INTEGRATED MICROSYSTEMS SERIES

Acoustic Wave and Electromechanical Resonators

CONCEPT TO KEY APPLICATIONS

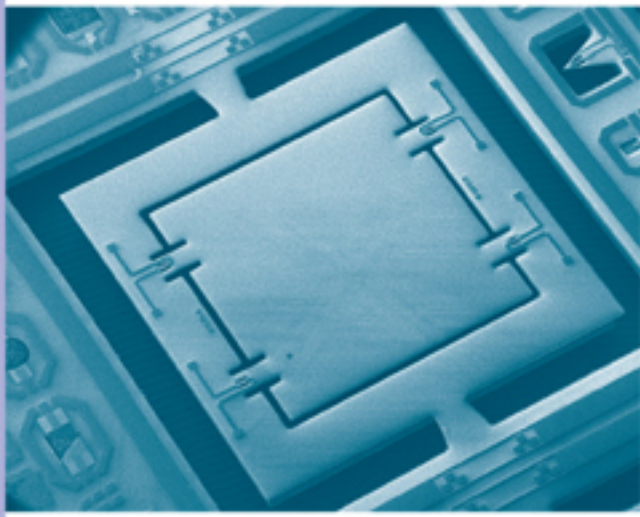

Humberto Campanella

Acoustic Wave and Electromechanical Resonators

Concept to Key Applications

For a listing of recent titles in the
Artech House Integrated Microsystems Series,
turn to the back of this book.

Acoustic Wave and Electromechanical Resonators

Concept to Key Applications

Humberto Campanella

ARTECH HOUSE
BOSTON | LONDON
artechhouse.com

Library of Congress Cataloging-in-Publication Data
A catalog record for this book is available from the U.S. Library of Congress.

British Library Cataloguing in Publication Data
A catalogue record for this book is available from the British Library.

ISBN-13: 978-1-60783-977-4

Cover design by Igor Valdman

685 Canton Street
Norwood, MA 02062

10 9 8 7 6 5 4 3 2 1

Aura matutinae: nivea et bianchissima
Alba del Mar, Aire, Río, Bosque . . .

Contents

Preface

Micro- and nanoresonators have become key components of virtually all modern radio frequency (RF) systems and sensors. As fabrication and packaging technologies have enabled high-production yield and high-performance devices, miniature resonators have left the laboratory to take up industrial applications. However, the complexity and huge variety of acoustic and electromechanical resonator technologies sometimes make it difficult to understand the mechanisms involved in their operation. Efficacy on decision making with regard to choosing the right technology for our application is thus often prevented. Also required is mastery of several disciplines, from applied physics and materials to manufacturing and system level applications.

How can we give an effective answer to these issues so as to benefit design, process, and application engineers? Keeping them in mind, this book provides comprehensive and wide coverage of thin-film bulk acoustic wave resonators (FBAR), microelectromechanical (MEMS), and nanoelectromechanical (NEMS) resonators, at both the technology and application levels. Hence, this work contributes to the field with a thorough and practical resonator description that gathers, for the first time, state-of-the-art design and modeling, fabrication and characterization techniques, integration with standard integrated circuit (IC) technologies, and industrial and laboratory applications. Moreover, practical case studies complement the theoretical and laboratory background.

The book assumes basic undergraduate-level preparation in physics, material science, electronics, chemical, mechanical, or electrical engineering. The intended audience includes the following:

1. Senior undergraduate or beginning graduate students involved in advanced education related to MEMS, RF systems, or sensors;
2. Process and design engineers, related to clean room and micro- and nanofabrication processes and modeling of MEMS devices;
3. MEMS, NEMS, and FBAR device researchers who are already familiar with the fundamentals of both MEMS and circuit design.

The contents of this book stem largely from academic and clean room experience. They follow what is to the author's view the logical sequence of FBAR, MEMS, and NEMS resonator production flow.

Chapter 1 is an introductory chapter to MEMS and NEMS resonator technologies. It covers the context and theoretical background of electromechanical devices. The discussion differentiates between MEMS and NEMS, their transduction mechanisms, and current fabrication technologies.

Chapter 2, on the other hand, specializes in bulk and surface acoustic wave resonators, like thin-film bulk acoustic wave resonator (FBAR), solidly mounted resonator (SMR), and surface acoustic wave resonator (SAW) technologies. As in the previous chapter, physical fundamentals of acoustic wave propagation, piezoelectricity, and applications are discussed.

Chapter 3 addresses the varied universe of resonator models by first defining a design flow and the role of modeling in the production of resonators. Electromechanical transformers, equivalent circuits, analytical models, and finite element models are covered.

Chapter 4 explains the fabrication and technological details of resonator fabrication by illustrating the case of FBAR manufacturing. Materials, processes, and structure characterization are described.

Chapter 5 deals with characterization. The contents provide the reader with concepts and experimental setup of electrical, atomic force microscope, and optical interferometry techniques.

Chapter 6 discusses performance optimization, thus dealing with frequency stability, temperature compensation, and frequency tuning. Detailed coverage of a novel focused-ion-beam-assisted technique for FBAR tuning is provided.

Chapter 7 deals with technological issues of FBAR, MEMS, NEMS resonator, and complementary metal oxide semiconductor (CMOS) technologies integration. As the MEMS-CMOS concept expands in current implementations, the subject is of central concern of process engineers and IC designers.

Chapter 8 reviews state-of-the-art sensor applications of FBAR, MEMS, and NEMS resonators. A balanced discussion of academic research and industrial products is preserved in the chapter.

Chapter 9 reviews classical passive and active RF applications. It revisits them under the light of the latest FBAR and MEMS resonator technologies, enabling the development of new architectures. Special attention is given to high-impact commercial RF microdevices and microsystems.

Chapter 10 closes the book by studying three implementation cases. Practical examples of FBAR fabrication, conceptual design of a temperature-compensated (TC) oscillator, and 434-MHz MEMS resonator read out circuit design are studied.

Acknowledgments

Writing a book cannot be accomplished without the support and encouragement of family, friends, and colleagues. Auto-motivation and faith also aid the author to foresee the "light at the end of the tunnel" with no significant loss of sanity and common sense.

First, I thank the Consejo Superior de Investigaciones Científicas (CSIC) and particularly the management and staff of the Instituto de Microelectrónica de Barcelona–Centro Nacional de Microelectrónica (IMB-CNM) for allowing me to undertake this project. I specially thank the clean room staffers for their support on fabrication and characterization. I have no words to express my gratitude to my former advisor and mentor at CSIC, Professor Jaume Esteve, from whom I have learned my best lessons. What I have learned from him will be transmitted through this book. I am indebted to present or former colleagues with which I have had the privilege to work on several MEMS and FBAR projects. I would like to thank Maria Calle and C. Golden for reading the manuscript and providing valuable feedback. I thank the anonymous reviewer for thorough revision of the manuscript. His or her suggestions contributed to significantly improve the quality of the contents. I would like to thank Dr. Zachary Davis and the intellectual property rights and permissions departments at the IEEE, IOP, NPG-Macmillan, Elsevier, ACS, AIP, SPIE, Sony, TriQuint, Epcos, iSupply—WTC, Avago Technologies, IBM, Agilent Technologies, Seiko EPSON, and Discera, for granting permissions to reproduce copyrighted figures. I gratefully acknowledge the active cooperation of the Artech House staff—particularly, Mark Walsh, senior acquisitions manager, for having paved the way to publish this book, and Penelope Comans, assistant editor, for her support throughout the manuscript development. Finally, I thank you, Alba, my beloved wife and companion, for designing and preparing high-quality artwork and, most important, for your unconditional patience and love.

CHAPTER 1

MEMS and NEMS Resonator Technologies

This introductory chapter addresses the fundamentals of micro- and nanoelectromechanical (MEMS and NEMS) resonators. Throughout this book, we employ the acronym MEMS to designate electron devices based on silicon. In the Section 1.1, MEMS and NEMS are defined and their main attributes described so we can identify their main differences from the beginning. Next, in the Section 1.2, a theoretical background on the physics behind the operating principles of MEMS and NEMS resonators is presented. The fundamental relationships of mechanical harmonic oscillators and transduction mechanisms are reviewed, thus supporting the discussion on the resonance modes and different resonator structures.

Second 1.2 deals with production and technological aspects of MEMS and NEMS resonator design and fabrication. Section 1.3, the production cycle of MEMS and NEMS shows the steps to develop and fabricate a resonator, from concept to application dimensioning. The section also describes the technologies currently employed in MEMS and NEMS fabrication. Two approaches are considered: the common to integrated circuit (IC), which is suitable for MEMS, and the nanofabrication-based techniques, more suitable for NEMS.

1.1 What Is MEMS and What Is NEMS?

Microelectromechanical systems (MEMS) are movable structures and systems with micrometer sizes. The concept also involves the related fabrication technology. Nowadays, it is generally accepted that MEMS have at least one of their dimensions in the range from hundreds of nanometers to hundreds of micrometers. Nanoelectromechanical systems (NEMS) have dimensions below the 100-nm conventional limit. Although some MEMS may also have submicron dimensions, a more determinant aspect differentiating MEMS and NEMS is their base technology. MEMS have been conceived under the integrated circuit (IC) paradigm, in which silicon is the base material for substrate, integration, and device fabrication. MEMS are fabricated according to the same fabrication techniques and processes of ICs, especially from complementary-metal-oxide-semiconductor (CMOS) technologies. Actually, MEMS and CMOS circuits can coexist for integrated applications. CMOS has become the predominant IC technology, whose potential is not only exploited for ICs but also for a variety of MEMS-based applications. Recently integrated microsystems featuring calibration by digital programming, self-testing, and

digital interfaces have been implemented on a single chip, demonstrating the strength of CMOS-based MEMS [1].

NEMS devices, on the other hand, are not scaled-down MEMS, but a quite different technological approach. Although it is widely implemented, silicon is no longer the main base technology of NEMS. New materials and structures like carbon nanotubes, nanowires, and organic composites are being investigated and implemented in many NEMS demonstrators [2–5]. Scaling down has been achieved by IC technology reduction, but mainly by introducing new fabrication tools, like electron beam lithography (EBL) [6], atomic force microscope [7], and nano-imprint [8], among others. The dominant physical phenomena are also different at the MEMS and NEMS scales, which imposes new engineering challenges. Due to technological development at both fabrication and material levels, new applications have appeared, many of them relying on NEMS devices. This integrated approach of NEMS technology and applications is known as the nano-bio-info-cognitive (NBIC) convergence. The schema of Figure 1.1 illustrates the different approaches of MEMS and NEMS technologies and the NBIC concept. Three different technologies can be differentiated: microelectronics, MEMS, and NEMS. The baseline material for both microelectronics and MEMS is silicon, and applications can be found in information technologies, neuroscience, biotechnology, cognitive science, and learning, among many others [9].

Materials, base technology, and applications of micro- and nanodevices are diverse and go beyond traditional fields of electronics after the conception of the NBIC convergence. Figure 1.2 shows how, before the NBIC, silicon is almost exclusively the material for fabricating microprocessors, digital signal processors (DSP), microcontrollers, analog devices, silicon MEMS, and integrated circuits in general (at left). After the NBIC, new materials and structures like polymers, organic composites, carbon nanotubes, or nanowires make part of specialized systems on the same chip. The situation has given rise to the bio-MEMS, lab-on-a-chip (LoC), micro total analysis systems (μTAS) and system-on-a-chip concepts (SoC) [10–12].

MEMS and NEMS play a central role on the miniaturization of electronic SoC, LoC, and μTAS. Information and communication technologies (ICT) have bene-

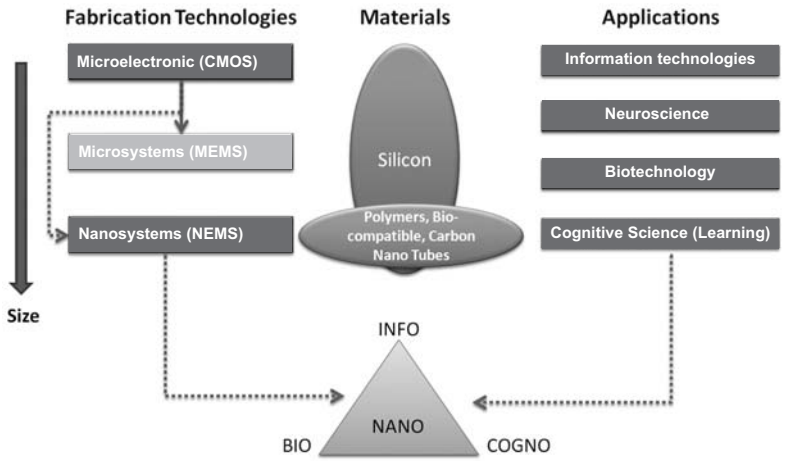

Figure 1.1 The NBIC convergence concept.

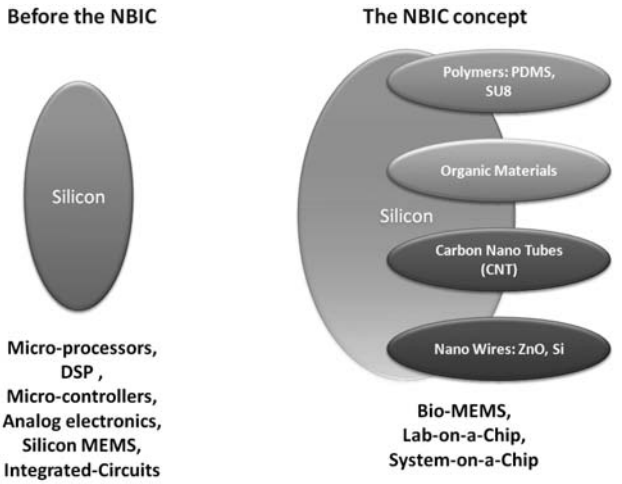

Figure 1.2 Impact of the NBIC on the materials and applications of technology.

fited from the MEMS and NEMS boom as well. Technological advances of micro- and nanoelectronic engineering fields have led to a drastic reduction of size and price in sensors and radio frequency (RF) components. New technologies have also enabled their integration into single microelectronic chips. Ultrahigh sensitivity, faster response times, and power and size efficiency are some of the benefits that have leveraged the implementation of MEMS in integrated sensor systems and modern mobile communication transceivers.

A detailed, comprehensive, and rigorous discussion on MEMS and NEMS history would take a complete book. If one has to elect the first MEMS device produced in history, it is the gold resonating MOS gate transistor invented by H. C. Nathanson at the Westinghouse Laboratories in 1967, which implemented the surface micromachining technique [13]. Thus, we see how the technological breakthroughs of microelectronics and micromachining techniques have allowed the evolution of MEMS and NEMS. Therefore, one can say that the MEMS era began with the pressure microsensor in the 1970s. It was followed by the actuator, microlenses and accelerometers in the 1980s; the RF devices, chemical sensors, micromirrors, antennas, and gears in the 1990s; and the medical applications, the LoC, μTAS, bio-MEMS, and NEMS devices developed in the following decade. This list shows a representative group of the major advancements of electronics, MEMS, and NEMS history [14]:

- 1947: Germanium transistor invention (Bell Labs: W. Shockley, J. Bardeen, W. Brattain);
- 1958: Silicon-made force sensor commercialization;
- 1958: First integrated circuit (Texas Instruments: J. Kilby);
- 1961: First silicon sensor (Kulite, *bare silicon strain gages*);
- 1967: Surface micromachining invention (Westinghouse: J. Nathanson, *resonant gate transistor*);
- 1967: Anisotropic silicon etching (R. M. Finne and D. L. Klein);

- 1970: First silicon accelerometer (Kulite);
- 1971: Microprocessor invention (Intel, *Intel 4004*);
- 1977: First capacitive pressure sensor (Stanford University: J. Angell);
- 1979: Micromachined inkjet nozzle for thermal printer (Hewlett-Packard Labs);
- 1980: Silicon torsional scanning mirror (K. E. Petersen);
- 1982: Blood pressure transducer (Foxboro/ICT, Honeywell);
- 1982: LIGA process (Karlsruhe Nuclear Research Center);
- 1986: Atomic force microscope invention (G. Binnig, IBM);
- 1988: Rotary electrostatic side drive motors (U. California Berkeley: Fan, Tai, and Muller);
- 1989: Lateral comb drive (U. Michigan: Tang, Nguyen, and Howe);
- 1990: BIACORE microfluidic chip;
- 1991: Polysilicon hinge (Pister, Judy, Burgett, Fearing);
- 1993: Multiuser MEMS processes-MUMPS program (Microelectronics Center North Carolina);
- 1993: First sold accelerometer (Analog Devices: ADXL50);
- 1994: Deep reactive ion etching patented (Bosch);
- 1996: First carbon nanotubes systematically produced (R. Smalley);
- 1999: Optical micro switch for the Internet (Lucent Technologies);
- 2000s: NEMS;
- 2001: First carbon nanotube transistors (IBM);
- 2005: First MEMS-based RF front end (Martina Consortium);
- 2007: First MEMS oscillator commercialized (Discera).

The MEMS market is very dynamic, and it has grown fast, especially during the past few years. To date, MEMS devices have broken many economical and conceptual barriers, enabling them to penetrate consumer segments of the market in a massive way. During the past five years, consumer electronics based on MEMS have passed from 6% to 22% of the global $25 billion MEMS market. The pie diagram of Figure 1.3 illustrates the situation. IT peripheral applications still dominate, although to a lesser extent, a segmented market in which automotive, medical, telecom, industry, aerospace and defense, household, and other applications complete the share [15]. MEMS are close to the big market of street consumer—and not only in the IT sense. This is evident in the explosion of sophisticated mobile devices and game consoles incorporating MEMS technology [16, 17].

This book concentrates on the study of a specific kind of the many MEMS and NEMS existing devices: resonators. A resonator can be defined as a frequency-selective amplifier, which, after appropriate excitation, goes into vibration. The resonance frequency is determined by physical properties of the materials composing the resonator, its layout, dimensions and mechanical configuration, and the excitation signal. MEMS and NEMS resonators have multiple applications as sensors and telecommunication system devices. Miniature mass, force, pressure, acceleration, torque, and flow detectors can be implemented with resonant MEMS and NEMS

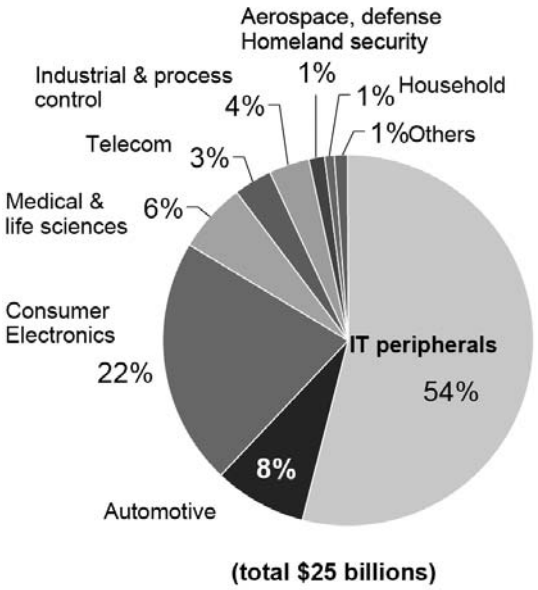

Figure 1.3 MEMS application fields in 2009: the global $25 billion market is dominated by IT and consumer electronics. (© 2009 Nexus [15].)

sensors. In the telecommunications field, resonators are utilized to build filters, oscillators, and mixers, for example. The quality factor (Q), which is studied in the next section, is the main parameter defining the performance of a resonator.

1.2 Physical Fundamentals of MEMS and NEMS Resonators

As a physical body, the structure of MEMS and NEMS resonators has an infinite number of eigenfrequencies, also referred to as eigenvalues. Under certain conditions, virtually any of them can be excited to drive the structure into resonance. Through the transduction mechanism exciting the MEMS or NEMS, electromechanical energy conversion causes the resonator to mechanically vibrate. Various approaches exist to implement MEMS/NEMS resonators: the micro- or nanomechanical and the acoustical. The approaches refer to the resonance modes excited, which lead to different vibration modes of the structure. In the micro- or nanomechanical modes, the structure vibrates at the fundamental modes, in general, and the resonator deflects, expands, or twists. Because the resonator deforms when excited at the corresponding frequencies, these are also known as structural modes. In the acoustical mode approach, deformation of the resonator is negligible, in comparison to its structural dimensions. An acoustic wave of the corresponding frequency propagates through the bulk, the surface, or both due to the excitation signal and the acoustic properties of the resonator. The mechanisms and physics behind acoustic resonators are studied in detail in Chapter 2. Let us review the physical fundamentals of resonance and transduction mechanisms in MEMS and NEMS resonators.

1.2.1 The Mechanical Damped Harmonic Oscillator

The resonant behavior of a MEMS or NEMS resonator can be described by the model of the mechanical damped harmonic oscillator:

$$m_{eff}^{n}\ddot{x} + D\dot{x} + k\dot{x} = F_{ext}(x,t) = F_0 \cdot \sin(2\pi ft) \tag{1.1}$$

where x is the time-varying harmonic oscillation, m_{eff}^{n} is the equivalent mass, D is the damping constant, k is the spring constant, F_{ext} is the external force applied to the resonator, and F_0 is the amplitude of the harmonic force signal with frequency f. The first term on the right side of (1.1) is the inertial force of the system, the second term is the damping and is related to the losses, and the third one is the restoring force. The eigenfrequencies of the oscillator are calculated by setting $F_0 = 0$ in (1.1), by only considering the mass and spring constants:

$$f_n = \frac{1}{2\pi}\sqrt{\frac{k}{m_{eff}^{n}}} \tag{1.2}$$

where f_n is the resonance frequency of the nth mode. By looking at (1.2), we can point out that the effective mass depends, of course, on the physical mass of the resonator, but also on its dimensions, geometry, and resonance mode, and then we can make some interesting remarks:

- Scaling down the dimensions of the resonator leads to a reduction of the absolute value of the effective mass. This increases the resonance frequency of the current mode.
- The effective mass is inversely proportional to the order of the resonance mode. Higher-order modes have less energy than fundamental ones.
- Scaling down from the MEMS to the NEMS regime leads to a reduction of the effective mass normalized to the physical mass. Thus, the vibration amplitude of NEMS resonators is smaller than it is for its MEMS counterpart.

In (1.1) the value of D determines the amount of damping in the system:

$$D = \frac{2\pi f_n m_{eff}^{n}}{Q} \tag{1.3}$$

where Q is the quality factor of the resonator. When operated in a fluid, like air or a liquid, the Q factor mainly depends on friction, and it is an important design parameter of the resonator applications. The energetic interpretation of the harmonic oscillator gives us a clear definition of the Q factor:

$$Q = 2\pi \cdot \frac{\text{max. energy stored in one period}}{\text{energy dissipated per period}} \tag{1.4}$$

According to the resonance frequency definition, the maximum energy is stored when the resonator vibrates at the frequency f_n. Due to losses, the oscillation energy is spread on a bandwidth B around f_n, which makes (1.4) equivalent to:

$$Q = \frac{f_n}{B} \tag{1.5}$$

B is defined between the –3-dB frequencies around f_n. The definition is illustrated in Figure 1.4, and it is widely used in tuned circuit and resonator characterization. Later in Chapter 5 we will return to practical aspects of the Q value characterization. Depending on whether the resonator vibrates in an elastic medium or in vacuum, the losses experimented are different. When the medium is air, for example, the Q factor is loaded by friction, anchoring, surface damping, and thermo-elastic damping, among other loss mechanisms. In good vacuum, the friction contribution to the Q factor can be neglected, and its value is higher than in liquid or gas. Because of this situation, the resonator characterization results have to specify the measurement conditions.

With the actual state of technology, it is not strange to reach Q factors between 10^3 and 10^5 with MEMS resonators. High Q values allow low power operation and high force sensitivity in sensor applications. Besides, high Q is equivalent to low dissipation, which translates into low insertion loss as well, which is very convenient for radio frequency (RF) applications. Nevertheless, the Q factor diminishes in a linear way with the resonator size [18]. The idea is illustrated in Figure 1.5, where the historical evolution of size reduction is compared against Q factor. A high Q factor implies a reduction in bandwidth, which is useful for the selectivity of sensors and filters. The situation relates also to the power handling of the resonator: the minimum power is defined at signal levels comparable to the thermal fluctuations of the system. The minimum power is estimated by dividing the thermal energy K_BT° over the energy-exchange time constant τ:

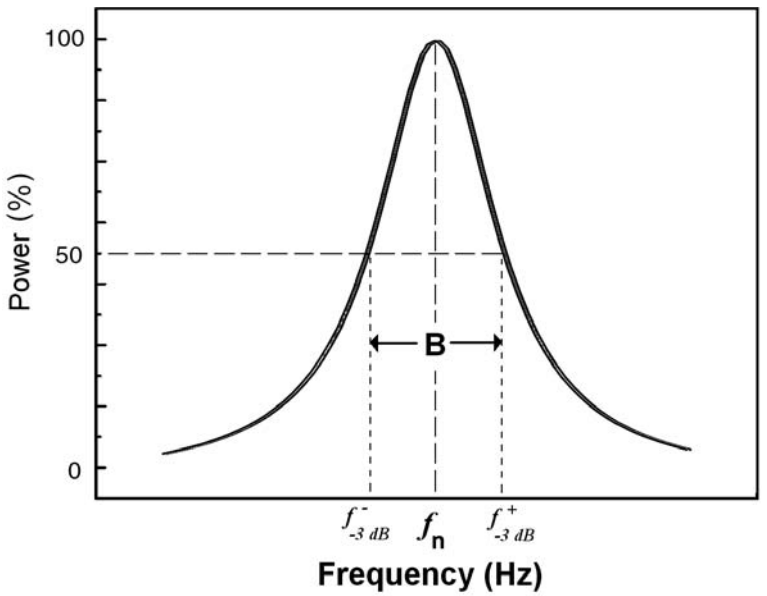

Figure 1.4 Quality factor of resonators: the oscillation energy is spread on a bandwidth B around the resonance frequency f_n. B is defined between the –3-dB frequencies around f_n.

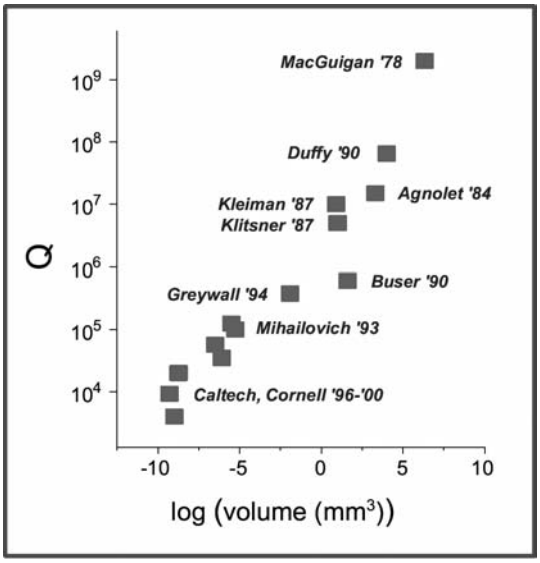

Figure 1.5 Quality factor and size of MEMS and NEMS resonators: the *Q* factor diminishes with dimensions. (© 2000 IEEE [18].)

$$P_{MIN} = \frac{K_B T^{\circ}}{\tau} \tag{1.6a}$$

$$= \frac{K_B T^{\circ} f_n}{Q} \tag{1.6b}$$

where τ is the quotient between Q and the resonance frequency f_n. For a given noise density of the environment, (1.6) means that a high-Q resonator will be able to reject more thermal noise power than low-Q devices, because noise integration is performed over a smaller bandwidth. This allows enhanced discrimination of the in-resonance signal and, equivalently, we can say that the high-Q resonator has bigger signal amplitudes than the low-Q resonator, for the same noise levels. Some characterization techniques are based on the thermal limit operation to extract some resonator parameters [19].

1.2.2 Quality Factor and Damping Mechanisms

In the previous section, we have defined the damping D and quality factor Q under the light of the damped harmonic oscillator model. Now, we examine the physical damping mechanisms inherent to MEMS and NEMS resonator operation.

First, we say that the overall Q factor of the resonator (Q_{TOTAL}) relays on diverse mechanisms, namely:

1. Air damping ($1/Q_{AIR}$);
2. Support damping ($1/Q_{SUPPORT}$);
3. Surface-effect damping ($1/Q_{SURFACE}$);
4. Thermoelastic damping ($1/Q_{THERMOELASTIC}$).

Depending on the resonator design and the operation environment, these mechanisms contribute to a lesser or large extent to the Q_{TOTAL} value. Q_{TOTAL} is calculated as the sum of the inverse Q factors attributed to each mechanism:

$$\frac{1}{Q_{TOTAL}} = \frac{1}{Q_{AIR}} + \frac{1}{Q_{SUPPORT}} + \frac{1}{Q_{SURFACE}} + \frac{1}{Q_{THERMOELASTIC}} \tag{1.7}$$

Air damping relates to the energy released by the resonator when it collides with the air surrounding the device at its vibrational state. At its time, three mechanisms contribute to air damping: viscous or Stoke's damping [20], acoustic radiation [21], and squeezed-film damping [22], the value of Q_{AIR} being given by:

$$\frac{1}{Q_{AIR}} = + \frac{1}{Q_{Stroke}} + \frac{1}{Q_{Squeezed}} + \frac{1}{Q_{Acoustic}} \tag{1.8}$$

Viscous damping, or viscous drag, removes the fluid around the resonator, whereas acoustic radiation occurs when the resonator excites the air in the direction perpendicular to the device motion. The energy loss parallel to the direction of motion is described by the Stoke's damping:

$$Q_{Stroke} = \frac{m_{eff}}{A}\sqrt{\frac{2\pi f_0}{2\rho\eta_{atm}}} \tag{1.9}$$

where m_{eff} is the effective mass, A is the area of the bottom and top surfaces, and f_0 is the resonance frequency of the resonator; η_{atm} is the viscosity at atmospheric pressure; and ρ is the air density depending on the air's molar mass, gas constant, and operating temperature. For example, in parallel-plate resonators with capacitive transduction, the fluid is pushed out of the gap: the air motion parallel to the plates produces Couette damping, while the motion perpendicular to the plate surfaces generates squeezed-film damping:

$$Q_{Squeezed} = \frac{\pi^5 h_0 m_{eff} f_0}{48\eta L_{eff} W_{eff}^3} \tag{1.10}$$

where h_0 and η are the air gap thickness and viscosity at the operating point, and L_{eff} and W_{eff} are the effective length and width of the air gap [23]. Squeezed-film damping is the dominant loss mechanism of electrostatically driven MEMS and NEMS resonators [23]. Nevertheless, the shape of the resonator determines the ultimate environmental conditions of the dominant mechanism. Vignola et al. found out that, at a pressure greater than 10^{-2} Torr, acoustic radiation dominates for their MEMS paddle resonators, while for a diamond-shaped oscillator, 10^{-3} Torr is the low-pressure condition when radiation damping is dominant [24]. More details on the analytical description of air damping can be found in [25].

Support damping, also known as anchor losses, results when the resonator anchors are stressed at the clamping points as a consequence of resonator displacement during vibration. Thus, a fraction of the vibrational energy is lost from the res-

onator through elastic wave propagation into the substrate. All the elastic energy transferred to the substrate is lost, although the mechanisms are only partially understood. Anchor losses can be significant if contributions from other loss mechanisms are negligible, and they degrade the Q factor and may introduce coupled-to-clamping spurious resonances.

Analytical expressions for anchoring losses derived by Judge et al. distinguish between two cases: supports that can be treated as plates, and supports that act as semi-infinite elastic media, with effectively infinite thickness. The former case is applicable to many MEMS resonators, while the latter is more appropriate for NEMS devices [26]. However, since the losses depend on the clamping design of the resonator, no general expression exists for calculating the $Q_{SUPPORT}$ value. Instead, it should be inferred from experiments, after de-embedding the contributions of air, surface, and thermoelastic damping.

To face the support damping, the designer balances the MEMS structure to compensate for the losses at the resonance frequency. The tuning fork is perhaps one of the most popular and studied MEMS structures, largely implemented in oscillator and filter applications [27]. More recently, other innovative structures have been explored as well, like the mesa-dome resonator proposed by Pandey et al. In this design, the resonator is surrounded by a trench, or mesa, that partially reflects wave energy back to the resonator. Depending on the distance from the resonator to the mesa, the reflected wave interferes either constructively or destructively with the resonator, increasing or decreasing the Q factor. Due to the constructive-interference anchor decoupling, Q factor improvements of up to 400% are achieved [28].

Surface-effect damping induced at the surface of the resonator increases as the surface to volume ratio increases. This is the case of devices approaching the NEMS scale. Roughness, contaminants, and etching residues contribute to damping and Q factor reduction [29]. Surface losses include structural dissipation (crystallographic defects) and surface effects, which are more significant when the dimensions of the resonator approach to those of the surface roughness and crystallographic defects.

Thermoelastic damping is an intrinsic-material damping source due to thermoelasticity present in most materials, and it is caused by irreversible heat flow across the thickness of the resonator. As its name suggests, it describes the coupling between the elastic field in the structure caused by deformation and the temperature field. TED is the dominant loss mechanism in MEMS resonators in thicker and long cantilevers. TED losses become less relevant when the thickness is reduced, anchoring and surface losses being the ultimate loss mechanisms limiting the Q factor at low pressure.

The earliest study of thermoelastic damping is dated back to 1937 in Zener's classical work [30, 31], in which he studied thermoelastic damping in beams undergoing flexural vibrations. Although the design of the resonator influences the $Q_{THERMOELASTIC}$ contribution to the global factor Q_{TOTAL}, other strategies like torsional-mode operation have proven to be effective on reducing the thermoelastic losses. For a reference on MEMS resonator design with low thermoelastic damping, refer to the work of Duwel et al. [32].

1.2.3 Transduction in MEMS and NEMS Resonators

Transduction in MEMS and NEMS resonators occurs through a variety of mechanisms involving the physical domain conversion of the input signal. Such mechanisms and the physical response of the resonator generate an output signal after the excitation. According to this idea, the resonator is both a sensor and an actuator, whose working principle is illustrated in Figure 1.6. The excitation signal causes the mechanical structure of the resonator to vibrate, if this signal is of a frequency close to one of the eigenvalues of the structure. An external component or circuit detects the resonance in the electrical domain, through an electric current or voltage proportional to the vibration amplitude. Then, a feedback electronic circuit processes and delivers the output current to a digital signal processor (DSP) to figure out the resonance frequency value f_0.

Often, "resonant" is considered a detection-actuation mechanism because the information of the transduction process is directly related to the frequency response of the resonator. As we will study later, in sensor applications the resonator vibrates at a resonance frequency f_0 that is proportional to the magnitude of the physical signal sensed by the resonator. This is the operation principle of resonant mass detectors, inertial force sensors, and many other applications we review in Chapter 8.

The resonant principle for sensor applications has many advantages, if we compare it with other mechanisms. Perhaps, high sensitivity and resolution, low noise, and frequency-domain output are the most attractive. It has been demonstrated that the absolute sensitivity is directly proportional to the working frequency of the sensor. Also, the low-frequency noise sources become less significant when operating the resonator at higher frequencies. If the Q factor is high, then the resonator is a quasi-binary device whose response to the excitation signal is highly selective. Nevertheless, resonators suffer from high temperature sensitivity, which cause thermal drifting that can degrade its frequency response. In such cases, a thermal-compensation mechanism is required to overcome the fluctuations of the resonance frequency. Another aspect to be considered is that, due to its resonating operation, resonators present high strain sensitivity and mechanical fragility. The situation imposes the need of hermetic packaging able to absorb shocks and external vibrations.

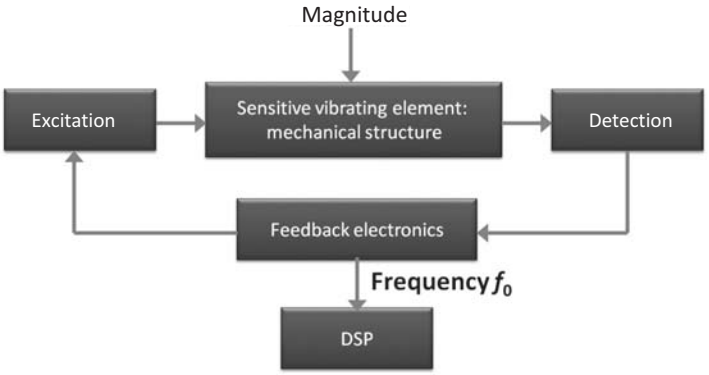

Figure 1.6 Working principle of a resonator.

There exists a variety of physical principles currently exploited in MEMS and NEMS resonators operation. Some of them are usually combined to offer a complete transduction system. The list in Table 1.1 shows just some of the possibilities, along with their advantages and drawbacks. Of course, other combinations are also possible, depending on the system and the size of the resonator.

Piezoelectric resonators are used as sensors, actuators, or both. An electric potential applied to the piezoelectric material of the resonator produces a mechanical strain and the resonator bends. Alternatively, a mechanical stress applied to the piezoelectric material induces an electric charge on the resonator surface proportional to the mechanical force. Piezoelectric crystals used in the fabrication of MEMS resonators include lead-zirconium-titanate (PZT), zinc oxide (ZnO), and aluminum nitride (AlN), among others. Most acoustic resonator technologies involve the piezoelectric effect, which is discussed in detail in Chapter 2.

Electrostatic actuation of a MEMS cantilever with capacitive detection of the resonance frequency is illustrated in the drawing of Figure 1.7. The cantilever is driven into resonance when an AC electric signal of the appropriate frequency is applied to one electrode—namely, the *driver* electrode. The cantilever is biased with a DC voltage to induce the electrostatic charge of the structure at the parallel-capacitance system formed by the driver and the cantilever. At the other side, a read-out electrode collects the capacitive-transduced current i_0. The system is modeled as a two-port configuration, because two independent ports are used for the driver and read-out electrodes. In a simpler model, the same electrode is employed for driving the cantilever and reading out the transduced current.

The variable capacitance formed between the cantilever and the electrodes can be described by the parallel-plate capacitor model $C(x)$:

$$C(x,t) = \frac{\varepsilon A}{\left(d_0 - x(t)\right)} \tag{1.11}$$

where A is the parallel-plate area formed between the faced surfaces of cantilever and electrode, d_0 is the rest distance between the plates, and $x(t)$ is the time-varying separation induced by the actuation. The voltage V applied to the driver and cantilever causes an electrostatic force F_E acting on the cantilever, related to the electric work W_E:

Table 1.1 Transduction Mechanisms in MEMS and NEMS Resonators

Excitation	*Detection*	*Advantage (+)*	*Drawback (–)*
Piezoelectric	Piezoelectric	Large dynamic range; acoustical isolation technologies available	Needs IC-compatibility development
Electrostatic	Capacitive	Surface micromachining	Complex process if only bulk micromachining is available
Electrothermal	Piezoresistive	Effective and simple; bulk micromachining available	Heat generation power; bandwidth
Optothermal	Optical	Electrical isolation; immunity to most electromagnetic noise	Hard to integrate
Magnetic	Magnetic	Effective and simple; variety of excitation mechanisms	Magnetic materials or magnets required; magnetic fields in the system

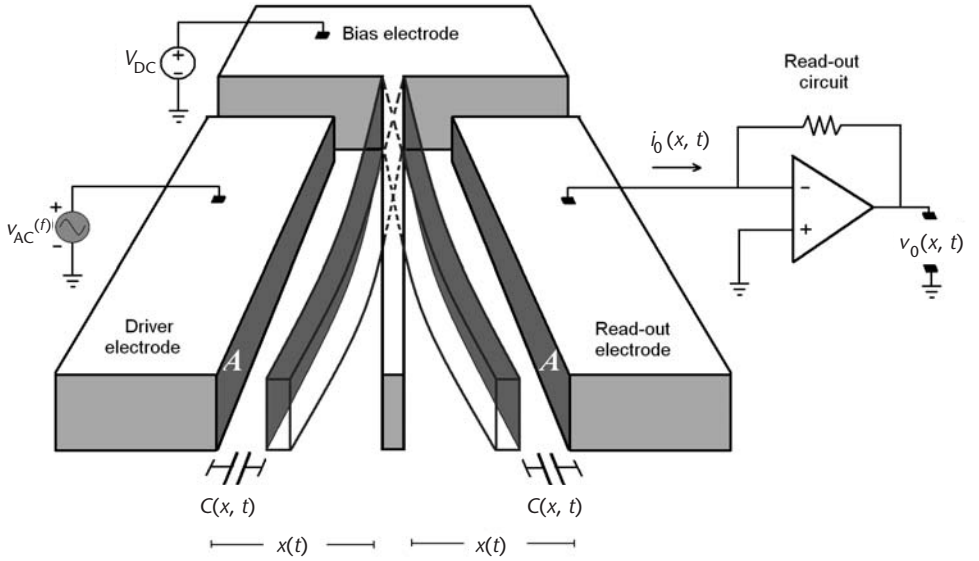

Figure 1.7 Electrostatic actuation of a cantilever resonator and capacitive detection of the resonance: AC voltage is applied to the driver electrode, which generates the electrostatic force acting on the cantilever. The resonance is detected by the read-out electrode in the form of a collected AC current. The cantilever is biased to maximize the amplitude of the current.

$$F_E(x) = \frac{\partial W_E}{\partial x} = \frac{\partial}{\partial x}\left(\frac{1}{2}CV^2\right) = \frac{1}{2}\frac{\varepsilon A V^2}{(d_0 - x)^2} \tag{1.12}$$

V accounts for both the driving and biasing voltages v_{AC} and V_{DC}, and C includes both the static capacitance C_0 and $C(x, t)$. The relationship between F_E, v_{AC}, and V_{DC} is defined through the change of $C(x)$:

$$F_E(x) = V_{DC}\frac{\partial C(x)}{\partial x}v_{AC} \tag{1.13}$$

According to the displacement current definition of capacitors, the electric current at the read-out electrode $i_0(t)$ is expressed as:

$$i_0(t) = \frac{\partial}{\partial t}\left(C(x,t)\cdot V\right) \tag{1.14}$$

The current $i_0(t)$ is calculated as:

$$i_0(t) = \left(C_o + C(x)\right)\frac{\partial v_{AC}}{\partial t} + \left(V_{DC} + v_{AC}\right)\frac{\partial C(t)}{\partial t} \tag{1.15}$$

Since $C(x)$ and v_{AC} are small in comparison to C_0 and V_{DC}, respectively, (1.15) can be approximated to:

$$i_0(t) \approx C_o \frac{\partial v_{AC}}{\partial t} + V_{DC} \frac{\partial C(t)}{\partial t} \tag{1.16}$$

In (1.16) the second term at the right side is dominant, so this equation could be further simplified if needed. Note that the restoring force of the cantilever F_X opposes to F_E. Along with the dimensions and geometry, it imposes the mechanical conditions for the resonance frequency. The images of Figure 1.8 show a cantilever placed between the two electrodes, when it resonates at the fundamental and second flexural modes (upper and lower images, respectively). Considering the previous analysis, one can conclude that the magnitude of the collected current at the read-out electrode will be higher when the resonator and electrode gap is reduced, their faced surfaces increased, and the biasing voltage augmented. Such parameters need careful design to avoid sticking, collapsing, or saturation of the resonator.

Magnetic transduction of MEMS devices can be implemented through different physical mechanisms. The main are electromagnetic induction [33], Lorentz force [34], and ferromagnetic attraction. Specifically, resonant magnetic transducers vibrate when they are in the presence of a time-varying magnetic field with oscillation frequency equal to one of the natural frequencies of the MEMS.

The Lorentz force explains the motional force acting on a conductor on a point charge due to electromagnetic fields, which is done in terms of electric and magnetic fields by:

$$F = q(E + v \times B) \tag{1.17}$$

where F is the force, E is the electric field, B is the magnetic field, q is the electric charge of the particle, v is the instantaneous velocity of the particle, and $\times$ is the vector cross product. According to the Lorentz force mechanism, the MEMS resonator will be accelerated and orientated in the same axis of the E field, with perpendicular

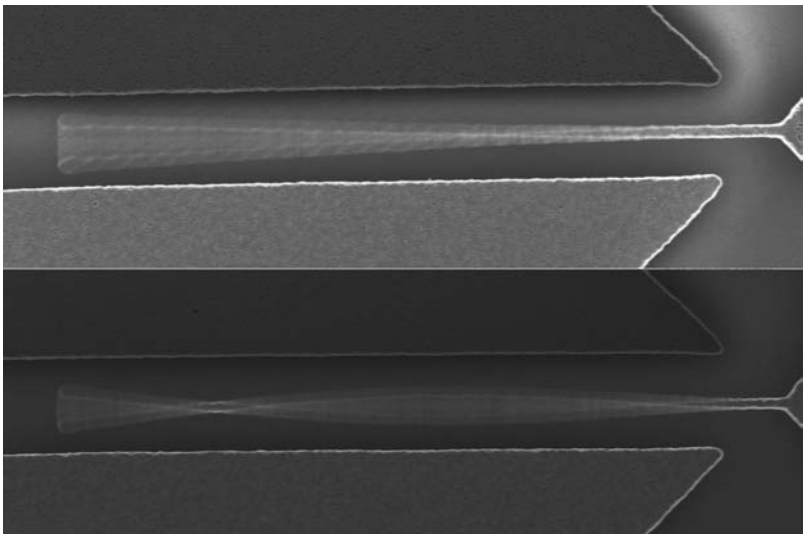

Figure 1.8 Cantilever resonator electrostatically actuated: the first and second flexural modes are observed in the scanning electron microscope (SEM) image. (Image courtesy of Dr. Zachary J. Davis, DTU Nanotech, Copenhagen, Denmark.)

and instantaneous variations following the instantaneous velocity vector v and the B field according to the right-hand rule. The term qE is called the electric force, while the term $qv \times B$ is the magnetic force. Some definitions simplify the term "Lorentz force," referring specifically to the magnetic force component:

$$F = q(v \times B) \tag{1.18}$$

The magnetic force component of the Lorentz force manifests itself as the force that acts on a current-carrying wire in a magnetic field. This is the principle used in the design of Lorentz force–driven MEMS magnetic transducers. When magnetomotive excitation is employed, the MEMS structure is covered by a metallic layer and placed in the magnetic field, where an electric current is guided through the metal conductor. This induces the Lorentz force used to drive the MEMS into resonance. Alternatively, the MEMS can detect the presence of a magnetic field. Current flowing through the conductive loop of the resonator aligns with the magnetic field. The MEMS is driven into resonance to maximize the sensitivity.

In ferromagnetic-based transducers, the MEMS resonator incorporates a soft magnetic material or a hard magnet, as depicted in Figure 1.9. The resonance frequency of the MEMS shifts due to the strain added to its structure when the external magnetic field and magnetic component of the resonator interact. The magnitude of the frequency shifting is used to determine the amplitude or the direction of the external magnetic field.

Referring to (1.1), the external force F_{ext} is the ferromagnetic attraction force F_M:

$$F_M = \nabla(\vec{m} \cdot B) \tag{1.19}$$

where $\vec{m}$ is the magnetic moment and B is the time-varying magnetic field. If a permanent magnet is attached to the resonator, (1.19) can be rewritten as:

$$F_M = \vec{m} \cdot \nabla B \tag{1.20}$$

$$F_M = \vec{m} \cdot \frac{\partial B(x,t)}{\partial x} \tag{1.21}$$

Thus, the time-varying ferromagnetic force attraction between the external field source and the MEMS depends on the variations of the magnetic field with both dis-

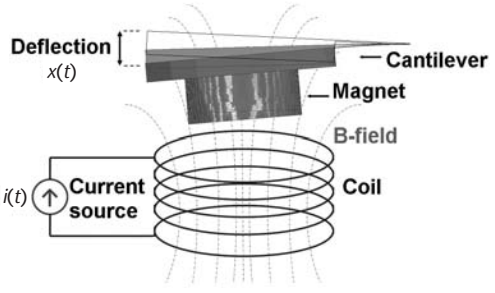

Figure 1.9 Ferromagnetic actuation of a MEMS cantilever.

tance and time. As in the case of electrostatic transduction, the restoring force of the MEMS F_X given by Hooke's law:

$$F_X = -k \cdot x \tag{1.22}$$

opposes to the resonator deflection caused by F_M in order to balance the system:

$$F_X = -F_M \tag{1.23}$$

The spring constant k of the MEMS/NEMS resonator, along with its dimensions and geometry, imposes the mechanical conditions leading the structure to resonate at a certain frequency. Figure 1.10 shows a quad-beam MEMS resonator with a NdFeB permanent magnet attached to it. The structure resonates at a frequency of 270 Hz when an AC current induces the external magnetic field. A coil placed underneath the resonator generates the current. The detection of resonance is carried out by optical systems (the resonance curve is shown in the inset).

Electrothermal actuation implements a heating resistor located on a movable MEMS/NEMS structure. The heater dissipates the power of an electric signal flowing through it. The dissipated power is converted into heat and the MEMS experiments thermal expansion or contraction according to its mechanical configuration, temperature, and environmental conditions. Since the thermal signal follows the voltage waveform, the MEMS can be driven into resonance if the electric signal is chosen to be of a frequency corresponding to one of the MEMS eigenvalues. The driving moment of the MEMS is proportional to the power dissipation P in the heater:

$$P = \frac{V^2}{R} \tag{1.24}$$

where V is the voltage signal and R is the resistance of the heater, and the voltage-dependent component of P is:

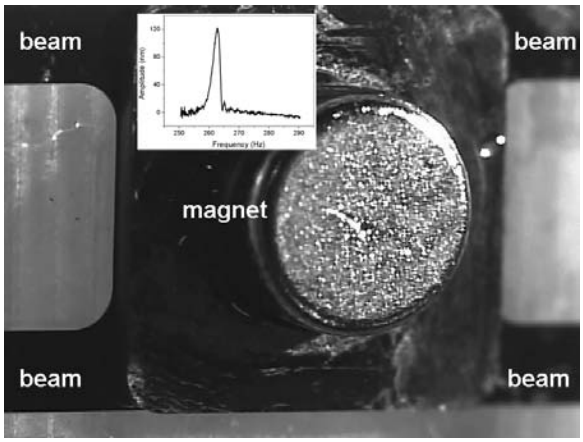

Figure 1.10 Magnetic transducer implemented with MEMS resonator and permanent magnet attached to it (resonance curve in the inset).

$$V^2 = \left(V_{DC} + v_{AC} \sin 2\pi ft\right)^2 \tag{1.25}$$

$$= \left(V_{DC}^2 + \frac{v_{AC}}{2}\right) + 2 \cdot V_{DC} \cdot v_{AC} \cdot \sin 2\pi ft - v_{AC}^2 \cos 4\pi ft \tag{1.26}$$

In (1.26) V_{DC} and v_{AC} are the DC and AC voltage components of V, respectively, and f is the frequency. If this excitation signal frequency f equals one of the natural frequencies of the MEMS f_0, it resonates. The second term in (1.26) shows that the dissipated power on the resistor depends on both the DC and AC signal amplitudes and their frequencies. The situation will drive the MEMS with more or less vibration energy.

The detection of resonance can be performed by using implanted piezoresistors of resistance R_P, and taking advantage of their piezoresistive behavior:

$$\Delta R \propto \frac{1}{2} \prod \cdot \sigma \tag{1.27}$$

where ΔR is the change of the resistance value due to deformation of the piezoresistor, Π is its piezoresistive coefficient, and σ is the stress in the MEMS structure caused by the heating-induced deformation. In silicon MEMS, the heaters and the piezoresistors are implanted in the substrate by ion implantation techniques currently employed in standard IC processes. The implantation can be made of boron, phosphorus, or a suitable material according to the available process and the designed resistivity values. In sensor applications, the resistors are placed at a stress-sensitive point of the MEMS, as illustrated in Figure 1.11. The piezoresistors are usually arranged in a Wheatstone bridge configuration to balance the output voltage signal v_{OUT}, given that the bridge is biased with the DC voltage V_{BIAS}. In the example, the MEMS device is a beam, although cantilevers or membranes are also often implemented. At resonance, v_{OUT} is the time-varying signal of frequency f_0 expressed by:

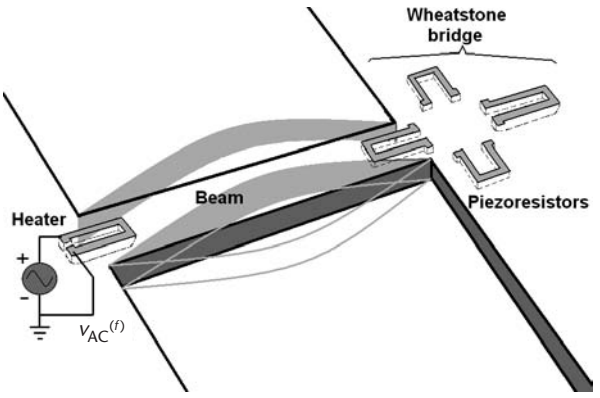

Figure 1.11 Electrothermal actuation with piezoresistive detection: the heater induces time-varying power dissipation on the beam, which resonates if the driving voltage corresponds to the beam's natural frequency. The piezoresistors detect the resonance, converting the mechanical signal into the electrical domain by a Wheatstone bridge.

$$v_{OUT}(t) = \frac{\Delta R(t)}{R_P} V_{BIAS} \tag{1.28}$$

Many other transduction mechanisms can induce resonance of MEMS and NEMS devices, too, like piezoelectric excitation and detection, which will be discussed in detail in Chapter 2. Most of them are suitable for both MEMS and NEMS. However, not all can be scaled down to the NEMS dimensions (e.g., optical detection of resonance of NEMS with dimensions less than the spot diameter of lasers in AFM systems or other microscopy systems). On the other hand, NEMS resonators are sensitive to electrostatic and magnetic actuations, among other mechanisms [35, 36]. When placed in the middle of electron-beam fields, the resonance can be induced due to electrostatic mechanisms [37]. The gallium nitride (GaN) shown in the TEM image of Figure 1.12 resonates due to the electrostatic excitation of a probe approaching to the nanowire and carrying the oscillating signal, while the nanowire substrate, TEM stage, and signal generator are grounded to the same voltage reference [38]. In the end, the suitability of transduction depends on the structure and excited mode of the resonator, as we will study next.

1.2.4 Resonance Frequency, Mode Shaping, and Aspect Ratio

There are no restrictions to design the structure of MEMS resonators. Nevertheless, they are usually designed with certain geometries that have demonstrated their efficiency: clamped-clamped beams, cantilevers, disks, rings, squares, membranes, combs, and triple and multiple beams, for example. NEMS resonators typically have the form of clamped-clamped beams, cantilevers, nanotubes, or nanowires, among others. Each one of them has its own process and performance characteristics.

Rigidity, intrinsic and design-related stress, and the layout and structural material of the resonator make the actuation more efficient at certain resonance modes. The mode shaping strongly links with the preferred mechanical configuration and aspect ratio of the device, provided it is driven with a signal of the corresponding

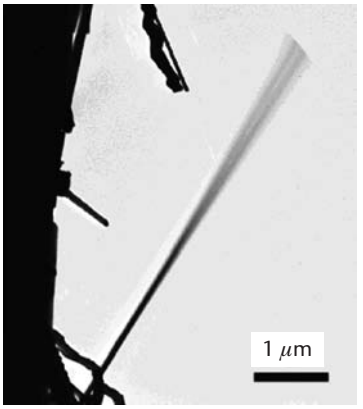

Figure 1.12 Gallium nitride (GaN) nanowire resonating at 2.2 MHz due to electrostatic excitation mechanisms: the nanowire is excited with an oscillating signal provided by a probe approaching to it, while the nanowire's substrate is grounded to the voltage reference of the system. (© 2006 American Chemical Society [38].)

frequency. Thus, long beams and cantilevers resonate at flexural, torsional, or extensional modes with good electromechanical conversion [39, 40]. By changing the aspect ratio of dimensions, bulk acoustic modes can be promoted in beams as well [41]. Disk resonators, on the other hand, exhibit good electromechanical performance at their fundamental radial and wine-glass modes [42, 43]. The natural modes of square and ring resonators also have preferred radial resonances [44, 45]. Long beams can resonate at higher-order radial modes, but the electromechanical conversion efficiency will be low at those modes. The schematics and pictures of Figure 1.13 show various examples of MEMS resonators and the mode shaping of their resonance modes.

The generic model of the harmonic oscillator described by (1.1) and (1.2) is adapted to each resonator design, according to its mechanical particularities and the

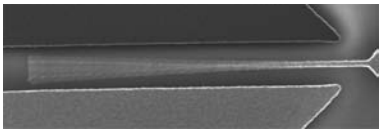

(a)

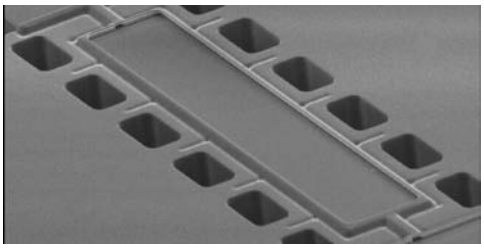

(b)

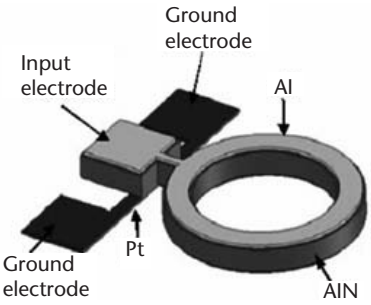

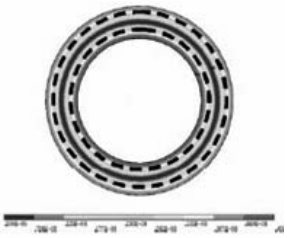

(c)

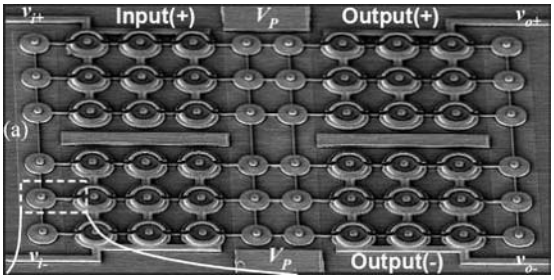

(d)

(e)

Figure 1.13 MEMS resonators and their resonance-mode shaping: (a) flexural (cantilever) (courtesy of: Zachary J. Davis, DTU Nanotech, Copenhagen, Denmark); (b) bulk (beam) (© 2007 IEEE [41]); (c) radial (ring) (© 2005 IEEE [45]); (d) radial (disk) (© 2007 IEEE [42]); and (e) wine-glass (disk) (© 2005 IEEE [43]).

Euler-Bernoulli equation. For example, the formulation of the resonance frequency of flexural-mode beams, equivalent to (1.2), is:

$$f_n = \frac{1}{2\pi}\left(\frac{\gamma_n}{L}\right)^2 \sqrt{\frac{E \cdot I \cdot L}{m}} \tag{1.29}$$

where E is the Young's module, I is the inertia moment, L is the length of the beam, m is the mass, and γ_n is a dimensionless parameter. Its value is numerically calculated for the nth mode and defined by the components of the Euler-Bernoulli equation leading to (1.29). Whether the beam is clamped at both sides or only by one of its ends—a cantilever—the values of γ_n are different for a given resonance mode (n). Similarly, the cross-section area and the vibration plane of the resonance define the value of I. If the oscillation is in the vertical plane, and the beam is a cantilever with rectangular section of width w and thickness t, the inertia moment is:

$$I_{vert}^{rect} = \frac{w \cdot t^3}{12} \tag{1.30}$$

Replacing (1.30) in (1.29), the spring constant k of (1.2) can be rewritten as

$$k = \frac{E \cdot w \cdot t^3}{4L^3} \tag{1.31}$$

And the effective mass nth mode of the cantilever is

$$m_{eff}^n = \left(\frac{3}{\gamma_n^4}\right)m \tag{1.32}$$

The first three-mode values of γ_n calculated for a cantilever are $\gamma_1 = 1.875$, $\gamma_2 = 4.694$, and $\gamma_3 = 7.854$. Now we ask ourselves: can this analysis be extendable to clamped-clamped (c-c) beams or to other MEMS or NEMS resonator geometries? The answer is yes. However, because of their different boundary conditions, c-c beams and cantilevers have different inertia moments, spring constants, and effective masses. For the rectangular-section c-c beam, k and m_{eff}^n are, respectively:

$$k = \frac{16 \cdot E \cdot w \cdot t^3}{L^3} \tag{1.33}$$

$$m_{eff}^n = \left(\frac{192}{\gamma_n^4}\right)m \tag{1.34}$$

Finally, the first three-mode values of γ_n calculated for the c-c beam are $\gamma_1 = 2.365$, $\gamma_2 = 3.927$, and $\gamma_3 = 5.498$. These examples have shown us how the resonance frequency and model constants of the resonator change by applying different boundary conditions. According to (1.31) to (1.34), we see that, for a given resonance mode, the cantilever is more flexible, has a bigger effective mass, and resonates at a lower frequency, if we compare it with the c-c beam.

By using the previous equations, Table 1.2 shows calculated values of the flexural-mode resonance frequencies of c-c beam and cantilever of resonators of different dimensions. We assume silicon-made beams with $E = 160$ GPa and $\rho = 2{,}330$ kg/m^3, and we corroborate that the higher rigidity of the c-c beam makes it resonate at higher frequencies. The calculations also demonstrate that by reducing the dimensions of the cantilevers and the beams from the MEMS to the NEMS scale, it is possible to reach fundamental frequencies in the range of gigahertz. With these dimensions, not only are higher resonance frequencies achieved, but also the force constants are kept at small values. These attributes make NEMS resonators highly sensitive in force-detection applications with ultralow power operation, as we study in Chapter 8.

From the previous analysis and observing Table 1.2, it seems logical to be interested in scaling down the size of MEMS to enter the NEMS regime. However, several difficulties arise if MEMS technologies are scaled from micrometers to nanometers. High resonance frequencies can only be achieved if the aspect ratio of the resonator is close to unity ($L/w \sim 1$, $L/t \sim 1$). This implies very high force constants, thus requiring high power levels of the excitation signal to obtain an appreciable mechanical response. Therefore, if the force constants are high, the low-power feature is diluted, and then the minimum power, the dynamic range, the tuning capability, and the Q factor performances are negatively affected. Besides, the same fabrication technology is employed to go down from the MEMS to the NEMS scale. As we study in Section 1.4, the planar IC-like approach for fabricating MEMS requires that thickness is the same for big surface or small surface devices. Thus, it is impossible to perform scaling down in three dimensions, but just on the lateral (width and length) axes. The images and resonance curves of Figure 1.14(a–d) show four resonators made of silicon carbide (SiC) within the same process and scaled down in its lateral dimensions. The 70-nm thickness is the same in all resonators. We can see how the aspect ratio changes, and, as we reduce the dimensions, the resonance frequency increases. However, the vibration amplitude diminishes, thus reducing the Q factor. From the figures, it is also noticeable that the Q factor reduction causes the in-resonance signal to approach the noise levels. Similar analysis can be done for the more complex geometries commented earlier, in order to synthesize their spring-mass constants and design equations (see [46]).

The previous ideas illustrate the reasons for investigating and implementing nanofabrication techniques to fabricate NEMS devices, rather than current IC-based processes, widely used in MEMS fabrication. This matter and the production cycle of MEMS and NEMS resonators are studied in the next sections.

Table 1.2 Flexural-Mode Resonance Frequencies of Si Cantilever and c-c Beam Resonators (Three Dimensions Are Compared)

Boundary condition	*Dimensions ($L \times w \times t$)*		
	10 mm × 200 nm × 100 nm	*1 mm × 50 nm × 50 nm*	*100 nm × 10 nm × 10 nm*
Clamped-clamped beam	2.13 MHz	106 MHz	2.13 GHz
Cantilever	1.34 MHz	66.9 MHz	1.34 GHz

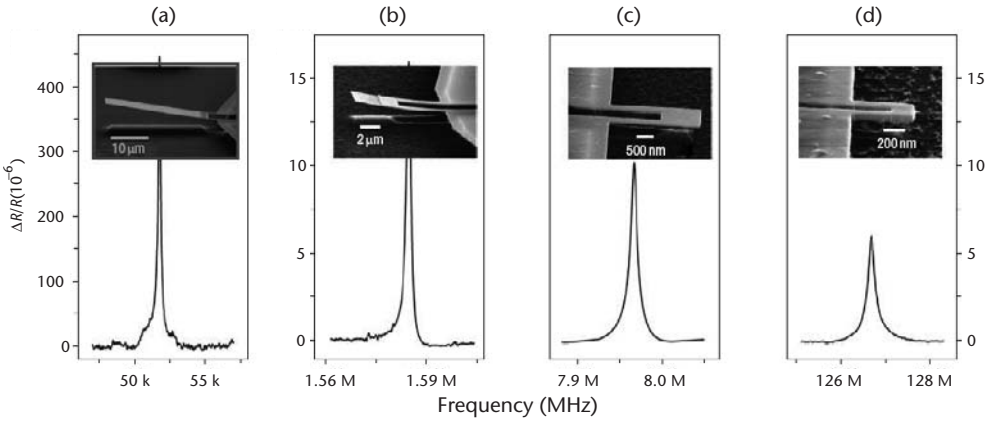

Figure 1.14 The aspect ratio of fabricated MEMS and NEMS resonators: the four resonators in the SEM images have a thickness of 70 nm and lateral dimensions of: (a) 33 μm $\times$ 5 μm; (b) 10 μm $\times$ 2 μm; (c) 2.5 μm $\times$ 0.8 μm; and (d) 0.6 μm $\times$ 0.4 μm. (© 2007 Nature Publishing Group [47].)

1.3 Key Fabrication Technologies

The resonator fabrication technologies are the same as those used in other MEMS and NEMS device fabrication. We divide them in two categories: (1) common to IC fabrication (suitable for MEMS), and (2) nanofabrication techniques (suitable for NEMS). In both cases, MEMS and NEMS fabrication is costly in time, materials, services, equipment, and man power. Thus, the design and production infrastructures are not affordable for most of the companies or research centers. External foundries have adapted their production lines to MEMS manufacturing and offer fabrication services to universities and small companies through public access programs like Europractice. The turnaround times for fabricated devices are about three months.

For these reasons, fabrication is critical, and previous design activities have to be rigorously completed to guarantee successful manufacturing results. From concept to application, there is a production cycle involving a set of engineering activities, which follow a logical sequence within the process. The section explains this cycle and describes some of the fabrication technologies of MEMS and NEMS devices in a general way. Later in Chapters 4 and 10, we will provide an extensive description of these technologies applied to acoustic microresonators fabrication.

1.3.1 The Production Cycle

Once we have defined the geometry, boundary conditions, and materials, the design equations presented in the previous section aid the analytical modeling of the resonator. Figure 1.15 depicts the flow diagram of the production cycle.

First, we define the resonator concept basing our decision on the expected application and the possible integration with IC technologies. The concept involves defining the generalities of the fabrication process and the interconnection technology with the IC, compatibility issues with the IC, temperature budget, and materials. At the layout level, it also requires previsions of the resonator active area,

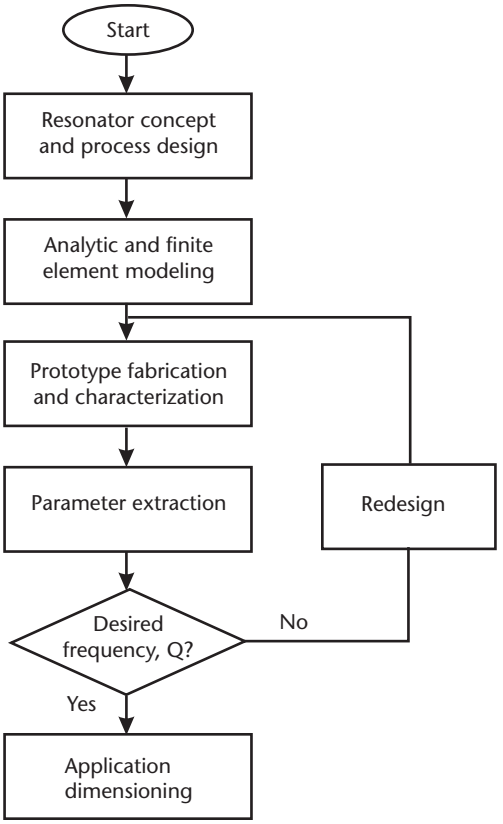

Figure 1.15 The production cycle of MEMS and NEMS resonators.

electrode design and contact pad area, dicing areas (if needed), or via holes for interconnection (if needed). If we intend to fabricate the resonator by using the layers of a microelectronic process, we need to choose the appropriate layers of the technology. Later in Chapter 7, we will study the integration strategies for this purpose.

Then, we perform analytical and finite element modeling (FEM) of the resonator. In a first approximation, the design equations presented in the previous section are enough to estimate the spectral range in which we expect to find the resonance frequency. With the design dimensions, we can build a finite element model. The FEM analysis is useful to extract the eigenvalues of the structure and to predict the structural and harmonic response due to external signals or forces. Commercial FEM tools offer many possibilities, so we can succeed in building a complex and reliable resonator model, which we will use to fix the final resonator process and dimensions.

A MEMS prototype can now be fabricated. Different test and de-embedding structures are used at this stage to extract the resonator material constants, quality factor, equivalent-circuit parameters, insertion losses, and parasitic impedances. Fabricated devices are then characterized with available measurement instrumentation. The main characterization results are the resonance frequency and the quality factor, whose values will validate our design or will force us to redesign the resonator to reach the design values.

If the resonance frequency has acceptable design values, extraction of the equivalent-circuit parameters is carried out. These parameters are a circuit-like electrical representation of the harmonic oscillator, and they can be used in further analyses, especially when we intend for future IC integration or read-out circuit interconnection. Even when the resonance frequency fits with acceptable tolerance within the design values, other design elements have to be considered, like the insertion losses or the quality factor. These elements are, as we commented before, key aspects of the application design. Since the success of the production cycle mainly depends on the fabrication technologies, we provide a detailed analysis of them in the next section.

1.3.2 Common to Integrated Circuit (MEMS)

Microfabrication technologies common to IC are a wide family of processes and techniques comprising the following: carrying substrates—mainly silicon, photolithography, etching, implantation, dielectric and conductive layer deposition, and, in general, all processes currently employed in integrated circuit manufacturing. Most of them have been adapted to produce MEMS devices, but not necessarily modified in their essence and principle: parallel processing and planar technology. Besides, micromachining complements the list to produce movable structures. The process cycle involving these technologies is depicted in Figure 1.16. The following sections discuss some of them.

1.3.2.1 Silicon Substrates

Silicon (Si) is the most employed substrate in MEMS and NEMS device fabrication. Si crystal orientation, doping, and wafer size are chosen depending on the application. Si wafers of types N or P with diameters of 100 to 300 mm and thicknesses from 300 μm to 1 mm are available in the market. Crystal's orientation (e.g., 100, 111) and doping types determine the wafer resistivity and fabrication time of micromachined MEMS, among other parameters. Different methods exist to fabricate Si wafers. Thus, the resistivity varies from the 0.002–50 Ω·cm obtained with the Czochralski technique, to the 20–100 Ω·cm in the Floating Zone method [48,

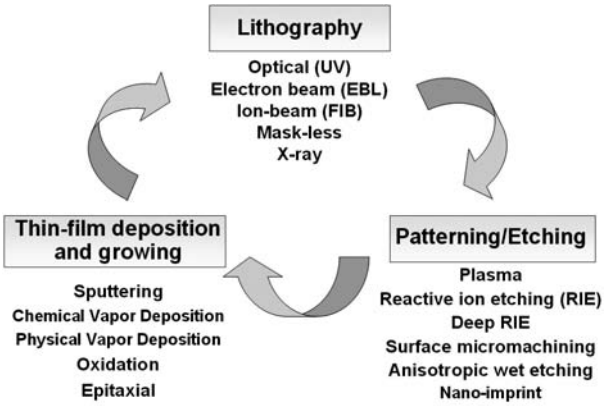

Figure 1.16 Process of common-to-IC MEMS fabrication.

49]. Nevertheless, the presence of impurity materials in Si wafer fabrication is unavoidable, with concentrations of oxygen lower than 1×10^{14} atoms/cm^3, carbon impurities between $1 \times 10^{12} - 1 \times 10^{14}$ atoms/cm^3, and heavy metals being the main materials found in the wafers.

P-type and N-type wafers are fabricated by introducing impurities of the III and V groups of the periodic table in the Si, respectively. III-group materials widely used are arsenic (As) and phosphorus (P), whereas boron (B) is the V-group material most employed in P-type doping. Ion implantation using accelerated isotopes to 50–200 keV achieves doping at rates between $10^{11} - 10^{14}$ atoms/cm^3. However, the carrier concentration, which depends on the wafer type (N or P), is not uniform and may change within the wafer and between the different wafers of a lot. Impurity diffusion contributes to a redistribution of charges through high temperature processes (1,000°C).

Silicon-on-insulator (SOI) wafers are another kind of substrate widely used in MEMS and NEMS fabrication [50]. SOI wafers are constituted by a Si device layer (DEV), a highly resistive buried oxide layer (BOX), and the Si substrate, as depicted in Figure 1.17. Commercial SOI wafers are available with DEV and BOX layers having thicknesses in the range of 1 to 100 μm and 0.5 to 5 μm, respectively [51]. The SOI technology finds good application in MEMS micromachining because it provides high control of etching. MEMS structures can be fabricated with the DEV or BOX layers, whose thicknesses are previously known. Also, SOI wafers aid in reducing the high coupling losses of standard Si wafers, because the DEV and BOX layers offer less resistance and better isolation, respectively. In RF applications, this is a key feature for obtaining good performance.

Other substrates for MEMS and NEMS applications offer high resistivity and flexibility so far [52]. Additionally, transferable electronics and MEMS have promoted the development of flexible substrates different from silicon [53].

1.3.2.2 Oxidation of Silicon

Oxidation of silicon wafers has several applications in microdevice fabrication—substrate passivation (the formation of a chemically, electronically, and electromechanically stable surface), diffusion, ion implantation, dielectric thin-film making, and intersubstrate material interfacing, among others [54]. Generally speaking, two kinds of oxides are fabricated: thermal oxide and deposited oxide.

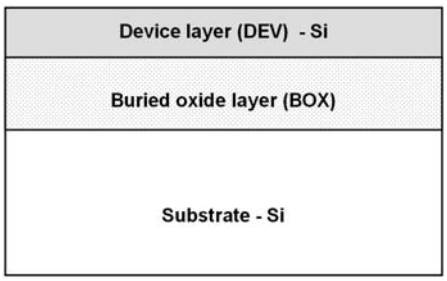

Figure 1.17 Silicon-on-insulator (SOI) technology as a high-performance substrate for MEMS and NEMS resonators.

Thermal silicon oxide (SiO_2) grows on Si when the air-Si interface is oxidized at room temperatures. Therefore, nanometer-thick SiO_2 thin films cover the whole Si wafer surface. Thicker SiO_2 layers can be grown at elevated temperatures after dry or wet atmosphere reactions:

- Dry reaction (with oxygen): $Si + O_2 \rightarrow SiO_2$;
- Wet reaction (with water): $Si + 2H_2O \rightarrow SiO_2 + H_2$.

Growth rate and oxide characteristics depend on concentration and quality of the oxidant, pressure, temperature, diffusivity, and oxide thickness, among others. For constant-temperature oxidation, the relationship between oxide thickness and time is parabolic. The oxygen-based process is slow but it offers high-quality oxide, whereas the water-based oxidation is faster but at the cost of lower oxide quality. In both cases, typical oxidation temperatures vary from 950ºC to 1,050ºC.

Deposited SiO_2 is obtained through thin-film deposition techniques, and it can be processed on Si or on other substrates as well. The obtained oxide may have thicknesses of hundreds of nanometers and is, in general, of better quality than the thermal oxide, thus exhibiting higher resistivity and dielectric properties. The deposition techniques of SiO_2 are common to other dielectric materials, as we review in the following section.

1.3.2.3 Dielectric Layer Deposition

Dielectric layers—as SiO_2—can be deposited using a variety of techniques, such as epitaxial growing, chemical vapor deposition (CVD), and molecular-beam growing. Epitaxial is especially useful for synthesizing high-quality dielectric layers in a monolayer basis, where low processing times and high temperature promote highly oriented crystal growing. Highly doped buried monocrystalline silicon or columnar piezoelectric materials like aluminum nitride (AlN) are two application examples. High deposition temperatures—above 950ºC–1,250ºC—restrict the application of epitaxial for previous-CMOS processing.

CVD is based on chemical reaction of the vapor-phase reactant with chemical radicals found inside the CVD machine chamber. The product of reaction is then deposited on the substrate, usually at a slow rate, as represented in the schematic of Figure 1.18. Many variants of the CVD process exist, namely:

- High temperature chemical vapor deposition (HTCVD);
- Low temperature chemical vapor deposition (LTCVD);
- Plasma enhanced chemical vapor deposition (PECVD);
- Low pressure chemical vapor deposition (LPCVD).

The versatility of CVD allows the fabrication of polysilicon, numerous kinds of oxides, BSG, PSG, BPSG, SiO_2, and nitrides, Si_2N_3, Si_3N_4, among others.

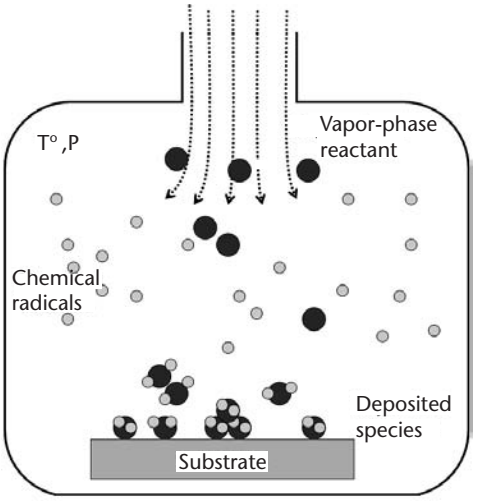

Figure 1.18 Chemical vapor deposition.

1.3.2.4 Conductive Layer Deposition

Metal evaporation, physical vapor deposition (PVD), and electroplating a deposition are the main techniques for conductive layer deposition. Sputtering, for example, is a technique of the PVD family that creates a source of particles being subsequently condensed onto the substrate, thus forming a thin film. Physical sputtering is the process where atoms are ejected from a surface as a consequence of the bombardment of the latter by heavy energetic particles (ions). Under the adequate energetic conditions and low-pressure environment, low-density plasma is formed by electron impact ionization of the gas in a controlled electrical gas discharge. Low ionization degrees in the range of 10^{-5} to 10^{-2} and processing pressures of 1–30 mTorr correspond to an ion density of 10^{9} to 10^{12} cm^{3} [55]. Due to these physical conditions, the sputtering process can be accomplished at relatively low temperatures (i.e., below 400°C, which is a favorable condition for CMOS compatibility). Figure 1.19 illustrates the concept of physical sputtering.

A combination of AC, magnetron, and reactive sputtering reports several advantages to single sputtering deposition. AC sputtering allows discharging of the target (ion charging occurs in DC sputtering), magnetron increases the attracting forces and acceleration of ions to the cathode, and reactive sputtering enables dielectric and compound material deposition using metallic targets. At the end, higher ion density and more efficient deposition are achieved with lower energy levels (in the hundreds of electron-volts, instead of kilo-electron volts) and power supplies.

With respect to other deposition techniques, sputtering offers several advantages. Among them, we can mention film uniformity, surface smoothness and thickness control, versatility (virtually any material can be introduced into a gas discharge or sputtered from the target), good adhesion, conformal or planarized coating, and higher deposition rates. Most important, the low process temperature makes the sputtering technique compatible with CMOS fabrication [56].

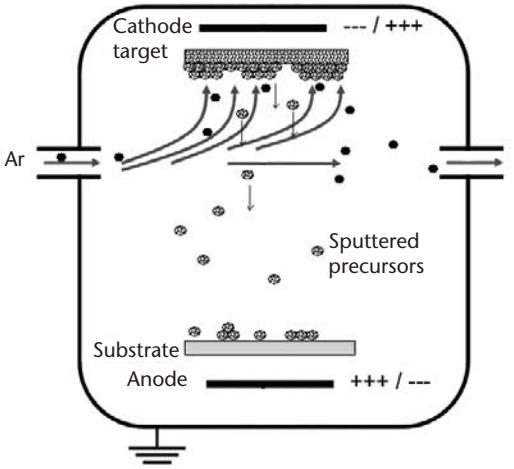

Figure 1.19 Physical sputtering.

1.3.2.5 Conventional Photolithography

Photolithography is an optical technique to transfer the patterns from a photo mask or reticule to the wafer. Thus, the system involves four elements: ultraviolet (UV) light source, mask or reticule, photoresist, and the wafer where the patterns are to be transferred to. Each mask or reticule contains only one layer of devices. Thus, the photolithography exposure is repeated as far as all chip patterns are transferred to the wafer. The process involves a consecutive number of resist spinning and coating, baking, developing, layer patterning, and resist removal [57].

The conventional photolithography process is illustrated with one example in Figure 1.20, which shows a simplified schema of the patterning of a SiO_2 layer. First, the photo-resist is uniformly deposited on the wafer by spin coating. Then, the mask or reticule is charged in the exposure line and aligned with the wafer. When

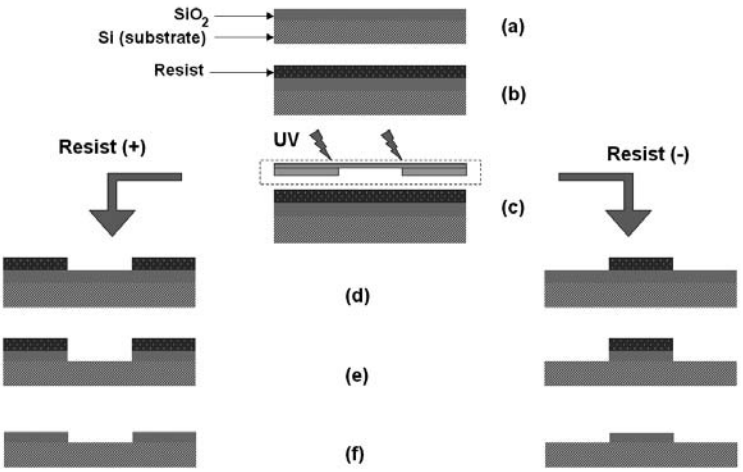

Figure 1.20 Conventional optical photolithography of a SiO_2 pattern: (a) SiO_2 layer deposition; (b) photo-resist coating; (c) mask alignment and UV exposure; (d) resist developing; (e) SiO_2 etching; and (f) resist removal.

exposed to UV radiation, the molecular structure of the light-sensitive resist is broken. After resist developing, two cases are considered, depending on whether the resist is *positive* or *negative*. With positive resist, only resist areas under the patterns in the mask remain after developing, while the opposite occurs for negative resist. After the wafer is cleaned, the resist remaining on the wafer serves as mask to selectively pattern the SiO_2, according to the resist case. After SiO_2 etching, the resist is removed and the wafer can be subsequently been processed.

The mask is made of a transparent, rigid dielectric, typically fused silica glass or quartz covered with a chrome film defining a pattern that allows UV light to pass through the transparencies. In standard contact photolithography, patterns are designed at 1:1 scale, whereas stepper and scanner technologies shrink them by four or five, thus obtaining reduced-size devices. Photo masks are manufactured by large commercial companies, as the cost of setting up a mask shop is some hundred million dollars [58–60]. However, major semiconductor companies fabricated their own masks [61–64]. UV-light wavelength identifies the different types of exposure lines: 365-nm i-line, 436-nm g-line, and deep UV (DUV) below 300 nm. DUV examples are the 248-nm krypton fluoride, 193-nm argon fluoride, and 157 nm. Phase shifting and immersion lithographies are other photolithographic techniques intended for enhanced resolution below 150 nm. The immersion technique, for example, achieves resolutions as small as 37 nm. Extreme UV (EUV, 13.5 nm), x-ray, and electron-ion sources technologies have been developed to reduce the pattern sizes to even smaller wavelengths of few nanometers.

1.3.2.6 Bulk Micromachining

Bulk and surface micromachining are etching techniques for MEMS, which are based on the modified CMOS technology. In bulk micromachining, the substrate is patterned to form the three-dimensional, movable structure of the MEMS device (it is rarely used for NEMS).

Bulk micromachining of Si was developed to fabricate movable microstructures. It uses wet- and dry-etching techniques in conjunction with masks and etch-stop layers to define three-dimensional microstructures [65]. Bulk micromachining can be performed by the front or the back of the substrate through wet- and dry-etching processes as depicted in Figure 1.21. Wet-etching processes utilize etchants attacking the different crystallographic directions at slower or faster rates. Examples of anisotropic etchant solutions are potassium hydroxide (KOH), sodium hydroxide (NaOH), and ethylene-diamine-pyrocatecol (EDP).

Dry etching is carried out through reactive-ion etching (RIE) and deep reactive-ion etching (DRIE). RIE and DRIE make use of plasma to etch straight-walled structures (e.g., cubes or rectangles). Depending on the recipe, RIE-based dry etching is useful for both isotropic and anisotropic etching. Taking advantage of isotropy, etching can be performed in both the vertical and lateral directions. The feature is exploited to release movable structures from the front of the wafer. Alternatively, the RIE recipe can be modified to provide an effective means of back-side processing with no considerable lateral etching. In this case, the whole bulk of the wafer is etched, whereas in most front-side etching applications, it is just partially etched [66].

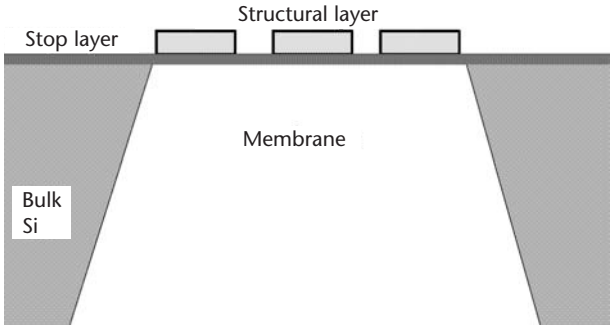

Figure 1.21 Bulk micromachining.

RIE and DRIE are kinds of sputtering systems in which reactive species are accelerated to the substrate. Accelerated plasma ions perform the bombardment of substrate, which is achieved through appropriate biasing conditions and reactive species. Figure 1.22 illustrates the process. Given a reactive species, etching is selective to certain materials. Thus, the application and target materials fix the reactive species to avoid undesired etching of other materials on the substrate [67].

1.3.2.7 Surface Micromachining

In surface micromachining, a sacrificial layer deposited on the surface of wafers is patterned to form the movable structure of MEMS and NEMS devices. The process must guarantee high patterning accuracy of the sacrificial layer. After etching, it leaves free volume for the device.

The thickness of thin films is usually limited to up to 5 μm, thus leading to planar-type microstructures [54]. In this sense, surface micromachining can be called a thin-film technology. The advantage of surface micromachining is the use of standard CMOS fabrication processes and facilities, which makes the fabrication of integrated sensors and actuators affordable to research institutes, small companies, and universities. The typical surface micromachining process depicted in Figure 1.23 implements a sacrificial layer to provide mechanical support to the subsequent

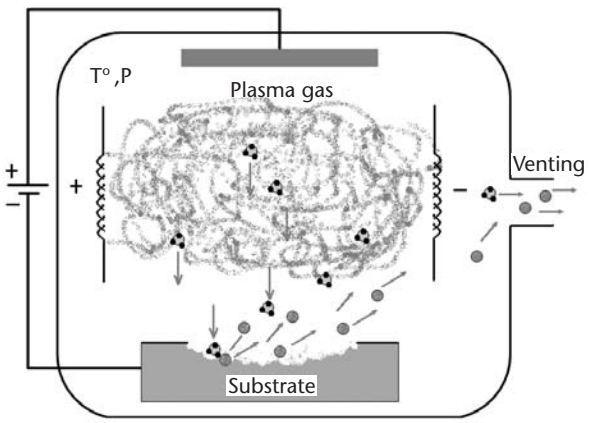

Figure 1.22 Reactive ion etching.

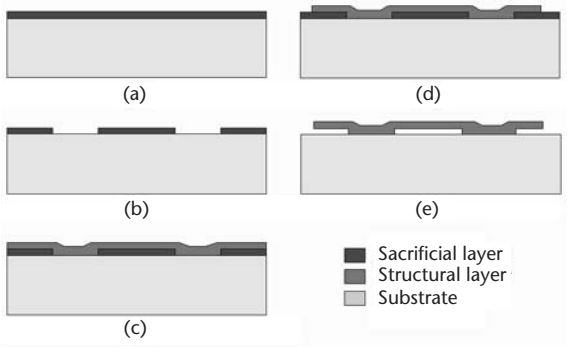

Figure 1.23 Surface micromachining: (a) deposition and (b) patterning (sacrificial layer); (c) deposition and (d) patterning (structural layer); and (e) etching (sacrificial layer).

layers, and it is removed to release the microstructures. Hence, one or more thin-film layers made of structural—the final device—and sacrificial materials are deposited and patterned on the surface of the wafer. After completion of the structural layer deposition, the sacrificial layer is removed, and the whole device is released [68].

Usually, the sacrificial layer is a dielectric material, although a conductive or semiconductor material may also be employed. Currently implemented sacrificial layers are made of SiO_2, phosphorous-doped silicon dioxide (PSG), or silicon nitride (Si_3N_4) [69]. After fabrication of the structures, wet etching of the sacrificial layer forms cavities underneath the surface components, which allows releasing and eventually the motion of the device. The wet etching can be done by using hydrofluoric acid (HF), buffered hydrofluoric acid (HF), KOH, EDP, TMAH, or NaOH, among others.

The size of patterned features that can be obtained with the foregoing techniques is in the order of microns, although smaller features can be obtained with ultra-thin films—tens or hundreds of nanometers—and the help of appropriate tools, like critical point dryers (CPDs). CPDs are useful to avoid sticking of submicron-sized membranes, cantilevers, and other structures resulting from the sacrificial layer etching. Nevertheless, NEMS resonators usually require advanced fabrication technologies to guarantee accuracy and process repeatability. The next section introduces the main nanofabrication techniques.

1.3.3 Nanofabrication Techniques (NEMS)

Nanofabrication mainly refers to lithography techniques that allow manufacturing of nanometer-sized structures for nanoelectronic circuits and NEMS. Nanofabrication is addressed by two complementary approaches: top down and bottom up. Top down is the nanoscale-updated methodology common to IC manufacturing. Top down involves the fabrication of small structures by patterning the "big" structural layer (top) to obtain the nanosized feature. On the other hand, bottom up denotes structuring the matter from the "small" scale of molecules—even atoms with the current techniques—to achieve a nanodevice. Nanosphere lithography and molecular self-assembly are two examples of this approach [70, 71]. These

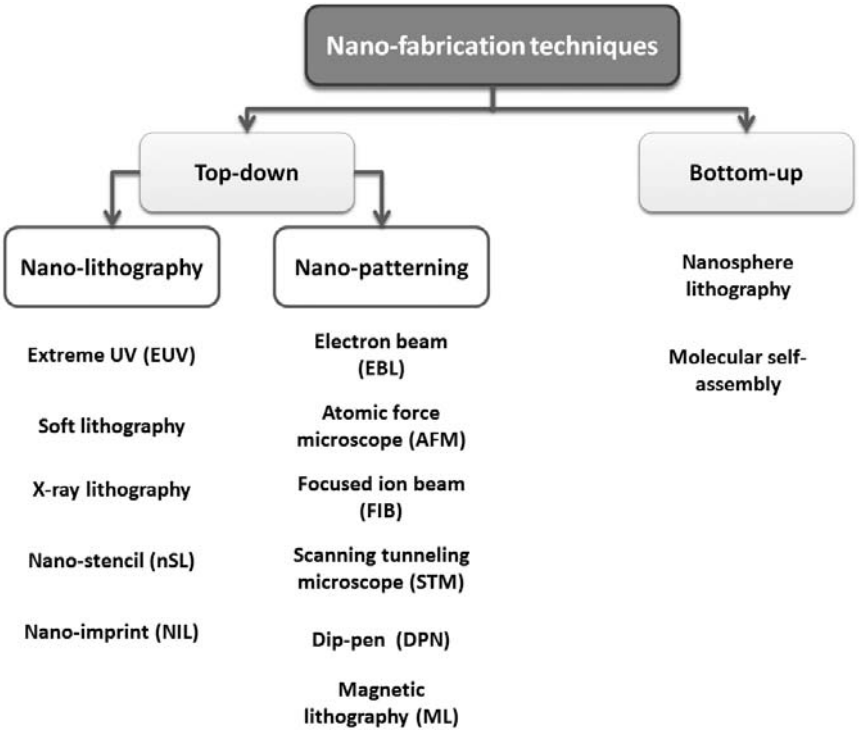

Figure 1.24 Taxonomy of nanofabrication techniques.

nanofabrication techniques and categories are depicted in the taxonomic tree of Figure 1.24.

Top-down techniques can be categorized in two groups: nanolithography and nanopatterning. Although the difference may be subtle, nanolithography implements additional elements to pattern the structure of interest, whereas in nanopatterning direct interaction between the layer and the patterning tool occurs. The nanolithographic tools are photo masks, stencils, molds, and printing buffers, among others. Extreme UV (EUV), soft lithography implementing polymers, x-ray lithography, nanoimprint lithography (NIL), and nanostencil lithography (nSL) are examples of the nanolithography group.

Nanopatterning techniques are the subject of intensive research activity. Commercial equipment is available to produce final devices, too. Because they do not use masks or similar elements, they are also known as *maskless lithography*. The expression, though, refers more accurately to a computer-aided serial technique that implements a mirror and laser or another light source to transfer the patterns to the wafer in a layer basis. Remarkable examples of the nanopatterning category are electron beam lithography (EBL), atomic force microscopy (AFM) lithography, focused ion beam (FIB) lithography, scanning tunneling microscope (STM), dip-pen nanolithography (DPN), magnetolithography (ML), and a daily growing list of novel lithography techniques.

Nanofabrication techniques offer many opportunities for NEMS production. Their main features are lower cost, suitability for NBIC applications, increased device complexity, biocompatibility and plastic materials implementation, and

Table 1.3 Engineering Attributes of MEMS and NEMS Resonators

Characteristic	*MEMS*	*NEMS*
Dimensions	100 nm–1 mm	Below 100 nm
Resonance frequency (fundamental flexural mode)	kHz–MHz	MHz–GHz
Q factor	Higher	Lower
Power	Higher	Lower
Aspect ratio	>1 (high, in general)	~1 (about unity, in general)
Surface-to-volume ratio	Lower	Higher
Dynamic range	Higher	Lower
Active mass (normalized to physical mass)	Bigger	Smaller
Sensitivity	Good	Better
Phase noise	Lower	Higher
Current applications	Sensors, radio frequency	Sensors
Technology	IC-based (top-down); parallel production	IC-based (top down) and bottom up (nanostructuring); serial production (if nanofabrication tools are employed)

smaller sizes. Nevertheless, several challenges of nanofabrication are still to be dealt with, like reproducibility of nanosized patterns, manufacturing throughput, and their compatibility to current IC processes.

1.4 Summary

This chapter has introduced the main concepts regarding MEMS and NEMS resonators. Physical phenomena, modeling and transduction principles of resonant devices, and fabrication techniques have been examined (piezoelectric transduction will be described in Chapter 2). We have learned that MEMS and NEMS resonators are differentiated from each other by their size and by their fabrication approach and physics scaling. Current NEMS engineering is facing challenges solved for MEMS many years ago. Among them, we find packaging, Q factor, high surface-to-volume ratio, and repeatability. Table 1.3 is a nonexhaustive list of engineering items we need to consider when comparing MEMS and NEMS. The goal is to contextualize the technologies, performance, applications, and challenges of both devices ("lower" and "higher" are relative to MEMS and NEMS).

References

[1] Baltes, H., et al., "CMOS MEMS—Present and Future," *Proc. IEEE Intl. Conf. MEMS 2002*, January 20–24, 2002, Las Vegas, NV, pp. 459–466.

[2] Bauerdick, S., et al., "Direct Wiring of Carbon Nanotubes for Integration in Nanoelectromechanical Systems," *J. Vac. Sci. Technol.*, Vol. B24, 2006, p. 3144.

[3] Husain, A. et al., "Nanowire-Based Very-High-Frequency Electromechanical Resonator," *Appl. Phys. Lett.*, Vol. 83, 2003, pp. 1240–1242.

[4] Ozin, G. A., A. C. Arsenault, and L. Cademartiri, *Nanochemistry: A Chemical Approach to Nanomaterials*, Cambridge, U.K.: RSC Publishing, 2009.

[5] Bachand, G. D., and Carlo D. Montemagno, "Constructing Organic/Inorganic NEMS Devices Powered by Biomolecular Motors," *Biomedical Microdev.,* Vol. 2, 2000, pp. 179–184.

[6] McCord, M. A., and M. J. Rooks, *Handbook of Microlithography, Micromachining and Microfabrication*, Vol. II, Bellingham, WA: SPIE, 2000.

[7] Binnig, G., C. F. Quate, and C. Gerber, "Atomic Force Microscope," *Phys. Rev. Lett.*, Vol. 56, No. 9, 1986, pp. 930–933.

[8] Chou, S. Y., P. R. Krauss, and P. J. Renstrom, "Imprint Lithography with 25-Nanometer Resolution," *Science*, Vol. 272, 1996, pp. 85–87.

[9] National Science Foundation (NSF), *Converging Technologies for Improving Human Performance (Nanotechnology, Biotechnology, Information Technology and Cognitive Science)*, 2002.

[10] ST Microelectronics, "System on Chip," http://www.st.com/stonline/products/technologies/soc/soc.htm.

[11] Geschke, O., H. Klank, and P. Telleman, (eds.), *Microsystem Engineering of Lab-on-a-Chip Devices*, New York: John Wiley & Sons, 2004.

[12] Herold, K. E., and A. Rasooly, (eds.), *Lab-on-a-Chip Technology: Fabrication and Microfluidics*, San Francisco, CA: Caister Academic Press, 2009.

[13] Nathanson, H. C., and R. A. Wickstrom, "The Resonant Gate Transistor," *IEEE Trans. on Electron Dev.*, Vol. 14, 1967, pp. 117–133.

[14] Southwest Center for Microsystems Education and the University of New Mexico, *History of Microelectomechanical Systems (MEMS)*, 2008.

[15] Salomon, P., "NEXUS_MNT_Market_Report_III-2005-2009," NEXUS Task Force (coordination: WTC), 2004.

[16] Apple, http://www.apple.com/iphone/.

[17] Nintendo, http://www.nintendo.com/wii.

[18] Roukes, M. L., "Nanoelectromechanical Systems," *Tech. Dig. of the 2000 Solid-State Sensor and Actuator Workshop*, Hilton Head, SC, June 4–8, 2000, pp. 1–4.

[19] Gibson, C. T., D. Alastair Smith, and C. J. Roberts, "Calibration of Silicon AFM Cantilevers," *Nanotechnology*, Vol. 16, 2005, pp. 234–238.

[20] Blom, F. R., et al., "Dependence of the Quality Factor of Micromachined Silicon Beam Resonators on Pressure and Geometry," *J. Vac. Sci. Tech.,* Vol. B10, 1992, pp. 19–26.

[21] Mangiarotty, R. A., "Acoustic Radiation Damping of Vibrating Structures," *J. Acoust. Soc. Am.*, Vol. 35, 1963, pp. 369–377.

[22] Hosaka, H., K. Itao, and S. Kuroda, "Damping Characteristics of Beam-Shaped Micro-Oscillators," *Sens. Actuators A: Phys.*, Vol. 49, 1995, pp. 87–95.

[23] Vemuri, S., G. K. Fedder, and T. Mukherjee, "Low-Order Squeeze Film Model for Simulation of MEMS Devices," *Proc. 2000 Intl. Conf. on Modeling and Simulation of Microsystems Semiconductors, Sensors and Actuators*, San Diego, CA, March 27–29, 2000, pp. 205–208.

[24] Vignola, J. F., et al., "Loss Mechanisms in MEMS Oscillators," *Proc. SPIE Fifth International Conference on Vibration Measurements by Laser Techniques: Advances and Applications*, Vol. 4827, Ancona, Italy, June 18–21, 2002, pp. 466–477.

[25] Brotz, J., "Damping in CMOS-MEMS Resonators," M.Sc. thesis, Carnegie Mellon University, 2004.

[26] Quevy, E. P., and R. T. Howe, "Redundant MEMS Resonators for Precise Reference Oscillators," *Dig. Tech. Papers Radio Frequency Integrated Circuits Symp. RFIC 2005*, Long Beach, CA, June 12–14, 2005, pp. 113–116.

[27] Judge, J. A., et al., "Attachment Loss of Micromechanical and Nanomechanical Resonators in the Limits of Thick and Thin Support Structures," *J. Appl. Phys.,* Vol. 101, 2007, 013521.

[28] Pandey, M., et al., "Reducing Anchor Loss in MEMS Resonators Using Mesa Isolation," *J. Microelectromech. Syst.*, Vol. 18, 2009, pp. 836–844.

[29] Ono, T., and M. Esashi, "Effect of Ion Attachment on Mechanical Dissipation of a Resonator," *Appl. Phys. Lett.*, Vol. 87, 2005, 044105.

[30] Zener, C., "Internal Friction in Solids, I: Theory of Internal Friction in Reeds," *Phys. Rev.*, Vol. 52, 1937, pp. 230–235.

[31] Zener, C., "Internal Friction in Solids, I: General Theory of Thermoelastic Internal Friction," *Phys. Rev.*, Vol. 53, 1938, pp. 90–99.

[32] Duwel, A., et al., "Engineering MEMS Resonators with Low Thermoelastic Damping," *J. Microelectromech. Syst.*, Vol. 15, 2006, pp. 1437–1445.

[33] Kim, Y.-S., et al., "A Class of Micromachined Magnetic Resonator for High-Frequency Magnetic Sensor Applications," *J. Appl. Phys.*, Vol. 99, 2006, 08B309.

[34] Greywall, D. S., "Sensitive Magnetometer Incorporating a High-Q Nonlinear Mechanical Resonator," *Meas. Sci. Tech.*, Vol. 16, 2005, pp. 2473–2482.

[35] Lassagne, B., et al., "Ultrasensitive Mass Sensing with a Nanotube Electromechanical Resonator," *Nano Lett.*, Vol. 8, 2008, pp. 373–3738.

[36] Vasquez, D. J., and J. W. Judy, "Flexure-Based Nanomagnetic Actuators and Their Ultimate Scaling Limits," *Proc. IEEE Intl. Conf. MEMS 2008*, Tucson, AZ, January 13–17, 2008, pp. 737–741.

[37] Huang, Y., X. Bai, and Y. Zhang, "In Situ Mechanical Properties of Individual ZnO Nanowires and the Mass Measurement of Nanoparticles," *J. Phys.: Cond. Matter*, Vol. 18, 2006, pp. 179–184.

[38] Nam, C. Y., et al., "Diameter-Dependent Electromechanical Properties of GaN Nanowires," *Nano Lett.*, Vol. 6, 2006, pp. 153–158.

[39] Holmgren, O., et al., "Analysis of Vibration Modes in a Micromechanical Square-Plate Resonator," *J. Micromech. Microeng.*, Vol. 19, 2009, 015028.

[40] Pang, W., et al., "Ultrasensitive Mass Sensor Based on Lateral Extensional Mode (LEM) Piezoelectric Resonator," *Proc. IEEE Intl. Conf. MEMS 2006*, Istanbul, Turkey, January 22–26, 2006, pp. 78–81.

[41] Pourkamali, S., G. K. Ho, and F. Ayazi, "Low-Impedance VHF and UHF Capacitive Silicon Bulk Acoustic-Wave Resonators—Part II: Measurement and Characterization," *IEEE Trans. on Electron Dev.*, Vol. 54, 2007, pp. 2024–2030.

[42] Li, S.-S., et al., "An MSI Micromechanical Differential Disk-Array Filter," *Dig. of Tech. Papers 14th Intl. Conf. on Solid-State Sensors, Actuators & Microsystems TRANSDUCERS 2007*, Lyon, France, June 10–14, 2007, pp. 307–311.

[43] Lin, Y.-W., et al., "Low Phase Noise Array-Composite Micromechanical Wine-Glass Disk Oscillator," *Dig. of Tech. Papers IEEE Intl. Electron Devices Meeting IEDM 2005*, Washington, D.C., December 5–7, 2005, pp. 281–284.

[44] Demirci, M. U., M. A. Abdelmoneum, and C. T.-C. Nguyen, "Mechanically Corner-Coupled Square Microresonator Array for Reduced Series Motional Resistance," *Dig. of Tech. Papers 12th Intl. Conf. on Solid-State Sensors & Actuators TRANSDUCERS 2003*, Boston, MA, June 8–12, 2003, pp. 955–958.

[45] Piazza, G., et al., "Low Motional Resistance Ring-Shaped Contour-Mode Aluminum Nitride Piezoelectric Micromechanical Resonators for UHF Applications," *Proc. IEEE Intl. Conf. MEMS 2005*, Miami Beach, FL, January 30–February 3, 2005, pp. 20–23.

[46] Teva, J., "Integration of CMOS-MEMS Resonators for Radiofrequency Applications in the VHF and UHF Bands," Ph.D. thesis, U. A. Barcelona, 2004.

[47] Li, M., H. X. Tang, and M. L. Roukes, "Ultra-Sensitive NEMS-Based Cantilevers for Sensing, Scanned Probe and Very High-Frequency Applications," *Nature Nanotechnology*, Vol. 114, 2007, pp. 114–120.

[48] Czochralski, J., *Z. Phys. Chem.*, Vol. 92, 1918, pp. 219–221; *Encyclopædia Britannica*, "Czochralski Method," http://www.britannica.com/EBchecked/topic/149253/Czochralski-method.

[49] Pfann, W. G., "Principles of Zonemelting," *T. AIME*, Vol. 194, 1952, p. 747.

[50] IBM, "IBM Advances Chip Technology with Breakthrough for Making Faster, More Efficient Semiconductors: Silicon-on-Insulator Technology," 1998, http://www-03.ibm.com/press/us/en/pressrelease/2521.wss.

[51] Silicon Materials, http://www.si-mat.com/.

[52] Polyakov, A., et al., "High-Resistivity Polysilicon as RF Substrate in Wafer-Level Packaging," *Electron. Lett.*, Vol. 41, 2005, pp. 100–101.

[53] Organic Electronics Association, http://www.oe-a.org/.

[54] Lyshevski, S. E., *MEMS and NEMS: Systems, Devices and Structures*, Boca Raton, FL: CRC Press, 2002.

[55] Engelmark, F., "AlN and High-K Thin Films for IC and Electroacoustic Applications," Ph.D. thesis, Uppsala University, Uppsala, Sweden, 2002.

[56] Parsons, R., "Sputter Deposition Processes," in *Thin Film Processes II*, J. L. Vossen and W. Kern, (eds.), San Francisco, CA: Academic Press Limited, 1991, p. 178.

[57] Jaeger, R. C., "Lithography," in *Introduction to Microelectronic Fabrication*, 2nd ed., Upper Saddle River, NJ: Prentice-Hall, 2002.

[58] Dai Nippon Printing Co.-Ltd., http://www.dnp.co.jp/index_e.html.

[59] Photronics, Inc., http://www.photronics.com/.

[60] Toppan Photomasks, Inc., http://www.photomask.com/.

[61] Intel Mask Operations, http://www.intel.com.

[62] Advanced Micro Devices (AMD), http://www.amd.com/.

[63] Industrial Business Machines (IBM), "Semiconductor Solutions," http://www-03.ibm.com/technology/index.html.

[64] Nippon Electric Co. (NEC), "Pioneering Development of Immersion Lithography," http://www.nec.co.jp.

[65] Lyshevski, S. E., *Micro- and Nano-Electromechanical Systems: Fundamentals of Micro- and Nano-Engineering*, Boca Raton, FL: CRC Press, 2000.

[66] Serre, C., et al., "Test Microstructures for Measurement of SiC Thin Film Mechanical Properties," *J. Micromech. Microeng.*, Vol. 9, 1999, pp. 190–193.

[67] Coburn, J. W., and H. F. Winters, "Ion- and Electron-Assisted Gas-Surface Chemistry: An Important Effect in Plasma Etching," *J. Appl. Phys.*, Vol. 50, 1979, pp. 3189–3196.

[68] Benítez, M. A., et al., "A New Process for Releasing Micromechanical Structures in Surface Micromachining," *J. Micromech. Microeng.*, Vol. 6, 1996, pp. 36–38.

[69] Calaza, C., et al., "A Surface Micromachining Process for the Development of a Medium-Infrared Tuneable Fabry-Perot Interferometer," *Sens. Actuators A: Phys.*, Vol. 113, 2004, pp. 39–47.

[70] Haynes, C. L., and R. P. Van Duyne, "Nanosphere Lithography: A Versatile Nanofabrication Tool for Studies of Size-Dependent Nanoparticle Optics," *J. Phys. Chem.*, Vol. B105, 2001, pp. 5599–5611.

[71] Whitesides, G. M., J. P. Mathias, and C. T. Seto, "Molecular Self-Assembly and Nanochemistry: A Chemical Strategy for the Synthesis of Nanostructures," *Science*, Vol. 254, 1991, pp. 1312–1319.

CHAPTER 2

Acoustic Microresonator Technologies

Acoustic microresonators are fueling the reduction in size and power consumption of mobile radio equipment and sensing systems that the telecommunication and sensors industries have been undertaking during the past few years. The kind of acoustic resonators we study herein are microelectromechanical devices. They experience acoustic wave propagation and eventually vibrate at a resonance frequency related to their dimensions and mechanical configuration, when driven with the appropriate conditions. Roughly, they are classified in two categories: surface acoustic wave (SAW) and bulk acoustic wave (BAW) resonators. Two types of the latter are found: the solidly mounted resonator (SMR) and the thin-film bulk acoustic wave resonator (FBAR). In Chapter 1 we studied how silicon-MEMS resonators can be excited at frequencies promoting acoustic wave propagation. Now, the discussion is restricted to those resonators implementing an acoustic layer made of piezoelectric materials.

Despite the need for compatibility between CMOS and piezoelectric thin-film processes, SAW, SMR, and FBAR devices can be fabricated within standard IC technologies. Additionally, FBAR manufacturing entails micromachining steps, like MEMS resonator processes. On the other hand, FBARs resonate at far-from-fundamental acoustic modes, instead of purely mechanical modes. Both circumstances have thus created certain controversy regarding whether FBARs are considered MEMS resonators.

In Section 2.1, we define the fundamental concepts of acoustic wave propagation and its differences with the electromagnetic-wave actuation in "classical" MEMS. Moreover, emphasis is put on the working principle of acoustic wave resonators. Then, Section 2.2 begins with the basics of piezoelectricity and acoustic wave theory, and we study some of the most exploited acoustic vibration modes. Section 2.3 goes into more detail about acoustic wave propagation, device design, and applications of SAW resonators. Similar discussion is continued in Section 2.4, which is devoted to BAW resonators.

2.1 Introduction to Acoustic Wave Resonators

By taking advantage of acoustic-wave propagation, acoustic wave resonators are built. Many kinds of acoustic resonators exist. Musical instruments, for example, amplify the vibration of a string or a shock by using resonant cavities or pipes, like drums, guitars, pianos, and organs do. Thus, the instrument produces sound waves of specific tones regarding the size of the acoustic cavity. Music instruments in which the air vibrates inside the cavity with one opening are known as Helmholtz

resonators [1]. Herein we focus on microelectromechanical acoustic resonators and, more specifically, on piezoelectric-based acoustic resonators.

2.1.1 Acoustic Waves

An acoustic wave is a disturbance in an elastic medium that propagates in space and time, thus transferring the energy supplied by an excitation source along the medium in the form of oscillation or vibration. Acoustic wave propagation entails elastic deformation of the medium along the propagation axis or in other axes as well. In contrast to electromagnetic waves, acoustic waves do require a medium to propagate, and their propagation speeds depend on the mechanical properties of the wave-supporting material. Virtually any material is capable of supporting acoustic wave propagation, including silicon, as we reviewed in Chapter 1. Nevertheless, the piezoelectric properties of certain materials facilitate the wave propagation, thus improving the electromechanical energy conversion, so piezoelectrics are usually chosen as the acoustic layer of many acoustic-wave resonators. Also known as *sound speed*, the acoustic-wave phase velocities are several times slower than those of the electromagnetic wave traveling in the same medium [2].

In a first approach, there exist two types of acoustic waves: surface acoustic waves (SAW) and bulk acoustic waves (BAW). Strictly speaking, a combination of both is normally found in the form of longitudinal, shear, mixed longitudinal-shear Rayleigh waves [3], Love waves [4], or Lamb waves [5], among others. The waves we can see propagating on the surface of a lake after hitting the water mass with a stone illustrate the concept of a SAW. On the other hand, the sound waves traveling through the air until reaching our ears are of the BAW type. In these examples, the water and the air are the propagation media of the SAW and BAW, respectively. Figure 2.1 through Figure 2.4 let us understand the differences between surface—Rayleigh and Love—and bulk—longitudinal and shear—acoustic waves.

As illustrated in Figure 2.1, the surface particles of an isotropic solid move in ellipses in planes normal to the surface and parallel to the direction of the *Rayleigh*

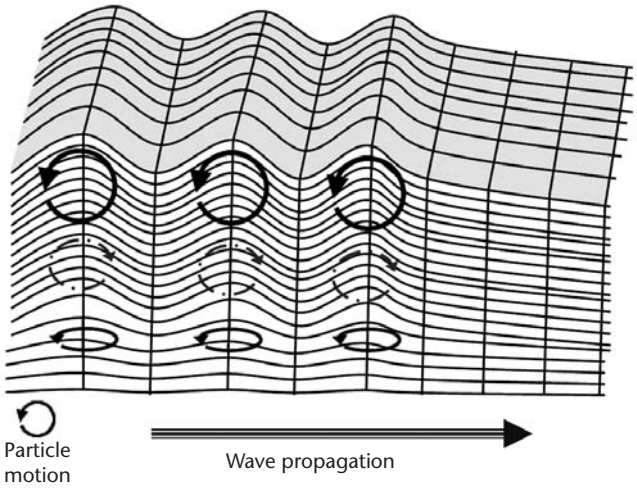

Figure 2.1 Rayleigh wave propagation: the surface particles of an isotropic solid move in ellipses in planes normal to the surface and parallel to the wave direction.

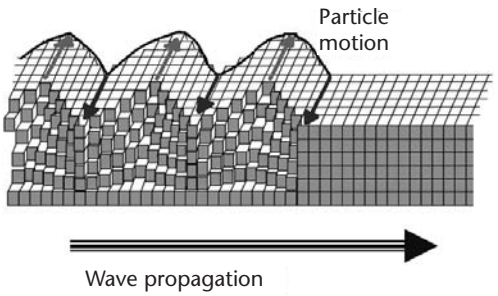

Figure 2.2 Love waves: the surface particles move in horizontal lines perpendicular to the wave propagation.

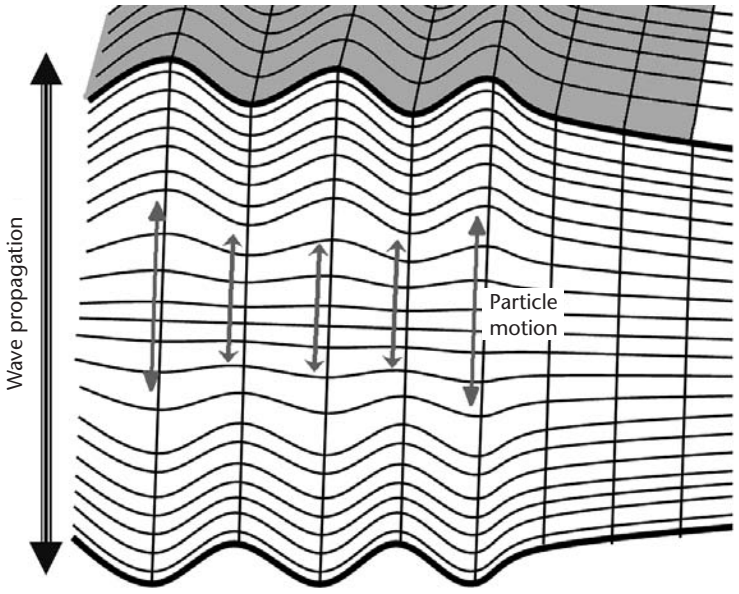

Figure 2.3 Longitudinal-mode waves: the bulk particles oscillate or vibrate in the same axis of the wave propagation.

wave propagation. The particle displacement is significant at a depth of about one wavelength. This motion is retrograde at the surface and thin depths, and becomes prograde at greater depths, as the size of the ellipses is smaller and its eccentricity changes for particles deeper in the material. This behavior was predicted by Lord Rayleigh in 1885, hence its name.

Love waves travel faster than Rayleigh waves. The particle motion of a *Love wave*, depicted in Figure 2.2, forms a horizontal line perpendicular to the direction of propagation, creating horizontally polarized shear waves (SH waves). Moving deeper into the material, motion alternately increases and decreases as one examines deeper layers of particles. The amplitude, or maximum particle motion, decreases rapidly with depth, and it decays with the squared root of the distance traveled by the wave.

On the other hand, bulk acoustic waves are longitudinal, shear-mode, or combination of both. *Longitudinal waves* travel through the medium parallel to the

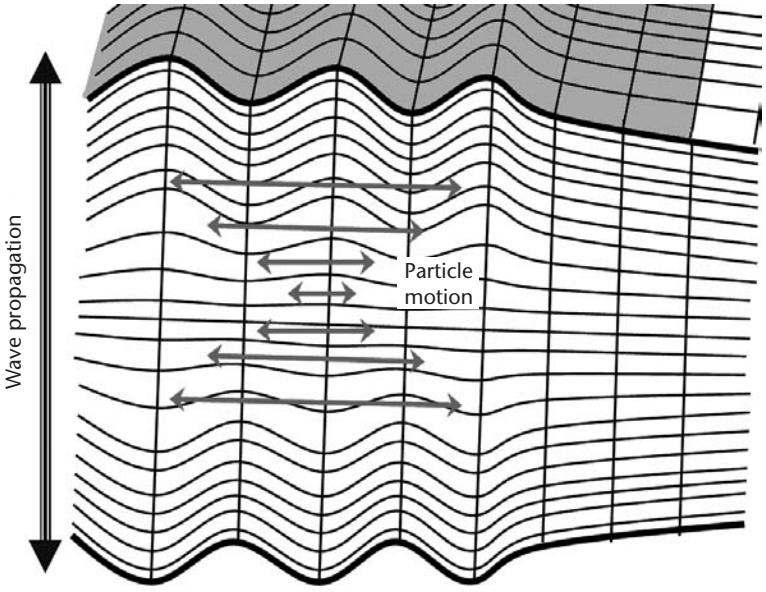

Figure 2.4 Shear or transverse-mode waves: the bulk particles oscillate in the plane perpendicular to the wave propagation and energy transfer.

same axis of the oscillations or vibrations of the particles in the medium; that is, in the same or opposite direction as the motion of the wave as shown in Figure 2.3. Longitudinal mode waves are confined in a resonant cavity, thus displaying a particular standing-wave pattern. The longitudinal modes are reinforced by constructive interference after many reflections from the cavity's reflecting surfaces for wavelengths corresponding to entire fractions of twice the length of the cavity. All other wavelengths experience destructive interference and are suppressed.

While longitudinal modes have a pattern with their nodes located axially along the length of the cavity, transverse modes, with nodes located perpendicular to the axis of the cavity, may also exist. A transverse or *shear-mode* wave propagates and transfers its energy in the direction perpendicular to the oscillations occurring in the medium. If the shear wave moves in the positive x-direction, for example, particles in the medium oscillate in the y-z plane, as represented in Figure 2.4. Shear-mode resonance occurs at longer wavelengths than longitudinal-mode vibrations.

Another type of complex quasi-surface wave is the Lamb waves propagating in solid plates. In this case, particle motion lies in the plane defined by the plate normal and the direction of wave propagation. The mathematical description of Lamb waves is quite complex, and due to its complexity Lamb waves have not been systematically explored in experimental implementations until recently. Similar but still different than Rayleigh waves, they are also often called *Rayleigh-Lamb waves*.

2.1.2 Acoustic Microresonators

Acoustic microresonators are kind of microelectromechanical devices experiencing acoustic wave propagation and eventually vibrating at a resonance frequency related to their dimensions and mechanical properties. In some sense, the resonator

behaves as an acoustic cavity trapping the wave in the medium. To do that, transmission and reflection of the wave are promoted by the appropriate means, such as electrodes and acoustic layer functionally designed of the type and frequency of the acoustic wave. Thus, the amplitude of the wave achieves its maximum when the transmitted and reflected waves have λ, $\lambda/2$, or $\lambda/4$ phase shifting, according to the separation of the electrodes, dimensions of the acoustic layer, and acoustic mode.

To illustrate, let's consider the case of longitudinal waves of wavelength λ propagating along the bulk of a $\lambda/2$-long resonant cavity. Because of the in-phase alignment of the transmitted and reflected waves, the constructive interference between them reinforces the energy inside the cavity. Otherwise, the incident and reflected waves are out of phase, and they are suppressed after destructive interference. This happens not only for the fundamental wavelength λ, but also for the shorter waves of wavelength λ/n equal to an entire fraction n of the fundamental wavelength λ. The sequence of Figure 2.5 depicts the propagation of the first five longitudinal modes through the $\lambda/2$-long resonator.

Silicon and other materials have been used to manufacture acoustic resonators. Nevertheless, the high-frequency requirements of modern systems, the electronic technology evolution imposing the need for miniaturization, and the development of thin-film piezoelectric technologies paved the way to the new generation of thin-film acoustic resonators. In this way, new fabrication processes and materials were developed and thin-film aluminum nitride (AlN) and zinc oxide (ZnO) became the standard for the new kind of SAW and BAW miniature resonators. In the next sections, we concentrate the discussion on these devices and the physics of acoustic wave propagation based on the piezoelectricity theory.

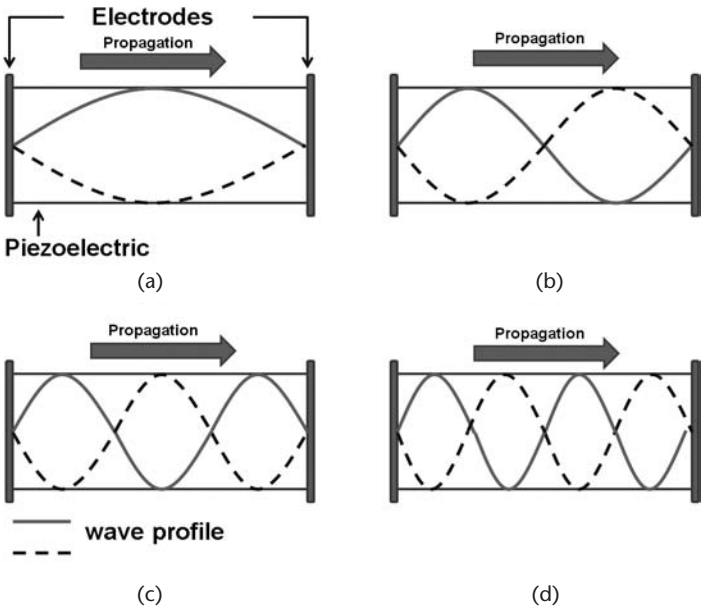

Figure 2.5 (a–d) Propagation of longitudinal-mode waves inside $\lambda/2$ resonators: constructive interference between the incident and reflected waves occurs for waves of length λ/n, where n is an entire number.

2.2 Fundamentals of Piezoelectricity and Acoustic Wave Propagation

Piezoelectricity is the property of some crystalline materials to deform after electric field excitation or, alternatively, to undergo electrical displacement when an external strain is applied to the crystallographic structure. We refer to these properties as the piezoelectric and inverse piezoelectric effects. They promote the medium deformation due to electric potentials or currents, thus easing the wave propagation and its implementation in electronic circuits integrating sensors and/or radio frequency components. Next, the basics of piezoelectricity theory and acoustic wave modes in piezoelectric resonators are examined.

2.2.1 Theory of Piezoelectricity

Piezoelectric materials in commercial application like quartz, AlN, or ZnO are crystalline solids arranged in a polycrystalline structure presenting symmetries on certain axes. At the macroscopic level, they can exhibit orientation in a determined direction due to a poling process. Since piezoelectric ceramics are anisotropic, their physical constants—elasticity, permittivity, and so on—are tensor quantities. For this reason, the study of piezoelectricity theory starts with previous definition of a reference system of coordinates.

The constants are generally expressed with two subscript indices. The first index refers to the axis of the excitation and the second one to that of the actuation. These variables are in the mechanical (stress or strain) and electrical (electric displacement or electric field) domains. We can define the crystallographic axes by using the notation of a Cartesian rectangular system, where we usually choose the direction of positive polarization to coincide with the *Z*-axis of a Cartesian rectangular system, as Figure 2.6 depicts. Directions of *X*, *Y*, and *Z* are represented by 1, 2, and 3, respectively, whereas the shear about these axes is done by 4, 5, and 6, respectively. In crystallography, the natural coordinate system is provided by the dimensions of the unitary crystal cell, denominated by the letters *a*, *b*, and *c*. Thus, we choose *X*, *Y*, and *Z* to coincide with the natural axes of the crystal *a*, *b*, and *c*, respectively.

In longitudinal-mode resonators, the electric field is applied in the direction of the *Z*-axis ("3"), thus coinciding with the preferred crystal orientation (*c*-axis), and, due to the electric field, the crystal will experience strain/stress in the *Z*-axis ("3"), too.

As stated before, the sound speed is some orders of magnitudes less than the electromagnetic-wave propagation speed. This is the case of piezoelectric materials,

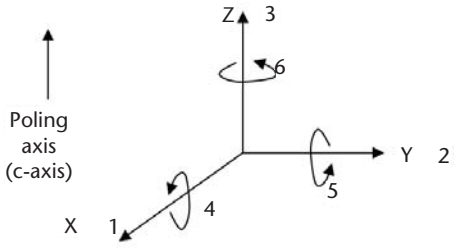

Figure 2.6 Axes convention and directions of deformation.

where the acoustic wave is about five times slower than electromagnetic waves. For this reason, the quasi-electrostatic approximation is enough to describe the wave propagation in piezoelectric materials, as the magnetic effects are neglected in the analysis. Thus, the description of piezoelectricity couples the equations of linear elasticity with the charge equation of electrostatics through the piezoelectric constants of the crystal. Due to the domain coupling, the electric variables are only quasi-static, as previously commented, and the formulation of the mutual relationship between the quasi-static electric field and the applied mechanical stress is:

$$\begin{aligned} T_{6\times1} &= c^{E}_{6\times6} \cdot S_{6\times1} - e_{6\times3} \cdot E_{3\times1} \\ D_{3\times1} &= e_{3\times6} \cdot S_{6\times1} - \varepsilon^{S}_{3\times3} \cdot E_{3\times1} \end{aligned} \tag{2.1}$$

This is known as the stress-charge form of the piezoelectric equations, where T is the stress matrix, S is the strain matrix describing the deformation of the crystal, c is the stiffness matrix, e is the piezoelectric constant matrix, E is the electric field applied to the resonator, D is the electric density displacement matrix, and ε is the permittivity matrix of the piezoelectric material [6]. The super-indices in the c and ε matrices point out that they are evaluated at constant electric field and strain, respectively.

Alternate forms of the constitutive equations describe in an equivalent fashion the electromechanical coupling. A certain equation of the group is employed depending on the boundary conditions that more easily simplify the description of the system. The strain-charge form is:

$$\begin{aligned} S_{6\times1} &= s^{E}_{6\times6} \cdot T_{6\times1} + d_{6\times3} \cdot E_{3\times1} \\ D_{3\times1} &= d_{3\times6} \cdot T_{6\times1} + \varepsilon^{T}_{3\times3} \cdot E_{3\times1} \end{aligned} \tag{2.2}$$

The strain-voltage form is:

$$\begin{aligned} S_{6\times1} &= s^{D}_{6\times6} \cdot T_{6\times1} + g_{6\times3} \cdot D_{3\times1} \\ E_{3\times1} &= -g_{3\times6} \cdot T_{6\times1} + \beta^{T}_{3\times3} \cdot D_{3\times1} \end{aligned} \tag{2.3}$$

The stress-voltage form is:

$$\begin{aligned} T_{6\times1} &= c^{D}_{6\times6} \cdot S_{6\times1} - h_{6\times3} \cdot D_{3\times1} \\ E_{3\times1} &= -h_{3\times6} \cdot S_{6\times1} - \beta^{S}_{3\times3} \cdot D_{3\times1} \end{aligned} \tag{2.4}$$

where s is the compliance matrix (reciprocal of the stiffness matrix), β is the inverse matrix of permittivity, and d, g, and h are the alternate forms of piezoelectric constants. Although (2.1) to (2.4) are exact, some of the right-hand variables simplify to zero upon certain boundary conditions, greatly simplifying the analysis and implementation.

One can pass from one description to another one by rewriting the stiffness, compliance, and piezoelectric constant matrices. This latter, for example, can be restated to their corresponding alternate form by the relations:

$$\begin{aligned} e &= dc^E \quad d = \varepsilon^T g \\ g &= \beta^T d \quad h = gc^D \end{aligned} \tag{2.5}$$

In the next section, some vibration modes are analyzed in the light of these equations. There we will see how the specific boundary conditions of the system make some variables vanish, thus simplifying the formulation of electromechanical coupling.

2.2.2 Excitation and Vibration Mode Description

In Section 2.1.1, acoustic wave propagation was introduced. Now, a more rigorous analysis of different excitation and vibration modes of acoustic resonators can be carried out, by using the constitutive equations studied in the previous section. Following, we revise some of the most representative vibration modes, their boundary conditions, and simplified equations resulting from the analysis of a specific excitation mode.

Acoustic resonances are high-order modes often denoted with the nomenclature of the excitation-actuation axes, instead of designating them in the mode-sequence manner of fundamental and first modes of electromechanical resonators. For example, excitation in the vertical axis (3), leading to strain in the same axis, is referred to as the "33" mode of the resonator (one could erroneously think that this is the 33rd-order mode). The crystal poling also gives a reference for defining the excitation axis. The schemas of Figure 2.7 illustrate the excitation-wave propagation notations of four configurations:

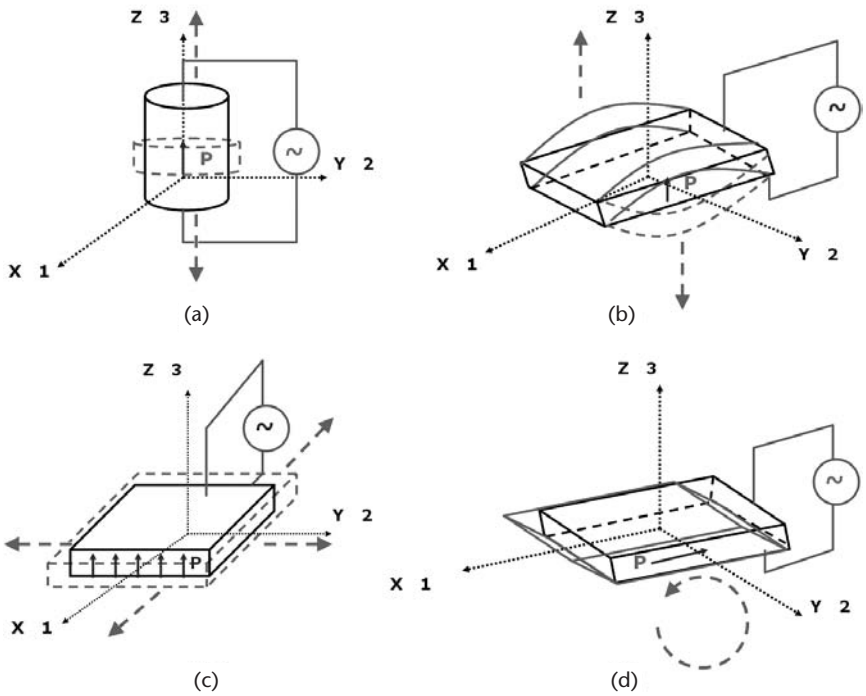

Figure 2.7 Vibration modes of acoustic resonators: (a) longitudinal ("33" mode); (b) extensional ("31" mode); (c) thickness-transversal ("31" shear mode); and (d) lateral-shear ("15" mode).

- Thickness excitation of the thickness vibration ("33" longitudinal mode);
- Thickness excitation of the extensional vibration ("31" flexural mode);
- Thickness excitation of the transversal vibration ("31" shear mode);
- Lateral excitation of the shear-mode vibration ("15" shear mode).

The poling axis, P in the figures, determines the wave propagation. The reference axes are considered according to this, as in the 15-shear-mode vibration of Figure 2.7(d), where the poling axis is along the one-axis orientation (despite the electric field is applied along the three-axis).

The boundary conditions of these resonator configurations simplify the constitutive equations of (2.1) to (2.4), easing the implementation of models and calculations. Considering the longitudinal-mode resonator of Figure 2.7(a), the electric field E_3 and mechanical stress T_3 applied in the three-axis generate electrical displacement D_3 and mechanical strain S_3. With these conditions, using the strain-charge form of (2.2) is very convenient:

$$\begin{bmatrix} S_1 \\ S_2 \\ S_3 \\ S_4 \\ S_5 \\ S_6 \end{bmatrix} = \begin{bmatrix} s_{11}^E & \cdot & \cdot & \cdot & \cdot & \cdot \\ \cdot & s_{22}^E & \cdot & \cdot & \cdot & \cdot \\ \cdot & \cdot & s_{33}^E & \cdot & \cdot & \cdot \\ \cdot & \cdot & \cdot & s_{44}^E & \cdot & \cdot \\ \cdot & \cdot & \cdot & \cdot & s_{55}^E & \cdot \\ \cdot & \cdot & \cdot & \cdot & \cdot & s_{66}^E \end{bmatrix} \cdot \begin{bmatrix} 0 \\ 0 \\ T_3 \\ 0 \\ 0 \\ 0 \end{bmatrix} + \begin{bmatrix} d_{11} & \cdot & \cdot \\ d_{21} & d_{22} & \cdot \\ d_{31} & d_{32} & d_{33} \\ \cdot & \cdot & \cdot \\ \cdot & \cdot & \cdot \\ d_{61} & \cdot & \cdot \end{bmatrix} \cdot \begin{bmatrix} 0 \\ 0 \\ E_3 \end{bmatrix}$$

$$\begin{bmatrix} D_1 \\ D_2 \\ D_3 \end{bmatrix} = \begin{bmatrix} d_{11} & \cdot & \cdot \\ d_{21} & d_{22} & \cdot \\ d_{31} & d_{32} & d_{33} \\ \cdot & \cdot & \cdot \\ \cdot & \cdot & \cdot \\ d_{61} & \cdot & \cdot \end{bmatrix} \cdot \begin{bmatrix} 0 \\ 0 \\ T_3 \\ 0 \\ 0 \\ 0 \end{bmatrix} + \begin{bmatrix} \varepsilon_{11}^T & \cdot & \cdot \\ \cdot & \varepsilon_{22}^T & \cdot \\ \cdot & \cdot & \varepsilon_{33}^T \end{bmatrix} \cdot \begin{bmatrix} 0 \\ 0 \\ E_3 \end{bmatrix} \tag{2.6}$$

In a more compact representation, (2.6) simplifies to:

$$\begin{aligned} S_3 &= s_{33}^E \cdot T_3 + d_{33} \cdot E_3 \\ D_3 &= d_{33} \cdot T_3 + \varepsilon_{33}^T \cdot E_3 \end{aligned} \tag{2.7}$$

This shows that we need to know only a reduced set of elastic, dielectric, and piezoelectric constants if some restrictions are imposed to the system. Analog procedure is carried out to analyze and simplify the description of the thickness-transversal "31" mode of the plate in Figure 2.7(b). The electric field E_3 and mechanical stress T_1 applied in the three-axis and one-axis directions, respectively, generate electrical displacement D_3 and mechanical strain S_1, in the three-axis and one-axis directions, respectively, thus simplifying (2.2) to:

$$\begin{aligned} S_1 &= s_{11}^E \cdot T_1 + d_{31} \cdot E_3 \\ D_3 &= d_{31} \cdot T_1 + \varepsilon_{33}^T \cdot E_3 \end{aligned} \tag{2.8}$$

Transversal and lateral modes are promoted in SAW resonators, and longitudinal and shear modes are usually excited in BAW resonators. Of course, due to process and design issues, spurious generation of nondesired modes can also occur. However, assuming that the preferred crystal orientations and excited modes are the expected, the piezoelectric, elastic, and dielectric constants of (2.1) to (2.8) can be used to characterize the electromechanical performance of the piezoelectric, as we will study in Chapter 5. Actually, a SAW resonator can be used as a test structure in order to extract the material constants of the piezoelectric layer employed in a BAW resonator. In the next section, the principles, design, and applications of SAW resonators are revisited.

2.3 Surface Acoustic Wave (SAW) Resonators

SAW resonators exploit SAW propagation and electromechanical transduction to implement electronic circuits as filters, oscillators, and sensors. The transduction is performed by two or more metallic electrodes and a piezoelectric layer, and, typically, wave propagation SAW resonators of the Rayleigh or leaky-SAW types [7]. A SAW resonator is basically a resonant cavity in which a first transducer electrode converts the electric signal into a lateral mechanical wave. The resulting SAW propagates on the piezoelectric to reach the second electrode, where it is transduced back into the electrical domain. When arriving at the second electrode, and typically aided by one or more reflector electrodes, the acoustic wave bounces back in the direction of the first electrode, and the electromechanical conversion is repeated indefinitely, as depicted in Figure 2.8. Thus, the acoustic wave is trapped in the cavity formed by the resonator electrodes.

The electrodes are one or more interdigitated transducers (IDTs) being fabricated by state-of-the-art photolithography techniques. Many piezoelectric crystals and ceramics have been implemented in the fabrication of SAW resonators, like quartz, lithium niobate, lithium tantalate, lanthanum gallium silicate (langasite-LGS), lead zirconate titanate (PZT), and, more recently, AlN and ZnO. Because of its low temperature drifting, quartz has been preferred to other materials and, to date, it dominates the high-accuracy SAW-resonator implementations.

The available photolithography resolution limiting the dimensions of the IDTs and the piezoelectric layer determine the maximum operating frequency of the fundamental mode of the resonator. However, as well as other electromechanical resonators, SAW devices can be operated at over-tone modes to bypass near-to-fundamental bulk or other resonance modes. Typical frequencies for SAW-resonator-based applications are in the UHF band below 1 GHz, although high-performance commercial devices in the 1.5-GHz GPS and 1.9-GHz PCS bands are available so far [8, 9]. The fundamental frequency of the SAW resonator mainly depends on the pitch of the IDTs, which is chosen to be equal to the SAW wavelength λ, and the sound speed of the piezoelectric layer v:

$$f_0 = \frac{v}{\lambda} \tag{2.9}$$

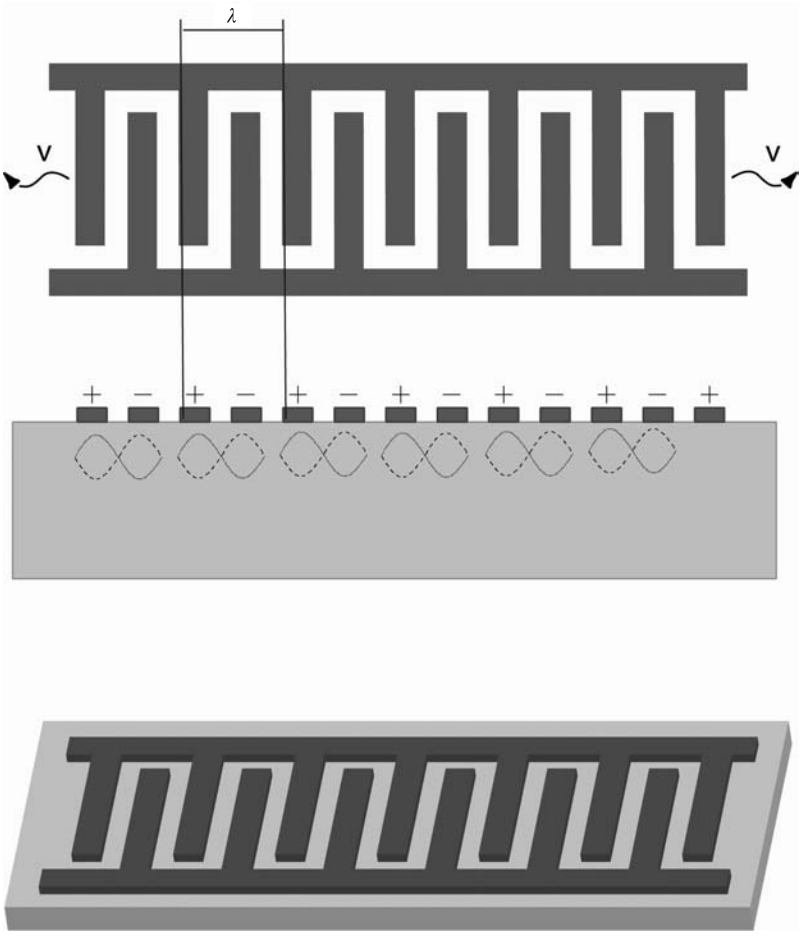

Figure 2.8 Surface acoustic wave (SAW) resonator.

Other aspects influence the final performance of the resonator, like the cavity and reflector grating design. To date, many companies fabricate SAW resonators, some of the major manufacturers being Epson Toyocom Corporation [10], Epcos AG [11], Murata Corporation [12], Fujitsu Corp. [13], Hitachi Corp. [14], Samsung [15], and NEC Corp. [16]. Commercial resonators exhibit low insertion losses, which make them ideal for high-performance radio frequency applications. Besides, they are relatively simple to fabricate because no micromachining techniques are required, although standard photolithography techniques have imposed a 3-GHz limit on SAW device fabrication (which will be overcome with leading-edge photolithography at sure). Through the years, design and fabrication of SAW resonators have been improved to achieve better application performance and device efficiency. In the following, we discuss the basic topics of SAW resonator design.

2.3.1 One-Port and Two-Port Configurations

SAW resonators are found in two types of port configurations: one-port and two-port resonators. One-port resonators are two-terminal devices, and they find

application in oscillator circuits like VCOs or Colpitts oscillators. Two-port resonators behave more like narrow bandpass filters. One-port SAW resonators have a single IDT generating and receiving the SAW, and two grating reflectors, which reflect the SAW and generate a standing wave between the two reflectors. The IDT and reflectors are fabricated on quartz crystal substrate or another piezoelectric material and patterned by photolithographic processes [17]. The IDT, input and output ports, and reflectors of a one-port resonator are depicted in Figure 2.9. The SAW escapes out from the IDT fingers and is picked back to them through the reflectors.

On the other hand, two-port SAW resonators exhibit two IDTs, one of them generating the SAW, and the second one picking it. As with one-port devices, two grating reflectors aid the SAW to be reflected and confined between the IDTs. The generic connections to the first and second IDTs, their layout, and their placement between the reflectors are drawn in Figure 2.10.

One-port SAW resonators can be of the synchronous or the nonsynchronous type, while many configurations of the two-port SAW resonator exist. Examples of the two-port type are the synchronous single pole, the single-phase unidirectional transducer (SPUDT), the proximity-coupled resonator, and the withdrawal-weighted-reflector resonator. The different configurations attempt to balance design, cost and manufacturability, and performance issues [18]. To illustrate, Figures 2.11(a) and 2.11(b) depict one-port resonators of both synchronous and nonsynchronous types, respectively, and a two-port proximity-coupled resonator is drawn in Figure 2.11(c).

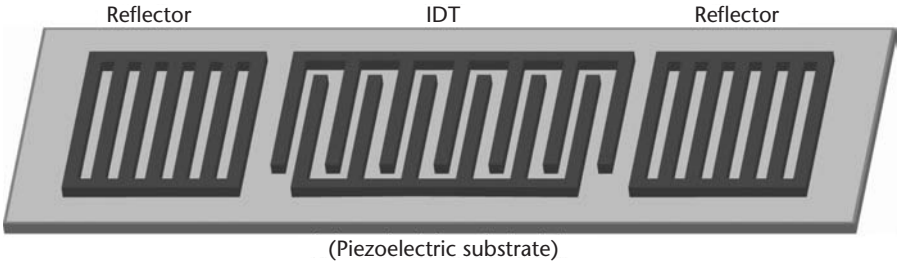

Figure 2.9 One-port SAW resonator.

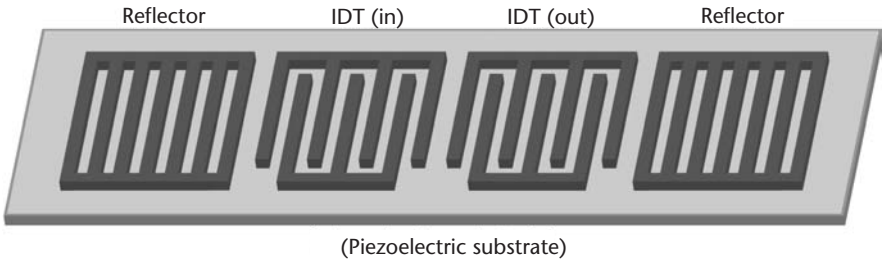

Figure 2.10 Two-port SAW resonator.

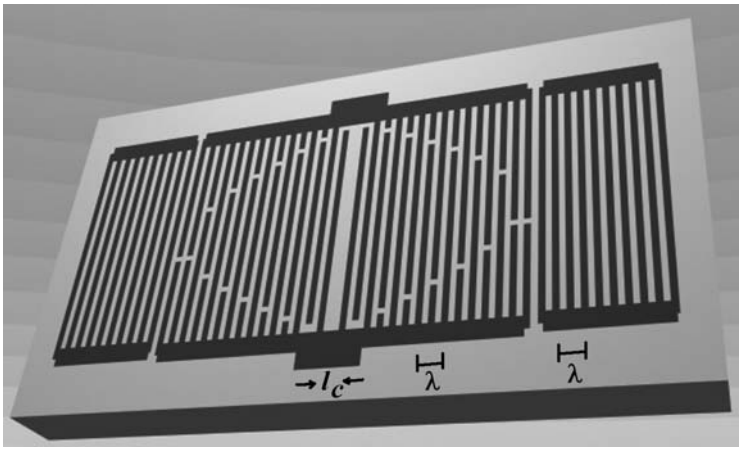

(a)

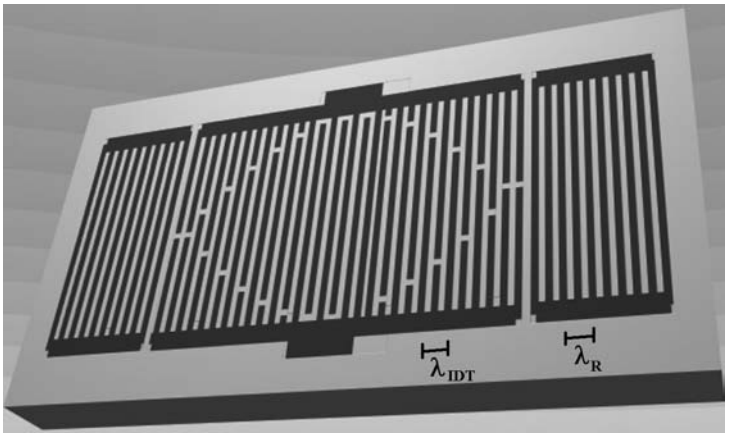

(b)

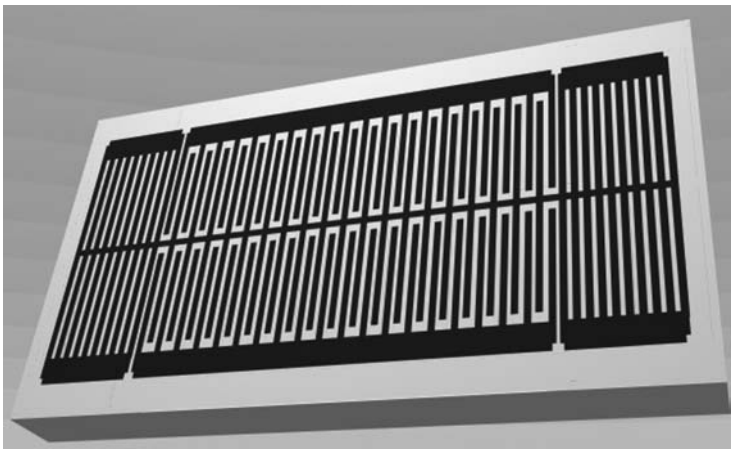

(c)

Figure 2.11 One-port and two-port configurations: (a) synchronous (one-port); (b) nonsynchronous (one-port); and (c) proximity-coupled (two-port). (Figure based on designs of P. V. Wright.)

2.3.2 SAW Resonator Design

The design parameters of SAW resonators are, essentially: (1) the IDT and grating periods; and (2) the width of the cavity and the total beam width of the IDTs and grating. The IDT period λ_{IDT} controls the resonance frequency, while the reflector grating period λ_R determines the total reflectivity (and thus the energy concentration in the center of the IDT region). The resonant cavity width l_C also plays a role in the frequency response. We can consider the next cases:

1. The one-port synchronous, with equal λ_{IDT} and λ_R values, and l_C equal to

$$l_C = \frac{(2n+1)\lambda}{4} \tag{2.10}$$

   where n is an integer, and λ equals λ_{IDT}. The advantages of this configuration are that, due to the periodicity of the structure ($\lambda_{IDT} = \lambda_R$), the resonance frequency does not depend on the reflectivity of the electrodes and the manufacturability yield is high. However, this is achieved at the cost of higher insertion losses or, equivalently, having increased die area: the number of fingers in both the IDT and grating has to be increased to make the overall beam wider, thus diminishing the insertion losses.
2. The one-port nonsynchronous, with different λ_{IDT} and λ_R values. In addition, the cavity width is no longer that of (2.10). In this case, the resonance frequency depends on the reflectivity of the electrodes and the conductance can be enhanced, which allows controlling the insertion losses at the cost of manufacturability.
3. Two-port designs, in which we control the frequency stability and introduce multiple poles in the frequency response through the cavity design, the symmetry between the first and second IDTs, the grating finger design, and coupled-resonator designs. The transducer electrodes are apodized in both one-port and two-port SAW resonators in order to suppress transverse modes. Thus, the apodizing strategy is also a design parameter of the frequency response. For a complete and rigorous guide on SAW resonator, the designer should consult the work of P. V. Wright [18–21].

So far, we have considered that the resonator operates at the SAW fundamental frequency predicted by (2.9). Nevertheless, they can also work at selected harmonic frequencies, depending on the IDT metallization ratio $\eta = a/b$. Thus, the SAW operates at only odd or odd and even harmonic frequencies [22]. Figure 2.12 shows some examples of modified IDTs for fundamental and harmonic frequency operation.

The role of novel quartz-cutting angles and the new materials employed in SAW device fabrication has been increasing the performance and resonance frequency of SAW resonators as well. For example, Epson-Toyocom developed a 2.5-GHz resonator with 6-dB insertion losses and high-frequency stability, by using a novel ST-cut quartz technique [23].

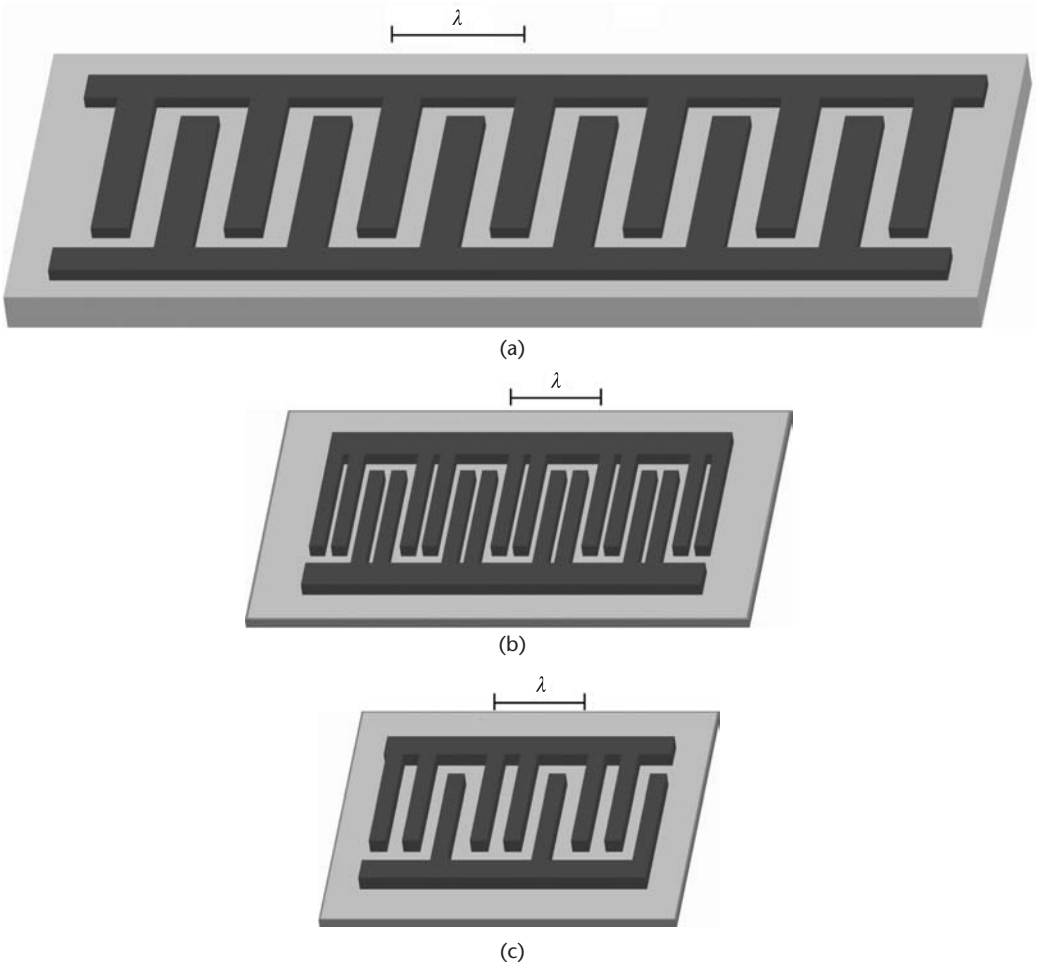

Figure 2.12 SAW IDT structures for fundamental and harmonic frequency operation: (a) solid electrode (odd-harmonic); (b) split electrode (odd-harmonic); and (c) three-electrode IDT (odd-even harmonic).

2.3.3 SAW Applications

SAW resonators have been a commercial success on radio frequency applications, especially for filter and oscillator implementations. Their impact has made possible considerable reductions in size and power of the chipsets of mobile devices [24, 25]. More modest, but also important, has been the impact of SAW resonators in mass detector and pressure sensor devices, with application in bioparticle detection [26, 27]. A detailed discussion on both RF and sensor applications is carried out in Chapters 8 and 9, respectively.

2.4 Bulk Acoustic Wave Resonators

Bulk acoustic wave (BAW) resonators are boosting the reduction in size and power consumption of mobile radio equipment experienced by the telecommunication industry during the past few years. Due to their commercial success, the motivation

for developing new, integrated applications based on BAW devices has caught the attention of many industry and academic research groups all over the world. Nowadays, this interest comes not only from the telecom industry, but also from sensing-application companies. Keeping both features in mind—CMOS integration and new applications—the implication is that BAW fabrication processes should be successful in producing high-quality devices and, at the same time, integrating them with standard CMOS technologies. This section focuses on introducing the key concepts and state-of-the-art technologies related to BAWs, ideas that will be further developed later in the book.

2.4.1 Acoustic Wave Propagation in BAW Devices

BAW devices experience acoustic wave propagation through the bulk of its active layer structure, hence their name (Figure 2.13). This feature differentiates BAW and surface acoustic wave (SAW) devices, the acoustic waves propagating in longitudinal or shear-transversal modes. In both cases, the acoustic wave causes deformation of the active layer, which is typically a piezoelectric material made with a thin-film technology. As in SAW resonators, piezoelectric and the inverse piezoelectric effects are the actuation and detection mechanisms involved in BAW device operation. According to these principles, a voltage applied to the resonator's electrodes induces strain of the acoustic layer and vice versa, after a mechanical strain of the acoustic layer a voltage can be read out the electrodes.

Another difference between BAW and SAW devices is their physical layout. In BAW, the acoustic layer is a component element of a stacked structure in which the acoustic wave is confined. A couple of metal layers acting as electrodes complete the structure of BAW resonators. Therefore, the BAW device is fabricated on top of a carrying substrate, typically silicon, and the acoustic layer and electrodes are located on top of said substrate. In SAW, the acoustic layer may be the carrying substrate by itself, and the IDT electrodes are located on top of it, both in the same plane. Typical operation frequencies for SAW range from 30 MHz to 1 GHz, while the central frequency of BAW can be found in the 1- to 10-GHz band (typical: 2 GHz). For both technologies, however, the value of the central frequency or the frequency-band range might be extended depending on the operating resonant mode—fundamental or overtone—and the available fabrication technologies [28].

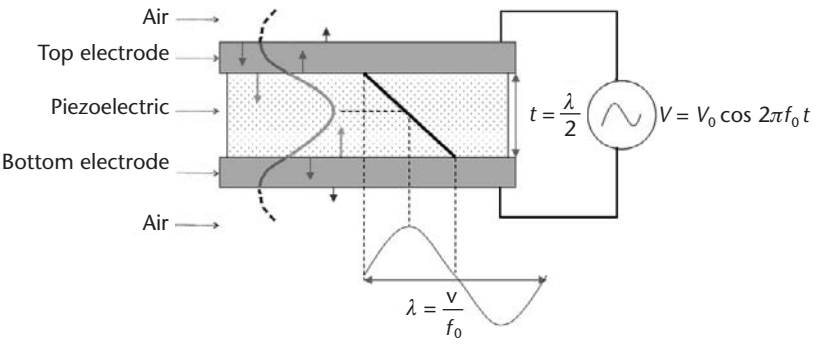

Figure 2.13 Acoustic-wave propagation in BAW resonators.

The resonance frequency of a BAW resonator operating in fundamental, longitudinal mode is mainly determined by the thickness t of the acoustic layer from [29]:

$$\theta = \frac{2\pi f_0 t}{v} \tag{2.11}$$

In (2.11), θ, v, and f are the phase, sound velocity, and frequency of the acoustic wave propagating through the bulk of the acoustic layer, and t is the thickness of the thin film. At resonance ($f = f_0$), the acoustic phase in the film is $\theta = \pi$. Under these conditions, and solving f in (2.11), it leads to:

$$f_0 = \frac{v}{2t} \tag{2.12}$$

This result is equivalent to saying that the thickness of the thin film is equal to half the wavelength of the acoustic wave for the first longitudinal resonance mode. However, in an electrode-piezoelectric-electrode resonator, the electrodes' contribution to this equation must also be accounted for, since their added thickness reduces the resonance frequency [30]. Looking at Figure 2.13, t must be half a wavelength of the acoustic wave, in order to confine the energy between the electrodes. At resonance, this energy is magnified by the quality factor Q of the device. The mechanism is illustrated in Figure 2.14(a). Due to the piezoelectric effect, an electric

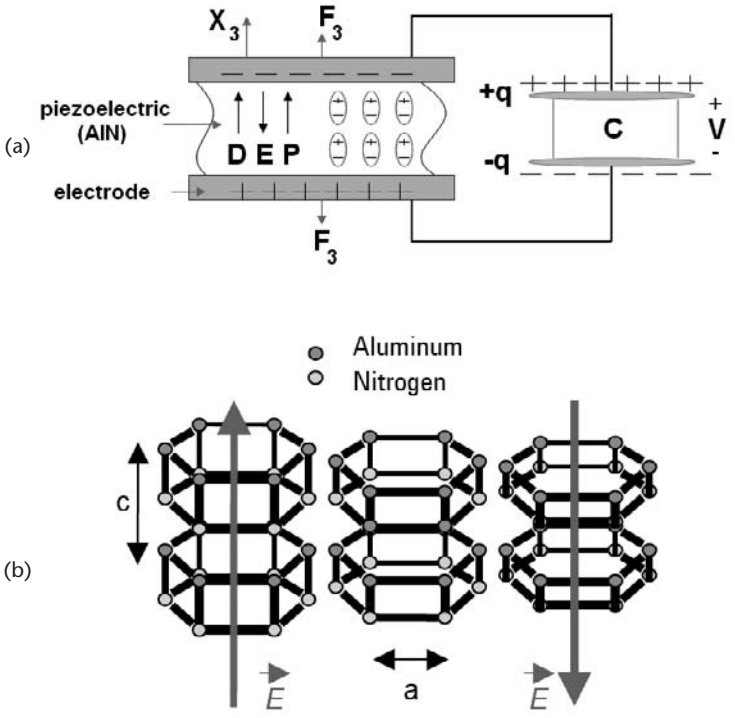

Figure 2.14 (a) Electric charge displacement and poling in a BAW resonator due to an electric potential applied to its electrodes, and (b) deformation of the crystal structure after electric fields of opposite magnitudes induced in the c-axis. (© 2001 Agilent Technologies [31].)

potential V applied to the electrodes of the resonator induces an electric field E and an electric density displacement D in the poling axis of the crystallographic structure, also referred to as the *c-axis* in Figure 2.14(b). Also observed in the figure, the crystal suffers from mechanical deformation in the axis of the electric field. Nevertheless, strain in other directions may occur, depending on the crystal orientation and resonance mode. Extensional and shear-mode resonances are two examples of different operating modes of the device.

The constitutive equation (2.7) previously described explains this mechanism for longitudinal-mode BAW resonators. As it will have been noticed, design parameters and physical behavior of BAW devices are completely different from those of SAW devices, in which the resonance frequency is a layout-design function of the interdigitated transducers. At the manufacturing level, these differences translate into more complex processes for the BAW device case, because acoustical isolation between the resonator and the substrate should be provided by some means.

Among BAW, we find two kinds of devices, namely, thin-film bulk acoustic wave resonators (FBAR) and solidly mounted resonators (SMR) [32]. The operation and physical principles of FBAR and SMR are the same, the only difference being the fabrication technology providing the acoustical isolation mentioned earlier.

Both kinds of BAW are a metal-piezoelectric-metal stack of materials. However, the FBAR exhibits a micromachined air gap to reduce the electromechanical coupling to the carrying substrate, while the SMR device implements an array of reflecting materials, known as a reflecting mirror or Bragg's reflector [33] (Figure 2.15). Careful selection of the mirror materials and configuration guarantees full impedance mismatching and improved isolation between the SMR and the substrate [28]. In both FBAR and SMR, the purpose of the acoustical isolation is to obtain a high-quality factor resonator.

2.4.2 Thin-Film Bulk Acoustic Wave Resonators (FBAR)

The first FBAR device was disclosed by Lakin and Wang in 1981 [29]. Micromachining of the FBAR takes advantage of well-established technologies and processes largely implemented in microelectromechanical systems (MEMS) and CMOS processes.

Concerning technological aspects, fabrication technologies and processes are the most described matter in FBAR devices. Key points in describing the FBAR technology are the piezoelectric-layer deposition process, the FBAR-stack configuration, and the micromachining implementation to obtain a high-quality factor device.

The piezoelectric layer composing modern FBAR devices is usually made of aluminum nitride (AlN), zinc oxide (ZnO), or lead zirconate titanate (PZT). Other materials like magnesium zinc oxide (MgxZn1-xO) or lanthanum gallium silicate (langasite - LGS) are currently being explored as well [34, 35]. Its electromechanical and piezoelectric properties, and the possibility of CMOS compatibility, have made AlN the preferred material for FBAR implementation. According to Table 2.1 and (2.12), the high acoustic wave velocity of AlN allows handy fabrication of a typical device to resonate in the gigahertz range, for a thin-film thickness in the order of few

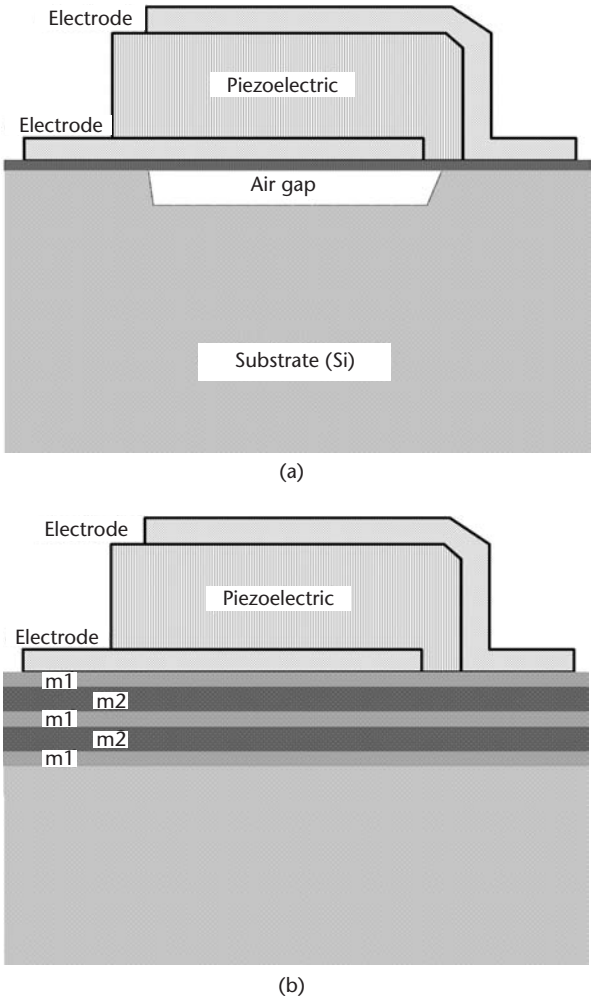

Figure 2.15 Stacked structure of BAW devices with acoustical isolation provided by: (a) a micromachined air gap (FBAR), and (b) a Bragg reflector (SMR).

microns or less. This feature makes FBARs known as "thin-film" devices. Table 2.1 compares the main properties of AlN and some piezoelectric materials.

The deposition technique of the piezoelectric layer is another important aspect influencing the performance of FBARs. Common fabrication techniques for achiev-

Table 2.1 Electromechanical Properties of Some Piezoelectric Materials

Material	*Density (kg/m^3)*	*Dielectric Constant*	*Acoustic Velocity (m/s)*	*Acoustic Impedance (10^6 kg/m^2s)*	*Acoustic Coupling*	*Acoustic Loss dB/μs at 1 GHz*
AlN	3,270	8.5	10,400	34.0	0.17	~5
ZnO	5,680	8.8	6,330	36.0	0.28	8.3
CdS	4,820	9.5	4,465	21.5	0.15	>50
$LiNbO_3$	4,640	29	7,320	30.6	0.17	0.5–0.9
$LiTaO_3$	7,450	43	6,160	46.4	0.19	0.8

ing a high-quality piezoelectric layer are radio-frequency sputtering [36–38], epitaxial growth [39], DC sputtering [40], or combination of the same, among others. Additional postprocessing techniques such as annealing of the piezoelectric-deposited wafer may be employed to improve the crystal's quality [41]. Several parameters condition the quality of the piezoelectric layer, some of the most relevant being the deposition technique and the temperature of the substrate. Some deposition techniques like sputtering are compatible with CMOS processes, whereas others like epitaxial growth are unsuitable for CMOS integration due to their processing at high temperatures over 400ºC [39].

Another critical topic influencing the quality of the piezoelectric layer is the substrate on which it is deposited (i.e., the FBAR's bottom electrode). It is well known that some metals lead to better c-axis-oriented crystal structures than others, mainly due to crystallographic compatibility between them and the AlN layer [42, 43]. Molybdenum (Mo), tungsten (W), aluminum (Al), and platinum (Pt) are some of the materials commonly employed in AlN-based FBAR fabrication.

Taking the previously mentioned process parameters into consideration, the crystallographic quality of the AlN is evaluated through atomic force microscopy (AFM) and x-ray diffraction (XRD) characterization, among other techniques. AFM aids in measuring the granularity of the crystal, whereas XRD provides information on the preferred orientation of the crystal. Additional techniques like scanning electron microscopy (SEM) may also help in the visual inspection of the polycrystalline structure of the piezoelectric. The AFM and SEM images of Figure 2.16(a) to Figure 2.16(c) show surface and cross-sectional views of AlN crystals deposited on different substrates. It can be noted how different the AlN's grain quality and the crystal orientation are when deposited under different conditions on Au/Cr [Figure 2.16(b)] and Al [Figure 2.16(c)] substrates [44].

As previously set out, micromachining is needed to release the FBAR, thus providing acoustical isolation between the device and the substrate in order to achieve high-quality factors. The result of the process is a structure with an air gap, a cavity, or a membrane underneath the resonator's structure. Front-side or back-side surface and bulk micromachining are the technological options for device releasing. According to the surface micromachining technique, a sacrificial layer placed in between the substrate and the resonator is attacked by wet etching. Processes implementing germanium [45] and silicon oxide [46] as sacrificial layers for surface micromachining, among others, have been described. On the other hand, bulk micromachining can be implemented through wet or dry etching, either from the front or from the back of the wafer. Different implementations of wet etching of silicon in KOH solutions are presented in [44, 47]. Dry etching of the silicon substrate may also be carried out by using RIE [48] or DRIE [49]. In Figure 2.17, the profiles of FBAR processes using some of these micromachining techniques are illustrated.

Less described is the influence of the electrodes' layout in the FBAR's performance. Some electrode geometries have been demonstrated to suppress or diminish spurious resonance modes better than others [50]. At the same time, the size of the electrodes affects the electrical performance of FBARs [51, 52].

Tuning of FBARs is also of special interest. Due to process deviations or variation of the physical properties of the materials employed in the fabrication, the resonance frequency may be slightly different from that corresponding to the process

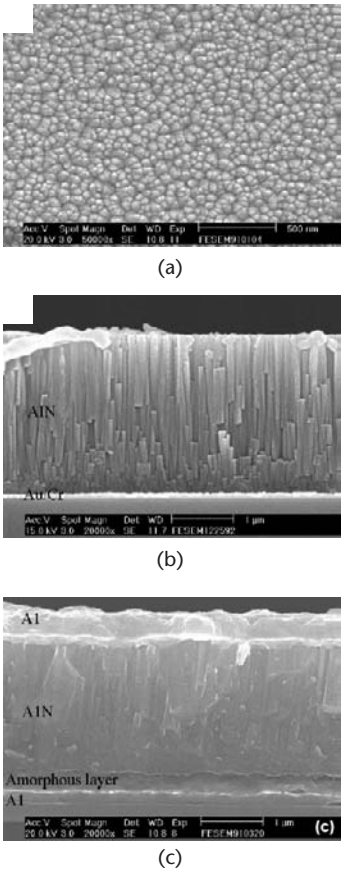

Figure 2.16 Evaluation of the thin-film quality in AlN: SEM image of AlN deposited on Au/Cr substrate, (a) top and (b) cross-sectional views; and (c) cross-sectional SEM of AlN on Al electrode showing amorphous layer and random crystal orientation. (© 2005 Elsevier [44].)

design. Different approaches, such as electrostatic tuning [53] or mass-loading [54, 55], for example, have been conceived in order to change the resonance frequency of FBARs. Related to this topic, the temperature coefficient factor (TCF) of FBARs is also an important factor conditioning the performance of the device, especially for RF applications. Temperature-compensation strategies based on the deposition of an opposite-TCF thin-film material on the FBAR have been studied [56, 57].

2.4.3 Solidly Mounted Resonators (SMR)

The device structure and working principle of SMRs are basically the same as those of FBARs. Instead of the air gap in FBARs, SMR devices implement a stack of $\lambda/4$-thick acoustically mismatched layers, which are placed underneath the resonator to provide acoustic isolation from the substrate, thus ameliorating the Q factor. The $\lambda/4$ thicknesses l_i are the quarter wavelength λ_i of the BAW at the ith layer evaluated at the resonance frequency f_0:

$$l_i = \frac{\lambda_i}{4} \tag{2.13}$$

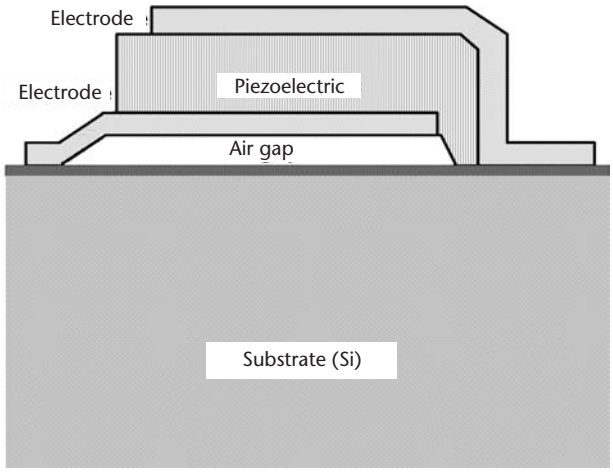

(a)

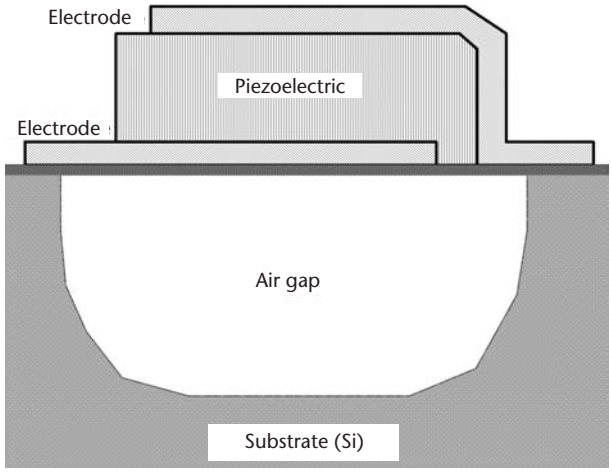

(b)

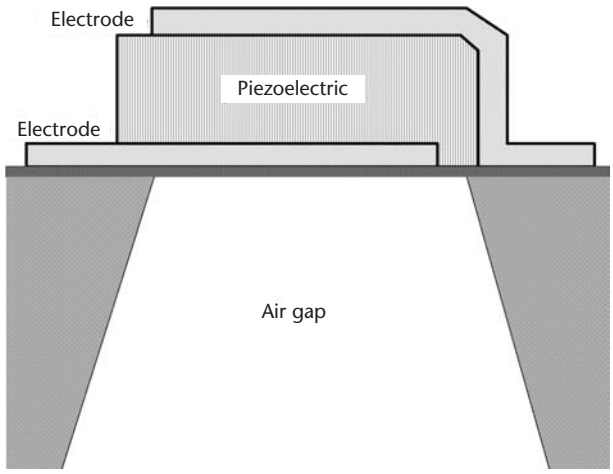

(c)

Figure 2.17 Different micromachining processes for releasing of FBAR: (a) surface, (b) front-side, and (c) back-side bulk micromachining.

$$l_i = \frac{v_i}{4f_0} \tag{2.14}$$

The large acoustic-impedance mismatching between the alternating $\lambda/4$-thick materials causes the BAW to be systematically reflected to the resonator, thus confining the energy in the acoustic layer of the device. For this reason, the stack is called a reflecting mirror, or *Bragg reflector*, after W. L. Bragg. A significant percentage of the BAW is effectively reflected with this method, and the energy of the escaped acoustic wave diminishes with depth along the traveled path down to the substrate. Figure 2.18 illustrates the operation of SMRs.

Typically, the impedance mismatching is achieved by alternating dielectric and conductor materials, with low and high acoustic impedances, respectively. Silicon oxide (SiO_2) and tungsten (W), for example, are two materials commonly employed in SMR implementations. SMRs exhibit good robustness, low stresses, and practically no risk of mechanical damage in dicing and assembly [58]. On the other hand, FBARs exhibit higher Q factors and thermal isolation due to the air gap. However, the Q factor of SMRs can be tailored to achieve design specifications as a function of the number of reflector periods N [28]:

$$Q = \frac{\pi}{4} p_d^s \left(p_h^l\right)^{2N} \left[1 + \frac{p_h^d}{p_h^l - 1}\right] \tag{2.15}$$

where p_d^s is the ratio of acoustic impedances of substrate (s) and piezoelectric (d) layer, p_h^l is the ratio of acoustic impedances of the low-impedance (l) and high-impedance (h) reflector layers, and p_h^d is the ratio of piezoelectric and high-impedance reflector layer. The direct relation between N and Q in (2.15) let us calculate the loaded Q factor (due to acoustic coupling).

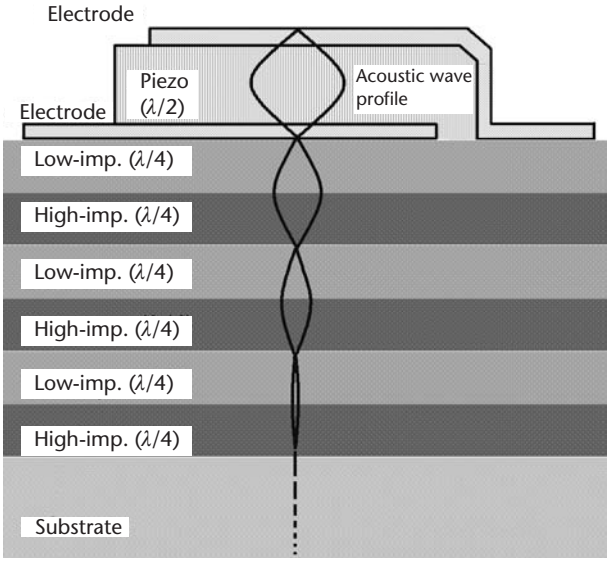

Figure 2.18 Wave propagation through SMRs and the Bragg reflector.

Controlling the Q factor enables the design and fabrication of highly selective filters for radio frequency applications, a field where the SMRs are being vastly exploited. Filter topologies as varied as ladder filters, solidly mounted stacked crystal filters (SCF) [32], and coupled resonator filters (CRF) [59] have been implemented. By implementing a grounded electrode in the middle of the stack, the input and output terminals of SCFs and CRFs are shielded to attain high out-of-band rejection. Figure 2.19 shows both SCF and CRF topologies, where the CRF exhibits additional layers in order to decrease the mechanical coupling between the top and bottom resonators. Because these topologies are based on resonator stacking, SCF and CRF are smaller than ladder filters, offering them competitive advantages in reduced-size mobile applications.

2.4.4 FBAR and SMR Applications

FBAR finds application in a variety of systems ranging from radio frequency (RF) to sensing components. Although the telecommunication industry has been the very first engine stimulating the development of FBAR applications, new sensing

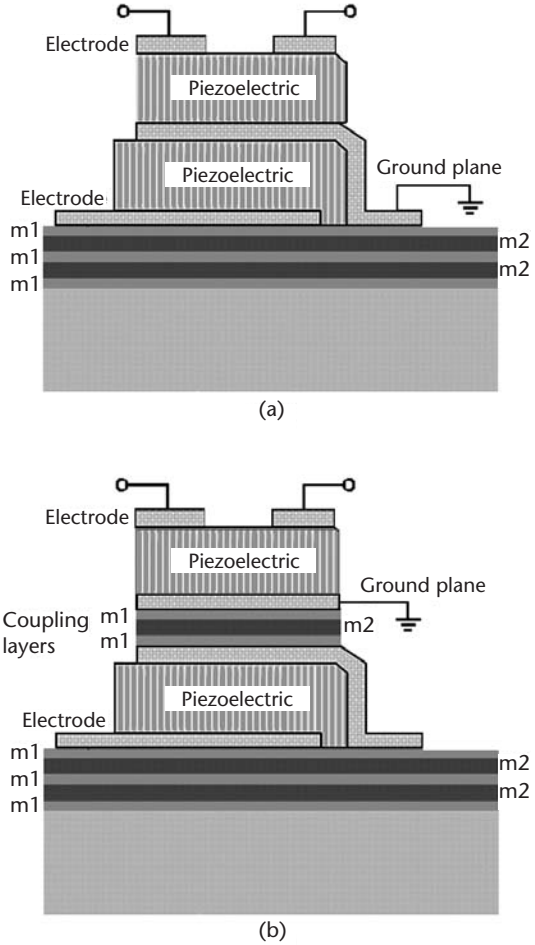

Figure 2.19 SMR-based filters: (a) stacked crystal filter (SCF); and (b) coupled resonator filter (CRF).

applications have been demonstrated in the past few years. This can boost even more the increasing presence and importance of FBARs in the MEMS device and system markets, as reported by independent market forecasting, reproduced here in Figure 2.20 [60]. Nowadays, BAW devices (FBAR+SMR) represent over 90% of the RF MEMS share, which is roughly 10% of the RF MEMS market [61]. The BAW-based duplexer market is expected to grow from 300 million pieces in 2005 to a total demand of well over 900 million pieces in 2010. This represents revenues over $1.5 billion by 2010. At this time, Avago Technologies (FBAR) and TriQuint (SMR) are the major players, with Avago having a market share 60% over of the total BAW device business.

The demanding requirements of emerging third generation (3G) mobile telecommunication systems have justified the search for new RF passive technologies, FBAR among them. All these systems operate in the 2-GHz frequency band, which is the typical FBAR's resonance frequency (fabricated with a 1-μm-thick AlN layer). The first RF applications of FBARs were thus devoted to supply fully passive components, able to compete with SAW and ceramic technologies, such as filters and duplexers. A duplexer is an RF system comprising two filters for simultaneous bidirectional communication, the first one being the transmission (TX) filter and the second one the reception (RX) filter. These components succeeded in offering lower insertion losses, higher out-of-band rejection, and a smaller size than those made with on-the-market technologies [62–67]. Also, FBAR's temperature coefficients are in the order of –20 to –35 ppm/°C, which is less than the typical range of –35 to –94 ppm/°C of SAW devices. An FBAR-duplexer implementation from Agilent Technologies is shown in Figure 2.21, where the six-FBAR layout [Figure 2.21(a)] and demonstration package system with two filter and assembly board [Figure 2.21(b)] are observed [31, 68].

In FBAR-based sensor applications, one or more FBAR devices are the constituent elements of a system operating under piezoelectric actuation or detection mechanisms. Mass sensors and biochemical, liquid, or gas detectors are some examples.

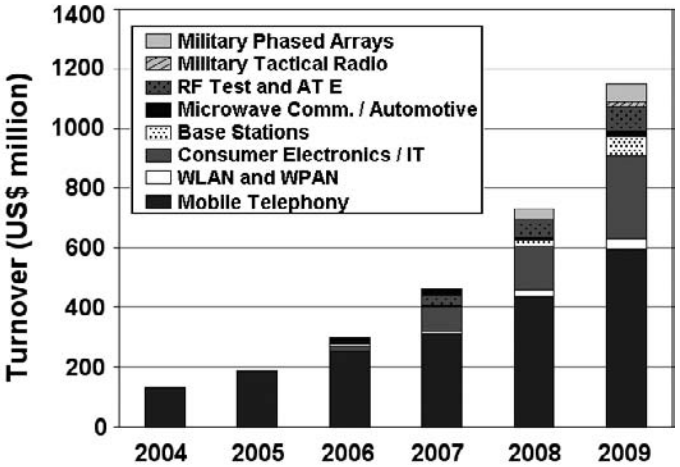

Figure 2.20 RF MEMS market forecasting 2005–2009: nowadays, BAW devices (FBAR+SMR) represent over 90% of the RF MEMS share. (© 2005 WTC [61].)

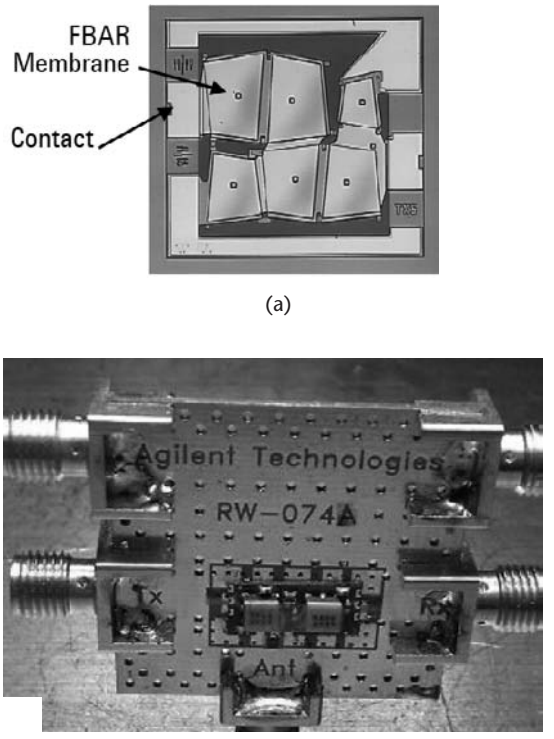

Figure 2.21 Agilent FBAR filter implementation: (a) layout of one of the six-FBAR filters of the duplexer (© 2001 Agilent Technologies [31]); and (b) demo package system comprising TX and RX FBAR-filters, assembly board and connectors (© 2002 Agilent Technologies [68].)

All these applications work under the same principle of quartz crystal microbalances (QCM) [69]: mass loading of the resonator's structure [70].

According to this principle, mass deposition on one of the FBAR electrodes gives rise to down-shifting of the resonance frequency, due to changes on the acoustic-impedance mismatching and consequent phase-shifting of the acoustic wave between the different FBAR-layer interfaces. The performance of mass-loading-based detectors is evaluated through the mass sensitivity [Hz $\times$ cm^2/ng] and the minimum detectable mass [ng/cm^2]. Since the operating environment of the FBAR-based sensor determines its sensitivity and the Q-factor loading, different aspects of the fabrication process and resonance mode are considered. In this way, longitudinal or shear-mode operation is desired, depending on whether the sensing medium is air, gas, or liquid.

The 2-GHz longitudinal-mode-FBAR biosensor system presented by Gabl et al. performs DNA and protein detection operating in a liquid environment [71]. An improved shear-mode FBAR version of the biodetection system was also implemented by the same group. In this case, the sensor performance ruled by the smallest detectable mass attachment is already better (2.3 ng/cm^2) than that of QCMs [72]. Another electro-acoustic chemical sensor based on FBAR detected low concentrations of the analyte upon exposure to H_2, CO, and ethanol, with a fast and repeat-

able response [73]. An FBAR mass sensor at its tip, inserted into biological and chemical environments to sense various chemical-bio species, has been shown to detect mercury ions in water [74]. Optical images of the sensor and schematic of the operating principle are shown in Figure 2.22.

Based on the same metal-piezoelectric-metal structure and process of the FBAR, but operating at nonlongitudinal resonance modes, different kinds of applications have recently appeared. For example, mechanically coupled contour-mode MEMS filters using a thin-film AlN process have been demonstrated. The use of contour modes whose frequencies are set by lithographically defined dimensions permits the cofabrication of multiple filters at arbitrary frequencies on the same chip, with the filters having center frequencies of 40 and 100 MHz [75]. Also, a resonant mass sensor that is based on a lateral extensional mode (LEM) ZnO resonator and has a minimum detectable mass (MDM) of 10^{-15}g in air at room temperature has been demonstrated by Pang et al. This resonator exhibits a quality factor higher than 1,400 at 60 MHz and mass detection uncertainty of only about 4.6×10^{-15}g [76]. Some of these applications are shown in Figure 2.23.

At this point, we still need to cover CMOS-integrated FBAR applications. Chapter 7 presents a detailed discussion on the different integration philosophies, requirements, and fabrication processes concerning CMOS integration.

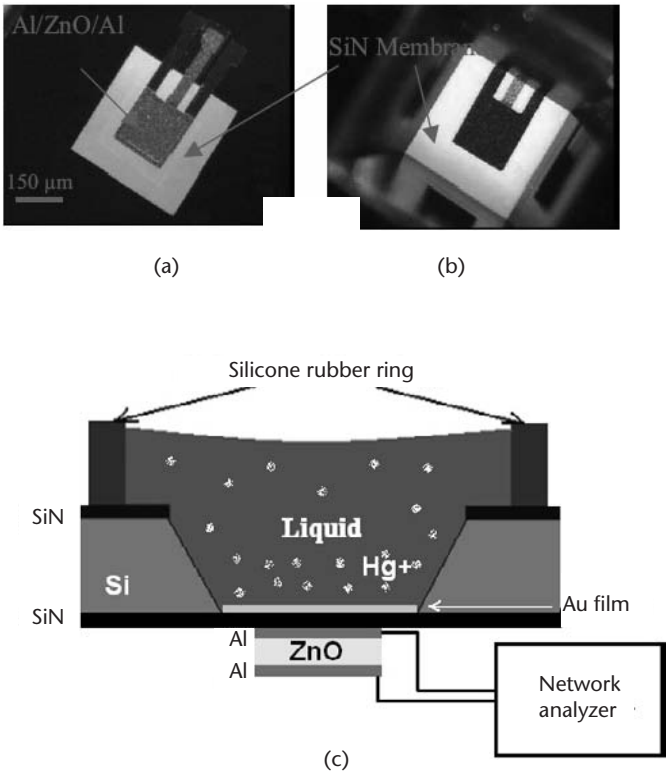

Figure 2.22 Mass sensor for biological applications: (a) top and (b) bottom views of the sensor and membrane; and (c) schematic of the mercury-ion detecting principle, where the ions interact with the gold coating, adding mass to the resonator and thus changing the resonance frequency. (© 2005 IOP Publishing Ltd. [74].)

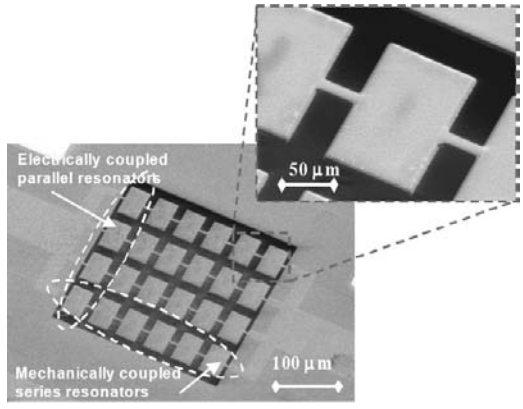

(a)

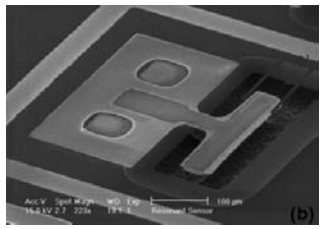

(b)

Figure 2.23 Other FBAR-based applications (nonlongitudinal resonance modes): (a) mechanically coupled contour-mode MEMS filters (© 2006 IEEE [75]); and (b) resonant mass sensor based on a lateral extensional mode (LEM) ZnO resonator (© 2006 IEEE [76]).

2.5 Summary

This chapter introduced the physics fundamentals, technologies, and applications of acoustic wave resonators. We discussed surface and bulk acoustic wave propagations and examined some of the types of acoustic waves, including Rayleigh, longitudinal, and shear-mode waves. The constitutive equations of piezoelectric and inverse piezoelectric effects provided us the formal background to understand the different excitation and vibration modes of acoustic resonators.

We examined SAW and BAW devices as well, providing an overview of SAW resonator operation, design, and typology. We paid more attention to BAW devices due to their booming performance on the radio frequency market and recently in new sensor applications. The mechanism of BAW propagation, the characteristics of the two types of BAW devices—FBAR and SMR—and their fabrication technology and applications were examined. The in-depth study of these aspects constitutes the core of this book, and extensive attention will be dedicated to them in the next chapters.

References

[1] Helmholtz, H. L. F., *On the Sensations of Tone as a Physiological Basis for the Theory of Music*, 4th ed., London, U.K.: Longmans, Green, and Co., 1912.

[2] Auld, B. A., *Acoustic Fields and Waves in Solids*, Vols. I and II, 2nd ed., Malabar, FL: Krieger Publishing Company, 1990.

[3] Lord Rayleigh, "On Waves Propagated Along the Plane Surface of an Elastic Solid," *Proc. London Math. Soc.*, Vol. s1–17, 1885, pp. 4–11.

[4] Love, A. E. H., *Some Problems of Geodynamics*, Cambridge, U.K.: Cambridge University Press, 1911, and New York: Dover, 1967.

[5] Lamb, H., "On Waves in an Elastic Plate," *Proc. Roy. Soc. London*, Ser. A 93, 1917, pp. 114–128.

[6] ANSI/IEEE Std. 176-1987, "IEEE Standard on Piezoelectricity," Institute of Electrical and Electronics Engineers, New York, 1988.

[7] Yamanouchi, K., and M. Takeuchi, "Applications for Piezoelectric Leaky Surface Waves," *Proc. IEEE Ultrason. Symp. 1990*, Honolulu, HI, December 4–7, 1990, pp. 11–18.

[8] Epcos AG, "1855 MHz Low-Loss Filter for Mobile Communications," 2002, http://www.epcos.com.

[9] TriQuint Semiconductor. "881.5/1960 MHz SAW Filter," 2009, http://www.triquint.com.

[10] Epson Toyocom, http://epsontoyocom.co.jp/english/.

[11] Epcos AG, http://www.epcos.com.

[12] Murata Manufacturing Co., Ltd., http://www.murata.com.

[13] Fujitsu Global, http://www.fujitsu.com.

[14] Hitachi Global, http://www.hitachi.com.

[15] Samsung Electronics, http://www.hitachi.com.

[16] Nippon Electric Company, http://www.hitachi.com.

[17] Murata Manufacturing Co., Ltd., "Surface Acoustic Wave Resonators," 2001, http://www.murata.com.

[18] Wright, P. V., "A Review of SAW Resonator Filter Technology," *Proc. IEEE Ultrason. Symp. 1992*, Tucson, AZ, October 20–23, 1992, pp. 29–38.

[19] Wright, P. V., "Low-Cost High-Performance Resonator and Coupled-Resonator Design: NSPUDT and Other Innovative Structures," *Proc. 43th Ann. Symp. Frequency Control*, Denver, CO, May 31–June 2, 1989, pp. 574–587.

[20] Wright, P. V., "Analysis and Design of Low-Loss SAW Devices with Internal Reflections Using Coupling-of-Modes Theory," *Proc. IEEE Ultrason. Symp. 1989*, Montreal, Quebec, October 3–6, 1989, pp. 141–152.

[21] Thompson, D. F., and P. V. Wright, "Wide Bandwidth NSPUDT Coupled Resonator Filter Design," *Proc. IEEE Ultrason. Symp. 1991*, Orlando, FL, December 8–11, 1991, pp. 181–184.

[22] Campbell, C. K., "Understanding Surface Acoustic Wave (SAW) Devices for Mobile and Wireless Applications and Design Techniques," 2008, http://www3.sympatico.ca/colin.kydd.campbell/.

[23] Epson Toyocom, "GHz Band, High Accuracy SAW Resonators and SAW Oscillators," http://epsontoyocom.co.jp/english/.

[24] Fujitsu Media Devices Ltd., Cellular SAW Duplexer, FAR-D5GA-881M50-D1AA, 2006, http://www.fujitsu.com.

[25] Epcos AG, Surface Acoustic Wave Components Division, "SAW Frontend Module GSM 850/EGSM/DCS/PCS/WCDMA 2100," 2008, http://www.epcos.com.

[26] Martin, F., "Pulse Mode Shear Horizontal-Surface Acoustic Wave (SH-SAW) System for Liquid Based Sensing Applications," *Biosensors and Bioelectr.*, Vol. 19, 2004, pp. 627–632.

[27] Talbi, A., et al., "ZnO/Quartz Structure Potentiality for Surface Acoustic Wave Pressure Sensor," *Sens. Actuators A: Phys.*, Vol. 128, 2006, pp. 78–83.

[28] Tsarenkov, G. V., "10+ GHz BAW Resonators Based on Semiconductor Multilayer Heterostructures," *Proc. IEEE Intl. Ultrason. Symp. 1999*, Tahoe, NV, October 17–19, 1999, pp. 939–942.

[29] Lakin, K. M., and J. S. Wang, "Acoustic Bulk Wave Composite Resonators," *Appl. Phys. Lett.*, Vol. 38, 1981, pp. 125–127.

[30] Chao, M.-C., et al., "Modified BVD-Equivalent Circuit of FBAR by Taking Electrodes into Account," *Proc. IEEE Intl. Ultrason. Symp. 2002*, Munich, Germany, October 8–12, 2002, pp. 973–976.

[31] Mueller, W., *A Brief Overview of FBAR Technology,* Agilent Technologies, technical report AB-WCM200701a, July 20, 2001.

[32] Lakin, K. M., G. R. Kline, and K. T. McCarron, "Development of Miniature Filters for Wireless Applications," *IEEE Trans. on Microwave Theory Tech.,* Vol. 43, 1995, pp. 2933–2939.

[33] Aigner, R., "Volume Manufacturing of BAW-Filters in a CMOS Fab," *Proc. Second International Symposium on Acoustic Wave Devices for Future Mobile Communication Systems*, Chiba, Japan, March 3–5, 2004, pp. 129–134.

[34] Emanetoglu, N. W., "MgxZn1-xO: A New Piezoelectric Material," *Proc. IEEE Intl. Ultrason. Symp. 2001*, Vol. 1, Atlanta, GA, October 7–10, 2001, pp. 253–256.

[35] Fritze, H., and H. L. Tuller, "Langasite for High-Temperature Bulk Acoustic Wave Applications," *Appl. Phys. Lett.*, Vol. 78, 2001, pp. 976–977.

[36] Engelmark, F., "Structural and Electroacoustical Studies of AlN Thin Films During Low Temperature Radio Frequency Sputtering Deposition," *J. Vac. Sci. Technol. A*, Vol. 19, 2001, pp. 2664–2669.

[37] Shiosaki, T., "Low Temperature Growth of Piezoelectric Films by RF Reactive Planar Magnetron Sputtering," *Jap. J. Appl. Phys.*, Vol. 20, 1981, pp. 149–152.

[38] Uchiyama, S., et al., "Growth of AlN Films by Magnetron Sputtering," *J. Crystal Growth*, Vol. 189–190, 1998, pp. 448–451.

[39] Vispute, R. D., H. Wu, and J. Narayan, "High Quality Epitaxial Aluminum Nitride Layers on Sapphire by Pulsed Laser Deposition," *Appl. Phys. Lett.*, Vol. 67, 1995, pp. 1549–1551.

[40] Dubois, M.-A., and P. Muralt, "Stress and Piezoelectric Properties of Aluminum Nitride Thin Films Deposited onto Metal Electrodes by Pulsed Direct Current Reactive Sputtering," *J. Appl. Phys.* Vol. 89, 2001, pp. 6389–6395.

[41] Shen, L., R. K. Fu, and P. K. Chu, "Synthesis of Aluminum Nitride Films by Plasma Immersion Ion Implantation–Deposition Using Hybrid Gas–Metal Cathodic Arc Gun," *Rev. Scient. Instrum.*, Vol. 75, 2004, pp. 719–724.

[42] Lee, J.-B., et al., "Effects of Bottom Electrodes on the Orientation of AlN Films and the Frequency Responses of Resonators in AlN-Based FBARs," *Thin Solid Films*, Vol. 447–448 2004, pp. 610–614.

[43] Akiyama, M., et al., "Influence of Metal Electrodes on Crystal Orientation of Aluminum Nitride Thin Films," *Vacuum*, Vol. 74, 2004, pp. 699–703.

[44] Huang, C.-L., K.-W. Tay, and L. Wu, "Fabrication and Performance Analysis of Film Bulk Acoustic Wave Resonators," *Mater. Lett.*, Vol. 59, 2005, pp. 1012–1016.

[45] Hara, M., et al., "Surface Micromachined AlN Thin Film 2 GHz Resonator for CMOS Integration," *Sens. Actuators A: Phys.*, Vol. 117, 2005, pp. 211–216.

[46] Saravanan, S., et al., "A Novel Surface Micromachining Process to Fabricate AlN Unimorph Suspensions and Its Application for RF Resonators," *Sens. Actuators A: Phys.*, Vol. 130–131, 2006, pp. 340–345.

[47] Pang, W., H. Zhang, and E. S. Kim, "Micromachined Acoustic Wave Resonator Isolated from Substrate," *IEEE Trans. on Ultrason. Ferroelectr. Freq. Control,* Vol. 52, 2005, pp. 1239–1246.

[48] Piazza, G., et al., "Single-Chip Multiple-Frequency RF Microresonators Based on Aluminum Nitride Contour-Mode and FBAR Technologies," *Proc. IEEE Intl. Ultrason. Symp. 2005*, Rotterdam, the Netherlands, September 18–21, 2005, pp. 1187–1190.

[49] Satoh, Y., et al., "Development of 5GHz FBAR Filters for Wireless Systems," *Proc. 2nd International Symposium on Acoustic Wave Devices for Future Mobile Communication Systems*, Chiba, Japan, March 3–5, 2004, pp. 141–144.

[50] Rosén, D., J. Bjursttröm, and I. Katardjiev, "Suppression of Spurious Lateral Modes in Thickness-Excited FBAR Resonators," *IEEE Trans. on Ultrason. Ferroelectr. Freq. Control*, Vol. 52, 2005, pp. 1189–1192.

[51] Kim, Y.-D., et al., "Highly Miniaturized RF Bandpass Filter Based on Thin-Film Bulk Acoustic-Wave Resonator for 5-GHz-Band Application," *IEEE Trans. on Microwave Theory Tech.*, Vol. 54, 2006, pp. 1218–1228.

[52] Su, Q., et al., "Thin-Film Bulk Acoustic Resonators and Filters Using ZnO and Lead-Zirconium-Titanate Thin Films," *IEEE Trans. on Microwave Theory Tech.*, Vol. 49, 2001, pp. 769–778.

[53] Pan, W., "A Surface Micromachined Electrostatically Tunable Film Bulk Acoustic Resonator," *Sens. Actuators A: Phys.*, Vol. 126, 2006, pp. 436–446.

[54] Ruby, R. C., and P. P. Merchant, "Tunable Thin Film Acoustic Resonators and Method for Making the Same," U.S. Patent No. 5587620, December 24, 1996.

[55] Ylilammi, M. A., "Method for Performing On-Wafer Tuning of Thin Film Bulk Acoustic Wave Resonators (FBARS)," U.S. Patent No. 6051907, April 18, 2000.

[56] Vanhelmont, F., et al., "A 2 GHz Reference Oscillator Incorporating a Temperature Compensated BAW Resonator," *Proc. IEEE Intl. Ultrason. Symp. 2006*, Vancouver, B.C., October 3–6, 2006, pp. 333–336.

[57] Larson III, J. D., "Acoustic Wave Resonator and Method of Operating the Same to Maintain Resonance When Subjected to Temperature Variations," U.S. Patent No. 6,420,820, July 16, 2002.

[58] Aigner, R., "High Performance RF-Filters Suitable for Above IC Integration: Film Bulk-Acoustic-Resonators (FBAR) on Silicon," *Proc. IEEE 2003 Custom Integrated Circuit Conference 2003*, San Jose, CA, September 21–24, 2003, pp. 141–146.

[59] Lakin, K. M., et al., "Bulk Acoustic Wave Resonators and Filters for Applications Above 2 GHz," *Dig. Tech. Papers IEEE Intl. Microwave Symposium MTT-S 2002*, Seattle, WA, June 2–7, 2002, pp. 1487–1490.

[60] Inouye, S., "Electronics.ca Research Network, 2006 MicroElectroMechanical Systems (MEMS)," Research Report # DB2563, November 2006, pp. 1–48.

[61] Wicht Technologie Consulting, "RF MEMS Market II, 2005-2009," 2005.

[62] Bradley, P., et al., "A Film Bulk Acoustic Resonator (FBAR) Duplexer for USPCS Handset Applications," *Dig. of Tech. Papers IEEE International Microwave Symp. MTT-S 2001*, Phoenix, AZ, May 20–25, 2001, pp. 367–370.

[63] Ruby, R., et al, "Ultra-Miniature High-Q Filters and Duplexers Using FBAR Technology," *Dig. of Tech. Papers IEEE Intl. Solid-State Circuits Conf.*, San Francisco, CA, February 5–7, 2001, pp. 120–121.

[64] Ylilammi, M., et al., "Thin Film Bulk Acoustic Wave Filter," *IEEE Trans. on Ultrason. Ferroelectr. Freq. Control*, Vol. 49, 2002, pp. 535–539.

[65] Nishihara, T., et al., "High Performance and Miniature Thin Film Bulk Acoustic Wave Filters for 5 GHz," *Proc. IEEE Intl. Ultrason. Symp. 2002*, Munich, Germany, October 8–12, 2002, pp. 969–972.

[66] Morkner, H., et al., "An Integrated FBAR Filter and PHEMT Switched-Amp for Wireless Applications," *Dig. of Tech. Papers IEEE International Microwave Symp. MTT-S 1999*, Anaheim, CA, June 13–19, 1999, pp. 1393–1396.

[67] Feld, D., et al., "A High Performance 3.0 mm × 3.0 mm × 1.1 mm FBAR Full Band Tx Filter for US PCS Handsets," *Proc. IEEE Intl. Ultrason. Symp. 2002*, Munich, Germany, October 8–12, 2002, pp. 913–918.

[68] Agilent Technologies, Applications Engineering Team, Personal Systems Division, "Using the HPMD-Series and QPMD-Series CDMA Duplexers," *Design Tip* (technical report), April 12, 2002.

[69] Lu, C. S., *Applications of Piezoelectric Quartz Crystal Microbalance*, London, U.K.: Elsevier, 1984.

[70] G. Z. Sauerbrey, "Verwendung von Schwingquarzen zur Wägung dünner Schichten und Microwägung," *Z. Phys.*, Vol. 155, 1959, pp. 206–222.

[71] Gabl, R., et al., "First Results on Label-Free Detection of DNA and Protein Molecules Using a Novel Integrated Sensor Technology Based on Gravimetric Detection Principles," *Biosens. Bioelectron.*, Vol. 19, 2004, pp. 615–620.

[72] Weber, J., et al., "Shear Mode FBARs as Highly Sensitive Liquid Biosensors," *Sens. Actuators A: Phys.*, Vol. 128, 2006, pp. 84–88.

[73] Benetti, M., et al., "Microbalance Chemical Sensor Based on Thin-Film Bulk Acoustic Wave Resonators," *Appl. Phys. Lett.,* Vol. 87, 2005, p. 173504.

[74] Zhang, H., et al., "A Film Bulk Acoustic Resonator in Liquid Environments," *J. Micromech. Microeng.*, Vol. 15, 2005, pp. 1911–1916.

[75] Stephanou, P. J., et al., "Mechanically Coupled Contour Mode Piezoelectric Aluminum Nitride MEMS Filters," *Proc. IEEE Intl. Conf. MEMS 2006*, Istanbul, Turkey, January 22–26, 2006, pp. 906–909.

[76] Pang, W., et al., "Ultrasensitive Mass Sensor Based on Lateral Extensional Mode (LEM) Piezoelectric Resonator," *Proc. IEEE Intl. Conf. MEMS 2006*, Istanbul, Turkey, January 22–26, 2006, pp. 78–81.

CHAPTER 3

Design and Modeling of Micro- and Nanoresonators

Modeling is a fundamental task in the production cycle of FBAR, MEMS, and NEMS resonators. Modeling allows prediction of the resonator static and dynamic responses, and, ideally, it is performed at the early stages of the design process, when the decisions of choosing materials, geometries, and dimensions are to be made. Besides aiding the designer in defining the fabrication technology, modeling allows analysis of the performance of a working device, so we can fit the actual frequency response to given models in order to extract their parameters. Design of modern system-on-a-chip blocks composed of resonators and integrated circuits is largely based on modeling activity, where the physical interconnection of the system creates a mutual and complex interaction that has to be quantified.

The design of resonators is addressed by different modeling approaches, each having its own context and usefulness. Analytical models are based on mechanical, electromechanical, and purely electrical equivalent-circuit representations of the resonator physics. In this chapter, we study these models, getting started with the stages of design and modeling introduced in Section 3.1. Next, Section 3.2 examines the electromechanical transformer concept, which gives the analytical elements and initial criteria to build more complex resonator models. Then, the circuit theory perspective of equivalent-circuit parameter models is presented in Section 3.3. With this at hand, the components, structure, and analyses types of finite element models are studied in Section 3.4.

3.1 The Stages of Resonator Design and Modeling

In Chapter 1, we studied the production cycle of MEMS and NEMS resonators. In that cycle, the design stages previous to manufacturing are based on models and modeling tools that represent the physics of the resonator. Each model defines an input-output relationship with regard to its level of abstraction, assuming that the system and manufacturing levels are the highest and lowest ones in the design hierarchy, respectively.

Starting from the system-level specifications and descending in the direction of manufacturing, the design goes through successive modeling stages involving less abstraction and more physics and fabrication parameters, as depicted in Figure 3.1. Mature, independent, and well-established modeling tools exist in the market to accomplish the calculations and analysis. These tools specialize in the different stages of the modeling process. If the resonator is part of a bigger system—like an IC

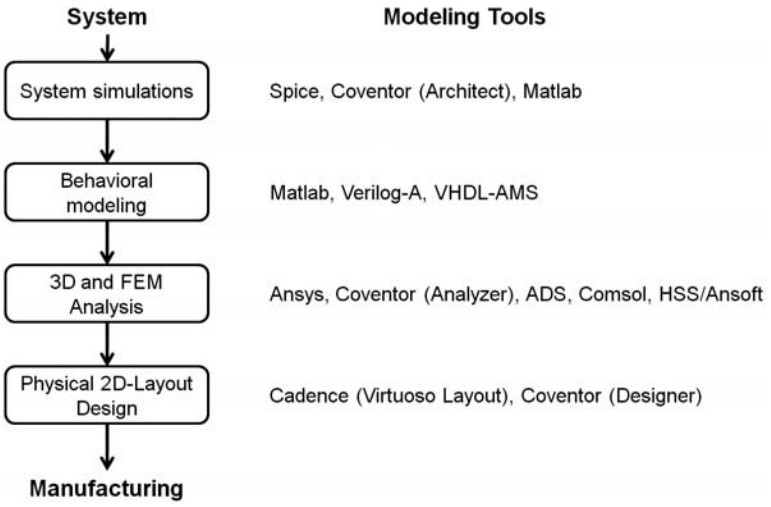

Figure 3.1 Modeling hierarchy for micro and nanoresonator design.

or a network of MEMS/NEMS devices, its design can be structured or nonstructured as long as the resonator and IC design tasks go in parallel or nonparallel ways [1, 2].

System simulations are performed at the schematic level, and the components of the model are connected by nets. Each component implements a behavioral model or transfer function. Commercial tools like CADENCE (Virtuoso Schematic), COVENTOR (Architect), and MATLAB-Simulink feature net-connection capabilities for interconnecting different building blocks of a system [3–5]. COVENTOR, for example, provides libraries for MEMS-IC interconnection. In the CADENCE environment, Virtuoso Schematic offers powerful networking capabilities, thus connecting Spice or Spectre models with behavioral customized models made by the user in Verilog-A or VHDL-AMS [6–9]. Figure 3.2 shows the level of abstraction of a system model comprising a MEMS resonator and amplifier integrated circuit for read out of the MEMS current.

However, in the user's eyes, the system-level model does not necessarily make explicit reference to the inner relations of the input-output variables of the building blocks. In this way, the user only instantiates and connects the blocks, and the simulator calculates the values of the variables according to the transfer functions of the

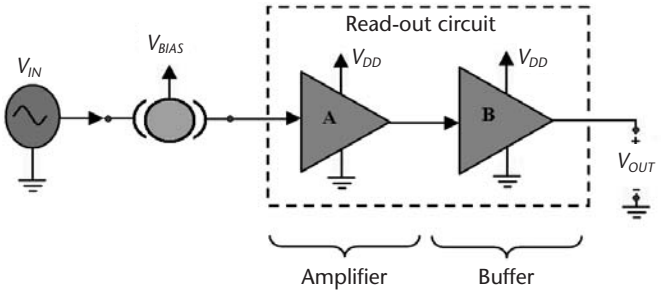

Figure 3.2 System-level model of a read-out circuit of a MEMS resonator (circuit schematic of the resonator and the read-out circuit).

blocks and the analysis type. AC analysis, for example, is performed by sweeping a user-selected variable to obtain the response of the interest variable against time, frequency, temperature, or any other independent variable. Figure 3.3 plots the bode (frequency response) of the read-out circuit and the MEMS resonator [10]. The user only needs to specify the MEMS Q factor, insertion loss, and resonance frequency, which are enough to build its second-order transfer function. Alternatively, the MEMS block can be specified by its lumped-circuit elements, and the amplifier described by its AC gain and bandwidth, in a first approximation.

The transfer function of the system can also be implemented by the user. MATLAB is very efficient in coding the transfer function and analysis type as a new function by following the MATLAB syntax rules. Also, the user takes advantage of preexisting MATLAB functions to simplify its own function and make the script more compact and readable. This approach gives the user more control of the model, although it requires manual building of the blocks. Much of the physical-level information of the components, like layout, geometries, and process parameters, is not considered at this stage. Figure 3.4 plots the root locus of the open-loop system composed by an amplifier and a 2-GHz resonator. The amplifier is assumed to be a CMOS circuit in common-source configuration and transimpedance gain g_m, which is serially connected to the second-order resonator so their transfer functions are multiplied in the frequency domain. With the root-locus plot, the system stability is studied through the amplifier and resonator parameters [11].

At this point, the physical nature of the system becomes less intuitive and begins to be more explicitly described by the lower-level behavioral models. A behavioral model reproduces the physical behavior of the system by integrating its mathematical model and underlying physics in an attempt to make the model as full and realistic as the physical system. Behavioral modeling has become a current-day circuit

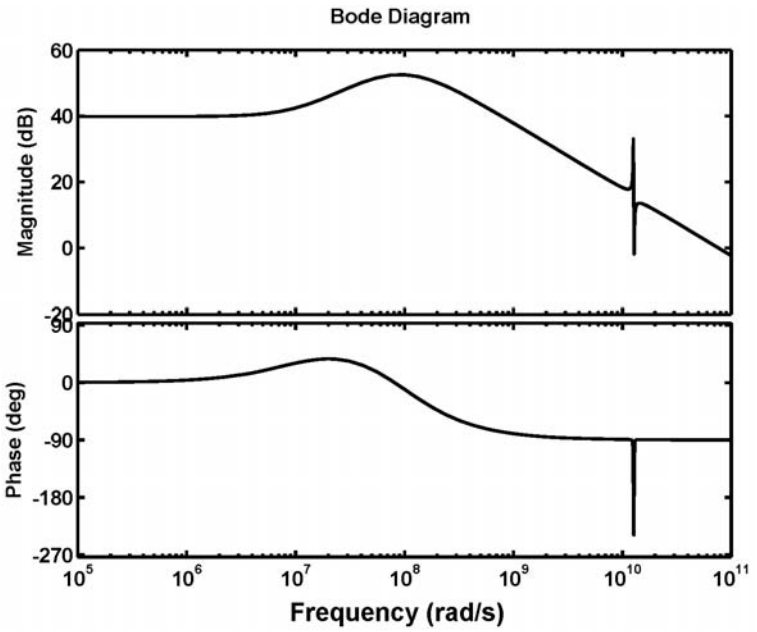

Figure 3.3 Bode plot (frequency response) of the read-out circuit and resonator.

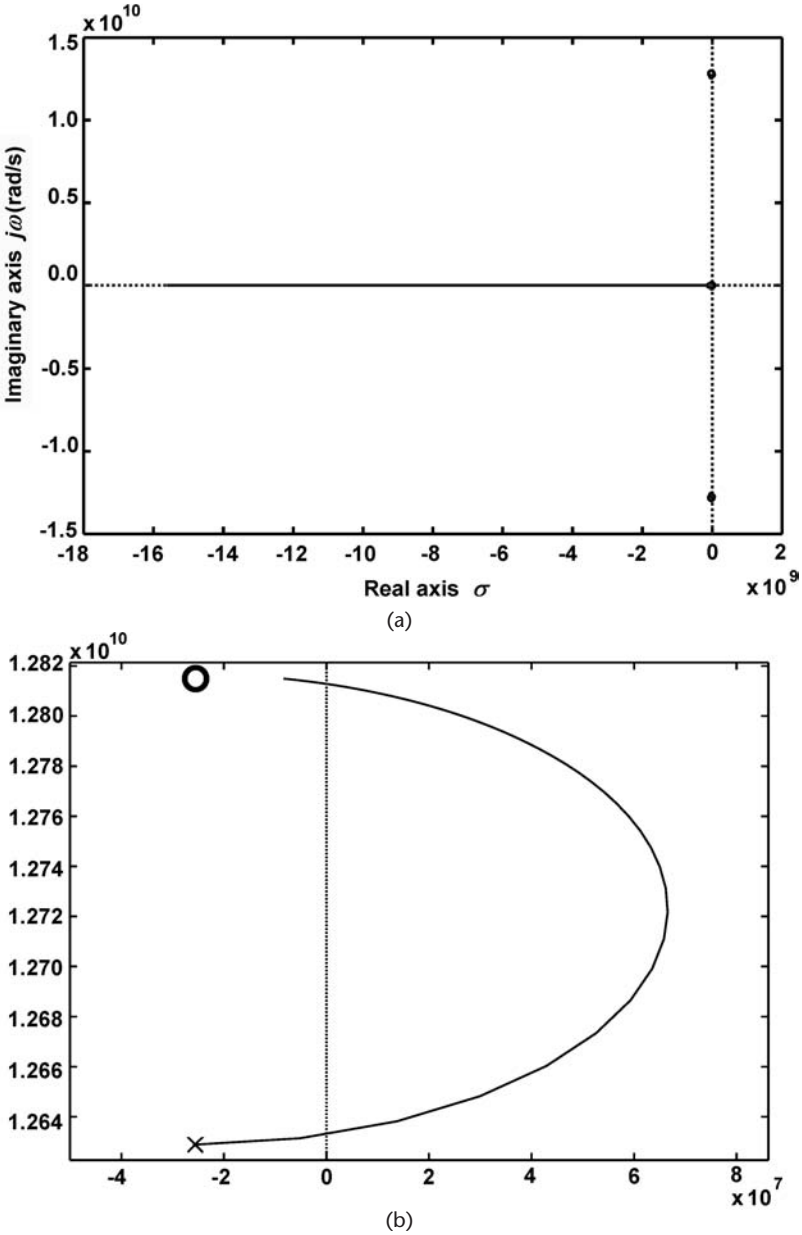

Figure 3.4 (a, b) Root locus of the open-loop FBAR and amplifier circuit.

and MEMS design technique supported by computer-aided design (CAD) tools and description languages like VHDL-AMS and Verilog-A [12].

The behavioral model of an FBAR with linear thermal coefficient factor (TCF) is built from its equivalent lumped-element RLC model and the TCF (the equivalent-circuit model of FBARs and other resonators will be studied in Section 3.3). The TCF, reference temperature, and RLC values at that temperature are the main parameters of the model: the TCF is fixed, the RLC elements are extracted from experimental measurements, and a reference temperature is fixed is chosen. This example deals with an electrothermal model, thus integrating both electrical and

thermal elements. The data plot of Figure 3.5 shows the evolution of resonance frequency as a function of temperature, described by this behavioral model. Simulations in the –20°C to +80°C temperature range were performed in 10°C steps, with a TCF equal to –25 ppm/°C and a reference temperature of 40°C (it can be noted that the TCF equals to 0 ppm/°C at that temperature). The resonance frequencies in the temperature range are found in the 2.2-GHz band. This model is useful for designing complete systems that integrate the resonator, like RF oscillators. The design of a temperature-compensated FBAR-based oscillator is studied in Chapter 10, where the behavioral model of the FBAR and the circuit are described in detail.

The system and component-level models give us a vision of the expected resonance frequencies and physical parameter influence in the performance of the resonator. After that, 3D finite element modeling (FEM) links the analytical formulation, the geometry, and the materials of the resonator, so we can predict its static and dynamic responses with high precision. Later in Section 3.4, we study the characteristics and design flow of a reliable FEM analysis.

The ANSYS model of Figure 3.6 compares the equilibrium (edged) and deformed (solid) configurations of a resonating gallium arsenide (GaN) nanowire. In the FEM, the user introduces the mechanical properties of GaN—elasticity, density, Poisson modulus—as simulation parameters. The FEM is composed of a number of elements, typically hundreds or thousands, which are represented in the figure by the small "bricks." After modal analysis, the fundamental resonance frequency of the 2-μm-long nanowire with a diameter of 50 nm equals 11.9 MHz.

A reliable FEM analysis gives the designer enough confidence to complete the physical 2D layout, which will be used in the resonator manufacturing. The layout is designed in layers that represent the different processes being implemented in the fabrication. Depending on the available technology, each one of these layers is employed in photolithography mask fabrication, laser photolithography, or other suitable lithography or patterning means. The layout is drawn in accordance with the design rules and process restrictions of the target technology. Commercial tools like CADENCE offer sophisticated options to develop complex designs and to perform design-rule checking.

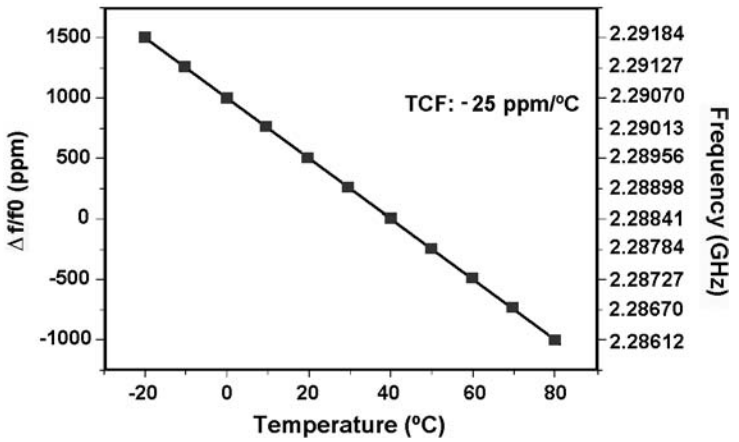

Figure 3.5 Behavioral description of an FBAR: parametric frequency response of the model as a function of temperature.

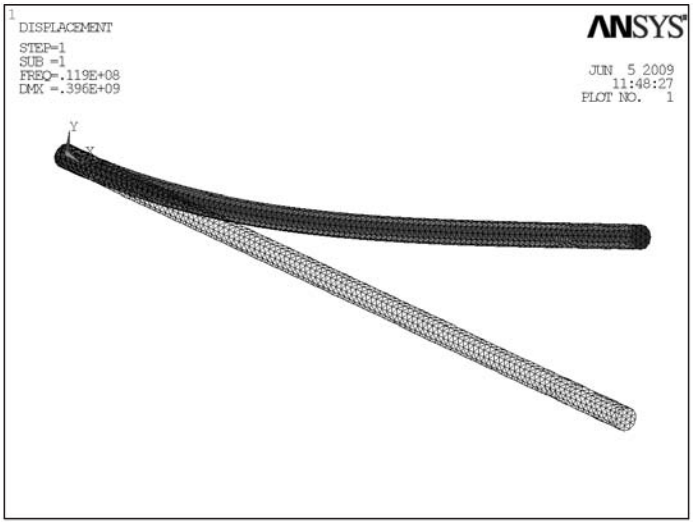

Figure 3.6 3D finite element model of a GaN nanoresonator: the nanowire is 2 μm long with a diameter equal to 50 nm, and it has a resonance frequency of 11.9 MHz.

In MEMS and NEMS manufacturing, the involved micromachining or nanopatterning techniques add complexity to the layout design. Due to the lack of standard processes for movable-structure releasing, the layout has to consider the performance of the etching techniques developed for the specific case of the interest resonator technology. Anisotropy, etching times, and selectivity are some of the factors conditioning the geometry and size of the structural and sacrificial layers of the technology. In deep silicon etching processes like DRIE, for example, the etching times are different for small and big-sized features. Underetching or lateral etching can also be important, so enough margins must be kept in the lateral dimensions to guarantee the integrity of the structure at the end of the process. Figure 3.7 depicts the three-layer layout of an AlN-made FBAR resonator (the etching layer is not included). As seen in the drawing, the bottom electrode is designed to have less width than both the AlN and top electrode layers. Also, the AlN layer is wider than the top and bottom electrodes. This is due to different reasons: First, to cover possible misalignment during photolithography (the tolerance of the photolithography process is assumed to be known and smaller than the width margin). This guarantees that the bottom electrode will always be underneath both the AlN and the top electrode, thus fixing the duty resonator area. Second, short circuits of the top and bottom electrodes are prevented. This may happen if the undesired lateral etching of the AlN causes it to be narrowed beyond the acceptable limits imposed by the AlN thickness and the etching rates. The fabrication details regarding FBARs and the issues of lateral and underetching are covered in Chapter 4.

So far, we have given a rapid overview to the stages of the design flow. The design and modeling processes conclude with the manufacturing of devices. Further modeling can be carried out on fabricated resonators when the equivalent-circuit parameters are extracted, for a given circuital model. In the next sections, we discuss in detail each level of the modeling workflow, from the higher abstraction of equivalent circuits to the more physical FEM and layout optimization.

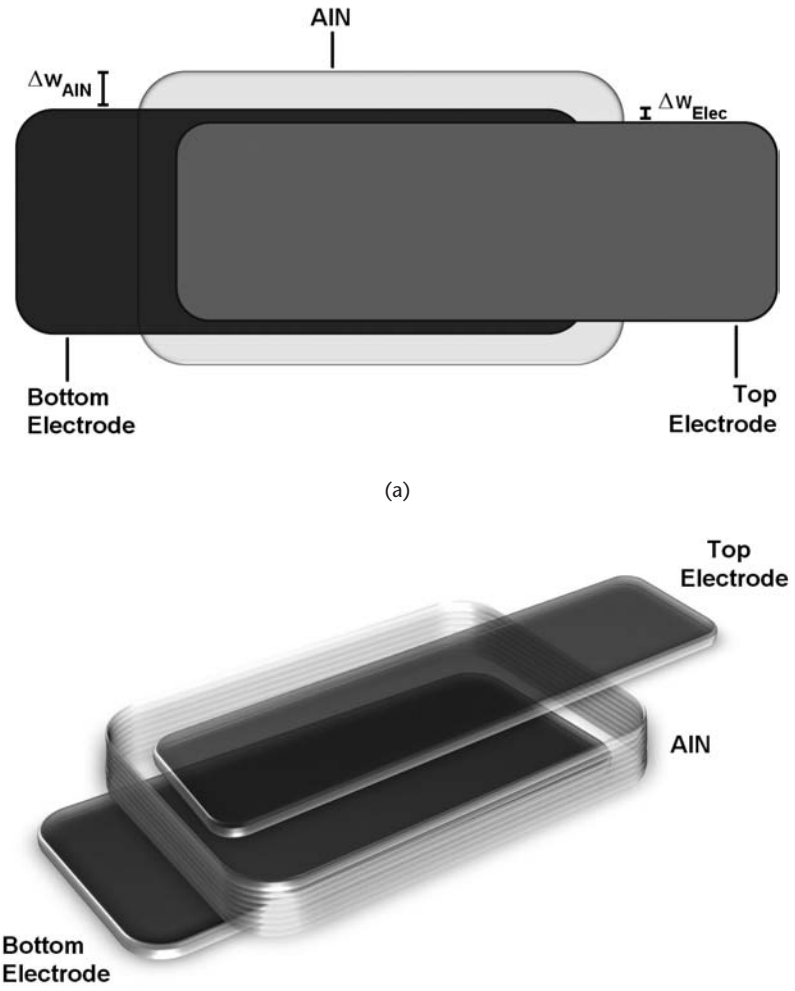

Figure 3.7 Physical layout view of an AlN-based FBAR: (a) 2D top view as seen by the designer and (b) 3D view.

3.2 The Electromechanical Transformer

FBARs, MEMS, and NEMS resonators convert the input energy from the electrical to the mechanical domains, and vice versa. This process entails, on the one hand, input-to-output domain coupling and, on the other hand, an effective electromechanical energy-conversion factor. The resonator is, in this sense, an electromechanical transformer, and it can be modeled by lumped-circuit electrical and mechanical components linked through the transformer, among other components in the model. The components of such an electromechanical transformer-based model are chosen depending on the transduction mechanism. These models help the designer understand the operation principles and their relationship with transduction, topology, and geometry of the resonator, thus providing useful infor-

mation to the FEM design and analysis. The modeling particularities of electromechanical and acoustic resonators are discussed next.

3.2.1 MEMS and NEMS Resonators

The mass-spring damped system depicted in Figure 3.8 illustrates the mechanical oscillation of MEMS and NEMS resonators. This model is in close relation with the mathematical description of the oscillatory movement and the resonance frequency provided by (1.1) and (1.2), respectively, which we reproduce herein for the reader convenience [13]:

$$m_{eff}\,\ddot{x} + D\dot{x} + kx = F_{ext}(x,t) = F_0 \cdot \sin(2\pi f t) \tag{3.1}$$

$$f_0 = \frac{1}{2\pi}\sqrt{\frac{k}{m_{eff}}} \tag{3.2}$$

where x is the time-varying harmonic oscillation, m_{eff} is the equivalent mass of the fundamental resonance mode with frequency f_0, D is the damping constant, k is the spring constant, F_{ext} is the external force applied to the resonator, and F_0 is the amplitude of the harmonic force signal with frequency f.

Figure 3.8 and (3.1) and (3.2) illustrate the oscillation and include the excitation force as the system input. However, they lack a description of the physical mechanism causing the vibration, because it depends on the transduction type. To exemplify, let's consider a MEMS resonator electrostatically driven by both AC and DC voltage signals, such as that previously depicted in Figure 1.7. The mechanical circuit constituted by the mass-spring-damper system is fed by the electric voltage signals v_{AC} and V_{DC}, as it represents the circuital model of Figure 3.9(a). Since certain equivalence between the mechanical and electrical domains exists, this circuit can also be depicted in terms of the electrically equivalent RLC parameter circuit of Figure 3.9(b).

A stricter equivalence between the mechanical and the RLC elements is done by adding a couple of electromechanical transformers in the circuit, as shown in

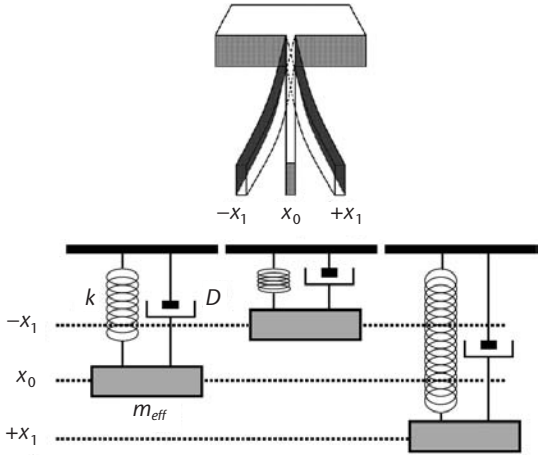

Figure 3.8 Mass-spring damped mechanical model of a MEMS resonator.

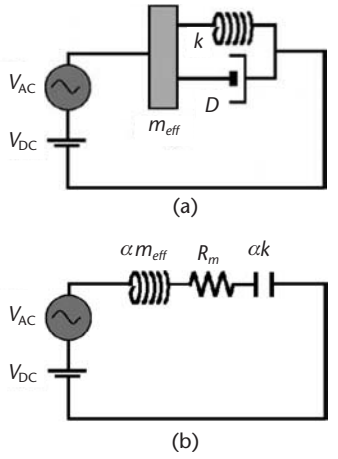

Figure 3.9 Equivalent circuits of the electrostatically driven MEMS resonator: (a) mechanical model and (b) electrically equivalent RLC model.

Figure 3.10. On the left side, the voltage source v_{elec} shunts the transformer and the static capacitance C_0 formed between the walls of the driver electrode and the resonator. The source velec includes both the AC and DC voltages, and the electromechanical transformer has efficiency η_e. Thus, the arrangement models the transformation of input voltage into mechanical motion. Note that, while the circuit at the left side of the transformer is electrical, its right side links to the mechanical-side circuit formed by the mass meff, spring k, and damper D. The electrical analogy is the same of Figure 3.9. That is, the inductance equals meff, the capacitor equals $1/k$, and the resistance equals D. At right, the second transformer models the mechanical impedance transformation due to the mechanical coupling between the beam and the clamping system [14].

At the driving electrode port (shunted by C_0), the equivalent RLC resonator circuit elements are transformed by the electromechanical ratio η_e, and their values are [14]:

$$R_m = \frac{D}{\eta_e^2} \tag{3.3}$$

$$L_m = \frac{m_{eff}}{\eta_e^2} \tag{3.4}$$

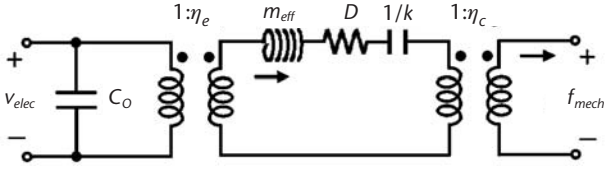

Figure 3.10 Electromechanical model of the MEMS resonator coupling the electrical and mechanical domains through the electromechanical transformers: the circuit is bidirectional and has both electrical (voltage v_{elec}) and mechanical (force F_{mech}) inputs and outputs. (*After:* [14].)

$$R_m = \frac{\eta_e^2}{k} \tag{3.5}$$

where R_m, L_m, and C_m are the motional resistance, inductance, and capacitance of the equivalent circuit, respectively, seen at the driving electrode port.

The electromechanical transformer model is completely bidirectional to reproduce the transduction physics. This means that the input voltage v_{elec} induces an electrostatic force on the MEMS, thus causing mechanical vibration and the subsequent mechanical force F_{mech}. Alternatively, an input mechanical force F_{mech} creates an electromotive displacement, and the resulting displacement current flows through C_0, where the output voltage v_{elec} can be read out.

3.2.2 FBAR and Other Acoustic Resonators

Electromechanical transformer models of FBAR, SMR, and other acoustic resonators are mainly based on the Mason's or the Krimholtz-Leedom-Matthaei's (KLM) models [15, 16]. The Mason's model, for example, shows that most of the difficulties in deriving the solutions for the wave propagation through the acoustic layer are overcome by using the network theory approach. Thus, the Mason's model presents an exact equivalent circuit that separates the piezoelectric material into one electric port and two acoustic ports through the use of an ideal electromechanical transformer. Each acoustic port represents the acoustic paths to the top and bottom electrodes, while the electric port sees the electric input impedance Z_{in} opposing to current circulation. For longitudinal-mode FBARs, the equivalent circuit representation of the FBAR, according to the Mason's model, is depicted in the schematic drawings of Figure 3.11. A similar approach is followed by the KLM model.

The input impedance Z_{in} seen from the half-phase line of the AlN layer, between the two parallel electrodes is [17]:

$$Z_{in} = \frac{1}{j\omega C_0} \times \left(1 - k_{eff}^2 \frac{\tan\phi}{\phi} \frac{(Z_T + Z_B)\cos^2\phi + j\sin 2\phi}{(Z_T + Z_B)\cos 2\phi + j(Z_T + Z_B + 1)\sin 2\phi} \right) \tag{3.6}$$

where ϕ is the half phase across the piezoelectric plate, k_{eff}^2 is the piezoelectric coupling coefficient of the AlN film, C_0 is the parallel-plate capacitance between the two electrodes, and Z_T and Z_B are normalized acoustic impedances at the piezoelectric layer boundaries (with respect to the acoustic impedance of the AlN layer). Equation (3.6) can be divided into three components: the electrical one, the purely mechanical one, and the electromechanical transformer with gain N:

$$N = k_{eff}^2 \frac{\tan\phi}{\phi} \tag{3.7}$$

The phase across the piezoelectric layer is equal to:

$$\phi = \kappa \times t \tag{3.8}$$

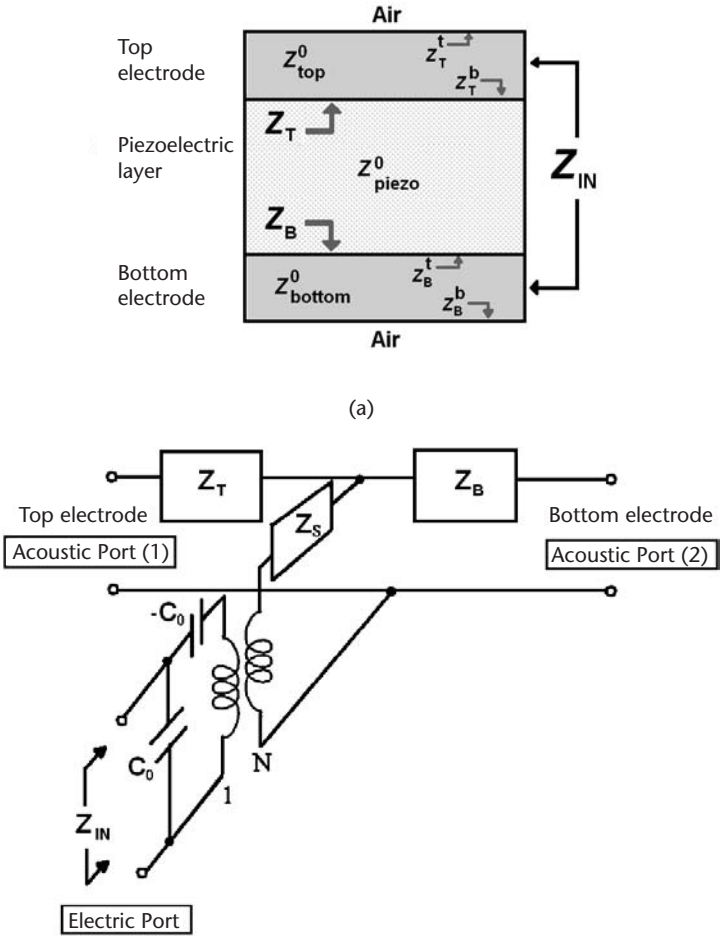

Figure 3.11 FBAR electromechanical model: (a) cross-section view of the FBAR with equivalent impedance values and input and output ports, and (b) equivalent circuit representation of the FBAR, according to the Mason's model.

where κ and t are the wave vector and the thickness of the piezoelectric layer, and κ depends on the frequency f and acoustic velocity v in the piezoelectric film, as given by:

$$\kappa = \frac{2\pi f}{v} \tag{3.9}$$

The boundary impedances Z_T and Z_B at the interface between the AlN and the electrodes are determined by the acoustic impedance matching between both media. If more than one metal is used in the fabrication of electrodes, or if another material is stacked, both the acoustic path and the input impedance seen from the electrical side change. The values of Z_T and Z_B can be found by [18]:

$$Z_{T/B} = Z_0^{T/B} \times \left(\frac{Z_{Load} \cos \phi_{T/B} + jZ_0^{T/B} \sin \phi_{T/B}}{Z_0^{T/B} \cos \phi_{T/B} + jZ_{Load} \sin \phi_{T/B}} \right) \tag{3.10}$$

where $Z_0^{T/B}$ is the characteristic acoustic impedance of either the top (T) or bottom (B) electrode's layer, Z_{Load} is the input load impedance seen by either the top or bottom electrode's layer at the next interface, and $\phi_{T/B}$ is the acoustic-wave phase across either the top or bottom electrode's layer. In FBARs, the top and bottom electrode surfaces have an air interface (although in real implementations, some area of the electrodes still contacts the substrate). Since air has low acoustic impedance, the air-to-electrode interfaces have boundary impedances equal to zero. Final calculation of the electrical impedance Z_{in} requires recursive calculation of Z_T and Z_B, beginning with the air interfaces and ending at the AlN layer. The circuit of Figure 3.12 represents the acoustic and electric impedances of the FBAR Mason's model. This is equivalent to the analytical formulation of (3.6) and (3.10), and it gives a graphic understanding of the transmission line formed by the different layers of the resonator (it may be useful to complete the recursive calculations of Z_T and Z_B as well).

This model can be implemented by computing software like Mathematica [19] or MATLAB, and it may be served to rapid prediction of the fundamental and harmonic acoustic modes of the resonator and its sensitivity to material properties or layer configuration. The curve of Figure 3.13 shows the ideal, lossless transmission response of an FBAR from 1 to 20 GHz. Five modes are observed in the plot, the first and main one being around 2 GHz.

A similar approach can be employed to model the wave propagation and the input impedance seen from the electric port of solidly mounted resonators (SMRs). By adding the Bragg's mirror reflector layers to the model [20], the input impedance Z_{in} can be calculated, as depicted in Figure 3.14. In this case, what is modified is the

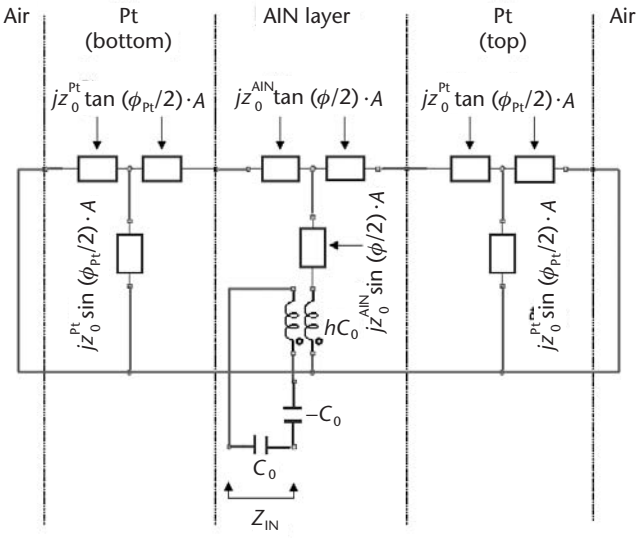

Figure 3.12 Transmission-line representation of the acoustic and electric paths of the Mason's model of FBARs.

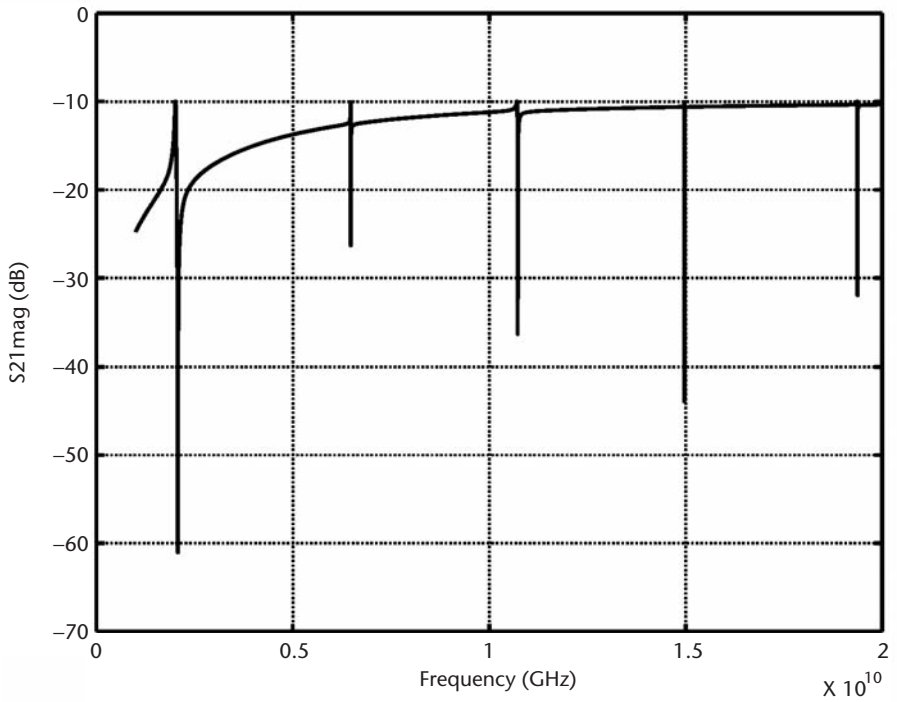

Figure 3.13 Frequency response of an FBAR predicted by the Mason's model (MATLAB simulation).

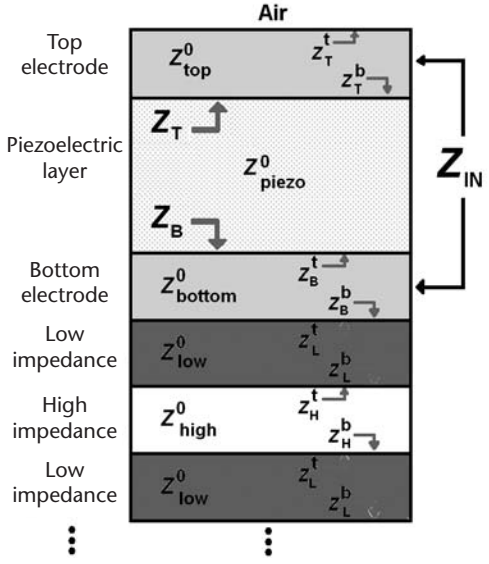

Figure 3.14 Equivalent acoustic impedances of solidly mounted resonator (SMR): the bottom impedance Z_B is modified.

acoustic impedance Z_B seen by the bottom electrode due to the added layers underneath the resonator.

The circuit of Figure 3.15 represents the equivalent transmission line of an SMR that includes the acoustic impedances of the Bragg's mirror. According to (3.6) and (3.10), it shows how the calculation of Z_B requires more steps than in the FBAR model, because the transmission line is longer due to the reflecting layers of the mirror. Electromechanical models of FBARs and SMRs are served to predict the impedance mismatching and resonance frequency changes due to new layers in the stack, which is useful for analyzing sensor and filter applications.

3.3 Equivalent-Circuit Models

Equivalent-circuit modeling is a powerful resonator analysis and design tool, which represents the resonator as a lumped-element circuit in the electrical domain. The parameters of the equivalent circuit characterize the physics and fabrication process of the resonator, and they are also an electrical abstraction of the motional response of the resonator (related to processing but without physical meaning). At the system level, electrical equivalent-circuit models aid the fitting and parameter extraction used in the design of circuits integrating FBARs, MEMS, and NEMS resonators.

3.3.1 The Resonant LC Tank

The basic equivalent circuit of resonators is the lossless resonant LC tank depicted in Figure 3.16. The tank is a second-order, frequency-selective impedance that stores electromechanical energy, whose resonance frequency f_0 is given by [21]:

$$f_0 = \frac{1}{2\pi\sqrt{L_t C_t}} \tag{3.11}$$

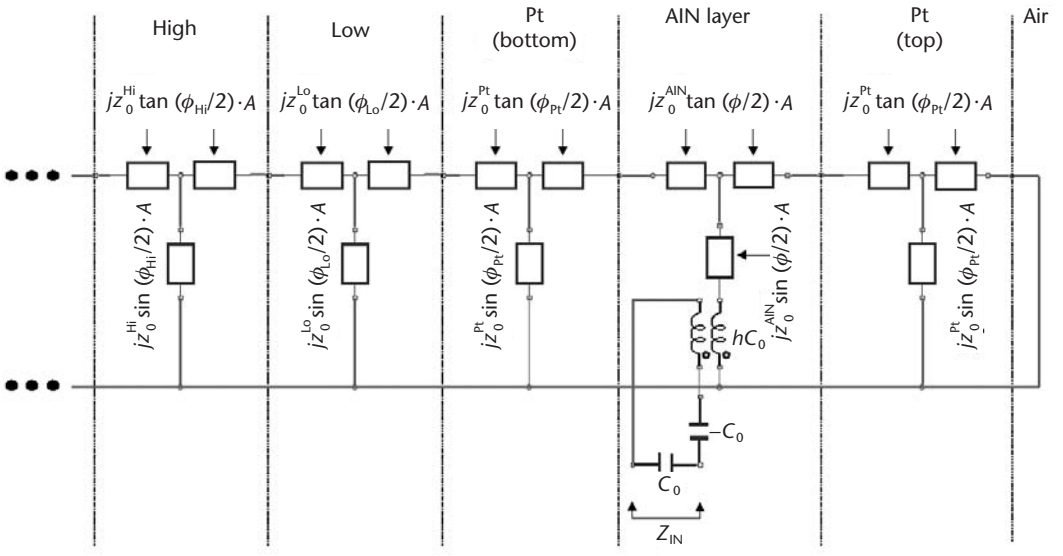

Figure 3.15 Transmission line model of an SMR.

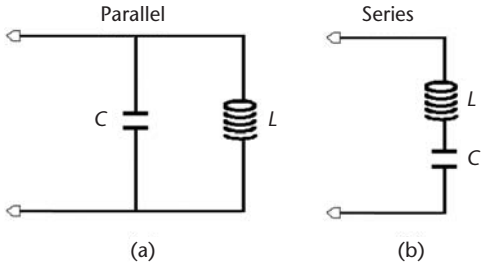

Figure 3.16 The resonant LC tank: (a) parallel circuit (at resonance: maximum impedance, minimum admittance); and (b) series circuit (at resonance: minimum impedance, maximum admittance).

where L_t and C_t are the equivalent inductance and capacitance of the tank. The parallel and serial LC tanks behave like resonant circuits, but the frequency-dependent impedances are opposite. At the low frequencies, far below the resonance frequency, the series LC tank is essentially a capacitor of impedance $1/j\omega C_t$. Far above resonance, the tank presents an inductive behavior with impedance approximately equal to $j\omega L_t$. At resonance, the series inductive and capacitive impedances compensate among them, and the overall impedance is minimized. The parallel tank works in the opposite way. At the resonance frequency, its impedance and admittance reach maximum (infinite) and minimum (zero) values, respectively.

However, physical systems are lossy circuits that prevent infinite energy storage in the tank. Thus, the basic lossless LC circuit is complemented with a resistor representing the losses in the tank that allows calculation of the quality factor [22]:

$$Q = \frac{1}{2\pi f_0 RC} \tag{3.12}$$

In terms of L, this is equivalent to:

$$Q = \frac{2\pi f_0 L}{R} \tag{3.13}$$

The resonant tank models to a large extent the behavior of radio frequency components, antennas, waveguides, and transmission lines, which are actually tuned resonant circuits. Nevertheless, the process and transduction particularities of acoustic and electromechanical resonators require models whose parameters describe their physics and operation. We examine this subject in the following section.

3.3.2 The Butterworth-Van-Dyke Model

The Butterworth-Van-Dyke (BVD) model is an equivalent-circuit representation suitable for crystal resonators, FBARs, and electrostatically actuated MEMS and NEMS resonators [23]. Figure 3.17 shows the BVD circuit, which has two parallel branches—namely, the motional and static capacitance arms. The motional arm comprises the series motional inductance L_m, capacitance C_m, and resistance R_m.

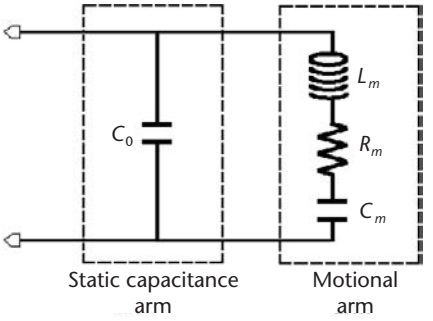

Figure 3.17 Butterworth-Van-Dyke model of micro- and nanoresonators depicting the motional and static-capacitance branches.

Although without physical meaning, motional elements relate to process-dependent parameters and material constants. The static capacitance branch is formed by the parallel-plate capacitance C_0 formed between the top and bottom electrodes of FBAR and SMR resonators, or between the cantilever and the electrodes of MEMS resonators.

As a two-branch parallel circuit, BVD models explain the series and parallel resonance frequencies found in FBAR and electrostatic MEMS resonators, given by:

$$f_S = \frac{1}{2\pi\sqrt{L_m C_m}} \tag{3.14}$$

$$f_P = \frac{1}{2\pi\sqrt{L_m \cdot \left(\frac{C_m C_0}{C_m + C_0}\right)}} \tag{3.15}$$

where f_S and f_P are the series and parallel resonance frequencies, respectively. Because the impedance is minimized at f_S, this frequency is often referred to as simply the *resonance* frequency, while f_P is the *antiresonance*, as the motional impedance is maximum at this frequency.

The link between the circuital BVD model and the physics of its elements depends on the transduction mechanism. For example, the circuit elements of crystal resonators and FBARs are [24]:

$$C_0 = \frac{\varepsilon \cdot A}{t} \tag{3.16}$$

$$\frac{C_m}{C_0} = \frac{8 \cdot k_{eff}^2}{N^2 \cdot \pi^2} \tag{3.17}$$

$$L_m = \frac{v}{64 f_S^3 \varepsilon A k_{eff}^2} \tag{3.18}$$

$$R_m = \frac{\eta\varepsilon}{16 f_S \rho A v k_{eff}^2} \tag{3.19}$$

where A is the area of the parallel-plate capacitor; ε, t, ρ, and v are the absolute permittivity, thickness, density, and speed sound of the piezoelectric material, respectively; N is the acoustic mode ($N = 1, 3, 5, \ldots$), and η is the acoustic viscosity related to the imaginary part of the wave vector $\kappa = \tilde{k}_r + j \cdot \tilde{k}_i$ by:

$$\tilde{k}_i = \frac{\eta\omega}{2\rho v^2} \times \left(\frac{\omega}{v}\right) \tag{3.20}$$

We carried out a similar analysis in Section 3.2.1 to find the RLC equivalent-circuit parameters of MEMS and NEMS resonators. Through (3.16) to (3.20), we can infer the physical constants of the process from the BVD circuit elements and curve fitting to experimentally obtained data. Process characterization based on this approach is explained in Chapter 5.

The modified Butterworth-Van-Dyke (MBVD) model allows us to obtain a more realistic representation of FBARs and acoustic resonators. The MBVD accounts for dielectric and ohmic losses in the piezoelectric material and the transmission line by using resistances R_P and R_S, respectively [25]. The MBVD circuit is depicted in Figure 3.18, which results from adding R_P and R_S to the BVD circuit. In the parallel-plate capacitance arm, R_P is serially added to C_0, whereas the transmission lines connecting the resonator are split in two components of resistance $R_S/2$, each one corresponding to the bottom and top electrode line losses.

The technological availability has made possible the application of FBAR, MEMS, and NEMS resonators in the field of radio frequency circuits to build competitive-performance blocks like filters, mixers, and oscillators. In this way, they are designed to operate at very and ultrahigh frequencies (VHF, UHF) and microwave bands. Typically, resonators are connected to other circuits and supported on silicon or SOI substrates. In the microwave regime, however, the substrate plays a major role in the performance of the circuit. Due to the high frequency, parasitic effects like ohmic losses and reactances become important in the working band [26]. These effects cause signal drifting from the RF path to the substrate, thus degrading the performance of the circuit.

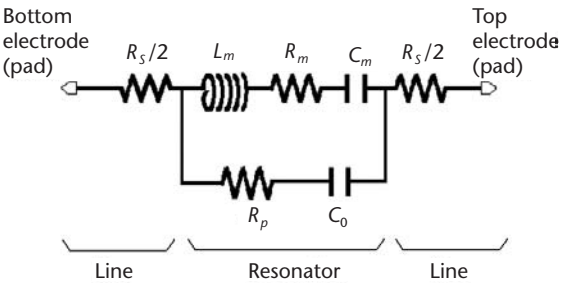

Figure 3.18 The modified Butterworth-Van-Dyke model: the circuit adds ohmic losses of the acoustic layer and the contact lines.

Three main sources of signal loss in microwave resonator circuits have been identified: conduction losses in the metal lines, dielectric losses in the substrate, and radiation losses. Conduction and radiation losses can be minimized by proper design of the RF conducting path, whereas high-resistivity substrates aid reducing the dielectric losses [27]. Depending on the frequency regime, a proper model has to be adopted to accurately describe these losses. This model is then employed to de-embed the resonator response from the parasitic effects of the circuit, which is useful in final-application circuit design. To exemplify this subject, we study next the equivalent-circuit model of an FBAR embedded in a coplanar transmission line and supported on a silicon substrate.

3.3.3 Case Study: FBAR Process and Modeling

The FBAR of our case study is fabricated on top of a SiO_2 layer and a 500-μm-thick silicon (Si) substrate. This substrate is a 10^{15} cm^3-boron-doped low-resistivity Si wafer. The FBAR is comprised by bottom and top titanium-platinum (Ti/Pt) electrodes with thicknesses of 30 and 150 nm, a 700-nm-thick aluminum nitride (AlN) layer. Front-side RIE-assisted micromachining releases the resonator. With this configuration, we expect to find the resonance frequency in the 2-GHz band.

Due to characterization purposes, the resonator is embedded in a coplanar transmission line with ground-to-signal-to-ground (GSG) connections to the FBAR. Although the isolating SiO_2 is between the signal line and the substrate, part of the RF signal energy diverts to the substrate through the oxide, thus promoting dielectric losses. In the 2-GHz regime, the SiO_2-Si substrate can be modeled by resistive and reactive elements [28], as it represents the drawing of Figure 3.19. The oxide capacitance C_{ox} depends on the thickness, area of the electric contact, and dielectric constant, which is determined by the fabrication process. The resistance R_{sub} and capacitance C_{sub} values depend on the substrate thickness and resistivity, the latter being primarily influenced by the doping characteristics.

Assuming that the FBAR is accurately modeled by the MBVD elements, the equivalent circuit of the system is the superposition of the resonator's MBVD, transmission line, contact pads, and substrate models. Figure 3.20 shows the cross-sec-

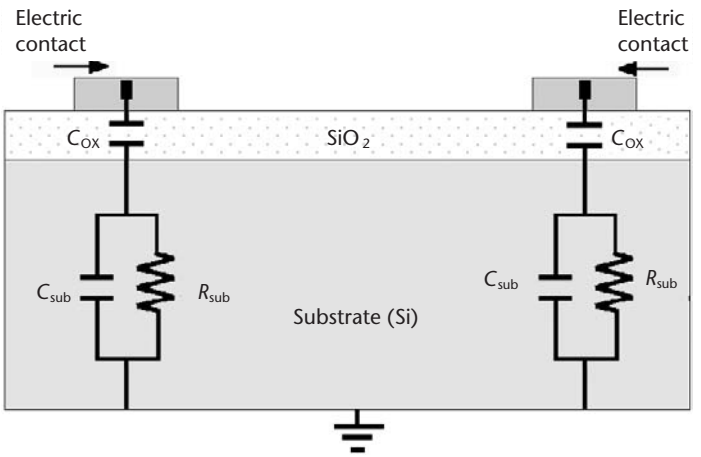

Figure 3.19 Equivalent-circuit model of substrates at the microwave regime.

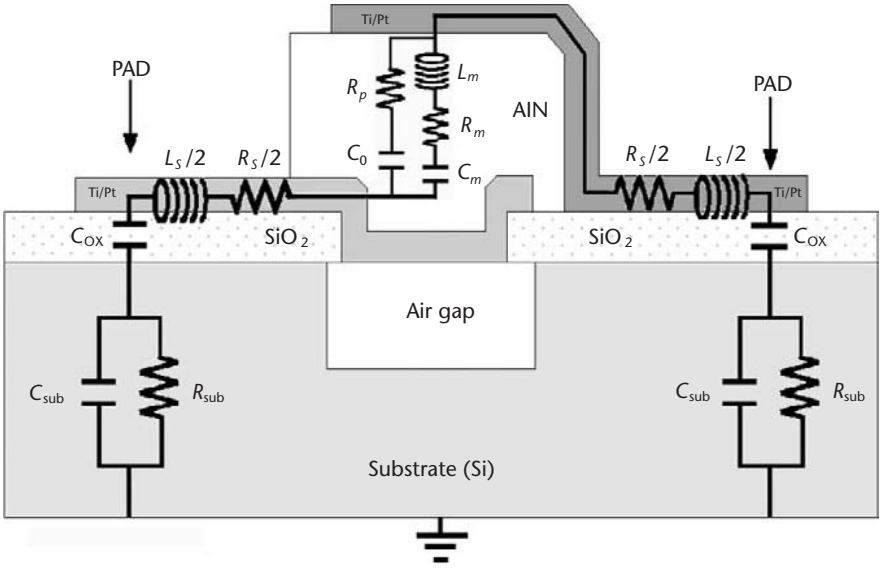

Figure 3.20 Equivalent circuit model of FBAR, including substrate loss and reactance elements (the FBAR is embedded in a coplanar transmission line).

tion of the process and the model elements. In addition to the MBVD elements—R_m, L_m, C_m, C_0, R_p, and R_s—and substrate elements—R_{sub}, C_{sub}, and C_{ox}—the model includes the line inductance L_s, which describes the parasitic inductance becoming of significance in long transmission lines [29].

Figure 3.21 shows the circuit, with the duty FBAR area in the center of the image, the long transmission lines connecting the electrodes to the contact pads at both the right and left side of the FBAR, and the substrate. The circuit elements are annotated in the picture to illustrate the model. The width and length of the transmission line are 70 μm and 150 μm, respectively, which gives theoretical $R_s/2$ and $L_s/2$ values of 1Ω and 60 fH, respectively. Calculation of C_{ox} for a 400-nm-thick thermal-SiO_2 layer with pad area of $70 \times 70\ \mu m^2$ leads to a theoretical value of 420 fF. Concerning the 500-μm-thick Si substrate, theoretical calculations of R_{sub} and C_{sub} result in values found in the range of 4,500Ω and 1 fF, respectively.

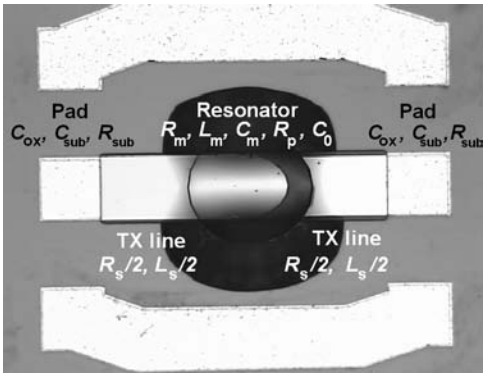

Figure 3.21 FBAR embedded in transmission line: the resonator, contact pads, and substrate loss and reactance elements are signaled.

These calculations give a general idea of the magnitude orders of the circuit elements, and they are useful to define the initial conditions of parameter extraction algorithms, as we study in Chapter 5.

3.4 Finite Element Modeling (FEM)

Finite-element modeling (FEM) is a vast field that merits full coverage in a complete book. The FEM analysis field spans from the formulation of numerical analysis and computational efficiency to the operational aspects of FEM commercial tools [30, 31]. Instead of going in depth on these topics, this section introduces general ideas about concepts, procedures, and working flow of FEM analysis. Computer-aided FEM is a powerful numerical-analysis tool that allows accurate prediction of the static and dynamic responses of a multiple-domain physical system. FEM analysis reproduces the geometry and forces interaction of complex systems whose analytical formulation is unfeasible. Starting from the structural model of the system, FEM analysis couples the structural physics with electrostatic, magnetostatic, piezoelectric, thermal, optic, fluidic, and electromagnetic domains, among others (Figure 3.22). A number of commercial software tools are available in the market for FEM analysis, like ANSYS (Ansys Inc., Canonsburg, Pennsylvania) [32], Coventor [4], IDEAS [33], and COMSOL [34], to mention some of the most popular.

The FEM of FBAR, MEMS, or NEMS resonators is a system constituted of the following components:

1. The resonator itself;
2. The environment—air, vacuum;
3. The degrees of freedom or boundary conditions;
4. The excitation sources—atmospheric or relative pressure, gravity or another inertial force, mechanical acceleration, fluidic pressure, magnetic field, electric potential, and so on.

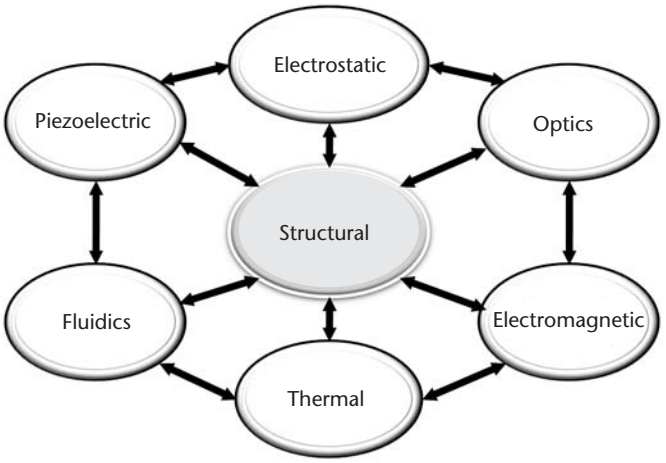

Figure 3.22 Physical domains in MEMS and NEMS finite element analysis.

As its name suggests, the fundamental component of an FEM is the *element*: the model geometry is structured by a group of elements, typically thousands of them, in the same way as bricks construct the shape and structure of a building. Being connected among them, such elements receive from and transmit to the rest of elements the forces that they are the object of from external excitation sources. When modeling the complete system, the FEM analysis software implements a set of equations pertinent to the physical domains involved in the interaction. These equations are applied and solved at the element level, and the results are stored in the system memory and used as an input parameter for the next element to be analyzed. In the end, all these results are scaled up and superposed to evaluate the global system response, whose quality will depend on the accuracy, correction, and complexity of the built model.

FEM analysis is a process that involves a set of necessary actions whose sequence is observed in the flow of Figure 3.23. First, the system characteristics and physical interactions between the system components are defined (this is not necessarily done with the FEM tool). From here on, the model of the system is built, by using a compiler or preprocessor (the /PREP primitive of ANSYS, for example). First, we define the materials and element types; then we generate the geometry; and next we mesh this model with a number of elements that can be specified by the designer. Once the model is made and meshed, the degrees of freedom (DOF) or boundary conditions of the system are applied to it. This establishes the physical reference frame, and it involves initial force definition, initial charging, and clamping of the structure, among others. Once this task is completed, we proceed to solve the model according to the simulation settings defined by the user. Structural, modal, and harmonic analyses can be carried out, with or without initial stresses or loads included in the analysis. Linear and nonlinear analysis options are also available in commercial tools. When the analysis finishes, the postprocessing system of the FEM

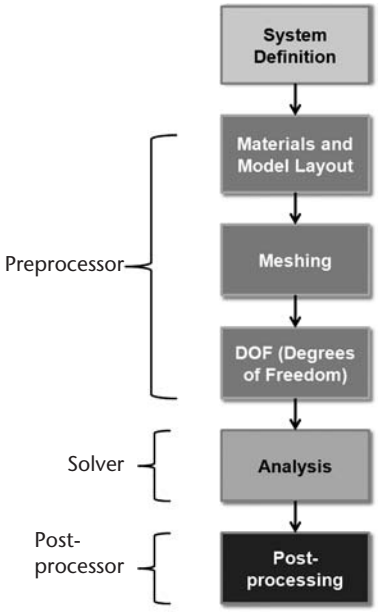

Figure 3.23 Finite element modeling flow.

tool allows evaluation of the simulation results, as they are provided in the form of graphs, charts, tables, or 3D plots. Specific primitives of the program are invoked to enter in postprocessing mode (e.g., /POST in ANSYS).

Generally speaking, the analyzer solves the second-order differential equations relating the mechanical response to an external force applied to the system, which was already defined by (3.1) and reproduced here for convenience:

$$m\ddot{x} + D\dot{x} + kx = F \tag{3.21}$$

where m is the mass, k is the spring constant, D is the damping, and F is the applied force. It should be noted that $F = 0$ in the modal analysis because it aims to find the eigenvalues of the system when no external forces are applied. The end products of the FEM analysis are the material deformations, stress, induced currents or electromagnetic fields, current flows, resonance frequencies, frequency responses, and many other results. The nature of applied forces will determine the implemented models, elements, and physical domain coupling. When the system response of a model defined in a certain physical domain to forces applied forces in another one is studied, we speak in terms of coupled-field response. Modern tools implement the design options to cover multiple-domain physical interaction.

3.4.1 Building the Model

Building the model starts from the concept of the desired FEM of the resonator. This includes taking a priori decisions with regard to four topics: (1) geometry and materials of the device; (2) type of analysis; (3) type of elements; and (4) degrees of freedom (DOF) of the structure. Creation of the model geometry and of the material and element database is possible due to different tools available in commercial simulators, which are useful for building complex geometries, conics, and micromachined-like 3D structures, for example. In general, the more realistic the geometry of the model, the more accurate the simulation results will be obtained.

However, simplified geometries and 2D models are often enough to get accurate results. This mainly depends on the DOFs and symmetry, thus limiting the model generation and meshing to the active resonator volume. Also, the chosen element types have to be prepared to couple the physical domains involved in the analysis type. Experienced designers let a program routine select the element type in the function of the analysis when different simulations are to be run with the same model. Figure 3.24 shows the conceptual drawing of a MEMS cantilever that has been prepared to define the geometry and DOF in order to build its FEM. The spatial orientation, dimensions, shape, and materials of the cantilever, the clamping area (U_X, U_Y, $U_Z = 0$), and electrostatic configuration ($\phi_T = 1\text{V}$, $\phi_B = 0\text{V}$) have been chosen in this example.

Once the geometry is built and the element and material types are chosen, the model is meshed with a number of elements that can be specified by the designer. Again, many options exist to complete this task, including manual, automatic, mapped, or free meshing. The designer has to be aware of the compatibility between the element and analysis types, which vary with the simulation software and depend on the shape, available DOFs, and number of nodes of the element, among other

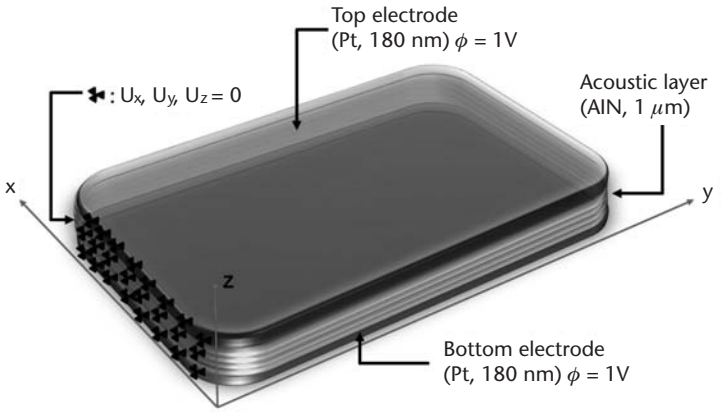

Figure 3.24 Conceptual drawing of the FEM model of a MEMS cantilever resonator depicting the geometry and degrees of freedom.

factors. Figure 3.25 shows the 2D model of a meshed system consisting of a resonant silicon-MEMS cantilever, a magnet inserted in the MEMS, the air surrounding the device, and the space region where the magnetic field lines are parallel to the infinite boundary. The different material types are differentiated by their tone: the lightest tone is the *infinite* region, mid-gray is the air around the MEMS, the gray in the central region represents the cantilever, and the darker tones are the elements of the magnet.

Accuracy of the simulation is determined by the number of elements and their aspect ratio. The aspect ratio definition depends on the element shape and model, although, as a general rule, it is the quotient of the largest over the shortest element

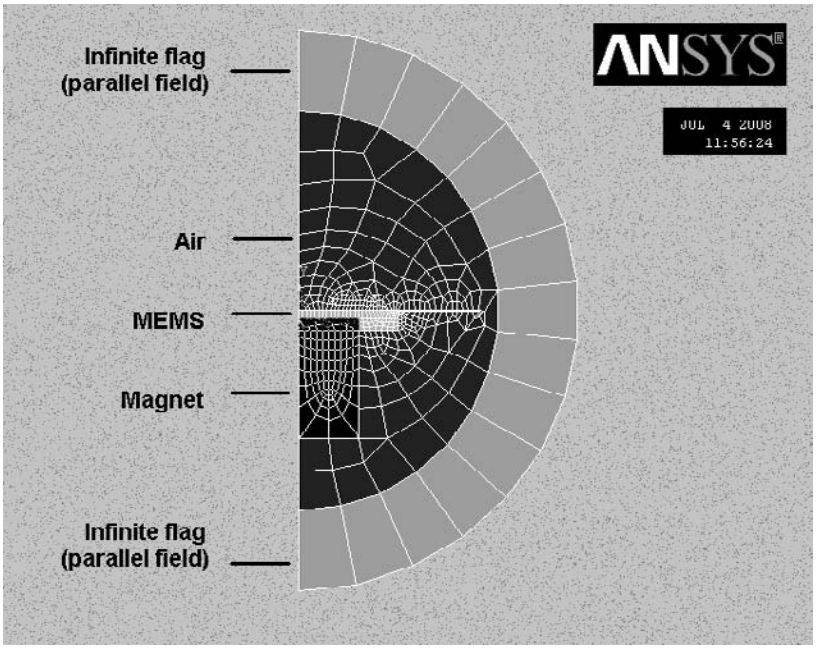

Figure 3.25 FEM meshing: MEMS cantilever resonator (light gray in the center) with inserted magnet (dark), air, and infinite boundary elements around them.

dimension in the mesh. Sometimes, high-aspect ratio elements are created, which degrades the numerical approximations assumed for regular elements. This will alter the solution superposition and the global response of the system, which also depends on the relative element size with respect to the structure dimensions. Thus, denser meshing leads to better superposition and model quality. It is a good design practice to perform a mesh testing to ensure the quality and reliability of the simulations. The example of Figure 3.26 shows the influence of the aspect ratio (AR) and element size in the resonance frequency of an FBAR. Figure 3.26(a) shows the simulated results of resonance frequency against element size (the aspect ratio is constant and equal to 11). The response of Figure 3.26(b) evidences a dependence on the aspect ratio of elements. Therefore, we obtain different aspect ratios by changing the element size. Although slight differences arise, they can be enough to degrade the performance of the prediction, especially when the resonator is designed for high-sensitivity applications.

3.4.2 Structural, Modal, and Harmonic Analyses

Once the model is meshed and the DOFs are defined, the corresponding analyses of the MEMS are carried out. Structural, modal, and harmonic are the most-performed

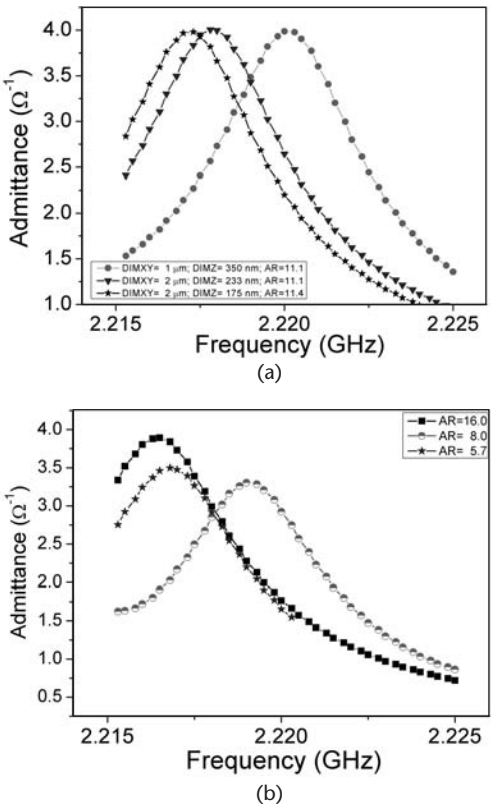

Figure 3.26 Mesh study to analyze the frequency stability of the model as a function of (a) constant aspect ratio (AR) equal to 11; and (b) fixed element thickness of 87 nm and variable *xy* dimensions to obtain a variable AR.

analyses for studying FBAR, MEMS, and NEMS resonators, although many other analysis options exist, depending on the physics of the resonator transduction.

Structural analysis aims to determine stresses, strains, deformations, and deflections of the resonator due to static force loading like gravity, pressure, inertial acceleration, or another constant force applied to the nodes, the elements, or one of the structure surfaces. Figure 3.27 shows the contour plot of a MEMS cantilever with silicon mass and a magnet inserted in the mass. The picture compares the initial and equilibrium positions of the system after considering the effect of gravity force (+1g) applied to the structure. The calculated deflection at the maximum displacement edge of the mass is about 168 μm.

Modal analysis extracts the natural frequencies (eigenvalues) of the MEMS device. In this analysis, the external forces are set to zero values ($F = 0$), as stated before. Thus, the analysis searches for modes existing between given frequency ranges. Otherwise, the simulator runs freely to find the first N eigenmodes of resonance, which is a user option. Modal analysis does not quantify the deformation or vibration amplitude of the structure at the so-found natural frequencies. Instead, it solves (3.21) to calculate the node displacement, thus finding the frequencies of maximum displacements. Commercial software can produce contour plots representing the shape of the studied modes. Contour plots of two eigenmodes of a silicon-FBAR resonant accelerometer are seen in Figure 3.28. While the geometry of the silicon mass shown in Figure 3.28(a) mainly determines the 3-kHz mode, the 800-kHz mode is attributed to the fundamental frequency of the sensing FBAR resonator [35]. In the latter case, the mass remains essentially immobile [Figure 3.28(b), detail of the resonator shape in the inset].

Harmonic analysis studies the dynamic response of the resonator to an excitation signal ($F \neq 0$), between user-defined starting and ending frequencies. Thus, it assumes that one or more modes with significant amplitude are found in the span of interest. It gives understanding of the relative amplitude of the different modes (something that is impossible to do with modal analysis) and allows detecting

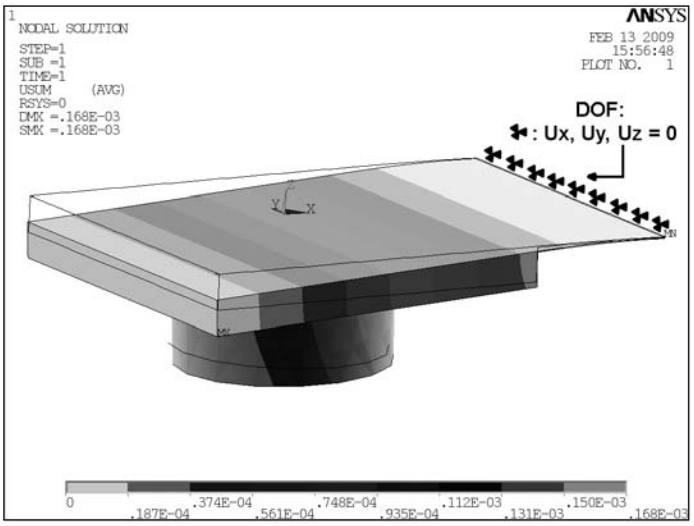

Figure 3.27 Structural analysis results: static deflection of the cantilever due to gravity force.

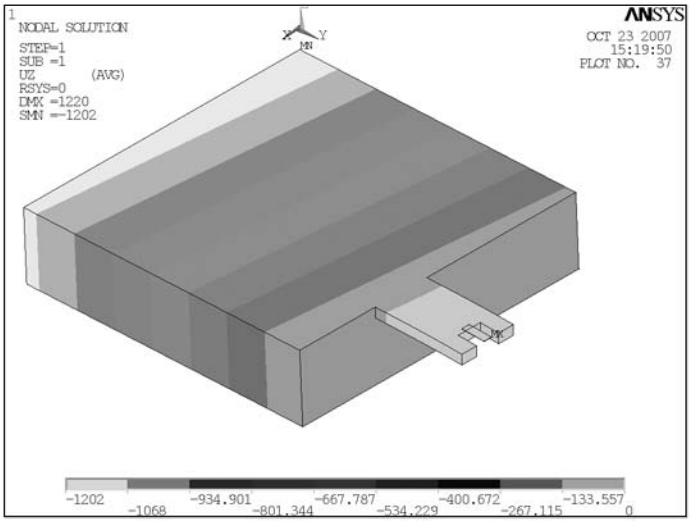

(a)

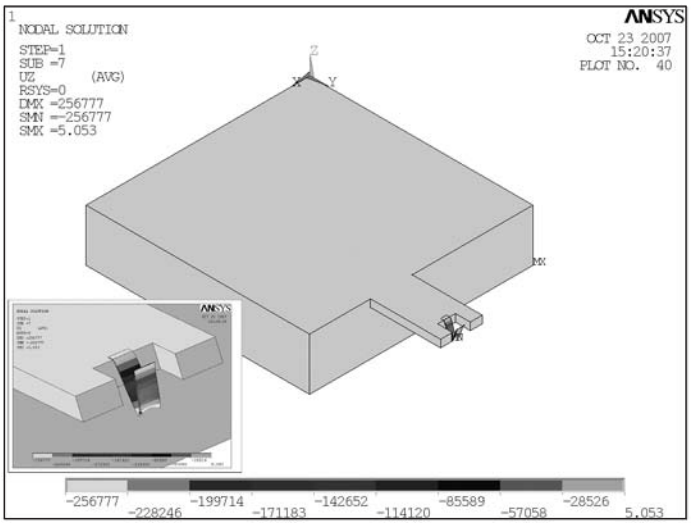

(b)

Figure 3.28 Modal FEM analysis of a Si-FBAR accelerometer: (a) 3-kHz mode shape of the fundamental value of the structure (it corresponds to the Si mass eigenfrequency); and (b) 800-kHz mode corresponding to the sensing resonator (detailed in the inset).

small-amplitude modes that may pass unseen by the user when performing the modal analysis. Output data of harmonic analysis include tables relating amplitude against frequency or time, and nodal solutions used in the generation of mode-contour plots.

3.4.3 Coupled-Domain Analysis

A coupled-domain or coupled-field analysis is performed when the designer wants to evaluate the influence of external forces in one domain in the static or dynamic response in other domains. For example, the magnetic force attracting the magnet

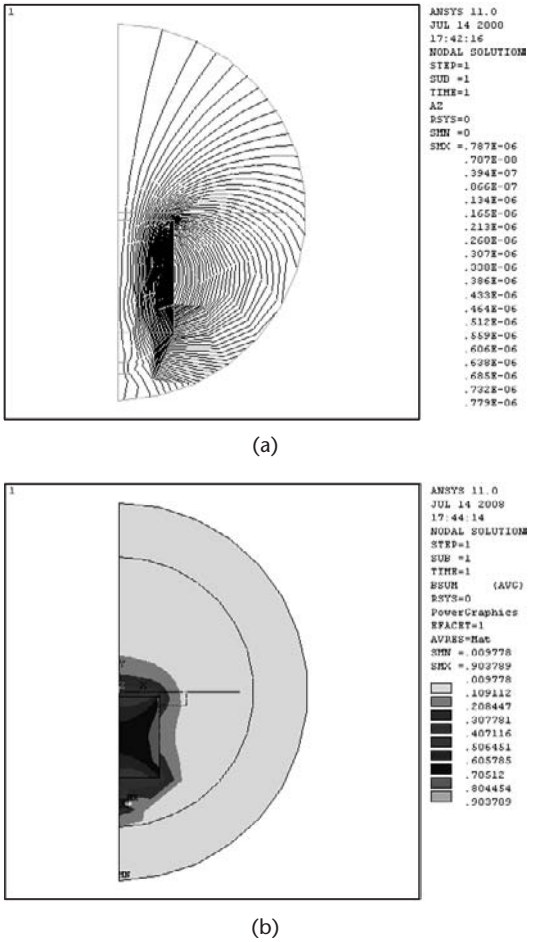

Figure 3.29 Magnetic-structural coupled-field FEM analysis: (a) magnetic flux lines; and (b) magnetic flux density.

inserted in the MEMS shown in the previous example generates a structural deflection of the cantilever. The magnitude of the deflection can be predicted if the amount of magnetic force is estimated in advance. This result is employed in structural design of the MEMS. In this example, the first question is, how we can determine the amount of force to apply to the structure? This case requires coupling the magnetic and the structural domains in order to design the structure and to know the magnetic force arising between the magnetic components.

There are two different strategies to perform a coupled-field analysis:

- Multifield solver;
- Complete transient simulation.

ANSYS Multiphysics solves the multifield strategy by defining two or more sets of single-domain elements, grouping the element types into physical fields, and selecting the quantities to be passed between the fields and the order in which such

fields are to be solved. Additional commands control the loading of simulation vectors to proceed with the system solving [36].

The second strategy proposes performing independent simulations, each one with its own inputs and element types. Following with the example of the magnetic MEMS-magnet system, the model is meshed with magnetic elements, and the magnetostatic solution is calculated. The results are then saved and stored in the simulation database to be used as inputs for the second structural analysis. Next, the model is remeshed with structural elements, and the solver executed. Several iterations may be required to design a system with desired values, which is typically done by a loop. Figure 3.29 shows the magnetic flux lines and magnetic flux density after magnetostatic analysis of the magnetic sensor 2D model. Pursuant to this analysis, the magnetic force arising between the magnet and the excitation source is obtained, which is used in the structural analysis to excite and calculate the displacement of the MEMS-magnet ensemble.

3.4.4 Case Study: Modal and Harmonic Analysis of a Resonant Mass Sensor

We now examine the model of an FBAR-based resonant mass sensor built in ANSYS. The resonator is made of Pt electrodes and an AlN acoustic layer. Figure 3.30 depicts a section of the model meshing, with the electrodes and the AlN being tone-differentiated by their material types. As observed in the figure, the meshing is uniform, as the model has a total of 15,000 elements with a maximum aspect ratio of 5.7.

The eight-node hexahedral SOLID5 and SOLID45 options were selected for the element geometry, and the lateral dimensions (xy) of all elements were of 1 μm. The ANSYS element types SOLID5 and SOLID45 are served to implement the piezoelectric and electrode materials. SOLID5 has a 3D magnetic, thermal, electric, piezoelectric, and structural field capability with limited coupling between the fields. The element thus has eight nodes with up to six degrees of freedom at each node and hexahedral or prism geometry options. When used in structural and

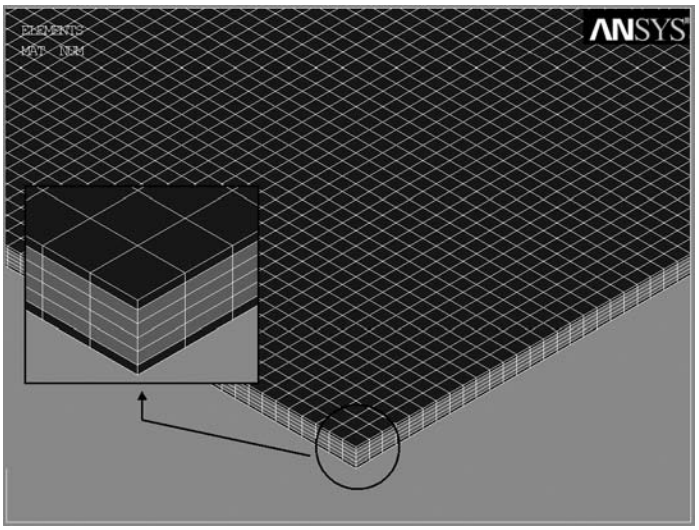

Figure 3.30 Section of the FBAR sensor meshing built-in ANSYS.

piezoelectric analyses, SOLID5 has large deflection and stress stiffening capabilities. SOLID45 is used for the 3D modeling of solid structures and has geometry similar to that of SOLID5. However, the element is defined by eight nodes having only three degrees of freedom at each node: translations in the nodal x, y, and z directions. In this model, coupled-field and translational DOFs are defined for the SOLID45 elements, whereas only translational DOFs are defined for the SOLID5 elements. According to this meshing, the model comprises 18,200 nodes.

The material properties used in the simulations are those presented in Table 3.1. The damping D equal to 110^{-3} is defined for the AlN material type. The assigned value of D uses the ANSYS definition of $D = 1/(2Q)$, where the Q factor is chosen to have a value similar to that of FBARs available in the market and literature ($Q \sim 500$). The resonator is a clamped-clamped beam that has lateral dimensions of $50 \times 70\ \mu m^2$, and electrode and AlN thicknesses of 180 nm and 1,000 nm, respectively. The DOFs include displacement ($U_{x,y,z}$) and voltage ($VOLT$) boundary conditions defined at all the nodes located at the clamping lateral-wall surfaces and the electrodes of the FBAR. Thus, a 1-V voltage is applied to the top electrode, while the bottom electrode is grounded to 0V, respectively. The structural DOFs translate into mechanical displacements U_x, U_y, and U_z equal to 0 at the corresponding nodes. With this configuration, the DOF matrix has a size of 7,344 nodes; 2,142 of them defined for $U_{x,y,z}$ and 5,202 devoted for $VOLT$ [37].

ANSYS performs modal and harmonic analyses on this model around the design 2-GHz frequency band. The user defines the number of extracted and expanded modes in the frequency span. Figure 3.31 shows the contour plot of the 2.22-GHz longitudinal mode of the FBAR, which is seen at its perspective and side views. In this "breathing-like" mode, the nodal displacements are bigger at the resonator's center, whereas they are negligible near the clamping zones.

Parametric harmonic analysis was carried out to observe the impact of the material properties on the resonance frequency of the longitudinal mode. In Figure 3.32 the frequency response between 2.35 GHz and 2.55 GHz is plotted. There, major peaks near 2.40 GHz and 2.48 GHz correspond to the longitudinal-mode resonance and antiresonance frequencies. If we look into the frequency range close to the resonance peak, we find that frequency and mode shaping differences arise between the three curves, due to the modified material properties. Besides the reso-

Table 3.1 Material Properties Used in the FEM Simulations of the FBAR Sensor

	AlN	*Pt (Electrodes)*
ρ [kg/m^3]	3,000	21,450
υ	0.35	0.38
c^E_{33} [GPa]	200	144
ε^E_{33} [GPa]	8.81	—
e_{13} [C/m^2]	–0.6	—
e_{23} [C/m^2]	–0.6	—
e_{33} [C/m^2]	1.46	—
e_{52} [C/m^2]	–0.48	—
e_{61} [C/m^2]	–0.48	—

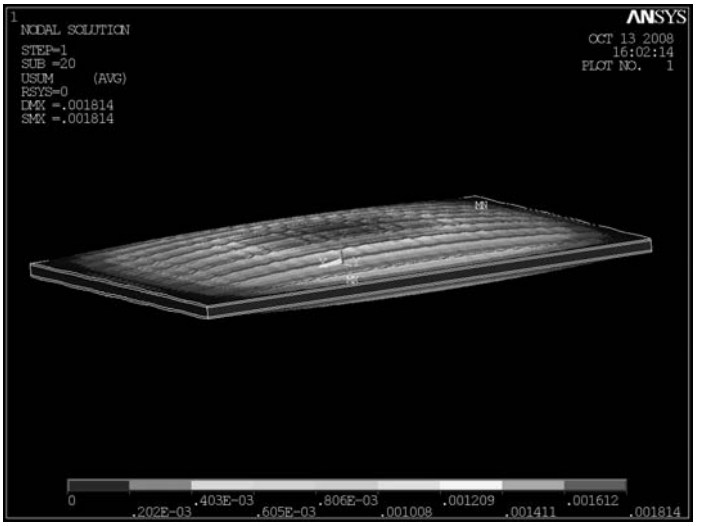

(a)

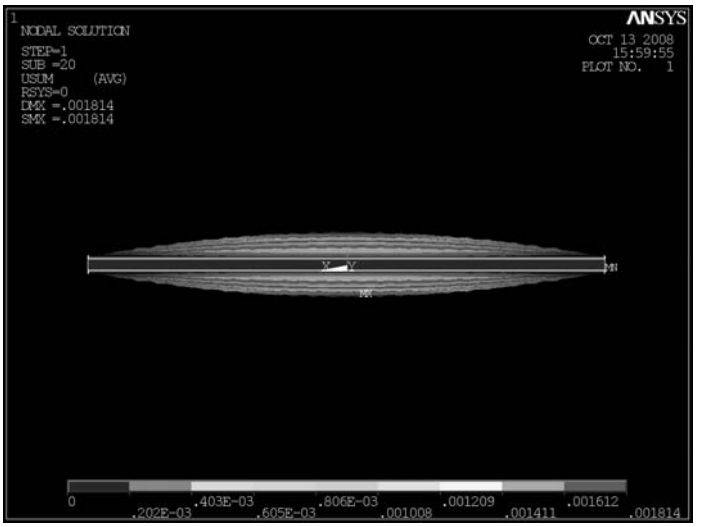

(b)

Figure 3.31 Contour plot of the longitudinal mode of the FBAR sensor (modal analysis): (a) perspective view and (b) side view.

nance frequency shifting, minor modes shift to a different value, diminish or augment their relative amplitudes, superpose to other modes, or simply disappear.

Harmonic and modal FEM analysis finds application in resonator chart-mode building. This is employed in full-mode resonator design where the evolution of longitudinal and transversal modes against dimensions of the resonator is examined through parametric studies. As another subject of interest concerning FEM, complete knowledge of the material properties is crucial for accurate modeling of the absolute harmonic response of the FBAR. As manufactured devices have process-dependent material properties, FEM simulations can also be served to extract their values from experimental device characterization.

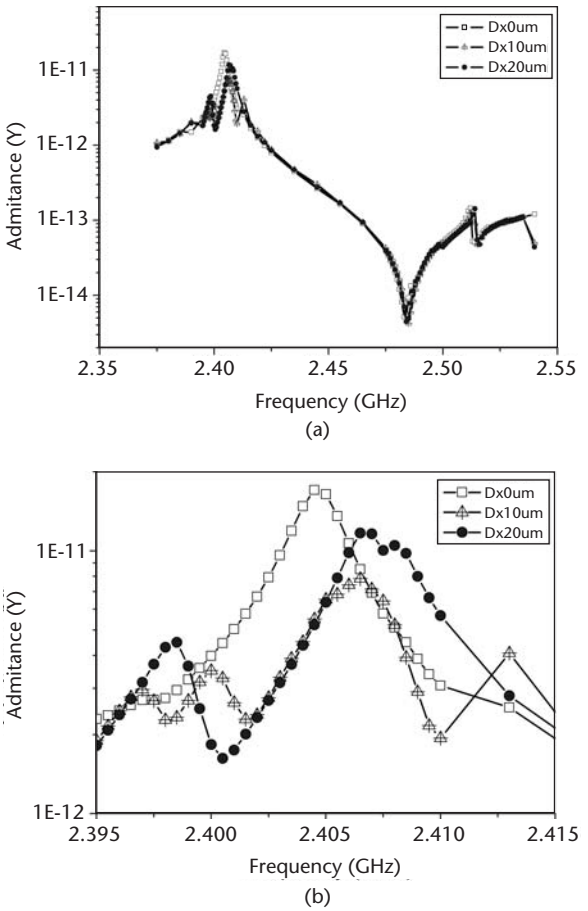

Figure 3.32 Parametric analysis of the FBAR frequency response after harmonic analysis: (a) 2.35-GHz to 2.55-GHz frequency span, and (b) zoomed in view around 2.4 GHz (the resonance frequency and mode shaping differences are observed at this scale).

3.5 Summary

The design of resonators passes through different modeling approaches. Therefore, we consider analytical models based on the physics of the resonator, electromechanical models, equivalent-circuit parameter models, and finite element models based on numerical methods and domain coupling analysis. In the end, these models serve to perform the physical layout design and, on the other hand, as characterization tools when fabricated devices are available.

Electromechanical transformer models offer the conceptual basis to comprehensive understanding of the resonator operation mechanisms. They analyze both the electrical and mechanical domains by using a unified approach, and they can be interconnected to model more complex resonator-based systems.

Equivalent-circuit modeling is, in general, an electrical-domain representation of the resonator. Equivalent-circuit parameters characterize the physics and fabrication process of the resonator, and they represent an electrical abstraction of the resonator motional response. At the system level, electrical equivalent-circuit models

aid the fitting and parameter extraction tasks performed for circuit design purposes. The technique is currently employed for designing FBAR, MEMS, and NEMS resonator-based integrated circuits.

Last but not least, we have gone into the physical implementation details of FEM analysis. Besides being a powerful prediction tool, FEM simulations with experimental characterization data are served to extract the process-dependent material constants. The sophistication level of commercial FEM design software makes the field of FEM analysis an enriching experience for designers and process engineers. The available tools support the execution of multidomain analysis of virtually any micro- or nanostructure.

While the design and modeling processes conclude with the manufacturing of devices, one can say that the modeling cycle always continues. Existing designs and processes need permanent refinement. Thus, modeling provides us with the valuable information needed for iterative device improvement, from the abstract to the physical levels.

References

[1] Fedder, G. K., "Structured Design of Integrated MEMS," *Proc. IEEE Intl. Conf. MEMS 1999*, Orlando, FL, January 17–21, 1999, pp. 1–8.

[2] Fan, Z., et al., "Structured Synthesis of MEMS Using Evolutionary Approaches," *Appl. Soft Comp.*, Vol. 8, 2007, pp. 579–589.

[3] Cadence Design Systems, Inc., http://www.cadence.com.

[4] Coventor, Inc., http://www.coventor.com/.

[5] The MathWorks, Inc., http://www.mathworks.com/.

[6] Pederson, D., "Simulation Program with Integrated Circuits Emphasis (SPICE)," University of California–Berkeley, 1975.

[7] Kundert, K., and J. White, "Spectre Circuit Simulator," Cadence Design Systems.

[8] IEEE Std. 1364-2001, "IEEE Standard Verilog Hardware Description Language," Institute of Electrical and Electronics Engineers, New York, 2001.

[9] IEEE Std. 1076.1-1999, "VHSIC Hardware Description Language Analog and Mixed-Signal," Institute of Electrical and Electronics Engineers, New York, 1999.

[10] Bode, H. W., "Bode Plots," AT & T Bell Labs, circa 1930.

[11] Evans, W. R., "The Root Locus Method," originally published in *AIEE Transactions*, 1948. Republished in *Control System Dynamics*, New York: McGraw-Hill, 1954.

[12] Polderman, J. W., and J. C. Willems, *Introduction to Mathematical Systems Theory: A Behavioral Approach*, New York: Springer, 1998.

[13] Tipler, P., *Physics for Scientists and Engineers: Vol. 1*, 4th ed., New York: W. H. Freeman & Co., 1998.

[14] Bannon, F. D., J. R. Clark, and C. T.-C. Nguyen, "High-Q HF Microelectromechanical Filters," *IEEE J. Solid-State Circuits*, Vol. 35, 2000, pp. 512–526.

[15] Mason, W. P., *Electromechanical Transducers and Wave Filters*, Princeton, NJ: Van Nostrand, 1948.

[16] Krimholtz, R., D. A. Leedom, and G. L. Matthaei, "New Equivalent Circuit for Elementary Piezoelectric Transducers," *Electron. Lett.*, Vol. 6, 1970, pp. 398–399.

[17] Lakin, K. M., G. R. Kline, and K. T. McCarron, "Development of Miniature Filters for Wireless Applications," *IEEE Trans. on Microw. Theory Tech.*, Vol. 43, 1995, pp. 2933–2939.

[18] Heaviside, O., "Electromagnetic Induction and Its Propagation," *The Electrician*, 1885, 1886, and 1887.

[19] Wolfram Research, Inc., http://www.wolfram.com/.

[20] Aigner, R., "Volume Manufacturing of BAW-Filters in a CMOS Fab," *Proc. Second International Symposium on Acoustic Wave Devices for Future Mobile Communication Systems*, Chiba, Japan, March 3–5, 2004, pp. 129–134.

[21] Razhavi, B., *Design of Analog CMOS Integrated Circuits*, New York: McGraw-Hill, 2001.

[22] Davis, W. A., and K. K. Agarwal, *Radio Frequency Circuit Design*, New York: John Wiley & Sons, 2001.

[23] Lin, Y. W., et al., "Series-Resonant VHF Micromechanical Resonator Reference Oscillators," *IEEE J. Solid State Circuits*, Vol. 39, 2004, pp. 2477–2491.

[24] Kim, K.-W., et al., "Resonator Size Effects on the TFBAR Ladder Filter Performance," *IEEE Microw. Wirel. Compon. Lett.*, Vol. 13, 2003, pp. 335–337.

[25] Larson III, J., et al., "Modified Butterworth-Van Dyke Circuit for FBAR Resonators and Automated Measurement System," *Proc. IEEE Intl. Ultrason. Symp. 2000*, San Juan, Puerto Rico, October 22–25, 2000, pp. 863–868.

[26] Wittstruck, R. H., et al., "Properties of Transducers and Substrates for High Frequency Resonators and Sensors," *J. Acoust. Soc. Am.*, Vol. 118, 2005, pp. 1414–1423.

[27] Polyakov, A., et al., "High-Resistivity Polycrystalline Silicon as RF Substrate in Wafer-Level Packaging," *Electron. Lett.*, Vol. 41, 2005, pp. 100–101.

[28] Hasegawa, H., M. Furukawa, and H. Yanai, "Properties of Microstrip Line on Si-SiO_2 System," *IEEE Trans. on Microw. Theory Tech.*, Vol. 19, 2001, pp. 869–881.

[29] Campanella, H., et al., "Automated On-Wafer Extraction of Equivalent-Circuit Parameters in Thin-Film Bulk Acoustic Wave Resonators (FBAR) and Substrate," *Microwave Optical Tech. Lett.*, Vol. 50, 2008, pp. 4–7.

[30] Chandrupatla, R., and A. D. Belegundu, *Introduction to Finite Elements in Engineering*, 2nd ed., Upper Saddle River, NJ: Prentice-Hall, 1997.

[31] Zienkiewicz, O. C., and Y. K. Cheung, *The Finite Element Method in Structural and Continuum Mechanics*, New York: McGraw-Hill, 1967.

[32] ANSYS, Inc., http://www.ansys.com/.

[33] IDEAS Ltd., http://www.ideas-eng.com.

[34] COMSOL, Inc., http://www.comsol.com.

[35] Campanella, H., et al., "Accelerometer Based on Thin-Film Bulk Acoustic Wave Resonators," *Proc. IEEE Intl. Ultrason. Symp. 2007*, New York, October 28–31, 2007, pp. 1148–1151.

[36] ANSYS Inc. "Low Frequency Electromagnetic," Training manual, 2004.

[37] Campanella, H., et al., "Analytical and Finite-Element Modeling of a Localized-Mass Sensor Based on Thin-Film Bulk Acoustic Resonators (FBAR)," *IEEE Sensors J.*, Vol. 9, 2009, pp. 892–901.

CHAPTER 4

Fabrication Techniques

There exist a great variety of MEMS, NEMS, and FBAR processes and fabrication techniques. The fundamentals of some of those techniques were already discussed in Chapters 1 and 2. Next, we take the particular case of FBAR devices to illustrate a complete microfabrication process. Although FBARs are just one example of microresonators, the techniques presented in this chapter are also applicable to the general case of MEMS and NEMS resonators.

The main processes involved in the fabrication of FBARs are the piezoelectric layer and electrode's deposition and patterning, and the micromachining technology for the resonator releasing. Nowadays, these processes are implemented by using a variety of technologies to obtain high-quality factor devices.

The chapter discusses different realizations of the FBAR fabrication process, putting special emphasis on the aluminum nitride (AlN) layer deposition technology and material characterization. At the same time, it explains compatibility issues and the actions to solve them. Pursuant to the compatibility development, fully released devices can be fabricated and characterized. By using scanning-electron-microscope (SEM), interferometer, and confocal inspection techniques, the FBAR's structural analysis is carried out, as we explain at the end of the chapter.

4.1 Process Overview

FBARs are a sandwiched piezoelectric membrane, typically made of aluminum nitride (AlN), zinc oxide (ZnO), or lead zirconate titanate (PZT). Membranes for current 2.4-GHz devices have a thickness of about 1 μm. Sputtering or epitaxial are current techniques for deposition, which is performed on metallic layers of few hundred nanometers.

FBARs are typically fabricated on a silicon (Si) substrate and released by surface or bulk micromachining techniques to obtain a free-moving device with high-quality factors. Surface micromachining employs a sacrificial layer made of either a metallic or a dielectric material. An etchant solution reacts with the sacrificial layer, etching it. At the end of the process, the resonator exhibits its characteristic cavity once the sacrificial layer is removed. Because the sacrificial layer is a thin film of a few micrometers, surface micromachining produces quasi-2D devices.

On the other hand, bulk micromachining processes remove a considerable volume of the substrate, thus making the "3D" structure more fragile. The substrate is usually Si (100), although high-resistivity substrates are implemented in RF applications to diminish the signal coupling [1]. Two main techniques accomplish this process: dry and wet etching. Dry etching is based on RIE, DRIE, or ICP. The process is

carried out from either the front or the back side of the wafer. At its time, potassium hydroxide (KOH) or similar solutions etch Si (100) in an anisotropic way, by immersing the wafer in the solution. The schemas of Figure 4.1 depict side views of FBAR processes using these technologies.

Before the bottom electrode deposition, the first step consists of depositing a passivation layer on top of the Si substrate. The passivation provides a window for

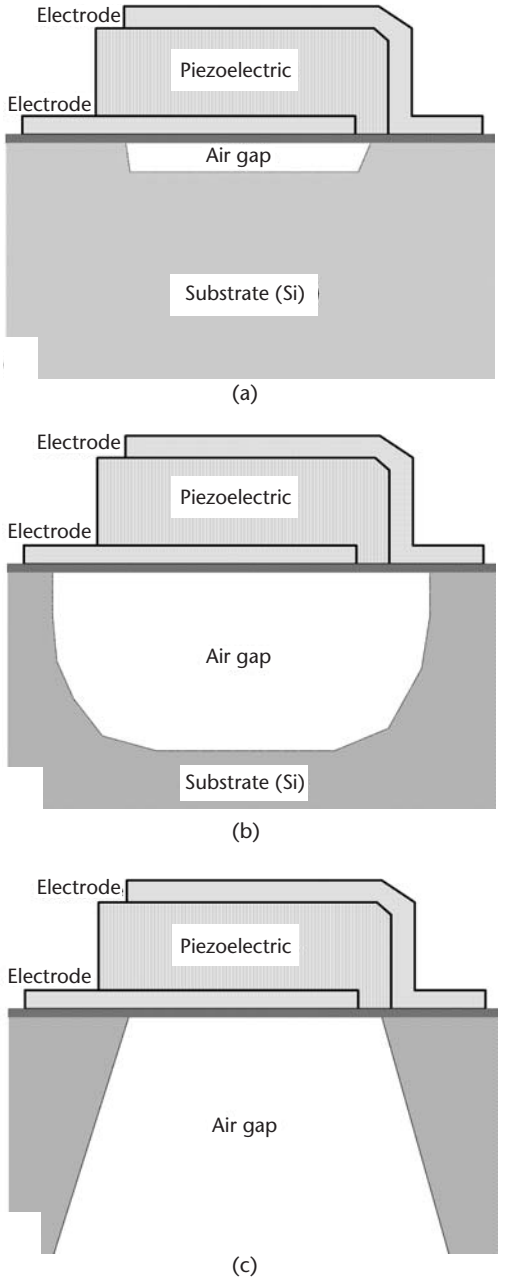

Figure 4.1 Micromachining technologies of FBAR processes: (a) surface, (b) front-side, and (c) back-side bulk micromachining.

etching and reduces the electrical coupling between the FBAR and the substrate, thus diminishing RF losses. Typical implementations of this layer involve silicon oxide (SiO_2) or silicon nitride (Si_3N_4) thin films with thicknesses of hundreds of nanometers.

Top and bottom electrodes are made of metallic materials of the same or different thicknesses, which is a design choice. Metals compatible with the crystallography and piezoelectric layer deposition are preferred to implement the bottom electrode. Platinum (Pt), molybdenum (Mo), tungsten (W), and chromium (Cr) are some examples [2]. The top electrode has fewer compatibility requirements. Thus, it can be fabricated using aluminum (Al), cupper (Cu), one of the metals previously mentioned, or another material compatible with standard integrated-circuit processes. The resonator contact pads may follow the current trends of standard CMOS processes, so they can be implemented with gold (Au) or Al. Some metals, like Pt, require an extra metal layer to allow proper adhesion to the substrate. Commonly used for the adhesion layer are titanium (Ti) or chromium (Cr), typically deposited with thicknesses of about 100 nm.

The three processes can be implemented through standard microfabrication clean room facilities and equipment. To further illustrate, Section 10.2 revises the step-by-step fabrication of a real device. In the following sections, we study the concepts, physical principles, fabrication equipment, materials, and chemical products involved in FBAR manufacturing. The study comprises fundamental definitions on oxidation, metallization, sputtering deposition, and micromachining techniques regarding FBAR and MEMS fabrication.

4.2 FBAR Fabrication Techniques

This section takes the particular case of FBAR to illustrate fabrication techniques that are common to MEMS and NEMS fabrication. Already in Chapter 1 we defined the physical and chemical concepts explaining the techniques. Now, we discuss the application of some of those techniques to the particular case of FBAR fabrication.

4.2.1 Oxidation of Silicon

Previously, in Section 1.3.2 the processing and applications of SiO_2 were explained. In the specific case of FBAR, oxidation will be used to passivate and interface the substrate and the device through a dielectric SiO_2 film. SiO_2 grown at high temperatures as previously described is also known as *thermal oxide*. However, SiO_2 can also be deposited on other materials (different from Si). In this case, chemical vapor deposition (CVD) is usually employed to obtain a high-quality oxide. In the case of FBAR implementations, either the thermal or the deposited SiO_2 may have thicknesses of hundreds of nanometers. Another application of CVD-deposited SiO_2 will be discussed in Chapter 6. There, we will see how a SiO_2 layer of appropriate thickness may optimize the temperature coefficient factor (TCF) of FBARs implemented with AlN.

4.2.2 Metallization and Piezoelectric Layer Deposition

As defined in Chapter 1, metallization is the formation of metal films for interconnections, ohmic contacts, rectifying metal-semiconductor contacts, and protections. Metallic thin films can be deposited on the surface of dielectric, conductor, or semiconductor materials. Vacuum evaporation (deposition of single element conductors, resistors, and dielectrics), sputtering, CVD, platting, and electroplating are some of the employed techniques. The FBAR metallization allows the application of the electric field through the acoustic layer, providing ohmic contacts for read-out purposes. In FBAR processes, Pt, W, Al, Ti, Cr, Ir, and Mo may be deposited on top of the SiO_2 passivation layer by RF sputtering. Sputtering is the deposition of compound materials and refractive metals through removal of the surface atoms or molecular fragments from a solid cathode (target). By bombarding it with positive ions from an inert gas (argon), removed atoms or molecular fragments deposit on the substrate forming the thin film.

Now, we center the discussion on the acoustic, piezoelectric layer deposition. The piezoelectric material is perhaps the layer that mostly determines the ultimate quality of BAW and SAW devices. Throughout this book, we discuss the particular case of AlN fabrication, due to its popularity, relatively simple processing, and CMOS compatibility. As well as metallization, there are a variety of AlN deposition methods, which are currently employed for FBAR and SAW fabrication, including sputtering, epitaxial growth, and physical vapor deposition (PVD), among others [3–5]. The crystallographic and piezoelectric quality of the AlN will strongly depend on the implemented technique. In this context, sputtering succeeds on achieving standard AlN quality with the benefits of low-temperature processes, making it more attractive to CMOS-compatible processes.

An example setup of the sputtering system for AlN deposition is shown in Figure 4.2. Sputtering can be performed by applying DC, AC, or a combination of DC and AC voltages. The voltage is applied between a cathode to which the target is attached and an anode grounded to the chamber. Vacuum conditions exist when the inert gas enters in the chamber, which is usually argon. Due to the potential difference between cathode and anode, positively charged argon ions are attracted and accelerated toward the cathode. Thus, they collide with the target, conveniently located near the cathode. As a consequence of the collision, different processes occur:

- Ion reflection and returning of the same to the gas phase;
- Emission of secondary electrons;
- Deep ion penetration and implantation in the target material;
- Ion-induced mixing as well as diffusion;
- Most important: ion-energy transfer to atoms located in the target's surface and ejection of some of them (i.e., sputtering of target's atoms).

If a combination of argon and another gas enter in the chamber (e.g., nitrogen), a reaction occurs between the gas and ejected atoms, leading to *reactive sputtering*. In this case, deposition of dielectric and compound materials using metallic targets can be carried out. The AlN deposition process by reactive sputtering is illustrated

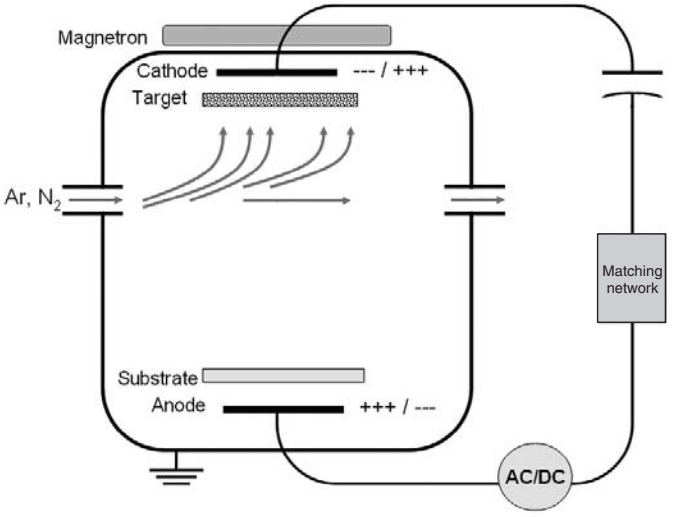

(a)

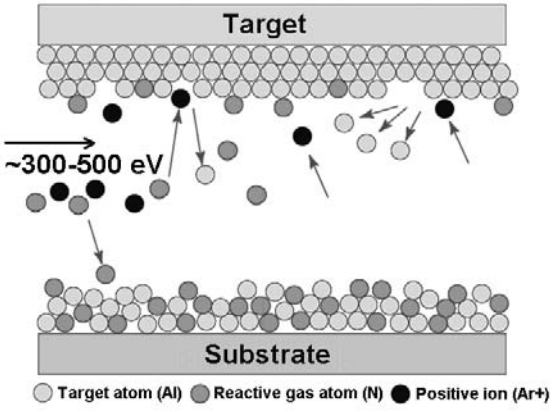

(b)

Figure 4.2 RF/magnetron sputtering for AlN deposition: (a) setup for AC/DC magnetron sputtering; and (b) illustration of the reactive sputtering process, where the Ar+ ions impact the target and the Al reacts with N_2 to form AlN. (*Source:* F. Engelmark, 2002.)

in Figure 4.2(b). The control system injects the Ar/N_2 gas in the chamber and, due to the biasing and magnetron, the Ar+ ions accelerate toward the target. The ejected Al atoms react with the reactive N_2 atoms, thus forming the AlN deposited on the substrate.

As pointed out in Section 2.3.2, process parameters have an influence on the quality, grain size, and orientation of the AlN crystals. Gas concentration and flow, pressure inside the sputtering chamber, DC bias, and AC power are the main variables [6]. The tilting angle and position of the wafer on the sample's holder are process parameters that also control the crystal orientation [7].

4.2.3 Surface-Micromachining-Based Process

Surface micromachining enables full releasing of fabricated FBARs in a fast and clean way. In this section, we study the required steps and technologies to accomplish this purpose.

The simplified fabrication sequence of Figure 4.3 features a sacrificial layer, implemented to release the FBAR. First, we deposit a passivation film of SiO_2 or Si_3N_4 layer on the Si substrate. When patterned, the thin film contributes to define the region containing the sacrificial layer. This is deposited and patterned in the next step of the process [Figure 4.3(b)]. An additional buffer layer, SiO_2, for example, may be deposited between the sacrificial layer and the substrate to reduce the etching impact on the substrate during the micromachining process. Next, fabrication continues with a first metal deposited on the passivation layer through RF and magnetron sputtering [Figure 4.3(c)]. The process requires high etching selectivity between the sacrificial layer and the bottom electrode. Thus, we need to choose suitable metals according to this requirement and the etchant solution. Next, we sputter the AlN and pattern it by wet etching in TMAH or a TMAH-based solution [Figure

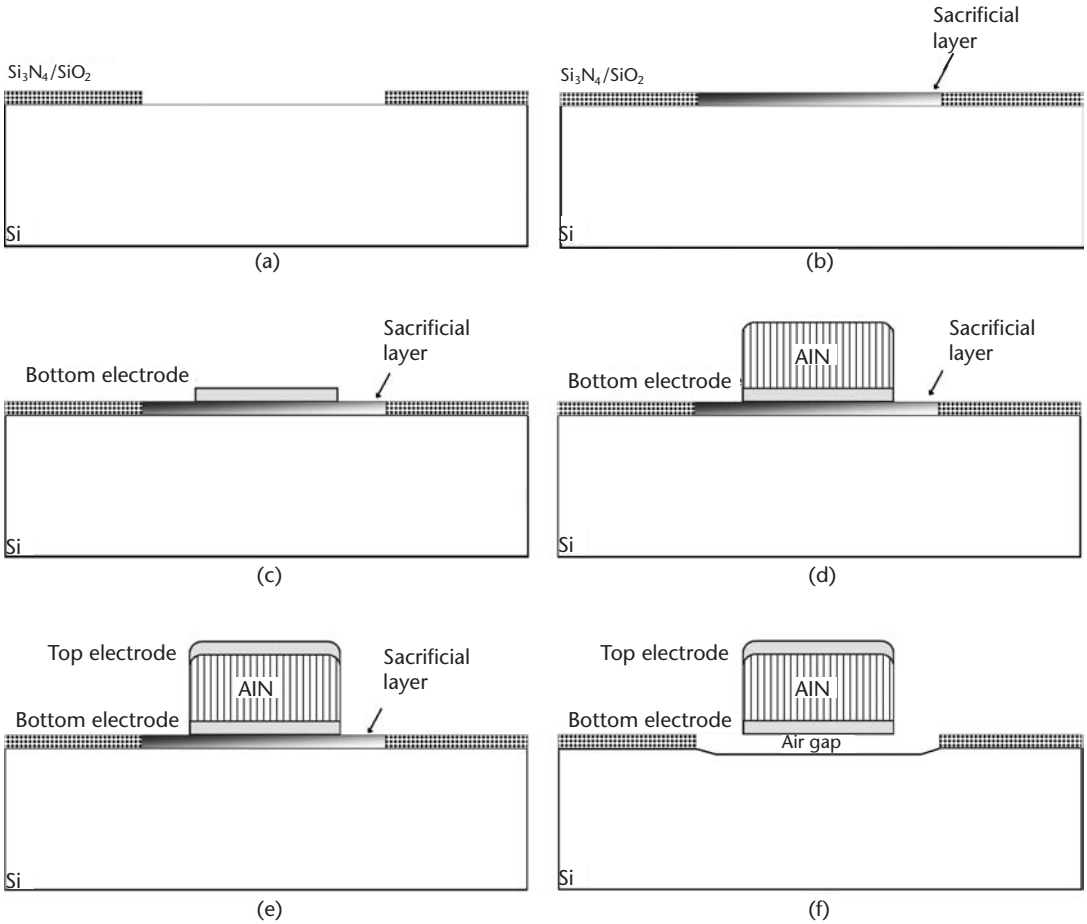

Figure 4.3 Surface-micromachining-based FBAR processing: (a) buffer and mask layers deposition and etching; (b) sacrificial layer deposition and patterning; (c) first electrode, (d) AlN, and (e) second electrode deposition and patterning, respectively; and (f) etching of the sacrificial layer (in HF solution).

4.3(d)]. Then, we proceed with deposition and patterning of the top electrode, according to the techniques already described for the bottom electrode [Figure 4.3(e)]. In the last step, immersing the wafer in the etchant removes the sacrificial layer [Figure 4.3(f)]. The sacrificial layer can be a metallic—Ti or Al—or a dielectric material—SiO_2 or PSG. Popular etchants for sacrificial layer removal are HF solutions. At this point, the device exhibits two air interfaces.

4.2.4 Bulk-Micromachining-Based Processes

4.2.4.1 Reactive-Ion Etching-Based Process

The first bulk-micromachining-based process implements front- or back-side RIE of the Si substrate. In the front-side case, partial or total etching of Si is carried out, while total etching of Si is performed from the back-side of the wafer. The simplified fabrication sequence of Figure 4.4 depicts the cross-sectional schematic view of a front-side RIE process. After passivation deposition and patterning, we deposit the first metal layer by RF and magnetron sputtering [Figure 4.4(a)], defining the layout of the bottom electrode. In the next step, the AlN layer is also deposited by RF/magnetron sputtering and etched according to the process described in the previous section [Figure 4.4(b)]. After a second metallization and patterning of the resulting metal layer, the top electrode is created and the device structure is completed [Figure 4.4(c)]. Finally, the front-side RIE completes the process by releasing the FBAR. This achieved by using the etching window provided by the SiO_2 layer [Figure 4.4(d)].

The process description and step sequence of the back-side RIE-based process is similar to that of the previously described front-side process. However, the photolithography of the etching window is done at the back side of the wafer. Although

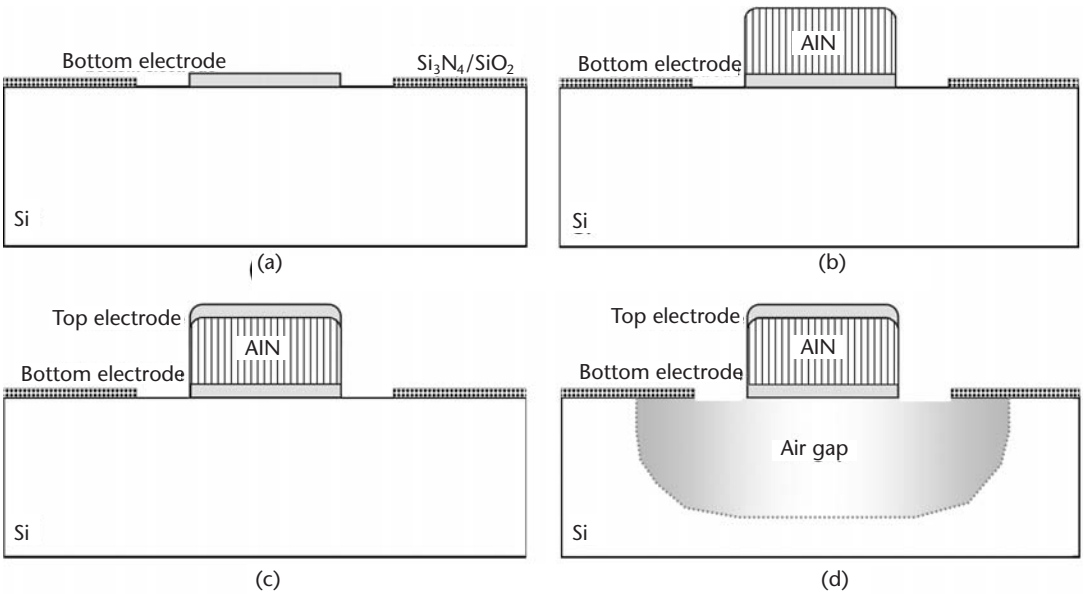

Figure 4.4 Front-side RIE process overview: (a) first electrode; (b) AlN; (c) second electrode deposition and patterning, respectively; and (d) device releasing from the front side of the wafer (RIE).

the photomask may have the same features in both cases, double-sided alignment capabilities should be provided for the back-side mask (strictly speaking, the features may be different, since the front-side etching needs larger etching windows to allow the etching plasma to attacking the substrate). Despite the layout design similarities, different compatibility issues arise in front-side and back-side fabrication processes.

4.2.4.2 Wet-Etching Process

Anisotropic wet etching of silicon follows, in general, the same fabrication sequence as the processes previously described, depicted in Figure 4.5. First, the passivation deposited on top of the Si substrate also serves as a buffer to stop the back-side etching. As in the RIE process, a resist layer and an etching-selective material are deposited on the back side of the wafer, and they will serve to mask etching during the last step of the process. The process is essentially the same as before: bottom electrode, AlN layer, and top electrode deposition and patterning [Figure 4.5(a–c)]. In the last step, anisotropic etching of the Si substrate succeeds in releasing the FBAR after immersion of the wafer in KOH or in a KOH-based solution [Figure 4.5(d)]. The remaining resist and etching mask can be removed. Since the Si etching stops at the passivation layer on the front side of the wafer, this step can be avoided.

4.3 Instrumentation and Materials for Fabrication

There is a vast amount of technology, techniques, and processes available in the market for FBAR and MEMS fabrication. For that reason, the list provided in Table

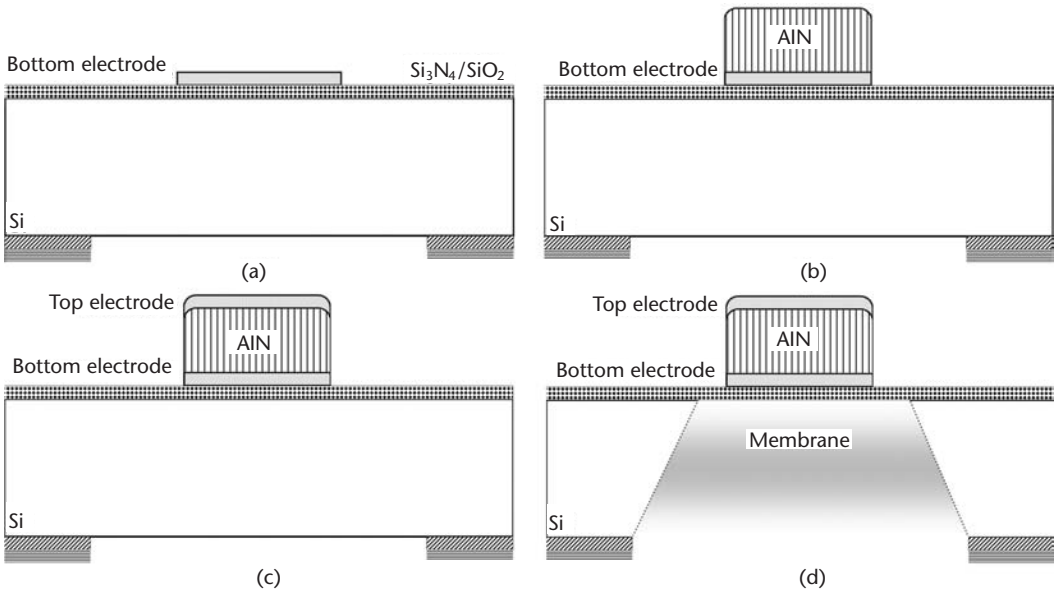

Figure 4.5 Wet-etching-based bulk-micromachining process for FBAR fabrication: (a) bottom electrode; (b) AlN layer; (c) top electrode; and (d) anisotropic etching of the Si substrate from the back side of the wafer (in KOH solution).

4.1 is only an example of the techniques, process parameters, materials, chemical products, and processing conditions that may be involved in the device manufacturing. The table lists the main processes under the assumption that (100) silicon wafers are used as a substrate for device fabrication. This table should be used only as an orientation to illustrate the complexity of the process, and it is suitable for MEMS and FBAR fabrication using microfabrication techniques. The example of the table includes the main processes involved in FBAR fabrication: photolithography, thin-film deposition (sputtering), thermal oxidation, dielectric thin-film deposition (CVD), and dry and wet etching for micromachining.

Table 4.1 Instruments, Chemical Products, and Materials Implemented in FBAR Fabrication

Process	*Technique and Process Parameter(s)*
Photolithography (conventional UV)	Priming: solution and contact time (e.g., HMDS, 25 seconds for SiO_2 substrates)
	Coating: resist density and thickness (e.g., HiPR 6512, 1.2 μm)
	Spinning: coating time and angular velocity (RPM)
	Soft baking: temperature and time (e.g., 100°C, 20 seconds)
	Alignment and exposure: UV line, proximity mode, exposure time (e.g., i-line, contact-3-μm, 10 seconds)
	Developing: time, temperature, developer, and solvent (e.g., 10–30 seconds, 22°C, OPD4262, RER)
	Hard baking: temperature and time (e.g., 115°C, 30–60 seconds)
	Cleaning-resist removal (dry etching by O_2 plasma): plasma flow, pressure, RF power, time (e.g., 10%, < 1 mbar, 500W, 30–45 minutes.)
Sputtering (AlN and metal deposition)	Target: sputtered precursor material (e.g., Ti, Pt, Al, W)
	Gas concentration (e.g., Ar, Ar/N_2—50–50%, reactive)
	Gas flow of the inert gas (e.g., 50 sccm (Ar))
	RF power: between the anode and cathode (e.g., 100W)
	DC power: between the anode and cathode (e.g., 500W)
	DC bias: between the anode and cathode (e.g., 300 VDC)
	Pressure (e.g., 10^{-3}–10^{-2} mbar)
	Typical sputtered thickness (e.g., 10–2,000 nm)
Thin-film growth and deposition (oxides, nitrides)	Thermal oxidation: oxidation temperature, dry oxidation time, wet oxidation time; gas flow (e.g., 1,100°C, 10–15 minutes, 90–120 minutes, 5–10 sccm—O_2: dry, H_2+O_2: wet)
	PECVD deposition: oxidation temperature (e.g., 1,100°C)
	Typical grown/deposited thickness (e.g., 10–2,000 nm)
Etching (AlN, metals, oxide, sacrificial layers)	Dry etching (RIE): inert gas buffer (e.g., Ar); atmosphere (e.g., SF_6+O_2 (Si), CHF_3 (SiO_2)); pressure (e.g., 75 mTorr); RF power (e.g., 100W); DC bias (e.g., 80 VDC); etching rates (e.g., 5,000 Å/min); etched quantities (e.g., 10–500 μm (thickness)).
	Wet etching (isotropic, surface): etchant solution (e.g., OPD4262-TMAH (AlN)), HF 49% (Ti, SiO_2); etching rate (e.g., 300–500 Å/min (AlN in OPD4262)), 50,000 Å/min (Ti in HF); drying (e.g., oven, critical point dryer (CPD, if sticking is critical)); etched quantities (typical) (e.g., 1 μm (AlN, thickness), 50 mm (Ti, lateral)).
	Wet etching (anisotropic, bulk, Si): etchant solution (e.g., KOH 40%, TMAH 25%); etching rate (e.g., 56 μm/hour (75°C), anisotropy 400:1 (100-Si in KOH)); etched quantities (typical) (e.g., 500 μm (Si wafer))

4.4 Process Compatibility and Characterization

Different issues need to be considered for achieving compatibility between the different steps of the FBAR fabrication process, among them:

1. AlN deposition with good crystallographic quality and with no significant alteration of the seed metal layer (bottom electrode);
2. AlN etching with no significant metal electrode etching;
3. Metal layer patterning with no significant AlN etching;
4. Si etching with no significant damage to the FBAR's structure (for bulk micromachining) and Si etching selectivity (against SiO_2 and AlN);
5. Sacrificial-layer etching selectivity (in the case of surface micromachining).

Achieving process compatibility thus requires the development of testing and characterization strategies, tailored for the particular case of the materials employed during the process. To implement these strategies, testing wafers made with the FBAR composing materials have to be prepared. These wafers are to be processed according to the expected process sequence and etchants. Depending on the results of these tests, variations in the processing sequence in the materials or in the etchants may be introduced. Usually, several iterations are required until full compatibility is achieved.

During and after completion of the process testing, both quality and structural characterization of the resonator will help to determine the right process or, at least, the most convenient process combination. The characterization techniques available may include atomic force microscopy (AFM), scanning electron microscopy (SEM), optical and confocal microscopy, and x-ray diffraction. In the following sections, we study different compatibility and quality issues.

4.4.1 Thin-Film Attributes

The thickness and profile of thin films will depend on the deposition rate, which is determined by the type of material and the deposition conditions. Deposited thin films are, in general, nonplanar. That means that, in the absence of planarization processes, the thin film will display a nonuniform thickness across the wafer. Evaluation of the thin-film uniformity and the thickness profile can be measured with a system implementing standard spectroscopy and reflectometry techniques, like the Nanospec family from Nanometrics [8]. The Nanospec system exhibits angstrom resolution and is particularly useful for nitrides, oxides, and other transparent films. The topographic profile of Figure 4.6 shows how the thickness of a nonplanar AlN layer shifts as a function of the distance of the measured point to the center of a 100-mm wafer. According to this plot, the thickness standard deviation is 74 nm for the scanned devices, which corresponds to a variation of around 10% (taken from a mean value of 853 nm). These results show that high deviations may occur if no external planarization means is employed (e.g., example chemical polishing).

Another topographic technique especially employed in metallic thin-film characterization is mechanical profilometry. Thus, the profilometer scans the surface of the sample with the tip of the scanner being physically in contact with the sample

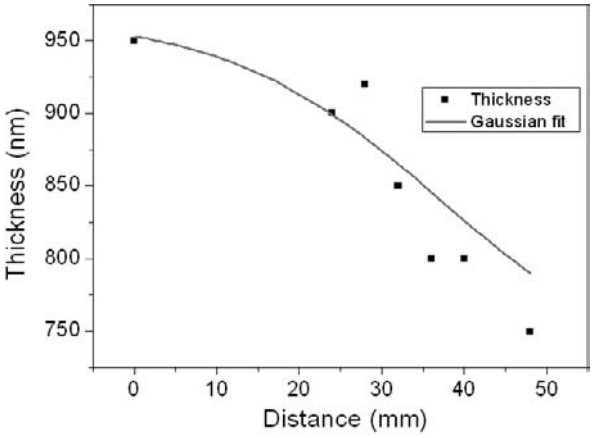

Figure 4.6 AlN thickness profile measured by the Nanospec AFT-200 system (distance is measured from the center of the wafer). (© 2007 IOP Publishing Ltd. [9].)

and scratching its surface. The plot of Figure 4.7 shows the profile of an FBAR with W (750Å), AlN (5,000Å), and resist (12,000Å or 1.2 μm), measured with a Veeco profiler. The FBAR has two W layers for bottom and top electrodes. The photolithographic resist used for patterning of the top electrode is still on the W. The FBAR is located on top of a passivation SiO_2 layer.

The surface roughness of thin films also provides information about the success and repeatability of the deposition process. Under certain deposition conditions, the size of the surface's grains is usually an indicator of some properties of the material. A useful tool for measuring the grain size and the surface grain is the AFM.

For example, an AFM can be implemented to perform a detailed analysis of the surface roughness of AlN film. In this application, AFM measurements relate the size of the grain to the crystallographic quality of the AlN. The scanned samples from Figure 4.8(a–c) present statistical analysis results of the surface roughness of AlN films deposited onto Si, Al, and Pt bottom electrodes, respectively. In the fig-

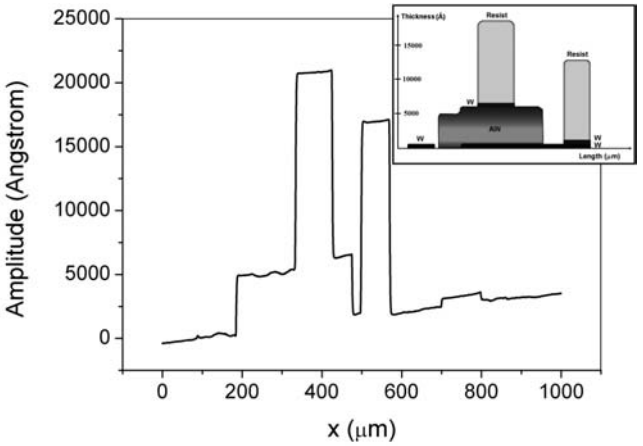

Figure 4.7 Profilometry of an FBAR for supervision of thickness and profile of the layers: W (750Å), AlN (5,000Å), and resist (12,000Å), measured with a Veeco profiler.

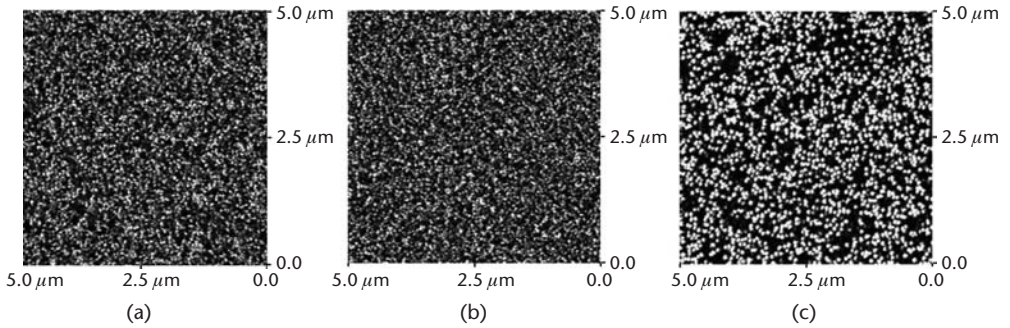

Figure 4.8 AFM analysis of the AlN surface roughness for different substrates: (a) Si; (b) Al; and (c) Pt.

ures, the scanning area on the surface of each sample is $5 \times 5\ \mu m^2$. For each case, the measured roughness at root-mean-square (RMS) values is 12, 8.7, and 31.9 nm, respectively. These results are a first indicator of the AlN crystal's quality, taking into account that higher grain sizes prompt higher crystallographic quality in the preferred (002) orientation for a given deposited material [10]. In these examples, the best grain size—and presumably best crystal quality—is obtained for the AlN film deposited on Pt substrate.

4.4.2 Crystallography

A crystallographic study allows us to determine the material configuration and crystal orientations of the evaluated sample. X-ray diffraction (XRD) equipment performs this study, which is useful to analyze the presence and intensity of certain orientations of the AlN crystals. Thus, one measures the full-width-half-maximum (FWHM) aperture angle $2\ \theta/\omega$ of the diffraction pattern and the rocking curves for the set of materials expected to be in the tested wafer.

Diffraction occurs as waves interact with a regular crystalline structure whose size is periodically repeated in a distance about the same as the wavelength of the incident x-ray source. X-rays happen to have wavelengths on the order of a few angstroms, the same as typical interatomic distances in crystalline solids. For this reason, x-rays can be diffracted from minerals, which, by definition, are crystalline and have periodic atomic structures. When certain geometric requirements are met, x-rays scattered from a crystalline solid can constructively interfere, producing a diffracted beam. In 1912, W. L. Bragg recognized a predictable relationship among several factors [11]:

1. The distance between similar atomic planes in a mineral (the interatomic spacing), which is called the *d*-spacing and is measured in angstroms.
2. The angle of diffraction, which is called the theta angle q and is measured in degrees. For practical reasons, the diffractometer measures an angle that is twice θ. That is why the measured angle is also called *2-theta* (2θ).
3. The wavelength of the incident x-radiation, symbolized by the Greek letter lambda (λ).

These factors are combined in Bragg's law:

$$n \cdot \lambda = 2d \sin\theta \tag{4.1}$$

For the case of copper, which is the target material of the x-ray radiation in most of the commercial XRD machines, $\lambda = 1.54$, and n is assumed to equal 1 ($n = 1$).

A diffractometer, a goniometer, and a scintillation counter for measuring the x-ray intensity, among other setup elements, are used to make a diffraction pattern of the samples. The goniometer is motorized and moves through a range of 2θ angles. Because the scintillation counter is connected to the goniometer, we can measure the x-ray intensity at any angle to the specimen. That is how the 2θ angles for Braggs's Law are determined (see Figure 4.9).

The sample patterns of Figure 4.10(a–d) show the $2\theta/\omega$ diffraction peak intensity for different AlN crystal orientations, including the (002), c-axis orientation. In this example, the AlN was deposited on a Pt seed layer. The 2θ angles for each orientation are 33.24 (100), 36.12 (002), 37.94 (101), and 59.40 (110) degrees. As observed in Figure 4.10, the AlN (002) orientation peak is several orders of magnitude more intense than in the AlN (101), (100), and (110) orientations, the relationships being 40, 48, and 54 dB, respectively. This means that the AlN crystal in the example exhibits a preferred orientation in the c-axis.

Assuming a hexagonal crystal structure and that each 2θ-angle peak corresponds to a specific crystal orientation, the network parameters of the AlN crystal can be calculated. The network parameters are the dimensions and distances of the crystal-plane structure in a certain coordinate space. All the lattice planes and directions of the crystal are described by a mathematical description known as a Miller index [12]. This allows the specification, investigation, and discussion of specific planes and directions of a crystal. In the hexagonal lattice system, the direction [hkl] defines a vector direction that is normal to the surface of a particular plane or facet, where h, k, and l are coordinate axes. Referring to lattice's d-spacing in (2.1), the value of each network parameter is given by:

$$\left(\frac{1}{d}\right)^2 = \left(\frac{h}{a}\right)^2 + \left(\frac{k}{b}\right)^2 + \left(\frac{1}{c}\right)^2 \tag{4.2}$$

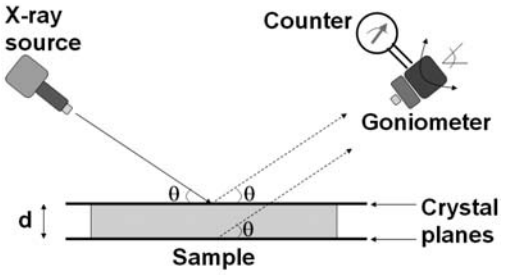

Figure 4.9 X-ray diffraction measurement: simplified setup including x-ray source, target material, sample wafer, goniometer, and counter.

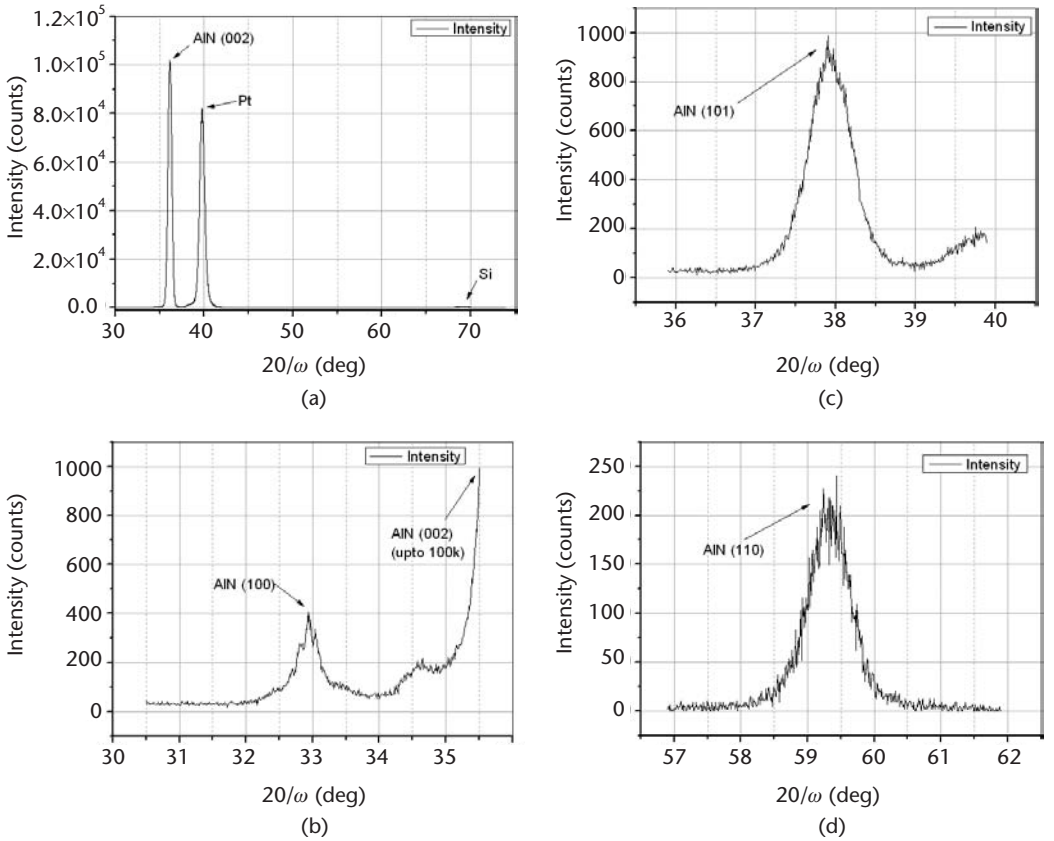

Figure 4.10 X-ray diffraction peak intensity: (a) global XRD pattern (biggest peak: (002) AlN); and detail of (b) (100) AlN (33.24°), (c) (101) AlN (37.94°), and (d) (110) AlN (59.40°) peaks.

where *a*, *b*, and *c* are the corresponding network parameters. In Figure 4.11(a) the hexagonal structure of the AlN crystal is depicted. According to this geometry and using (4.1) and (4.2), the values of a, *b*, *c*, and *d* are calculated to be 2.837Å, 2.941Å, 4.973Å, and 2.487Å, respectively. These results are very close to 3.084Å, 3.084Å, 4.948Å, and 2.474Å, which are reference values for hexagonal AlN crystals [13]. The SEM image of Figure 4.11(b) shows the columnar structure of the analyzed AlN sample. The columnar-crystal orientation is often associated with good piezoelectric properties, although adequate poling is also a necessary condition [14].

Additional information concerning the AlN quality can be extracted from the XRD analysis. The full width half maximum (FWHM) aperture angle is also an important parameter to evaluate the quality of the crystal: the narrower the angle, the higher the orientation in a certain axis. FWHM is measured in relation to reference materials, and its aperture angle depends on the width dispersion values for the different planes of the crystalline structure (network parameters of crystal). As a rule of thumb, values of less than 1° are expected for crystalline materials strongly oriented in a specific axis.

As the fabrication technique strongly determines the crystallographic orientation, Table 4.2 compares the AlN deposition for different implementations and pro-

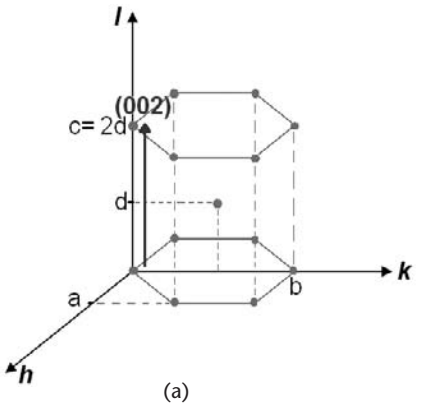

(a)

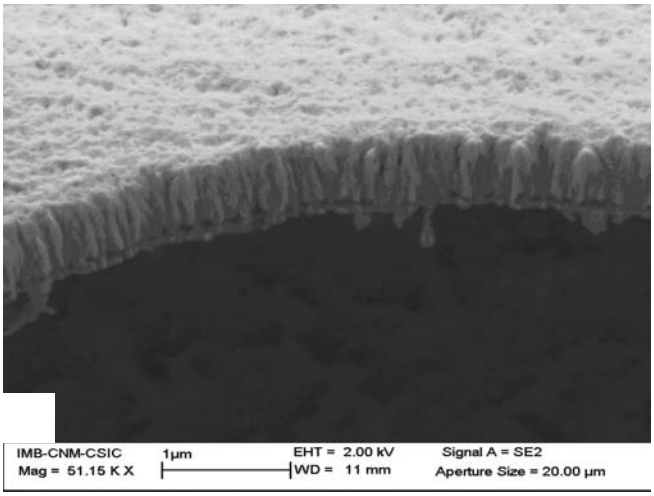

(b)

Figure 4.11 AlN crystal orientation: (a) hexagonal lattice structure of AlN and (b) SEM image showing the columnar structure of an AlN sample.

cesses. This table shows the relationship between deposition temperature, full-wave-half-maximum (FWHM) width, and fabrication technique. Although the comparative could be more exhaustive, it still contributes to estimate the quality of films as a function of the fabrication techniques with reference information. As

Table 4.2 Different AlN-Deposition Implementations

Source	*FWHM (°)*	*Temperature (Max. °C, Process)*	*Thickness (µm)*
[15]	1.6	Low (350, RF sputtering)	2.0
[16]	1.3	Low (<400, RF sputtering)	2.0
[9]	0.11	Low (<400, DC+RF sputtering)	1.0
[17]	>0.4	Low (<500, epitaxial)	N/A
[15]	0.4	High (500, epitaxial)	2.0
[3]	0.03	High (>600, epitaxial)	N/A

observed, high-temperature processes offer, in general, more quality than low-temperature-deposited AlN films, at the cost of CMOS-compatibility loss.

In this sense, the comparison of sputtering with epitaxial processes is not straightforward. In spite of FWHM evaluation, further analyses must be carried out to determine the ultimate crystal quality and piezoelectric properties of the AlN film. Sanz-Hervás et al. found out that no direct relationship exists between low FWHM values and the piezoelectric coefficient of sputtered AlN films, suggesting the influence of domain inversion of the poling structure due to crystal defects [14]. On considering this background, characterization of poling domains and comparatives of different process conditions are required. Once the AlN is deposited on the appropriate substrate, a device fabrication process is to be defined. Compatibility between deposition, patterning, and micromachining at the different fabrication stages has to be ensured in order to obtain a full and operational device.

4.4.3 Etching Performance

Appropriate releasing of the resonator is a requirement to obtain a high-quality factor. For this purpose, the micromachining technique has to provide a membrane or cavity that allows the device to move freely with no significant damage of its structure. While insufficient etching may prevent satisfactory releasing, excessive processing times may cause irreversible damage to the device. For this reason, supervision and evaluation of the etching rates and selectivity is crucial to achieve a successful fabrication. Optical microscope inspection, SEM, profile meter, and confocal microscopy, among others, can be used to calculate the anisotropy and etching rates of the implemented micromachining process.

Prior to final device fabrication, we need to perform selectivity and compatibility testing of the different layers of the device. Evaluation of etching rates and integrity of the device are the main goals of this testing. For this purpose, test wafers with different layer configurations are prepared and the etching rates for the passivation, electrodes, piezoelectric, and sacrificial layers are measured. With this information, the etching times are adjusted to obtain a released device with minimum damage and the shortest processing times. The selectivity of the structural layers of the resonator is prioritized, especially that of the piezoelectric layer.

To illustrate the testing, let's take the case of HF-based wet etching of a sacrificial Ti layer in a surface micromachining process. The electrodes are made of Pt with an adhesive layer of Cr; the piezoelectric layer is AlN; and the FBAR is fabricated on a Si_3N_4 passivation layer. AlN and Pt have proven to be highly selective to HF, since they do not suffer significant damage during testing. Thus, the selectivity of Cr and the etching rate of Ti are evaluated. Figure 4.12(a) shows the layout of a test wafer with Si/Ti/Cr configuration and etching windows in the Cr layer (openings in light color). The Ti lies underneath the Cr layer and is exposed to the etchant through the etching windows. (Ti and Cr thicknesses are 1,000 and 400 nm, respectively). Figure 4.12(b) shows a detailed view of the wafer with underetching dimensions after 12 minutes of etching. Thus, for this specimen, the Ti etching rate is calculated to be 40,000 Å/min. No change in the dimensions or shape of the Cr layer is observed. However, slight differences in the Ti etching rate are observed when measuring the size of different patterns. In considering the window-size factor and

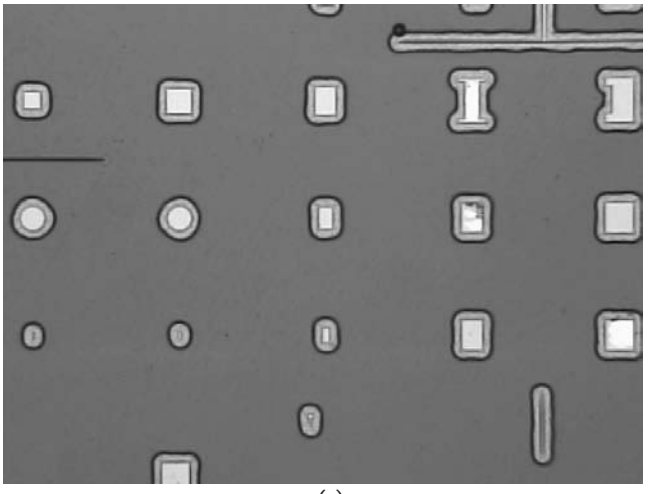

(a)

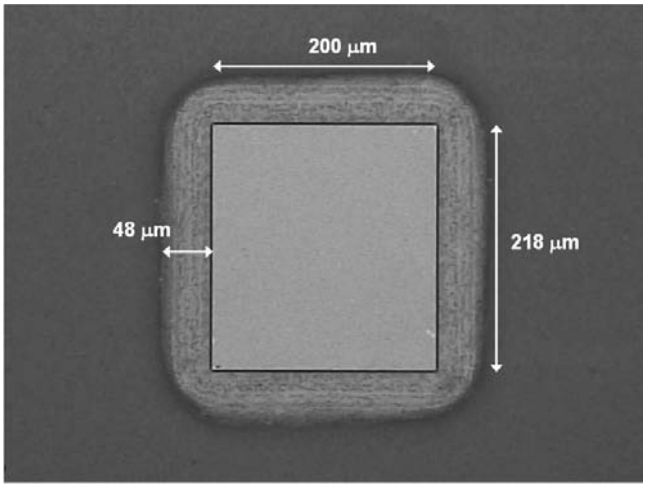

(b)

Figure 4.12 Ti/Cr etching-selectivity testing: (a) sample with Si/Ti/Cr configuration (opening windows in light color showing underlying Ti layer); and (b) detailed view of the etch window with underetching observed underneath the Cr layer.

after several measurements, the etching rate range is determined to be within the range of 35,000–70,000 Å/min.

In addition, SEM is particularly useful for analyzing the anisotropy and etching rates of bulk micromachining. By taking a cross section of the sample, the depth and lateral underetching are measured and these parameters are calculated. The SEM images of Figure 4.13(a) and Figure 4.13(b) show cross-sectional views of sample profiles after RIE of the Si substrate. The RIE recipe of the example specifies an SF_6+O_2 atmosphere with Ar buffer at 75 mTorr pressure, and 100W of RF power. A patterned metallic layer highly selective to the RIE recipe covers the substrate to allow selective etching. The metal patterning constitutes an etching window that is opened in those areas around the FBAR where the etching is to be performed, thus protecting the substrate and other regions of the device. Looking into Figure 4.13(a), the lateral versus vertical etching rates can be estimated to be between 1:3

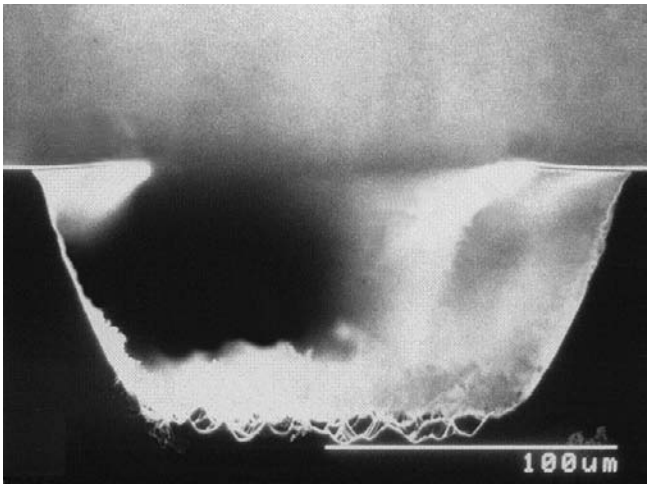

(a)

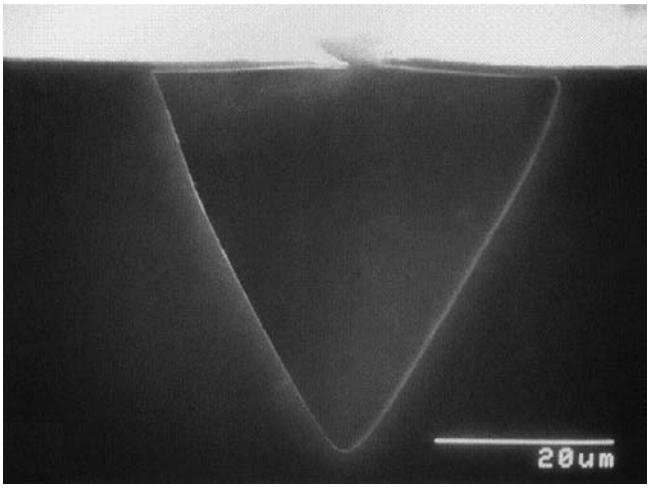

(b)

Figure 4.13 RIE profile and etching rate evaluation (SEM images): (a) big etching window (> 20 μm); and (b) small etching window (< 10 μm).

and 1:4. According to the scale, the vertical etching is around 100 μm, whereas the lateral underetching is around 30–35 μm. Thus, the lateral etching rate can be calculated to be 1,500–1,600 Å/min. However, the small-windowed structure of Figure 4.13(b) reveals a lower lateral-to-vertical aspect ratio in the order of 1:2. Also, the etching rate is reduced for this case. Clearly, there exists a dependence between the size of the etching window and the etching rate. Thus, the size of devices and etching windows should be carefully designed to find the best combination: small windows make the layout design more efficient, but they reduce the etching rate, whereas bigger windows increase the etching rate at the cost of bigger underetching areas. According to this example, releasing a 50-μm-wide device would require a minimum etching time of around 3 hours.

After completion of the fabrication process, the SEM images in Figure 4.14(a) show the layout of the stacked structure of an FBAR comprising top and bottom electrodes, the AlN, and the passivation layer. The Si substrate is found under the

etching window (in dark). In Figure 4.14(b) the stacked configuration displaying the electrode-AlN-electrode sequence can be seen. Applying a correction factor of the vertical scale—due to the setup tilting of the electron beam—the thickness of the composing materials can be measured (given the topographic scale, annotated in the image). In this example, the tilting angle is 52°, as the metal-AlN-metal layers have thicknesses of 180 nm, 1,000 nm, and 180 nm, respectively. Also, the air cavity underneath the structure is observed. In partially released devices, some Si still remains underneath the bottom electrode, as seen in Figure 4.14(c). In this case, further etching is required to finish the FBAR fabrication.

4.4.4 Structural Performance

Interferometer and confocal microscopy are other useful techniques to evaluate the structural performance of fabricated devices. Stress levels, sticking, and releasing of the resonator are some of the aspects that can be studied.

The image of Figure 4.15(a) shows a partially released cantilever. Interferometer bands are observed in the released region of the device (lower side of the image, the area near the border of the electrode). The topographic image (up) corroborates this observation, where bending of the device due to residual stress can be deduced from the higher-scale levels near the border of the device (light gray). The central, dark-gray region is still clamped to the Si substrate. At its time, the FBAR of Figure 4.15(b) exhibits relatively homogeneous scale levels (up) and interferometer bands (down). In this case, the square-shaped, beam-type device has been fully released from the substrate, thus vibrating at its natural mechanical frequency (MHz) all along its structure. However, we can observe considerable stress of the beam when contrasting the topographic levels at the center and lateral regions, where one of the clamped electrodes is found (at left). A RIE-based bulk micromachining process was served to fabricate both the cantilever and beam devices.

Confocal microscopy allows us to get additional details on the structure of certain processes, specifically for thin-film devices like FBARs [18, 19]. Flatness, stress, and sticking of the structure can be analyzed. Also, the etching status of a micromachining process can be supervised.

After micromachining, the structure or the contour regions of the resonator may suffer damage, sticking, or deformation due to residual stress after releasing. In Figure 4.16, two devices fabricated within bulk and surface micromachining processes are compared. In Figure 4.16(a), the accumulated stress in the underetched region of the passivation layer (SiO_2) is observed in dark gray after Si underetching. Such stress is evidenced by deformation and, in some parts, cracking of the membrane (around the etching window in black). The situation of a surface micromachined device is fairly different, as shown in the confocal image of Figure 4.16(b). Lower processing times and fewer fabrication steps alleviate induced stress, thus providing relatively flat structures, in comparison to those obtained by the bulk-based process. A quasi-flat topographic profile of the same device along the A-A' axis can be seen in Figure 4.16(c). In this example, the 1.5-μm-thick sacrificial layer has already disappeared after etching. The top electrode and the overall FBAR structure also have an almost-flat conformation.

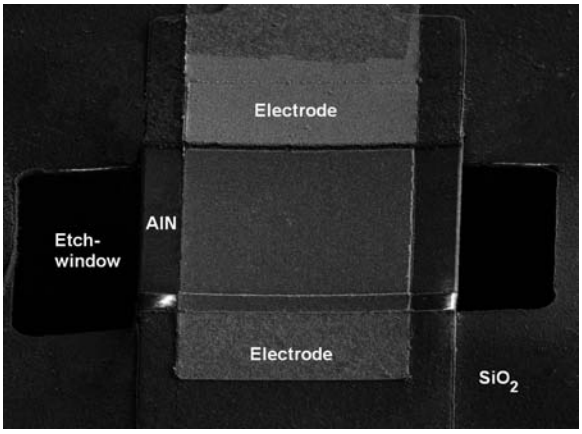

(a)

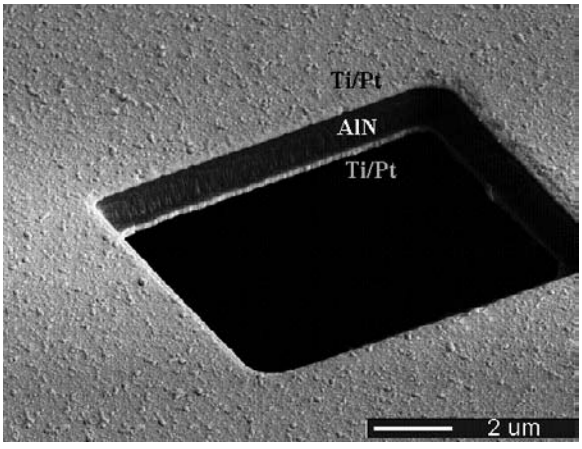

(b)

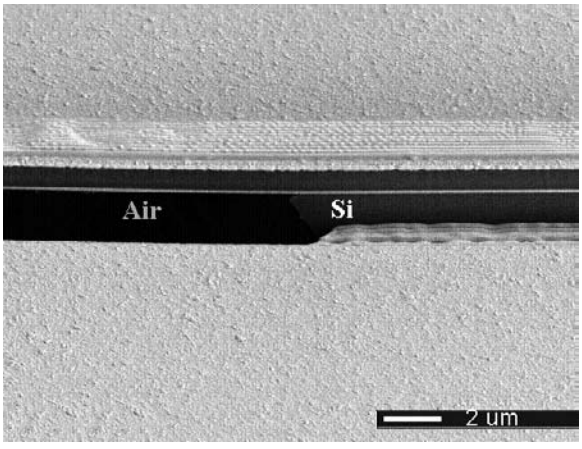

(c)

Figure 4.14 FBAR structure after fabrication: (a) overall layout; (b) insight into the layered metal-AlN-metal structure (tilting angle of 52°, thicknesses of Pt, AlN, and AlN of 180, 1,000, and 180 nm, respectively); and (c) partially released device (Si substrate is still observed underneath the device). (© 2007 IOP Publishing Ltd. [9].)

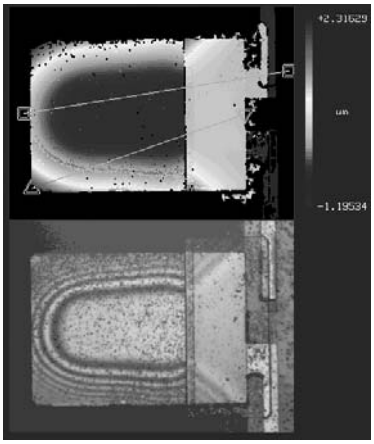

(a)

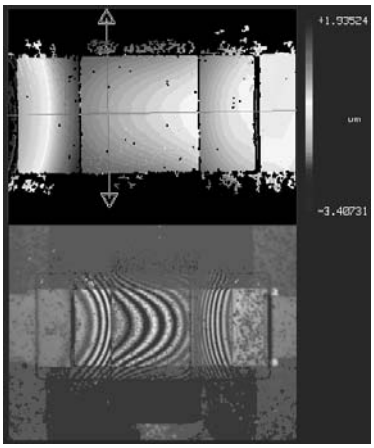

(b)

Figure 4.15 Interferometer analysis of the FBAR structure: (a) partially released, cantilever-type device (partial bending and nonhomogeneous interferometer bands are observed); and (b) fully released, beam-type resonator (homogeneous bands and topographic levels all along the device).

4.5 Summary

The FBAR fabrication technology comprises many steps and has to be developed to achieve full-process compatibility. Among these steps, piezoelectric layer deposition and a variety of micromachining processes are the key technologies. Also, different characterization techniques have to be implemented in order to evaluate the main steps of the process. Structural, crystallographic, and etching analysis can be studied by current-art instrumentation like AFM, SEM, interferometer, and confocal microscopy. Although a variety of process parameters should be considered, Table 4.3 attempts to compare the different aspects concerning FBAR-related microfabrication. Advantages and challenges of each technology should be sought on considering the possibilities and limitations of the technology available to the designer.

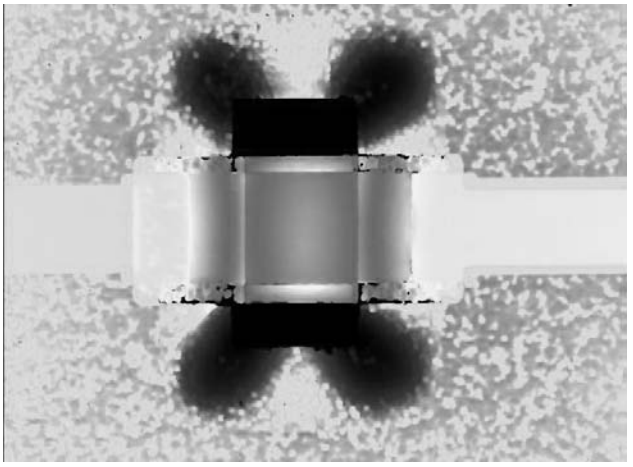

(a)

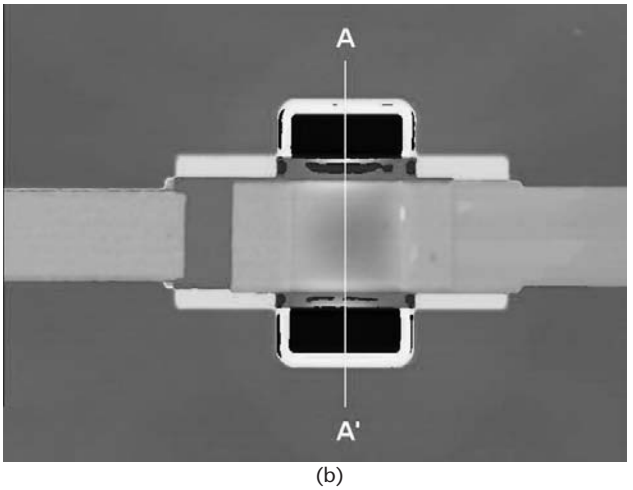

(b)

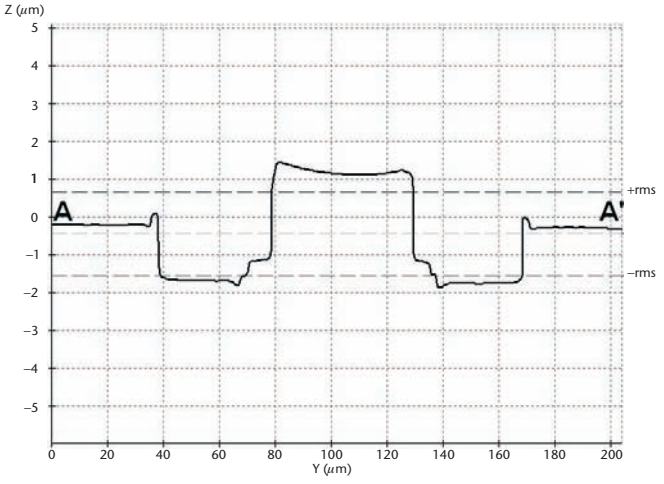

(c)

Figure 4.16 Stress and flatness confocal supervision: (a) RIE-based FBAR (accumulated stress in the SiO_2 membrane is observed); (b) surface-micromachined FBAR (sacrificial layer cavity after etching in dark gray); and (c) topographic profile of the device (along the *A-A′* axis).

Table 4.3 Micromachining Implementations in the Fabrication of FBAR

Fabrication Issue	*Bulk Micromachining (Dry Etching)*	*Surface Micromachining (Wet Etching)*	*Bulk Micromachining (Wet Etching)*
Design complexity	4-mask set, including RIE mask	4-mask set, including sacrificial layer mask	5-mask set, including additional back-etching mask
Fabrication complexity	High metal step (top and bottom)	Sticking, critical etching time (to avoid metal lift-off)	Front-to-back mask alignment, residual silicon on back side
Etching rate	High	Highest	Low
Etching time ($50\,\mu m \times 50\,\mu m$, wafer: $500\,\mu m$)	Short	Shortest	Long
Cleanness	More clean	Less clean	Less clean
Residual stress	Medium	Low	High
Etching control	Time-supervised	Time-supervised	Self-controlled
Wafer area required	Underetching of non-FBAR regions	Less than RIE	More than RIE

References

[1] Ylilammi, M., et al., "Thin Film Bulk Acoustic Wave Filter," *IEEE Trans. on Ultrason. Ferroelectr. Freq. Control*, Vol. 49, 2002, pp. 535–539.

[2] Lee, J. B., et al., "Effects of Bottom Electrodes on the Orientation of AlN Films and the Frequency Responses of Resonators in AlN-Based FBARs," *Thin Solid Films*, Vol. 447–448, 2004, pp. 610–614.

[3] Uchiyama, S., et al., "Growth of AlN Films by Magnetron Sputtering," *J. Crystal Growth*, Vol. 189–190, 1998, pp. 448–451.

[4] Vispute, R. D., H. Wu, and J. Narayan, "High Quality Epitaxial Aluminum Nitride Layers on Sapphire by Pulsed Laser Deposition," *Appl. Physics Lett.*, Vol. 67, No. 11, 1995, pp. 1549–1551.

[5] Dubois, M. A., and P. Muralt, "Stress and Piezoelectric Properties of Aluminum Nitride Thin Films Deposited onto Metal Electrodes by Pulsed Direct Current Reactive Sputtering," *J. Applied Physics*, Vol. 89, No. 11, 2001, pp. 6389–6395.

[6] Oshmyansky, Y., et al., "Sputtering Processes for Bulk Acoustic Wave Filters," Semiconductor International, 2003, http://www.semiconductor.net/article/CA282270.html.

[7] Chung, C.-J., et al., "Synthesis and Bulk Acoustic Wave Properties on the Dual Mode Frequency Shift of Solidly Mounted Resonators," *IEEE Trans. on Ultrason. Ferroelectr. Freq. Control* Vol. 55, No. 4, 2008, pp. 857–864.

[8] Nanometric Inc., http://www.nanometrics.com.

[9] Campanella, H., et al., "Focused-Ion-Beam-Assisted Tuning of Thin-Film Bulk Acoustic Wave Resonators (FBAR)," *J. Micromech. Microeng.*, Vol. 17, 2007, pp. 2380–2389.

[10] Clement, M., et al., "SAW and BAW Response of C-Axis AlN Thin Films Sputtered on Platinum," *Proc. IEEE Intl. Ultrason. Symp. 2004*, Montreal, Quebec, August 24–27, 2004, pp. 1367-1370.

[11] Perutz, M. F., "How W. L. Bragg Invented X-Ray Analysis," *Acta Cryst. A*, Vol. 46, 1990, pp. 633–643.

[12] Ashcroft, N. W., and N. D. Mermin, *Solid State Physics*, New York: Harcourt, 1976.

[13] Wright, A. F., and J. S. Nelson, "Consistent Structural Properties for AlN, GaN, and InN," *Phys. Rev. B: Condens. Matter*, Vol. 51, 1995, pp. 7866–7869.

[14] Sanz-Hervás, A., et al., "Degradation of the Piezoelectric Response of Sputtered C-Axis AlN Thin Films with Traces of Non-(0002) X-Ray Diffraction Peaks," *Appl. Phys. Lett.*, Vol. 88, 2006, p. 161915.

[15] Engelmark, F., et al., "Structural and Electroacoustical Studies of AlN Thin Films During Low Temperature Radio Frequency Sputtering Deposition," *J. Vac. Sci. Technol. A.*, Vol. 19, 2001, pp. 2664–2669.

[16] Hara, M., et al., "Surface Micromachined AlN Thin Film 2 GHz Resonator for CMOS Integration," *Sens. Actuator A-Phys.*, Vol. 117, 2005, pp. 211–216.

[17] Shiosaki, T., et al., "Low Temperature Growth of Piezoelectric Films by RF Reactive Planar Magnetron Sputtering," *Jap. J. Appl. Phys.*, Vol. 20, 1981, pp. 149–152.

[18] Semwogerere, D., and E. R. Weeks, "Confocal Microscopy," *Encyclopedia of Biomaterials and Biomedical Engineering*, London, U.K.: Taylor & Francis, 2005.

[19] Prasad, V., D. Semwogerere, and E. R. Weeks, "Confocal Microscopy of Colloids," *J. Phys.: Cond. Mat.*, Vol. 19, 2007, p. 113102.

CHAPTER 5

Characterization Techniques

Characterization of FBAR and MEMS resonators comprises different methods and techniques, and is performed through successive measurement stages. Material and equivalent-circuit parameter extractions enable for a complete description of the device, which can be used to design specific applications. Nowadays, several resonator characterization techniques are available through commercial systems or specific laboratory setup. Electrical, optical, or mechanical methods, among others, can aid the parameter-extraction process of micro- and nanodevices, although the electrical techniques are perhaps the most powerful for MEMS resonator measurement.

Electrical characterization involves understanding the basics of network theory and measurement techniques necessary to extract the equivalent circuit parameters, the quality factor, the electromechanical coupling, and the elastic, dielectric, and piezoelectric constants of the resonator. In this chapter, we discuss two electrical characterization approaches based on scattering parameter analysis. The setup and applications of the low- and high-frequency techniques are explained by exemplary applications. Other techniques are also being used to evaluate the resonant behavior of FBAR and MEMS. In particular, the concepts and measurement setup of interference microscopy and AFM techniques are introduced at the end of the chapter.

5.1 Low- and High-Frequency Electrical Characterization

Electrical characterization entails the feeding of an electric current or voltage to the circuit composed by the resonator, a signal generator, and, optionally, a matching or read-out electric circuit. In general, what is characterized is the change of the current delivered to a loading impedance when it flows through the resonator's frequency-dependent impedance Z_m. The schema of Figure 5.1 depicts the typical setup of a resonator's electrical characterization.

The definition of "low" frequency is relative to the actuation mechanism and design of the resonator, but in general it comprises the range of frequencies between DC and tens of megahertz. On the other hand, the "high" frequency behavior is described in terms of energy delivered to the load, rather than in the traditional, low-frequency circuit representation. Thus, the energetic description focuses on the energy passing through and returning from a distributed transmission line in which the resonator is inserted, when a lumped-circuit representation of the system is impractical or hard to establish. In the following sections, we define both the low- and high-frequency measurements and their usefulness in the parameter extraction of the resonator.

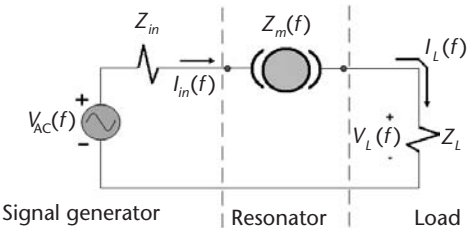

Figure 5.1 Electrical characterization of a MEMS resonator: the resonator's frequency-dependent current $I_L(f)$ flows through the load impedance Z_L. The current $I_{in}(f)$ is provided by an AC signal generator and the loading impedance may be a passive or an active circuit matched to a signal analyzer (like a network analyzer).

5.1.1 Short-Open DC and Low-Frequency Measurements

We define "low-frequency" as the frequency range between DC and a few megahertz. This is the frequency band in which the first mechanical modes of MEMS resonators are found. Low-frequency measurements can monitor the success of the fabrication process. For example, one can verify short- and open-circuit conditions of the resonator's electrodes. At the same time, measurements enable the extraction of the low-frequency material constants.

First, the integrity of the resonator's structure is verified by DC short-open measurements. As FBARs and several MEMS and NEMS resonators implement two or more electrodes to allow read out, it is crucial to assure ohmic contact between the lines connecting the resonator and the read-out electrode system (short-circuit condition). Electrical isolation between different electrodes also has to be guaranteed (open-circuit condition).

After verification of the correctness of the structure, we evaluate DC or low-frequency material constants and layout parameters. For example, in FBARs or parallel plate electrostatic resonators, the pad-to-transmission-line DC resistance ($R_s/2$) and the static capacitance C_0 can be measured. Then, one extracts the static permittivity ε value from the measured C_0 value, for known resonator dimensions (electrode area A and thickness t of the AlN layer, or equivalently the plate-to-plate distance). On the other hand, characterization of the first electromechanical-mode resonance frequencies provides useful information for the extraction of elastic constants of the resonator's materials.

Short and open-circuit can be performed using a DC probe station, a semiconductor parameter analyzer, and a capacitance meter, among other instruments. A fully functional device must accomplish both the short- and the open-circuit conditions. These conditions are evaluated through current-to-voltage testing, or I/V testing. In the setup of the measurement system, a saturation current is defined for the short-circuit measurement. Thus, $I(V)$ plots are used to evaluate the line resistance: a high resistance prompts for the open-circuit verification, while low-resistance values indicate the short-circuit condition (line resistance in the units of ohms or less).

The short-circuit condition of a given electrode is verified by connecting two DC probes at different points of the line, as shown in Figure 5.2(a, b). Due to the fabrication process and to the device's layout, it may be of special interest to check out this condition on those electrodes with thin-film layers and high fabrication

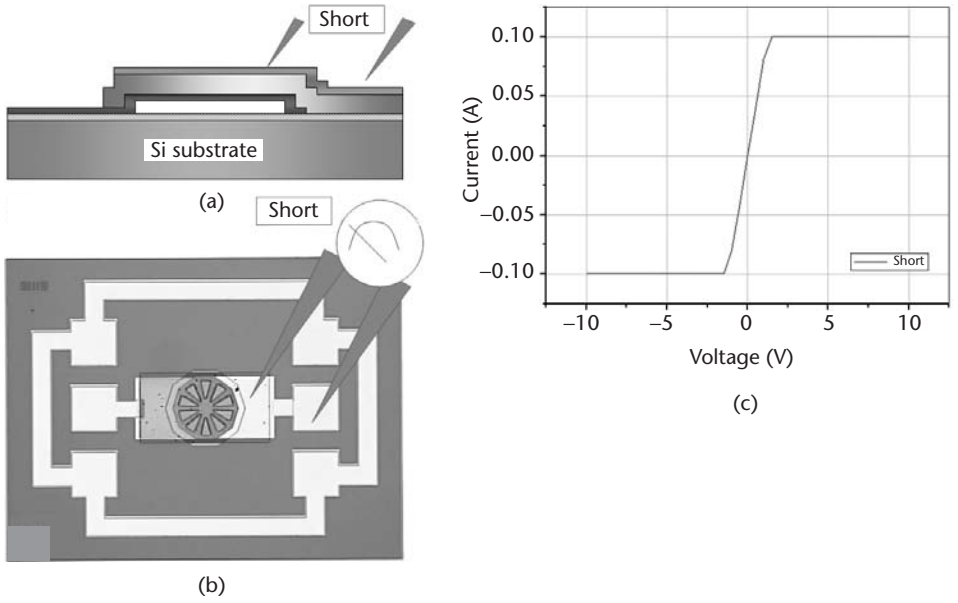

Figure 5.2 Setup and connections for verification of the short-circuit condition: (a) side-view schematic of the probe location; (b) top-view optical photograph of an FBAR indicating the probe location; and (c) I/V plot for a typical device (line resistance $R_s/2$ of 12Ω).

steps. In these cases, there is a high risk of open circuit between the resonator's electrodes and the transmission line, a situation which has to be evaluated.

The short-circuit condition is affirmatively verified if the electrode shows current-continuity between the points where the two probes are located. The experimental I/V plot of a device verifying the condition is shown in Figure 5.2(c). In this example, the current limitation is 100 mA. The line is made of Pt with thickness of 150 nm, width between 30–100 μm and length between 50–200 μm. With these values, the line resistance $R_s/2$ equals 12Ω. Let us note that the locations in which the probes touch the electrode have not been systematically controlled. Hence, this experiment is conceived only to give a rough estimation of the magnitude of $R_s/2$ (or of the short-circuit condition). The value depends on the dimensions and material (Pt) of the transmission line, which explains the high value of $R_s/2$, in comparison to Mo or Al implementations ($R_s/2$ less than 1Ω). Since Pt is a material with higher resistivity than Al or Mo, for example, relatively short transmission lines lead to $R_s/2$ values of units of ohms. Thus, with appropriate layout and process optimization $R_s/2$ may be significantly reduced.

In two-electrode resonators, the open-circuit measurements are carried out by connecting each probe to each one of the electrodes. In Figure 5.3(a, b), the measurement configuration and connections are observed. Verification of the open-circuit condition guarantees that both electrodes are isolated between them (i.e., no electrical contact occurs), thus keeping the low-frequency static-capacitance behavior of the device. Mask misalignment during the fabrication process could derive into electrode contacting and short-circuiting of them. The open-circuit condition is thus verified if current discontinuity is observed between the two probing points. Figure 5.3(c) shows the I/V plot for a device verifying the open-circuit condition (the

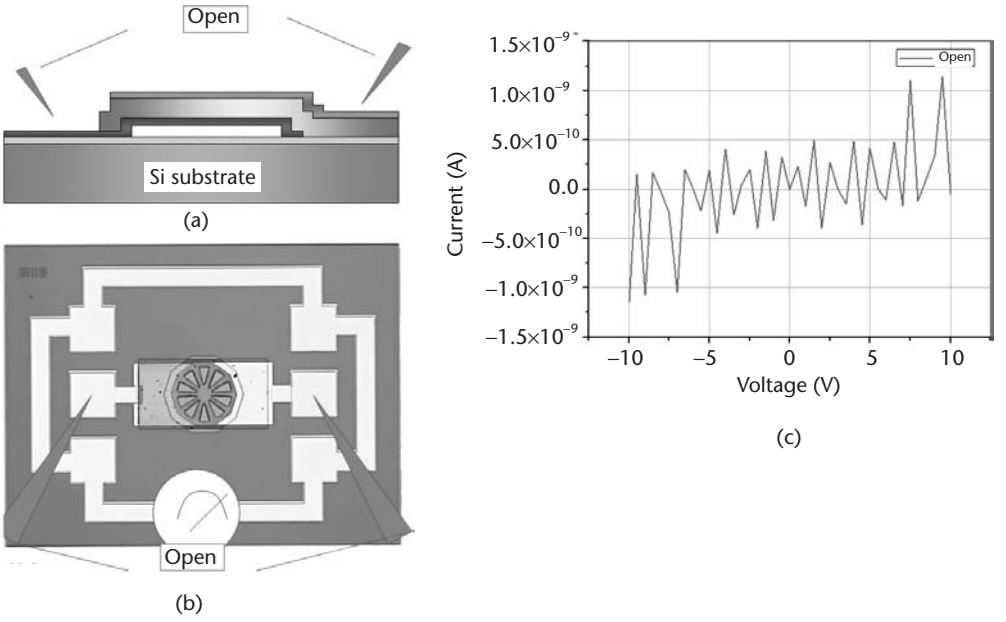

Figure 5.3 Verification of the open-circuit condition: (a) side-view schematic of FBAR with probe location; (b) top-view optical photograph of an FBAR indicating the probe location; and (c) I/V plot for a device verifying the condition (minimum through-resistance of 25 GΩ (i.e., the open-circuit condition).

current was also limited to 100 mA). By calculating the mean value and standard deviation of the current, the DC through-resistance was estimated to be between 25–90 GΩ (equivalent to an open-circuit condition).

5.1.2 Microwave Network Theory and the Scattering-Parameter Description

Transmission and reflection measurements are the best way to describe the electrical response of resonators working in the gigahertz frequency regime. In particular, the scattering-parameter representation—or S-parameters—is very useful to explain the impedance and energy relationships of the RF system comprised by the resonator, the transmission line connecting said device to the measurement system, and the probing pads at which the test instrumentation is connected to the circuit. S-parameters are used to evaluate microwave circuits and come from the two-port circuit representation shown in Figure 5.4, where two sets of ingoing (a_i) and outgoing (b_i) waves are generated. The indices $i = 1, 2$ stand for the input port and output port, respectively.

The four quantities are related together by the scattering matrix S:

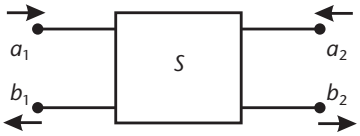

Figure 5.4 Two-port circuit representation with scattering parameters.

$$\begin{bmatrix} b_1 \\ b_2 \end{bmatrix} = \begin{bmatrix} S_{11} & S_{12} \\ S_{21} & S_{22} \end{bmatrix} \begin{bmatrix} a_1 \\ a_2 \end{bmatrix} \tag{5.1}$$

Setting one of the independent variables to zero allows us to find the individual S-parameters by:

$$\begin{aligned} S_{11} &= \left.\frac{b_1}{a_1}\right|_{a_2=0} \\ S_{12} &= \left.\frac{b_1}{a_2}\right|_{a_1=0} \\ S_{21} &= \left.\frac{b_2}{a_1}\right|_{a_2=0} \\ S_{22} &= \left.\frac{b_2}{a_2}\right|_{a_1=0} \end{aligned} \tag{5.2}$$

where S_{11} is the reflection coefficient at port 1 when port 2 is terminated with a matched load, S_{12} is the reverse transmission coefficient when port 1 is terminated with a matched load, S_{21} is the forward transmission coefficient when port 2 is terminated with a matched load, and S_{22} is the reflection coefficient at port 2 when port 1 is terminated with a matched load (S_{11} and S_{22} are closely related to the input and output impedances, respectively) [1].

Typically, the transmission line can be implemented as a coplanar waveguide (CPW). In this way, the *S*-parameters can also be defined in terms of the circuit and the CPW electrical characteristics [2]:

$$\begin{aligned} S_{11} &= \frac{Z_{in}}{(2Z_S + Z_{in})(1+\lambda L)} \\ S_{21} &= \frac{2Z_S}{(2Z_S + Z_{in})(1+\lambda L)} \end{aligned} \tag{5.3}$$

where Z_{in} and Z_s are the resonator's input and source impedance, respectively, and λ and L are the propagation constant and length of the CPW, respectively. These equations are simplified forms of the S-parameters for the special case: $Z_0 = Z_S$, where Z_0 is the characteristic impedance of the CPW. These relationships are very useful when S-parameter measurements are performed with a network analyzer and a probing system with calibrated and known impedance values (typically $Z_0 = 50\Omega$).

5.1.3 High-Frequency Measurement Setup

The setup to perform high-frequency electrical characterization requires the use of microwave network analyzer and probe stations or prototypes to connect the resonator to the measurement equipment. A first setup comprises the network analyzer and a coplanar probe station (ground-signal-ground system). The network analyzer performs automated evaluation of the resonator's S-parameters. The use of

coplanar transmission lines provides a very convenient method to contact the resonator because they offer a well-defined ground plane and avoid the introduction of parasitic and strain inductances [1]. The typical setup for a CPW connecting an FBAR is depicted in Figure 5.5, where the FBAR's circuit representation and the system-level interconnection are shown. By using appropriate calibration standards and routines, the measurement plane is translated to the probing-pad location, thus compensating the effects of the probing system—including cables and connectors—and matching the network analyzer's port impedance of 50Ω. Commercial network analyzers may be employed for gigahertz-range measurements [3], whereas the interconnection may be carried out with microwave probe stations [4].

Nowadays, different calibration standards are implemented in RF measurements, as the coplanar thru-open-short-and-load (TOSL) structures are very popular. TOSL standards are commercially available in the form of printed-circuit substrates and are provided by microwave-instrumentation companies [5]. The

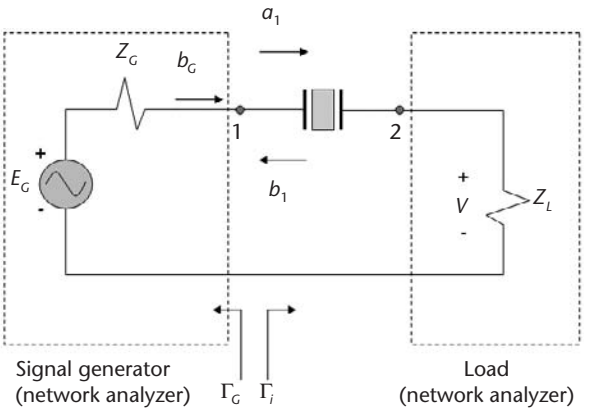

(a)

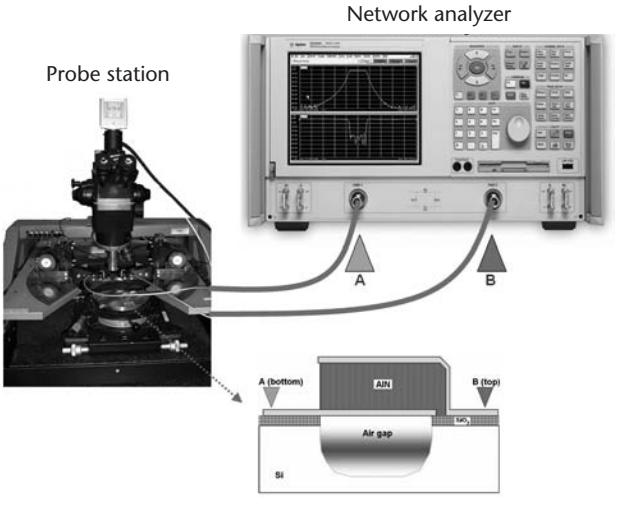

(b)

Figure 5.5 First setup for electrical characterization of the scattering parameters in FBAR: (a) circuit representation; and (b) physical connection of the instrumentation and probe station.

name of the TOSL standard describes the network components employed in the calibration routine. This standard is conventionally used with an automatic network analyzer and is suitable for calibration routines limited to coaxial transmission lines in the frequency range from DC to 6 GHz. To perform the calibration, the standard kit implements two components: the printed-circuit TOSL substrate and the standard software against which the measurements are compared during calibration. For higher frequency calibrations, other standards are implemented [6].

In a second setup, a printed circuit board (PCB) will replace the coplanar probe station. In this PCB, a CPW is designed to connect the resonator die to the measurement instrumentation. The die is attached to the PCB and connected to the PCB-made transmission lines by wire-bonding. For this purpose, the PCB's CPW design has to guarantee impedance matching to the 50Ω value of the port impedance of the network analyzer (appropriate PCB design and careful selection and knowledge of the dielectric constants of the PCB's laminate are required). The circuit representation of this setup is the same as that depicted in Figure 5.5(a). A schematic representation of an exemplary PCB-FBAR system is depicted in Figure 5.6(a), and the physical setup comprising the PCB and the network analyzer is shown in Figure 5.6(b). The calibration standards used in this setup are coplanar TOSL structures implemented as coaxial connectors fabricated by Agilent Technologies. The PCBs were fabricated using laminates made of the high-frequency dielectric material Rogers 3010, which is a ceramic-filled PTFE composite with low dielectric loss and application up to 10 GHz [7].

The measurement setup also influences the characterization results and has to be considered when performing the evaluation of results and the parameter extraction. As previously discussed, PCB-based and coplanar probe station characterization setups can be implemented. This decision has an impact on the measurement's performance and leads to different de-embedding approximations. While the PCB-based setup is practical for complex systems involving more than one FBAR device, such as nonconventional devices or hybrid FBAR-CMOS circuits, its flexibility is achieved at the cost of added losses and reactance due to the wire-bonding, and it is not very practical for single-resonator characterization. Also, additional—and nonnegligible—design and prototyping effort has to be dealt with.

To visualize the differences and impact of both systems, the same device can be characterized by first measuring it directly on the wafer, with the coplanar probe station. After data measurement and acquisition, the wafers can be diced, packaged, and tested on chips glued and bonded to the PCB. The plots of Figure 5.7 compare data from S-parameter measurements performed on the same resonator, where three main resonances are observed at 1.8, 2.4, and 2.6 GHz. Although the electrical response is similar in both setups, the effects of added losses and reactance affecting the S-parameter values can be observed. Wire-bonding and PCB design optimization would help diminish the differences between both measurements.

5.1.4 Quality Factor Extraction

The quality factor (Q) is a key parameter to evaluate the performance of both the resonators and the resonator-based applications. Hence, its evaluation is of great

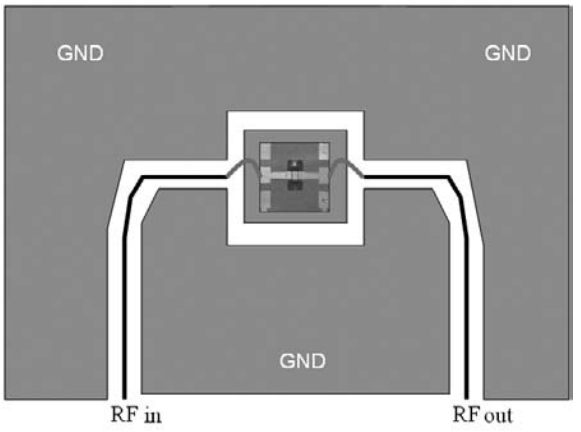

(a)

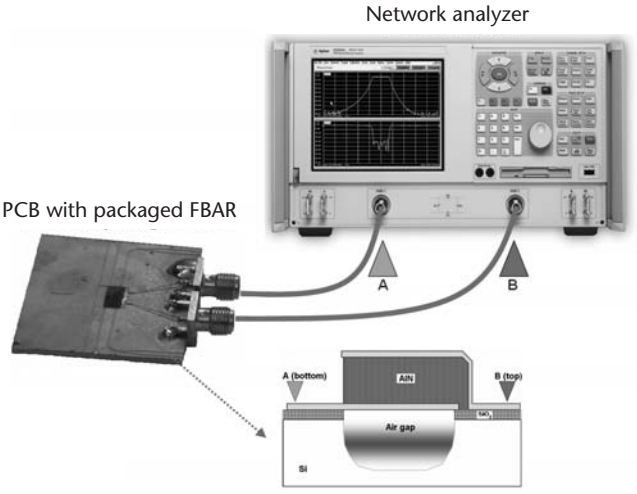

(b)

Figure 5.6 Second setup for electrical characterization in FBAR: (a) schematic representation of the PCB-FBAR system; and (b) physical interconnection of the PCB and the network analyzer.

concern in order to perform accurate estimations of the device's capabilities. There are different methods for calculating the Q factor of a resonant device. Based on electrical characterization, transmission and reflection S-parameters are useful tools to extract the Q factor. Its characterization in FBARs is important because it determines the selectivity of filters and phase noise of oscillators in RF applications, and the sensing capability of sensors [8, 9].

In a first method, which we will call the S_{21}-S_{11} *magnitude method*, the Q value of a resonator can be obtained from the measurements of two-port S parameters, by using the magnitudes of both the transmission (S_{21}) and reflection (S_{11}) parameters. According to this method and assuming source impedance Z_s of 50Ω, the Q factor is calculated by the following equation [2]:

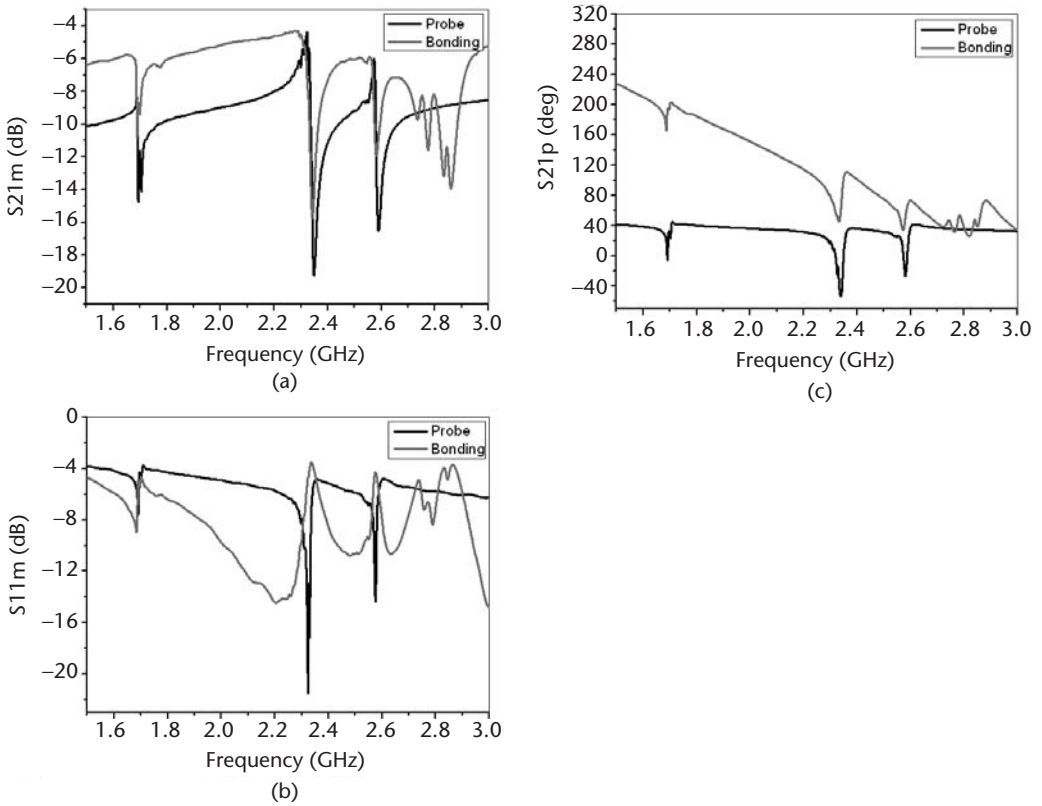

Figure 5.7 Comparison of the probe-station-based and the PCB-based characterization setups: (a) magnitude of S21; (b) magnitude of S11; and (c) phase of S21. The effects of added reactance are observed in the response of PCB-packaged resonators.

$$Q_S = \frac{\left(\frac{\omega_S}{\omega_p}\right)}{1-\left(\frac{\omega_S}{\omega_p}\right)^2}\sqrt{\frac{\left(1-|S_{21Min}|\right)}{|S_{21Min}|}\frac{\left(1-|S_{11Min}|\right)}{|S_{11Min}|}} \tag{5.4}$$

In (5.4) ω_s and ω_p are the serial and parallel resonance frequencies, and S_{21Min} and S_{11Min} are the minimum values of the S_{21} and S_{11} parameters, respectively. This method for determining the Q value has the advantage of taking account of all acoustic and electrical loss mechanisms [10].

According to the classical BVD model presented in Chapter 3, the Q factor at the series resonance frequency can also be defined as:

$$Q_S = \frac{1}{\omega_S R_m C_m} \tag{5.5}$$

From (5.3), (5.4), and (5.5), values for R_m and C_m can be extracted in a first approximation by:

$$R_m = \frac{|S_{11Min}|}{\left(1-|S_{11Min}|\right)} 2Z_S \tag{5.6a}$$

$$C_m = \frac{1}{\omega_S R_m Q_S} \tag{5.6b}$$

Another Q factor definition considers the open-loop phase response $\phi(\omega)$ of the resonator, examined at resonance. The Q factor is then defined as [9]:

$$Q = \frac{\omega_S}{2} \left| \frac{\partial \phi}{\partial \omega} \right| \tag{5.7}$$

If the phase slope is large, a significant change in the phase shift and Q factor arises. This definition has an interesting interpretation for oscillator-design applications in which the resonator drives the oscillation. Thus, the open-loop Q value measures how the closed-loop circuit will oppose the variations in the frequency of oscillation [9]. Using this method, in practice, the Q factor at resonance can be extracted from the S_{21} parameter by observing the derivative of the S_{21} phase. According to this method and to the plots of Figure 5.8, the phase of the S_{21} parame-

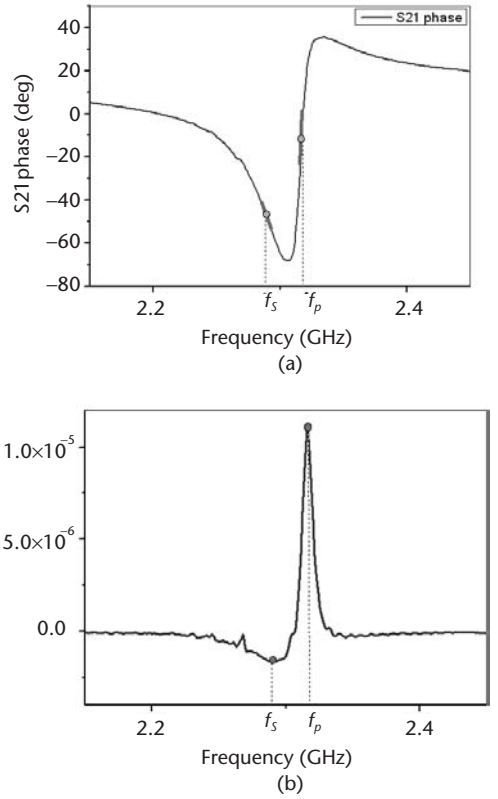

Figure 5.8 Phase response of a typical FBAR for *Q*-factor calculation: (a) phase of the S21 parameter indicating the minimum and maximum slope values (the same correspond to series and parallel resonance frequencies, respectively); and (b) derivative of the S21 phase (the most negative and positive peaks correspond to f_s and f_p).

ter of an FBAR is used to characterize the Q factor of the resonator. The most negative derivative value coincides with the most negative phase slope, corresponding to the series resonance frequency f_s. On the other hand, the most positive derivative value corresponds to the most positive phase slope (i.e., the parallel resonance frequency f_p). Characterization results of the Q factor by using this method are similar to those found by the S21-S11-magnitude method. In this example, a Q value bigger than 1,000 is extracted.

A third method widely employed for Q factor calculation uses the –3-dB definition of bandwidth: Q is then defined as the resonance frequency f_0 divided by the two-sided –3-dB bandwidth B ($Q = f_0/B$). This method is very popular for high-insertion-loss MEMS devices and bandpass filters with a several-decibel peak response. Figure 5.9 shows the frequency response of a clamped-clamped MEMS resonator fabricated within the UMC CMOS process [11]. The response was obtained by mixing technique measurements (circles) and the corresponding Lorentz fitting (continuous line). At the 25.475-MHz central frequency, the signal power level is about –115 dBm, and the curve fits the –3-dB levels of –118 dBm at the frequencies located at ± 15.75 kHz of the central frequency, or B = 31.5 kHz, thus leading to the Q value of 812. However, in low-loss devices such as FBARs, the resonance peak at the series resonance frequency is poorly defined, especially—and paradoxically—in high-Q factor resonators (insertion losses near to 0 dB are the rule on FBAR performance). For this reason, this method is rarely used to characterize FBARs.

To illustrate the impact of Q factor on FBAR and MEMS resonator-based applications, let's consider the example of a microwave ladder filter. Ladder filters and duplexers are nowadays the most popular and commercially successful applications of FBARs. Worldwide companies like Avago Technologies (formerly Agilent) or Infineon are selling millions of units each year, thus replacing RF components made with SAW and ceramic technologies [12, 13]. Such components offer lower insertion losses, higher out-of-band rejection, and a more reduced size than those made with previous technologies. Although FBAR filters are well developed and mature at the design and technology levels, their performance is very sensitive to the

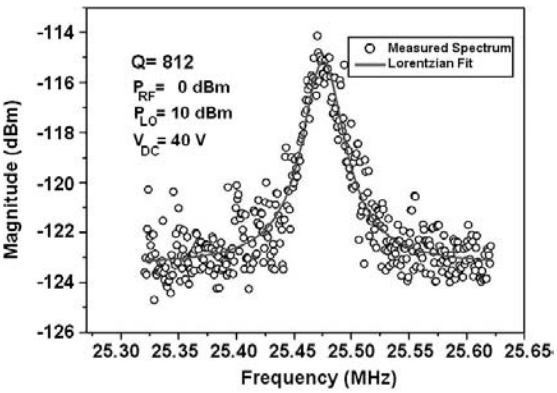

Figure 5.9 Frequency response around the resonance peak of a CMOS-MEMS clamped-clamped HF resonator: the Q factor equal to 812 was extracted with the –3-dB method after mixing technique measurements performed in vacuum. (© 2009 Institute of Physics [11].)

quality of their composing resonators. Since there are numerous references to FBAR filters [14, 15], this application has also become a useful benchmark tool in order to explore the limitations and possibilities of FBAR technologies.

A ladder filter is comprised by an *n*th-order interconnection of series and shunt-located FBARs. The schematic and equivalent-circuit models are depicted in Figure 5.10. The order of the filter refers to the number of series-to-shunt stages, counting from the input to the output port of the filter [14]. The series and shunt FBARs have different resonance frequencies and should ideally be of different size, in order to optimize the in-band and out-of-band performance of the filter [16].

The performance of the filter can be predicted by circuit-level simulations and the equivalent-circuit model of Figure 5.10(b). The equivalent-circuit model of a third-order filter ($N = 6$ resonators) with 2.2-GHz central frequency and corresponding simulation results are shown in Figure 5.11(a). Outstanding 2-dB insertion loss and 36-dB out-of-band rejection values can thus be predicted. However, the realization of the filter does not always lead to the expected specifications. If process variations or design issues significantly affect the quality factor of resonators, the global result is disastrous for the filter's performance. Following with the same example, the third-order filter performs the poor characteristics shown in Figure 5.11(b). Insertion losses higher than 14 dB, and 26-dB zeroes in the out-of-band region, are far below the standards required for modern filters.

If we analyze these results, we can obtain a good explanation regarding the Q factor of the FBARs. According to the insertion-loss expression for a passband filter [17], we can see how strong the link between the Q factor and insertion losses (IL) is:

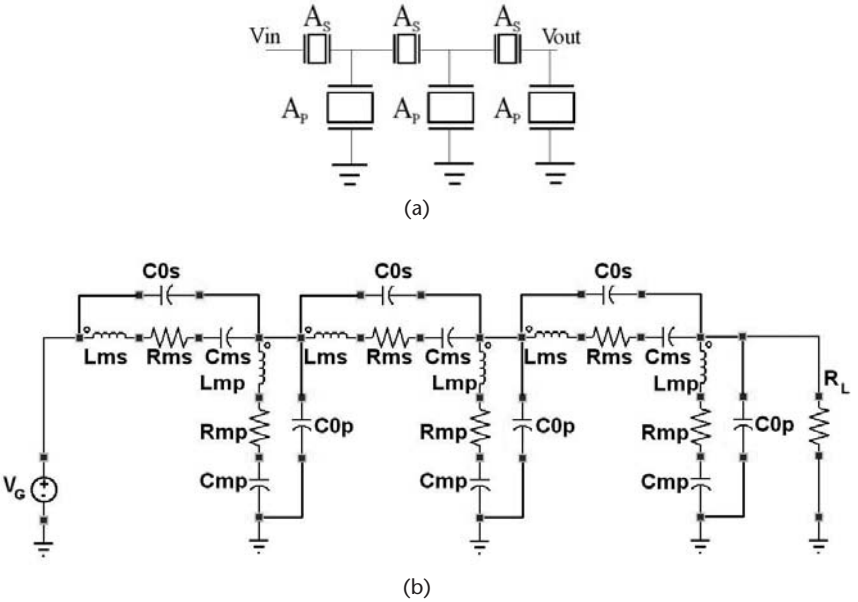

Figure 5.10 FBAR-based ladder filter (third order, six resonators): (a) ladder filter topology; and (b) circuit-level modeling.

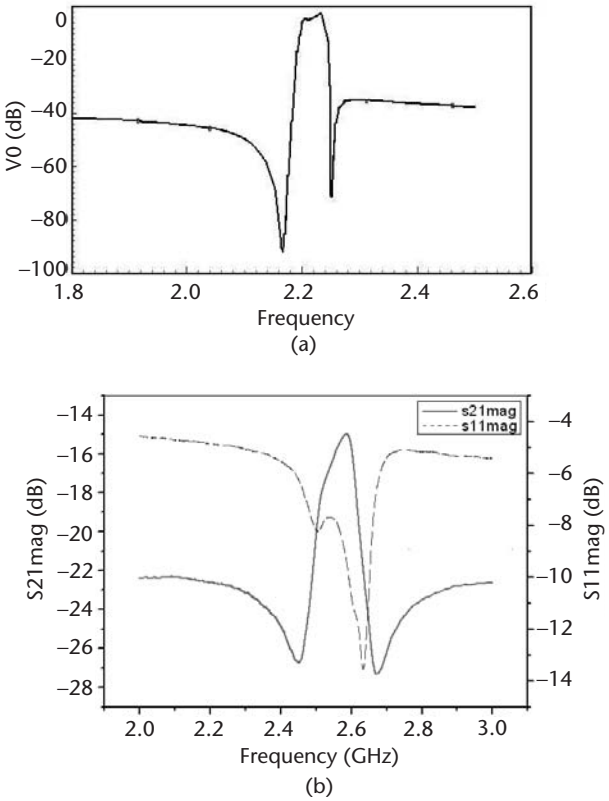

Figure 5.11 Frequency response of the ladder filter: (a) simulated response (2-dB insertion loss, out-of-band rejection > 36 dB); and (b) experimental characterization of fabricated filter (14-dB insertion loss, 26-dB out-of-band rejection).

$$IL(dB) = 20\log\left(\frac{4}{4+\frac{3\pi^2}{k_{eff}^2 Q}}\right) \tag{5.8}$$

For a k^2_{eff} of 3.0–3.4%, and IL values between 12–16 dB, Q factors in the range of 60 to 80 can be predicted. If we look at the filter-composing resonator and its S21 parameter magnitude, both shown in Figure 5.12, we can verify that the extracted Q factor value is in the same range. In summary, we see how low Q factor values of the resonators drastically increase insertion losses of the filter. Commercial filters meeting the stringent requirements of contemporary wireless mobile systems implement resonators with Q factors higher than 1,000. Precise understanding and careful extraction of the resonator physical constants enable fine-tuning of the fabrication process, thus promoting such high Q factors. Therefore, the following section describes the elastic, dielectric, and piezoelectric constants of FBARs and their extraction.

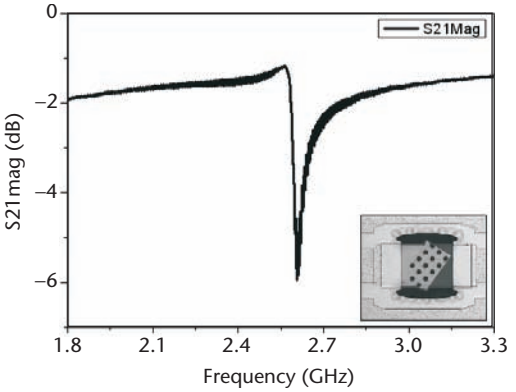

Figure 5.12 Characterization of one of the filter-composing FBARs: the S21 parameter of the resonator in the inset allows extraction of its *Q* factor (60–80), which explains to a great extent the poor performance of the filter.

5.2 Determination of Elastic, Dielectric, and Piezoelectric Constants

The electromechanical performance of FBAR, MEMS, and NEMS resonators depends on both their design and their transduction mechanism. Physical constant values of the materials composing the resonator ultimately determine their resonance frequency, quality factor, and other performance parameters. In the next sections, we analyze the extraction of physical constants by discussing the case of FBARs and AlN. The characterization procedures and parameter extraction methodology used for the elastic and dielectric constants are also extendable to other MEMS and NEMS devices, as we study. Moreover, the extraction of piezoelectric constants is of use to characterize FBARs, SMRs, SAW, and, in general, piezoelectric-based MEMS and NEMS resonators. The background and experimental methods for the extraction of such constants are described next.

5.2.1 Elastic Constants

The acoustic and mechanical properties of the structural layer of FBAR and MEMS resonators mainly determine their performance and frequency response. While the structural layer of MEMS resonators is typically fabricated by using silicon or polysilicon, it is a piezoelectric material in the case of BAW or SAW resonators. Recent resonator applications implement other materials as well, like diamond or carbon nanotubes (CNTs) [18, 19].

Among the elastic constants contributing to the resonator's characterization, we consider the elastic stiffness (or Young's modulus), the mass density, and the sound velocity. In order to extract these properties, the resonator's low-frequency mechanical resonance is estimated from the analytical model corresponding to its mechanical configuration. Let's consider the clamped-clamped beam resonator depicted in Figure 5.13, which has the same geometrical configuration of most FBARs.

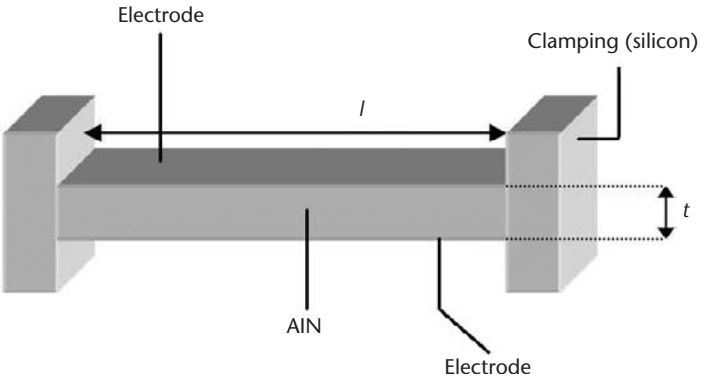

Figure 5.13 Clamped-clamped beam resonator with dimensions.

The resonance frequency of the beam depends on the thickness t and length l of the beam. Assuming a structural layer of AlN with thin-metal electrodes, one can calculate the frequency by [20]:

$$f_0 = \frac{4.73^2}{2\pi} \cdot \frac{t}{l^2} \sqrt{\frac{c}{12\rho}} \tag{5.9}$$

The quotient of the stiffness constant c and the mass density ρ of the AlN can be determined by measuring the fundamental resonance frequency f_0. Assuming the value of one of these constants, the other one can be extracted. Two independent measurements performed on beams of different dimensions allow completion of the evaluation of this quotient.

In our example, we take two beams with identical thicknesses t of 1 μm and different lengths l of 60 and 90 μm. Their experimental S21 parameters are plotted in Figure 5.14 (the resonator's layouts are observed in the insets). As observed in Figure 5.14(a), the 90-μm-long beam exhibits a fundamental frequency of 800 kHz, whereas Figure 5.14(b) shows the 60-μm-long device resonating at a higher frequency of 1.5 MHz. These results are in good agreement with the theoretical expectations of the clamped beam model described by (3.2). Furthermore, if we build finite element models (FEMs) of the beams and perform the modal analysis, we will find out similar frequency values within small error.

In Table 5.1 we compare the values of the first resonance modes of these AlN beams obtained by experimental, ANSYS, and analytical methods. Using these values and solving c and ρ in (3.5), the AlN stiffness and density values are estimated to be between 180–220 GPa and 3.0–3.7 g/cm^3, respectively. With these results at hand, the sound velocity can be derived through the well-known relationship [21]:

$$v = \sqrt{\frac{c}{\rho}} \tag{5.10}$$

According to the extracted stiffness and density values, the sound velocity of the AlN is calculated to be in the range of 7,000–8,500 m/s. As we reviewed in

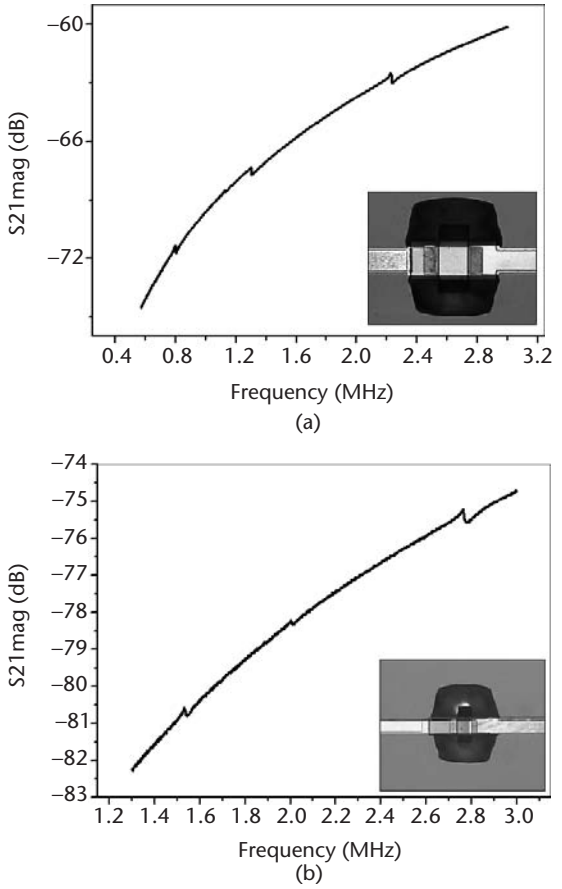

Figure 5.14 Mechanical resonances of the beam-shaped FBARs in the insets: (a) length of 90 μm, and (b) length of 60 μm (thickness is 1 μm for both devices).

Table 5.1 Low-Frequency Characterization of an FBAR, Comparing Experimental, Finite-Element-Modeling (ANSYS) and Analytical Calculations for a Clamped-Clamped Beam Resonator

Device	*Experimental (S-Parameter Data)*	*Finite-Element-Modeling (ANSYS)*	*Analytical (3.2)*
Large-sized beam (width: 50 μm, length: 90 μm, thickness: 1 μm)	First mode (fundamental): 800 kHz; second mode: 1.3 MHz; third mode: 2.2 MHz	First mode (fundamental): 877 kHz; second mode: 1.46 MHz; third mode: 2.47 MHz	First mode (fundamental): 885 kHz
Small-sized beam (width: 50 μm, length: 60 μm, thickness: 1 μm)	First mode (fundamental): 1.5 MHz; second mode: 2.75 MHz	First mode (fundamental): 1.98 MHz; second mode: 2.65 MHz	First mode (fundamental): 1.9 MHz

Chapter 2, the acoustic velocity affects the high-frequency resonant behavior of FBARs, although other electromechanical parameters must also be accounted for.

5.2.2 Dielectric Constants

In some MEMS as well as in BAW and SAW resonators, the structural layer is a dielectric thin film, whose properties we are interested in characterizing. Some test structures, like parallel-plate capacitors sandwiching the dielectric layer and forming a static capacitance C_0, allow evaluating the permittivity ε of the dielectric. For this purpose, two-probe measurements can be performed by using a capacitance meter and a probe station to contact each electrode of the capacitor. The absolute permittivity ε, also known as the dielectric constant, is defined as the dielectric displacement per unit electric field. Using the same notation defined in Chapter 2, the first subscript gives the direction of the dielectric displacement, and the second gives the direction of the electric field. If the material is anisotropic, ε is a matrix with nine elements of different values. In piezoelectric materials, ε_{11} and ε_{33} are particularly interesting, and they are defined as follows:

- ε_{11}^{T} [F/m] is the permittivity for the dielectric displacement and electric field in direction 1 under conditions of constant stress.
- ε_{33}^{S} [F/m] is the permittivity for the dielectric displacement and electric field in direction 3 under conditions of constant strain.

Given that the static capacitance C_0 formed by the electrodes and the dielectric is measured, the permittivity can be evaluated by implementing the following characterization procedure [22]:

1. Low frequency C_0 measurement;
2. Dielectric thickness (t) measurement (by means of profilometer, interferometer or SEM) [23];
3. Capacitor area (A): determined from the resonator's layout;
4. Calculation of permittivity (ε):

$$\varepsilon_{11/33}^{T/S} = \varepsilon_r \cdot \varepsilon_0 = C_0 \frac{t}{A} \tag{5.11}$$

The evaluation of ε_{11}^{T} or ε_{33}^{S} depends on the test structure we choose. For example, if we have a c-axis-oriented AlN thin film we want to evaluate the ε_{33}^{S}, which we do by using parallel-plate FBARs of known electrode sizes. If the plate has an area of $200 \times 140\ \mu\text{m}^2$ and the thin film has a thickness of 1 μm, a theoretical C_0 value of 2.21 pF is expected. From (5.11), a theoretical ε_{33}^{S} value of 7.8×10^{-11} F/m should be extracted.

Process and layout deviations may explain possible differences between experimental and theoretical dielectric-constant values. First, if the thickness of the dielectric is not uniform, C_0 may vary from one device to another. Also, device underetching may lead to capacitor areas bigger than expected to the design. Statistical analysis and parametric FEM may complement the experimental means described herein, which are good starting points for further refinement of the dielectric constants.

5.2.3 Piezoelectric Properties

5.2.3.1 The Piezoelectric Coupling Coefficient

The piezoelectric coupling coefficient is, together with the Q factor, the most important parameter characterizing the electrical performance of acoustic resonators like SMRs or FBARs. Strictly speaking, what is being characterized is the electromechanical conversion capability of the acoustic layer of the resonator (e.g., AlN, ZnO, or PZT). Furthermore, a mutual relationship exists between them, through the figure of merit (*FoM*) of the resonator:

$$FoM = Q \cdot k_T^2 \tag{5.12}$$

This means that, for a given technology, the value of the process is given by the combined Q by k_T^2 product, rather than by only one of them. Depending on the application, it will be interesting to optimize one of the Q or the k_T^2 values (the other one will diminish in the same proportion).

Since piezoelectric ceramics are anisotropic, their physical constants (elasticity, permittivity, and so on) are tensor quantities. For this reason, as explained in Chapter 2, the coupling coefficient k_T^2 of an FBAR can be measured in the longitudinal ("33") or transverse ("31") wave propagation directions. Depending on the available test structures, one or both coefficients can be measured.

Longitudinal Coupling Coefficient k^2_{33}

The longitudinal coupling coefficient k^2_{33} represents the electromechanical conversion efficiency in the c-axis ("3") when an electric field in the z-axis ("3") is applied to the piezoelectric. This is done by measuring the longitudinal-mode resonance frequency (mode "33") of an FBAR (or SMR), which is found in the 2-GHz band for a typical FBAR process. The crystal orientation and thickness of the piezoelectric layer mainly determine the coupling coefficient k^2_{33}. As the thickness decreases, the value of k^2_{33} increases, Q decreases, and the resonance frequency increases, and vice versa. The expression to derive the value of k^2_{33} from experimental measurements is [21]:

$$k_{33}^2 = \frac{\pi^2}{4}\frac{f_s}{f_p}\frac{f_p - f_s}{f_p} = \frac{\pi^2}{4}\frac{f_s}{f_p}\tan\left(\frac{\pi}{2}\frac{f_p - f_s}{f_p}\right) \tag{5.13}$$

In (5.13), f_s and f_p are series and parallel resonance frequencies of the FBAR or SMR. Table 5.2 shows the k^2_{33} values for various devices implemented with AlN thicknesses of 1,000 and 500 nm. While the resonance frequency augments for the 500-nm-thick AlN devices, k^2_{33} increases and Q decreases for similar values of the FoM.

The theoretical limits for the magnitude of k^2_{33} in AlN are around 6.7–7.0%, whereas typical Q factor values for commercial FBARs are between 700–2,000. Thus, reference values for the FoM between 50 and 100 can be found. Average values of 3% for k^2_{33} and 10% for the FoM are relatively low in comparison to reference processes. The low efficiency of the electromechanical conversion is probably due to inversion of the crystal's poling domain [24]. Annealing or other techniques

Table 5.2 Coupling Coefficient k^2_{33} Characterization for Different Devices and Thicknesses: The *Q* Factor Changes in an Inverse Proportion to k^2_{33}, for Similar Values of the FoM

Device	k^2_{33} *(%)*	*Q Factor*	*FoM*	*AlN Thickness (nm)*
Type I	2.42	731.5	17.72	1,000
Type II	2.53	519.0	12.34	1,000
Type III	0.85	1,517	12.90	1,000
Type IV	2.63	587	15.44	500
Type V	6.46	156.6	10.12	500
Type VI	3.45	276.3	9.54	500

intended for AlN-deposition refinement would contribute to future improvements of the crystal's quality.

Transverse Coupling Coefficient k^2_{31}

The k^2_{31} coupling coefficient measures the electromechanical conversion efficiency of a *c*-axis-oriented ("3") piezoelectric when an electric field is applied along the *x* axis ("1"). The measurement technique is basically the same previously described for the k^2_{33} characterization, although a surface wave test structure, like a SAW resonator, is required. Again, the electromechanical coupling is a function of the surface-wave series and parallel resonance frequencies f_S^T and f_P^T of the SAW device:

$$k_{31}^2 = \frac{\pi^2}{4}\frac{f_S^T}{f_P^T}\frac{f_P^T - f_S^T}{f_P^T} \tag{5.14}$$

Taking the AlN process of the previous example, a SAW device exhibiting series and parallel resonance frequencies of 211.75 MHz and 212.15 MHz allows the extraction of an effective k^2_{31} value of 0.47%. This value is between one-fourth and one-fifth of the k^2_{33} value, which is normal for *c*-axis-oriented piezoelectric films. Both k^2_{31} and k^2_{33} are utilized in the extraction of the piezoelectric constants of the thin film, which is explained in the following item.

5.2.3.2 Piezoelectric Constants

Piezoelectric constants of a fabricated material are process-dependent physical constants explaining the electromechanical performance of the crystal. Although reference values are available for commercially available material compounds, like AlN, specific crystal characterization has to be performed for a newly developed process. The piezoelectric constants can be expressed in voltage-to-strain (*g*), voltage-to-stress (*d*), charge-to-stress (*e*), and charge-to-strain (*d*) forms. Linear relationships exist between the different forms. Thus, the characterization of one form allows the knowledge of the other ones. In this section, the *d*-form of the piezoelectric constant is studied.

The piezoelectric constant *d* is defined as the electric polarization induced on a material per unit mechanical stress applied to it. Alternatively, it is the mechanical strain experienced by the material per unit electric field applied to it. The first sub-

script refers to the direction of polarization at zero-electric field ($E = 0$), or to the applied field strength. The second one refers to the direction of the applied stress, or to the direction of the induced strain. Two relevant components of the *d*-constant are as follows:

1. d_{33} [m/V] is the induced polarization the direction of *Z*-axis ("3") per applied unit stress in the same direction. Alternatively, it is the induced strain per unit electric field applied in the same direction.
2. d_{31} [m/V] is the induced polarization in the direction of the *Z*-axis ("3") per unit stress applied in the direction of the *X*-axis ("1"). Alternatively, it is the strain induced in direction 1 per unit electric field applied in direction 3.

The values of d_{33} and d_{31} can be extracted through different methods. One method performs an experimental measurement of the mechanical displacement of the film when an electric potential is applied to the electrodes. The measurement of the low absolute level of the displacements in thin films necessitates the use of a precise interferometer technique. Typically, a resolution of about 10^{-2} Å and a complex measurement setup—including a sensitive double-beam interferometer—are required to determine the low-field piezoelectric coefficients [25]. For that reason, an indirect evaluation is preferred, by calculating the values of d_{33} and d_{31} from previously extracted electromechanical constants.

In previous sections, FBAR and SAW resonators were useful to evaluate permittivity, stiffness, and coupling-coefficient constants. These constants can be used to obtain the piezoelectric charge constants from piezoelectric constitutive equations:

$$k_{33}^2 = \frac{d_{33}^2 \cdot c_{33}}{\varepsilon_{33}^T} \tag{5.15}$$

$$k_{31}^2 = \frac{d_{31}^2 \cdot c_{11}}{\varepsilon_{33}^T} \tag{5.16}$$

Solving the right-sided parts of (5.15) and (5.16) and using previously extracted parameters, the *d*-constants are calculated. Using the parameters of the previous example, the values of d_{33} and d_{31} are 2.85 and 1.12 pm/V. These magnitudes are roughly equal to half the value of previously reported epitaxial AlN films [26]. The higher deposition temperatures of epitaxial processes partially explain the better quality of the films obtained with this process, in comparison to sputtered-AlN films. On the other hand, the d_{33}/d_{31} ratio is 2.56, in the same order of the theoretical relationship for clamped wurtzite structures ($d_{33}/d_{31} = 2$) [27].

5.3 Equivalent-Circuit-Parameter Extraction

Previously, in Chapter 3, the BVD equivalent-circuit-parameter model of FBARs and other MEMS resonators was introduced. Electrical modeling and extraction of equivalent-circuit parameters in FBARs are well documented, the lumped-element

MBVD being the most accepted model for parameter extraction purposes [28]. The extraction of the model's parameters is carried out by evaluating and averaging the resistive and reactive components of the S-parameters evaluated at different points, in a frequency span where the resonance is expected to be found. Some optimization processes can be implemented in the extraction of the parameters, like least-mean-squares fitting. Additional dissipative elements due to substrate coupling may also be accounted for in the model, or they can be omitted if on-the-wafer calibration or de-embedding is performed. These dissipative elements are of great interest, since they could explain insertion losses and signal drifting from the RF signal paths connecting the resonator to the substrate wafer. An accurate resonator's model is particularly important to design MEMS-to-CMOS integrated applications. The MBVD model and the setup for parameter extraction are shown in the schema and optical image of Figure 5.15.

The optimization of parameter extraction in other RF devices is well known: extensive work has been done to extract, from measured S-parameters, the equivalent-circuit parameters of microwave resonators [29], FET transistors [30, 31], and filters [32]. In most of these cases, a least-squares strategy is adopted to optimize the extraction of the circuit parameters. In this section, we expand this discussion by studying a multistep procedure implementing a least-squares optimization strategy for the extraction of equivalent-circuit elements of the resonator and of the substrate carrying it. In this way, on-wafer calibration is avoided [28], allowing model-based de-embedding of the MBVD parameters.

5.3.1 Parameter-Extraction Algorithm

Assuming a given resonator's model, a least-square-based extraction algorithm aims to estimate the optimal values of one or more error functions, which describe the transfer function of the resonator by its equivalent circuit parameters. The extraction can be done in an iterative way, processing each one of the iterations either in a single step or in a multiple substep basis, the latter being more accurate in complex or selective functions. In this case and for a given iteration, each substep in the algorithm extracts a subset of one or more of the equivalent-circuit parameters. This implies that different error functions are defined and are to be optimized. Prior to this, the S-parameters' sensitivity to the different circuit elements has to be analyzed, in order to determine the most adequate function to be used in the extraction of each circuit element.

To illustrate this, let's consider the MBVD FBAR's model depicted in Figure 5.15(a). Thorough exploration of the model allowed us to find out that some equivalent-circuit elements are more sensitive to the reflection parameter S_{11}, whereas others are more sensitive to the transmission parameter S_{21}. Also, the execution sequence of the substeps has to be studied, with the aim of achieving acceptable numerical stability and convergence rates. Table 5.3 presents a summary of this study, where seven different error functions involve the equivalent-circuit parameters of both the FBAR and its substrate. This means that each one of the iterations will be comprised by the execution of each one of these functions on a seven-substep basis.

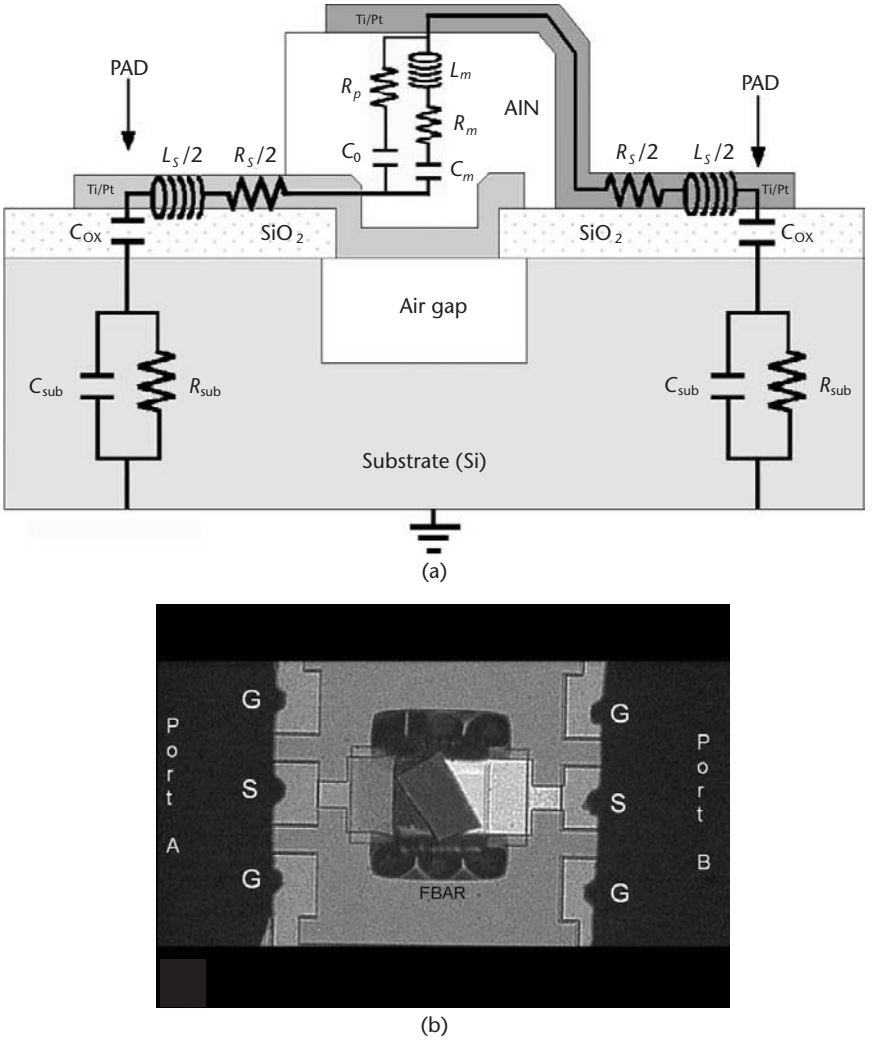

Figure 5.15 MBVD model of FBAR, substrate, transmission line, and characterization pads: (a) equivalent circuit representation and (b) characterization setup.

The number of iterations can be set in two ways: first, through an internal tolerance value of the error-function value, and, second, by user's setting as a running parameter at the time of execution of the algorithm. The execution of each substep may be controlled by various optimization criteria. Since each substep is also an iterative routine by itself, one of the optimization criteria may be the number of local execution cycles (for the substep, independentof the global number of iterations). Other optimization criteria may be the tolerance of the optimized variable or the tolerance of the error-function value. Around 10 global iterations are typically enough to achieve good convergence of the equivalent-circuit parameters in a standard Pentium processor–based PC platform.

The flow diagram of Figure 5.16 illustrates the sequence of the parameter extraction. As shown, a given iteration cycle may begin with the optimization of R_m. The remaining elements in the equivalent-circuit are then set to fixed values—the

Table 5.3 Error Functions of the Multisubstep Parameter-Extraction Algorithm on FBARs

Substep	*Circuit-Elements Optimized*	*S-Parameter Fitted*	*Error Function*
1	R_m	S11	S11mag(R_m)
2	L_m, C_m, C_0	S21	S21phase(L_m, C_m, C_0)
3	R_s	S11	S11mag(R_s)
4	R_p	S21	S21mag(R_p)
5	R_{sub}	S21	S21mag(R_{sub})
6	C_{sub}	S21	S21phase(C_{sub})
7	C_{ox}	S21	S21phase(C_{ox})

Source: [33].

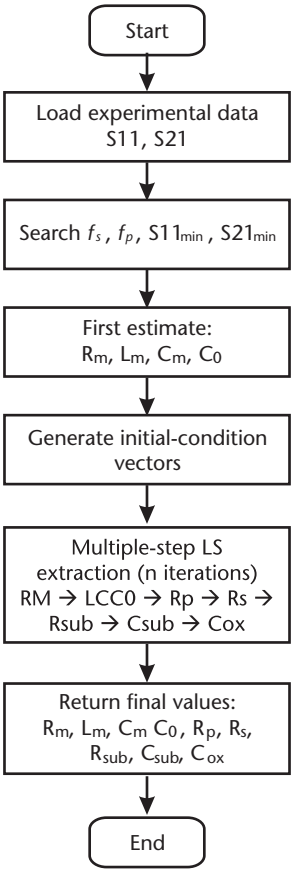

Figure 5.16 Flow diagram of an FBAR's equivalent-circuit parameter extraction algorithm.

ones obtained in the previous iteration cycle. In the second substep, the L-C-C_0 ensemble is optimized by implementing the second error-function *S21phase*(L_m, C_m, C_0), while R_m and the other model elements remain fixed to constant values, and so forth. After the substep is completed, the algorithm proceeds in the same way to execute the following steps until the last substep. In that moment a new global cycle starts, and the foregoing process is repeated until the last iteration is completed.

Additional routines may also be implemented in order to complete the fully automated parameter-extraction procedure, including loading of S-parameter ASCII data and first estimation of the BVD parameters [2], among others.

5.3.2 Case Study: Equivalent-Circuit-Parameter Extraction of an FBAR

The optical image of Figure 5.17(a) shows the top view of a rectangular-shaped FBAR with annotated model elements. The device was fabricated according to the RIE-based process described in Chapter 4. The transmission line is made of Ti/Pt and has a thickness of 30 nm/150 nm, a width of 50 μm, a length of 250 μm, and theoretical $R_s/2$ and $L_s/2$ in the range of 8–12 ohms and 90–140 fH, respectively. The dark area around the resonator is SiO_2 after Si underetching (an equivalent area can be found underneath the FBAR). Figure 5.17(b) plots experimental and extraction results where the transmission spectrum (S_{21}) magnitude is shown in a span of 1.5 GHz. These curves compare the BVD, MBVD, and MBVD with parasitic element models. The extracted $R_s/2$ and $L_s/2$ values are 12.25Ω and 34 fH, respectively, which are of the same order of magnitude as those expected from the theoretical analysis.

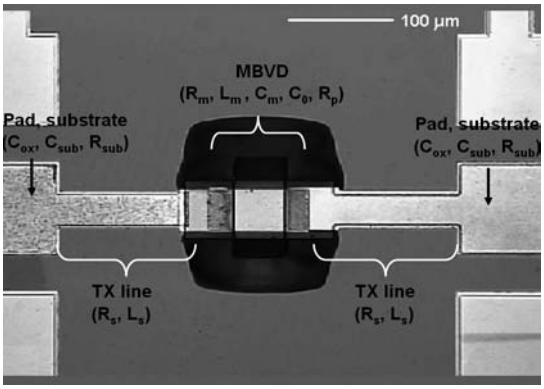

(a)

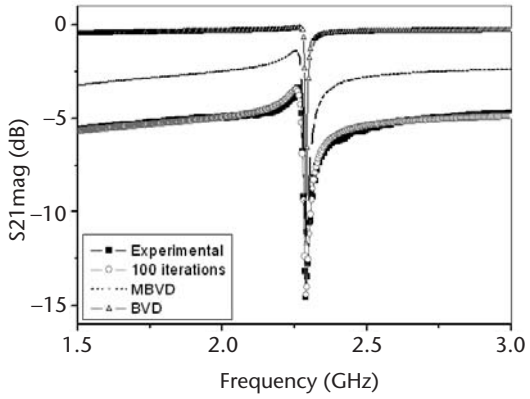

(b)

Figure 5.17 Experimental results on the extraction of FBAR's parameters: (a) exemplary FBAR with annotated model elements; and (b) fitting and experimental curves (BVD and MBVD curves are also plotted). (*After*: [34].)

Concerning the substrate of FBAR, an 800-nm-thick thermal-SiO_2 layer leads to a theoretical value of C_{ox} of around 430 fF, whereas the extracted value is 647 fF. On the other hand, theoretical calculations for our low-resistivity 500-μm-width Si wafers result in values in the range of 2,000–10,000Ω and 2 fF for resistance R_{sub} and capacitance C_{sub}, respectively. These values are of the same order as the extracted values obtained by the algorithm, –150Ω and 1 fF, respectively. The differences in the extracted and theoretical values of R_{sub} may be explained by a lower resistivity value of the wafer, with respect to the expected doping configuration. Further characterization of this process should allow refinement of this parameter. Whatever the case, the extracted values are consistent with the properties of a low-resistivity substrate.

Finally, the extracted BVD model values are also closely related to experimental observation. In particular, for the testing device, the measured coupling coefficient k_{33}^2 of 2.32% is very close to 2.22%. The latter is calculated from the extracted values of L_m, C_m, C_0; 435.5 nH, 11.1 fF, and 605.2 fF, respectively. The 10-Ω and 8.5-Ω values of R_m and R_p, respectively, are also in the range of those previously reported for resonators [33–35].

5.4 AFM, Optical, and Electron-Beam-Induced Characterization

Nonelectrical characterization techniques have been largely employed to characterize physical systems. In this section, we also discuss AFM and optical interferometer techniques.

5.4.1 AFM-Based Characterization with Optical Detection

AFM is a nanometer-scale-resolution tool able to measure the static and low-frequency mechanical parameters of some MEMS resonators, especially those with a cantilever shape and a frequency response between units of hertz to few megahertz. More recently, AFM has been used to perform high-frequency scanning of gigahertz-mode resonators like FBARs. Next, we discuss both characterization approaches.

5.4.1.1 Low-Frequency Mechanical Resonance of MEMS

In standard tapping-mode AFM measurements, a cantilever with a tip scans the surface of the sample after piezoelectric actuation of a device chip placed on the head of the AFM system, as shown in Figure 5.18(a). A piezoelectric actuator excites the cantilever substrate vertically, causing the cantilever to move up and down. In its encounter with the sample's surface, the tip located on the cantilever's vertex deflects. The reflected laser beam reveals information about the vertical height of the sample surface and material's characteristics. This setup, however, can be modified to perform MEMS resonator measurements. In the new system, depicted in Figure 5.18(b), the MEMS resonator replaces the AFM cantilever and is driven by the AFM's piezoelectric actuator and a signal generator.

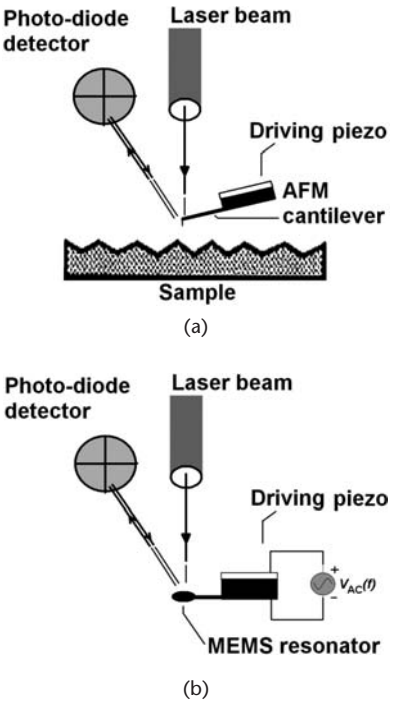

Figure 5.18 AFM-based MEMS resonator characterization: (a) standard SFM setup for sample characterization; and (b) modified setup for MEMS resonator characterization.

In the resonance measurements, the AFM is configured to work in tapping mode. Thus, the AC signal of the generator feeds the piezoelectric actuator, which is caused to move the cantilever to the extent of its natural modes and the transduced energy by the piezoelectric material. As the cantilever moves vertically, the reflected laser beam, or *return signal*, deflects in a regular pattern over a photodiode array, generating a sinusoidal, electronic signal. Such signal is postprocessed by frequency-analysis software to extract the resonance peaks and their quality factors within the frequency span [36].

Calibration and evaluation of the spring constants of MEMS cantilevers can also be performed with a similar setup. There exist a number of techniques to determine the spring constant of atomic force microscope (AFM) cantilevers. These methods can be divided into four categories: dynamic, theoretical, static, and indirect. The dynamic methods rely on analyzing the resonance response of the cantilever. Some of these methods require knowledge on the cantilever's material properties and dimensions, whereas others involve analysis of the lever's thermal noise spectrum. The theoretical methods involve the use of simple expressions that require accurate knowledge of the cantilever's Young's modulus and dimensions. In the static response methods, a known force is applied to an AFM cantilever to determine the spring constant. The known force can be supplied by a small added mass, a reference lever or artifact, or an indentation device. Indirect methods have also been employed. These techniques require that one cantilever on each chip is calibrated accurately, and then the spring constant of the other levers on the same chip is calculated indirectly [37].

5.4.1.2 High-Frequency Dispersion Amplitude of FBARs

High-frequency modes of MEMS and FBAR can also be supervised by AFM techniques. Reference [38] presents a setup based on the combination of an AFM with a lock-in detection technique to measure displacement amplitude of an FBAR.

For example, the desired main thickness vibration mode of FBAR resonators is observed in the gigahertz band, where lateral resonant modes are also excited around this frequency [39]. These modes exhibit very small displacement amplitudes of about units of nanometers due to the piezoelectric effect. Hence, the AFM scans the FBAR's surface in order to evaluate the mode shaping around the main resonance frequency. The characterization procedure implemented by San Paulo et al. [38] requires electrical characterization of the FBAR, prior to the AFM experiments (to estimate the resonance range and also for comparison purposes). The measurement setup of Figure 5.19 illustrates how the AFM tip is placed in contact with the top electrode of the FBAR while a sinusoidal amplitude-modulated RF signal is used to drive the resonator. The RF oscillation amplitude is then measured by using the modulation signal as the reference for the lock-in amplification of the cantilever deflection signal. The experiments require the use of AFM cantilevers with a high resonance frequency (> 20 kHz) and a low stiffness constant (< 1 N/m). Consequently, we have the selection of a particular modulation frequency, near but lower than the cantilever's resonance frequency. The RF driving signal has to be chosen in the range of the FBAR resonance frequency previously obtained in the electrical characterization. To analyze the topography, or equivalently the mode shaping maps, or *wavelength patterns*, the two-dimensional Fourier transform of the amplitude is calculated over a selected scanning line on the device geometry. The existence of a uniform thickness vibration mode at some driving frequency is checked as well. Finally, the average oscillation amplitude along the selected scan line against the line frequency is plotted.

Line-scanning the whole surface allows obtaining 2D mode shaping maps of the FBAR electrode at the thickness-mode frequency and the near lateral-mode frequencies. The method also evaluates the vibration amplitude as a function of the modulation and driving frequencies.

Another measurement technique of the resonator's displacement and mode shaping describes how images are recorded at normal video frame rates. This is done by using dynamic holography with photorefractive interferometric detection,

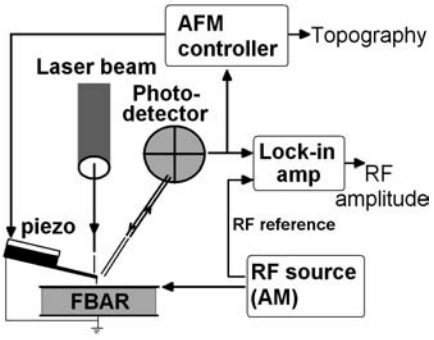

Figure 5.19 AFM and lock-in detection based experimental setup. (*After:* [38].)

coupled with microwave electrical impedance measurements [40]. The ability of the photorefractive technique to process optical interference over an extended area eliminates the need for rapid serial scanning of smaller size. The experimental setup includes a coherent solid state laser source (532 nm), a microwave generator, a photorefractive crystal, an electro-optic modulator (EOM), a photodetector or charge-coupled-device (CCD) camera, mirrors, lenses and optical beams.

5.4.2 Optical Microscope Interferometry with Piezoelectric Actuation

Interferometry is another characterization method employed in both static and dynamic resonator characterization. The method is performed by an optical microscope with objectives featuring light-interference capabilities at a specific wavelength λ. Interferometry takes advantage of the interference produced when the light passing through an object is caused to interfere with a reference beam of light that has followed a somewhat different pathway. Under these circumstances, the opaque surfaces of a reflected light specimen or transparent specimens are imaged when the path difference between the two light beams is converted into intensity fluctuations. Thus, interference bands appear on the structure's surface when the sample is placed on the microscope's stage and after appropriate focusing [41].

In static measurements, the levels of flatness or curvature of the resonator's structure can be analyzed through this method. By studying the orientation of the interference bands, the type of curvature—concave or convex—can be inferred. If the bands displace to the clamping zone after moving the sample away with respect to a reference observation point, the structure is down-tilted, or it has a concave shape. Otherwise, the sample is up-tilted, or it is convex. Bands appearing simultaneously across the surface of the resonator indicate that it is highly flat. The optical image of Figure 5.20 shows the interferometer bands of a MEMS cantilever whose central area is still clamped to the substrate (due to insufficient etching time). Looking at its interference bands, this device has a concave shape, which is explained by the difference of residual stress between the released and the nonreleased areas.

In dynamic characterization, interferometry is very useful for characterizing the frequency response of the resonator and its main mechanical parameters, like the resonance frequency, its vibration amplitude, and the quality factor. Apart from the microscope, the measurement setup comprises an AC signal generator and a commercially available piezoelectric actuator [42] whose frequency response is previ-

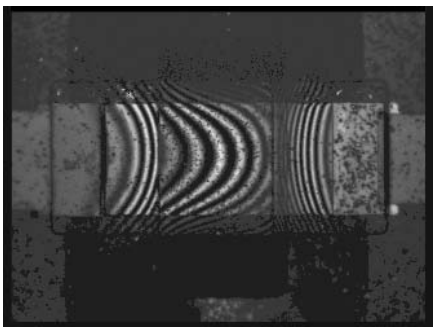

Figure 5.20 Interferometer bands of a resonating MEMS cantilever.

ously known and supposed to cover the resonator's frequency range of interest. Due to the piezoelectric effect, the AC signal provided by the generator induces an AC displacement of the piezoelectric actuator, which is mechanically attached to the resonator's die. Due to this coupling (and if the frequency of the signal generator approaches one of the natural modes of the resonator), it goes into resonance. When the resonance starts up, a group of zero-contrast bands become visible. In this way, the resonance frequency is related to the highest number of zero-contrast bands over the resonator's surface. Figure 5.21 shows out-of-resonance and in-resonance interferometer images of another MEMS resonator. The number of zero-contrast bands is determined by the implemented wavelength λ of the microscope's objective and helps to estimate the vibration's amplitude A, through first-order Bessel functions relating both variables [43]. The images of Figure 5.21 show the interferometry bands on the surface of a $1{,}000 \times 1{,}000\ \mu m^2$ MEMS cantilever Si resonator with thickness of 5 μm. In the static resonator image of Figure 5.21(a), the interference bands are seemingly observed, while the cantilever resonating at 4 kHz shows a diffuse image with four zero-contrast bands. The images were taken at $\lambda = 546$ nm. The wavelength leads to a resonating amplitude of about 500 nm [44].

Although practical and useful, it should be said that interferometry entails some limitations. Due to the optical nature of the measurement, only rough approximations of the quality factor's values can be obtained. Thus, calibration and evaluation of the 3-dB value amplitudes are not straightforward tasks and may lead to considerable error. Another drawback of this technique is the impossibility to state and compare the energy values delivered to the resonator and transduced by the excitation system at the different vibration modes. These limitations, however, can be overcome with postprocessing software and automated calibration routines.

5.4.3 Fabry-Pérot Interferometry

Fabry-Pérot interferometry is an optical technique based on a structure implementing reflective surfaces. They selectively transmit and reflect wavelengths of the incident light depending on the dimensions, incidence angle, and refractive index of the

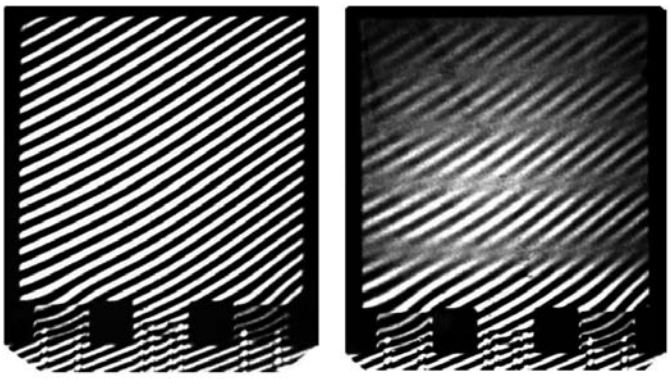

(a) (b)

Figure 5.21 Interferometer-based MEMS resonator characterization: (a) static resonator interferometer image; and (b) cantilever resonating at 4 kHz (zero-contrast bands are observed). (*After:* [44].)

interferometer [45]. The structure can be a transparent plate with two reflecting surfaces—also known as an *etalon*—or it can be two parallel highly reflecting mirrors—the *interferometer*. The spectrum of the interferometer exhibits transmission peaks as a function of wavelength corresponding to resonances of the etalon or interferometer structures, which is the base of Fabry-Pérot characterization of MEMS and NEMS resonators.

The technique can be used in two ways: in a Fabry-Pérot interferometer the distance l between the plates can be tuned in order to change the wavelengths at which the transmission peaks occur. On the other hand, the Fabry–Pérot etalon has a fixed size—the thickness of the MEMS or NEMS resonator—and the characterization aims for finding out which wavelengths are transmitted (corresponding to the thickness of the resonator). Due to the angle dependence of the transmission, the peaks can also be shifted by rotating the etalon with respect to the beam. The geometry of the Fabry-Pérot etalon is depicted in Figure 5.22.

How much of the light incident to the etalon is effectively transmitted? The answer relies on the transmission function T_F of the etalon and the interference between the multiple light reflections between its two reflecting surfaces. Depending on whether or not the transmitted light beams T_m are in phase, constructive or destructive interference occurs. In the case of constructive interference a high-transmission peak of the etalon is detected. Out-of-phase transmitted beams are destructed, thus corresponding to a transmission minimum. The phase conditions are thus dependent on the wavelength l of the light, the traveling angle through the etalon θ, and the thickness λ and refractive index n of the etalon. The phase shift δ for constructive interference is given by:

$$\delta = 2\kappa l \cos\theta \tag{5.17}$$

where κ is the wave number inside the etalon:

$$\kappa = \frac{2\pi n}{\lambda} \tag{5.18}$$

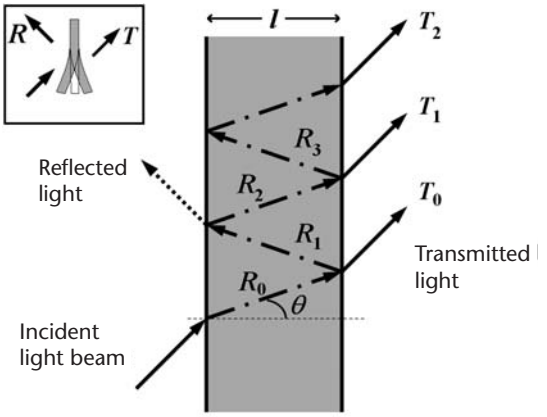

Figure 5.22 Fabry-Pérot interferometer (etalon): the incident light beams are selectively transmitted according to their wavelength and angle of incidence, and the thickness *l* and refractive index *n* of the etalon.

As the drawing of Figure 5.22 suggests, the amplitude of the transmitted beams A_T is the sum of the individual amplitude beams T_m:

$$A_T = \sum_{m=0}^{\infty} T_m \tag{5.19}$$

Assuming no absorption of the etalon, the energy of the transmitted and reflected light is conserved. The condition $T + R = 1$ is met, where T and R are the transmission and reflection magnitudes of the beams. The first transmitted beam T_0 results from direct transmission through the etalon, while the second beam T_1 is a phase-delayed version of T_0, and doubly attenuated by a factor R^2 due to the two reflections inside the etalon. By considering the m reflections of the $(m + 1)$th beam, (5.19) can also be expressed in terms of the phase shift, and the transmission and reflection amplitudes by:

$$A_T = T\sum_{m=0}^{\infty} R^m e^{jm\delta} \tag{5.20}$$

The amplitude sum of (5.20) can be expressed in an analytical form as the solution of the series by:

$$A_T = \frac{T}{1 - \mathrm{Re}^{j\delta}} \tag{5.21}$$

Finally, the energy of the transmission function T_F equals the product $A_T A_T^*$ as:

$$T_F = A_T A_T^* = \frac{T^2}{1 + R^2 - 2R\cos\delta} \tag{5.22}$$

The frequency spectrum of T_F gives us the transmitted-peak wavelengths of the incident light.

Fabry-Pérot interferometers or etalons are used in optical modems, spectroscopy, lasers, and dichroic filters to measure the wavelengths of incident light [46–48]. As a characterization tool, it is used in MEMS and NEMS resonator characterization to detect the resonance frequencies of the device. Since MEMS and NEMS resonators are relatively thin and transparent—thickness comparable with the wavelengths of incident light—part of the light is transmitted through the structure and is reflected by the structural layer. Indeed, MEMS and NEMS resonator act as Fabry-Pérot interferometers. This method was first used by Carr et al. to detect the vibration of NEMS resonators [49]. A general disadvantage of the technique is that the laser beam locally increases the temperature of the structure when illuminating it.

5.4.4 Electron-Beam Excitation

Electron-beam-induced excitation of NEMS resonators can be used to elicit vibration of the resonator. The technique is based on quasi-electrostatic charges induced on the surface of very thin dielectric resonators by the action of electrons in vacuum

environment. The NEMS is assumed to be inside the chamber of a scanning electron microscope (SEM), a transmission electron microscope (TEM), or similar equipment where electron beam imaging and high vacuum can be available.

In a first setup, the electron beam of the SEM or TEM illuminates the sample. Another mechanism for inducing the charges involves a conducting sharp probe connected to an external signal generator. As the probe approaches the NEMS at enough distance to generate charge accumulation, time-varying charges generate electromotive forces driving the NEMS into resonance. If we know the driving frequency of the signal generator, and we observe the vibration, the NEMS resonance frequency can be extracted.

Required forces make the mechanism suitable for resonator characterization at the NEMS scale. Under appropriate conditions, nanocantilever, nanotube and nanowire resonators [19, 50], and nanooscillators [51] have been characterized.

5.5 Summary

In this chapter, we have learned many lessons regarding the characterization of FBAR, MEMS, and NEMS resonators. First, we studied the basis of low- and high-frequency characterization. Different characterization setups have been described, and layout considerations affecting the performance of FBARs have been commented. Based on the electrical characterization method, we have seen how the main elastic, dielectric, and piezoelectric constants of the resonator are extracted, and we have seen how the quality factor and the electromechanical coupling coefficients are extracted.

The electrical characterization also supports the extraction of the equivalent-circuit parameters of FBAR and MEMS. This task is particularly useful for designing MEMS-based integrated circuit applications, as we will study in the next chapters. Although many methods exist for extracting these parameters, we have focused on explaining a least-mean-square-based algorithm to optimize the extraction. By this algorithm, on-wafer calibration can be avoided, thus achieving instantaneous de-embedding of the resonator's equivalent-circuit parameters. Of course, the performance of such a tool can be improved with classical test structures carrying out on-the-wafer calibration and parameter de-embedding.

NEMS characterization techniques are being developing to deal with submicron oscillation detection. AFM measurement, Fabry-Pérot interferometry, and electron-beam-induced resonance elicitation are suitable for structural and vibration analysis of NEMS resonators. They are replacing well-developed electrical techniques that cannot be implemented at the nanometer scale or due to the device configuration. Such techniques are increasingly leaving the laboratory to become part of robust applications where in situ characterization is required [52], and they are expected to deal with more application fields in the near future.

References

[1] Davis, W. A., and K. K. Agarwal, *Radio Frequency Circuit Design*, New York: John Wiley & Sons, 2001.

[2] Su, Q., et al., "Thin-Film Bulk Acoustic Resonators and Filters Using ZnO and Lead–Zirconium–Titanate Thin Films," *IEEE Trans. on Microw. Theory Tech.*, Vol. 49, 2001, pp. 769–778.

[3] Rohde & Schwartz International Network Analyzers, http://www2.rohde-schwarz.com.

[4] Süss Microtec Probe Systems, http://www.suss.com.

[5] Cascade Microtech RF Microwave Probes, http://www.cmicro.com.

[6] Agilent Technologies, Mechanical and Electronic Calibration Kits (Microwave Mechanical Calibration Kits & ECal Modules, up to 110 GHz): http://www.agilent.com.

[7] Rogers Corporation, "RO3000 Series High Frequency Circuit Materials," http://www.rogerscorporation.com/mwu/pdf/3000data.pdf.

[8] Ylilammi, M., et al., "Thin Film Bulk Acoustic Wave Filter," *IEEE Trans. on Ultrason. Ferroelectr. Freq. Control*, Vol. 49, 2002, pp. 535–539.

[9] Razhavi, B., *RF Microelectronics*, Upper Saddle River, NJ: Prentice-Hall, 1998.

[10] Kaitila, J., et al, "Spurious Resonance Free Bulk Acoustic Wave Resonators," *Proc. IEEE Intl. Ultrason. Symp. 2003*, Honolulu, HI, October 5–8, 2003, pp. 84–87.

[11] Lopez, J. L., et al., "Integration of RF-MEMS Resonators on Submicrometric Commercial CMOS Technologies," *J. Micromech. Microeng.*, Vol. 19, 2009, 015002.

[12] Avago Technologies, http://www.avagotech.com/pages/en/rf_for_mobile_wlan_mmw/fbar_filters/fbar.

[13] Infineon Technologies, http://www.infineon.com.

[14] Ruby, R., et al., "Ultra-Miniature High-Q Filters and Duplexers Using FBAR Technology," *Digest of Tech. Papers IEEE Intl. Solid-State Circuits Conf. ISSCC 2001*, San Francisco, CA, February 5–7, 2001, pp. 120–121.

[15] Lakin, K. M., et al., "Bulk Acoustic Wave Resonators and Filters for Applications Above 2 GHz," *Digest of Tech. Papers IEEE Intl. Microwave Symp. MTT-S 2002*, Vol. 3, Seattle, WA, June 3–7, 2002, pp. 1487–1490.

[16] Kim, K. W., et al., "Resonator Size Effects on the TFBAR Ladder Filter Performance," *IEEE Microw. Wirel. Compon. Lett.*, Vol. 13, 2003, pp. 335–337.

[17] Ruby, R., "Review and Comparison of Bulk Acoustic Wave FBAR and SMR Technology," *Proc. IEEE Intl. Ultrason. Symp. 2007*, New York, October 28–31, 2007, pp. 1029–1040.

[18] Gaidarzhy, A., et al., "High Quality Factor Gigahertz Frequencies in Nanomechanical Diamond Resonators," *Appl. Phys. Lett.*, Vol. 91, 2007, 203503.

[19] Lassagne, B., et al., "Ultrasensitive Mass Sensing with a Nanotube Electromechanical Resonator," *Nano Lett.*, Vol. 8, 2008, pp. 3735–3738.

[20] Lin, Y. W., et al., "Series-Resonant VHF Micromechanical Resonator Reference Oscillators," *IEEE J. Solid State Circuits*, Vol. 39, 2004, pp. 2477–2491.

[21] ANSI/IEEE Std. 176-1987, "IEEE Standard on Piezoelectricity," Institute of Electrical and Electronics Engineers, New York, 1988.

[22] Alexander, T. P., et al., "Dielectric Properties of Sol-Gel Derived ZnO Thin Films," *Proc. Tenth IEEE Intl. Symp. on Applications of Ferroelectrics Ferroelectrics ISAF'96*, Vol. 2, East Brunswick, NJ, August 18–21, 1996, pp. 585–588.

[23] Makkonen, T., et al., "Estimating Materials Parameters in Thin-Film BAW Resonators Using Measured Dispersion Curves," *IEEE Trans. on Ultrason. Ferroelectr. Freq. Control*, Vol. 51, 2004, pp. 42–51.

[24] Sanz-Hervás, A., et al., "Degradation of the Piezoelectric Response of Sputtered C-Axis AlN Thin Films with Traces of Non-(0002) X-Ray Diffraction Peaks," *Appl. Phys. Lett.*, Vol. 88, 2006, 161915.

[25] Kholkin, A. L., et al., "Piezoelectric Characterization of Pb(Zr,Ti)O3 Thin Films by Interferometric Technique," *Proc. 10th IEEE Intl. Symp. on Applications of Ferroelectrics Ferroelectrics ISAF'96*, Vol. 1, East Brunswick, NJ, August 18–21, 1996, pp. 351–354.

[26] Tsubouchi, K., K. Sugai, and N. Mikoshiba, "AlN Material Constants Evaluation and SAW Properties on AlN/Al2O3 amd AlN/Si," *Proc. IEEE Intl. Ultrason. Symp. 1981*, Vol. 1, Chicago, IL, October 14–16, 1981, pp. 375–380.

[27] Berlincourt, D., H. Jaffe, and L. R. Shiozawa, "Electroelastic Properties of the Sulfides, Selenides, and Tellurides of Zinc and Cadmium," *Phys. Rev.*, Vol. 129, 1963, pp. 1009–1017.

[28] Larson III, J., et al., "Modified Butterworth-Van Dyke Circuit for FBAR Resonators and Automated Measurement System," *Proc. IEEE Intl. Ultrason. Symp. 2000,* San Juan, Puerto Rico, October 22–25, 2000, pp. 863–868.

[29] Wheless, W., and D. Kajfez, "Microwave Resonator Circuit Model from Measured Data Fitting," *Digest of Tech. Papers IEEE Intl. Microwave Symp. MTT-S 1986*, Baltimore, MD, June 2–4, 1986, pp. 681–684.

[30] Kondoh, H., "An Accurate FET Modeling from Measured S-Parameters," *Digest of Tech. Papers IEEE Intl. Microwave Symp. MTT-S 1986*, Baltimore, MD, June 2–4, 1986, pp. 377–380.

[31] Kompa, G., and M. Novotny, "Highly Consistent FET Model Parameter Extraction Based on Broadband S-Parameter Measurements," *Digest of Tech. Papers IEEE Intl. Microwave Symp. MTT-S 1992*, Albuquerque, NM, June 1–5, 1992, pp. 293–296.

[32] Seyfert, F., et al., "Extraction of Coupling Parameters for Microwave Filters: Determination of a Stable Rational Model from Scattering Data," *Digest of Tech. Papers IEEE Intl. Microwave Symp. MTT-S 1992*, Philadelphia, PA, June 8-13, 2003, pp. 25–28.

[33] Campanella, H., et al., "Automated On-Wafer Extraction of Equivalent-Circuit Parameters in Thin-Film Bulk Acoustic Wave Resonators (FBAR) and Substrate," *Microwave Optical Tech. Lett.*, Vol. 50, 2008, pp. 4–7.

[34] Campanella, H., et al., "Instantaneous De-Embedding of the On-Wafer Equivalent-Circuit Parameters of Acoustic Resonator (FBAR) for Integrated Circuit Applications," *Proc. 20th Symp. on Integrated Circuits and Systems Design SBCCI'07*, Rio de Janeiro, Brazil, September 3–6, 2007, pp. 212–217.

[35] Campanella, H., et al., "Automated On-Wafer Characterization in Micro-Machined Resonators: Towards an Integrated Test Vehicle for Bulk Acoustic Wave Resonators (FBAR)," *Proc. IEEE Intl. Conf. Microelectronic Test Structures ICMTS 2007*, Tokyo, Japan, March 19–22, 2007, pp. 157–161.

[36] Digital Instruments, Dimension 3100 SPM AFM measurement system, Dimension 3100 Manual, Rev. B, 2009.

[37] Gibson, C. T., D. A. Smith, and C. J. Roberts, "Calibration of Silicon AFM Cantilevers," *Nanotechnology*, Vol. 16, 2005, pp. 234–238.

[38] San Paulo, A., X. Liu, and J. Bokor, "Atomic Force Microscopy Characterization of Electromechanical Properties of RF Acoustic Bulk Wave Resonators," *Proc. IEEE Intl. Conf. MEMS 2004*, Maastrich, the Netherlands, January 25–29, 2004, pp. 169–172.

[39] Telschow, K. L., V. A. Deason, and D. L. Cotte, "Full-Field Imaging of Acoustic Motion at Nanosecond Time and Micro Length Scales," *Proc. IEEE Intl. Ultrason. Symp. 2002,* Munich, Germany, October 8–11, 2002, pp. 601–604.

[40] Telschow, K. L., et al., "Full-Field Imaging of Gigahertz Film Bulk Acoustic Resonator Motion," *IEEE Trans. on Ultrason. Ferroelectr. Freq. Control*, Vol. 50, 2003, pp. 1279–1285.

[41] NIKON Microscopy U., http://www.microscopyu.com/articles/optics/objectivespecial.html.

[42] Physik Instrumente (PI) GmbH & Co., "PICMA ® Chip Monolithic Multilayer Piezo Actuators (LVPZT)," Data Sheet, 2008.

[43] Lizorkin, P., "Bessel Functions," in *Encyclopaedia of Mathematics*, M. Hazewinkel, (ed.), Boston, MA: Kluwer Academic Publishers, 2001.

[44] Morata, M., "Resonadores micromecanizados para su aplicación en la detección de gases," Ph.D. Thesis, U. A. Barcelona. 2004.

[45] Fabry, C., and A. Pérot, *The Interferometer*, 1899.

[46] Langdon, R. M., and D. Dowe, "Photoacoustic Oscillator Sensors," in *Fiber Optic Sensors II*, Vol. 798, A. M. Scheggi, (ed.), The Hague, the Netherlands: SPIE, 1987, pp. 86–93.

[47] Stokes, N. A. D., R. M. A. Fatah, and S. Venkatesh, "Self-Excitation in Fibre-Optic Microresonator Sensors," *Sens. Actuators A: Phys.*, Vol. 21, 1990, pp. 369–372.

[48] Kouh, T., et al., "Diffraction Effects in Optical Interferometric Displacement Detection in Nanoelectromechanical Systems," *Appl. Phys. Lett.*, Vol. 86, 2005, 013106.

[49] Carr, D. W., and H. G. Craighead, "Fabrication of Nanoelectromechanical Systems in Single Crystal Silicon Using Silicon on Insulator Substrates and Electron Beam Lithography," *J. Vac. Sci. Technol. B*, Vol. 15, 1997, pp. 2760–2763.

[50] Nam, C.-Y., et al., "Diameter-Dependent Electromechanical Properties of GaN Nanowires," *Nano Lett.*, Vol. 6, 2006, pp. 153–158.

[51] Tanner, S. M., et al., "High-Q GaN Nanowire Resonators and Oscillators," *Appl. Phys. Lett.*, Vol. 91, 2007, 203117.

[52] "First Atomic Force Microscope on Mars," Scientific payload in the NASA's Phoenix Mars Lander mission to Mars, http://monet.physik.unibas.ch/famars/index.htm.

CHAPTER 6

Performance Optimization

After ideal-device characterization, the main process and equivalent-circuit parameters are obtained. However, process deviations and stability issues introduce new variables to the study of the resonator's behavior. These issues may include time and frequency stability due to differences between the designed and the implemented fabrication process. Furthermore, frequency drifting due to the thermal conditions of the operation has to be kept at low values, for accomplishing the competitive performance of resonators.

This chapter presents the main process optimization techniques to achieve improved performance of resonators. The optimization of an FBAR is studied in detail as a representative case for the illustration of the concept. We begin this chapter by explaining the sources of time and frequency instability of the resonance frequency, mainly due to fabrication process deviations and the thermal configuration of the resonator's structure. In this way, the thermal coefficient factor is evaluated. Afterward, we learn about the concept, implementation, and characterization of different temperature-compensation techniques.

Process-based tuning of the resonance frequency in batch resonators is also required to face the performance uniformity required in commercial, mass-produced devices. Some postfabrication tuning techniques of the FBAR's resonance frequency are studied herein, expanding the study of tuning to a novel, low-impact technique based on focused-ion-beam.

6.1 Frequency Stability

Tolerances of the fabrication process, the layout design of the resonator, the process design, and the physical environment of operation may affect the frequency response of resonators. These parameters cause the resonance frequency to be changed or to exhibit poor stability. Also, nondesired resonance modes of lower energy may superpose in a nonconstructive way to the main resonance mode, leading to quality factor reduction and diminishing the overall resonator's performance. These deviations are related to inaccurate or low-controlled thin-film deposition, oxide growing, or micromachining, among other sources, and they lead to unexpected material properties, dimension, or layout variations of the resonators. In this section, it will become evident how the resonance frequency depends on these materials and layout properties.

6.1.1 Thin-Film Thickness Tolerance

The performance of the resonator and resonator-based systems depends on how accurately the resonance frequency's value is predicted. In certain applications, like FBAR-based ladder filters, the resonance frequencies of the series and the shunt resonators have to be fixed within very small tolerances. This allows preserving the bandwidth-to-central frequency ratio, in-band insertion loss, and out-of-band-rejection specifications. Since the size and frequency relationships of devices have a big impact on the filter's response, the design allows only small tolerances. As discussed in previous chapters, the thickness of the piezoelectric layer is the key process parameter controlling the resonance frequency of the filter-composing FBARs. For example, the analysis in [1] shows that a deposition process of ZnO with thickness tolerance of ±86Å is required to obtain a competitive ladder filter with application in the PCS band (1.9 GHz).

In Section 4.4.1, thickness and profile measurements showed how the AlN layer may suffer variations due to fabrication in a nonplanar process. If we look at the S-parameter characterization results, it can be seen that the resonance frequency deviations are between 10% and 15%. This is in the same order of thickness deviations previously found, as observed in the plot of Figure 6.1. The variations obligate to implement a planarization step, a postprocess tuning technique, or both. The planarization process is mandatory to reduce the variation of the AlN thickness, and it can be performed by chemical mechanical polishing (CMP), which is a technique widely used in semiconductor fabrication. By combining the chemical and mechanical actions of a reactive and abrasive component, and a polishing pad, the layer is flattened to guarantee a uniform thickness across the wafer within very small tolerances. CMP is an on-process technique, because it is performed during the fabrication process, and it can be performed on such layers requiring planarization that are critical to the resonance frequency's control (not only the AlN, as we will see later). Other fabrication and postfabrication-based frequency control techniques exist as well, as we will study in the next sections of this chapter.

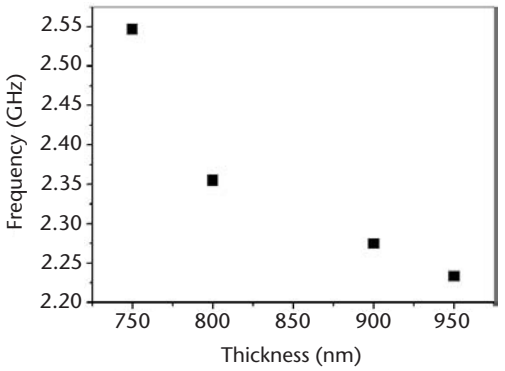

Figure 6.1 Resonance frequency of FBARs with different AlN thicknesses: due to process deviations and nonplanar AlN deposition, both the thickness and resonant frequency present a 10–15% tolerance (respective to the nominal value). (© 2007 IOP Publishing Ltd. [2].)

6.1.2 Layout Design Effects

In addition to fundamental-mode resonances, the low frequency response of resonators involves static and quasi-static mechanisms. On the other hand, the high frequency behavior of resonators accounts for layout- and process-dependent phenomena, including parasitic effects due to the packaging setup, substrate, transmission line, and design-related higher-order modes.

Regarding the layout design of FBAR and other MEMS resonators, the presence of higher-order modes in the proximity of the main resonance frequency may affect performance at the frequency of interest. In FBARs, for example, some electrode geometries suppress or diminish the presence of "spurious" resonance modes, while others enhance them in a negative way [3]. These modes are lateral, Lamb-like modes superposing to the main longitudinal-mode resonances, which may appear due to the resonator's layout, the crystalline characteristics of the piezoelectric layer, or both. At the same time, the size of the electrodes has an effect in the insertion losses of FBARs [4, 5].

For the sake of illustration, let's take the example of two groups of FBARs fabricated within a RIE-based process. Resonators of the first group have electrodes with nonparallel walls, whereas those of the second group are designed with parallel-wall electrodes. Examples of the S-parameter responses of resonators from both groups are observed in the optical pictures of Figure 6.2. Looking at the S21 and S11 parameter's response of the second group in Figure 6.2(a), two resonances comparable in size with the main peak (2.2 GHz) can be observed around the frequencies 1.6 and 2.6 GHz. However, only a main resonance mode is observed in the resonators of the first group, according to the plots of Figure 6.2(b). The parallelism of the FBAR's electrode walls contributes to the appearance of important spurious resonances, due to the systematic transmission and reflection of lateral-mode waves.

Superposed modes of lower energies can also be notoriously close to the main resonance frequency. While the main resonance is due to longitudinal-wave propagation, as previously discussed in Chapter 2, superposed modes are caused by lateral waves. The energy of these lateral modes can be diminished by the addition of an "overlap" electrode, which has proven its effectiveness on this task [5, 6]. An overlap electrode is an annular-shaped structure built on the top electrode of the FBAR to modify the wave propagation conditions near the layout boundaries of the electrode. In this way, a more uniform resonance shape is obtained, and the energy of lateral-mode resonances attenuated. The plots of Figure 6.3 compare the frequency response of two resonators of similar geometry fabricated within the same process, with and without overlap electrode. Both the electrode design and the overlap-electrode addition strategies should be addressed to optimize the FBAR's frequency response.

6.1.3 Time and Frequency Stability

Time stability is also an important factor to be considered when studying the resonator's frequency response. To analyze the fluctuations of the resonance frequency, we distinguish two cases: short-term and long-term stability.

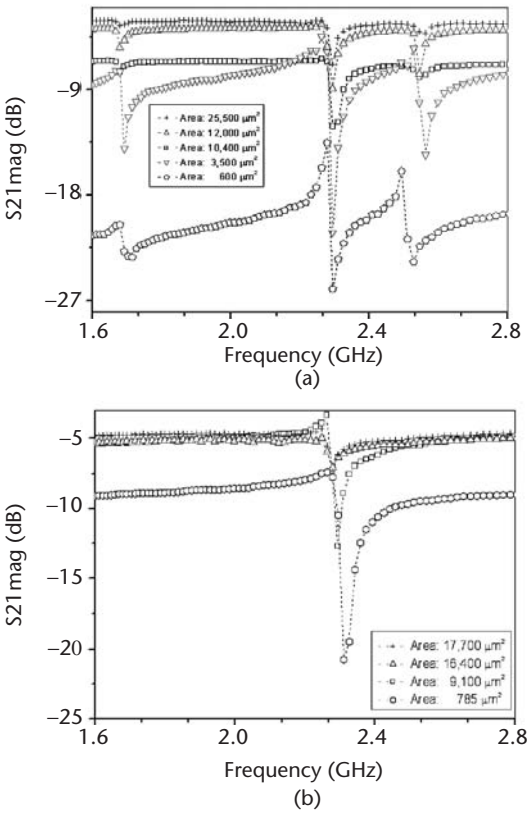

Figure 6.2 Electrode geometry influence in the S-parameter response of the FBAR (f_0= 2.25 GHz): (a) parallel-side resonators (big resonances at 1.6 and 2.6 GHz); and (b) nonparallel side devices (a single resonance peak is observed at 2.25 GHz; small lateral-mode resonances are not observed at this scale).

Short-time stability can be explained by noise sources in the setup, and it can be studied by two different methods:

1. Observing a wideband frequency span of the resonant signal of the FBAR and acquiring various sets of data to calculate the frequency deviation;
2. Observing a 0-Hz frequency span near the resonance frequency to evaluate the phase deviation.

From the conceptual point of view, results of the first method are equivalent to those of the second one. Regarding the first method, data acquisition of the magnitude of the S11 or S21 parameters is performed, and the resonance frequencies of each curve labeled and compared among them. In the second method, we acquire the S11 or S21 parameter phase data, we identify the resonance frequency (using the marker tool of the network analyzer), and then we reduce the frequency span to 0 Hz. Then we start a new data acquisition and store phase values in order to make some statistical analysis, by extracting the mean value and standard deviation. The plot of Figure 6.4 shows the phase response of the S21 parameter of a rectangular-shaped FBAR. Data acquisition is carried out along a representative number of

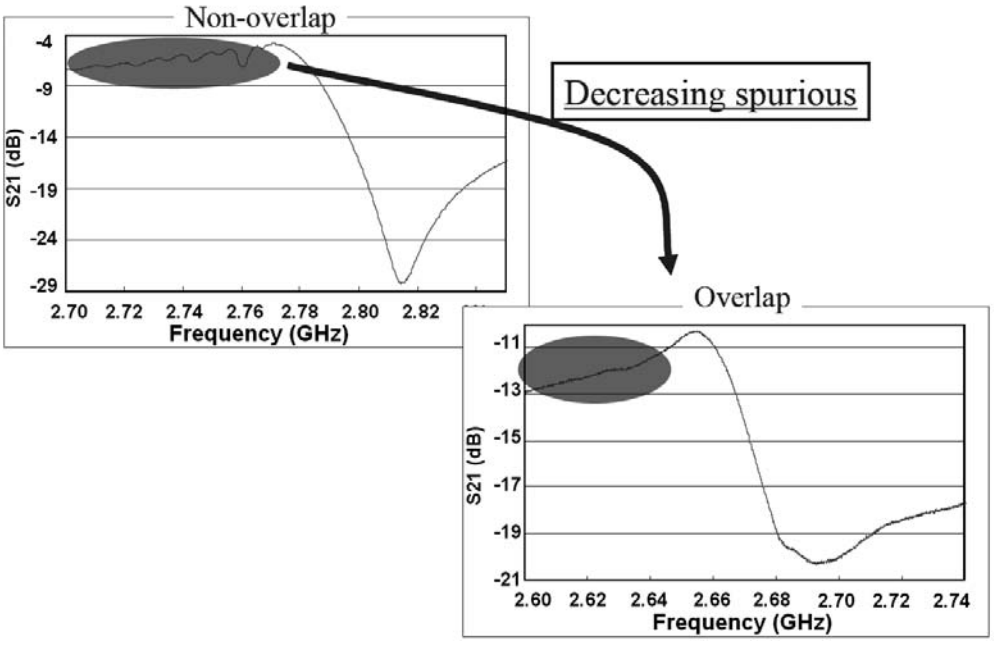

Figure 6.3 Overlap electrode effects on the high-frequency response of FBARs. (Courtesy of Seiko EPSON Corp., 2008.)

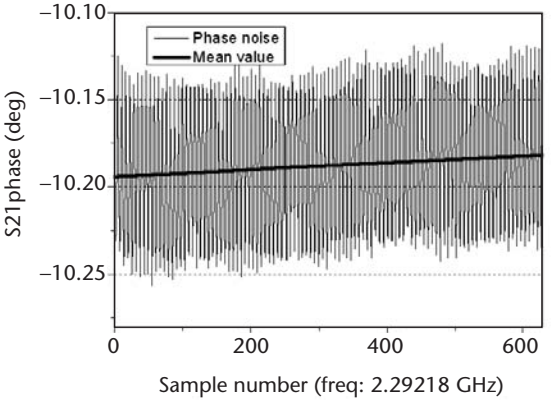

Figure 6.4 Short-term time stability characterization: zero-span frequency-domain acquisition of the S21 phase response.

samples to give the study statistical validity. To calculate the short-time frequency stability, the mean value of the phase is divided by the phase slope at the resonance frequency, which is calculated by differentiating the S21 parameter phase data of the first acquisition (see an example of S21 phase differentiation in Figure 5.8). In this example, the phase deviation is ±0.08° and the phase slope is 2.6×10^{-6} deg/Hz. Consequently, the frequency drifting has a value of 30 kHz.

The long-term stability is, at its time, observed over a longer window of time. To study it, S-parameter acquisition is performed on different devices along days, weeks, months, or even years depending on the quality and goals of the study. In

such a long window, it is hard to compare the environmental variables of the characterization setup among different samples, but some conclusions regarding the devices may be extracted. The curves of Figure 6.5 illustrate the magnitudes of the S11 parameter of an exemplary FBAR device, taken with a 1-month difference. Measurements were performed at room temperature and, as it can be seen in the figure, with no significant difference among the resonance frequencies. This example can be improved and done in a more systematic way, thus exploring the minimum frequency resolution needed to establish accurate reference-frequency values. Environmental conditions, like temperature or vibration, can also be controlled.

6.1.4 Temperature Stability and Thermal Coefficient Factor (TCF)

The temperature stability of resonators is a third aspect worth studying to understand the importance of process optimization. In reference oscillator applications of FBAR, QCMs, or other MEMS resonators, for example, a low temperature coefficient (TCF) of the resonator is particularly important to guarantee the best phase-noise performance [7]. The TCF of the structural layer mainly determines the overall TCF of the resonator; thus, measuring it gives process and application design elements to optimize the resonator and its applications.

First, the TCF characterization of the resonator is performed. The required setup includes a network analyzer, a heater stage and temperature controller, and an adequate probe station to connect the resonator and the network analyzer. Also, the temperature range and values to perform the measurements between a minimum and maximum value are defined, the temperature of the chamber is set up, and the S-parameter data acquisition is performed. New data acquisitions are carried out for each temperature value after appropriate control of the heater stage. Gathering the data of all measurements in a postprocessing tool allows identification of the changes of the resonance frequency. In the end, one obtains the curve relating the resonance frequency against the chamber's temperature and calculates the TCF. Since the frequency change is usually low, it is expressed in parts per million (ppm), referred to a reference frequency as:

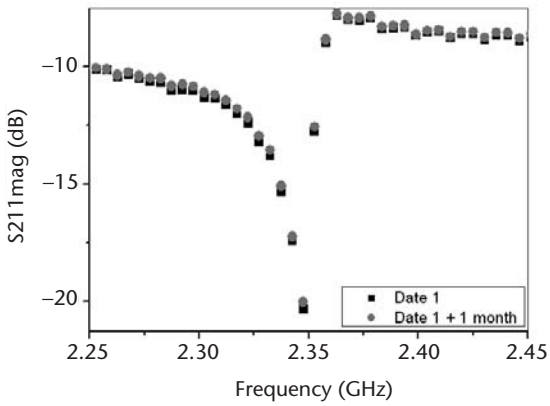

Figure 6.5 Time stability characterization: two independent measurements of the S11 parameter were performed on the same device with a 1-month difference between them.

$$\frac{(f_i - f_0)}{f_0} \times 10^6 [\text{ppm}] = \frac{\Delta f}{f_0} \times 10^6 [\text{ppm}] \tag{6.1}$$

In (6.1), f_i is the measured resonance frequency at temperature i, and f_0 is the resonance frequency at a known temperature of reference. The plot of Figure 6.6 shows the TCF characterization of a rectangular-shaped FBAR. The chosen temperature range is in a range of 100°C from –20°C to +80°C. The resonator has electrodes of Ti/Pt with a thickness of 30 nm/150 nm and a layer of AlN with thickness equal to 1,000 nm. The TCF value of this resonator is about –20 ppm/°C, which is in accordance to FEM simulations (–16 ppm/°C), and is typical of FBARs fabricated with sputtered AlN films (TCF between –20 to –40 ppm/°C). However, this value is rather high to accomplish the requirements of modern RF applications, in comparison to technologies like quartz crystals (TCFs in the units of ppm/°C). Optimization of the TCF toward a temperature-compensated device is discussed in the next section, where we examine the compensation strategies and the involved processes.

6.2 Temperature Compensation

As commented in the previous section, high TCF values degrade the frequency stability and phase-noise response of the system in which the resonator is integrated. Different authors have proposed various strategies to reduce the magnitude of the TCF of AlN-based FBARs, and so stabilize the frequency response of FBARs. As a mainstream approach for temperature compensation, a thin-film layer made of a material with a TCF of opposite magnitude is added to the resonator's material stack.

Proper selection and dimensioning of the compensation-film material reduce the overall TCF of the device, to values even as low as 1–5 ppm/°C. Vanhelmont et al. [8] proposed a temperature-compensated FBAR (TCFBAR) for RF oscillator applications, by a SiO_2 layer deposited on top of the AlN layer, which is shown in

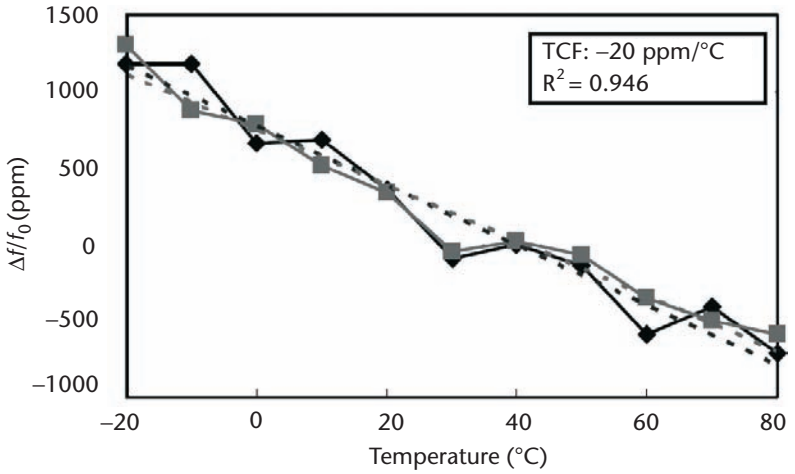

Figure 6.6 Thermal characterization of the FBAR process.

Figure 6.7(a). With this compensation, the resonator achieves thermal-coefficients as low as –5 ppm/°C. Alternative embodiments of the TCFBAR implement the thermal-compensation layer on top of the top metal electrode of the resonator, as shown in Figure 6.7(b) [9].

6.2.1 TCFBAR Fabrication Processes

The TCF compensation techniques rely mainly on modifying the thermal configuration of the resonator, as commented earlier. The fabrication process of a TCFBAR introduces additional steps concerning the deposition and patterning of a TCF-compensating layer on top of the AlN layer or in another place of the resonator's stack. This layer can be made, for example, of SiO_2, and its deposition can be done by plasma-enhanced chemical vapor deposition (PECVD) or thermal growing. The PECVD-oxide exhibits a positive TCF that compensates the negative TCF of the AlN layer. One simplification of the design process allows choosing the photolithography layer of the PECVD-oxide to be the same as for the AlN layer (thus saving a mask).

In considering such a TCFBAR fabrication process, let's study the TCF compensation with an example in which we have three wafers with FBAR devices. Two of

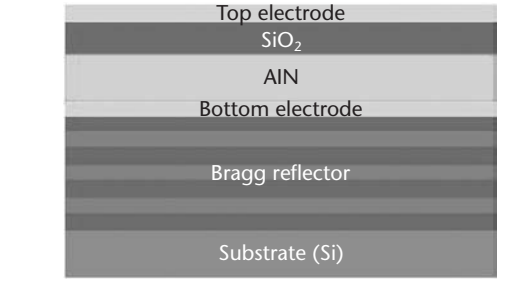

(a)

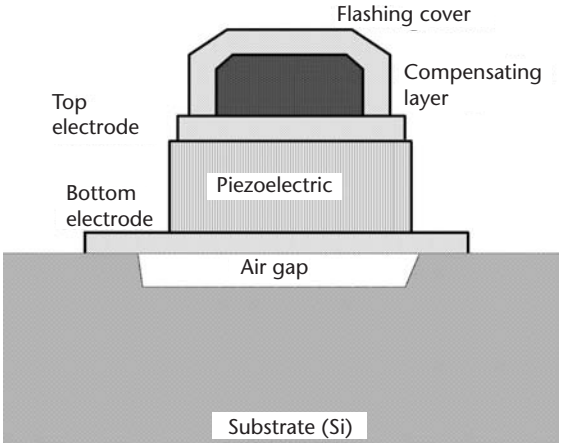

(b)

Figure 6.7 Temperature-compensated FBAR process alternatives: (a) a compensation layer of silicon oxide is deposited on top of the AlN layer (© 2006 IEEE [8]); and (b) the compensation layer is deposited on top of the second metal electrode of the FBAR (*From:* © 2005 J. D. Larson [9]).

them have chips with a SiO_2 compensation layer and the third one, without it. The two wafers containing the TCFBAR devices have the TE/SiO_2/AlN/BE layered structure, where TE and BE stand for the top and bottom electrodes, respectively. Each wafer has the same configuration for the TE (180 nm), BE (180 nm), AlN (700 nm) layers, although they differ in the thickness of the SiO_2 layer. The first wafer has a 50-nm-thick SiO_2 layer, whereas the second one's layer has a thickness of 300 nm. The third, noncompensated wafer serves as a reference of the technology's TCF.

Thermal characterization of the three wafers is performed to extract their TCFs. Thus, we introduce the wafers in the probe station and close the chamber to modify the temperature between –20°C and +80°C. Then, we measure the S-parameters of each device and we store resulting data for postprocessing, according to the procedures described in Section 6.1.4. Measurements are done in the temperature range of –20°C to +80 °C, with steps of 10°C among them. Figure 6.8 shows thermal characterization results.

As can be seen, the compensation-oxide layer has the effect of changing the TCF of the resonator. According to these results, the oxide layer should have a thickness between 50 and 300 nm in order to achieve a TCF value near to 0 ppm/°C. This example shows how the SiO_2 layer mitigates the negative TCF of the AlN layer. Different thicknesses of the SiO_2 layer evidence a compensation trend. In this way, the target TCF value should be designed using both experimental and modeling tools, regarding the specific fabrication process.

6.2.2 Behavioral Description and Modeling of a TCFBAR

A behavioral model is a mathematical tool that helps predict the response of a component as a function of a group of variables. In parallel to experimental characterization, the behavioral modeling of TCFBARs describes the temperature-dependent performance of the resonator. To accomplish this task, we create a mathematical model relating process, equivalent circuit, and temperature variables. Assuming linear temperature dependence of the resonance frequency, the frequency-shift relationship can be described by:

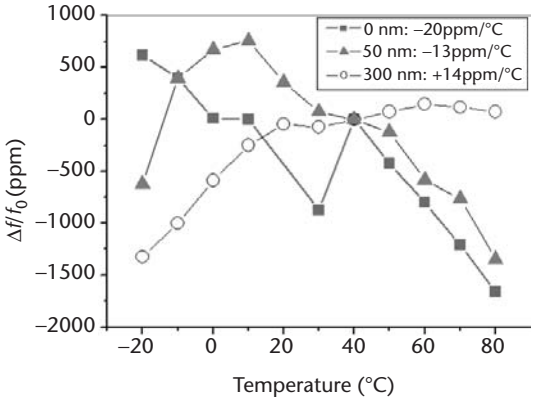

Figure 6.8 Thermal characterization of TCFBARs: the positive-TCF value of the SiO_2 layer has the effect of compensating the negative TCF of the AlN layer.

$$f_0^{Ti} = f_0^{ref}\left(1 - TCF \times \left(T_{ref} - T_i\right)\right) \tag{6.2}$$

where f_0^{Ti} is the resonance frequency at the temperature T_i, and f_0^{ref} is the resonance frequency at the reference temperature T_{ref}. Previously, we studied the equivalent-circuit equation for the resonance frequency of a crystal resonator, which is given by:

$$f_0 = \frac{1}{2\pi\sqrt{L_m C_m}} \tag{6.3}$$

Assuming that either the motional inductance L_m or motional capacitance C_m can be used to describe the linear TCF of the FBAR, a high-level behavioral model of the TCFBAR can be built. For example, the L_m described by:

$$L_m^{Ti} = \frac{L_m^{ref}}{\left(1 - TCF \times \left(T_{ref} - T_i\right)\right)^2} \tag{6.4}$$

where L_m^{Ti} is the L_m value at temperature T_i, and L_m^{ref} is the L_m value at the reference temperature T_{ref}. Replacing L_m^{Ti} in (6.4) with L_m in (6.3) describes the high-level linear behavior of f_0. Figure 6.9(a) depicts a schema of the equivalent-circuit model of the FBAR with the behavioral model of L_m within the Cadence design environment. The plot of Figure 6.9(b) shows the frequency shift-to-temperature curve of a 2.3-GHz FBAR. A TCF of –25 ppm/°C and a reference temperature $T_{ref} = 40$°C were set up in the model.

This model can be used for system-level and circuit design purposes. Once the temperature dependence of the TCFBAR with a specified thermal coefficient is described, the TCFBAR model can be integrated in a circuit-design environment and implemented by using commercial CAD tools, like Verilog-A descriptors and Cadence design suite.

6.3 Frequency Tuning

Due to process deviations or modification of the electromechanical properties of the materials used for FBAR fabrication, its target resonance frequency may be slightly different from that originally designed. For these reasons, several tuning procedures have been incorporated in the FBAR and MEMS manufacturing processes. This subject has become a requirement for industrial production and repeatability of the frequency response. Some of these procedures implement postfabrication techniques for changing the resonance frequency, whereas others are intended for tuning of the device during its operation.

For example, an electrostatic-tunable FBAR is presented in [10]. Taking advantage of a similar principle, it has been demonstrated that the electrical properties of its composing materials can be changed by applying an electric field, thus modifying the resonance frequency [11]. Indeed, some applications using this approach have been patented for the integration of acoustically active materials or devices, as well

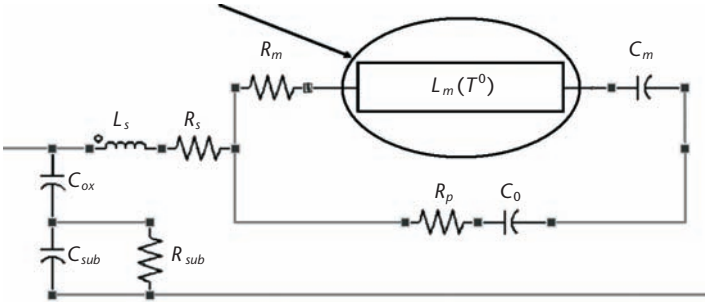

(a)

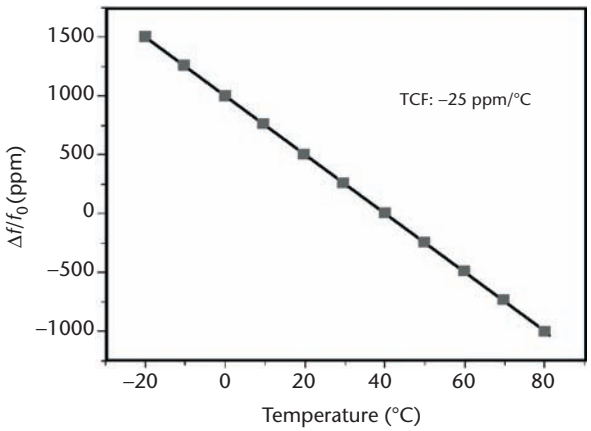

(b)

Figure 6.9 Behavioral description of FBAR: (a) equivalent-circuit model of the FBAR with Verilog model of L_m (in the box); and (b) frequency-to-temperature curve for a 2.3-GHz FBAR with TCF equal to –25 ppm/°C and reference temperature T_{ref} = 40°C.

[12, 13]. Frequency adjustment of microelectromechanical cantilevers by using electrostatic pull down has also been explored in [14]. This approach could be especially useful in piezoelectric-based resonators (in FBAR, for example, induced strain may change the resonance frequency). Also, an electrostatic mechanism to tune upward and downward the resonance frequency of nanomechanical resonators was demonstrated in [15]. Even more, the impedances of piezoelectric resonators exposed to moderate magnetic fields have been efficiently tuned in their resonance windows [16]. The setup and characterization results of a basic electrostatic-tuning procedure are discussed in Section 6.3.1.

On the other hand, postfabrication techniques have had a remarkable impact on industrial implementations for mass production. For example, FBAR tuning based on the mass-loading principle has attracted the attention of many research groups, mainly oriented to depositing a metal or isolating layer on top of the FBAR stack [17, 18]. In this line of research, recent investigations have shown how the electrical performance of FBAR boosts up when covered with carbon nanotubes, too [19]. The mass loading is performed by growing or depositing a thin film on one of the electrodes of the resonator. The mass loading affects the FBAR's frequency response, changing its resonance frequency $f_0 = v_0/2t_0$, where v_0 and t_0 are the sound

velocity and the thickness of the unloaded resonator, respectively. The added mass changes the phase condition of the acoustic wave propagating through the bulk of the acoustic layer due to impedance modification. The effect is down shifting of the resonance frequency value [20, 21]. The mass loading in FBAR is carried out by covering the whole surface of one of the electrodes with a uniform thin film. The thin film is deposited by physical vapor deposition (PVD) or grown by chemical vapor deposition (CVD) techniques. In Section 6.3.2 the uniform-film-based mass loading of FBARs is described.

New techniques have also demonstrated their suitability for the tuning of micro- and nanosized devices. Thus, the tools implemented in the process are able to perform postfabrication, localized mass loading of MEMS resonators. For example, Chiao et al. present in [22] a postpackaging tuning process for microresonators by pulsed laser deposition (PLD). By adding materials on the surface of the structure, the desired resonant frequency could be achieved. In the past few years, focused-ion-beam (FIB) has become a powerful tool for the postfabrication of a wide variety of MEMS devices. Subtractive or additive implementations of FIB techniques have enabled the fabrication of three-dimensional structures on a micrometer scale [23–25]. In another example of an elegant FIB application, the milling of optical waveguide MEMS is performed for both characterization and postfabrication tool of a cantilever sensor [26]. Also, the fabrication process of metal-oxide nanowires showing gas sensing capabilities being contacted by a dual-beam FIB machine is revealed in [27]. In Section 6.3.3, we introduce a FIB-based technique for tuning of FBARs.

6.3.1 DC Tuning

The resonance frequency of FBARs can be controlled by changing the electrostatic configuration of the device. By applying a DC-bias voltage to a third electrode of the FBAR, its resonance frequency can be tuned, because the static capacitance formed by the FBAR is modified when the DC voltage is applied to the new electrode [10]. A different two-electrode biasing approach has been demonstrated so far. In this case, the DC and AC voltages are applied to the same FBAR's electrode, thus injecting both signals to one of the electrodes. With the aid of a bias tee or similar DC coupling system, both the DC and AC voltages are superposed with no need for additional signal lines.

According to this strategy, the measurement setup for DC tuning is depicted in Figure 6.10 where the circuit representation, and the physical interconnection of the FBAR to the network analyzer, the DC-power supply, the bias-tee, and the probe station are shown. As for the AC excitation–only setup, appropriate calibration standards and routines have to be initiated in order to compensate for the effects of the layout-defined transmission line and probing system, keeping the matching impedance of the network analyzer's ports to 50Ω.

Using that setup, let's say that we apply a DC voltage between 0 and 30 VDC to the first electrode of an FBAR. As we observe in the curves of Figure 6.11(a), the magnitude of the S11 parameter changes in a linear way and shifts down the resonance frequency to a maximum value of 3 MHz. This leads to a DC-tuning sensitivity of around 100 kHz/VDC, which is about half the sensitivity obtained with the

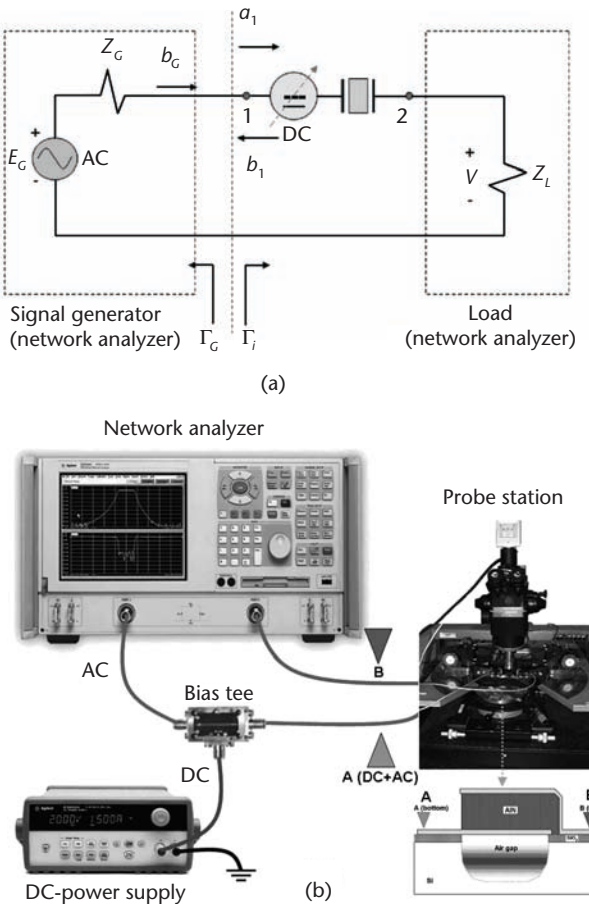

Figure 6.10 Measurement setup for DC tuning using a single electrode for DC+AC voltage supply: (a) circuit representation and (b) physical connection of the FBAR to the instrumentation and the probe station.

three-electrode tunable FBAR of [10]. Those FBARs, at a resonance frequency of 6.8 GHz, need actuation voltages between 0 to 9 VDC to get a tuning range of 1.9 MHz, thus achieving a tuning sensitivity of 211 kHz/V. Nevertheless, the FBARs of the second example exhibit an expanded tuning range with high linearity, as illustrated in the plot of Figure 6.11(b). Due to its simplicity, this method is demonstrated to be suitable for fine tuning in certain RF applications.

6.3.2 Uniform-Film Deposition

Uniform-film deposition is a well-known postfabrication method to change the resonance frequency to lower values by taking advantage of the mass loading principle of the electrode. The mass loading–based tuning performance of microelectromechanical resonators may be described by one or more metrics, though the mass responsivity is the main parameter being considered. The inverse mass-responsivity R^M is defined as the number of grams deposited on the device needed to produce a change of 1 Hz in its resonance frequency.

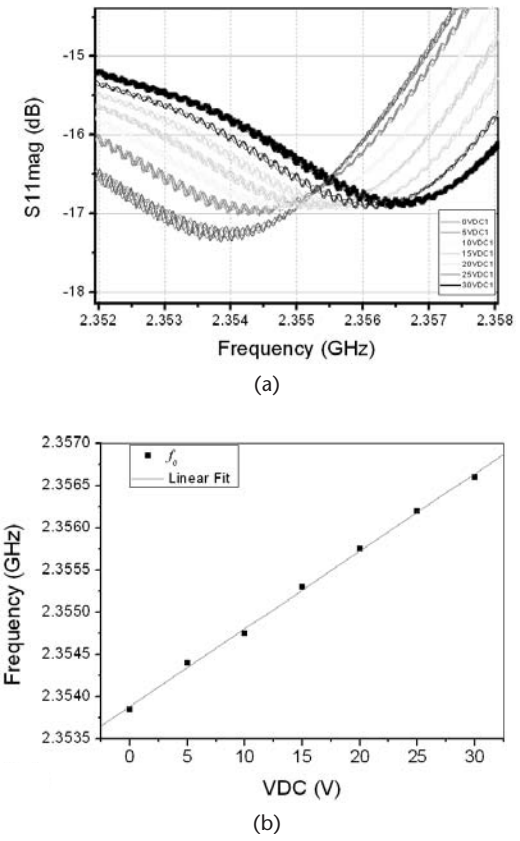

Figure 6.11 DC tuning in FBARs: (a) magnitude of the S11 parameter for different DC-tuning voltages; and (b) frequency shifting against DC-tuning voltage (tuning sensitivity of 100 kHz/VDC).

Uniform-film deposition can be performed by physical vapor deposition (PVD), chemical vapor deposition (CVD), or thermal-growing techniques. In this way, either a metallic or nonmetallic thin film is deposited all over one of the electrodes of the resonator. This method is suitable for tuning of a wide variety of resonators, from MEMS to FBAR, and many implementation examples are available in the literature [11–13].

Magnesium fluoride (MgF_2) is a dielectric material that can be used to demonstrate the uniform-film–based mass-loading concept. If we use PVD to deposit MgF_2 on the surface, we will experiment the down-shifting of the resonance frequency. For instance, if we have a rectangular FBAR with electrode dimensions of 50×70 μm^2, and we deposit MgF_2 with thicknesses between 2 and 20 nm, we obtain the highly linear down-shift of the resonance frequency shown in the curves of Figure 6.12. The responsivity achieved with this method is of 1.4×10^{-17} g/Hz. Since the PVD process is not easily controllable for thin-film deposition under 1 nm, it is hard to accomplish mass loading to a lower value, given a certain electrode area. However, if we reduce the size of the deposited mass, improved sensitivity may be obtained, as we study in the next section.

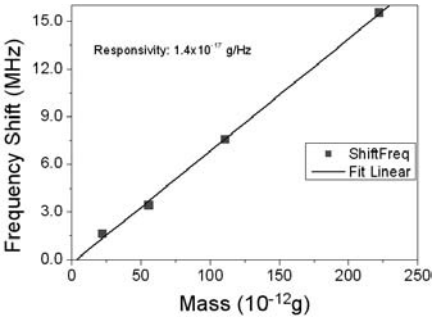

Figure 6.12 Uniform-film deposition: frequency shifting of the resonance frequency against the amount of an MgF_2 thin film deposited on top of FBARs.

6.3.3 FIB-Assisted Tuning Technique

6.3.3.1 Ion-Assisted Chemical Vapor Deposition

So far, we have discussed the uniform-film, mass-loading approach to frequency tuning of resonators. We previously stated that the electrode size and the thin-film deposition techniques limit the responsivity of the method. However, new localized-mass-deposition techniques may improve the tuning performance of micro- and nanoresonators. In this section, we study FIB deposition and effects on FBARs, although it is suitable for silicon nanocantilevers, nanobridges, and other MEMS and NEMS resonator geometries. This tuning technique has been developed and extensively demonstrated by our group at the IMB-CNM (CSIC) [2].

First, we define the expression *localized-mass deposition*, which is the deposition of a material whose size is small, in comparison to the effective resonator's or electrode's area (typically, the mass area is a fraction of less than the 10% of the electrode's area). Localized-mass deposition can be performed using machines with nanopatterning capabilities like FIB.

To perform the deposition, a precursor material containing Pt, for example, is injected close to the resonator in the sample's chamber of the FIB machine and decomposed by the ion beam. Gallium ion beams (Ga+) are accelerated at kV, which gives them enough energy to promote the decomposition of the precursor gas crossing their path. The technique is also known as ion-assisted chemical vapor deposition (IACVD). If we properly adjust the dwell time of the ion beam, positioning, and current density, the amorphous compound resulting from the precursor decomposition is locally deposited on the area scanned by the beam. According to Auger Electron Spectroscopy measurements and the precursor materials, this compound may contain C, Pt, and Ga [28]. Its mass density can be estimated in proportion to these materials [personal communication with H. Mulders, FEI Company, 2006]. Depending on the desired size and thickness of the deposited mass, the ion current and deposition time need to be adjusted. The schematic diagram of Figure 6.13 represents the mass deposition procedure: the Pt injector introduces the metalorganic precursor inside the vacuum chamber, while the same is decomposed by the Ga+ ion-beam scanning the resonator's electrode area. The result is a mass deposited on the top electrode of the cantilever, illustrated in this figure as a square spot. In addition, the electron beam of the dual beam machines is used for imaging and calibration purposes without structural damaging of the sample.

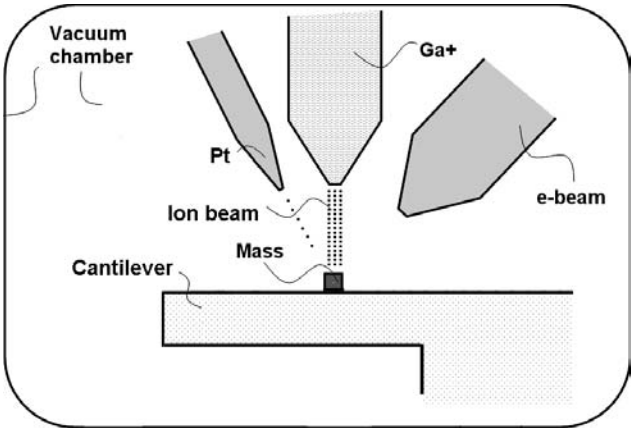

Figure 6.13 FIB-based tuning setup and procedure: the Pt injector introduces the metalorganic precursor inside the vacuum chamber, whereas the same is decomposed by the Ga+ ion-beam scanning the cantilever's area.

The FIB-assisted tuning technique is very versatile and allows a wide variety of geometries and types of resonators' configurations being tuned. The SEM images of Figure 6.14(a, b) were obtained inside the dual-beam FIB-SEM machine and show a mass deposited on the center of the top electrode of an FBAR. The mass has a contact surface of $1.5\,\mu\text{m} \times 1.5\,\mu\text{m}$, while the FBAR electrode's area was of $50\,\mu\text{m} \times 50\,\mu\text{m}$. The tilting angle of the electron beam is 52°, so dimensioning of patterns at the vertical scale has to be compensated for accurate calculations.

The SEM images of Figure 6.15(a–c) show examples of other FBAR geometries in which localized tuning of the resonance frequency was performed. FBARs with a rhomboidal shape [Figure 6.15(a)], a cantilever [Figure 6.15(b)], and a piezoelectric bar [Figure 6.15(c)] illustrate different layout configurations with their corresponding tuning load deposited on the top electrode. Since the location and size of tuning loads give valuable information about the tuning performance, calibration and adjustment of the setup need to be performed prior to deposition on target FBAR devices.

Some undesired effects, like charging of the sample's surface, may occur during deposition, thus causing the ion beam to be shifted away from the desired location.

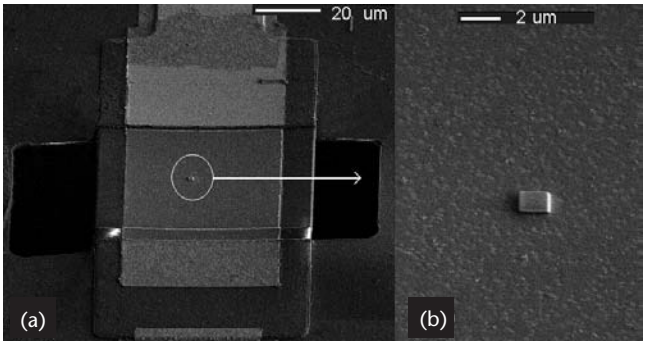

Figure 6.14 FIB-based deposition of a C/Pt/Ga composite on top of FBAR (SEM images): (a) general view; and (b) detailed view of the deposited spot. (© 2007 IOP Publishing Ltd. [2].)

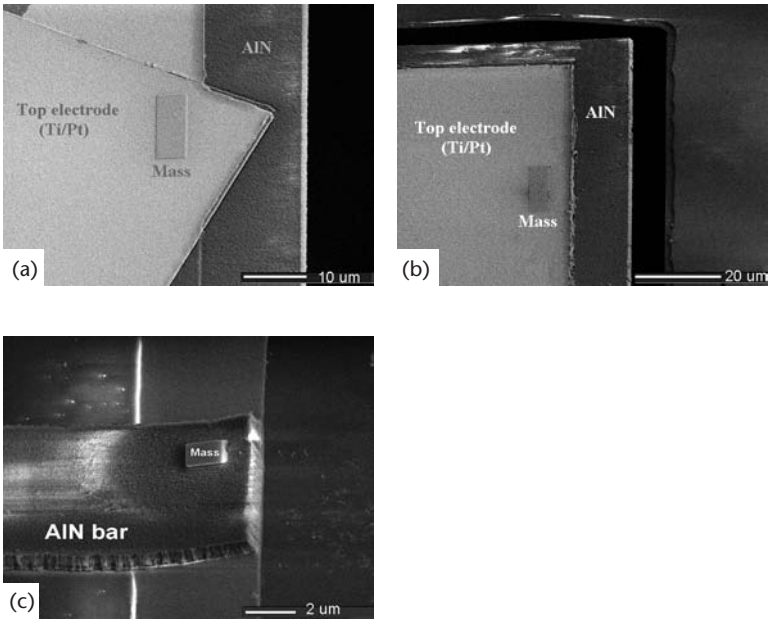

Figure 6.15 Examples of other FBAR geometries in which tuning of the resonance frequency was performed: (a) rhomboidal-shaped; (b) cantilever; and (c) piezoelectric bar. (© 2007 IOP Publishing Ltd. [2].)

Although not significantly for small-sized mass deposited on big electrode resonators, it could cause the tuning load to be deposited out of the surface of narrower devices like cantilevers. In this way, a calibration procedure helps the improvement of the deposition accuracy. Calibration is also important for analyzing the performance of the frequency tuning. Two aspects mainly influence this performance:

1. The size of the deposited mass;
2. Collateral effects of the ion beam in the sample's surface like residual etching or deposition in the surroundings of the target area (this could happen due to inappropriate selection of the ion-current or scanning conditions).

In this way, the calibration has to ensure the appropriate size and thickness of the mass and, at the same time, minimum damage to the resonator when irradiated by the ion beam (we will return later to this point). Also, efficiency is important in IACVD, because a certain deposition goal can be achieved with lower or higher current densities. This will depend on the scanning area and will affect the deposition (or milling) time.

6.3.4 Milling of FBAR as Another FIB-Tuning Procedure

At this point, we have discussed a localized-mass-deposition–based tuning procedure of resonators. However, under certain ion-beam setup conditions, milling (etching) of the device structure can be performed, thus *deloading* the resonator. This can happen for current densities of the ion beam above about pA/îm^2, but other considerations, such as scanning speed, also influences the process. While the reso-

nance frequency may be down-shifted by the mass-loading procedure, with the *mass deloading* this frequency is expected to be up-shifted. Since the localized etching modifies the structure of the device, we can suppose a change of the mode-shaping of the resonance, too. Thus, it is important to understand the interaction between deloading, frequency tuning, and resonance's mode shaping. The SEM image of Figure 6.16 shows a region of a deloaded FBAR, in which the Ti/Pt top electrode has been locally milled by the ion beam. In this image, the underlying AlN layer is observed in the milled area.

Based on the same principle, we can change the shape of the resonance modes of the device by transversal milling of the structure. To illustrate this concept, let's look at the rectangular FBAR shown in the SEM image of Figure 6.17. Suppression of the spurious modes was achieved by transversal cuts of the layered FBAR structure, as observed in the image. Electrical characterization of the magnitude of the S21 parameter, before and after milling, demonstrates how rippling and some resonance modes are no longer visible after the FIB processing [curves of Figure 6.17(b)]. Looking at the curves, the new resonance shape coincides with the shape and frequency of smaller modes observed in the nonmilled device. Before the milling, these modes were superposed to the main resonance and other small spurious modes. Now, they can be enhanced due to the ion-beam processing. Of course, systematic engineering of the mode shape requires finite element analysis, but the presented examples illustrate the potential of this tool for mode shaping.

6.3.5 Frequency-Tuning Sensitivity and Responsivity

At this point, we wonder whether or not the FIB-based tuning has a better tuning performance in comparison to uniform-film deposition. As long as IACVD is a complex process, the answer will depend on several deposition parameters and on the configuration of the deposited mass. Nevertheless, one example of FIB-deposited FBARs illustrates the advantages of this tuning method. Let's say that we perform localized-mass deposition on the geometric center of the top electrode of a group of rectangular resonators with electrode area of $50 \times 70\ \mu m^2$. The squared-shaped localized masses had a size of $1.5 \times 1.5\ \mu m^2$ and different thicknesses to change the amount of mass; in the range of 9.0×10^{-15}g to 3.6×10^{-12}g. The frequency shift against the amount of deposited mass is shown in the plot of Figure 6.18 (the x-axis

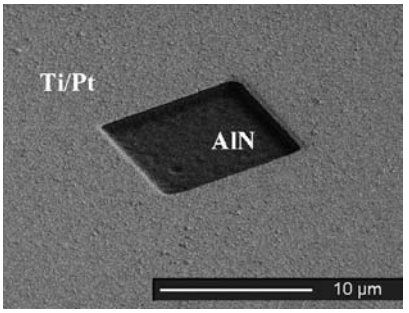

Figure 6.16 Illustration of the milling-based deloading concept: ion-assisted etching locally removes the Ti/Pt top electrode of FBAR (the square-shaped etching allows observation of the AlN layer). (© 2007 IOP Publishing Ltd. [2].)

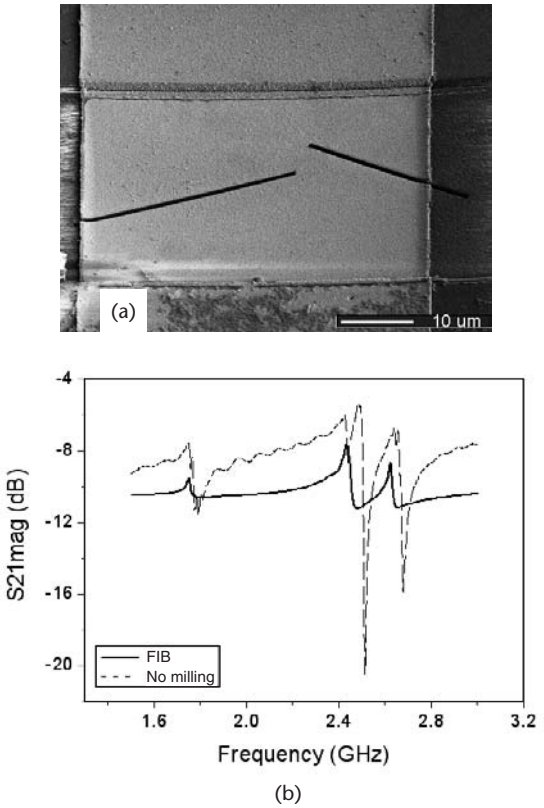

Figure 6.17 FIB-based engineering of mode shaping in FBAR: (a) SEM image of FBAR with transversal cuttings (intended for suppression of spurious modes); and (b) magnitude of the S21 transmission parameter, before (dotted line) and after (continuous line) FIB-assisted milling (ripple and some spurious modes disappeared for the after-FIB case). (© 2007 IOP Publishing Ltd. [2].)

is represented in log-scale, due to the wide range of deposited masses). Regarding these results, the responsivity may be calculated, its average value being 7.4×10^{-19} g/Hz. This value is competitive with respect to other NEMS technologies previously reported [29–31].

The curves also show the extrapolated linear fit of the uniform-film deposition case. Thus, we can see how the localized-mass deposition exhibits better responsivity in comparison to the uniform-film case. In this way, the extrapolated curve shows that the improvement is between one and three orders of magnitude for the ion-beam-tuning procedure. However, as we have also seen in the curves, this happens for low-mass depositions. Above the crossing value of the curves, uniform-film deposition would be more efficient to resonator's tuning.

6.3.6 Quality Factor

The quality (Q) factor of the resonator mainly determines its mass sensitivity, since it is related with a minimum change of frequency. In this sense, the Q factor is an important issue to be considered in mass-loading-based tuning of resonators. During deposition, however, the ion beam might induce heat damages in the resonator's

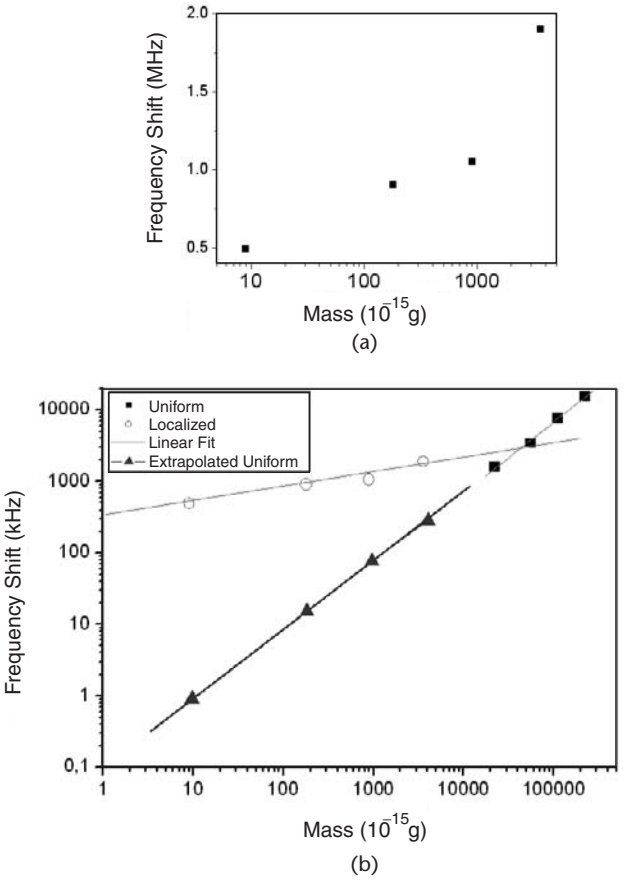

Figure 6.18 Frequency shift of the resonance frequency against the amount of tuning load: (a) detailed sensitivity plot; and (b) FIB-tuning performance in comparison to uniform-film deposition. (© 2007 IOP Publishing Ltd. [2].)

structure, due to possible heating of the materials, thus reducing its Q factor. Some practical experiments may help us know the effects of ion-beam radiation. Starting from ion-beam–based imaging of a test resonator, the electrical response can be evaluated before and after ion-beam irradiation.

To do that, we can take one or more resonators and extract the Q factor by evaluating their S-parameter responses. Next, the resonators are irradiated with the ion beam to perform imaging or very-small mass deposition (in order to not significantly change the resonance frequency). Again, we characterize the S-parameters and the Q factors to see if some change in the electrical response arises. The plot of Figure 6.19 compares the magnitudes of the S21 parameter before and after ion-beam imaging practiced on a sample FBAR. The S parameters and the Q factor remained at a constant value of about 500 in both cases.

Some explanations can explain these results. First, not enough heating of the structure occurs to modify the piezoelectric properties of the AlN. Also related to this idea, the longitudinal resonance mode and the reduced size of the mass—compared to the FBAR—inhibits to a great extent the mass-related damping. As a difference to flexural MEMS resonators, FBAR works in longitudinal resonance modes.

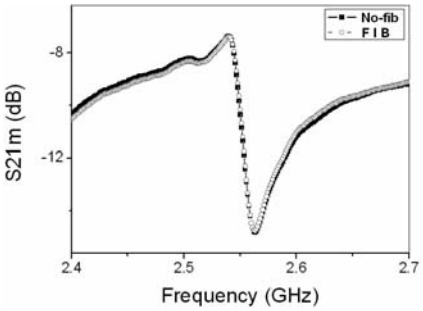

Figure 6.19 S21 magnitude of FBAR before and after i-beam operation (no mass deposition, only i-beam imaging). No significant change of the response is observed. (© 2007 IOP Publishing Ltd. [2].)

In low-frequency mechanical resonance modes, as with the case of vibrating cantilevers, the electromechanical damping of deposited masses strongly reduces the Q factor [32].

Another aspect is that the mass is deposited on top of the Pt layer of the FBAR, and no interaction occurs between the ion beam and the AlN, due to the Pt shielding. In this case, the AlN quality mainly determines the Q factor of the FBAR.

6.4 Summary

In this chapter, we have learned about different resonator optimization techniques. First, we have reviewed the main issues degrading the expected performance of resonators. We have studied how process deviations change the thickness of the structural layer, which affects the resonance frequency. Also, thermal noise sources may affect the short- and long-term frequency stability. The thermal coefficient factor (TCF) of the structural layers of the resonator is another important issue determining the stability, which has importance in oscillator applications, for example.

Different resonator optimization techniques have been explored. First, we described a process-based temperature compensation method. To start, we evaluated the TCF of FBAR. With this information, the temperature-compensation strategy was implemented by modifying the fabrication process with an additional thermal-compensation layer. We studied different examples of TCFBARs with reduced TCF and compared their performance with noncompensated FBARs.

On the other hand, we have made a review on various state-of-the-art frequency-tuning techniques. Beginning with electrostatic tuning of the resonance frequency, we studied the uniform-film deposition technique, too. However, we have taken significant space to explain the leading-edge FIB-assisted tuning technique, its advantages and its possibilities. Different ion-beam-tuning procedures, including IACVD and milling of resonators, were described. Also, we have performed benchmarking of the ion-beam and uniform-film tuning techniques, finding out that the FIB-based procedure offers improved responsivity under small-mass-deposition conditions, which are very useful for fine tuning of sensitive devices, like FBARs. Improved responsivities of at least one and two orders of magnitude were achieved with this method. The possible influence of ion-beam irradiation in the physical

structure and electrical response of the resonators was also analyzed. We conclude that it depends on the type of resonator and on the resonance mode. For example, no significant variation in the Q factor or the S parameters of FBARs was observed, whereas low-frequency cantilevers suffer from significant damping and Q-factor reduction.

References

[1] Andersen, B. D., and N. A. Belkerdid, "Measurement Sensitivity Analysis of One Port BAW Resonators," *Proc. 50th IEEE International Frequency Control Symposium 1996*, Honolulu, HI, June 5–7, 1996, pp. 357–362.

[2] Campanella, H., et al., "Focused-Ion-Beam-Assisted Tuning of Thin-Film Bulk Acoustic Wave Resonators (FBAR)," *J. Micromech. Microeng.*, Vol. 17, 2007, pp. 2380–2389.

[3] Rosén, D., J. Bjursttröm, and I. Katardjiev, "Suppression of Spurious Lateral Modes in Thickness-Excited FBAR Resonators," *IEEE Trans. on Ultrason. Ferroelectr. Freq. Control*, Vol. 52, 2005, pp. 1189–1192.

[4] Su, Q., et al., "Thin-Film Bulk Acoustic Resonators and Filters Using ZnO and Lead-Zirconium-Titanate Thin Films," *IEEE Trans. on Microw. Theory Tech.*, Vol. 49, 2001, pp. 769–778.

[5] Kim, Y. D., et al., "Highly Miniaturized RF Bandpass Filter Based on Thin-Film Bulk Acoustic-Wave Resonator for 5-GHz-Band Application," *IEEE Trans. on Microw. Theory Tech.*, Vol. 54, 2006, pp. 1218–1228.

[6] Kaitila, J., et al., "Spurious Resonance Free Bulk Acoustic Wave Resonators," *Proc. IEEE Intl. Ultrason. Symp. 2003*, Honolulu, HI, October 5–8, 2003, pp. 84–87.

[7] Gribaldo, S., et al., "Experimental Study of Phase Noise in FBAR Resonators," *IEEE Trans. on Ultrasonics, Ferroelectrics, Freq. Control*, Vol. 53, 2006, pp. 1982–1986.

[8] Vanhelmont, F., et al., "A 2GHz Reference Oscillator Incorporating a Temperature Compensated BAW Resonator," *Proc. IEEE Intl. Ultrason. Symp. 2006*, Vancouver, BC, October 3–6, 2006, pp. 333–336.

[9] Larson III, J. D., "Method of Making an Acoustic Wave Resonator," U.S. Patent 6,874,212, April 2005.

[10] Pan, W., et al., "A Surface Micromachined Electrostatically Tunable Film Bulk Acoustic Resonator," *Sens. Actuator A-Phys.*, Vol. 126, 2006, pp. 436–446.

[11] Lancaster, M. J., J. Powell, and A. Porch, "Thin-Film Ferroelectric Microwave Devices," *Supercond. Sci. Technol.*, Vol. 11, 1998, pp. 1323–1334.

[12] Ella, J., "Device Incorporating a Tunable Thin Film Bulk Acoustic Resonator for Performing Amplitude and Phase Modulation," U.S. Patent 5714917, 1998.

[13] Korden, C., T. Ostertag, and W. Ruile "Component Having an Acoustically Active Material for Tuning During Operation," U.S. Patent 6847271, 2005.

[14] Kafumbe, S. M. M., J. S. Burdess, and A. J. Harris, "Frequency Adjustment of Microelectromechanical Cantilevers Using Electrostatic Pull Down," *J. Micromech. Microeng.*, Vol. 15, 2005, pp. 1033–1039.

[15] Kozinsky, I., et al., "Tuning Nonlinearity, Dynamic Range, and Frequency of Nanomechanical Resonators," *Appl. Phys. Lett.*, Vol. 88, 2006, 253101.

[16] Maglione, M., W. Zhu, and Z. H. Wang, "Evidence of a Strong Magnetic Effect on the Impedance of Integrated Piezoelectric Resonators," *Appl. Phys. Lett.*, Vol. 87, 2005, 092904.

[17] Ruby, R. C., and P. P. Merchant, "Tunable Thin Film Acoustic Resonators and Method for Making the Same," U.S. Patent 5587620, December 24, 1996.

[18] Ylilammi, M. A., "Method for Performing On-Wafer Tuning of Thin Film Bulk Acoustic Wave Resonators (FBARS)," U.S. Patent 6051907, April 18, 2000.

[19] Dragoman, M., et al., "High Performance Thin Film Bulk Acoustic Resonator Covered with Carbon Nanotubes," *Appl. Phys. Lett.*, Vol. 89, 2006, 143122.

[20] Sauerbrey, G. Z., "Verwendung von Schwingquarzen zur Wägung dünner Schichten und Microwägung," *Z. Phys.*, Vol. 155, 1959, pp. 206–222.

[21] Lostis, P., "Etude, realisation et contrôle de lames minces introduisant une difference de marche déterminée entre deux vibrations rectangulaires, Part 2: Nouvelle methôde de controle de l'epaisseur pendant l'évaporation," *Rev. Opt., Theor. Instrum.*, Vol. 38, 1959, pp. 1–28.

[22] Chiao, M., and L. Lin "Post-Packaging Frequency Tuning of Microresonators by Pulsed Laser Deposition," *J. Micromech. Microeng.*, Vol. 14, 2004, pp. 1742–1747.

[23] Fujii, T., et al., "A Nanofactory by Focused Ion Beam," *J. Micromech. Microeng.*, Vol. 15, 2005, pp. S286–S291.

[24] Reyntjens, S., and R. Puers, "Focused Ion Beam Induced Deposition: Fabrication of Three-Dimensional Microstructures and Young's Modulus of the Deposited Material," *J. Micromech. Microeng.*, Vol. 10, 2000, pp. 181–188.

[25] Reyntjens, S., and R. Puers, "A Review of Focused Ion Beam Applications in Microsystem Technology," *J. Micromech. Microeng.*, Vol. 11, 2001, pp. 287–300.

[26] Pruessner, M. W., et al., "End-Coupled Optical Waveguide MEMS Devices in the Indium Phosphide Material System," *J. Micromech. Microeng.*, Vol. 16, 2006, pp. 832–842.

[27] Hernández-Ramírez, F., et al., "Fabrication and Electrical Characterization of Circuits Based on Individual Tin Oxide Nanowires," *Nanotechnol.*, Vol. 17, 2006, pp. 5577–5583.

[28] Vilà, A., et al., "Fabrication of Metallic Contacts to Nanometer-Sized Materials Using a Focused Ion Beam (FIB)," *Mater. Sci. Eng. C*, Vol. 26, 2006, pp. 1063–1066.

[29] Forsen, E., et al., "Ultrasensitive Mass Sensor Fully Integrated with Complementary Metal-Oxide-Semiconductor Circuitry," *Appl. Phys. Lett.*, Vol. 87, 2005, 043507.

[30] Ekinci, K. L., X. M. H. Huang, and M. L. Roukes, "Ultrasensitive Nanoelectromechanical Mass Detection," *Appl. Phys. Lett.*, Vol. 84, 2004, pp. 4469–4471.

[31] Ilic, B., et al., "Attogram Detection Using Nanoelectromechanical Oscillators," *J. of Appl. Phys.*, Vol. 95, 2004, pp. 3694–3703.

[32] Enderling, S., et al., "Characterization of Frequency Tuning Using Focused Ion Beam Platinum Deposition," *J. Micromech. Microeng.*, Vol. 17, 2007, pp. 213–219.

CHAPTER 7

Integration of Resonator to CMOS Technologies

Complementary-metal-oxide-semiconductor (CMOS) is, nowadays, the most popular integrated-circuit (IC) technology. Although other IC technologies—like bipolar, BiCMOS, or GaAs, for example—exhibit improved performance in specialized applications such as radio frequency (RF), the presence of CMOS in the IC market field has grown at a faster rate. Virtually all the industrial and consumer-oriented applications are built of low-cost, low-power electronics systems implementing CMOS circuits. Furthermore, the development of the system-on-chip (SoC) and system-on-a-package (SoP) concepts has contributed to increase the popularity of CMOS. More recently, the technological and application convergences between traditional IC technologies and the emerging nano-bio-info-cogno (NBIC) devices have boosted and motivated the integration of CMOS with other processes, materials, and devices, like FBARs, MEMS and NEMS resonators, SOI/CMOS mixed signal ASICs, microscale passive components, micropower systems, and biocompatible materials. Low cost, reduced size, and low power are the main requirements and promises of such convergence.

This chapter deals with the case of resonator-based, IC-integrated systems. Thus, the different approaches to integrate CMOS and resonator technologies are studied. First, we define the current-art integration strategies and technologies, including hybrid, monolithic, and the more recent heterogeneous integration. Then, we review leading-edge IC applications based on integrated MEMS, NEMS, FBAR, and SAW resonators. At this point, we pay our attention to the advanced 3D, heterogeneous integration with CMOS processes. The wafer-level-transfer integration of diverse micro- and nanotechnologies and target CMOS technologies are discussed. The chapter closes with a case study on the development and implementation of a wafer-level-transfer process for the heterogeneous integration of FBAR and CMOS technologies.

7.1 Integration Strategies

Over the past decades, CMOS has become the predominant fabrication technology for integrated circuits (IC). Research and development efforts have been made to continuously improve process yield and reliability, while minimal feature sizes and fabrication costs continue to decrease. Nowadays, the power of CMOS technology is exploited for ICs and also for a variety of microsensors and MEMS benefiting from well-established fabrication technologies and the availability of on-chip cir-

cuitry. Recently integrated microsystems featuring calibration by digital programming, self-testing, and digital interfaces have been implemented on a single chip, demonstrating the strength of CMOS-based MEMS [1].

SoC technologies integrate multiple function systems on a single silicon chip. This concept involves the double integration of processes and functions, and it promises increased capability, lower power consumption, and improved economy, in comparison to the multiple-chip technologies [2]. Whether technology constraints of the SoC definition arise at the time of implementation, the more general concept of SoP enables the integration of multiple systems fabricated within the same or different IC processes into a single-packaged chip, through advanced packaging technologies. With the contribution of MEMS technologies, the LoC and the micro total analysis systems (μTAS) are some of the application-level concepts developed from the SoC or SoP [3–5]. More and more, we see how MEMS and NEMS play a central role in the miniaturization of electronic SoC, LoC, and μTAS. In all these systems, CMOS is the transversal technology that supports the conditioning and signal processing functions, and it provides, in most of the cases, the physical substrate of the system.

Nevertheless, the engineering of integration and process compatibility of MEMS to CMOS-based IC technologies is a tricky and challenging task at both the technology and application levels. Several challenges, like manufacturing temperature, packaging, postprocessing of MEMS, integrity of CMOS, and reliability and modeling of the MEMS-to-CMOS interface, are just some of the considerations that can be mentioned [6–8]. Nowadays, hybrid and monolithic-integration are the mainstream strategies in CMOS-to-MEMS integration. The CMOS-to-NEMS and CMOS-to-FBAR integrations have been demonstrated as well. More recently, heterogeneous integration has become an important evolution of the hybrid strategy in CMOS integration. According to the way in which the CMOS and the MEMS substrates are processed and interconnected, each strategy is defined as follows.

7.1.1 Hybrid Integration

In hybrid integration, the MEMS or NEMS chip is fabricated on a different substrate within various technological processes involving micromachining of the device structure, and it is combined with a separate CMOS-processed IC chip. The integration of both processes is performed at the chip level by wire bonding or packaging techniques after fabrication of both the MEMS/NEMS and the CMOS chips. Thus, dicing is carried out prior to process integration [1].

The CMOS integration may be performed for read-out or functional purposes. For example, the temperature-compensated silicon I-shaped bulk acoustic resonator (IBAR) reference oscillator of Figure 7.1 connects the IBAR and the CMOS circuit through wire-bonding to close the oscillation loop [9]. The IBAR is an electrostatic micromechanical MEMS resonator whose current is amplified by the transimpedance amplifier incorporating a mixed bandgap PTAT temperature compensation stage. The IBAR is fabricated using the HARPSS-on-SOI process [10], and the CMOS circuit is a transimpedance amplifier with a self-biased folded-cascode operational transconductance amplifier (OTA) fabricated in a two-poly three-metal (2P3M) 0.5-μm CMOS process.

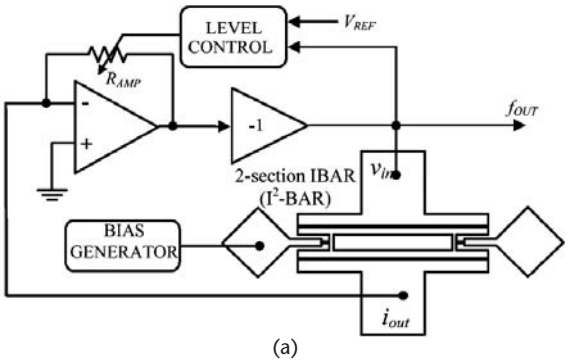

(a)

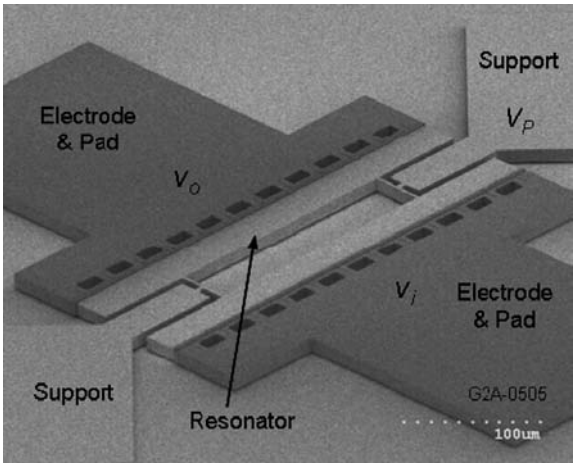

(b)

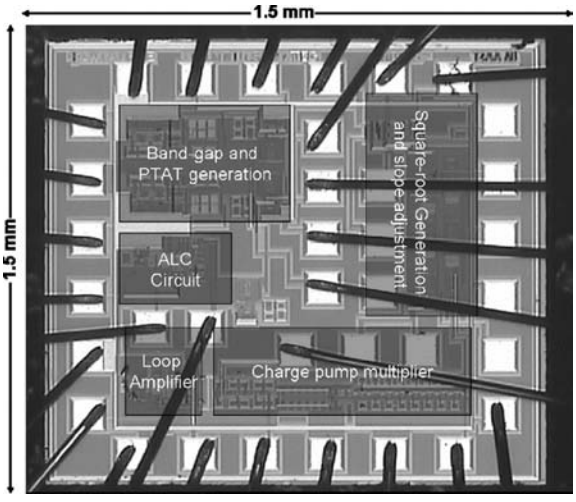

(c)

Figure 7.1 Temperature-compensated silicon I-shaped bulk acoustic resonator (IBAR) reference oscillator: (a) block diagram of the reference oscillator; (b) SEM picture of the IBAR; and (c) die picture of the interface IC. (© 2007 IEEE [9].)

Hybrid integration is the oldest and simplest way to integrate different technologies, because it does not concern on-process compatibility issues. Regarding such compatibility, it is fast because it avoids technological developments to harmonize the requirements of the processes to be integrated. The integration can be performed with commercial wire bonding or multichip-module (MCM) platforms, which are the cheapest option in most cases, instead of suffering the costs and engineering effort of technology development. On the other hand, hybrid integration is carried out in a one-by-one basis, which makes it slow for mass-production purposes. The diagrams of Figure 7.2 represent the process of hybrid integration when performed through wire bonding and stacked packaging. As long as wafers are diced to extract the chips, a pick and place system is needed to manipulate both the resonator and IC chips. As we can see, two technologies are available for carrying out the interconnection: wire bonding and packaging. While the MEMS die is placed onside of the IC chip in the case of the wire-bonded system, they are placed one above the other one when using the MCM packaging technology.

The wire-bonding system saves alignment effort but is area expensive. Also, the wires introduce parasitic reactive and resistive elements on the circuit, thus degrading the performance of the system, which is especially notorious for high-frequency applications. These parasitics must be considered to the equivalent-circuit model of

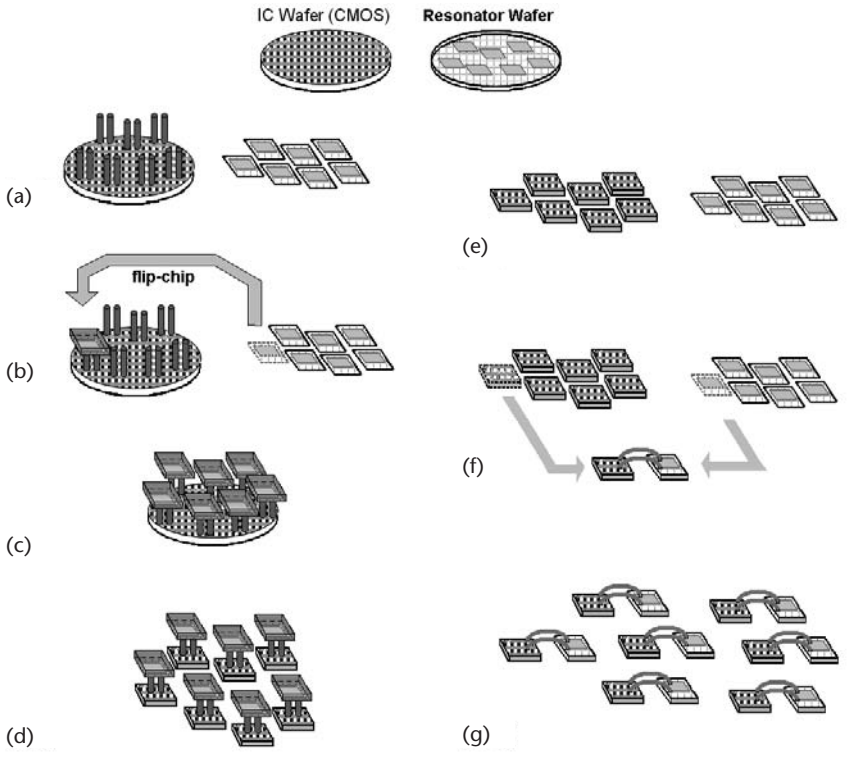

Figure 7.2 Process of hybrid integration: the MCM-based approach includes post deposition and resonator wafer dicing (a), flip-chip of the resonator die and connection to the IC wafer (b), full dice interconnection (c), and dicing of the IC wafer with the resonators (d). On the other hand, the wire-bonding–based hybridization involves dicing of both the resonator and the IC wafers (e), wire bonding of the first resonator-IC dice (f), and full dice interconnection (g).

the system to predict its response within reasonable margins. The packaging approach offers increased area efficiency and reduced parasitic effects, but it is more complex to implement, and requires careful alignment of the interconnection pads.

Hybrid integration is the most affordable option when, due to intrinsic features of the MEMS/NEMS technology, the CMOS line may be contaminated by the materials of the MEMS/NEMS process. The situation makes impossible the development of a compatibility protocol. Besides, MEMS/NEMS and CMOS manufacturers are often specialized, have dedicated resources, or simply lack the interest to disperse their expertise in exploring new processes or integration strategies. One explanation can be that they are busy enough continuously updating their own technology in order to remain competitive in the market place. For these manufacturers, hybrid integration offers a good tradeoff between functionality and cost.

7.1.2 Monolithic Integration

Monolithic integration appeared to overcome the limitations of hybrid technologies. According to this approach, the MEMS device and the IC are made and combined on a single substrate, according to the same standard, CMOS-compatible technology. The combination is performed using read-out circuitry to compensate for MEMS deficiencies or to provide the desired functionality. Depending on the order of fabrication, monolithic integration can be grouped into: (1) pre-CMOS (also known as *first-CMOS* or *before-CMOS*), (2) intermediate-CMOS (or *interdigitated fabrication*), and (3) post-CMOS (*add-on* or *after-CMOS*) [1].

In the pre-CMOS approach, the MEMS structures or part of them are formed before the regular CMOS process sequence. Necessarily, the MEMS/NEMS, as a movable device requiring micromachining, cannot be located under the IC layers so it must be placed at one side of the IC, which increases the die area. Remarkable examples of this approach are the embedded polysilicon microstructures (microengine) based on the iMEMS technology of Sandia National Laboratories shown in Figure 7.3 [11].

In the intermediate-CMOS approach, the CMOS process sequence is interrupted for additional thin-film deposition or micromachining steps. This approach is commonly exploited to implement surface micromachined polysilicon structures in CMOS technology. Either the standard gate polysilicon or an additional low-stress polysilicon layer is used as structural material. Examples of commercially available microsensors relying on intermediate process steps are the Infineon's pressure-sensor integrated circuits [12]. Figure 7.4 illustrates the side view of this process [13]. There, surface micromachining of a SiO_2 sacrificial layer is carried out to form the cavity of the polysilicon membrane. Hermetic sealing of the membrane is achieved when depositing subsequent layers of the CMOS process on the membrane.

In the post-CMOS approach, two general fabrication strategies can be distinguished. In the first strategy, the MEMS structures are completely built on top of a finished CMOS substrate, leaving the CMOS layers untouched. An example for this approach is the Texas Instruments' Digital Micromirror Device (DMD) [14]). Alternatively, the MEMS can be obtained by machining the CMOS layers after the completion of the regular CMOS process sequence. Both strategies are implemented by

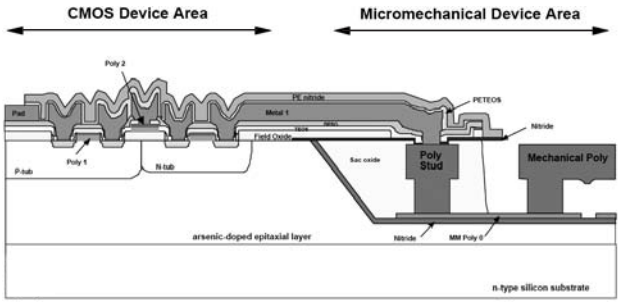

(a)

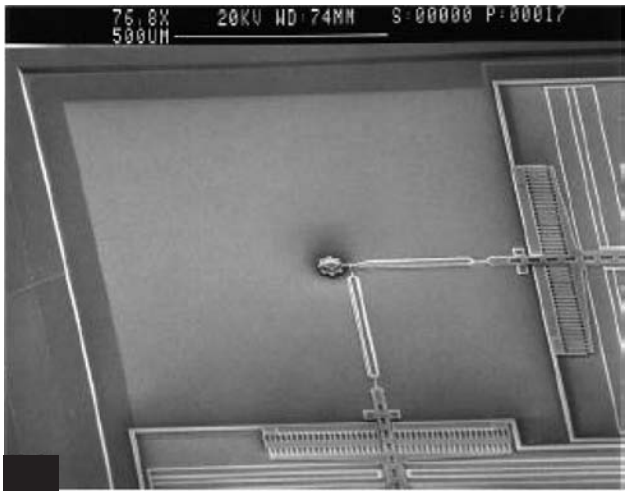

(b)

Figure 7.3 Pre-CMOS integration: (a) concept and (b) realization of a three-level polysilicon structure (micro-engine) built in a trench. (© 1995 IEEE [11].)

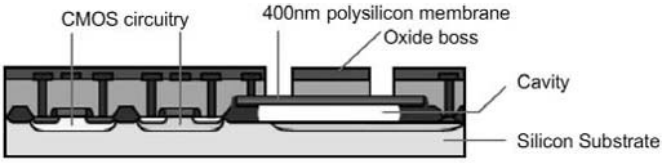

Figure 7.4 Intermediate-CMOS process: the Infineon's pressure-sensor IC is implemented through surface micromachining of the polysilicon layer to form the sensor's cavity. Sealing of the membrane is carried out by using the subsequent CMOS layers. (*After:* [13].)

using a variety of bulk-micromachining and surface-micromachining CMOS-compatible techniques. Figure 7.5 shows a bridge-shaped MEMS resonator fabricated in AMS035 CMOS technology. The MEMS has been released by wet-etching surface micromachining and using the second strategy (micromachining of the top-level CMOS layers after completion of the process) [15].

Monolithic integration is a complex process that requires a specific development to control the materials, temperatures, and the possible sources of contamina-

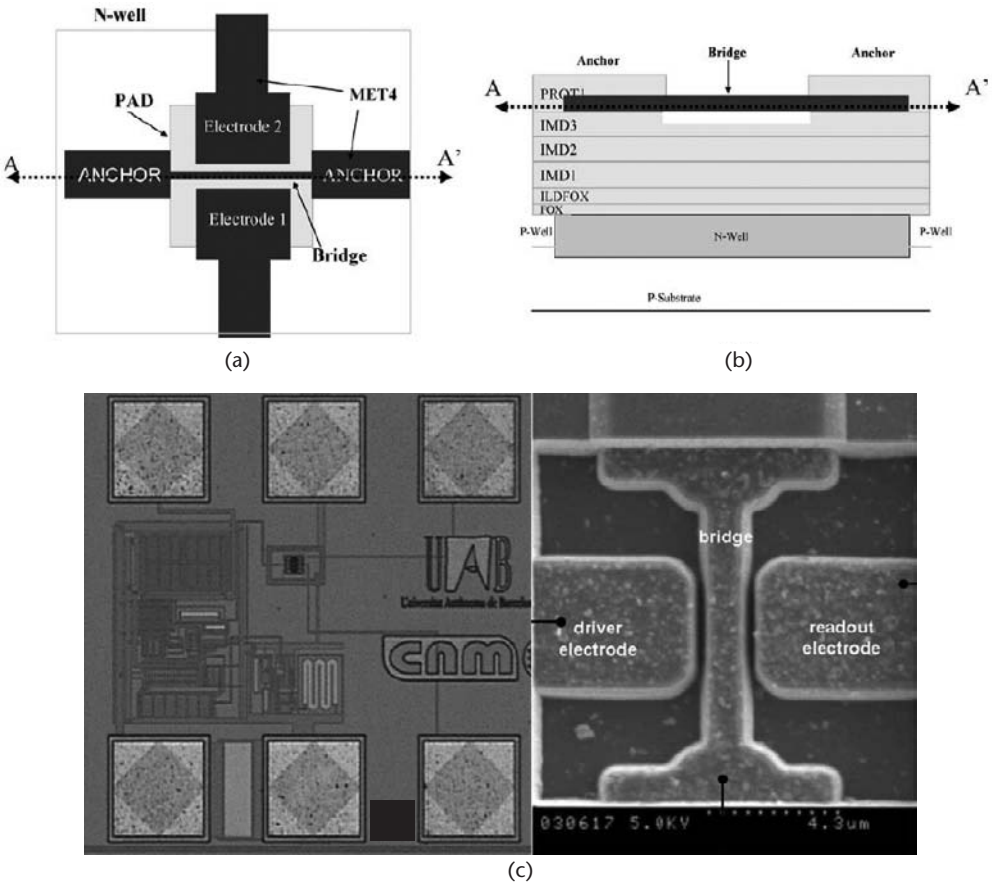

Figure 7.5 Post-CMOS bridge-shaped MEMS resonator fabricated in AMS035 CMOS technology: (a) top and (b) cross-sectional views, and (c) realization of the MEMS resonator-CMOS ensemble (SEM image of the bridge-shaped resonator at right). (© 2006 IEEE [15].)

tion. Therefore, it is highly specialized and exclusive for the modified CMOS technology, with the MEMS/NEMS technology subordinating its possibilities to the restrictions imposed by the CMOS process. Due to the achieved compatibility, the process parameters of the CMOS and the MEMS/NEMS devices are the same, as their electrical responses can be predicted with the same modeling tools. The parasitics effects of the MEMS/NEMS-CMOS interconnection are drastically reduced, in comparison to hybrid integration, because of the efficiency achieved by the shorter paths provided by the CMOS via/through hole technology. However, the development costs and the risks are high, and the CMOS manufacturer must provide exclusive resources for the technology testing, which is not always in the best interest of an industrial company. However, the impact on mass production is very positive, thus guaranteeing higher volumes. Monolithic integration also enables the fabrication of nanosized NEMS devices through advanced patterning tools like electron-beam lithography (EBL) and FIB, among others. The impact of these tools on the CMOS performance after postfabrication of NEMS devices has been documented [16].

7.1.3 Heterogeneous Integration

In spite of the classical hybrid-monolithic classification of the CMOS integration approaches, a third strategy, *heterogeneous integration*, is to be defined. Heterogeneous integration is an evolution of hybrid integration and refers to technologies that can be integrated on one platform device. Also, it can designate materials that are not compatible and cannot be manufactured on the same substrate—at least not in a cost-effective manner [17]. The concept of heterogeneous integration enables the fabrication and assembly of complete electronic subsystems from components fabricated within a variety of processes. MEMS devices, SOI/CMOS mixed signal ASICs, microscale passive components, and micropower systems are some of these systems. The baseline technology incorporates bump attachment and flip-chip between the various components and the substrates. When possible, this will entail wafer bumping prior to dicing and attachment [18, 19]. This feature and the three-dimensional stacking of different substrates represent a fundamental difference from traditional hybrid-integration technologies. Concept and realizations of a Si-based system-in-package composed by passive and heterogeneous integration can be observed in the drawings and images of Figure 7.6. First, in Figure 7.6(a), the concept of integration of a variety of passive and active components is depicted. In

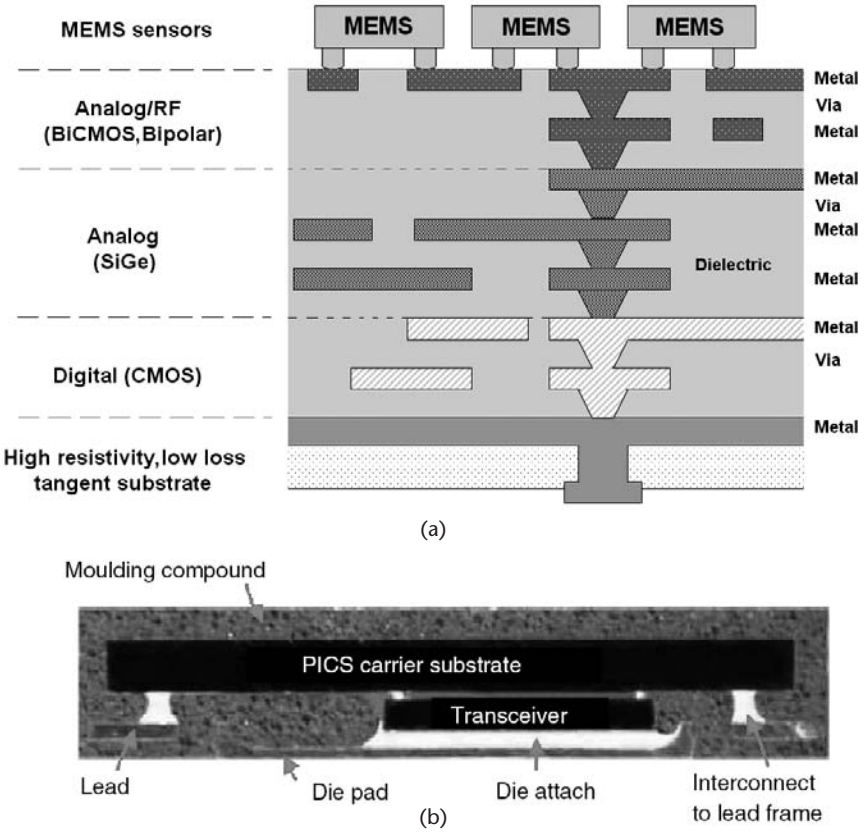

Figure 7.6 Heterogeneous integration: (a) concept of integrated high-resistivity substrate, CMOS digital processing, RF and analog BiCMOS sections, and MEMS sensors (on top); and (b) cross-section of a fully integrated radio module with active transceiver and passive die in a molded lead frame. (© 2006 Elsevier [19].)

Figure 7.6(b) a cross-section view of a fully integrated radio module with an active transceiver and passive die in a molded lead frame is observed.

Heterogeneous integration overcomes the technological restrictions of traditional hybrid and monolithic integrations. To complete the integration, no process compatibility between the MEMS/NEMS and the CMOS part is required. Processes involving diverse materials like high-temperature ceramics, piezoelectrics, and noble metals, among others, can be integrated to a CMOS substrate avoiding the need for CMOS line modification. Additionally, the same integration process may be suitable for different CMOS and MEMS/NEMS technologies, if they incorporate similar conditions. This is the case of standard CMOS processes implementing certain metals, dielectrics, and passivation layers. Thus, flexibility is an added value of the heterogeneous integration approach.

In addition to standard CMOS processes, the clean room incorporates MCM and postprocessing sections for stacking, interconnection, and micromachining of the parts. As a remarkable difference to traditional hybrid processes, heterogeneous integration can be performed either at the chip or the wafer level, which means that dicing is no longer prioritized over integration. Instead, new procedures like wafer-level transfer become key components of the integration technology. Micromachining may be carried out before or after the integration, leaving the dicing at the end of the process, if it is desirable. Because of this feature, heterogeneously integrated systems may be mass produced, thus benefiting from scale economies. The interconnection technology, as in the monolithic integration case, can be optimized to reduce the parasitic effects at the MEMS-to-CMOS interface. Via or through hole, electroplating, and bump attachment are some of the available technologies to provide the vertical connection of the stacked system, which is not limited to only a couple of processes as illustrated in the conceptual diagram of Figure 7.6. Traditional micromachining as well as advanced laser ablation techniques may be employed to release devices or substrates.

Table 7.1 synthesizes the requirements and features of the different integration strategies we have reviewed on this chapter. As we may suspect, any of the strategies can claim supremacy, and their implementation will depend more on the specific economical and application cases. As long as FBAR, MEMS and NEMS resonators, CMOS, and other IC processes have been integrated through these strategies, this table may aid as a checklist for defining application requirements and economical and technological possibilities. The design effort also has to be accounted for.

7.2 State-of-the-Art Integrated Applications

In this section, we review some of the latest integrated-resonator applications to date. Although the technology requirements for integrating MEMS, NEMS, and acoustic resonators may be the same, we organize the section in three main blocks. In the first one, we discuss the case of CMOS-integrated MEMS and NEMS resonators. In the second one, we explain the integration of SAW and FBAR devices. In the last block, focus is on advanced 3D integration technologies. This section is will describe some of the key technological aspects of the IC-to-resonator integration,

Table 7.1 Requirements and Features of Hybrid, Monolithic, and Heterogeneous Integration Strategies

Requirements	*Hybrid*	*Monolithic*	*Heterogeneous*
Process specialization	No	Yes	No
Complexity	Low	High	High
Compatibility requirements	Low	High	Low
Flexibility-versatility	High	Low	High
Development Costs	Low	High	High
Production Costs	High	Low	Low
Performance	Low	High	High
Integration Technologies	Wire-bonding, MCM, packaging	Via-through hole, planar, surface micromachining, advanced patterning tools (EBL, FIB)	Wafer-level-transfer, surface micromachining, laser ablation, MCM, packaging
MEMS-NEMS Possibilities	Features restricted to the available wire-bonding technology	Only CMOS-compatible materials, nanosized features	Suitable for a broad variety of MEMS (feature size restricted to the available MCM technology)
Geometry	Onside (wire-bonding), MCM-stacked (two chips)	Onside, above-IC	3D-stacked (more than two chips, in general)

thus giving emphasis to the process description rather than the application analysis. Numerous applications of integrated resonators will be discussed in Chapter 8.

7.2.1 MEMS and NEMS Resonators

MEMS and NEMS resonators integrated with CMOS technologies are being widely used in diverse sensor applications. Most recently, the resonators are monolithically integrated according to the post-CMOS approach. The NEMS-resonator-based mass sensors of Arcamone et al. implement a wafer-scale process based on post-processing the CMOS wafer that contains read-out integrated circuits [20]. They use nanostencil lithography (nSL) to pattern on top of the CMOS process several types of micro- and nanoelectromechanical resonators, whose dimensions range from 20 μm down to 200 nm. They have demonstrated the simultaneous nSL patterning with a throughput of about 2,000 resonators per wafer. The technique is a reliable method to define nanoscaled patterns and is also compatible with the CMOS process, thus avoiding damage to the CMOS circuits.

The sequence of fabrication is depicted in the schema of Figure 7.7. Once the CMOS process is completed, 80-nm-thick Al features are locally deposited and patterned in a single step through metal evaporation and nSL. In this way, the nSL wafer with the stencil is aligned on top of the CMOS wafer and the Al deposited by using electron-beam evaporation [Figure 7.7(a)]. The Al features serve as a mask to transfer its pattern to the resonator's 600-nm-thick polysilicon structural layer. This is carried out by RIE etching of the polysilicon layer (poly0), taking advantage of the very high dry etching selectivity of Al with respect to Si [Figure 7.7(b)]. Before completing the process, an UV-patterned photoresist mask is deposited and opened

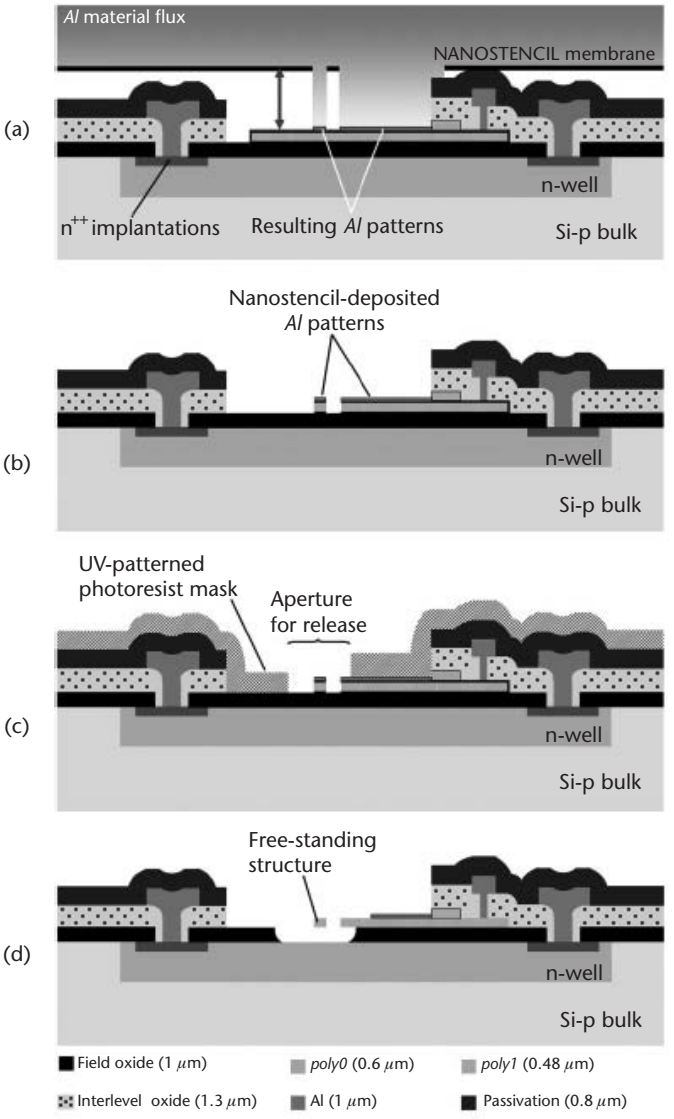

Figure 7.7 MEMS and NEMS resonators monolithically integrated with CMOS: (a) the post-CMOS resonator fabrication includes nanostencil lithography (nSL) to deposit an Al mask, (b) polysilicon etching to define the structural layer of the resonators, (c) photoresist protection of the CMOS circuits, and (d) and dry etching of the CMOS field oxide. (e) Nanocantilevers and (f) suspended beams connected to the CMOS circuits are obtained. (© 2008 IOP Publishing Ltd. [20].)

in selected areas around the resonators to protect the CMOS circuits [Figure 7.7(c)]. Finally, immersing the wafer in HF etches the field oxide of the CMOS process, thus releasing the resonators [Figure 7.7(d)]. The result of the process can be appreciated in the pictures of Figure 7.7(e, f). The resonators are onside placed and connected to signal interfacing and amplification CMOS circuits. Mechanical structures with line widths down to 150 nm can be routinely achieved by the presented process sequence.

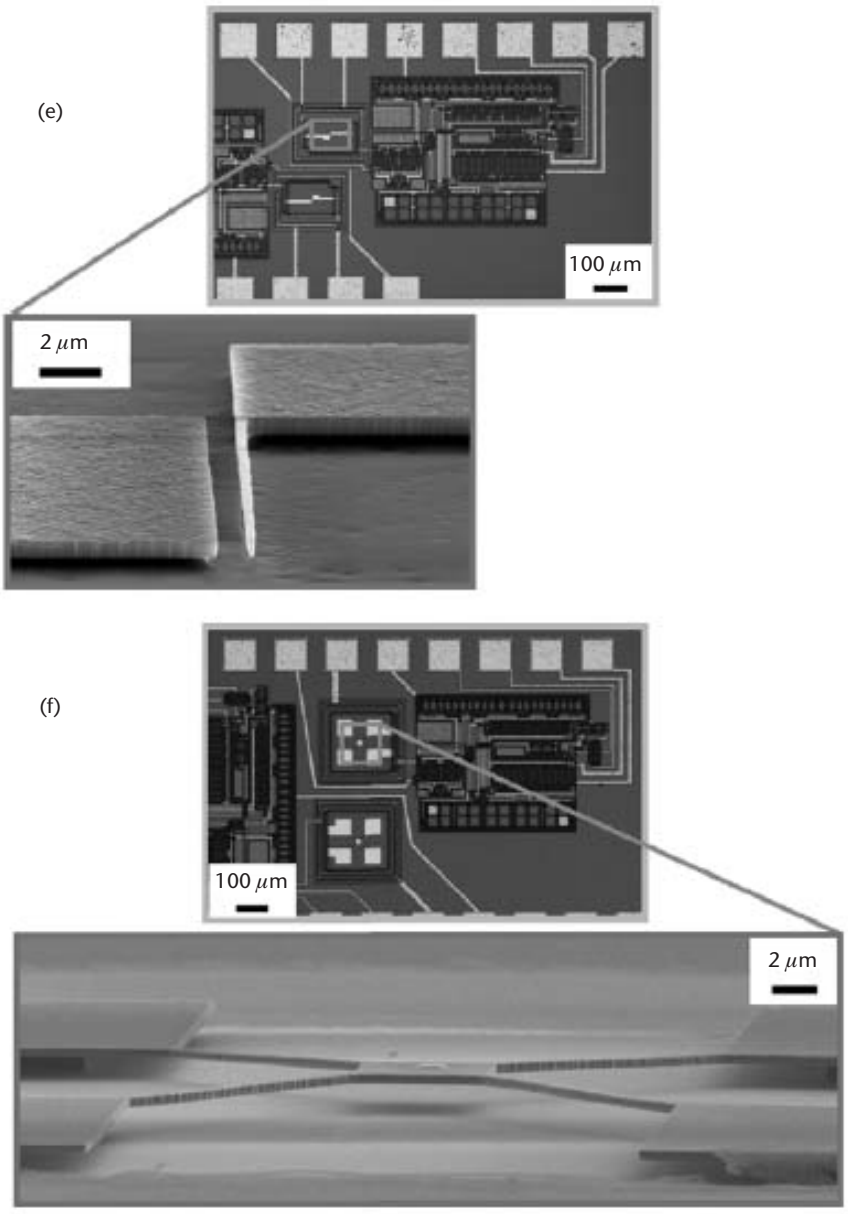

Figure 7.7 (continued)

A second example of post-CMOS monolithic integration is the MEMS cantilever resonator device fabricated through the Taiwan Semiconductor Manufacturing Company (TSMC) 0.35-μm double polysilicon quadruple metal (2p4m) CMOS process. According to this process, Chiou et al. fabricate a CMOS-MEMS prestress vertical comb-drive resonator with a piezoresistive sensor to detect its static and dynamic response [21]. The fabrication process of the comb-drive MEMS resonator is depicted in the sequence of Figure 7.8. First, Figure 7.8(a) illustrates the cross-section view of the CMOS process after full layer deposition and opening of the

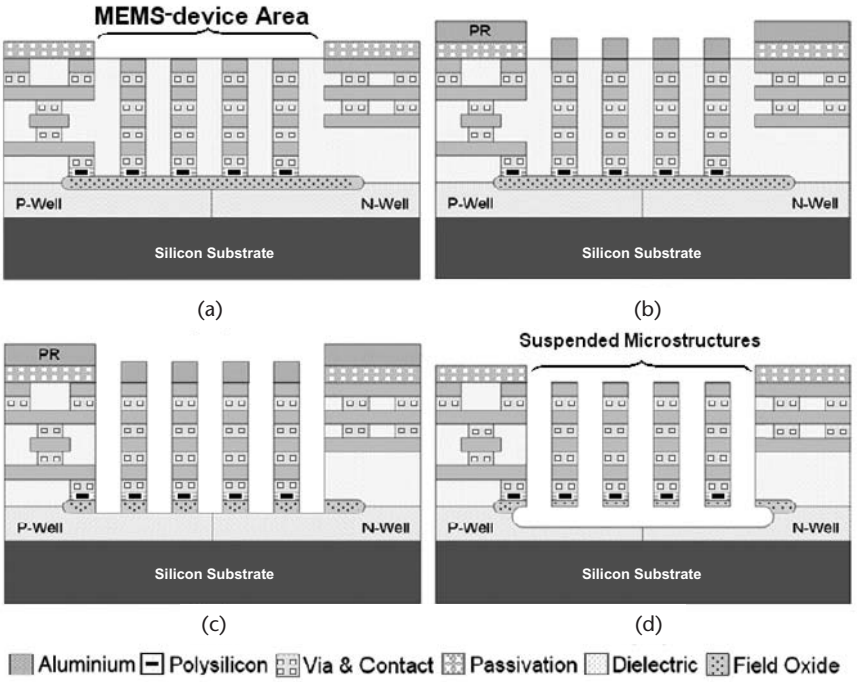

Figure 7.8 Fabrication process of the comb-drive MEMS resonator: (a) completion of the CMOS process (proving passivation apertures); (b) deposition and patterning a photoresist mask to protect the CMOS regions; (c) etching the field oxide by anisotropic RIE etching; and (d) etching the Si substrate to release the suspended microstructure and removal of the photoresist. (© 2008 IOP Publishing Ltd. [21].)

passivation. Prior to etching the interlayer dielectric, a thick photoresist is deposited and patterned to protect the nonresonator areas, as illustrated in Figure 7.8(b). Then, the dielectric is etched by anisotropic RIE with CHF_3/O_2 plasma, thus defining the sidewalls of the resonator and etching the field oxide as it shows Figure 7.8(c). Next, isotropic RIE of the doped region of Si is performed in a SF_6/O_2 atmosphere, thus releasing the suspended structures of the MEMS resonators. Finally, the photoresist is removed to complete the post-CMOS micromachining process, as shown in Figure 7.8(d).

As we have seen, many of the CMOS-monolithically integrated MEMS and NEMS resonators are placed onside of the CMOS process, and implemented through the upper layers of the CMOS process. In general, the processes involve the following:

1. The passivation layer is opened to allow etching of the structures.
2. The resonators are shaped by standard lithography. NEMS devices can be patterned by using advanced techniques like nSL or e-beam lithography (EBL).
3. The resonators are released by dry or wetetching of the dielectric layers of the CMOS process, as the interlayer dielectric or the field oxide.

7.2.2 SAW and FBAR

As a difference with most CMOS-integrated NEMS and MEMS resonators, in CMOS-based SAW and FBAR applications the process necessarily considers the addition of piezoelectric thin films, which are nonstandard in conventional CMOS technologies. In monolithic integration, these layers impose the need for CMOS-compatible processes, thus implying the development of a compatibility protocol. One of the issues is the low-temperature requirement for depositing thin-film piezoelectric materials like AlN or ZnO. The second issue may be the adaptation of the CMOS line to deposit nonstandard metals like Pt or Mo.

7.2.2.1 SAW Integration

Hybrid applications based on SAW and CMOS circuits exist since the miniaturization of SAW has made feasible the size fitting between the chips of both technologies. The polylithic integration of a quartz wafer on silicon (QoS) to fabricate a reference SAW-CMOS oscillator was demonstrated by Yunseong et al. [22]. The SAW resonator and its connection with the ICs were fabricated after wafer-level bonding of the quartz and silicon wafers. A few years later, Yeonwoo et al. improved the technology to provide temperature-compensated SAW-CMOS oscillators [23].

With the passing of time, the monolithic integration of SAW devices and CMOS circuits has made possible the fabrication of SAW-CMOS reference oscillators on the same chip. Furuhata et al. developed a reference oscillator that combined the SAW device and the IC into a single unit, with the total thickness of nearly the same as that of the IC [24]. They fabricated the IC in a standard CMOS 0.25-μm process and flattened the wafer through chemical-mechanical polishing (CMP). After CMP, they opened the passivation layer to access the upper Al metallization and deposited the ZnO thin film on the wafer, as depicted in Figure 7.9(a). Next, deposition and etching of an Al layer forms the IDTs of the SAW electrodes [Figure 7.9(b)]. A key feature of this approach is the low-temperature deposition of the ZnO layer at 400°C. This avoids damages to the circuits, especially the Al metallization. The oscillator has the layout shown in Figure 7.9(c) and exhibits a central frequency of 545 MHz and a low phase noise of –120 dBc/Hz at 10 kHz.

Another example of SAW-CMOS monolithic integration is the fully integrated two-port SAW resonator fabricated within the standard 0.6-μm American Microsystems Incorporated (AMI) CMOS three-metal two-poly CMOS process [25]. The metal layers M1 and M2 of the CMOS process were used to implement the IDTs, the reflectors, and the ground shield. The process entails three main steps: (1) RIE-based micromachining to etch the interlayer SiO_2, (2) ZnO deposition, and (3) wet etching of ZnO. The first step allows accessing the ground shield and patterning the IDTs. In the second step, the ZnO is sputtered to fill the space between the IDT fingers, and the third step opens the contact pads for characterization and interconnection. An improved implementation of this process employs the third CMOS metal layer M3 to provide the resonator with an extra layer of reflectors to contain the acoustic waves propagating above the transducer. Cross-sectional cut views of both implementations are depicted in the schematic drawing

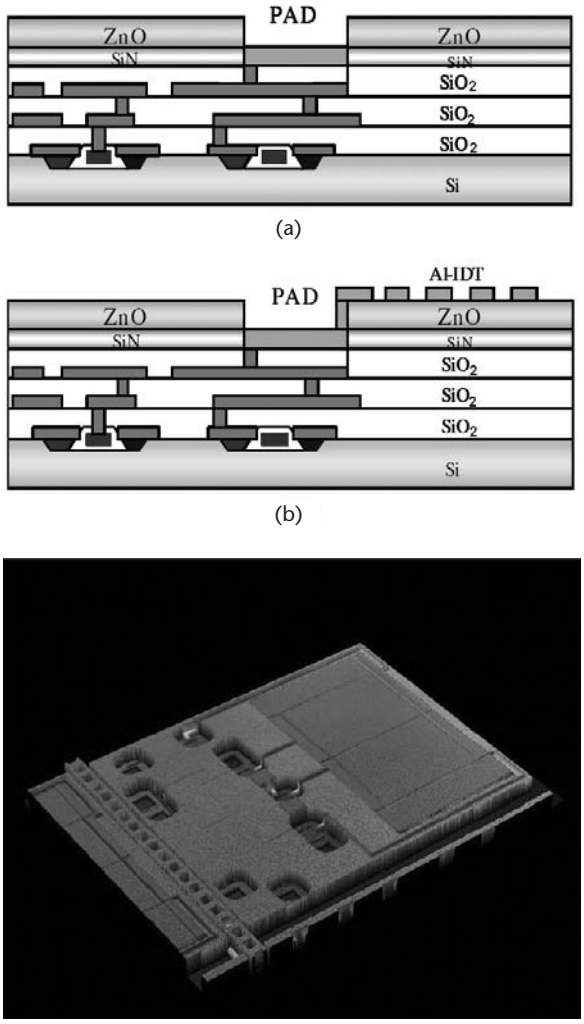

Figure 7.9 Monolithically integrated SAW-CMOS oscillator: the fabrication process involves: (a) CMP, pad opening, and ZnO deposition, and (b) the upper Al layer deposition to form the SAW electrode IDTs. (c) The layout of the SAW-CMOS oscillator. (© 2005 IEEE [24].)

of Figure 7.10. Resonators with different designs achieved parallel resonant frequencies of 1.02 GHz, 941 MHz, and 605 MHz.

7.2.2.2 FBAR

The integration of FBAR has a relatively short history, in comparison to other MEMS devices. As a high-Q factor device, FBARs have also attracted the attention of RF IC and sensor-application designers. Recent developments in FBAR-to-CMOS integration have stimulated the conception of integrated applications in which FBAR is a key component, with IC integration as a requirement for proper functionality of the system. Hybrid and monolithic integration strategies have been investigated and implemented so far.

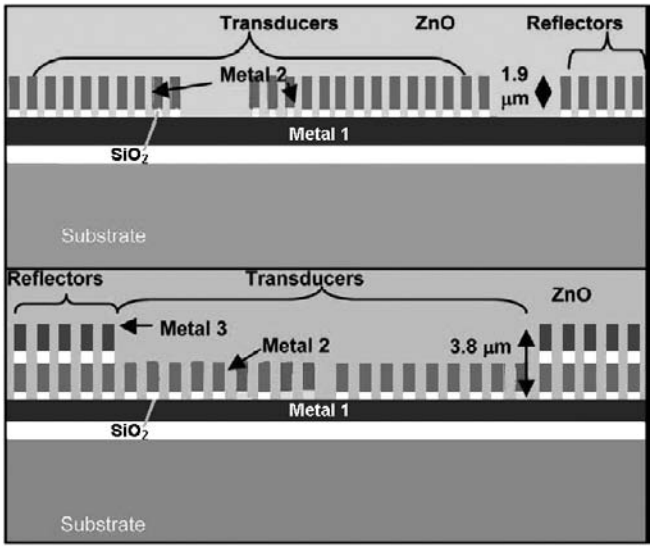

Figure 7.10 CMOS-based SAW resonator fabricated within the AMI standard CMOS process: two-metal implementation that uses the first metal layer M1 to form the ground shield and the second metal M2 to design the reflectors and the transducers; and three-metal process featuring improved reflector design implemented through the third metal M3. (© 2007 IEEE [25].)

In the case of hybrid integration, the FBAR and IC chips are bonded to their corresponding circuit nodes. Examples of this integration approach are the oscillators presented in [26–28], where the FBAR performs the crystal-like functionality in the system. More recently, Avago Technologies [29] introduced a temperature-compensated 604-MHz oscillator based on the FBAR-Colpitts topology. The quadratic temperature function of its FBAR is compensated for by an oxide layer of the opposite temperature coefficient factor (TCF) [30]. In Figure 7.11 the UC Berkeley–Agilent's implementation of a Pierce oscillator is shown. Double and short wire-bonding between both chips ensures reduction of losses and parasitic inductances. Area restrictions, added parasitic capacitances due to the bonding, and batch processing of the integrated devices are some of the limitations of the hybrid integration approach.

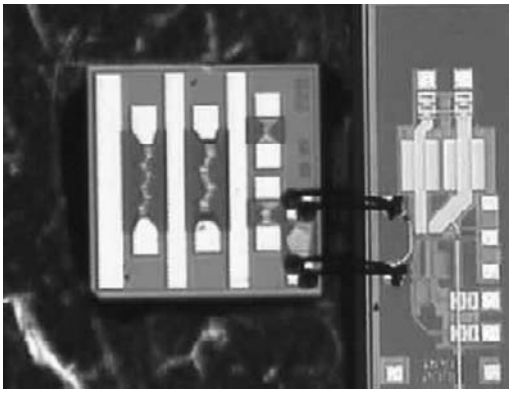

Figure 7.11 Hybrid integration of FBAR with low-power CMOS oscillator. (© 2003 IEEE [26].)

In the current art of monolithic integration, FBARs are placed above the circuit using a post-CMOS strategy, thus saving die area. The approach disclosed in 1993 showed the concept [31] and a system integrating FBAR and radio circuitry conceived in 2001 [32]. However, it was as late as 2005 when the first monolithic FBAR-above-IC RF systems were demonstrated by the Martina consortium. Using a 0.25-μm BiCMOS process, this group implemented double-lattice filters [33], filtering LNAs comprising two broadband amplifiers and one FBAR filter [34], and a 5-GHz FBAR-based low-phase noise oscillator [35], among others, as shown in Figure 7.12.

The interest in monolithic integration of FBAR spans from fully active ICs to passive components as well, like CMOS inductors [36]. On the other hand, CMOS-integrated MEMS, NEMS, and SAW resonators have already been demonstrated as well [37, 38]. In spite of the elegance of monolithic integration, its com-

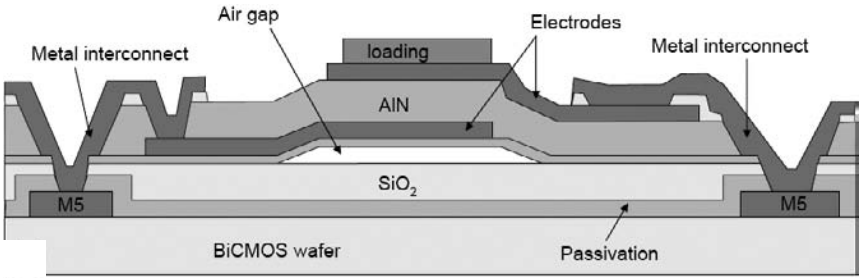

(a)

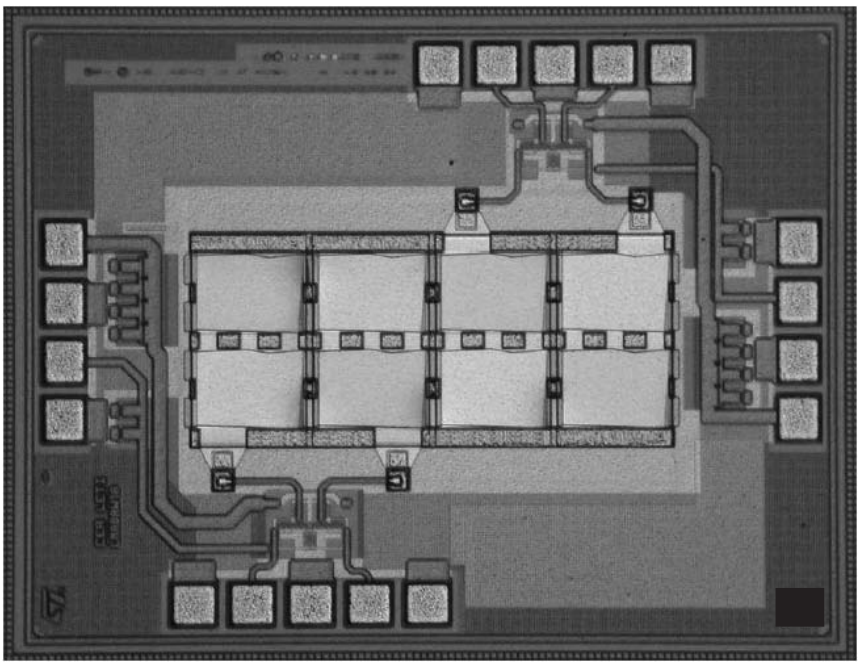

(b)

Figure 7.12 Post-CMOS monolithic integration of FBAR: (a) Martina's concept of the FBAR-above-IC integration; and (b) filtering LNA comprising two broadband amplifiers and differential-lattice filter. (© 2005 IEEE [34].)

plexity, compatibility issues, costs, and technology-specific nature are the main challenges of this approach.

7.2.3 Advanced 3D Integration Technologies: Wafer Level Transfer

Wafer level transfer (WLT) is an advanced 3D integration technology able to integrate CMOS, MEMS, and other IC technologies. To accomplish this purpose, the devices on a source wafer are transferred to a target wafer, all at the same time, hence its name. The WLT technologies must also be able to achieve full releasing of movable devices, as it is the case of MEMS and NEMS resonators. Nowadays, surface micromachining, flip-chip, multichip module, and laser ablation, among others, have been implemented to accomplish 3D CMOS integration of MEMS and NEMS devices.

Two examples are representative of the 3D heterogeneous integration. One of them was developed by IBM (Zurich Research Laboratory) in the context of the "Millipede" project [17], and consists of three main processes. In the first process, a cantilever array is fabricated according to conventional MEMS fabrication techniques. The second process fabricates the CMOS metal and studs on which the cantilevers will be supported. In the third process, the MEMS-CMOS alignment and lamination are carried out, and the cantilevers are released. Figure 7.13(a) depicts the processes, and the final device results are observed in the SEM image of Figure 7.13(b).

A second example is the EPSON's surface free technology by laser ablation-annealing (SUFTLA) technology. The SUFTLA process enables the transfer of thin-films or thin-film devices from their original substrate to any substrate by using selective laser annealing. Low-temperature (below 425°C) polycrystalline-silicon thin film transistors (poly-Si TFTs) and TFT circuits could be successfully transferred from a glass or quartz substrate to plastic film without affecting the circuit functionalities [39]. Using the SUFTLA technology, EPSON has demonstrated flexible TFT-LCD displays, polymer-based displays, TFT-SRAM memories, and the industry's first flexible 8-bit asynchronous microprocessor shown in Figure 7.14 [40].

Similar approaches have followed the 3D integrations of the monocrystalline silicon mirrors fabricated using CMOS-compatible transfer bonding [41], which is improved with nano-imprint resists to optimize the bonding of the CMOS and the MEMS wafers [42]. As described in the foregoing examples, the two wafers are placed one above the other and aligned, and their landing pads are bonded through interconnection posts. These technologies, as we have studied, are implemented at the wafer level, which is the main difference to previous hybridization of integrated systems.

7.3 Wafer-Level-Transfer-Based FBAR-to-CMOS Integration

Taking advantage of the WLT approach, we can also fabricate FBARs integrated to a standard CMOS process. As we have studied before, this will overcome the limitations of hybrid or monolithically integrated resonators. According to this method,

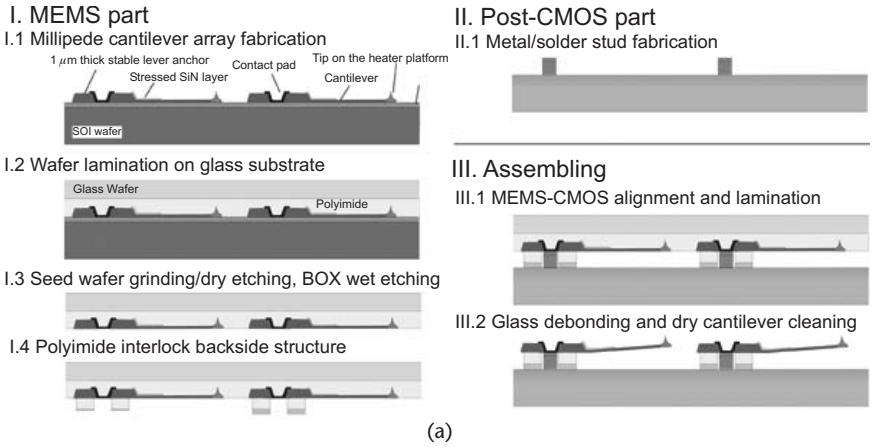

(a)

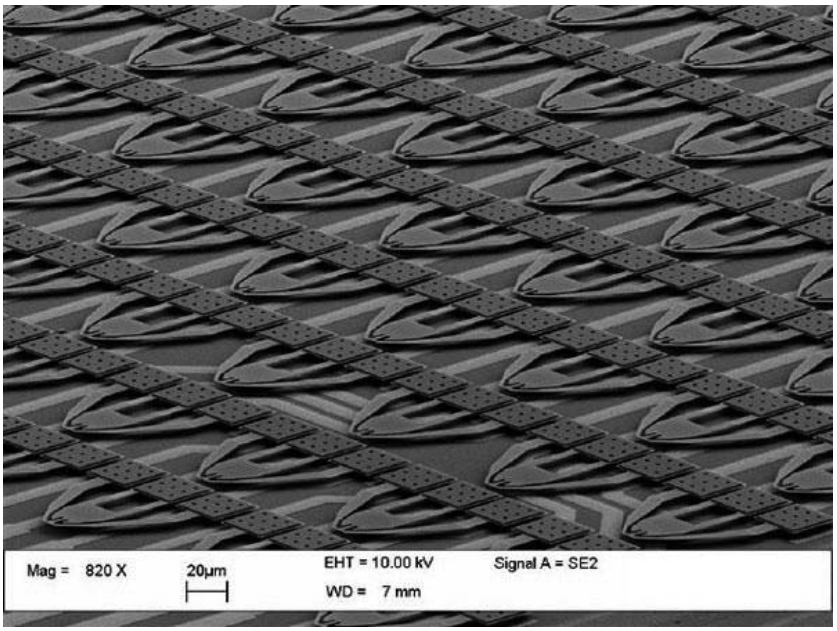

(b)

Figure 7.13 Heterogeneous integration technology for cantilever array fabrication: (a) process description and (b) SEM image of the cantilever array. (© 2009 IBM [17].)

the FBARs on a first device wafer are transferred all at a time to a target the CMOS wafer, thus obtaining 3D, floating structures. This approach is also suitable to other MEMS and NEMS resonators.

In the WLT-based integration approach, we need to distinguish between two main processes: (1) manufacturing of the resonator strictly speaking, and (2) its wafer-level transfer into a CMOS substrate. On the other hand, we have a previously fabricated CMOS wafer. For example, the schematic drawings of Figure 7.15 explain the simplified sequence of a fabrication process involving this couple of processes. First, both the CMOS and the FBAR wafers are fabricated according to independent technological processes [Figure 7.15(a)]. Next, in either the CMOS or the FBAR wafers, pillars providing future electrical connection and mechanical support

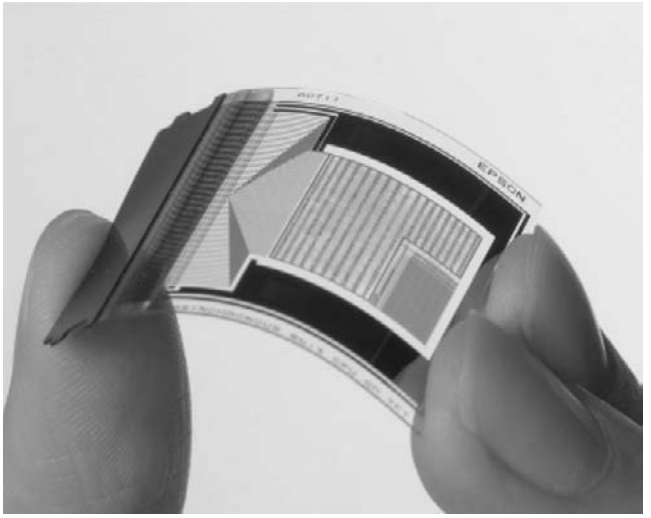

Figure 7.14 The industry's first flexible 8-bit asynchronous microprocessor, fabricated with the SUFTLA technology. (© 2005 EPSON [40].)

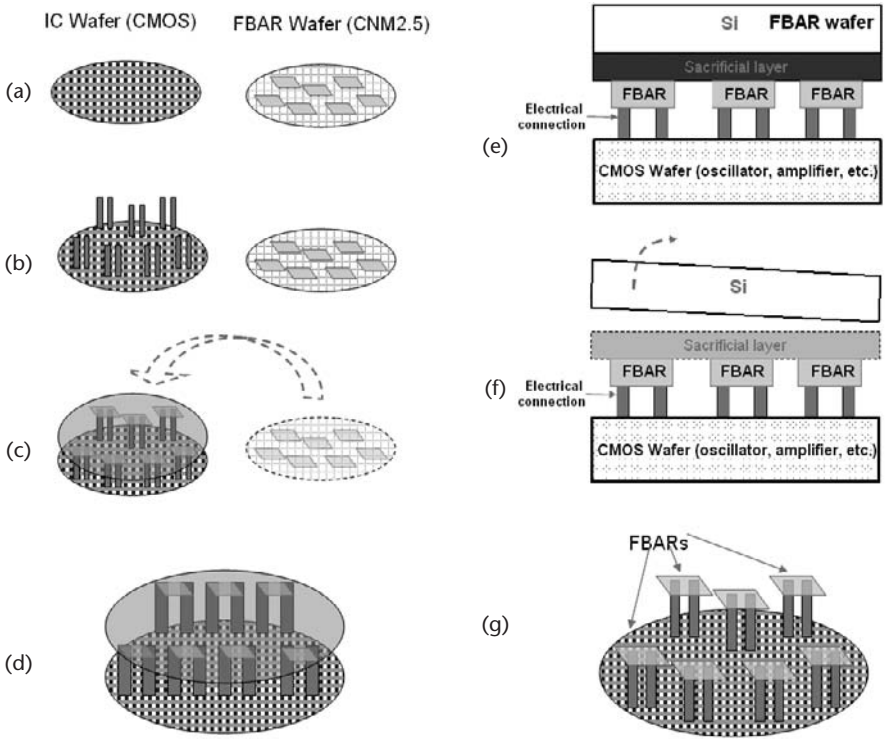

Figure 7.15 Heterogeneous integration process overview: (a) FBAR and CMOS wafers are fabricated within independent processes; (b) pillars are fabricated on the CMOS wafer (or the FBAR wafer, if desired); (c) the FBAR wafer is turned on and placed above the CMOS wafer (devices in contact with pillars); (d) after soldering, FBARs are hard-connected to both the FBAR and CMOS wafers; (e) side view of the FBAR-CMOS ensemble; (f) sacrificial layer wet etching and device releasing; and (g) FBARs are attached to the CMOS substrate, with no presence of the former FBAR-carrying Si substrate.

to the FBAR-CMOS ensemble are fabricated [Figure 7.15(b)]. Then, the FBAR wafer is placed above the CMOS wafer, in order for the FBARs to contact the pillars fabricated on the CMOS substrate [Figure 7.15(c)]. After hard interconnection at appropriate temperature conditions, the FBAR-CMOS ensemble is integrated as shown in Figure 7.15(d). A side view of the ensemble shows that a sacrificial layer between the FBARs and its origin substrate provides mechanical support to them [Figure 7.15(e)]. After the etching of the sacrificial layer, the substrate separates from the devices, thus releasing them above the CMOS wafer [Figure 7.15(f)]. We can appreciate that only the structural layers of the resonators remain above the CMOS substrate, as depicted in the bird's-eye scheme of Figure 7.15(g). This method entails a significant step away the conventional hybrid integration strategy, because wafer-level integration is prioritized to device-level dicing, among other features. At this point, the wafer can be diced to extract the chips.

One can implement this method to integrated FBAR and CMOS for RF and sensor applications. Its advantages are diverse: saving of die area, minimization of power losses, reduction of the fabrication time, process compatibility, and suitability to other MEMS devices, among others. As a difference to conventional FBARs or the floating structure presented in [43], the whole FBAR structure is completely transferred to the target substrate, which can also carry CMOS or another integrated circuit technology. As a floating structure, the FBAR is placed above the IC and is exclusively supported by two or more posts, which are also interconnecting points to the CMOS substrate.

7.3.1 The Resonator Process

First, we describe the resonator manufacturing process. We can assume that the CMOS wafer is fabricated according to a standard process and that it carries integrated circuits. As we said before, the FBAR wafer is placed above and connected to the CMOS substrate. The schematic drawings of Figure 7.16(a, b) show top and cross-sectional views of the integrated FBAR-CMOS ensemble, with the FBAR placed on top of the CMOS substrate. As observed, the pillars are the only supporting means of the FBAR, making it a three-dimensional, floating structure. At the same time, the posts provide electrical contact between the FBARs and the CMOS substrate. The CMOS wafer may carry passive devices, test structures, integrated circuits, or a combination of all.

The technology can integrate other microresonator and IC technologies as well. Since the floating configuration of the FBAR provides it with acoustical and mechanical isolation to the substrate, the same process principles may be applied to other micromachined movable structures, such as MEMS resonators, RF switches, varactors, and tunable capacitors. Also, this method is suitable to integrate functional blocks comprised of more than one resonator, like filters and duplexers.

Figure 7.17 depicts the main steps of the fabrication process. First, Figure 7.17(a) shows that a sacrificial layer made of a metal or dielectric material is deposited on top of the FBAR wafer substrate. This is a characteristic seal of the technology, because it enables the wafer-level releasing of the devices once transferred to the CMOS wafer. Thus, one avoids the patterning or mask-driven processing of the sacrificial layer. Instead, it is uniformly deposited on the wafer and etched at the

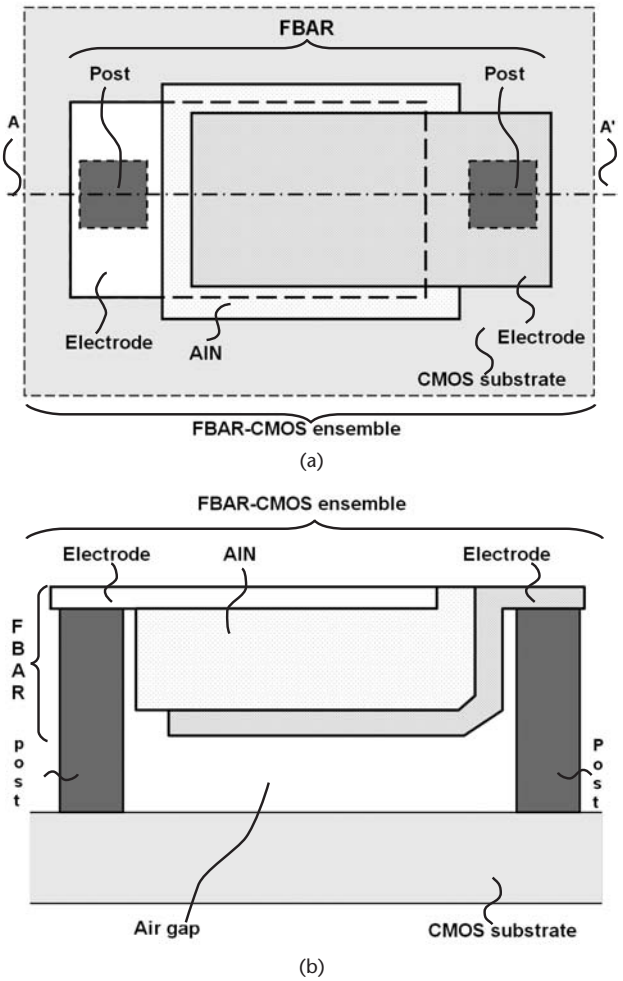

Figure 7.16 Schematic drawing of the floating FBAR structure, after fabrication using the heterogeneous integration method: (a) top view and (b) side view of the FBAR and CMOS substrate.

final step, when performing the FBAR and substrate integration. Next, Figure 7.17(b) illustrates the FBAR fabrication, where the metal of the first electrode is on top of the sacrificial layer. Then, the piezoelectric and second electrode layers are deposited at the steps shown in Figure 7.17(c, d), respectively. To achieve this purpose, one may employ the thin-film deposition or growing technologies previously described, like RF sputtering, epitaxial, or plasma-assisted deposition.

A realization of the previously described process may be as follows: the sacrificial layer can be made a 1-μm-thick phosphor silicate glass (PSG) film deposited on a 500-μm-thick silicon wafer. Next, an 180-nm-thick Cr/Pt layer—30 nm of Cr for Pt-adhering purposes—is deposited on top of the PSG, and the first electrode is defined by liftoff. Then, the acoustic layer can be a 1μm-thick AlN layer that is wet-etched by using OPD4262 developer to define the resonator shape. Finally, the second electrode is also made according to the same process of the first electrode. FBAR-device wafers fabricated with this process are observed in the optical pictures of Figure 7.18. Broadly, this process is similar to the surface micromachining pro-

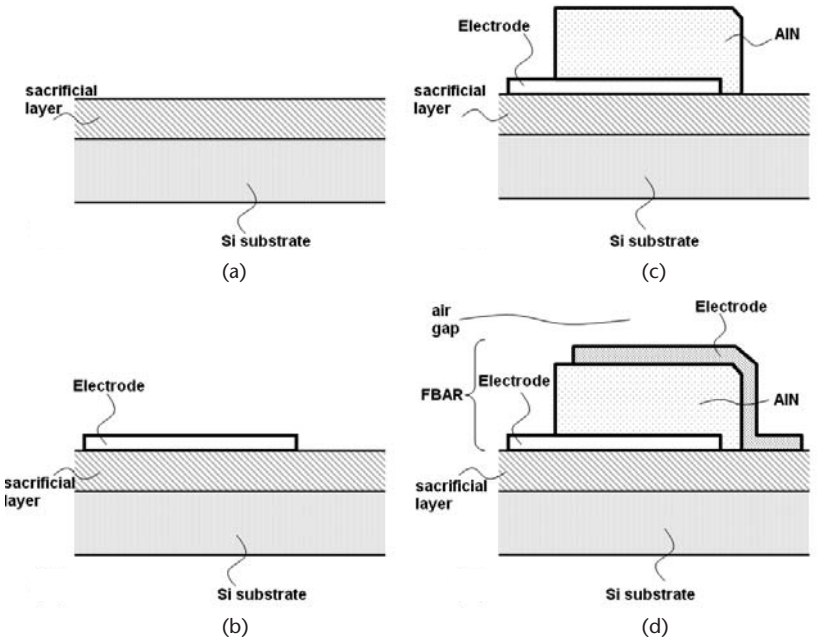

Figure 7.17 Schematic drawing of the FBAR fabrication process, before integration with the CMOS substrate: (a) sacrificial layer deposition on top of the substrate; (b) deposition and patterning of the first metal electrode; (c) deposition and patterning of the acoustic layer (AlN); and (d) deposition and patterning of the second metal electrode.

cess previously described in Chapter 4. The main differences between them are the sacrificial layer material and the photolithography step to define its geometry. In the surface-micromachined FBAR, the sacrificial layer is patterned only underneath the region occupied by the resonator, according to the photolithography. On the other hand, the 3D process described in this section performs etching on the whole wafer surface without photolithography. Additionally, the passivation layer implemented in the surface micromachining process disappears in this technology. Due to the floating configuration of the resulting devices, isolating layers are avoided with this process (the only contact points to the CMOS wafer are the pillars).

Although the previous example implements an AlN layer, compatibility issues with the CMOS technology are irrelevant to choosing the thin-film acoustic material, because the FBAR and the CMOS wafers have contact only after they have been fabricated. Such a process offers more flexibility to choose the piezoelectric material of the FBAR acoustic layer. This can be made of AlN, ZnO, lead zirconate titanate (PZT), lead tantalum zirconate titanate (PLZT), or any other material with good piezoelectric properties. Since an air interface between the FBAR and CMOS wafers is provided at the end of the integration process, the FBAR manufacturing is completed.

7.3.2 The CMOS Process

The target CMOS wafer may be fabricated following the standard process of commercial CMOS technologies, and the cross-sectional view of a typical process is

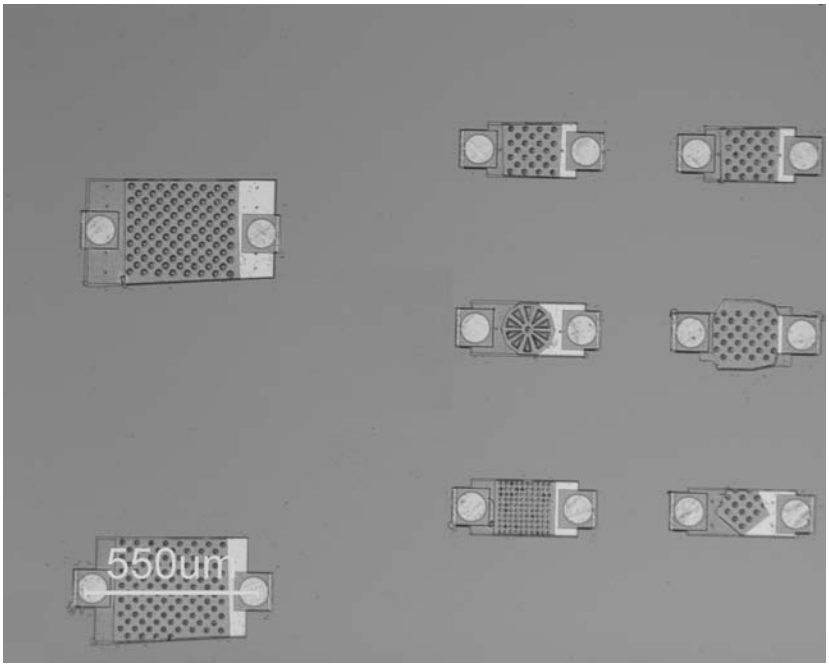

(a)

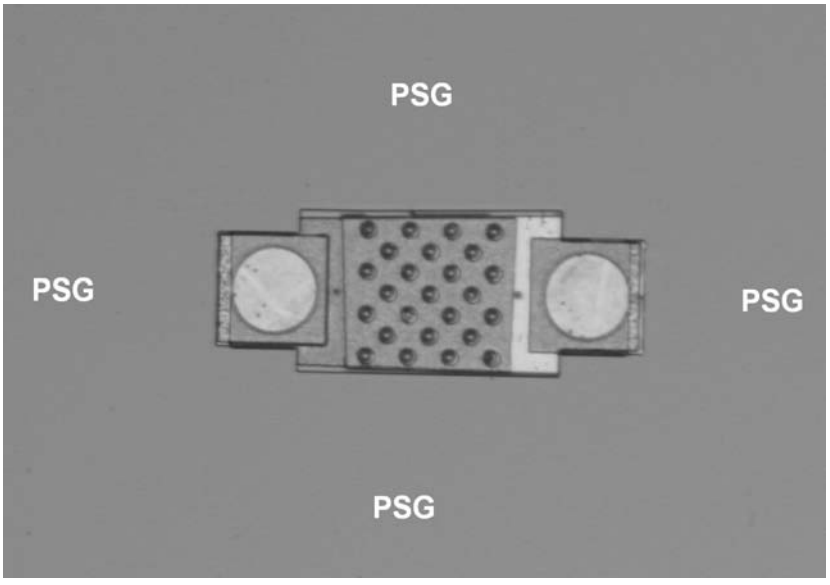

(b)

Figure 7.18 Optical images of the floating FBAR process, before integration with the CMOS substrate. The sacrificial PSG layer covers the whole surface of the wafer (no mask-driven patterning of the PSG is required prior to etching): (a) general view of a section of the device-wafer surface; and (b) detailed view of an FBAR device.

depicted in the schematic drawing of Figure 7.19. Alternative implementations in bipolar, BiCMOS, SOI, or other IC technologies are also suitable for integration. As usual, the CMOS process includes a passivation layer on top of the upper

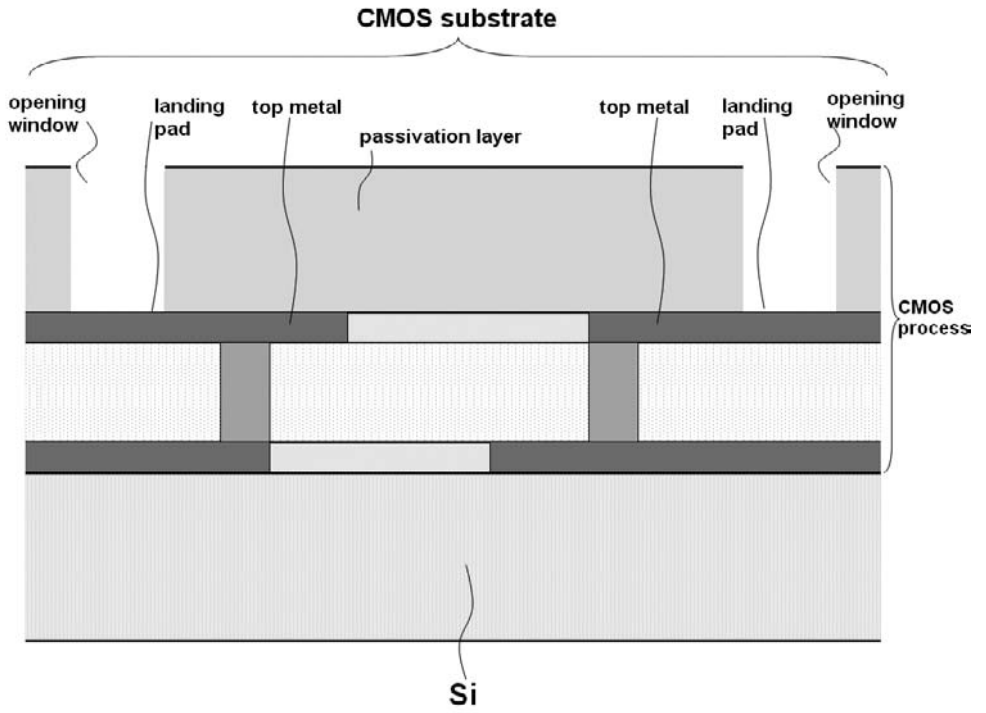

Figure 7.19 Schematic representation of an exemplary CMOS process, suitable for integration with the floating FBAR technology.

metallization layers. Also, opening windows are provided to allow for electrical connection of the IC. For integration purposes, the opening windows will serve as landing pads to the FBAR-to-CMOS interconnection. Although commercial CMOS technologies provide a top passivation layer to protect the circuits and opening windows to contact the circuit pads, rare cases without these features should be prepared to complete the integration process. In those cases, additional postprocessing steps would be required in the IC process, in order to deposit and open a passivation layer to define the pad area on top of the integrated-circuit layers.

The passivation layer may be, for example, a 500-nm-thick PECVD SiO_2 layer, patterned through standard photolithography to open the pad connections. Depending on the application of the CMOS technology (RF, high power, standard), the material of the upper metal layer is made of a combination of Pt on Cr, Al on Cr, or Al on Ti, among many possibilities. Depending on the available metal combination, the wet etching of the FBAR-CMOS ensemble has to be performed using suitable solutions in order to etch the sacrificial layer without damaging of the CMOS layers. Equivalently, if we have technological options for the CMOS metallization, we choose the upper metal configuration that meets the etching requirements of the FBAR wafer.

Let's study two CMOS technologies that we will consider for the heterogeneous integration of the previously described FBAR process. The first one implements the in-house CNM25 CMOS of the IMB-CNM (CSIC) (Barcelona), the cross-section schematic view of which is depicted in Figure 7.20(a). In this process, an isolating

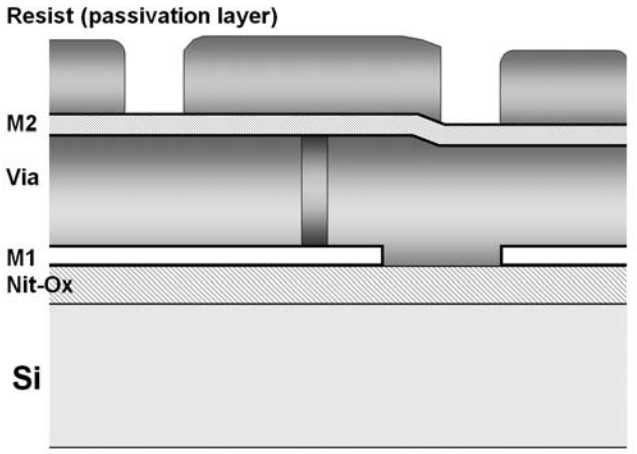

(a)

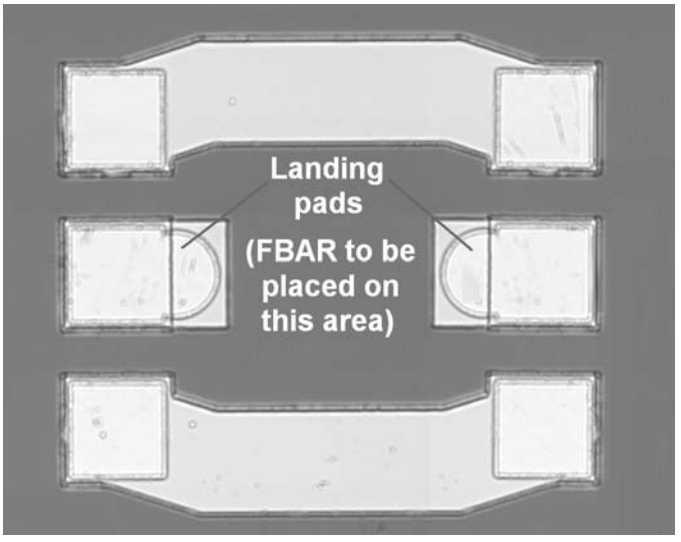

(b)

Figure 7.20 CNM25 2-metal technology implementation: (a) cross-sectional schematic view of the CNM25 process; and (b) a coplanar test structure fabricated according to this process.

Si_3N_4 layer is deposited on the surface of the Si substrate, prior to the first Pt/Cr metallization M1. In order to provide the process with adhesive metallization, a Ti/Ni/Au layer is deposited on the upper metal (M2) to form landing pads to interconnect the CMOS with the FBAR wafer. The passivation layer can be made of a resist or oxide. It serves as a mask for patterning of the Ti/Ni/Au, and, at the same time, it becomes the CMOS passivation. The aspect of the CMOS surface with a coplanar test structure designed with the M2 is observed in the optical micrograph of Figure 7.20(b). This structure will be used to perform electrical characterization of the FBARs once the heterogeneous integration is completed. The contact pads of the FBAR will be connected to the CMOS pads signaled in the figure, and the resonator will occupy the empty space in between them once the device transfer is completed.

The second CMOS process that we study herein is one of the 2-poly, 4-metal Austria Micro System's (AMS) 0.35-μm AMS035c3b4 technologies [44]. This is a commercial and standard CMOS process whose parameters depict Figure 7.21(a). The top layer metallization (Metal 4) is made of Al/Ti, which is accessible by appropriate mask design and pad opening through etching of the protection and passivation layers PROT1 and PROT2. The same coplanar structures of the previous example can be implemented with the Metal 4, as observed in the optical picture of Figure 7.21(b). Again, the region between the landing pads will be occupied by the FBAR once the interconnection process of the FBAR and CMOS wafers is completed.

7.3.3 The Wafer-Level-Transfer Process

Once the FBAR and the CMOS wafers are fabricated, they are heterogeneously integrated by a wafer-level-transfer process. First, the deposition and etching of an alloy or stack of metals suitable for soldering or electroplating is carried out on the FBAR electrodes, thus defining two or more landing pads for the interconnection, as shown in Figure 7.22(a). This is required if the FBAR electrodes are made of materials unsuitable to adherence with soldering or electroplating processes. Thus, the materials composing the landing pads may be selected from the group of Ni, Au, and Ti, among others. Next, Figure 7.22(b) illustrates how the pillars are placed on top of the landing pads. The techniques and methods required to implement them are diverse and include mask-driven deposition of soldering paste, metal deposition, and electroplating assisted deposition, among others. Then, the FBAR wafer is turned over and placed above the CMOS wafer, as represented in Figure 7.22(c). Both wafers are handled to align the FBAR pillars and the opening windows of the CMOS wafer. Manual or automatic pick-and-place systems may be used for positioning, alignment, and soft-contacting of FBAR and CMOS wafers. Since the FBAR wafer is flipped at this step, the second electrode becomes the closest one to the CMOS substrate, whereas the substrate is now the upper layer of the suspended structure. Current technologies provide pillars that are bigger than FBARs. Therefore, an air interface is created at the gap between the FBAR and the CMOS wafers. The mechanical interconnection can be done by soldering bumps heated and soldered to the CMOS pads, at one side, and to the FBAR pads, at the other one. Alternatively, electroplating or deposition techniques may replace soldering. In the last step of the process, depicted in Figure 7.22(d), the FBARs are released through wet etching of the sacrificial layer. Since the sacrificial layer is between the FBARs and their substrate, it is lifted off when the etching is completed, thus separating the FBARs and completing the transfer to the CMOS wafer. Now the FBARs exhibit two air interfaces, and they have mechanical freedom to vibrate, as no acoustical coupling exists between them and the CMOS wafer. This feature is a necessary condition to guarantee high-quality factors.

To perform the interconnection of the FBAR and CMOS wafers, the landing pads can be made of Ni, Au, and Ti, for example, with thicknesses of 30 nm, 20 nm, and 50 nm, respectively. The pillars may be soldering bumps, which are applied on the wafer by a masking-aided appliance and an alignment system. In the stereoscopic picture of Figure 7.23(a), a close-up of the pillars on the resonators can be

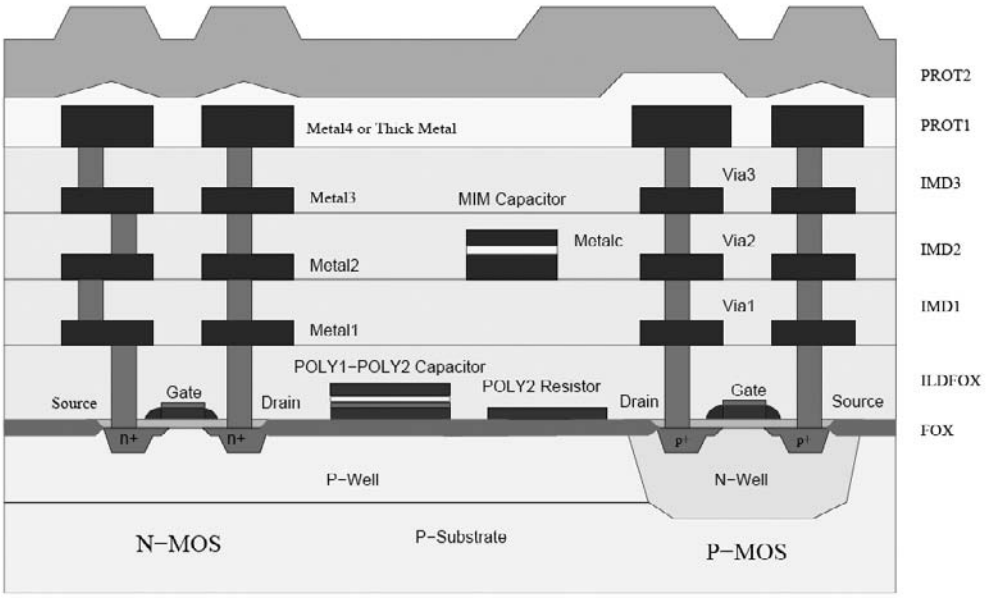

(a)

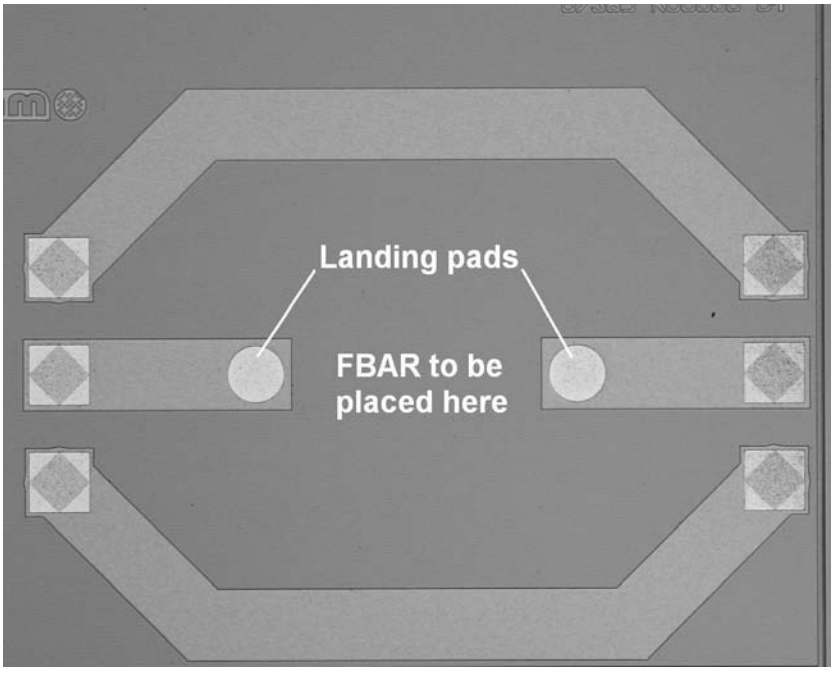

(b)

Figure 7.21 AMS035 technology implementation of the CMOS-substrate for heterogeneous integration with FBAR substrate. (a) Cross-sectional schematic view of the AMS035 process. (*After:* [44].) (b) Optical image of a coplanar test structure implemented within this process (the FBAR is to be located in between the landing pads).

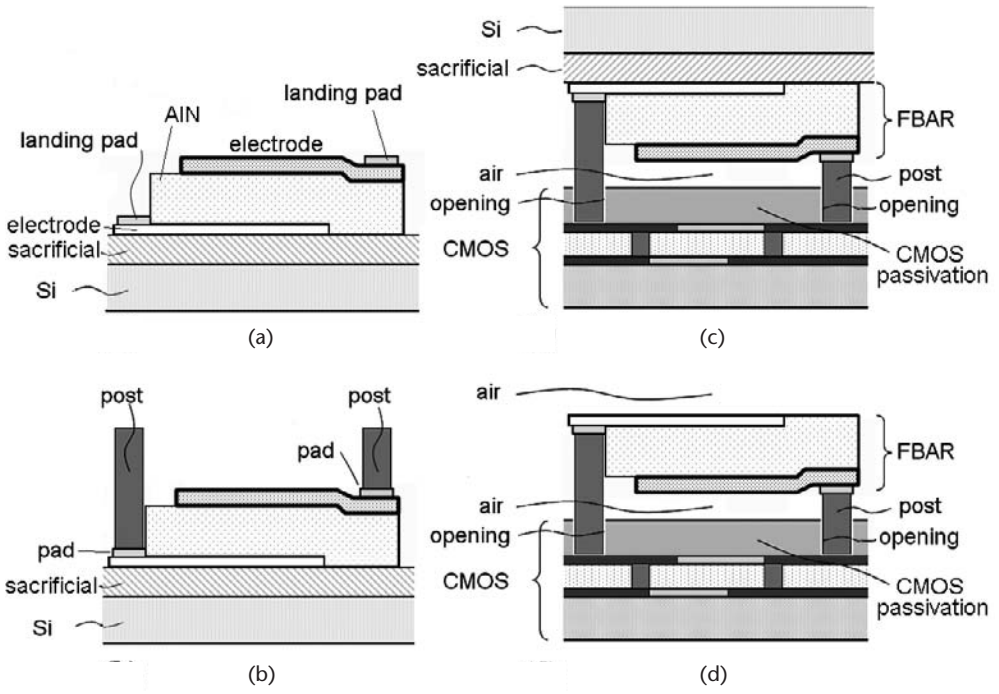

Figure 7.22 Cross-sectional view of the heterogeneous integration process of FBARs to CMOS substrates: (a) FBAR fabrication and landing-pad deposition; (b) contacting/supporting post deposition; (c) FBAR-to-CMOS interconnection (the FBAR wafer is flipped, face-down); and (d) sacrificial layer wet etching. (© IEEE 2008 [45].)

observed. The pick-and-place system is used now to align and contact the FBAR and CMOS wafers. In this example, the ensemble is introduced in an oven or a heater to accomplish the hard interconnection between both FBAR and CMOS substrates. Finally, the PSG sacrificial layer is attacked through wet etching on an HF buffered solution, thus releasing the Si substrate of the FBAR wafer. The SEM image of Figure 7.23(b) shows the integrated system, where the FBARs are connected to the CNM25 coplanar structures. It can be seen that the thin-film FBAR structure is placed about 40–50 μm above the substrate.

7.3.4 Characterization and Technology Optimization

We are interested on finding out whether the heterogeneous integration process is effective to obtain integrated devices with a high-quality factor. For this reason, we employ electrical characterization of the resonators to evaluate the process. The coplanar test structures will serve as this purpose. As commented in the previous section, the heterogeneous integration process was performed on two different standard CMOS technologies. Another example of CNM25-integrated FBARs is shown in Figure 7.24(a), whereas Figure 7.24(b) shows another resonator above an AMS035 CMOS substrate. Both devices are located 40–50 μm above their corresponding CMOS substrates (focus is laid on the resonators). In each case, the FBAR was integrated to a coplanar GSG test structure with pitch of 150 μm, in order to

(a)

(b)

Figure 7.23 Heterogeneous integration implementation: (a) stereoscopic image of the FBARs and the pillars placed on their contacting pads; and (b) SEM image of FBARs above the CNM25 CMOS substrate.

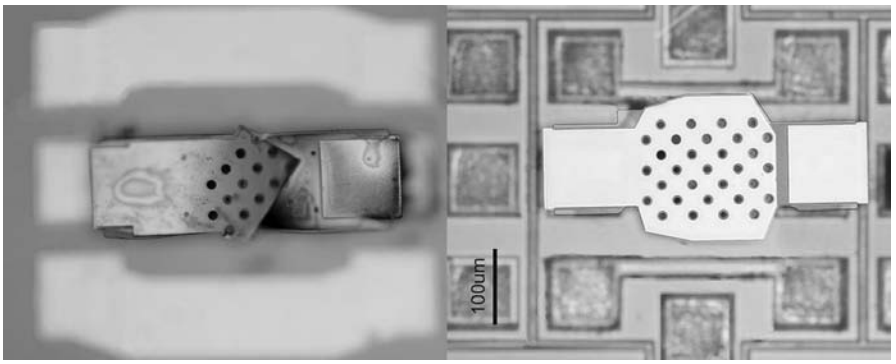

(a) (b)

Figure 7.24 Top-view optical images of floating FBAR integrated with two different CMOS substrates: (a) in-house standard CMOS, and (b) AMS 0.35-μm technology. (© IEEE 2008 [45].)

perform on-the-wafer characterization. The measurement setup comprises a coplanar RF-probe station and a network analyzer (the signal path is through the CMOS-FBAR-CMOS interfaces).

In Figure 7.25(a) the magnitude and phase of the S21 parameter of an exemplary device are plotted, with a resonance frequency of around 2.4 GHz observed. The Q factors of heterogeneously integrated FBARS and RIE-based FBAR devices with the same layout are compared in Figure 7.25(b). As observed, the floating FBAR process exhibits a better performance than the RIE-based process, thus suffering lower damping and achieving reduced substrate coupling. Looking at these curves, it should be said that larger variations in both the attenuation and phase shift are required to accomplish the in-band and out-of-band specifications of modern filter-applications. This goal can be achieved with higher Q-factor devices, which can be obtained after appropriate layout design of the electrodes, among other actions [46]. Due to the direct relationship between the Q factor and the FBAR electrode size, the high-Q-factor goal can be reached with bigger-sized devices.

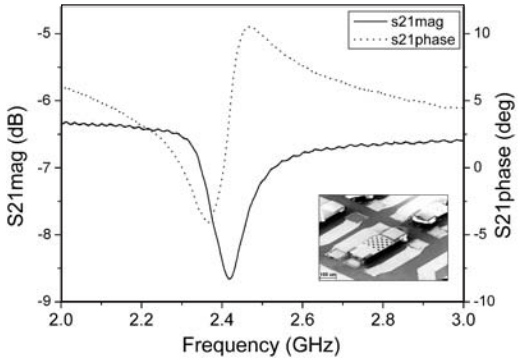

(a)

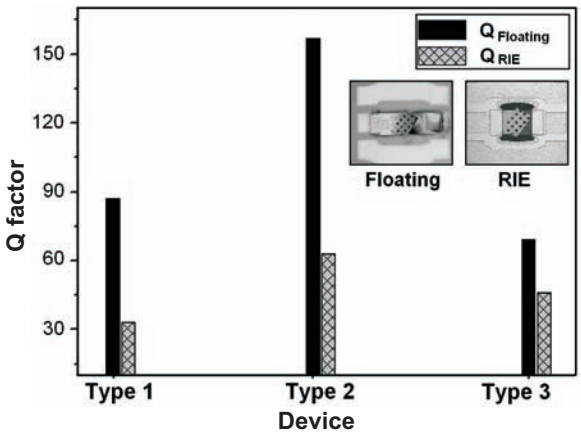

(b)

Figure 7.25 Electrical characterization of FBAR integrated with CNM25 standard-CMOS substrate: (a) magnitude and phase of the transmission (S21) parameter (characterized device in the SEM image of the inset); and (b) comparative performance of the Q factors of 3D-integrated and RIE-based FBARs (exemplary devices of each technology in the insets). (© IEEE 2008 [45].)

The thin-film structure of the FBAR makes it fragile and highly stressed. Thus, small devices should be fabricated to diminish the break-off risk and improve the process yield. On the other hand, the soldering technology requires deposition of bumps with a pitch of the order of 250 μm, each bump having a diameter of 80 μm (after heating). This leads to bigger-device layout design, thus increasing the die area. As a consequence, the mechanical rigidity and stability of the devices are reduced. A third issue is that postintegration cleaning of the integrated wafers is required, due to residual composites deposited on the surface of the CMOS wafer (and/or the FBAR wafer), as colateral products of bump melting. Additionally, the electrical properties of the soldering bumps as interconnecting paths are still to be studied, especially for the gigahertz-range frequency band.

Another technological possibility to pillar fabrication is electroplating. With this option, the soldering paste is replaced by a more uniform electroplated column, grown on top of either the CMOS or the FBAR wafers. The resulting product is a cleaner and sharper FBAR-CMOS ensemble, with reduced pitch dimensions, and, consequently, improved area efficiency. No additional layout design effort is required, since the same mask for landing pad and soldering bump definition is used for the electroplated pillar. The sequence of Figure 7.26 represents the technological process of the optimized FBAR-CMOS integration. The main difference in respect to Figure 7.22 is the description of the electroplating process for pillar construction.

Starting from the FBAR fabrication, the first electrode, AlN layer, and second electrode are successively deposited on top of a sacrificial layer (e.g., PSG), as depicted in Figure 7.26(a). Next, a passivation layer is deposited and patterned to feature the landing pads [Figure 7.26(b)]. Typically, this layer is a thick resist and

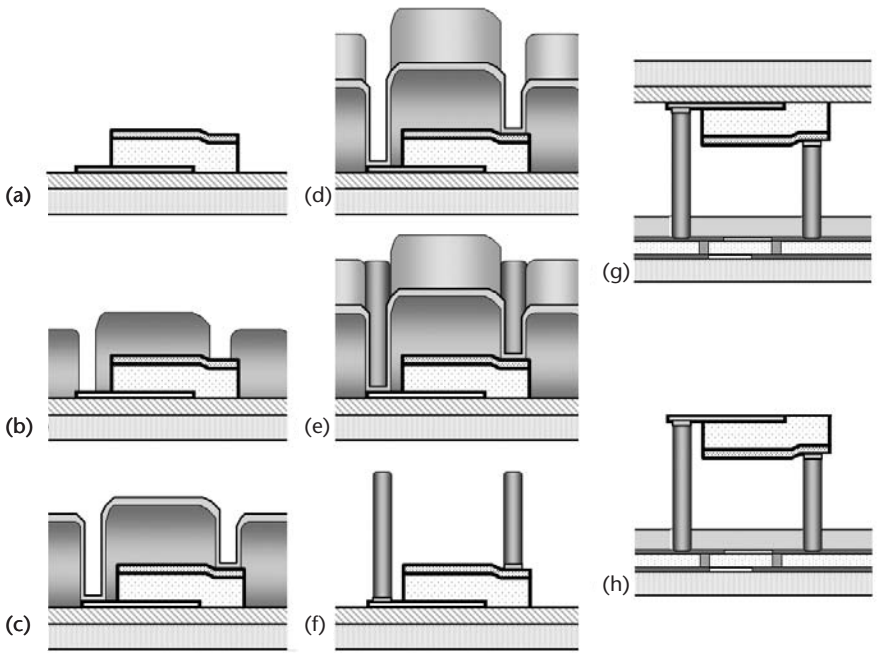

Figure 7.26 Electroplating-based optimized process sequence for heterogeneous integration of FBAR and CMOS wafers: (a) FBAR fabrication; (b) resist deposition; (c) seed material; (d) oxide deposition; (e) electroplating; (f) resist-oxide removing; (g) FBAR-CMOS wafers integration; and (h) sacrificial layer etching (FBAR released).

will be used to define the electroplating area. Then, a seed material for electroplating is deposited on the wafer as depicted in Figure 7.26(c). This material is a metal with good conductive properties, like Cu or Au. Since the process intends for wafer-level integration, the seed material is deposited along the whole wafer surface. Next, the same mask of Figure 7.26(b) is used to pattern another passivation layer, as depicted in Figure 7.26(d). This second passivation layer will contribute to limiting the growing area of the electroplated material, according to the supporting post mask design [Figure 7.26(e)]. Once the electroplating deposition is finished, the resist, seed material, and second passivation layer are removed to provide the final shape of the FBAR wafer before the integration [Figure 7.26(f)]. Note that Figure 7.26(b–f) could also be performed on the CMOS wafer. However, in spite of the standard nature of the CMOS process, this implementation describes a more general solution. The last two steps are basically the same as those already described at the beginning of this section, where the FBAR-CMOS interconnection is carried out [Figure 7.26(g)] and the sacrificial layer is attacked to release the Si substrate, thus completing the process [Figure 7.26(h)].

In considering this process, a new design with reduced pillar diameter and pitch can be achieved. In the previous example, they were equal to 80 μm and 250 μm, respectively. With the optimization introduced by this process, these values can be reduced to 25 μm and 100 μm. Shrinking the pillar dimensions and pitch is of special relevance to this integration approach, because it permits a more compact and robust design of the FBAR structure. Since the AlN and electrode intersections define the effective resonator area, the remaining electrode and AlN areas can be reduced to provide shorter structures. This alleviates the high stress of the floating FBAR structure. Additionally, this feature lets a higher FBAR density in the wafer, due to reduced distance between devices. Figure 7.27 illustrates these effects. Figure 7.27(a) shows top-view representations of FBARs, the landing pads, and the effects of optimized electroplating process in the pad size reduction. In the same way, the pitch reduction permits a higher number of FBARs to be located on a determined area, as depicted in Figure 7.27(b). Clearly, the new structures are expected to be more robust and efficient.

7.4 Summary

In this chapter, we have reviewed the concepts and technological approaches for CMOS integration of micro- and nanodevices. Hybrid, monolithic, and heterogeneous integration, along with implementation examples of them, was discussed. Special emphasis was given to MEMS, NEMS, SAW, and FBAR resonators, thus introducing state-of-the-art integrated-resonator technologies and applications. At this point, we paid our attention to the latest 3D integration techniques implementing advanced processes. With this review, we entered into Section 7.3 to study a method of heterogeneous integration of FBAR and CMOS technologies [47]. We have also studied two implementations of the heterogeneous integration of FBARs and two different CMOS processes. As we have seen, the integrated FBARs exhibit a floating, three-dimensional structure above the CMOS substrates [45]. This method has shown us how compatibility requirements can be minimized to achieve

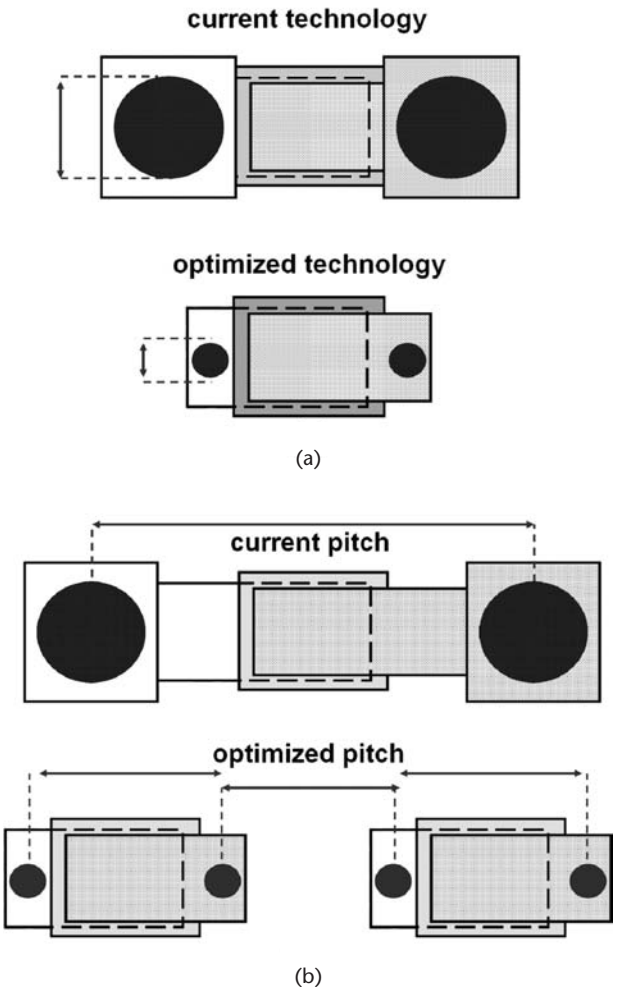

Figure 7.27 FBAR layout optimization due to the electroplating-based fabrication of the supporting posts: (a) pitch reduction; and (b) pad-size reduction, compared in both cases to the soldering bump process.

full integration of such different technologies. Since the processes do not require special manufacturing restrictions—like deposition temperature of the FBAR acoustic layer—enhanced flexibility and versatility may be achieved for the FBAR-to-CMOS interconnection technology.

Heterogeneous integration exhibits many benefits over traditional hybrid and monolithic integration of micro- and nanoresonators. Compared to standard flip-chip implementations [48], for example, this method presents two main advantages: wafer-level integration and no carrying substrate attached to the resonator. This saves the long processing time of batch resonator-to-CMOS integration. Heterogeneous integration can be seen as a kind of packaging technology serving as a protective means [49]. Additionally, it features interconnection to the integrated ensemble. On the other hand, it avoids the constraints of costly and technology-specific monolithic integration [50]. In summary, some of the main benefits introduced by heterogeneous integration can be stated as follows:

1. Technology-independent integration process;
2. No need for integration-oriented resonator technology (e.g., process temperature);
3. No need for integration-oriented IC technology;
4. Versatility and flexibility of the IC technology;
5. Possibility of wafer-level or die-level integration;
6. Reduced die area (compared to onside resonator integration);
7. Versatility and flexibility of the interconnection technology (e.g., solder bumping, electroplating).

References

[1] Baltes, H., et al., "CMOS MEMS—Present and Future," *Proc. IEEE Intl. Conf. MEMS 2002*, Las Vegas, NV, January 20–24, 2002, pp. 459–466.

[2] ST Microelectronics, System on Chip, http://www.st.com/stonline/products/technologies/soc/soc.htm.

[3] Geschke, O., H. Klank, and P. Telleman, (eds.), *Microsystem Engineering of Lab-on-a-Chip Devices*, New York: John Wiley & Sons, 2004.

[4] Herold, K. E., and A. Rasooly, (eds.), *Lab-on-a-Chip Technology: Fabrication and Microfluidics*, San Francisco, CA: Caister Academic Press, 2009.

[5] Royal Society of Chemistry, Lab on a Chip, http://www.rsc.org/Publishing/Journals/lc/index.asp.

[6] Tea, N. H., et al., "Hybrid Postprocessing Etching for CMOS-Compatible MEMS," *IEEE/ASME J. Microelectromech. Syst.*, Vol. 6, 1997, pp. 363–372.

[7] Latorre, L., et al., "Characterization and Modeling of a CMOS-Compatible MEMS Technology," *Sens. Actuator A-Phys.*, Vol. 74, No. 1-3, 1999, pp. 143–147.

[8] Lund, J. L., et al., "A Low Temperature Bi-CMOS Compatible Process for MEMS RF Resonators and Filters," *Proc. Solid-State Sensor, Actuator and Microsystems Workshop 2002*, Hilton Head Island, SC, June 2–6, 2002, pp. 38–41.

[9] Sundaresan, K., et al., "Electronically Temperature Compensated Silicon Bulk Acoustic Resonator Reference Oscillators," *IEEE J. Solid-State Circuits*, Vol. 42, 2007, pp. 1425–1434.

[10] Pourkamali, S., Z. Hao, and F. Ayazi, "VHF Single Crystal Silicon Capacitive Elliptic Bulk-Mode Disk Resonators—Part II: Implementation and Characterization," *IEEE/ASME J. Microelectromech. Syst.*, Vol. 13, 2004, pp. 1054–1062.

[11] Smith, J. H., et al., "Embedded Micromechanical Devices for the Monolithic Integration of MEMS with CMOS," *Proc. IEEE Intl. Electron Devices Meeting IEDM 1995*, Washington, D.C., December 10–13, 1995, pp. 609–612.

[12] Infineon Technologies, Pressure Sensors, http://www.infineon.com/sensors.

[13] Hierold, C., "Intelligent CMOS Sensors," *Proc. IEEE Intl. Conf. MEMS 2000,* Miyazaki, Japan, January 23–27, 2000, pp. 1–6.

[14] Florence, J. M., and L. A. Yoder, "Display System Architectures for Digital Micromirror Device (DMD)–Based," *Proc. SPIE Projection Displays II*, San Jose, CA, January 29, 1996, Vol. 2650, pp. 193–208.

[15] Verd, J., et al., "Integrated CMOS–MEMS with On-Chip Readout Electronics for High-Frequency Applications," *IEEE Electron Dev. Lett.*, Vol. 27, 2006, pp. 495–497.

[16] Campabadal, F., et al., "CMOS Degradation Effects due to Electron Beam Lithography in Smart NEMS Fabrication," *Proc. SPIE Symposium on Microtechnologies for the New Millennium 2005*, Sevilla, Spain, May 9–11, 2005, Vol. 5836, p. 667.

[17] IBM Zurich Research Laboratory, Device Integration, http://www.zurich.ibm.com/st/server/microdevice.html.

[18] Geske, J., et al., "Vertical and Lateral Heterogeneous Integration," *Appl. Phys. Lett.*, Vol. 79, 2001, pp. 1760–1762.

[19] Roozeboom, F., et al., "Passive and Heterogeneous Integration Towards a Si-Based System-in-Package Concept," *Thin Solid Films*, Vol. 504, 2006, pp. 391–396.

[20] Arcamone, J., et al., "Full-Wafer Fabrication by Nanostencil Lithography of Micro/Nanomechanical Mass Sensors Monolithically Integrated with CMOS," *Nanotechnology*, Vol. 19, 2008, 305302.

[21] Chiou, J.-C., L.-J. Shieh, and Y.-J. Lin, "CMOS-MEMS Prestress Vertical Cantilever Resonator with Electrostatic Driving and Piezoresistive Sensing," *J. Phys. D: Appl. Phys.*, Vol. 41, 2008, 205102.

[22] Yunseong, E., et al., "Reference SAW Oscillator on Quartz-on-Silicon (QoS) Wafer for Polylithic Integration of True Single Chip Radio," *IEEE Electron Dev. Lett.*, Vol. 21, No. 8, 2000, pp. 393–395.

[23] Yeonwoo, K., E. Yunseong, and L. Kwyro, "Polylithic Integration of a Reference SAW Quartz-on-Siliconoscillator for Single-Chip Radio," *Digest of Technical Papers IEEE International Solid-State Circuits Conference ISSCC 2002*, Vol. 1, 2002, pp. 186–459.

[24] Furuhata, M., et al., "Development of Monolithic CMOS-SAW Oscillator," *Proc. IEEE Intl. Ultrason. Symp., 2005*, Vol. 4, Rotterdam, the Netherlands, September 18–21, 2005, pp. 2194–2197.

[25] Nordin, A. N., and M. E. Zaghloul, "Modeling and Fabrication of CMOS Surface Acoustic Wave Resonators," *IEEE Trans. on Microwave Theory Tech.*, Vol. 55, No. 5, 2007, pp. 992–1001.

[26] Otis, B. P., and J. M. Rabaey, "A 300-μW 1.9-GHz CMOS Oscillator Utilizing Micromachined Resonators," *IEEE J. Solid-State Circuits*, Vol. 38, 2003, pp. 1271–1274.

[27] Chee, Y. H., A. M. Niknejad, and J. M. Rabaey, "An Ultra-Low-Power Injection Locked Transmitter for Wireless Sensor Networks," *IEEE J. Solid State Circuits*, Vol. 41, 2006, pp. 1740–1748.

[28] Zhang, H., et al., "5GHz Low Phase-Noise Oscillator Based FBAR with Low TCF," *Proc. 13th International Conference on Solid-State Sensors, Actuators and Microsystems Transducers 2005*, Seoul, Korea, June 5–9, 2005, pp. 1100–1101.

[29] Avago Technologies, http://www.avagotech.com.

[30] Pang, W., et al., "A Temperature-Stable Film Bulk Acoustic Wave Oscillator," *IEEE Electron Dev. Lett.*, Vol. 29, 2008, pp. 315–318.

[31] Dunn, W. C., et al., "Monolithic Circuit with Integrated Bulk Structure Resonator," U.S. Patent 5,260,596, November 1993.

[32] Lee, K., Y. S. Eo, and S. Hyun, "Single-Chip Radio Structure with Piezoelectric Crystal Device Integrated on Monolithic Integrated Circuit and Method of Fabricating the Same," U.S. Patent 6,285,866, September 2001.

[33] Dubois, M.-A., et al., "Integration of High-Q BAW Resonators and Filters Above IC," *IEEE Intl. Solid-State Circuits Conf. Dig. of Tech. Papers, 2005*, San Francisco, CA, February 6–10, 2005, pp. 392–393.

[34] Carpentier, J. F., et al., "A SiGe:C BiCMOS WCDMA Zero-IF RF Front-End Using an Above-IC BAW Filter," *IEEE Intl. Solid-State Circuits Conf. Dig. of Tech. Papers, 2005*, San Francisco, CA, February 6–10, 2005, pp. 394–395.

[35] Aissi, M., et al., "A 5 GHz Above-IC FBAR Low Phase Noise Balanced Oscillator," *Proc. IEEE Radio Frequency Integrated Circuits Symposium RFIC-2006*, Vol. 1, San Francisco, CA, June 11–13, 2006, pp. 25–28.

[36] Figueredo, D., et al., "Thin Film Bulk Acoustic Resonator (FBAR) and Inductor on a Monolithic Substrate and Method of Fabricating the Same," U.S. Patent 6,710,681, March 2004.

[37] Forsen, E., et al., "Ultrasensitive Mass Sensor Fully Integrated with Complementary Metal-Oxide-Semiconductor Circuitry," *Appl. Phys. Lett.*, Vol. 87, 2005, 043507-1-3.

[38] Ilic, B., et al., "Attogram Detection Using Nanoelectromechanical Oscillators," *J. Appl. Phys.*, Vol. 95, 2004, pp. 3694–3703.

[39] Shimoda, T., and S. Inoue, "Surface Free Technology by Laser Annealing (SUFTLA)," *IEEE Electron Devices Meeting IEDM 1999 Digest Tech. Papers*, Washington, D.C., December 5–8, 1999, pp. 289–292.

[40] Seiko Epson Corporation, "Epson Develops the World's First Flexible 8-Bit Asynchronous Microprocessor," http://www.epson.co.jp/e/newsroom/2005/news_2005_02_09.htm

[41] Niklaus, F., S. Haasl, and G. Stemme, "Arrays of Monocrystalline Silicon Micromirrors Fabricated Using CMOS Compatible Transfer Bonding," *IEEE/ASME J. Microelectromech. Syst.*, Vol. 12, No. 4, 2003, pp. 465–469.

[42] Populin, M., et al., "Thermosetting Nano-Imprint Resists: Novel Materials for Adhesive Wafer Bonding," *Proc. IEEE Intl. Conf. MEMS 2007*, Kobe, Japan, January 21–25, 2007, pp. 239–242.

[43] Kim, E. -K., "Thin Film Resonator and Method for Manufacturing the Same," U.S. Patent 6,849,475 B2, February 2005.

[44] Austria Microsystems, AMS035c3b4, 2-poly 4-metal 0.35 μm CMOS technology, http://www.austriamicrosystems.com.

[45] Campanella, H., et al., "Thin-Film Bulk Acoustic Wave Resonator Floating Above CMOS Substrate," *IEEE Electron Device Lett.*, Vol. 29, 2008, pp. 28–30.

[46] Su, Q. X., et al., "Thin-Film Bulk Acoustic Resonators and Filters Using ZnO and Leadzirconium-Titanate Thin Films," *IEEE Trans. on Microwave Theory Tech.*, Vol. 49, 2001, pp. 769–778.

[47] Campanella, H., et al., "Thin-Film Bulk Acoustic Wave Resonator and Method for Performing Heterogeneous Integration of the Same with Complementary-Metal-Oxide-Semiconductor Integrated Circuit," European Patent Office App. 07380041.9, February 2007.

[48] Vanhelmont, F., et al., "A 2GHz Reference Oscillator Incorporating a Temperature Compensated BAW Resonator," *Proc. IEEE Intl. Ultrason. Symp. 2006*, Vancouver, BC, October 3–6, 2006, pp. 333–336.

[49] Feld, D., et al., "A Wafer Level Encapsulated FBAR Chip Molded into a 2.0 mm/spl times/ 1.6 mm Plastic Package for Use as a PCS Full Band Tx Filter," *Proc. IEEE Intl. Ultrason. Symp. 2003*, Vol. 2, Honolulu HI, October 5–8, 2003, pp. 1798–1801.

[50] Dubois, M. -A., et al., "Integration of High-Q BAW Resonators and Filters Above IC," *IEEE Intl. Solid-State Circuits Conf. Dig. of Tech. Papers, 2005*, San Francisco, CA, February 6–10, 2005, pp. 392–393.

CHAPTER 8

Sensor Applications

A micro- or nanosensor is the part of a microsystem that inputs information into the system comprised of the electronic circuit that conditions the sensor signal, the actuator responding to the electrical signals generated within the circuit, and the sensor itself. Thus, the sensor is the interface to the outside world. It converts the input signal from its physical domain to the electrical domain (the actuator works in the opposite way). The technological advancements of the micro- and nanoelectronic engineering fields have led to a drastic reduction of size and prize in sensors and have enabled sensor integration into single microelectronic chips. In this way, many microsensors (and most recently nanosensors) take advantage of the silicon technologies and the well-known electrical and mechanical properties of this material. Other materials have also been studied and are important elements of modern miniature MEMS, NEMS, and acoustic sensors.

There exist many detection mechanisms including piezoresistivity, piezoelectricity, electrostatic, magnetic, optical, and resonant techniques. Resonant sensors offer many benefits, like improved sensitivity and accuracy, and reduced power consumption, among others. Due to the action of the external excitation, resonator-based sensors change their resonance frequencies, which is detected by a read-out electronic circuit. This change is directly proportional to the magnitude of the input signal, which can be given in one of the physical domains previously mentioned.

The chapter focuses on resonant sensors, and more particularly the main emphasis is on mass and mechanical sensors. Mass sensors detect the amount of mass deposited on the surface of the resonator and the physical mechanism of detection is known as the mass-loading effect. Thus, the added mass of a film or body deposited on the resonator brings about down shifting of its resonance frequency. On the other hand, mechanical sensors perform pressure, force, acceleration, torque, inertial, and flow sensing, and the physical mechanism involves a strain added to the resonator structure, thus increasing the resonance frequency of the device. In the following sections, we study the concepts, technologies, and some of the most popular MEMS-, NEMS-, and FBAR-based resonant sensor applications.

8.1 Resonant Sensing Performance

Resonant sensing has many benefits over nonresonant techniques, like improved sensitivity, resolution, and accuracy. The recent advances of material science and fabrication technology have also enabled the manufacturing of low-power and

highly temperature stable resonators. Table 8.1 compares the main features of resonant sensing against capacitive and piezoresistive techniques.

Nevertheless, performance benefits are achieved at the cost of added complexity of fabrication processes, in particular those related with packaging and vacuum operation. As we discuss next, the resonator's Q factor, its geometry, and the characterization technique determine the ultimate resolution and performance of the sensor.

8.1.1 The Role of the Q Factor on Resolution

In Chapter 1 we reviewed the damping mechanisms affecting the Q factor of resonators. Now, we revisit the Q factor from the sensor performance perspective and more specifically with the frequency resolution, because the measurand (mass, pressure, acceleration) is a function of frequency (or time). The smaller the frequency value that can be discriminated is, the smaller the measurand magnitude that we are able to quantify is. Thus, two aspects relate with frequency discrimination: phase stability of the resonator, and the frequency response evaluation method.

The phase stability issue arises from the Q factor definition considering the open-loop phase response $\phi(\omega)$ of the resonator, which we discussed in Chapter 4. We reproduce it convenience of the reader:

$$Q = \frac{\omega_S}{2}\left|\frac{\partial \phi}{\partial \omega}\right| \tag{8.1}$$

Determining the frequency resolution Δf passes from quantifying the phase stability $\Delta\phi$. The practical matter is how to proceed with experimental phase data and (8.1). Typically, we perform statistical analysis on phase data collected at the resonance frequency to extract mean values and standard deviation. The latter can be considered the actual phase deviation $\Delta\phi$ around a mean phase value, using Allan's deviation or similar criteria [2]. On the other hand, and referring to Figure 5.8(a), for example, we know that fast slope changes ϕm occur near the resonance frequency. With this at hand, the frequency resolution is expressed by:

$$\Delta f = \left.\frac{\Delta\phi}{\phi m}\right|_{f_0} \tag{8.2}$$

Table 8.1 Comparative Performance of Resonant, Piezoresistive, and Capacitive Sensing Techniques

Item	*Resonant*	*Piezoresistive*	*Capacitive*
Resolution	1 part in 10^8	1 part in 10^5	1–10 parts in 10^5
Accuracy	10–1,000 ppm	500–10,000 ppm	100–10,000 ppm
Power consumption	~1 nW	~1 mW	< 0.1 mW
Temperature factor	~1 ppm/°C	> 1,000 ppm/°C	1–10 ppm/°C

Source: [1].

The size of resonators also affects the Q factor, as we know from the damping models of electromechanical and acoustic resonators examined in previous chapters. Therefore, we state three considerations regarding the resolution of the sensor:

1. Sensitivity augments proportionally to the Q factor, because the frequency resolution grows with Q (regarding (8.2)).
2. Sensitivity augments proportionally to the size of the resonator [regarding (1.9), (3.12), (3.13), and, in general, the electromechanical models of MEMS and FBARs].
3. Sensitivity augments proportionally to the central frequency of the resonator [3].

Characterization method is the second aspect that determines the frequency resolution of the sensor. Frequency-domain techniques include S-parameter characterization, amplitude spectrum, and power spectrum, among others. These techniques do require specification of the intermediate frequency (IF) filter bandwidth, which determines the amount of out-of-band noise filtering. Time-domain techniques, on the other hand, allow the Q factor characterization and read-out circuits suitable for electronic integration with the sensor in full system implementation. Frequency-analysis integrated circuits [4], zero-crossing, and threshold-crossing frequency counting techniques [5], among others, have demonstrated outstanding resolution of 1 Hz and less. Actually, the characterization-related resolution is limited only by the available IC technology and instrumentation hardware, as the ultimate resolution of the sensor relies on the resonator design and physical damping mechanisms.

8.1.2 Performance Features and Parameters

Material properties, operation mode, and geometry also affect the sensitivity performance of resonant sensors. If we look into the design equations of resonators, and more specifically of the sensor, we realize that sensitivity is dependent on geometric parameters and the mechanical configuration of the structure on which the resonator is located.

In order to compare resonant and nonresonant techniques, we need to point out the sensitive elements of capacitive, piezoresistive, piezoelectric, and resonant devices. Sensitivity is measured in terms of a dimensionless quantity termed the gauge factor (GF), which equals the relative change in the detection variable divided by the actuated variable. For example, piezoresistive and piezoelectric devices are strain sensitive. Capacitive transduction is sensitive to the parallel-plate distance and overlap area. Electromechanical resonance depends on thickness and length, and acoustical resonance on the thickness. Additionally, the sensor application determines the GF form, as the case of mass sensors where the density (mass) is the actuated variable. Table 8.2 summarizes the gauge factors, gauge functions, and sensitive variables for resonant and other sensing techniques.

Sensitivity is maximized when the detection device is located at the point where the gauge factor is maximum (i.e., where the biggest response is obtained with a minimum effort on the actuated variable). The stress contour plot of the cantilever

Table 8.2 Performance Features and Parameters of Sensing Techniques

Sensing	*Gauge Function*	*Gauge Factor*	*Sensitive Variable*
Piezoresistive	$R = \frac{\rho L}{A}$;	$GF = \frac{\Delta R/R}{\varepsilon}$;	Length L
	R: resistance, ρ: density, L: length, A: area	ε: strain ($\varepsilon = \Delta L/L$)	
Capacitive	$C = \varepsilon_r \varepsilon_0 \frac{A}{t}$;	$GF_1 = \frac{\Delta C/C}{\Delta A/A}$;	Area A Thickness t
	C: capacitance, ε: permittivity, t: thickness	$GF_1 = \frac{\Delta C/C}{\Delta t/t}$;	
Piezoelectric	$Q_i = d_{ij} F_j$;	$GF_1 = \frac{\Delta Q/Q}{\varepsilon}$	Thickness t or length L
	Q: charge, d: piezoelectric constant, F: force	ε: strain (DL/L)	
Resonant (electromechanical)	$f_n = \frac{1}{2\pi}\left(\frac{\gamma_n}{L}\right)^2 \sqrt{\frac{E \cdot I \cdot L}{m}}$	ε: strain (DL/L)	Length L
Resonant (acoustical)	$f_0 = \frac{1}{4\pi t}\sqrt{\frac{E}{\rho}}$	$GF_1 = \frac{\Delta f/f_0}{\Delta t/t}$	Thickness t or density ρ

in Figure 8.1 illustrates the concept: stress is maximum near the clamping surface. Thus, a big change in piezoresistance or frequency will be achieved with low strain if the piezoresistor or the resonator is placed on these regions.

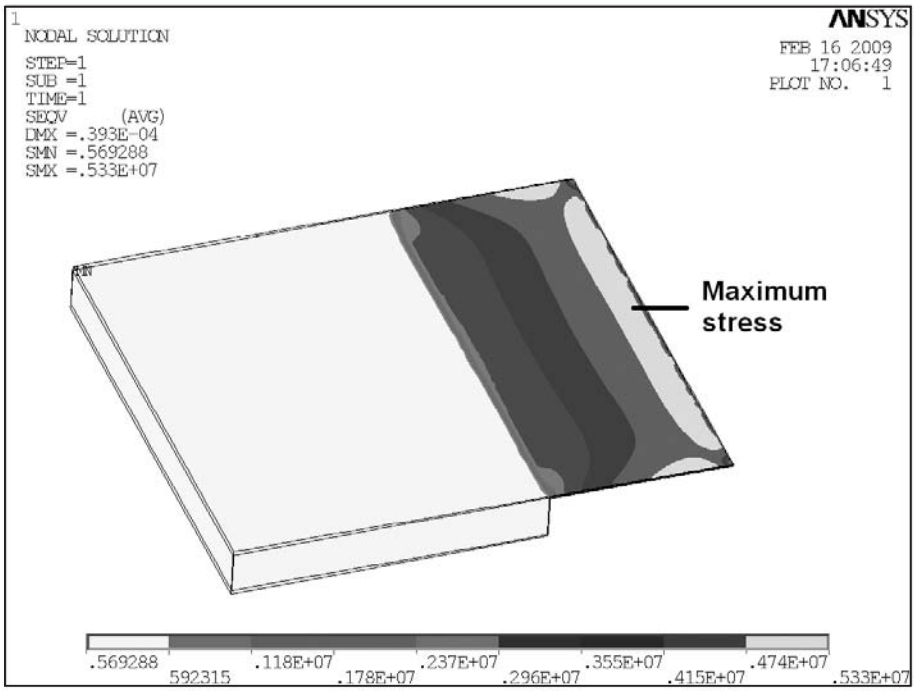

Figure 8.1 Stress contour plot of a cantilever: maximum sensitivity is obtained around the clamping points.

8.2 Mass Sensors

Miniature mass sensors have wide applications in physical, chemical, and biologic systems, and their sensitivities have made them starring devices in new, convergent microdevices and nanodevices. The operating principle behind mass sensors is the mass loading effect. Therefore, the mass deposited on the resonator brings about down shifting of its resonance frequency. Within the operation limits of the sensor technology, the frequency shifting is directly proportional to the amount of the deposited mass. The fabrication technology of the resonator conditions the manner in which the mass can be deposited.

Mass loading can happen in air, gas, or liquid media, and a physical or chemical interaction between the resonator surface and the medium is needed to fix the mass to the resonator. In some applications, the mass is temporarily deposited, because it is a volatile compound that evaporates or reacts with the media. Strictly speaking, mass loading occurs when a thin-film material grows or is deposited on the resonator in a localized or distributed way, thus covering part or the whole active surface of the device. For example, thin-film devices like FBARs experience mass loading when their composing layers are stacked to fabricate the device metal electrodes.

Resonant mass sensors are characterized by their frequency responses, which are evaluated through frequency-domain read-out circuits or instrumentation. Their sensitivity depends on the resonance frequency, the detection system resolution, and the Q factor of the resonator, among others. Thus, resonators with high resonance frequencies and Q factors and low-noise detection will exhibit improved sensitivity than that of low-frequency, low–Q factor, and poor-frequency resolution devices. An unavoidable consequence of mass loading is that it increases the damping, thus decreasing the resonator Q factor. For that reason, the resonator is designed with regard to the application and the sensing medium, which also contributes to the Q factor reduction (damping losses are severe in liquid and dense fluids).

Commercially available mass sensors are implemented with acoustic QCM, SAW, and BAW resonators. Also, MEMS- and NEMS-based sensors are being investigated to perform distributed or localized high-sensitivity mass detection. They can be used as distributed-mass or as localized-mass sensors. A distributed-mass sensor makes use of its whole surface to detect the amount of mass on it, which is deposited, grown, or adhered to it by physical or chemical means. On the other hand, the localized-mass sensor detects the mass of a body with lateral dimensions (in contact with the resonator surface) small enough in comparison to those of the electrode area. The mass sensing capabilities of each technology rely on the different mechanisms described in the following sections.

8.2.1 MEMS-Based Microbalances

The MEMS-based resonant mass sensors perform mass detection by detecting the frequency shifting of the fundamental mechanical or first-overtone resonance modes. As we study later, other sensors make use of higher-order flexural modes to detect the added mass on their surface. The sensing structure of most of the MEMS-based sensor is made of silicon (Si). In this way, MEMS sensors exhibit high

mass sensitivity due to the excellent mechanical properties of Si. Another advantage of Si-made sensors is their full compatibility with standard CMOS processes and low fabrication costs. Nevertheless, other materials can also be implemented as the structural layer of the resonator.

The MEMS sensors have physical dimensions with a high aspect ratio, typically ranging from units to hundreds of micrometers. The cantilever is the preferred structure of highly sensitive mass sensors. Optimization of its dimensions achieves mass sensitivity maximization through a high surface area–to-mass ratio. In Chapter 2 we examined the resonance frequency of the MEMS cantilever, reproduced here for convenience:

$$f_n = \frac{1}{2\pi}\frac{\alpha_n^2}{l^2}\sqrt{\frac{EIl}{m_{eff}}} \tag{8.3}$$

where f_n is the n-mode resonance frequency, E is the Young's modulus, l is the beam length, I is the moment of inertia, and m_{eff} is the effective mass of the cantilever. The coefficient α_n depends on the n-mode number [6]. Equivalently, (8.3) may be expressed in terms of the spring-damped-mass system:

$$f_n = \frac{1}{2\pi}\sqrt{\frac{k}{m_{eff}^n}} \tag{8.4}$$

where k is the spring constant of the cantilever and m_{eff}^n is the effective mass of the nth mode of resonance. The mass Δm deposited on the cantilever changes both the stiffness and the effective mass of it. If the added mass is small enough, in comparison to the cantilever mass, we can assume no change of the elastic properties and neglect the stiffness variation. Thus, the net effect of Δm contributes to decrease the resonance frequency to a value defined by the first-order approximation:

$$\frac{\Delta f}{f_n} = -\frac{1}{2}\frac{\Delta m}{m_{eff}^n} \tag{8.5}$$

where Δf is the resonance frequency shifting. The optimization of the cantilever design aims to maximize the mass sensitivity S_m of the device:

$$S_m = \frac{\Delta f}{\Delta m} \tag{8.6}$$

Looking at (8.4) and (8.5), we can see how smaller cantilevers will exhibit higher resonance frequencies and improved mass sensitivity. This can be controlled through different approaches. Hwang et al. optimized the design of a piezoelectric cantilever intended for biosensing applications by the Taguchi method [7], thus using the first resonance frequency, the separation factor between the resonance frequencies, and the sensing signal of the piezoelectric cantilever as the object functions [8]. According to this method, they optimize the sensitivity of the cantilever to the binding between the antigen and the antibody by considering the combined effect of the length, width, thickness, and width-to-length ratio of the cantilever. In

this way, they maximize the first resonance frequency and the separation factor between the first and the second resonance frequencies.

Narducci et al. have studied how the sensitivity of Si T-shaped cantilever resonators for mass sensing applications augments by detecting the higher-order resonance modes and reducing the device dimensions [9]. The T-shaped cantilevers shown in Figure 8.2 are released through back-side etching, and they are piezoelectrically actuated. The detection is carried out by four piezoresistors in a Wheatstone bridge configuration. They demonstrated how, for these resonators, performing the detection at the second resonance mode improves the mass sensitivity by a factor of 4.1. Also, the sensitivity gain is 16 when the length and width of the cantilever are halved, thus achieving an S_m value equal to 1.3 Hz/pg.

Further reduction of microcantilever dimensions has been proposed by Davila et al., with the purpose of detecting *Bacillus anthracis Sterne* spores in air and liquid [10]. They implement microcantilevers whose resonance frequency is detected with the use of a laser Doppler vibrometer (LDV) after thermal-noise source excitation. Aside from the investigations on the viscous effects in the cantilever response, Davila et al. performed biological experiments involving suspended spores on the cantilevers in air and water. Figure 8.3(a) shows a dark field photograph of a 20-μm-long cantilever with spores deposited on it and then after measurements in water, and the SEM image of Figure 8.3(b) details a small group of spores on the

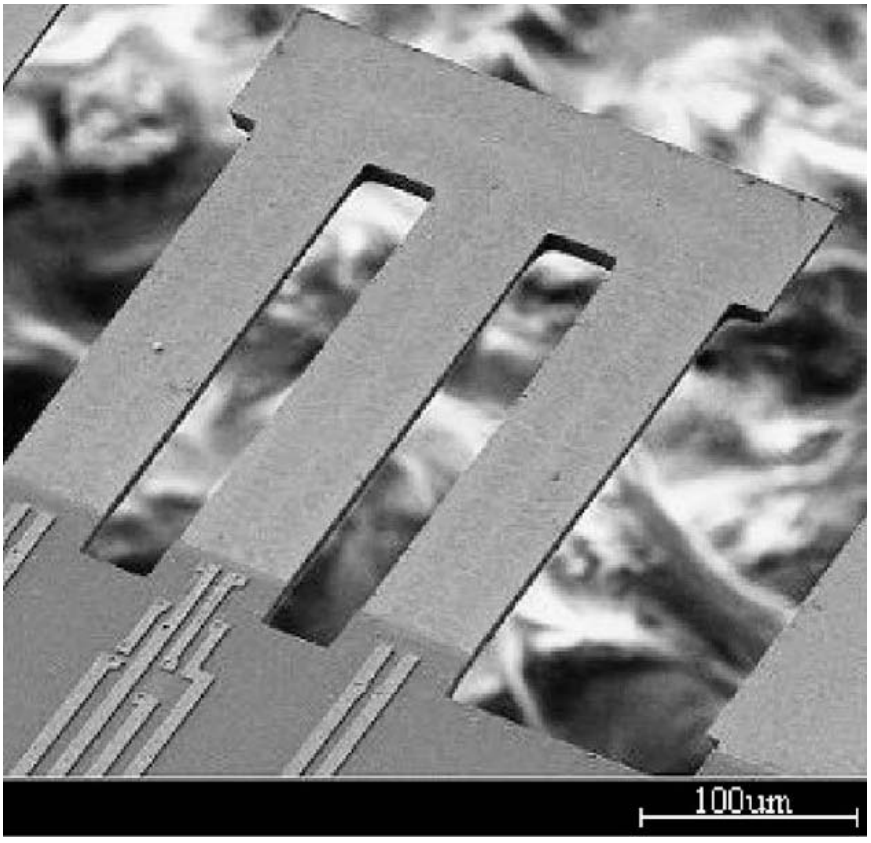

Figure 8.2 T-shaped cantilever for mass detection applications (length: 400 μm, width: 300 μm, thickness: 15 μm). (© 2009 Elsevier [9].)

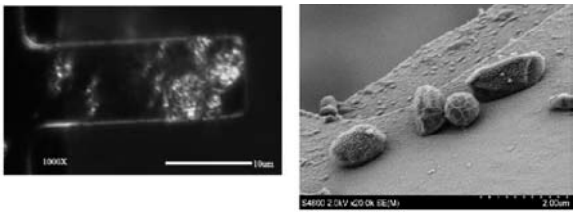

(a) (b)

Figure 8.3 Microcantilevers for detecting *Bacillus anthracis Sterne* spores in air and liquid: (a) dark field photograph of a 20-μm-long cantilever after measurements in water; and (b) SEM image showing different spores on the cantilever. (© 2007 Elsevier [10].)

cantilever in air. For detection of spores in water, the cantilevers were functionalized with antibodies in order to fix the spores onto the surface. With this setup, they could detect a minimum of 2 spores (740 fg) and 50 spores (139 pg) in air and water, respectively, with 20-μm-long, 9-μm-wide, and 200-nm-thick cantilevers, thus obtaining measurement sensitivities of 9.23 Hz/fg for air and 0.1 Hz/fg for water.

Aside from microcantilevers, other MEMS structures have been explored to perform high-sensitivity mass detection. Ismail et al. designed a degenerate mode resonant mass sensor with a cyclically symmetric structure [11]. The simplest structure with these features is a circular diaphragm, which supports pairs of independent modes of vibration sharing a common natural frequency, thus referred to as degenerated modes. If an extra mass is added to the structure over predefined regions, then the degeneracy can be broken, and this produces a separation of the previously identical frequencies. The frequency split is the output of the sensor and is proportional to the added mass. Due to its design, the sensor is frequency self-compensated and the ambient effects equally influence both modes, thus preserving the frequency split for a given mass. Figure 8.4 shows the layout of the polysilicon diaphragm resonator.

Other interesting MEMS structures are the high-frequency silicon columnar microresonators reported by Kehrbusch et al. [12]. Within their fabrication technique, they can control the dimensions of the microresonators on a scale of at least 1 μm, as the SEM images of Figure 8.5 show. According to the characterized mechanical properties of the silicon columns, they resonate at the lowest flexural mode of 3–7 MHz with quality factors of up to 2,500 in air and ~8,800 under vacuum conditions. The columnar microresonators were operated as a mass microbalance with a sensitivity of 1 Hz/fg and an experiment-deduced mass detection limit of 25 fg.

Multiple MEMS-based mass sensors implement arrays of devices intended for multiple particle detection. Villarroya et al. developed an on-chip array of polysilicon cantilevers, which are monolithically integrated with the CMOS read-out circuit [13]. They successfully demonstrated the electrostatic excitation and detection of 4-resonator and 8-resonator cantilever arrays with submicron dimensions of the integrated cantilevers. As long as they scaled the cantilever dimensions, they achieved a mass sensitivity of 28 Hz/fg, the expected mass resolution in vacuum being of units of femtograms (fg). The optical images of Figure 8.6

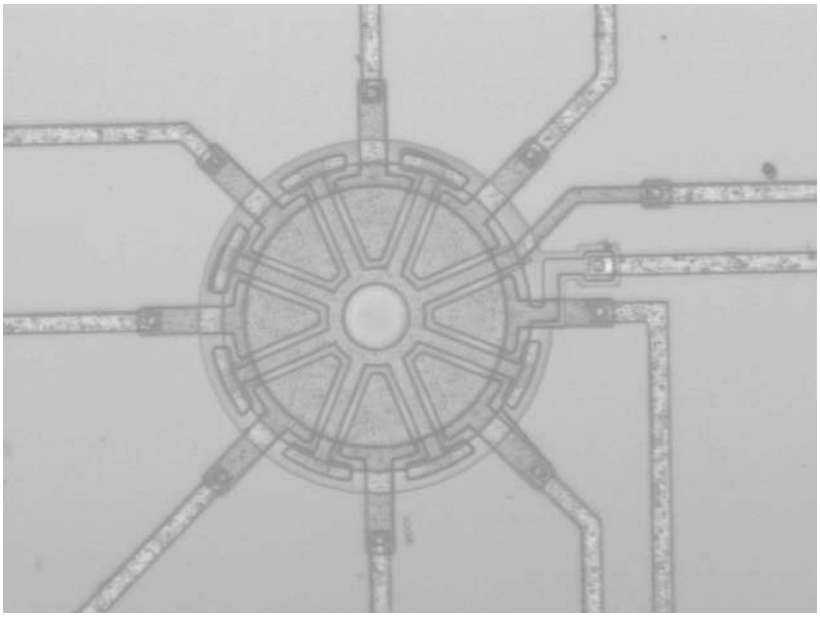

Figure 8.4 Polysilicon MEMS circular diaphragm for mass detection. (© 2006 Institute of Physics Publishing [6].)

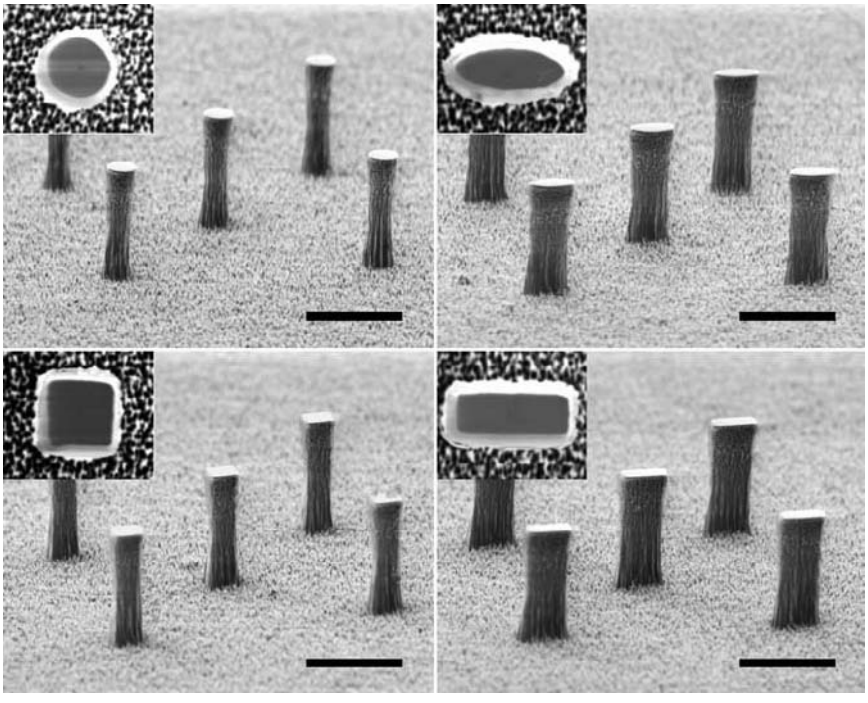

Figure 8.5 Silicon columns of various cross sectional geometries (scale bar: 30 μm). The insets reproduce SEM images from the top of a single column revealing the cross-sectional geometry after RIE etching (circular [9-μm diameter], elliptical [15.1 × 7.4 μm^2], square [9.1-μm width], and rectangular [14.9 × 7.3 μm^2]). (© 2008 American Institute of Physics [12].)

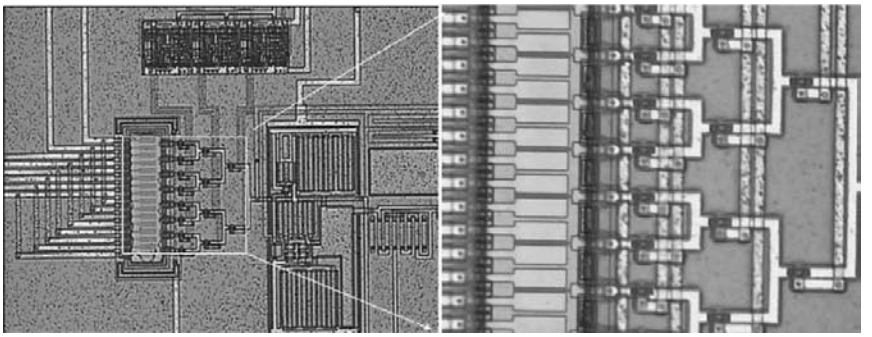

Figure 8.6 Monolithically integrated 8-cantilever mass sensor: the cantilevers are integrated with a multiplexing and read-out CMOS circuit (a zoomed-in view of the cantilevers is on the right side of the picture). (© 2006 Elsevier [13].)

show one of the 8-cantilever sensors monolithically integrated with a read-out and multiplexing CMOS circuit.

So far, we have reviewed some examples of MEMS-based resonant mass sensors. Although cantilevers are simple to fabricate and feature high mass-sensitivity, diaphragm or columnar structures have also been explored. We have noticed how the mass sensitivity is improved by reducing the dimensions of the resonator, from the units of hertz per picogram of microsized devices to the hertz per femtogram of nearly nanosized resonators. Hence, we would expect to improve even more the sensitivity through further reduction of the resonator dimensions.

8.2.2 Ultrasensitive NEMS Mass Sensors

The approach of nanoelectromechanical resonators for high-sensitive mass sensing applications has a notorious visibility in the NEMS field. Technological challenges and the broad spectrum of convergent applications that are being envisioned for the future explain their high impact. As long as nanomechanical resonators have been realized and achieved fundamental resonance frequencies exceeding 1 GHz, with Q factors in the range $10^3 < Q < 10^5$, their small active masses and high Q factors have translated into inertial mass sensitivities below 1 fg. Ekinci et al. have evaluated the ultimate mass sensitivity limits for nanomechanical resonators operating in a vacuum, and they related these limits with a number of fundamental physical noise processes. These analyses indicate that nanomechanical resonators have the potential for mass resolution at the level of individual molecules [14].

The advancements of NEMS resonator technology have also brought new concepts to mass detection and leading-edge applications, especially those in which different disciplines converge. Nowadays, detection of viruses is possible thanks to the nanoresonator mass sensor technology. Ilic et al., for example, used a resonating mechanical cantilever to detect immunospecific binding of viruses, captured from liquid. To demonstrate the concept, they used a nonpathogenic insect baculovirus to test the ability to specifically bind and detect small numbers of virus particles. Arrays of surface micromachined, antibody-coated polycrystalline silicon nanomechanical cantilevers were used to detect binding of various concentrations of baculoviruses in a buffer solution. The $0.5\ \mu\text{m} \times 6\ \mu\text{m}$ cantilevers shown in

Figure 8.7 exhibit mass sensitivities on the order of 10^{-19} g/Hz, thus enabling the detection of an immobilized antibody monolayer with a mass of about 3×10^{-15} g. This means that the mass of single-virus particles bound to the cantilever can be detected. Based on control experiments, they showed the nanocantilever's capability to adsorb very small amounts (<50 attograms) of the antibody layer [15].

NEMS resonators can also be used as self-detection instruments, and, due to their reduced size, they can be used in high-frequency applications. In scanning probe microscopy (SPM), the cantilever-based sensors generally use low-frequency mechanical devices of microscale dimensions or larger. The detection systems of these microscopes involves costly and nontransportable off-chip sensors, most of them based on laser or photo-diode arrays. Because the dispersion of such optical systems is greater than the actuation magnitude, they are unsuitable for detecting the nanoscale displacement of nanocantilevers. The implementation of self-sensing nanoresonators changes the paradigm of detection and notoriously improves the performance of SPM. Mo-Li et al. fabricated and described the operation of self-sensing nanocantilevers with fundamental mechanical resonances up to very high frequencies (VHF). The devices use integrated electronic displacement transducers based on piezoresistive thin metal films to perform the nanodevice read-out and are observed in Figure 8.8. This nonoptical transduction enables fast SPM and VHF force sensing (the detection of 127-MHz cantilever vibrations was demonstrated). With the smallest devices, they successfully achieved chemisorption measurements in air at room temperature, with a mass resolution less than 1 attogram [16].

Besides silicon-based resonators, carbon nanotubes (CNT) have also been demonstrated to be suitable for high-resolution mass detector implementation. Jensen et al. demonstrated that, at room temperature, carbon-nanotube-based nanomechanical resonators can achieve atomic mass resolution. They built the device depicted in Figure 8.9, which is essentially a mass spectrometer with a mass sensitivity of 1.3×10^{-25} kg/Hz$^{1/2}$ or, equivalently, 0.40 gold atoms /Hz$^{1/2}$. Unlike traditional mass spectrometers, nanomechanical mass spectrometers do not require

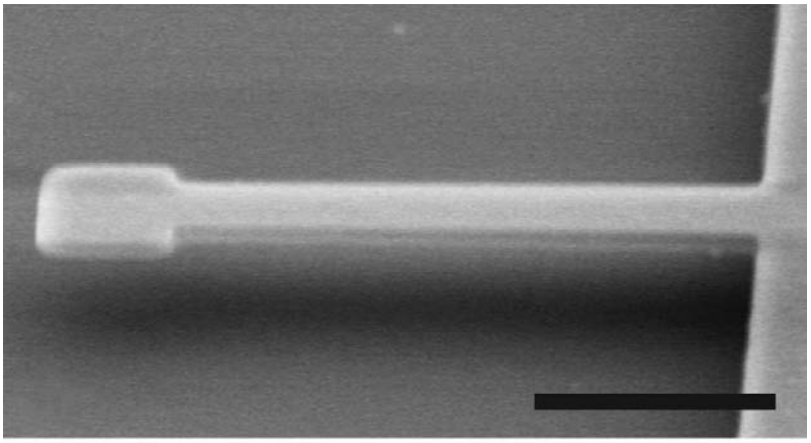

Figure 8.7 The nanocantilever used to detect immunospecific binding of viruses: the cantilever has length $l = 6\ \mu$m, width $w = 0.5\ \mu$m, and thickness $t = 150$ nm with a 1 μm × 1 μm paddle (the scale bar corresponds to 2 μm). (© 2004 American Institute of Physics [15].)

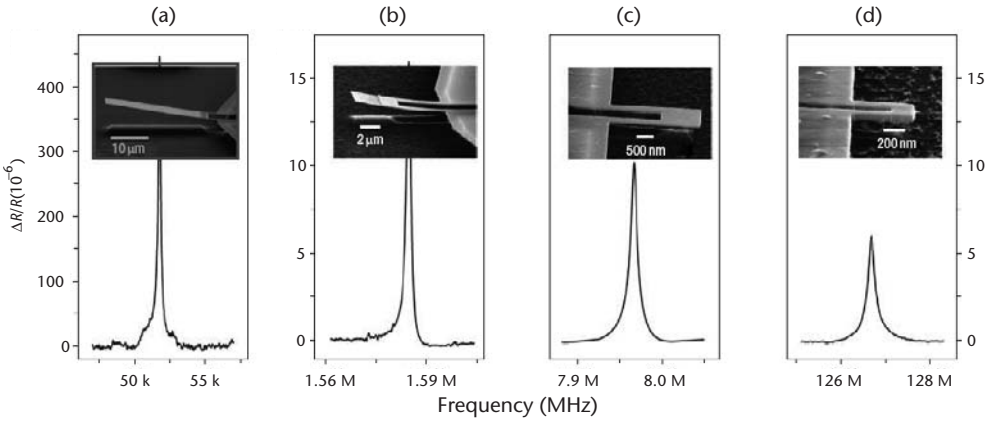

Figure 8.8 Piezoresistively detected frequency response from a family of SiC nanocantilevers to a 1 nN AC drive signal at room temperature in a vacuum: fundamental-mode resonance frequencies are: (a) 52.1 kHz, (b) 1.6 MHz, (c) 8 MHz, and (d) 127 MHz. The insets show SEM micrographs (angled perspective) of the devices, with dimensions 33 μm × 5 μm, 10 μm × 2 μm, 2.5 μm × 0.8 μm, and 0.6 μm × 0.4 μm, respectively. All are fabricated from a single-crystal, 70-nm-thick SiC epilayer. (© 2007 Nature Publishing Group [16].)

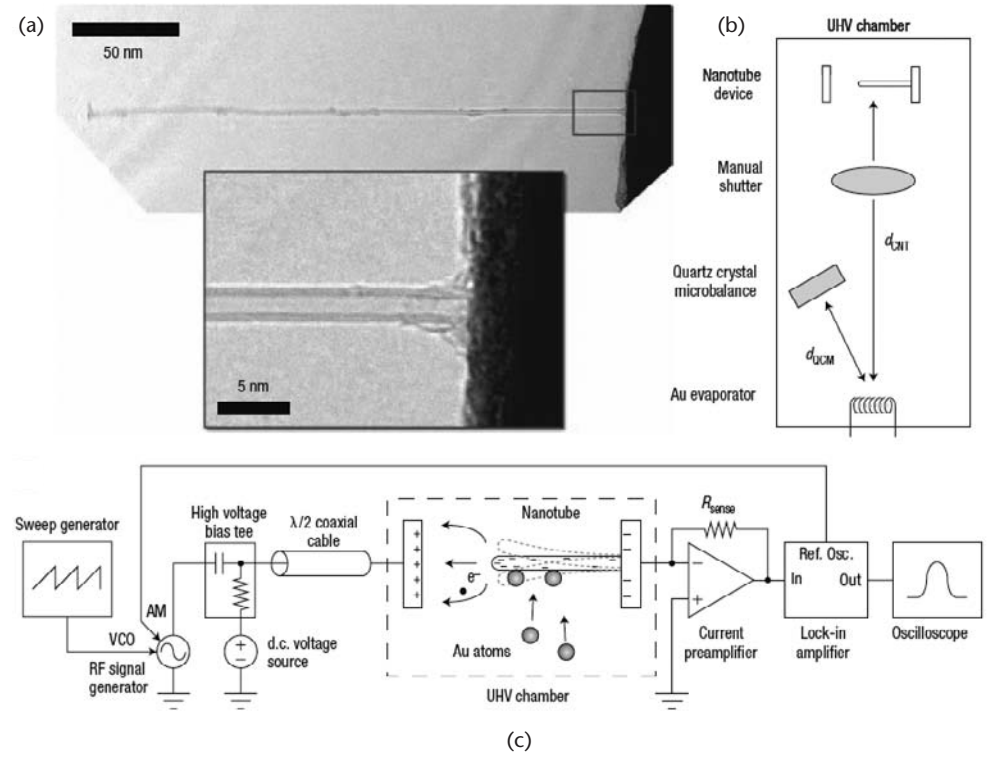

Figure 8.9 Nanomechanical mass spectrometer device and schematics of the measurement setup: (a) TEM images of a nanomechanical mass spectrometer device constructed from a double-walled carbon nanotube; and (b) physical layout of the entire nanomechanical mass spectrometer apparatus. Gold atoms are evaporated inside a UHV chamber and travel a distance d_{CNT} before adsorbing to the nanotube device and, consequently, lowering its resonant frequency. A shutter may be inserted to interrupt mass loading. The QCM provides an alternative means of calibrating the system through measurement of mass flux. (c) Schematic of the mechanical resonance detection circuit. (© 2008 Macmillan Publishers Ltd. [17].)

the potentially destructive ionization of the test sample. They are more sensitive to large molecules and could eventually be incorporated on a chip [17].

High resonance frequency and low mass are the main parameters driving a high mass sensitivity, and CNTs meet both conditions. Recent experiments have demonstrated the ultra high mass sensitivity of CNTs. Since the mass of a nanotube is as low as a few attograms, even a tiny amount of atoms deposited onto the nanotube makes up a significant fraction of the total mass. Also, nanotubes are ultrarigid mechanically, which is a key material property to push up the resonance frequency. The 1-nm-sized carbon nanotube resonator reported by Lassagne et al. is actuated by electrostatic interaction, as Figure 8.10(a) depicts. Using electron-beam lithography, nanotubes are connected in transistor geometry to two Cr/Au electrodes. The SEM image of Figure 8.10(b) shows the CNT and the electrodes. When an AC voltage V_g oscillating at a frequency f is applied on the back-gate of the wafer, an oscillating electrostatic force is generated on the nanotube at the same frequency. The motion of the nanotube, induced by the electrostatic force, modulates the gate capacitance C_g, and, in turn, it modulates the charge in the nanotube. The mass responsivity is 11 Hz/yg and the mass resolution is 25 zg at room temperature (1 yg = 10^{-24} g and 1 zg = 10^{-21} g). By cooling the nanotube down to 5K in a cryostat, the

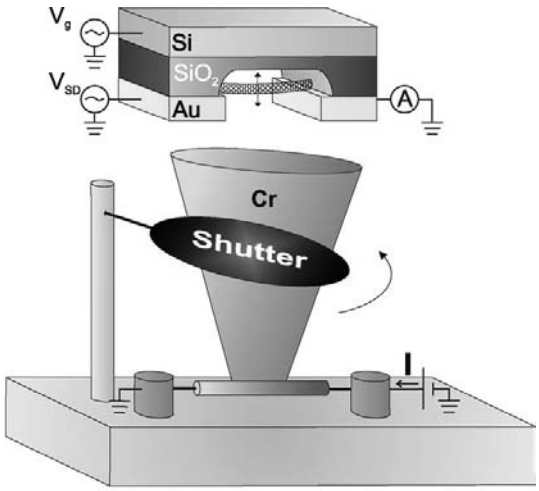

(a)

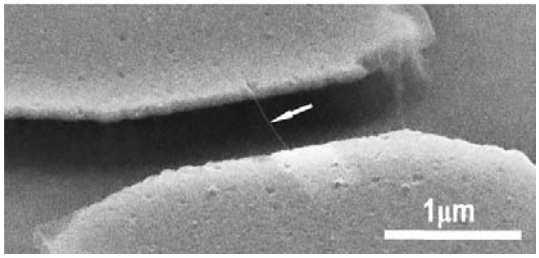

(b)

Figure 8.10 Carbon-nanotube-based mass sensor. (a) Experimental setup for mass sensing. Chromium atoms are deposited onto the nanotube resonator in a Joule evaporator and the mass of the atoms adsorbed on the nanotube is measured. (b) Scanning electron microscopy image of the nanotube resonator connected to the electrodes. (© 2008 American Chemical Society [18].)

signal for the detection of mechanical vibrations is improved to a resolution of 1.4 zg [18].

As we have seen, the NEMS resonator, microfluidics, silicon, and carbon nanotube technologies are integrated to offer ultrasensitive mass detection. The CNT-based resonators are the most sensitive mass detectors to date. Nevertheless, from the technological point of view, some issues should be resolved to implement nanoelectromechanical resonators in biodetection environments. In such cases, sample delivery is generally difficult and requires the entire device chip to be submersed into an analyte. Stiction problems are common to this scale as well. In addition, the viscous damping diminishes the mass sensitivity, so high vacuum is required. Some innovative solutions have been presented to address these issues, like the encapsulation of nanocantilever arrays in individually accessible, parallel microfluidic channels, which are used for delivery of liquids and nitrogen [19]. At a larger scale, and based on different transduction mechanisms, acoustic resonators are also being evolved to deal with the attogram-resolution and reduced-size technological challenges.

8.2.3 Acoustic Resonator Distributed-Mass Sensors

An acoustic resonator distributed-mass sensor features a piezoelectric layer to perform mass measurements, the most popular implementations being quartz crystal microbalances (QCM) and FBAR-based sensors.

In Section 3.3.4 we studied the Mason's model, which explains to a great extent the frequency shifting caused by the mass loading effect: an added film or body deposited on top of the resonator electrode changes the phase conditions of the acoustic wave propagation. The phase shifting translates into frequency shifting of the resonance modes of the device. Thus, the frequency change Δf is proportional to the amount of deposited mass (Δm) and is evaluated in the Sauerbrey-Lostis equation [20] by:

$$f_m = f_0\left(1 - \frac{\rho_m t_m}{\rho_0 t_0}\right) \tag{8.7}$$

In (8.5) the term at the right of f_0 corresponds to the frequency change Δf due to added mass Δm, where ρ_m and t_m are the density and thickness of the added-mass, and ρ_0 and t_0 are the density and thickness of the unloaded resonator. In this way, the frequency change relative to the unloaded resonance frequency can be solved as:

$$\frac{\Delta f}{f_0} \approx -\frac{\rho_m t_m}{\rho_0 t_0} = -\frac{\Delta m}{m_0} \tag{8.8}$$

Equation (8.8) is valid if Δm is less than 2% of the initial mass of the resonator m_0.

The sensing performance of distributed-mass sensors is evaluated by using four parameters. First, we consider the mass segnsitivity S_m [cm^2/g], which is defined as:

$$S_m = \frac{1}{\sum_i \rho_i t_i} \tag{8.9}$$

where ρ_i and t_i are the density and thickness of each layer in the resonator stack. The second parameter is the frequency responsivity $R_f = \Delta f/f_0$, where Δf is the minimum detectable frequency shift. Third, the minimum detectable mass change per unit area Δm [g/cm^2] can be evaluated from the mass sensitivity and the frequency responsivity as:

$$\Delta_m = \frac{R_f}{S_m} \tag{8.10}$$

Finally, the fourth parameter is the mass responsivity per area r_m [g/Hz/cm^2], whose definition is related to both the resonance frequency and the mass sensitivity as:

$$r_m = \frac{1}{f_0 \times S_m} \tag{8.11}$$

8.2.3.1 Quartz-Crystal Microbalance (QCM)

A QCM is a miniature mass sensor, or balance, that measures the amount of mass deposited on it as the change of its resonance frequency. It is used in most applications to operate in the thickness shear resonance mode at a frequency in the 1- to 30-MHz range. When a voltage is applied to the metal electrodes, it causes oscillation of the plate at the shear-mode resonance frequency.

The QCM, as a bulk acoustic wave resonator, is built as a parallel-plate device made of AT or SC-cut quartz crystal thin film sandwiched between two metallic electrodes. Due to the good piezoelectric properties of quartz, the oscillation is generally very stable with the high quality of oscillation, which enables QCM to be high sensitivity mass sensors. Its electrical behavior is described by the classical Butterworth-Van-Dyke model. Different crystals like α-cut quartz (shear) and new materials (langasite LGS $La_3Ga_5SiO_{14}$, gallium ortophosphate $GaPO_4$) are also employed in QCM fabrication.

QCMs are operated in air, gas, or liquid, although the damping and Q factor reduction caused by the contact of the resonator with the sensing medium imposes the need for designing the device and its operation mode according to the application. In air or gas phase interfaces, the damping is lower than in liquid media; for that reason, higher-sensitivity thickness-shear resonance modes are preferred in these cases. In liquid media the damping is very critical, thus drastically reducing the Q factor and sensitivity of the resonator. Because of this, shear horizontal surface acoustic wave (SH-SAW) mode [21, 22], Love-wave mode [23], and torsional mode resonators are implemented for liquid-media applications. Although less sensitive, lateral-wave resonances suffer less damping, and, in the end, the overall sensitivity of the QCM is improved.

Based on the previously defined operation modes, QCMs can be categorized in gravimetric and nongravimetric sensors. The thickness-shear mode sensors are

strictly gravimetric mass sensors. As stated by Mecea [24], mega-gravity inertial forces arise in this kind of sensor, which enable the mass-sensing measurement. On the other hand, nongravimetric sensors take advantage of viscoelasticity and viscosity effects. Thus, a change in the viscoelastic properties of the material in the liquid phase causes the resonance frequency to change because of the acoustic impedance variation. However, the viscoelastic parameters themselves usually depend on frequency, and it is often difficult to discriminate against inertial and viscoelastic effects. The resonance frequency shift of the QCM immersed in a liquid environment is explained by models similar to the Sauerbrey equation, although they include new terms related to the viscoelastic correction [25–28].

A typical QCM exhibits r_m in the units of pg/Hz/cm^2, and minimum detectable mass Δm of ng/cm^2. With these values, QCMs find application in gravimetry; particle detection in biotechnology, using functionalized surfaces, thin-film thickness monitoring in thermal, e-beam, sputtering, magnetron, ion, and laser deposition; and in situ monitoring of fluid properties. Karamollaoglu et al. developed a QCM-based DNA biosensor for detection of genetically modified organisms (GMOs), which promises real-time, label-free, direct detection of DNA samples for the screening of GMOs [29].

8.2.3.2 FBAR-Based Distributed-Mass Sensors

FBARs exhibit high frequency and mass sensitivities. Thus, it makes the FBAR technology a suitable candidate for biomolecular or chemical-detection applications. Mass-sensing systems, in which quartz microbalances (QCM) have been the key technology, are now rethought to be implemented with FBARs, taking advantage of their higher sensitivity in comparison to conventional QCMs [30–33]. As in QCMs, uniform loading of the active area of the electrode occurs when the FBAR is submersed in the sensing media (air or liquid).

As already discussed in Section 6.3.2, and based on the mass loading effect, the uniform thin-film deposition is a way of tuning the FBAR resonance frequency. The mass loading analysis of the FBAR with a magnesium fluoride (MgF_2) thin film deposited on its electrode showed that a responsivity R_m value as good as 1.4×10^{-17} g/Hz can be reached. Based on those experiments, we now study the performance of the thin-film-deposited FBAR as a distributed-mass sensor.

First, the theoretical and experimental values of the mass responsivity per area r_m are calculated. From the frequency shifting and deposited-mass data shown in Figure 6.12, the theoretical value of the mass sensitivity S_m is calculated from (8.9) by taking into account each layer in the FBAR's stack configuration. Once obtained S_m, the responsivity r_m is obtained by the inverse product of S_m by the series resonance frequency f_0 (2.4 GHz), as expressed in (8.11). Table 8.3 shows the sensitivities and responsivities for each layer and for the FBAR. A thin film of 20 nm of MgF_2 is used to calculate these parameters.

Then, we find the experimental sensitivity of the FBAR-based sensor. For this purpose, we evaluate the minimum mass change Δm and the minimum detectable frequency Δf. The experimental, minimum detectable mass change Δm is determined by the minimum detectable frequency shift Δf. To do that, the phase noise amplitude $\Delta\varphi$ is measured from zero-span S-parameter data acquired at the series

Table 8.3 Theoretical Mass Sensitivity and Responsivity of the FBAR-Based Uniform-Mass Sensor

FBAR's Layer	*Density* ρ_i *[g/cm^3]*	*Thickness* t_i *[cm]*	*Layer Sensitivity* $S_i=1/(r_i\, t_i)$	*Inverse Layer Sensitivity* $m_i=S_i^{-1}$
MgF_2	3.176	2.0×10^{-6}	157,430.73	6.35×10^{-6}
Pt (top)	21.45	1.5×10^{-5}	3,108.00	3.22×10^{-4}
Ti (top)	4.506	3.0×10^{-6}	73,975.44	1.35×10^{-5}
AlN	3.260	1.0×10^{-4}	3,067.48	3.26×10^{-4}
Pt (bottom)	21.45	1.5×10^{-5}	3,108.00	3.22×10^{-4}
Ti (top)	3.176	3.0×10^{-6}	73,975.44	1.35×10^{-5}
Distributed-mass sensitivity S_m *[cm^2/g]*	$S_m = m_0 = \dfrac{1}{\sum_i \rho_i t_i}$			997.12
Mass responsivity per area r_m *[g/Hz/cm^2]*	$r_m = \dfrac{1}{f_0 \times S_m}$			4.18×10^{-13}

resonance frequency f_0, and divided by the S21-phase slope φm, as given by (8.3). Figure 8.11 plots a zero-span acquisition of the S21 parameter phase. As observed in the figure, the maximum phase deviation from the mean value is ±0.08°, which is divided by the phase slope ϕm value -4.21×10^{-6} deg/Hz. This is calculated from differentiation and evaluation of the S21 phase at the series resonance frequency f_0 (see an example in the plots of Figure 5.8). The minimum frequency shifting is found to be $\Delta f = 19$ kHz.

Using the foregoing results, the experimental values of S_m, Δm, and r_m are calculated from (8.9) to (8.11), after the thin-film deposition. The S_m values are averaged to obtain Δm and r_m, given the minimum detectable frequency shift Δf previously calculated. Table 8.4 shows individual and averaged S_m, mass sensitivity and responsivity values.

According to the examples of Tables 8.3 and 8.4, the experimental uniform-film mass sensitivity and responsivity values are within the 80% of the theoretical values. Also, the experimental Δm equals to 9.8 ng/cm^2, which is pretty

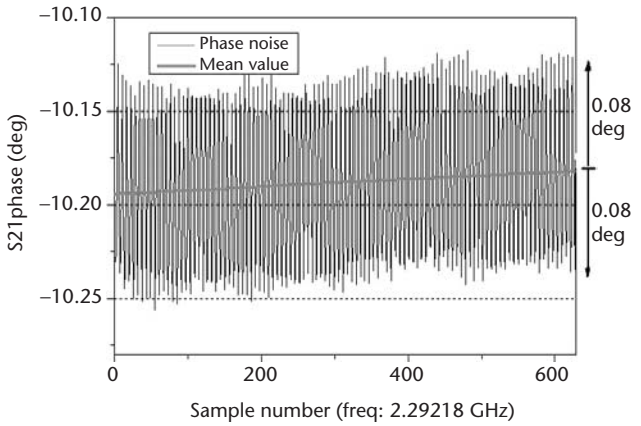

Figure 8.11 Zero-span frequency-domain acquisition of the FBAR response at resonance, for evaluation of the phase noise and minimum frequency shifting (with no loading).

Table 8.4 Experimental Mass Sensitivity and Responsivity of the FBAR-Based Uniform-Mass Sensor

	Thickness t_i *[cm]*	*Frequency Shift (Average)* Δf_i *[Hz]*	*Average Layer Sensitivity* $S_i = \Delta f_i/(f_0\, r_i\, t_i)$
MgF_2 density: 3.176 g/cm^3 *Δf= 19 kHz* *f_0 = 2.4 GHz*	2.0×10^{-7}	9.6×10^{5}	630
	5.0×10^{-7}	3.7×10^{6}	954
	1.0×10^{-6}	6.2×10^{6}	817
	2.0×10^{-6}	1.3×10^{7}	816
Average mass sensitivity S_m [cm^2/g]	$S_m = m_0 = \frac{1}{N}\sum_i \frac{\Delta f_i}{f_0 \rho_i t_i}$		804.4
Minimum detectable mass Δm [g/cm^2]	$\Delta_m = \frac{\Delta f}{f_0 \cdot S_m}$		9.84×10^{-9}
Mass responsivity per area r_m [g/Hz/cm^2]	$r_m = \frac{\Delta m}{\Delta f}$		5.18×10^{-13}

competitive to similar mass-sensing technologies. Table 8.5 compares four realizations of the uniform-film sensor, including a quartz-based QCM sensor. Although the Δf of QCMs is better, the highest resonance frequency of FBARs explains their improved S_m and r_m performance.

8.2.4 FBAR-Based Localized-Mass Detection

An FBAR-based localized-mass sensor performs high-sensitivity mass detection of a material or compound deposited on the electrode of the FBAR. The SEM image of Figure 8.12 shows an example of this concept, a C/Pt/Ga deposited by FIB on the top electrode of an FBAR being observed [30]. Parameters different than those of uniform-mass sensors evaluate the performance of localized-mass detectors. Mass responsivity R_m [Hz/g] is the first one, and it is defined as the change in the frequency response per unit mass change:

$$R_m = \frac{\Delta f}{\Delta m} \tag{8.12}$$

Table 8.5 Uniform-Mass-Sensing Performance for Different FBAR Realizations (Longitudinal-Resonance Mode)

	FBAR (2.2 GHz) (the Example of This Section)	*QCM (10 MHz) [34]*	*FBAR (1.5 GHz) [33]*	*FBAR (2GHz) [34]*
Minimum detectable frequency shift Δf [Hz]	19,000	1	400	15,400
Average mass sensitivity S_m [cm^2/g]	804.4	0.54	726	937.5
Minimum detectable mass Δm [g/cm^2]	9.8×10^{-9}	5.2×10^{-9}	1.0×10^{-9}	21×10^{-9}
Mass responsivity per area r_m [g/Hz/cm^2]	5.18×10^{-13}	1.79×10^{-12}	9.18×10^{-13}	1.36×10^{-12}

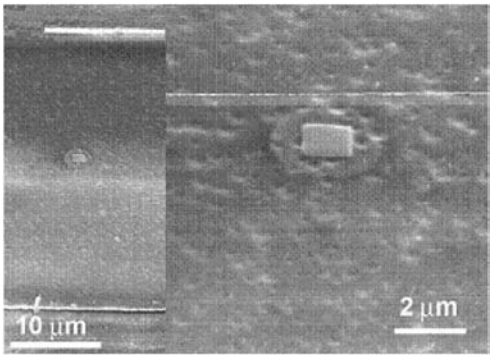

Figure 8.12 Localized mass deposited on the top electrode of an FBAR. (© 2006 American Institute of Physics [30].)

Due to the experimental approach of the sensor characterization, it is often more convenient to deal with the inverse responsivity R_m^{-1} [g/Hz]. Thus, the expressions *responsivity* and *inverse responsivity* are used indistinctly in this context. By taking the minimum detectable frequency $\Delta f_{\min}$ and R_m^{-1}, the minimum mass change $\Delta m_{\min}$ is calculated from [35]:

$$\Delta m_{\min} = \frac{\Delta f_{\min}}{R_m} \tag{8.13}$$

As we can see in (8.14), the minimum detectable frequency determines the ultimate sensitivity of the mass sensor. The value of $\Delta f_{\min}$ depends on the measurement setup and requires fine characterization of the noise sources to minimize it.

Localized-mass detection using FBARs as sensing devices was demonstrated in 2006. Through FIB-assisted experiments, FBARs achieved responsivities as high as 10^{-19} g/Hz and minimum detectable masses of units of femtograms [30]. Further studies on the FBAR-based sensitivity also demonstrated the sensor's dependence on the location and size of the deposited mass [36].

Localized-mass sensors are at least one order of magnitude more sensitive than uniform-mass sensors, although the sensitivity decreases with the area and location of the localized mass. It was found out that a change of the deposited mass location causes different magnitudes of the frequency shifting. Within the 2% mass limit imposed by the Sauerbrey-Lostis equations, the responsivity of the localized-mass sensor changes for different-sized mass deposition, which opens a broad variety of size-based applications. The mass-loading configuration can thus be designed according to the purpose of the target application. The plot of Figure 8.13 shows that the FBAR-based mass detection responsivity increases when the size or the mass of the localized-load are reduced.

Regarding the deposited mass location, the *center* of the FBAR sensor is the region of the electrode with the best responsivity, as the study of Table 8.6 details. Previous works on atomic-force-microscopy-based scanning of FBAR electrodes revealed that the amplitude of oscillation at resonance is related to the mode shape at this frequency. In [37], the vertical displacement of the FBAR's longitudinal resonance modes was bigger in the central region of the resonator. This could explain

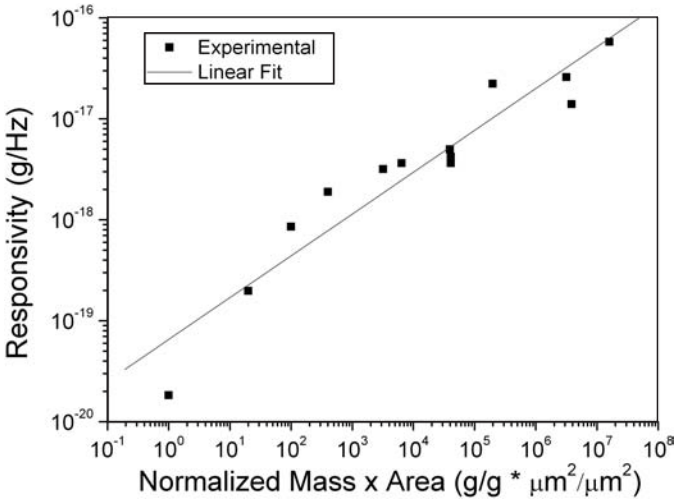

Figure 8.13 FBAR-based localized-mass detector responsivity [g/Hz] against normalized mass-by-area (the reference mass is 3.6×10^{-12}g with a contact-area of $1.5 \times 1.5\ \mu m^2$). (© 2007 Elsevier [36].)

the higher sensitivity and responsivity values for this region found in FBAR-based localized-mass detectors. This is also coherent with experimental data obtained for QCMs, in which localized silver spots are deposited on several positions along the diameter of quartz resonators [38]. Similar experiments have been carried out with crystal resonators immersed in liquid environments [39]. In these experiments, the mass sensitivity and amplitude distribution curves were found to follow a Gaussian function [40], the maximum value being obtained at the center of the resonator's electrode.

At resonance, vibration with a mode shaping induces a deformation in the vertical geometry of the FBAR. Thus, an explanation for improved sensitivity of the central region may be given in terms of different inertial fields generated on the surface of the electrode [24]. Regarding this explanation, the central region exhibits higher sensitivity, probably due to bigger acceleration forces—inertial field—in the center of the FBAR.

Analytical and finite-element modeling of FBAR-based localized-mass detectors have corroborated the location and mass size dependence on the sensor's responsivity, as previously referenced. The contour plots of Figure 8.14 show the high-frequency mode shaping of an FBAR before and after localized-mass deposi-

Table 8.6 Dependence of the FBAR Responsivity on the Axis of the Top Electrode on Which the Localized Mass Is Deposited

Region	*Mass (Estimated) (g)*	*Δf (MHz)*	*Responsivity (g/Hz)*
Center	3.6×10^{-12}	1.90	1.90×10^{-19}
Diagonal	3.6×10^{-12}	1.13	3.19×10^{-19}
Lateral	3.6×10^{-12}	0.98	3.65×10^{-19}

Source: [36].

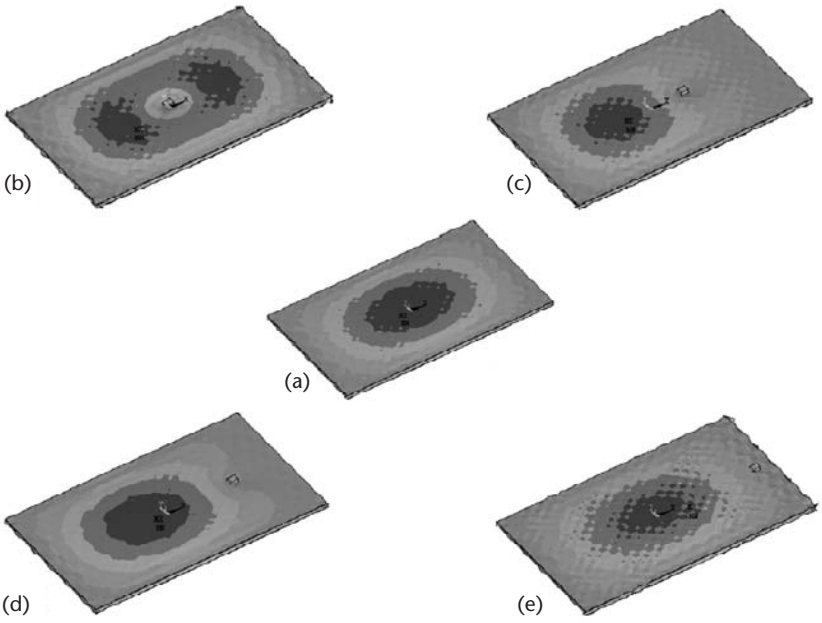

Figure 8.14 High-frequency mode shaping of an FBAR-based localized-mass sensor (FEM simulations performed in ANSYS): (a) the FBAR with no mass; (b) mass deposited at the center of the electrode; (c) the mass deposited 10 μm away from the center (along the y-axis); (d) mass located at $y = 20$ μm; and (e) mass located at $y = 30$ μm. The resonance frequency shifts down with the location of the deposited mass. (© 2009 IEEE [41].)

tion, obtained through FEM simulations in ANSYS. The FEM analysis reveals a modification of the mode shape and the down shifting of the resonance frequency. This is dependent on the position of the deposited mass (the center is the most sensitive location exhibiting higher frequency shift).

FBAR-based localized-mass sensors are a competing technology with great potential in highly sensitive biochemical applications. Evaluation of the active-sensor area of localized-mass sensors is an interesting subject of study. Since responsivity is location-dependent, it determines both the application and design of the sensor. Hence, the ultimate localized-mass sensor's sensitivity and mechanisms are to be studied with regard to the FBAR's size. Analytical and finite element models are suitable to accompany this topic.

8.3 Mechanical Sensors

In this section, we study the application of microresonators to mechanical sensors. In mechanical sensing applications, a strain applied to the MEMS structure is the most common mechanism for coupling the resonator to the measurand. In this way, the resonator becomes a resonant strain gauge that couples to the measurand when mounted in a suitable location on a sensing structure that deflects due to the application of the measurand. Such a structure is specifically designed for the application requirements and purposes.

The resonator output can be used to monitor the deflection of the sensing structure and thereby provide an indication of the magnitude of the measurand, which is directly proportional to the resonance frequency of the sensor. When used as a resonant strain gauge, the applied strain effectively increases the stiffness of the resonator, thus increasing its resonance frequency. This is the common principle of resonant force sensors, pressure transducers, and accelerometers [42].

The acoustic wave propagation through and reflection from a piezoelectric film is another mechanism to sense the inertial force applied to the sensor. When the incident pressure arrives at the piezoelectric sensor, an acoustic wave propagates and the amount of pressure can be quantified as a function of the propagated or reflected acoustic wave. In the following sections, mechanical sensors of both the strain gauge and acoustic wave kinds are discussed.

8.3.1 Pressure Sensors

Resonant pressure sensors are mature applications, which have been produced, commercialized, and exploited by different companies since the 1980s. The main sensing technology is a strain gauge integrated with a diaphragm, or it is the diaphragm by itself, which senses the resonance of the structure to determine the pressure value as a function of frequency. Piezoelectric sensors can also be used as resonant strain gauges to perform pressure measurement. SAW resonators have been implemented to detect the pressure changes as the delay in the path of the acoustic wave as well. MEMS industrial products and in-research pressure sensors are challenging the sensitivity limits of bulk devices. They offer improved performance in comparison to techniques.

Resonant pressure sensors have their origin at the early developments of Greenwood [43]. The strain gauge technology developed by Greenwood was later acquired and successfully commercialized by Druck Ltd. The sensor is a butterfly-shaped diaphragm attached to four pillars that deflects with pressure. Resonance frequency shifting happens when the diaphragm deflects by the action of pressure. Metal electrodes fabricated on the structure perform capacitive detection of the strain after electrostatic actuation of the diaphragm. The boron-etch stop technique developed by Greenwood, high vacuum, and hermetic packaging allow the device to achieve high Q factors and sensitivities. The Druck's Resonant Pressure Transducer (RPT) series fabricated with this technology exhibits high stability (<100 ppm) and resolution of 2–4 Hz/mbar in the 35–3,500-mbar range [44].

The Yokogawa's silicon resonant pressure sensor is another commercial technology of high market impact. The resonant sensors are fabricated from single crystal silicon using bulk micromachining techniques. Two H-shaped gauge resonators operating at resonance are patterned on the sensor's diaphragm. Resonance is electromagnetically elicited by placing the metallic gauges in an alternating high-frequency magnetic field. As pressure is applied, the bridge gauges are simultaneously stressed, one in compression and one in tension. The resulting change in resonance frequency produces a differential frequency output proportional to the amount of applied pressure. The thermal stability is higher than 10 ppm/°C with in vacuum Q factors above 50,000. The fabrication technology involves advanced

micromachining and packaging techniques, which are applied to Yokogawa's DPharp pressure transmitter and MT100/200 digital manometer [45].

The Quartzdyne's resonant pressure sensor is a quartz resonator that changes its frequency in response to pressure by the piezoelectric effect mechanism. The structure is a thick-walled hollow cylinder with closed ends that encapsulates a thickness-shear-mode disk resonator dividing the central portion of the hollow cylinder, as depicted in Figure 8.15. In this device, the gauge and the diaphragm are the same structure, namely the disk resonator. Fluid pressure on the exterior hydrostatically compresses the quartz cylinder, producing internal compressive stress in the resonator. The vibrating frequency of the sensor changes in response to this stress. Because quartz is highly frequency stable, the sensor's frequency output provides high-resolution pressure measurement [46].

Recent laboratory efforts have explored the mechanisms of resonant pressure sensing to discriminate the effects causing the resonance frequency variations. In 2003, Mertens et al. investigated the effect of pressure and temperature on the resonance response of Si microcantilevers. In their studies, they identified the ranges and mechanisms causing variations of the resonance frequency, and they demonstrated the potential of cantilevers to distinguish between the effects of pressure, temperature, and gas properties. The resonance response as a function of pressure shows that three different regions corresponding to molecular flow, transition, and viscous regimes are involved. The deflection in the flow transition regime resulting from thermal variation has a minimal effect on frequency. The frequency variation of the cantilever is caused mainly by changes in the mean free path of gas molecules [47].

Azevedo et al. introduced a silicon carbide (SiC) MEMS resonant strain sensor for harsh environment applications [48]. The sensor is built as a balanced-mass double-ended tuning fork (BDETF) fabricated from 3C-SiC deposited on a Si substrate. The fabricated device is shown in Figure 8.16. The resonance frequencies of the BDETF are about 207 kHz and 210 kHz in air, with and without the on-chip strain actuator, respectively. The resonators operate at atmospheric pressure and from room temperature to above 300°C, and they exhibit strain sensitivities of 66 Hz/$\mu\varepsilon$ and strain resolution of 0.11 $\mu\varepsilon$ in a bandwidth from 10 to 20 kHz with high linearity [48].

The SAW pressure sensor of Talbi et al. combines the physical properties of ZnO and quartz to produce high sensitivity and low temperature coefficient factor

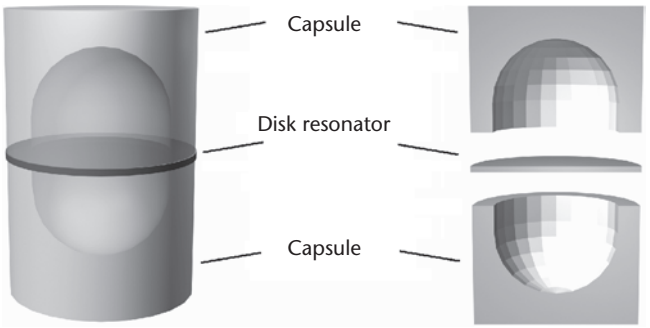

Figure 8.15 Quartzdyne's resonant pressure sensor: a hollow cylinder with closed ends encapsulates a thickness-shear-mode disk resonator (external pressure compresses the capsule and causes resonance frequency shifting of the disk). (*After:* [46].)

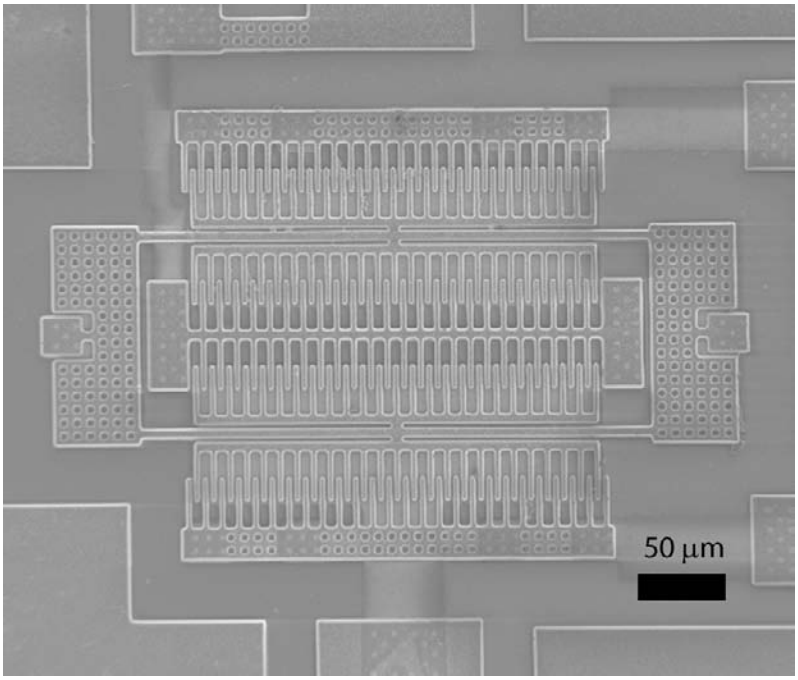

Figure 8.16 SiC MEMS resonant strain sensor for harsh environment applications. (© 2007 IEEE [48].)

(TCF). The quartz Y–X contributes to a nearly zero TCF value when it is combined with a thin ZnO film of particular thickness. The ZnO also increases the electromechanical coupling coefficient (k^2 = 1%) to seven times higher than that of quartz Y–X. The optimal structure of the 130-MHz SAW resonator yields a high electromechanical coupling factor k^2 of 1% and small temperature coefficient of frequency TCF of –0.21 ppm/°C, and it achieves the pressure sensitivity to around 35 ppm/mbar [49].

The concept and operating principle of another wireless pressure microsensor based on a SAW reflective delay line is depicted in the schematic of Figure 8.17. The contact antenna coupled to the SAW sensor receives an RF pulse. Then, the interdigitated transducer (IDT) transforms the received signal into an acoustic wave. Reflectors are placed in the propagation path of the SAW, and the reflected waves are reconverted into an electromagnetic wave by the IDT and transmitted to the reader unit through antennas. Phase shifting evaluation of reflected impulses determines the sensor signal. The 440-MHz SAW-based pressure sensor based on this reflective delay line is made of 41° YX $LiNbO_3$ with shorted circuit grating reflectors and single-phase unidirectional transducers (SPUDT). The obtained pressure sensitivity was 2.67°/kPa [50].

8.3.2 Accelerometers

Miniature accelerometers are a popular application of MEMS sensors. A resonant accelerometer integrates a strain sensitive resonator, seismic (proof) mass, and beam structures to support the proof mass and the resonator. The base technology is

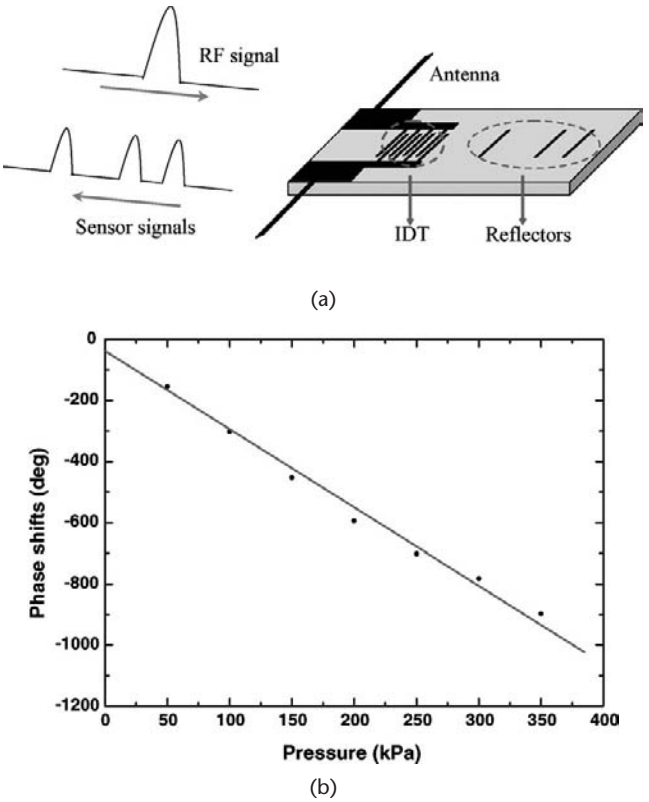

Figure 8.17 SAW-based pressure sensor: (a) operating principle; and (b) phase response against applied pressure. (© 2007 Elsevier [50].)

usually silicon, which is served to implement the mass and beams. The movable proof mass aids in improving the acceleration sensitivity. Sensing resonators are made of piezoelectric films or piezoresistive implantations. As the external force is applied to the mass, it deflects in the acceleration axis and the added strain produces frequency shifting of the resonator.

Ferrari et al. developed a resonant accelerometer manufactured in silicon bulk micromachining with electrothermal excitation and piezoresistive detection. The accelerometer's structure is a seismic mass supported by two parallel flexure hinges as a doubly sustained cantilever, with a resonating microbeam located between the hinges, as shown in the schematic drawing of Figure 8.18(a). AC voltage applied to the heaters induces a thermal excitation to the hinges, thus causing the structure to resonate. The piezoresistors detect the resonance of the micro beam: acceleration normal to the chip plane induces an axial stress in the microbeam and, in turn, a proportional change in its resonance frequency. The accelerometer shown in Figure 8.18(b) resonates at a frequency around 70 kHz, and it has an acceleration sensitivity of 35 Hz/g over the range of 0 to 3 kHz [51]. Another piezoresistive accelerometer with a similar performance was also demonstrated by Aikele et al. [52], thus obtaining frequency-to-static-acceleration sensitivity of 70 Hz/g.

In piezoelectric-based resonant accelerometers, the acoustic layer of the resonator is the sensitive element of the system. Current thin-film technologies employ

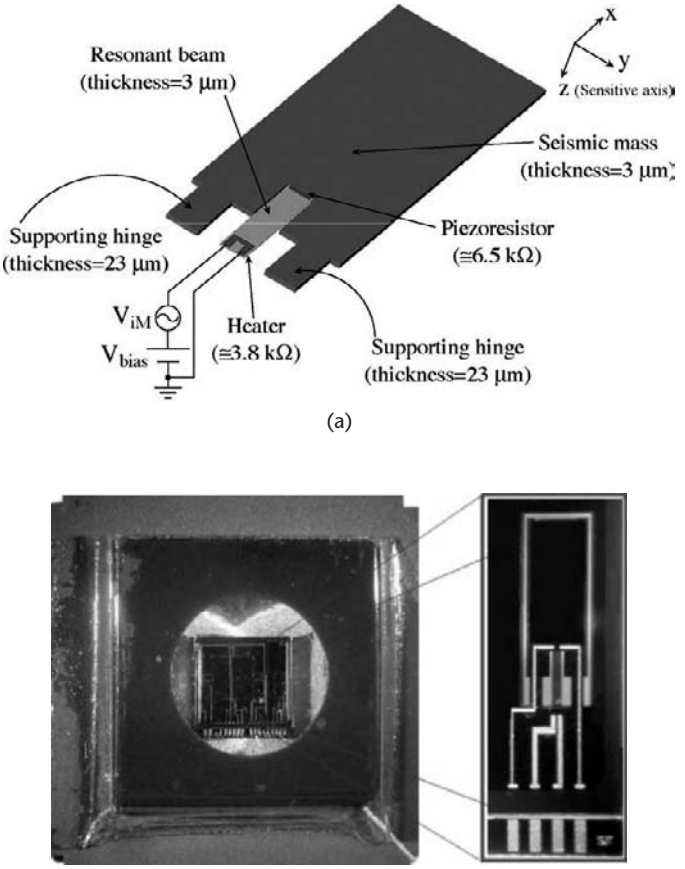

Figure 8.18 Piezoelectric accelerometer with electrothermal excitation and piezoresistive detection: (a) sensor's concept; and (b) physical realization of the sensor chip with the accelerometer (enlarged view). (© 2005 Elsevier [51].)

miniature FBARs fabricated on silicon accelerometers. The operating principle of such a kind of accelerometer is depicted in Figure 8.19: acceleration applied to the seismic mass adds stress to the device and causes strain. Since the FBAR and the Si are mechanically coupled, the strain induced on the mass is transmitted to the beam and FBAR. Thus, it produces charge displacement in the crystalline structure of the piezoelectric layer, and it causes shifting of the FBAR's resonance frequency. The electrical charge displacement within the crystal and the resonance frequency of the FBAR is proportional to the magnitude and orientation of the acceleration. This principle can be extended to the case in which the FBAR couples directly with the seismic mass. The fabrication technology of FBAR-based accelerometers requires process compatibility between silicon and FBAR technologies. The FBAR piezoelectric layer can be made of AlN, whose deposition and etching on a Si substrate is the biggest challenge to FBAR and Si compatibility [53].

The SEM images of Figure 8.20 show front and back-side views of a dual-beam accelerometer with embedded piezoelectric resonator and 500-μm-thick mass. Detail of one sensing FBAR is observed in Figure 8.20(c). The thickness of the seis-

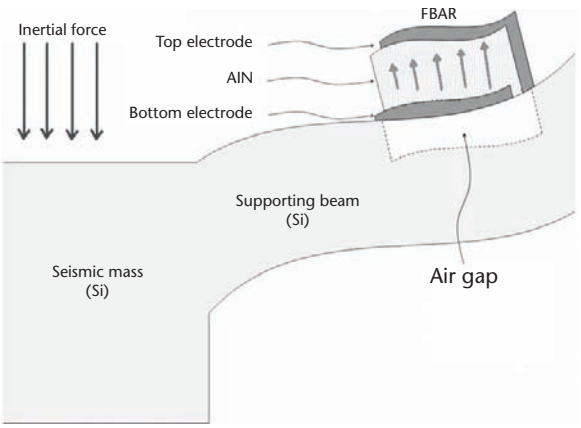

Figure 8.19 Operating principle of a piezoelectric, FBAR-based accelerometer. (© 2008 Elsevier [53].)

mic mass controls the accelerometer sensitivity; an example of an 80-μm thin mass device is shown in Figure 8.20(d). The FBAR has lateral size of $20\,\mu\text{m} \times 100\,\mu\text{m}$, and it is made of AlN and Pt electrodes, with thicknesses equal to 1,000 and 180 nm, respectively. The supporting silicon beam has a thickness of about 80 μm. According to this configuration, the resonance frequency of the FBAR is 2.4 GHz. Break-off tabs have been patterned on the Si to facilitate dicing. The device exhibits a frequency-to-static-acceleration sensitivity of 200 kHz/g. Due to its high-frequency operation mode, the embedded-FBAR accelerometer reaches a frequency sensitivity that is more than 2,000 times higher than that of the low-frequency devices previously discussed. However, the relative frequency shifting of the low-frequency piezoresistive accelerometer is one order of magnitude better than the 1×10^{-4} value of the embedded-FBAR accelerometer. Process variations can be introduced to fabricate accelerometers with supporting beams made with the structural layers of FBARs in order to achieve improved sensitivity [54].

8.4 Atomic Force Detection

An atomic force microscope (AFM) can perform nanometer-scale and atomic-scale force detection by implementing a MEMS cantilever as the sensing element. When operated in tapping mode, the cantilever resonates with a frequency response between units of hertz to few megahertz. The sharp tip located at the apex of the cantilever scans over a surface of the sample and detects the tip-sample interactions, while a feedback system controls the interaction force between the tip and the sample surface [55]. Using micromachining technologies, the dimensions of cantilevers can be tuned to optimize the sensitivity, resonance frequencies, elastic constants, and other properties of the cantilever [56]. Both the cantilever and the tip are usually made of polysilicon, although other materials, like quartz, have been implemented as well [57]. Examples of AFM probes made of crystalline silicon are observed in the SEM images of Figure 8.21. In AFM systems, the force detection is performed by measuring the deflection of the cantilever when it is attracted by the sample. This measurement is carried out by complex optical or interferometer tech-

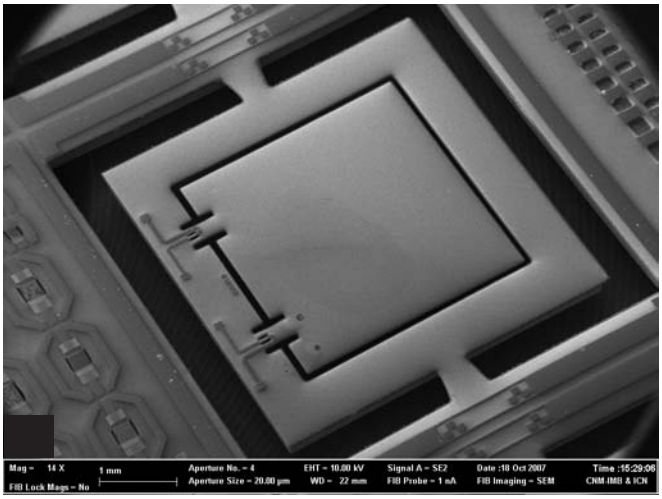

(a)

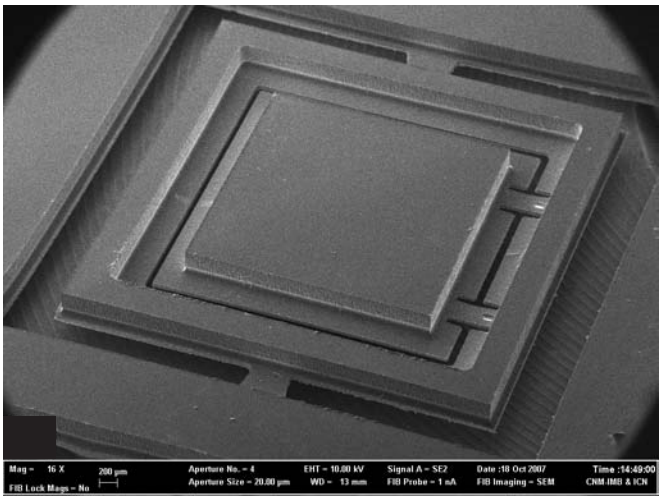

(b)

Figure 8.20 Dual-beam FBAR-based accelerometer: (a) front side; (b) back side (thick-mass); (c) detailed view of one of the embedded FBARs; and (d) back side (thin-mass).

niques, the setup comprising laser, optical detectors, signal generators, and lock-in amplifiers, among others [58]. Taking advantage on the same operating principle of FBAR-based accelerometers, a new generation of AFM-detection cantilevers can be implemented with the FBAR technology (a detailed discussion on AFM cantilever measurements is done in Section 5.4.1).

The concept of the FBAR-based force sensor for AFM applications is illustrated in the schematic drawings of Figure 8.22(a, b), where two cases are differentiated. In the configuration of Figure 8.22(a), the FBAR is embedded on the cantilever's structure, which can be made of silicon and has a tip close to its vertex. When the probe and the sample approach each other, the cantilever deflects, thus bending the FBAR and adding stress to the piezoelectric layer. The magnitude of deflection is directly proportional to the probe-sample attraction forces and is detected as a

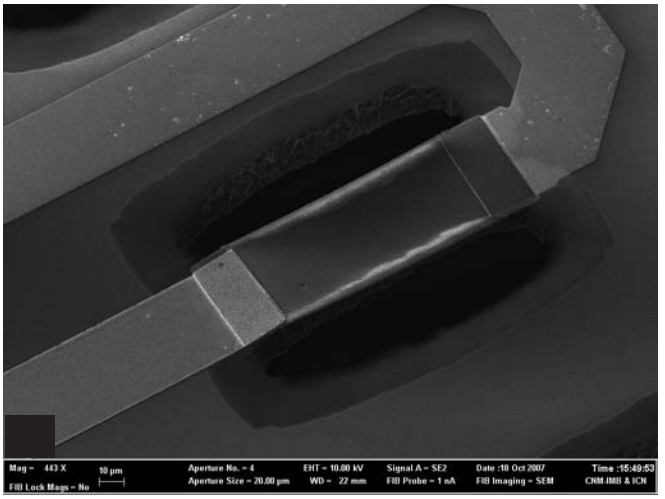

(c)

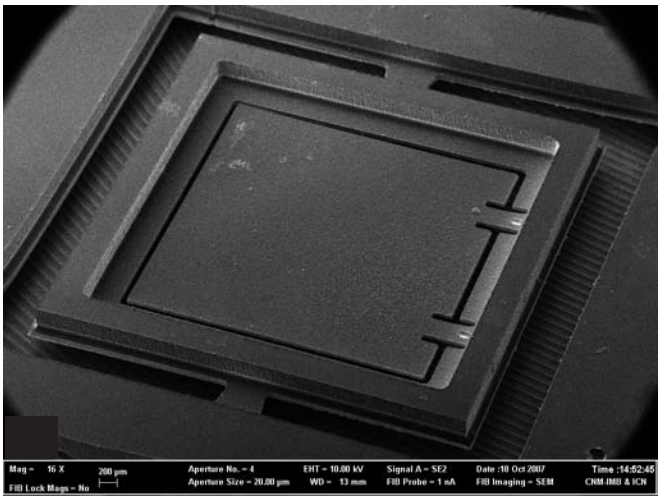

(d)

Figure 8.20 (continued)

change of the resonance frequency of the FBAR. The second concept is shown in Figure 8.22(b), in which the cantilever and the tip are the same V-shaped structure. This structure is fabricated according to the FBAR process (metal-piezoelectric-metal stack configuration). As depicted in the figure, the V-FBAR cantilever deflects when attracted by the sample, thus increasing its resonance frequency. The fabrication technology, operation, and detection principles are the same for both configurations. A combination of front- and back-side DRIE is performed to release both the cantilever and the FBAR (which are the same structure in the second case).

Although there exist several AFM-probe fabrication technologies, the development of FBAR-based force sensors is still in the early stages of analysis and design. The pictures of Figure 8.23(a, b) show fabricated devices of the first kind with embedded FBAR. The FBARs have a width of 40 μm, a length of 100 μm, and a thickness of 1 μm (AlN). The second type of force sensor is observed in Figure

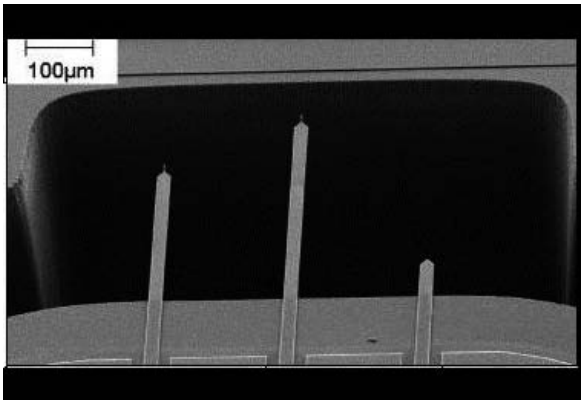

(a)

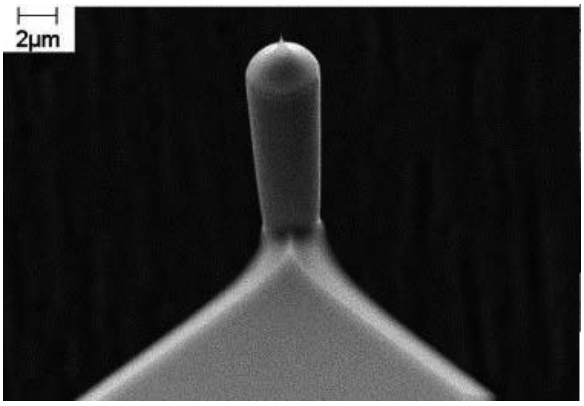

(b)

Figure 8.21 AFM probes made of crystalline silicon: (a) SEM micrographs of a typical AFM probe-chip, with a shaft diameter ~3.8 μm, apex radius ~10 nm, and vertex angle ~10°. Cantilever thickness is 1.5 μm, width is 25 μm, and length is 250 μm, 350 μm, and 50 μm (from left to right). (b) Detailed view of one tip. (© 2007 Elsevier [56].)

8.23(c, d). The V-shaped tips are designed and fabricated according to the FBAR process, and they have lengths between 5 and 50 μm, and widths of 5–20 μm. The AlN layer and the metal electrodes are 1 μm thick and 180 nm thick, respectively. The residual stress of the AlN layer presumably causes the bending observed on the tips.

Both kinds of sensors could be implemented in future AFM applications if a force tip is deposited on or grown near the FBAR [56]. In this application, the tip is placed above the analyzed sample to perform force interaction, and the FBAR detects the force intensity by reading out the resonance frequency's variation.

8.5 Magnetic Sensors

Magnetic sensors of many kinds have been designed and assisted different applications throughout the past and the present century. The existing magnetic sensing

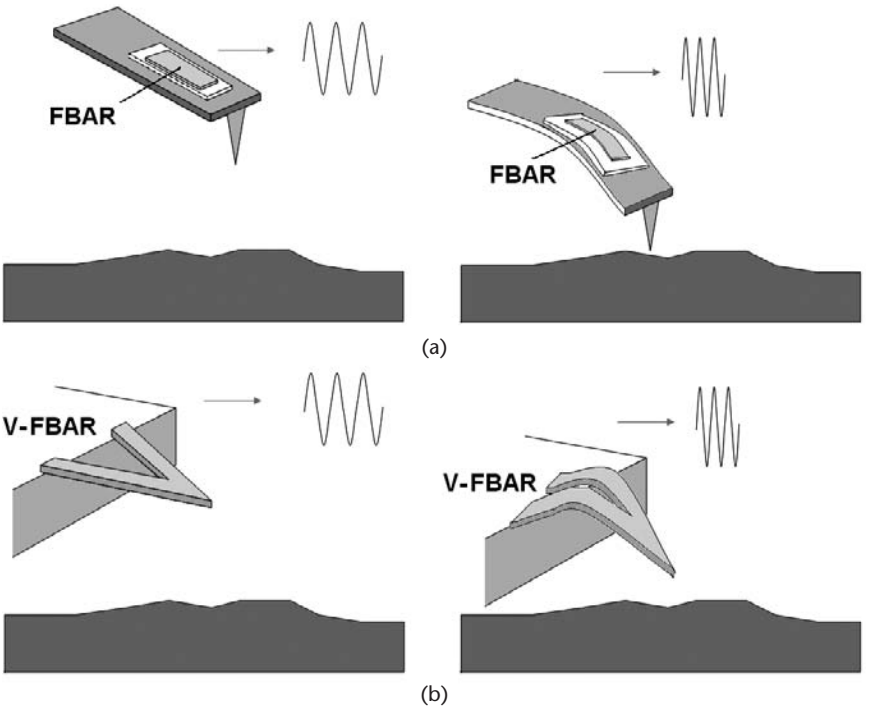

Figure 8.22 Concept of the FBAR-based AFM force detector: (a) first configuration: the FBAR is embedded on the Si cantilever's structure; and (b) second configuration: cantilever and tip are a V-shaped FBAR. In both cases, the probe-sample attraction causes deflection and frequency shifting of the FBAR.

technologies are capable of covering the wide range of magnetic field intensities from over the Earth's magnetic field down to the geomagnetic noise and below [59]. The earliest designs of magnetic sensors utilized simple magnetic attraction to ferrous objects to detect the magnitude or gradient of the magnetic field. In contrast, MEMS magnetometers and gradiometers typically implement a hard magnet or magnetic material integrated somehow to its micromachined structure. Whenever the MEMS sensor is under the influence of the magnetic field, it happens to move due to the ferromagnetic attraction arising between the magnetic material and the source of the magnetic perturbation. The resulting motion is then measured through electrical [60], optical [61], or magnetic [62] detection techniques, among others.

Current MEMS magnetometers have magnetic field sensitivities in the range from 1 μT to 1 mT. They are also referred to as *MEMS compasses* because they align in the direction of the magnetic field. Normally, MEMS compasses are designed to operate without power consumption, although they can be connected to an integrated read-out circuit. In the first case, optical detection is most commonly employed to detect the movement of the MEMS. The most popular structures to implement the compass are torsional beams with a magnetic plate [63–65] and cantilevers [66]. The sizes of such structures range from hundreds of micrometers to some millimeters, and they have mainly been used as magnetic field detectors, current meters, or optical scanners.

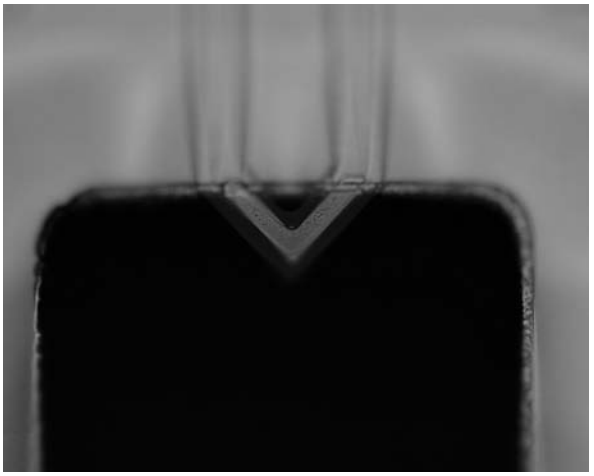

(a)

(b)

Figure 8.23 Force sensors for AFM applications: (a, b) V-shaped FBAR-made tips; and (c, d) embedded FBARs on Si cantilevers.

Resonant magnetic field sensors of the MEMS compass and LC types are based on magnetic resonant structures. The MEMS resonator is modified to incorporate a soft magnetic material or to integrate a hard magnet. The resonance frequency of the MEMS shifts due to the interaction of the external magnetic field and the magnetic component of the resonant system. The magnitude of the frequency shifting is used to determine the amplitude or the direction of the external magnetic field. According to this operation principle, Leichle et al. fabricated a CMOS-compatible and low-temperature process sensor based on surface micromachining. The sensor, depicted in Figure 8.24, has a resolution of 45° at 30 μT. The resonator's low power consumption—on the order of 20 nW—makes it useful as a magnetic compass [67].

Electromagnetic induction is a sensing mechanism that has also been implemented by MEMS sensors to detect magnetic field variations. A micro-LC resonator consisting of a solenoidal microinductor with a bundle of soft magnetic microwire cores and a capacitor connected in parallel to the microinductor was reported by

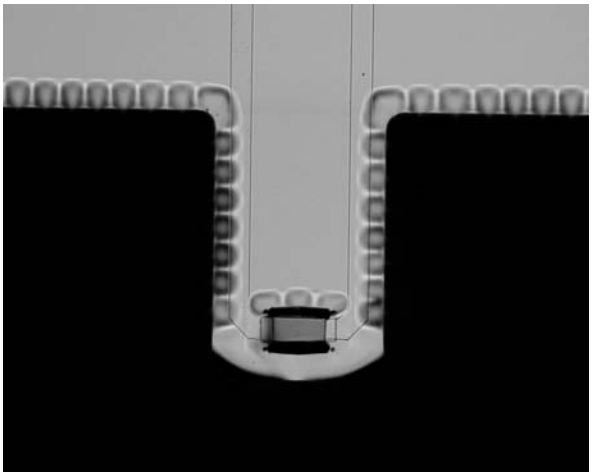

(c)

(d)

Figure 8.23 (continued)

Kim et al. [68]. The LC resonator detects the external magnetic field by measuring the inductance ratio as well as the magnetoimpedance ratio (MIR). The MEMS solenoids are manufactured within lithography, electroplating, and molding (LIGA) processes. The core magnetic material of the microinductor shown in Figure 8.25 is a tiny glass-coated $Co_{83.2}B_{3.3}Si_{5.9}Mn_{7.6}$ microwire fabricated by a glass-coated melt-spinning technique. The solenoidal microinductors fabricated by MEMS techniques are 500–1,000 μm in length with 10–20 turns. The resonance frequency of the microinductor and capacitor tank is near 105 MHz and, because the permeability of the ultrasoft magnetic microwires changes rapidly as a function of external magnetic field, the inductance ratio and the MIR vary very rapidly with the magnetic field as well [68].

The Lorentz force is another mechanism widely exploited for highly sensitive magnetic field measurements. The resonant Lorentz-force device is typically a mechanical resonator carrying an electrically conductive element designed for low

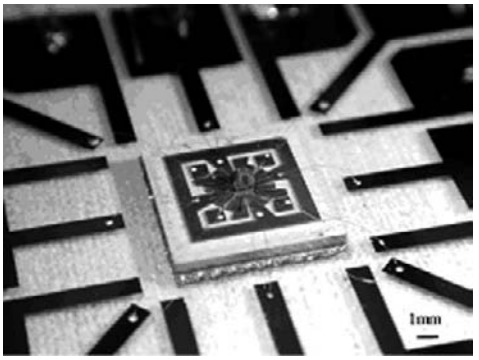

Figure 8.24 Photograph of a fabricated resonator incorporating a permanent magnet. (© 2004 Institute of Physics Publishing [67].)

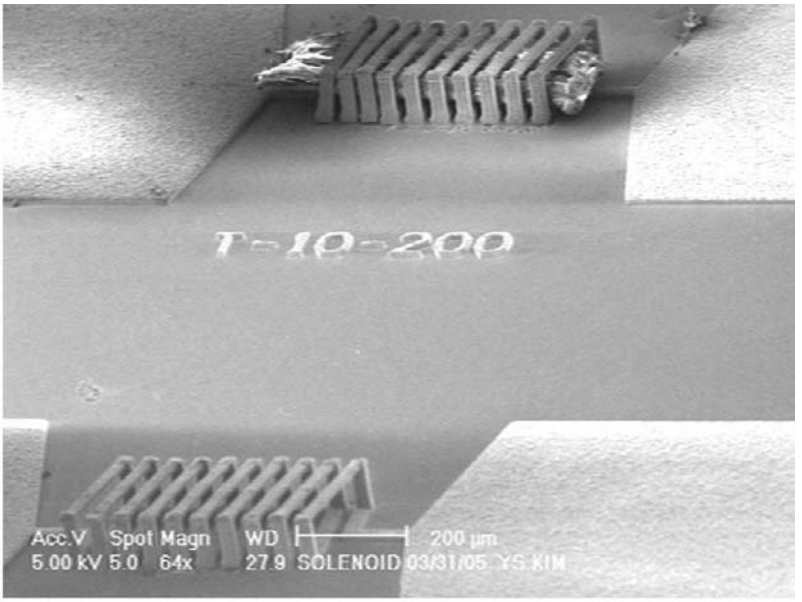

Figure 8.25 Microinductors for LC-resonator-based magnetic field sensing, with and without microwires as a core: the MEMS solenoids are made within a LIGA process, and the tiny glass-coated $Co_{83.2}B_{3.3}Si_{5.9}Mn_{7.6}$ microwires are fabricated by a glass-coated melt-spinning technique. (© 2006 American Institute of Physics [68].)

sensitivity to spurious vibration or magnetic perturbations of the environment. Oscillation of the conductor in a magnetic field generates an electric potential that drives a current around a closed resistive loop to damp the motion of the resonator. Variations in the magnetic field, therefore, alter the resonator's amplitude and so alter the measured frequency of the overdriven resonator. According to this mechanism, Greywall proposed a device that is capable of detecting perturbations in Earth's magnetic field smaller than one part per million (1 ppm) [69].

Herrera-May et al. reported another Lorentz-force-based resonant magnetic field sensor at atmospheric pressure [70]. This sensor does not require vacuum packaging to operate efficiently and presents a compact and simple geometry. The MEMS structures of Figure 8.26 are built in a SOI substrate, and their geometry consists of a seesaw plate ($400 \times 150 \times 15\ \mu m^3$), two torsional beams ($60 \times 40 \times 15\ \mu m^3$), four flexural beams ($130 \times 12 \times 15\ \mu m^3$), and a Wheatstone bridge with four p-type piezoresistors. The resonant device operates at its first resonant frequency of 136.52 kHz with a Q factor over 800. A sinusoidal excitation current of 22.0 mA with a frequency of 136.52 kHz and magnetic fields from 1G to 400G are considered. The sensor has the maximum magnetic sensitivity of 40.3 μV/G (magnetic fields <70G), theoretical root-mean square (rms) noise voltage of 57.48 nV/Hz$^{1/2}$, theoretical resolution of 1.43 mG /Hz$^{1/2}$, and power consumption less than 10.0 mW [70].

Resonant magnetic microsensors have been demonstrated at the micrometer scale, although nanometer-sized NEMS geometries are being developed to detect magnetic field perturbations, like the nanocantilever implementation of Vasquez et al. [71]. Even if these NEMS are nonresonant devices, they open new paths in magnetic sensor miniaturization.

8.6 Summary

In this chapter, we have studied several resonant sensor applications. First, we reviewed MEMS, NEMS, QCM, SAW, and FBAR mass detectors. The mass loading effect and the sensitivity analysis of each technology were discussed. In these

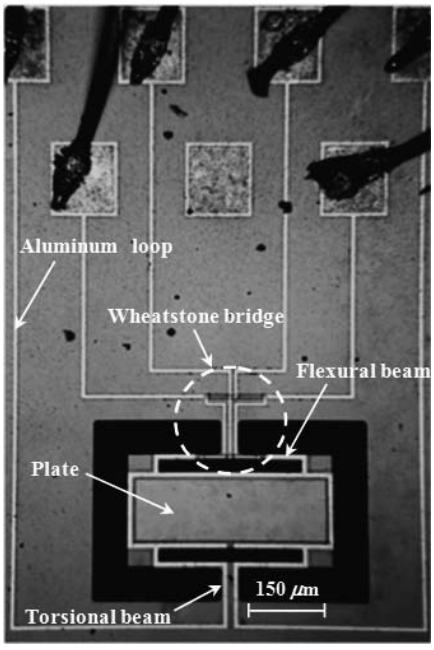

Figure 8.26 Photomicrograph of the magnetic field microsensor. (© 2009 Institute of Physics Publishing [70].)

analyses, we differentiated between distributed and localized mass sensing. Nowadays, NEMS resonators achieve the highest mass resolution and sensitivity between the current-art technologies, the latest sensors being able to detect masses as small as atoms. Nevertheless, the wide family of acoustic resonators is a more mature technology and is currently being implemented in both commercial and laboratory products. Applications of mass sensors are innumerable. Miniaturized mass sensors have enabled the high-sensitivity, high-resolution detection of chemical particles, biological particles like spores or viruses, DNA and proteins, gases, liquids, and a long and growing list of convergent applications.

In the Section 8.2 we studied mechanical sensors. First, micromachined accelerometers based on piezoresistive and piezoelectric actuations were introduced. The discussion followed with the concept and fabrication technology of FBAR-based high-frequency accelerometers. The benefits of the high-frequency detection of FBAR accelerometers were compared to other low-frequency resonant devices. Section 8.3 described another kind of force detector: AFM. The concept, operation principles, and available technologies of MEMS cantilevers for AFM applications demonstrated that a new generation of low-cost, low-size atomic-scale scanning probes is now possible. Self-detection is one of the main features of this new generation of AFM probes, thus simplifying the detected-signal measurement setup. Eventually, this feature will open the path for the future implementation of portable AFM systems.

Studied in Section 8.4, MEMS resonators also demonstrated their versatility as resonant magnetic sensors. Most of them are based on micro cantilever or torsional beam geometries and have made evident the advantages of miniaturization in magnetometry. The latest developments of NEMS resonator magnetometers promise future resonant detection of magnetic field perturbations.

The examined applications are a fruitful and stimulating research field. Although commercial products exist, most of them still need to solve a lot of challenges and design issues to enable the applications to pass from concept to industrial reality. A lot of modeling, testing, and optimization work is required to consolidate the sensor applications. Also, and related to previous chapters of this book, integration of these applications with CMOS technologies is to be considered. As has been fully proven, CMOS integration improves the impact and versatility of the sensors, boosting them to full systems-on-chip implementations.

References

[1] Greenwood, J. C., "Etched Silicon Vibrating Sensor," *J. Phy. E. Sci. Instrum.*, Vol. 17, 1984, pp. 650–652.

[2] IEEE Std. 1139, "IEEE Standard Definitions of Physical Quantities for Fundamental Frequency and Time Metrology—Random Instabilities," Institute of Electrical and Electronics Engineers, New York, 1999.

[3] Rodriguez-Pardo, L., et al., "Resolution in Quartz Crystal Oscillator Circuits for High Sensitivity Microbalance Sensors in Damping Media," *Sens. Actuators B: Chem.*, Vol. 103, 2004, pp. 318–324.

[4] Beeley, J. M., et al., "All-Digital Interface ASIC for a QCM-Based Electronic Nose," *Sensor Actuators B: Chem.*, Vol. 103, 2004, pp. 31–36.

[5] Zeng, K., and C. A. Grimes, "Threshold-Crossing Counting Technique for Damping Factor Determination of Resonator Sensors," *Rev. Sci. Instrum.*, Vol. 75, 2004, pp. 5257–5261.

[6] Gribaldo, S., et al., "Experimental Study of Phase Noise in FBAR Resonators," *IEEE Trans. on Ultrasonics, Ferroelectrics, Freq. Control*, Vol. 53, 2006, pp. 1982–1986.

[7] Phadke, M. S., *Quality Engineering Using Robust Design*, Englewood Cliffs, NJ: Prentice-Hall, 1989.

[8] Hwang, I.-H., and J.-H. Lee, "Self-Actuating Biosensor Using a Piezoelectric Cantilever and its Optimization," *J. Physics*, Vol. 34, 2006, pp. 362–367.

[9] Narducci, M., et al., "Sensitivity Improvement of a Microcantilever Based Mass Sensor," *Microelectronic Eng.*, Vol. 86, 2009, pp. 1187–1189.

[10] Davila, A. P., et al., "Microresonator Mass Sensors for Detection of Bacillus Anthracis Sterne Spores in Air and Water," *Biosensors and Bioelectr.*, Vol. 22, 2007, pp. 3028–3035.

[11] Ismail, A. K., et al., "The Principle of a MEMS Circular Diaphragm Mass Sensor," *J. Micromech. Microeng.*, Vol. 16, 2006, pp. 1487–1493.

[12] Kehrbusch, J., et al., "High Frequency Columnar Silicon Microresonators for Mass Detection," *Appl. Phys. Lett.*, Vol. 93, 2008, 023102.

[13] Villarroya, M., et al., "System on Chip Mass Sensor Based on Polysilicon Cantilevers Arrays for Multiple Detection," *Sens. Actuators A: Phys.*, Vol. 132, 2006, pp. 154–164.

[14] Ekinci, K. L., Y. T. Yang, and M. L. Roukes, "Ultimate Limits to Inertial Mass Sensing Based upon Nanoelectromechanical Systems," *J. Appl. Phys.*, Vol. 95, 2004, pp. 2682–2689.

[15] Ilic, B., Y. Yang, and H. G. Craighead, "Virus Detection Using Nanoelectromechanical Devices," *Appl. Phys. Lett.*, Vol. 85, 2004, pp. 2604–2606.

[16] Li, M., H. X. Tang, and M. L. Roukes, "Ultra-Sensitive NEMS-Based Cantilevers for Sensing, Scanned Probe and Very High-Frequency Applications," *Nature Nanotechnology*, Vol. 114, 2007, pp. 114–120.

[17] Jensen, K., K. Kim, and A. Zettl, "An Atomic-Resolution Nanomechanical Mass Sensor," *Nature Nanotechnology*, Vol. 3, 2008, pp. 533–537.

[18] Lassagne, B., et al., "Ultrasensitive Mass Sensing with a Nanotube Electromechanical Resonator," *Nano Lett.*, Vol. 8, 2008, pp. 3735–3738.

[19] Aubin, K. L., et al., "Microfluidic Encapsulated Nanoelectromechanical Resonators," *J. Vac. Sci. Technol. B*, Vol. 25, 2007, pp. 1171–1174.

[20] Sauerbrey, G., "Verwendung von Schwingquarzen zur Wägung dünner Schichten und zur Mikrowägung," *Z. Phys.*, Vol. 155, 1959, pp. 206–222.

[21] Martin, F., et al., "Pulse Mode Shear Horizontal-Surface Acoustic Wave (SH-SAW) System for Liquid Based Sensing Applications," *Biosensors and Bioelectr.*, Vol. 19, 2004, pp. 627–632.

[22] Gulyaev, Y. V., "Review of Shear Surface Acoustic Waves in Solids," *IEEE Trans. on Ultrason. Ferroelectr. Freq. Control*, Vol. 45, 1998, pp. 935–938.

[23] Gizeli, E., et al., "A Love Plate Biosensor Utilising a Polymer Layer," *Sens. Actuators B: Chem.*, Vol. 6, 1992, pp. 131–137.

[24] Mecea, V. M., "Is Quartz Crystal Microbalance Really a Mass Sensor?" *Sens. Actuators A: Phys.*, Vol. 128, 2006, pp. 270–277.

[25] Granstaff, V. E., and S. J. Martin, "Characterization of a Thickness-Shear Mode Quartz Resonator with Multiple Nonpiezoelectric Layers," *J. Appl. Phys.*, Vol. 75, 1994, pp. 1319–1329.

[26] Martin, S., V. Granstaff, and G. Frye, "Characterization of a Quartz Crystal Microbalance with Simultaneous Mass and Liquid Loading," *Anal Chem.*, Vol. 63, 1991, pp. 2272–2281.

[27] Domack, A., et al., "Swelling of a Polymer Brush Probed with a Quartz Crystal Resonator," *Phys. Rev. E*, Vol. 56, 1997, pp. 680–689.

[28] Voinova, M. V., et al., "Viscoelastic Acoustic Response of Layered Polymer Films at Fluid-Solid Interfaces: Continuum Mechanics Approach," *Physica Scripta*, Vol. 59, 1999, pp. 391–396.

[29] Karamollaoglu, I., H. A. Oktem, and M. Mutlu, "QCM-Based DNA Biosensor for Detection of Genetically Modified Organisms (GMOs)," *Biochemical Engineering J.*, Vol. 44, 2009, pp. 142–150.

[30] Campanella, H., et al., "Localized and Distributed Mass Detectors with High Sensitivity Based on Thin-Film Bulk Acoustic Resonators," *Appl. Phys. Lett.*, Vol. 89, 2006, 033507.

[31] Benetti, M., et al., "Microbalance Chemical Sensor Based on Thin-Film Bulk Acoustic Wave Resonators," *Appl. Phys. Lett.*, Vol. 87, 2005, 173504.

[32] Benetti, M., et al., "Thin Film Bulk Acoustic Wave Resonator (TFBAR) Gas Sensor," *Proc. Intl. IEEE Ultrason. Symp. 2004,* Montreal, Quebec, August 24–27, 2004, pp. 1581–1584.

[33] Zhang, H., and E. S. Kim, "Micromachined Acoustic Resonant Mass Sensor," *IEEE J. Microelectromech. Syst.*, Vol. 14, 2005, pp. 699–706.

[34] Weber, J., et al., "Shear Mode FBARs as Highly Sensitive Liquid Biosensors," *Sens. Actuators A: Phys.*, Vol. 128, 2006, pp. 84–88.

[35] Ekinci, K. L., Y. T. Yang, and M. L. Roukes, "Ultimate Limits to Inertial Mass Sensing Based upon Nanoelectromechanical Systems," *J. Appl. Phys.*, Vol. 95, 2004, pp. 2682–2689.

[36] Campanella, H., et al., "Localized-Mass Detection Based on Thin-Film Bulk Acoustic Wave Resonators (FBAR): Area and Mass Location Aspects," *Sens. Actuators A: Phys.*, Vol. 142, 2008, pp. 322–328.

[37] San Paulo, A., X. Liu, and J. Bokor, "Scanning Acoustic Force Microscopy Characterization of Thermal Expansion Effects on the Electromechanical Properties of Film Bulk Acoustic Resonators," *Appl. Phys. Lett.*, Vol. 86, 2005, 084102.

[38] Mecea, V. M., "Loaded Vibrating Quartz Sensors," *Sens. Actuators A: Phys.*, Vol. 40, 1994, pp. 1–27.

[39] Kanazawa, K. K., and J. G. Gordom, "Frequency of a Quartz Microbalance in Contact with Liquid," *Anal. Chem.*, Vol. 57, 1985, pp. 1770–1771.

[40] Martin, B. A., and H. E. Hager, "Velocity Profile on Quartz Crystals Oscillating in Liquids," *J. Appl. Phys.*, Vol. 65, 1989, pp. 2630–2635.

[41] Campanella, H., et al., "Analytical and Finite-Element Modeling of a Localized-Mass Sensor Based on Thin-Film Bulk Acoustic Resonators (FBAR)," *IEEE Sensors J.*, Vol. 9, 2009, pp. 892–901.

[42] Beeby, S., et al., *MEMS Mechanical Sensors*, Norwood, MA: Artech House, 2004.

[43] Greenwood, J. C., "Etched Silicon Vibrating Sensor," *J. Phy. E. Sci. Instrum.*, Vol. 17, 1984, pp. 650–652.

[44] Druck Ltd., Resonant Pressure Transducer (RPT) Series, http://www.druck.com.

[45] Differential Pressure High Accuracy Pressure (DPharp), Yokogawa Electric Corporation, http://www.yokogawa.com.

[46] Quartzdyne, http://www.quartzdyne.com.

[47] Mertens, J., et al., "Effects of Temperature and Pressure on Microcantilever Resonance Response," *Ultramicroscopy*, Vol. 97, 2003, pp. 119–126.

[48] Azevedo, R. G., et al., "A SiC MEMS Resonant Strain Sensor for Harsh Environment Applications," *IEEE Sensors J.*, Vol. 7, 2007, pp. 568–576.

[49] Talbi, A., et al., "ZnO/Quartz Structure Potentiality for Surface Acoustic Wave Pressure Sensor," *Sens. Actuators A: Phys.*, Vol. 128, 2006, pp. 78–83.

[50] Wang, W., et al., "Optimal Design on SAW Sensor for Wireless Pressure Measurement Based on Reflective Delay Line," *Sens. Actuators A: Phys.*, Vol. 139, 2007, pp. 2–6.

[51] Ferrari, V., et al., "Silicon Resonant Accelerometer with Electronic Compensation of Input-Output Cross-Talk," *Sens. Actuators A: Phys.*, Vols. 123–124, 2005, pp. 258–266.

[52] Aikele, M., et al., "Resonant Accelerometer with Selftest," *Sens. Actuators A: Phys.*, Vol. 92, 2001, pp. 161–167.

[53] Campanella, H., et al., "High-Frequency Sensor Technologies for Inertial Force Detection and AFM Applications Based on Thin-Film Bulk Acoustic Wave Resonators (FBAR)," *Microelectronic Eng.*, Vol. 86, 2009, pp. 1254–1257.

[54] Campanella, H., et al., "Accelerometer Based on Thin-Film Bulk Acoustic Wave Resonators," *Proc. IEEE Intl. Ultrason. Symp. 2007*, New York, October 28–31, 2007, pp. 1148–1151.

[55] Binnig, G., C. F. Quate, and C. Gerber, "Atomic Force Microscope," *Phys. Rev. Lett.*, Vol. 56, No. 9, 1986, pp. 930–933.

[56] Villanueva, G., et al., "DRIE Based Novel Technique for AFM Probes Fabrication," *Microelectronic Eng.*, Vol. 84, 2007, pp. 1132–1135.

[57] Hida, H., et al., "Fabrication and Characterization of AFM Probe with Crystal-Quartz Tuning Fork Structure," *Proc. IEEE Intl. Symp. Micro-NanoMechatronics and Human Science 2005*, Nagoya, Japan, November 7–9, 2005, pp. 97–101.

[58] San Paulo, A., X. Liu, and J. Bokor, "Atomic Force Microscopy Characterization of Electromechanical Properties of RF Acoustic Bulk Wave Resonators," *Proc. IEEE Intl. Conf. MEMS 2004*, Maastrich, the Netherlands, January 25–29, 2004, pp. 169–172.

[59] Lenz, J., and S. Edelstein, "Magnetic Sensors and Their Applications," *IEEE Sensors J.*, Vol. 6, 2006, pp. 631–649.

[60] Ciudad, D., et al., "Modeling and Fabrication of a MEMS Magnetostatic Magnetic Sensor," *Sens. Actuators A: Phys.*, Vol. 115, 2004, pp. 408–416.

[61] Keplinger, F., et al., "Lorentz Force Based Magnetic Field Sensor with Optical Read Out," *Sens. Actuators A: Phys.*, Vol. 110, 2004, pp. 112–118.

[62] Ripka, P., "Advances in Fluxgate Sensors," *Sens. Actuators A: Phys.*, Vol. 106, 2003, pp. 8–14.

[63] Yang, H. H., et al., "Ferromagnetic Micromechanical Magnetometer," *Sens. Actuators A: Phys.*, Vols. 97–98, 2002, pp. 88–97.

[64] Vasquez, D. J., and J. W. Judy, "Optically Interrogated Zero-Power MEMS Magnetometer," *IEEE/ASME J. Microelectromech. Syst.*, Vol. 16, 2007, pp. 336–343.

[65] Cho, H. J., and Ch. H. Ahn, "Magnetically Driven Bi-Directional Optical Microscanner," *J. Micromech. Microeng.*, Vol. 13, 2003, pp. 383–389.

[66] Goedeke, S. M., S. W. Allison, and P. G. Datskos, "Non-Contact Current Measurement with Cobalt-Coated Microcantilevers," *Sens. Actuators A: Phys.*, Vol. 112, 2004, pp. 32–35.

[67] Leichle, T. C., et al., "A Low-Power Resonant Micromachined Compass," *J. Micromech. Microeng.*, Vol. 14, 2004, pp. 462–470.

[68] Kim, Y.-S., et al., "A Class of Micromachined Magnetic Resonator for High-Frequency Magnetic Sensor Applications," *J. Appl. Phys.*, Vol. 99, 2006, 08B309.

[69] Greywall, D. S., "Sensitive Magnetometer Incorporating a High-Q Nonlinear Mechanical Resonator," *Measurement Science and Technology*, Vol. 16, 2005, pp. 2473–2482.

[70] Herrera-May, A. L., et al., "A Resonant Magnetic Field Microsensor with High Quality Factor at Atmospheric Pressure," *J. Micromech. Microeng.*, Vol. 19, 2009, 015016.

[71] Vasquez, D. J., and J. W. Judy, "Flexure-Based Nanomagnetic Actuators and Their Ultimate Scaling Limits," *Proc. IEEE Intl. Conf. MEMS 2008*, Tucson, AZ, January 13–17, 2008, pp. 737–741.

CHAPTER 9

Radio Frequency Applications

Radio frequency (RF) circuits are responsible for conditioning the signals transmitted and received by antennas of a wireless telecommunication system. Such signals carry the huge amount of information of modern telecommunication systems, like public and private mobile Internet applications. Thus, RF signals need to be accommodated into wireless channels to meet the power, bandwidth, and carrying-frequency requirements of the telecommunication standard implemented for the transmission and reception of the information. At the transmitter side, RF systems take digital baseband signals and convert them into analog counterparts able to access the channel and to cross the distances specified by the application. At the receiver, on the other hand, the incoming signal from the antenna has to be selected, amplified, and reconverted into the digital domain to recover the transported information.

RF systems are, in essence, analog circuits—with some exceptions—and their miniaturization and integration with their digital counterparts have been the object of intensive research work. Since the cost and failure rates of RF analog devices are notoriously higher than those of digital components, diminishing of the size and power consumption of wireless devices drives the development of new RF components. At a certain point of history, the miniaturization road path of RF components changed its technological paradigm and took advantage of the benefits of IC and MEMS processes, giving rise to the RF MEMS concept. Thus, RF MEMS are the application of MEMS technology in the fields of RF and microwave circuits. Inductors, varactors, transmission lines, switches, and resonators are some of the RF MEMS components fabricated with the methodologies and micromachining techniques used in current MEMS processes. Based on these components, RF circuits and systems like oscillators, mixers, filters, and amplifiers have dramatically reduced their size and improved their performance. Nowadays, most of the miniature RF MEMS applications have matured from the early R&D stages to reach the status of industrial and commercial products. Diverse companies are selling millions of units of RF MEMS components, which represent a significant share of the global MEMS market.

Resonator-based RF MEMS are an important group of the RF MEMS kind, and they are the study object of this chapter. RF MEMS resonators are useful to implement both passive- and active-circuit components and are, among the RF MEMS components, those achieving the greatest market impact and technological maturity. We have selected some of the most remarkable commercial products and laboratory demonstrators to explain the competitive advantages of resonant RF MEMS against other RF technologies. First, we contextualize the field of RF systems and RF MEMS, and their impact on modern telecommunication systems. Then, we

begin the study by describing the operation principles, functionality, specifications, and implementations of passive-circuit applications like filters, duplexers, triplexers, and multiplexers. These applications are implemented with either acoustic or electromechanical resonators. Next, focus is laid on active-circuit applications, as we study RF MEMS-resonator-based oscillators, low-noise amplifiers, and integrated RF front ends. The chapter concludes with a discussion on the latest state-of-the-art developments of resonant RF MEMS applications.

9.1 Introduction

The communication and information technologies revolution has carried an unprecedented development of services and appliances, which need a physical support to be efficiently offered. The explosion of both public and private wireless mobile Internet systems and the aggressive competition of service providers have stimulated the market to offer innovative end-user terminals. From the past ten years to now, several technological paradigms have been broken, passing from the mobile phone to the convergent, ubiquitous personal device.

Nowadays, functionality and aesthetics are combined on the same apparatus without sacrifice of portability. The requirements of modern third generation (3G) and beyond-3G (B3G) mobile systems involve a complex set of specifications. Among them, we find internetworking capability, multiple-band access, low power consumption, multimedia interfaces and services, and small size. In addition, personalized interfacing, tactile screens, navigation, positioning, and personal networking capabilities have been incorporated into the latest mobile systems. Provided with a variety of MEMS sensors, like silicon accelerometers and pressure and proximity transducers, the Apple's iPhone [1] combines a visual and energy-efficient interface with a powerful telecommunication system able to network to UMTS [2], Wi-Fi [3], HSDPA [4], GSM [5], EDGE [6], Bluetooth [7], and GPS [8]. Other manufacturers like Nokia [9], Samsung [10], and LG [11] offer competing devices as well. All are positioning as the paradigm of the convergent device.

3G specifications impose stringent requirements to the RF section of the telecommunication system of the mobile device, such as low power consumption, low noise amplification, and filtering low insertion losses and high selectivity. In background, the promise of the single-chip RF front end also remains a milestone of the low-cost, low-power device. These factors have motivated the development of compact technologies to replace the traditionally bulky analog components of the RF section. The role of RF MEMS in the miniaturization of key components, like switches, duplexers, and band-selection filters, is crucial for this purpose. RF MEMS are fabricated with the methodologies and micromachining techniques used in current MEMS processes. The recently demonstrated integration of RF MEMS with CMOS processes is boosting the size reduction of the RF sections and front ends. The now-classic diagram of Figure 9.1 illustrates the impact of RF MEMS in the miniaturization of modern transceivers [12]. As observed in the figure, a considerable number of RF components (the shadowed ones) are potentially replaceable by RF MEMS. Actually, commercial products have already been placed on most of the shadowed blocks of the diagram, instead of components made with

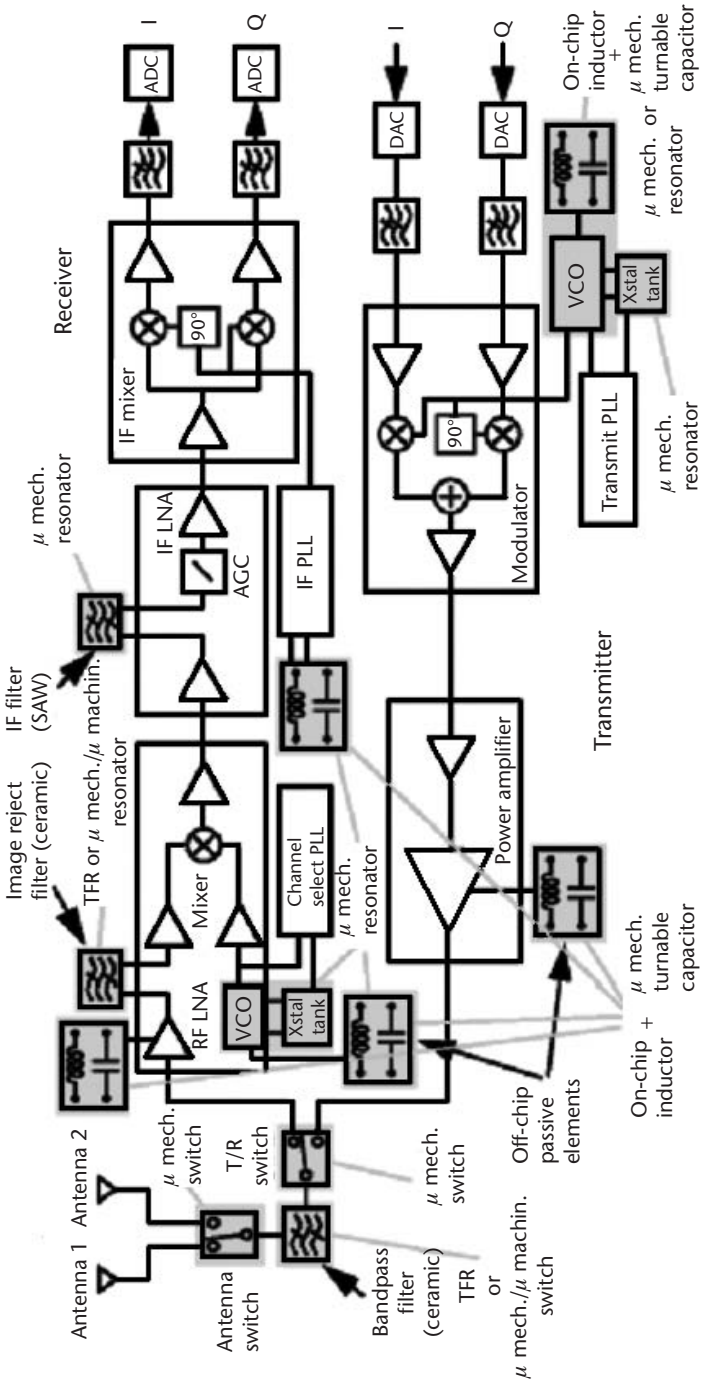

Figure 9.1 Block diagram of modern telecommunication transceiver with RF MEMS replacing traditional-technology components (highlighted). (© 2000 IEEE [12].)

traditional technologies like ceramics or bulky crystals, as we will review in the next sections.

RF MEMS offer many advantages against traditional technologies: low weight, low insertion losses, high off-state isolation, high precision, low power consumption, and high reliability, among others. Due to these characteristics, the multiple-band receiver integrating in-parallel filters and switches or multiplexers for channel selection has also been envisioned. To date, duplexers, triplexers, and quintplexers integrating band-selection filters on a single chip are available in the market, as detailed in Section 9.2.2. The schema of Figure 9.2 depicts the concept of the in-parallel multiple-band receiver. In this example, modern wireless standards like UMTS or Wi-Fi are selected for baseband processing by RF MEMS switches. The RF MEMS antenna might also be reconfigured to adapt its bandwidth to the different frequency bands of GSM-800/900 and UMTS-2000/3000.

Not all is rose-colored concerning RF MEMS. Due to its moving-structure nature, these devices often need hermetic packaging, and many of them are far from being robust in hazardous environments (e.g., vibrations, temperature). Besides, some of them need very high polarization/actuation voltages not compatible with standard CMOS processes, as it is the case of some resonators. Large time reliability is still to be demonstrated in switches, for example. Mass production also requires resolving process compatibility and test issues. Nevertheless, the RF MEMS market offers a variety of products like BAW filters, switches, inductors, and resonators. The size of the market is still limited, in comparison with other MEMS applications like inkjet heads or pressure and inertial sensors. However, RF MEMS components are expected to be a major breakthrough, thus satisfying the performance, miniaturization, and reconfiguration requirements of telecommunication systems [13]. The diagram of Figure 9.3 shows the RF MEMS commercialization status, discriminated by the different products available to date. We see how BAW filters and duplexers for microwave bands (1–10 GHz) have the largest industrial history with

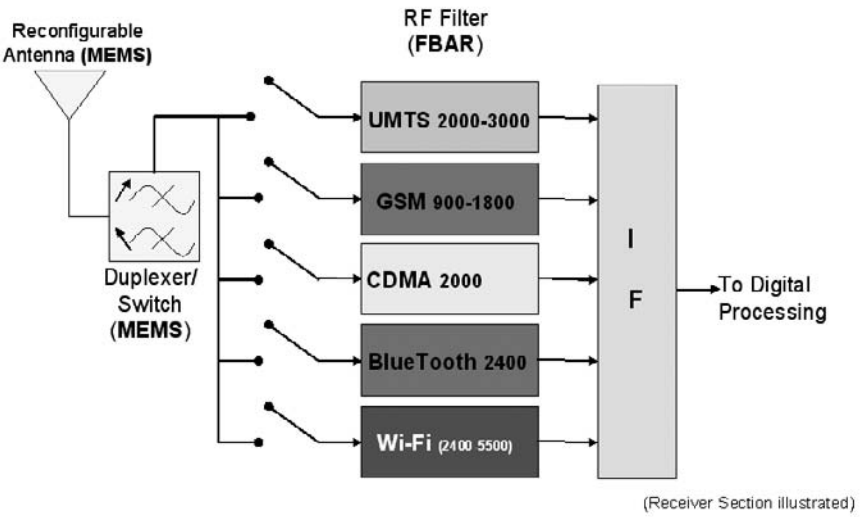

Figure 9.2 Vision of the in-parallel, multiple-band receiver integrating reconfigurable RF MEMS antenna, switches, and band-selection filters tuned at the central frequencies of current 3G and wireless Internet standards.

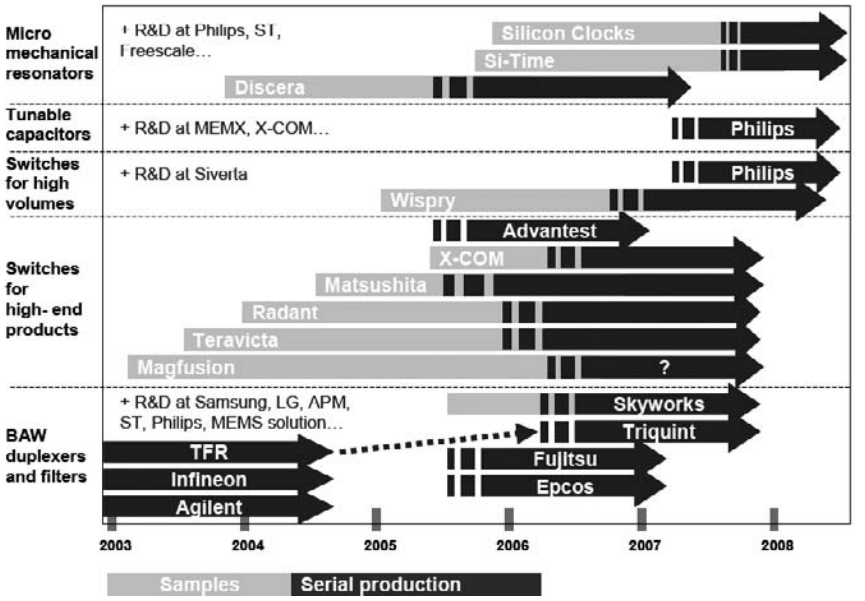

Figure 9.3 RF MEMS commercial products road path. (© 2005 WTC [13].)

a significant number of players competing for the market. Among them, Avago Technologies (formerly Agilent Technologies) [14] has the biggest share of the BAW market, followed by Epcos [15], TriQuint [16], and Skyworks [17]. RF oscillators and clocks based on micromechanical resonators (VHF and UHF bands) fabricated by Discera (mid-2005) [18] and Si-Time (2007) [19] are also available, and Philips and Baolab are still in the product development stage of MEMS switches [20, 21]. In this chapter, we will focus our attention on some of these commercial BAW filters, duplexers, resonant switches, and oscillators. Additionally, we make room for components and subsystems still in the R&D stages.

9.2 Passive-Circuit Applications

A passive circuit application is an all-passive component circuit without signal amplification functions. Typical examples are passive filters composed by more than one resonator. The components are integrated at the board level with RF integrated circuits (RFIC) to offer a specific RF function, mainly band selection and channel selection filtering. Filter-based multiplexing incorporates broadband multiple filtering in a single chip. In this section, we study some of the most popular resonator-based filters, multiplexers, and the resonant switch.

9.2.1 SAW, BAW, and FBAR-Based Band-Selection Filters

A band-selection filter rejects the signals of adjacent channels in communication systems. In typical wireless mobile systems, for example, the transmitted and received signals are channelized using different frequency bands. In current transceiver architectures, the transmit filter fits between the driver and power amplifiers.

When placed at the transmission path, the filter prevents the transmitted signal from feedback into the receiver path, thus increasing the sensitivity. With the proper design, the filter can also reject the out-of-band signals at the receiver path, including images of the RF incoming signal.

The history of RF filters began with ceramic filters, which were developed using technology similar to that of quartz crystal and electromechanical resonator filters. Based on the type of piezoelectric materials, four stages of historical development of ceramic filters may be identified. The first material was single-crystal quartz, the second was single-crystal Rochelle salt, the third was barium titanate ceramics, and the fourth was lead-zirconate-titanate (PZT) ceramics [22]. The electronic technology evolution imposed the need for filter miniaturization. Then, new fabrication processes and materials were developed and thin-film aluminum nitride (AlN) and zinc oxide (ZnO) became the standard for the new kind of SAW and BAW miniature resonators. Classical applications of crystal and ceramic filters provide selectivity in communications receivers at frequencies of 9 MHz or 10.7 MHz, or at higher frequencies as roll-off filters in receivers using up-conversion. Even a lower frequency (455 kHz) is used as the second intermediate frequency filters in some communication receivers. Ceramic filters at 455 kHz can achieve similar bandwidths to crystal filters at 10.7 MHz. However, the evolution of communication systems led to new services requiring more bandwidth and higher frequency bands, where the selectivity, insertion losses, and overall performance of traditional filter technologies were not enough to meet the requirements of new systems. By up-shifting the frequency to the VHF and UHF passbands, SAW filters opened the way to gigahertz band BAW filters, including both SMR- and FBAR-based filters.

BAW-based filters offer unprecedented performance, exhibiting lower insertion losses, higher out-of-band rejection, and a more reduced size than those made with previous technologies. Two topologies are mostly implemented in RF filter applications—namely, the stacked crystal filter (SCF) and the ladder filter. The SCF filter stacks two or more BAW resonators with the appropriate thicknesses to build the filtering shape, as illustrated in the schematic view of Figure 9.4 [23].

On the other hand, the ladder filter topology is comprised of an *N*th-order interconnection of series and shunt FBARs arranged in a planar way. The schematic and

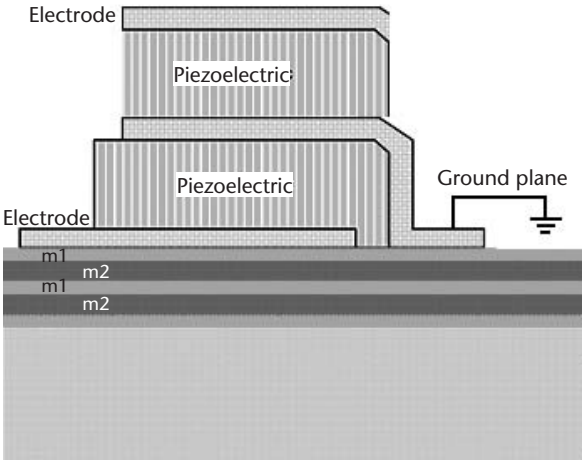

Figure 9.4 SCF topology (here the filter is mounted on a Bragg's reflector).

equivalent-circuit models of a filter with $N = 3$ are depicted in Figure 9.5(a, b), where N is the number of series-to-shunt cells, counting from the input to the output port of the filter [24]. As suggested by the process representation of Figure 9.5(c), series resonators are designed to be thinner than shunt FBARs. Also, shunt resonators have a bigger electrode area in order to optimize the in-band and out-of-band performances of the filter [25]. The pictures of Figure 9.5(d) show the physical layout of filters fabricated within the IMB-CNM's CNM25 technology [26].

In 2002 Avago Technologies (Agilent Technologies at that time) released the first FBAR-based filters of the market. This launching represented a breakthrough in miniaturization and performance and came in an opportune market moment to challenge SAW filters. Very soon, FBAR-based filters became a commercial success, replacing previous-technology filters in the at-the-time newest US PCS and UMTS mobile handsets. Figure 9.6(a–d) shows the RF performance of the Avago's ACPF-7003 1.6×2.0-mm high reception and image rejection transmission (TX) filter for the US PCS band. With a passband of 1,850–1,910 MHz and typical insertion losses of 2.5 dB, the filter features 35-dB minimum attenuation in the 1,930–1,990-MHz band and 25-dB image rejection at 1,830 MHz. Its main application is in US PCS band handsets and wireless data terminals [27]. A similar high rejection TX filter for US PCS band is presented in [28].

TriQuint Semiconductor also has a relevant market presence with their BAW filter products. TriQuint's filters implement solidly mounted resonators (SMRs) with Bragg mirrors to improve the quality factor of the resonators, instead of the micromachined air cavity of FBARs. Two examples of the TriQuint's BAW-device catalog are the 880404 GPS (1,575 MHz) and the 880369 Wi-Fi (802.11a, 5,775 MHz) filters, available in their $3.71 \times 2.51 \times 0.84$ mm and $3.26 \times 1.60 \times 0.84$ mm packages, respectively [29, 30]. Figure 9.7(a) shows the passband response of the GPS filter, with a central frequency of 1,575 MHz, typical insertion losses of 1.5 dB, and 3-dB bandwidth of 35 MHz. The Wi-Fi filter, at its time, performed insertion losses of 3.0 dB, and 3-dB bandwidth of 100 MHz at the central frequency of 5,775 MHz, as shown in the S21 plot of Figure 9.7(b).

SAW filters have also been an important technology in the RF market, because of their good performance and low manufacturing difficulty. Companies like Epcos and Epson Toyocom [31] are world leaders in producing components made with this technology. For example, the Epcos B7843 SAW filters for PCS applications exhibit maximum insertion losses of 3 dB and out-of-band attenuation bigger than 40 dB at the central PCS frequency of 1,850 MHz [32]. More recently, however, SAW filters are gradually being replaced by the newest and technology-compatible BAW filters. Furthermore, some products are been hybridized, thus integrating both SAW and BAW devices in the same chip. Epcos is also commercializing BAW-based filters for duplexer applications, which we discuss in the next section.

9.2.2 Duplexers, Triplexers, and More

A duplexer is a three-port component performing filtering of RF signals at the point closest to the antenna in the RF chain of a wireless handset or data terminal. The duplexer allows simultaneous transmission and reception of RF signals through a single antenna. Thus, it reduces the complexity, size, and cost of the RF system,

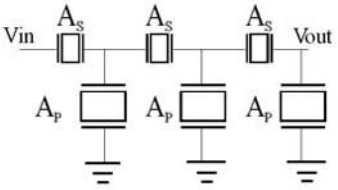

(a)

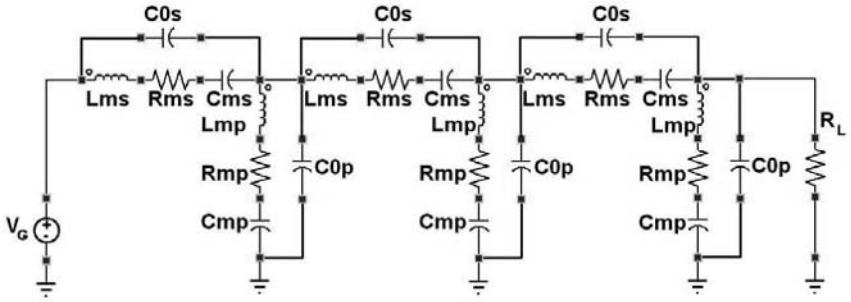

(b)

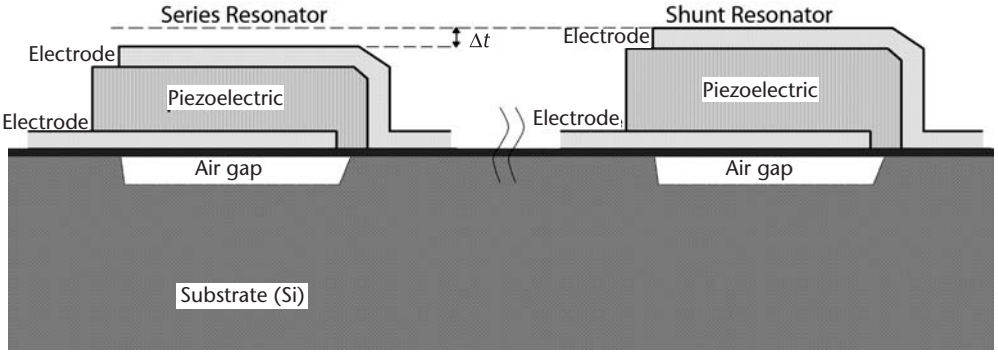

(c)

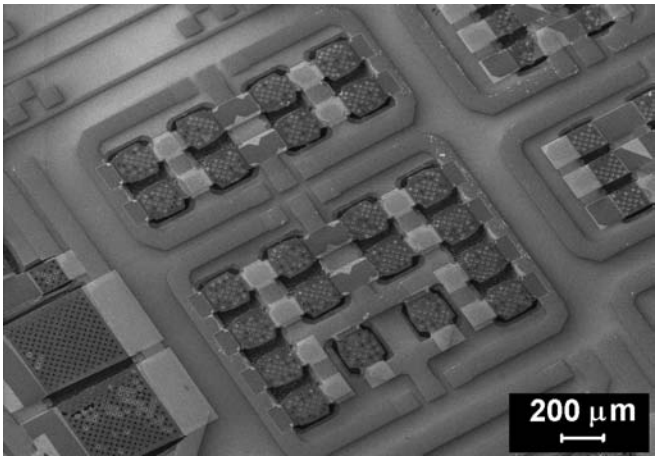

(d)

Figure 9.5 Ladder filter topology: (a) schematic view; (b) equivalent-circuit model; (c) process description; and (d) filter implementations within the CNM25 technology.

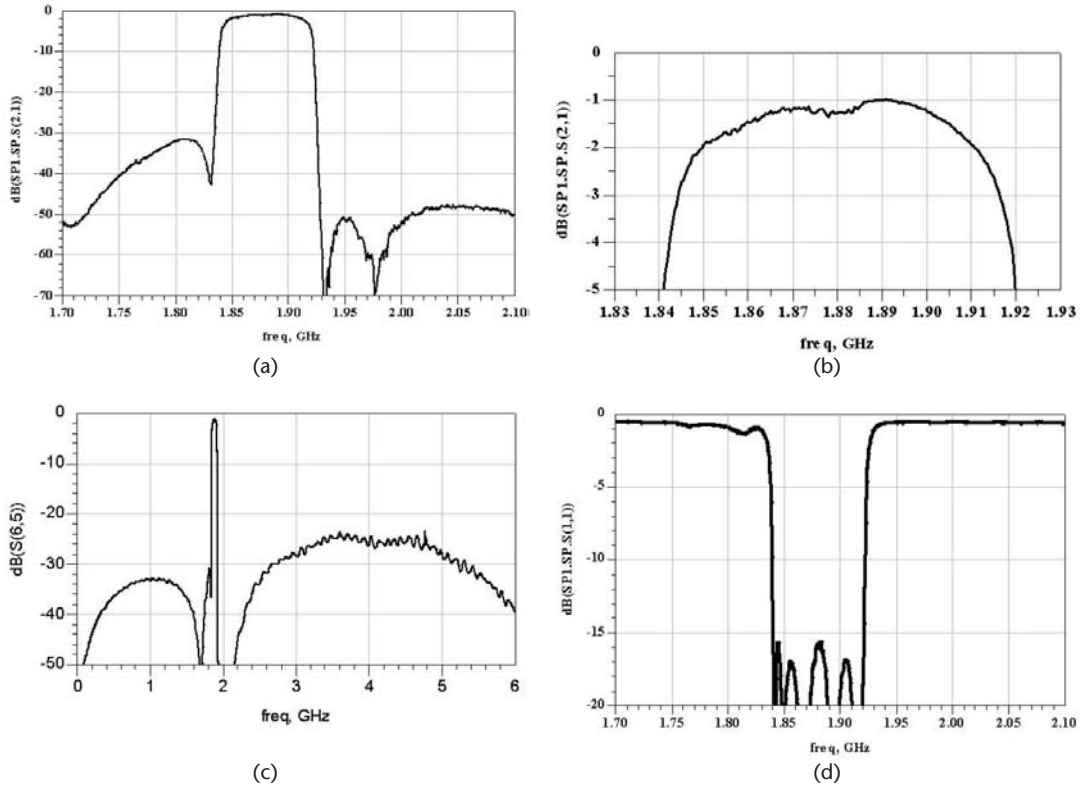

Figure 9.6 RF performance of Avago's ACPF-7003 high-reception and image-rejection transmission filter for the US PCS band: (a) attenuation versus frequency (narrowband); (b) insertion loss versus frequency (zoom in of (a) in the passband); (c) attenuation versus frequency (broadband); and (d) return loss versus frequency. (© 2006 Avago Technologies [28].)

which is particularly important in mobile phones. In this way, the duplexer avoids the need for dedicated antennas or switches to select the transmission (TX) and reception (RX) channels by implementing two filters within the same circuit, as depicted in the diagram of Figure 9.8. The first duplexer port (PORT 1) connects the output signal of the power amplifier to the transmitter filter, while the second port (PORT 2) is employed to connect the signal incoming from the antenna and filtered by the passband RX filter. The third port (PORT 3) connects the antenna to both filters. Two specifications mainly characterize a duplexer:

1. The TX and RX filters have disjoint passbands to allow proper selection of the TX and RX signals.
2. The isolation between the TX and RX ports PORT1 and PORT 2 must meet the application requirements. Thus, both the TX and RX filters must provide enough selectivity and out-of-band rejection to reduce the signal circulation occurring at the antenna port (PORT 3).

The Avago Technologies ACMD-7602 is a miniature duplexer designed for use in UMTS band I handsets [33]. The maximum insertion losses in the TX channel are only 1.5 dB, which minimizes current drain from the power amplifier into the RX

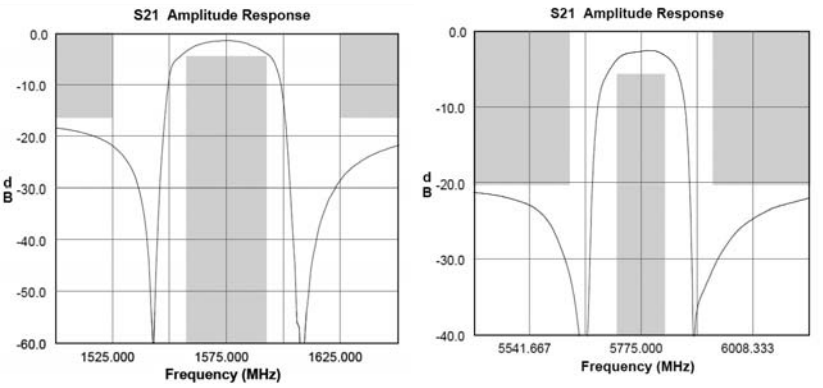

(a) (b)

Figure 9.7 GPS and 802.11a RF BAW Filters from TriQuint Semiconductor: (a) attenuation versus frequency (S21) of the 1,575-MHz GPS filter; and (b) attenuation versus frequency (S21) of the 5,775-MHz 802.11a filter. (© 2007 TriQuint Semiconductor Inc. [29, 30].)

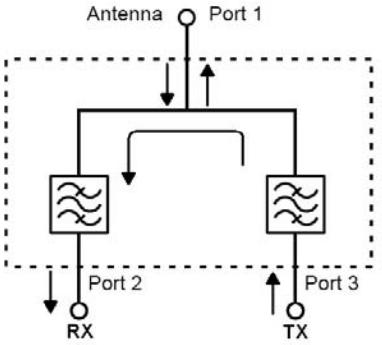

Figure 9.8 Schematic diagram of a duplexer: the three ports connect the transmitter output (PORT 1), the receiver input (PORT 2), and the antenna (PORT 3).

section. Insertion losses in the RX channel are achieved at a maximum of 2.0 dB, improving receiver sensitivity. The ACMD-7602 is designed with Avago's FBAR technology. The duplexer enhances the sensitivity and dynamic range of WCDMA receivers by providing more than 53-dB attenuation of the transmitted signal at the receiver input and more than 43-dB rejection of transmit-generated noise in the receiver band. The two duplexer filters are assembled in a molded chip-on-board module that is less than 1.2 mm high with a maximum footprint of only 2.5×3.0 mm. The high power handling capability of +33 dBm is another remarkable feature of this device. Figure 9.9(a) shows the insertion loss performances of the TX (1,920–1,980 MHz) and RX (2,110–2,170 MHz) filters. The Epcos' B7692 BAW duplexer is another high-performance device for use in the WCDMA band II (1,880–1,960 MHz) [34]. The maximum insertion losses in the usable 60-MHz passband are 2.2 dB and 2.6 dB in the TX and RX bands, respectively. TX-RX isolation levels of the transmitted signal at the receiver input and the transmit-generated noise in the receiver band are 50 dB and 48 dB, respectively. The insertion loss

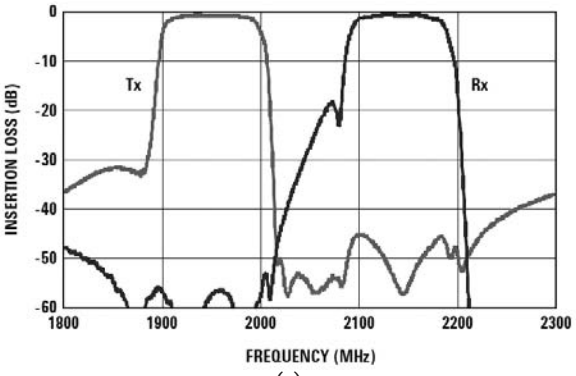

(a)

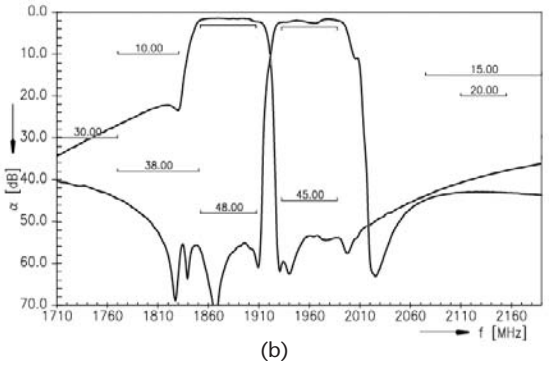

(b)

Figure 9.9 TX rejection in RX band and RX rejection in TX band of duplexers. (a) Avago's ACMD-7602 UMTS band I FBAR duplexer. (© 2008 Avago Technologies [33].) (b) Epcos B7692 WCDMA band II BAW duplexer. (© 2008 Epcos [34].)

performances of the Epcos' TX (1,850–1,910 MHz) and RX (1,930–1,990 MHz) filters are shown in the plot of Figure 9.9(b).

So far, we have mentioned the most common use of duplexers, where the antenna port is bidirectional, and the TX and RX are input and output ports. However, the duplexer can be designed to arbitrarily change the use of the three ports (e.g., a single input port and two output ports). In this case, the duplexer splits the signal incoming from the antenna and delivers filtered versions to the output ports, which receive signals in their respective band of interest. The philosophy of the three-port duplexer can be extended to triplexers, quintplexers, and, in general, multiplexers. To illustrate, just consider the triplexer and quintplexer depicted in Figure 9.10. The triplexer has four ports and the quintplexer has six ports, one of them devoted to the antenna connection. However, the use of the remaining ports is different in the triplexer and the quintplexer. In the Epcos B9100 SAW triplexer, the GPS, cellular, and PCS ports are outputs to connect the RX section [35]. On the other hand, Avago's ACFM-7102 quintplexer features an input S-GPS port, two TX cellular and PCS output ports, and two RX cellular and PCS input ports connecting to the receiver [36].

The frequency response of the Epcos B9100 SAW triplexer exhibits low insertion losses in its three passbands. Its features are maximum values of 0.8, 0.9, and 2.0 dB in the cellular, PCS, and GPS bands at central frequencies of 859, 1,920, and

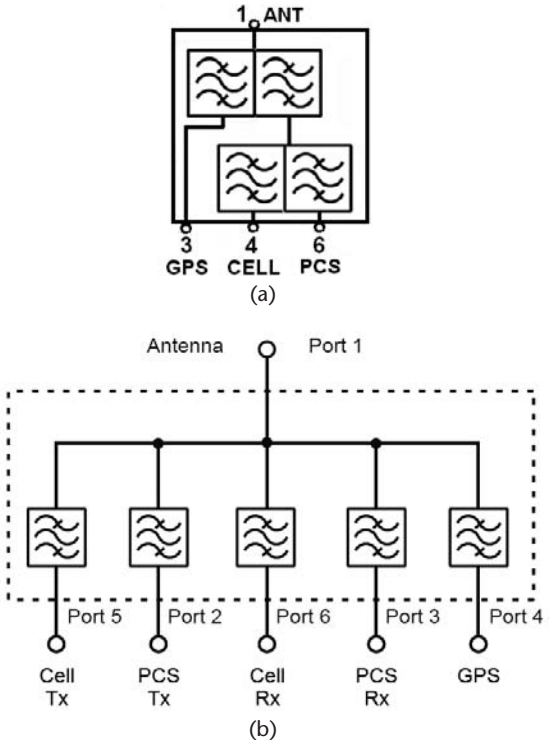

Figure 9.10 Schematic diagram of multiplexers. (a) Epcos B9100 SAW Cell/GPS/PCS triplexer. (© 2008 Epcos [35].) (b) Avago's ACFM7102 PCS/Cellular/S-GPS Quintplexer. (© 2008 Avago Technologies [36].)

1,575 MHz, respectively. Typical interband attenuations are 35 dB (cellular to GPS) and 23 dB (PCS to GPS), and power handling of +31 dBm. The transfer function of Figure 9.11(a) shows the antenna to PCS band attenuation, where the interband requirements specified by the standard are depicted with the rectangular masks at 850 and 1,575 MHz. Note the deep attenuations provided by the filter at the GPS and cell bands. The Avago Technologies ACFM-7102 quintplexer combines PCS and cellular duplexer functions with a GPS filter and is packaged in a module that is less than 1.2 mm high with a footprint of only 5×8 mm and high power handling of +33 dBm. The transfer functions of Figure 9.11(b) show the wideband insertion losses of both the PCS and cellular duplexers of the ACFM-7102. The insertion loss and attenuation performances of all the quintplexer ports are specified as follows [36]:

- GPS filter (1,574.4–1,576.4 MHz): insertion loss: 2.0 dB max., isolation in PCS/Cell Tx 45 dB min.;
- Cellular duplexer Rx (869–894 MHz): insertion loss: 3.6 dB max., noise blocking: 40 dB min.;
- Cellular duplexer Tx (824–849 MHz): insertion loss: 2.6 dB max., interferer blocking: 55 dB min.;

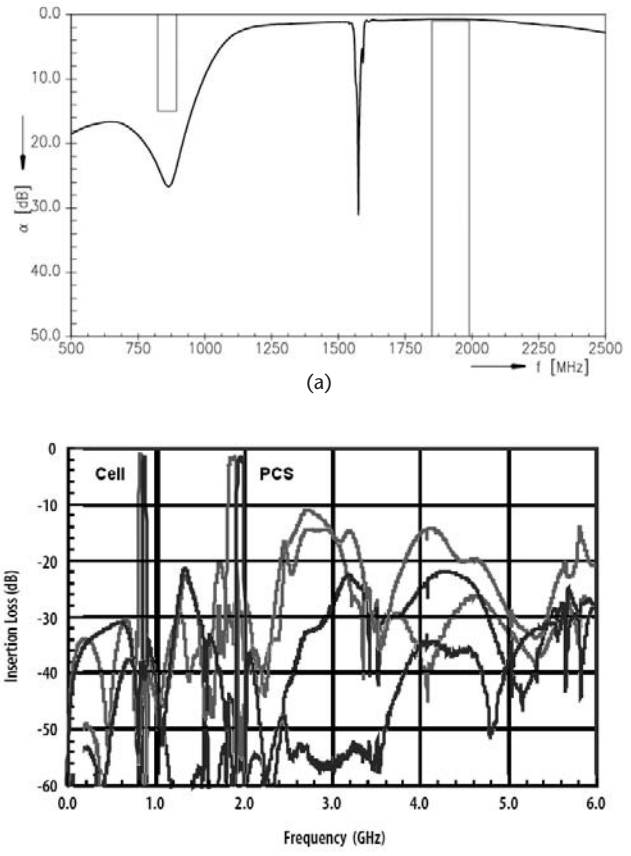

Figure 9.11 Transfer function of the insertion loss of multiplexers. (a) Epcos B9100 SAW cell/GPS/PCS triplexer. (© 2008 Epcos [35].) (b) Avago's ACFM7102 PCS/cellular/S-GPS Quintplexer. (© 2008 Avago Technologies [36].)

- PCS duplexer Rx (1,930.5–1,989.5 MHz): insertion loss: 4.4 dB max., noise blocking: 40 dB min.;
- PCS duplexer Tx (1,850.5–1,909.5 MHz): insertion loss: 3.9 dB max., interferer blocking: 53 dB min.

More than one acoustic technology can be combined to produce a duplexer. For example, Epcos also developed the hybrid B7686 SAW-BAW duplexer for WCDMA band II handsets. This combination allows the duplexer to have improved TX-to-RX and RX-to-TX attenuations of 45 and 50 dB [37]. The filters can also be combined to produce more complex RF front-end modules, as we study in Section 9.3.4.

9.2.3 Microelectromechanical Filters

Unlike the acoustic resonator applications previously studied, the design of silicon-based RF MEMS circuits considers different operation principles, actuation

mechanisms, and resonance modes. In this section, we study how movable resonant structures made of different materials, mainly polysilicon, are combined to produce filters. As a difference to the acoustic wave propagating through or at the surface of the piezoelectric layer of acoustic resonators, the micromechanical resonators move themselves in flexural, torsional, or extensional resonance modes (or combination of them). When several of these resonators are mechanically coupled, the frequency response is also combined, and the resulting system behaves as a filter, for example.

The concept of MEMS-resonator filters has extensively been developed at universities in the United States, Europe, and Japan. The groups of Professor C. T.-C. Nguyen at University of Michigan and UC–Berkeley have been among those proposing the first concepts and models [38–40]. One of these concepts is shown in the SEM image of Figure 9.12(a), where the perspective view of a two-resonator filter with electrodes is observed. In this example, the filter consists of two identical mechanical clamped–clamped beam resonators, coupled mechanically by a flexural-mode beam. Conducting strips underlie the central regions of each resonator and serve as capacitive transducer electrodes positioned to induce resonator vibration in a direction perpendicular to the substrate. The resonator-to-electrode gaps are 1,300Å. The MEMS filter can be modeled through an equivalent mechanical circuit. In the circuit, a mass-spring-damper system represents each resonator, while the coupling beam corresponds to a network of mechanical springs, as depicted in the model of Figure 9.12(b). Such a coupled two-resonator system exhibits two mechanical resonance modes with closely spaced frequencies that define the filter passband [38].

As studied by Nguyen et al. and according to the previous model, the center frequency of the filter is mainly determined by the frequencies of constituent resonators. On the other hand, the stiffness of the coupling spring largely determines the spacing between modes—the bandwidth. As it happens in mechanical resonators,

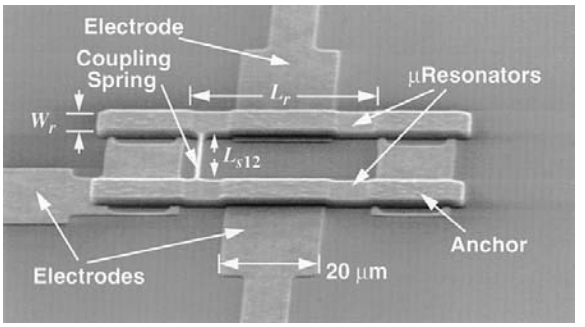

(a)

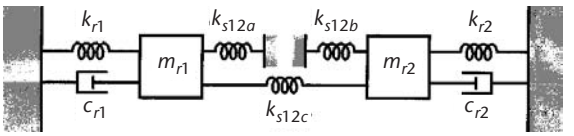

(b)

Figure 9.12 Two-resonator microelectromechanical filter: (a) SEM image showing the clamped-clamped resonators, coupling beam, and electrodes; and (b) mechanical model of the filter. (© 2000 IEEE [38].)

the application of an electrical input signal creates an electrostatic force between the input electrode and the first conductive resonator. The force induces vibration of the input resonator whenever the input signals have a frequency within the passband of the filter. In time, this vibration is transmitted to the output resonator via the coupling spring, causing it to vibrate as well. Vibration of the output resonator creates a dc-biased current and time-varying capacitor between the conductive resonator and the output electrode, which then sources an output current flowing through the termination, read-out impedance. If the value of the impedance is properly chosen, the filter exhibits a flattened passband as shown in Figure 9.13.

Sony Corporation proposes a bandpass filter for the VHF band using MEMS technology [41]. Additionally, Sony has succeeded in integrating a MEMS filter with peripheral circuits on a single chip by adding MEMS processing into the existing BiCMOS process. The bandpass filters are created by combining four resonators. Thus, they are a collection of parallel-coupled clamped-clamped beam structures, whereby the resonating beam is held fixed at its both ends. Sony's contribution is the three-port resonator design, depicted in Figure 9.14(a): the beam resonance mode is changed from first order (a single wave) to second order (two waves), and the input and output signal lines are placed under the beam independently. The design improves the signal-to-noise ratio and reduces the influence of manufacturing variations in the patterning because of the longer beam length required in the second-order flexion mode [41]. Next, Sony increased the signal level by arranging multiple resonators in parallel. By adjusting the resonator parallel coupling pattern, they achieve Q factors and insertion losses appropriate for the bandpass filter. Figures 9.14(b) and 9.14(c) show schemas of the four-resonator lattice-type bandpass filter and its frequency response, respectively. With a central frequency of 97 MHz, the filter performs a 3.9% bandwidth (3.8 MHz), a good 3.5-dB insertion loss, and out-of-band suppression of 33.8 dB.

Sony next created an embedded MEMS filter chip that consists of this MEMS filter and the impedance matching circuit as the next stage. Polysilicon resonators are formed after the front end of line (FEOL) process in their BiCMOS process. After the multilayer interconnect process has completed, the interlayer dielectric

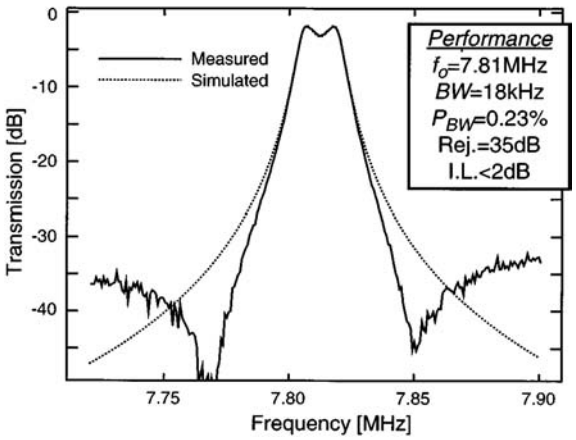

Figure 9.13 Frequency response of the two-resonator microelectromechanical filter: its central frequency is 7.8 MHz with a quality factor of 435. (© 2000 IEEE [38].)

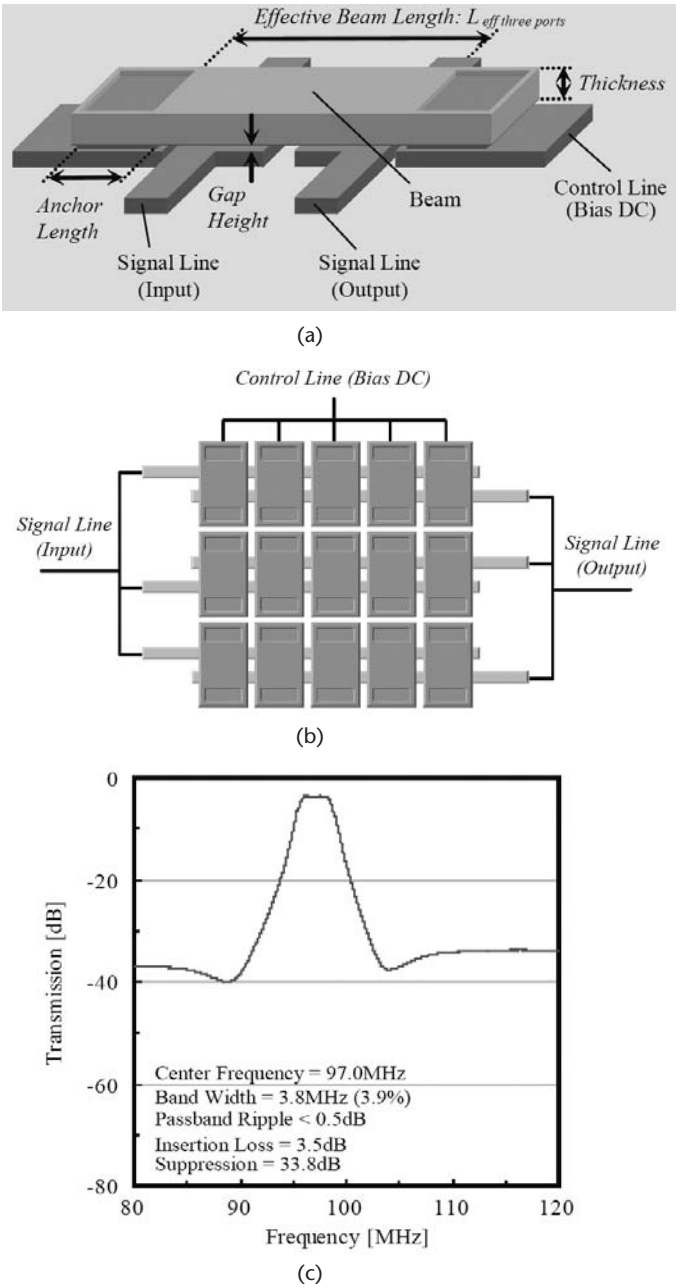

Figure 9.14 Sony's four-resonator MEMS filter: (a) three-port constituent MEMS resonator; (b) lattice-type bandpass filter circuit; and (c) frequency response of the filter. (© 2009 Sony [41].)

(ILD) and the sacrificial layer around the MEMS resonators are removed with buffered-HF treatment [41].

The design of MEMS filters can be done by following the same procedures and using the same network topologies and coupled-resonator ladder-filter synthesis techniques of electronic filters. The topology and the geometry of the filter resonators can be very diverse, such as those implemented using the disk and squared array

filters developed by Li et al. [40] and Clark et al. [42], respectively. The MEMS filter constituted by parallel-coupled arrays of microelectromechanical square resonators demonstrated by Demirci et al. [43] greatly reduces the equivalent impedance of the aggregate resonator by up to a factor of 30 in an array of 30 strongly coupled devices while retaining high quality factors near 10,000.

Figure 9.15 shows one of these resonator array filters and its frequency response with a central frequency of 68 MHz, stopband rejection of 25 dB, and insertion loss less than 2.7 dB. The MEMS filter design is based on mechanical soft-coupling of the resonators. They have been arrayed in parallel through hard mechanical coupling in order to reduce the overall impedance level and improve power handling. The hard-coupling serves to lock the frequencies of the resonators, eliminating spurious responses, which might otherwise arise from simple electrical parallelism. The single cell consists of one input resonator coupled to one output resonator, and the resulting filters are built from this basic cell up to arrays consisting of 30 cells [42].

A more sophisticated resonator array concept involves the design of the medium-scale integrated (MSI) vibrating microelectromechanical filter proposed by Li et al. [40]. Through a hierarchical building block approach, one of the most significant contributions of this work is the demonstration that mechanical circuit design methodologies can be just as powerful as those used in the transistor world to enhance functionality. The MSI filter circuit utilizes radial-mode disks and mechanical link elements to achieve low motional resistance while suppressing unwanted modes and feed-through signals with a 0.06% bandwidth insertion loss less than

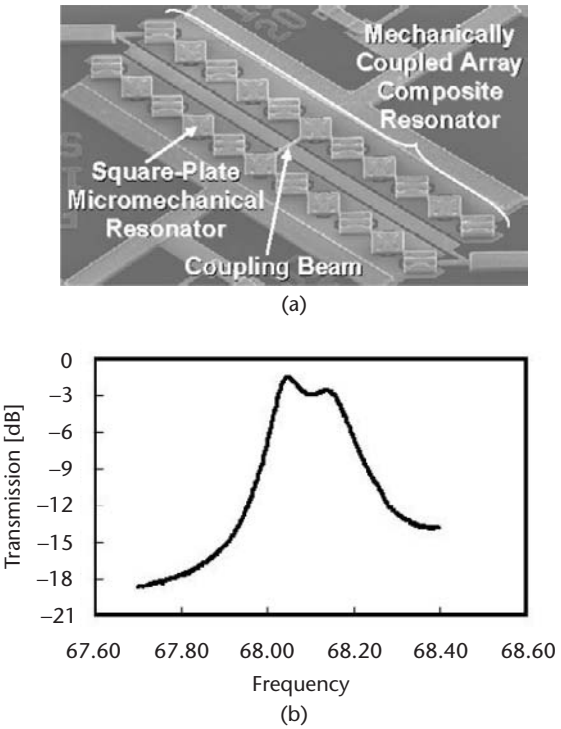

Figure 9.15 Square-resonator array filter: (a) parallel-coupled array of 11 microelectromechanical square-resonator cells; and (b) frequency response of the filter (central frequency is 68 MHz). (© 2003 IEEE [43].)

2.5 dB at the center frequency of 163 MHz. The design strategy overcomes the impedance deficiencies by optimizing the mechanical coupling between the resonators. This improves the stopband rejection of the filter response while also suppressing unwanted modes in the same footprint.

The MSI filter circuit shown in Figure 9.16(a) is comprised of four disk-array composites (assigned numbers from 1 to 4), each of which contains 15 contour-mode disk resonators. As shown in the schematic drawing of Figure 9.16(b), which zooms in on one of the arrays, its resonators are linked by $\lambda/2$ longitudinal mode array-coupling beams, thus promoting in-phase resonance among the resonators in each of the four arrays. This allows summing of their motional currents to achieve a lower overall impedance and higher power handling capability. Via the $\lambda/2$ mechanical coupling beams, each array behaves like a single composite resonator with much lower impedance. The coupling strategy can be summarized as: (1) half-wavelength $\lambda/2$ couplers accentuate the in-phase motion of disks; (2) λ couplers force disks to mechanically vibrate out-of-phase, hence enabling differential mode operation; and (3) $\lambda/4$ couplers spread the frequencies of the multiple-resonator system to form the bandpass response desired for the filter [40].

9.2.4 RF MEMS Switches

Microelectromechanical switches are one of the key RF MEMS components the market is paying more attention to. The MEMS switch can be used to select one or more RF channels or as a part of multiple-element reconfigurable RF circuits like phase arrays, matching networks, or reconfigurable antennas [44–46].

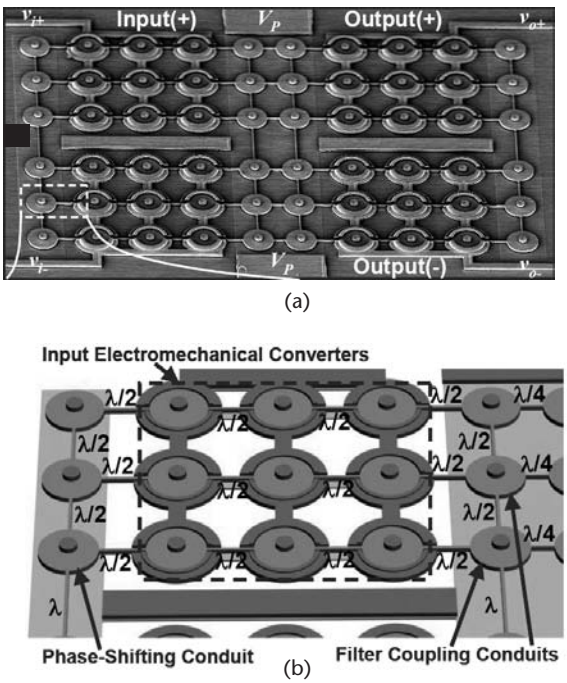

Figure 9.16 MSI disk-array MEMS filter: (a) 60-resonator four-array filter; and (b) zooming in on one of the arrays detailing the coupling strategy between the resonators. (© 2007 IEEE [40].)

Nowadays, no commercial RF MEMS switch product is available, although big R&D and funding efforts are being made for this purpose. The MEMS switch is a binary component having two operation states—namely, the on (down) and the off (up) states. Thus, the MEMS switch is placed on a microwave transmission line to isolate or to allow the RF signal to pass through the RF circuits. When operated in the on (or down) state, the switch is in a low impedance configuration and most of the RF signal passes through it. In the off (or up) state, the switch exhibits a high impedance to the transmission line and most of the RF signal is prevented from passing through the switch.

Two placement configurations of the MEMS switch on the transmission line are possible: the series and the shunt switch. Figure 9.17(a) depicts a conceptual drawing of the series switch. In the series connection, the switch connects two segments of the transmission line, and the RF signal flows from the first segment to the second when the switch is in the on (down) state, because it is aligned with the segments. In the up state (off) of the switch, the RF signal flow is interrupted because of the two segments isolation. On the other hand, the shunt switch derives the energy to a shunt branch of the circuit, and the operation is exactly the opposite: in the on state, most of the RF signal is derived to the shunt and the second segment of the transmission line is isolated from the first segment. During the off state, the switch opens, the shunt is isolated, and the RF signal energy flows between the two segments of the line. Figure 9.17(b) depicts the shunt switch concept.

Roughly, there exist three kinds of RF MEMS switches: the ohmic-contact, the capacitive, and the resonant switch. The performance of switches is evaluated in terms of power consumption, insertion losses, isolation, and linearity. The switching is controlled by an actuation voltage—not always as low as desirable for IC inte-

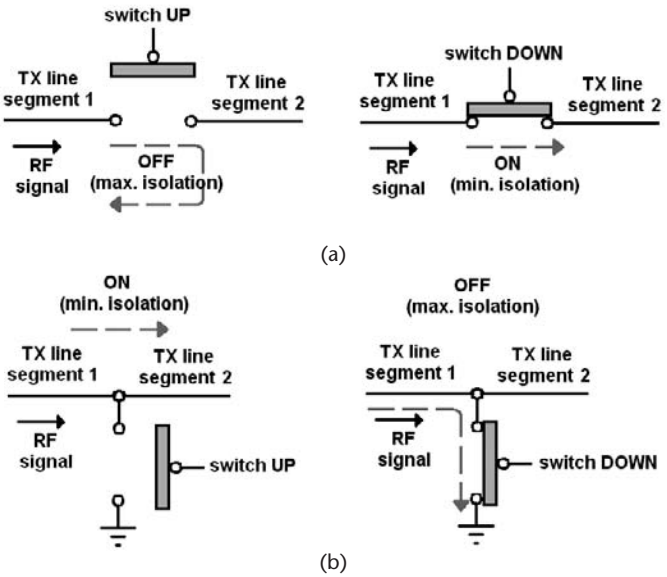

Figure 9.17 RF MEMS switch concepts: (a) the series switch (the down state coincides with closed-circuit and signal passing through the segments, and the up state with RF isolation between segments 1 and 2 of the transmission line); and (b) the shunt switch isolates the segments in the down state and allows signal passing in the up state.

gration—that causes the movable structure of the switch to bend or to deflect. The structure is typically a bridge or a cantilever, and it contacts the transmission line when deflected (the on state). In this state, the switch has to be as electrically matched as possible to the transmission line, so the insertion loss is to be at minimum values, less than 1 dB. In the off state, good isolation at a wide bandwidth is expected to be at least 25 dB or more [44]. The schematic of Figure 9.18 represents the operation states and the mechanical configuration of a bridge switch when it is actuated by the driving voltage.

Peroulis et al. realized that, with a proper design, the isolation properties of capacitive switches could be improved if the impedance of the switch is controlled by a driving AC signal. The signal makes the switch to resonate at a certain frequency, thus minimizing the impedance and improving the isolation in the down state [47–49]. Figure 9.19(a) depicts the resonant switch concept and simplified equivalent circuit. On the other hand, Figure 9.19(b) shows a picture of the fabricated MEMS switch. When the switch is in resonance, the impedance of the series inductance L and the capacitance C is null and the switch overall impedance reduces to R. The values of L, C, and R are designed to minimize at resonance and to maximize the isolation.

The relevance of MEMS switches in RF circuits is especially notorious in the state-of-the-art RF front end concepts, as we will study in Section 9.3.3. Nowadays, RF MEMS switch products are still in early production phases, although big R&D and funding efforts are being made to launch commercialization. Philips, Sivestra, and Baolab are at the industrial development stage and are expected to launch high-performance miniature MEMS switches in the next few years [20–22].

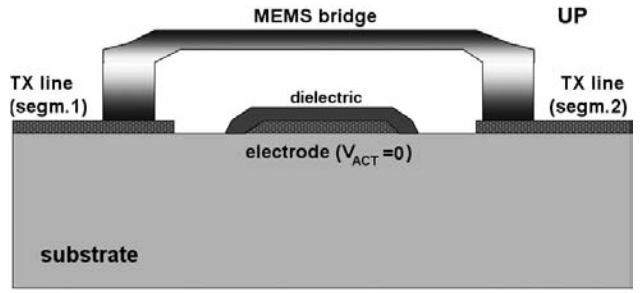

(a)

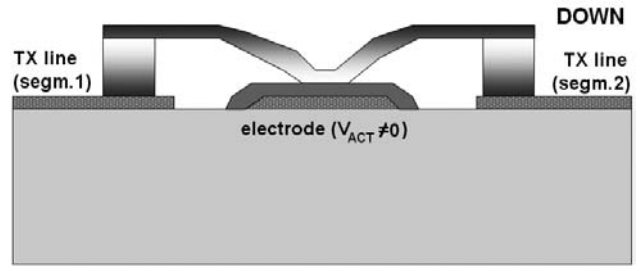

(b)

Figure 9.18 Operation states and mechanical configuration of a bridge switch: (a) off (up) state; and (b) on (down) state.

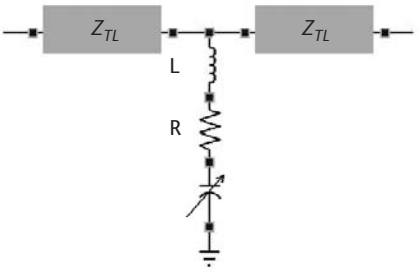

(a)

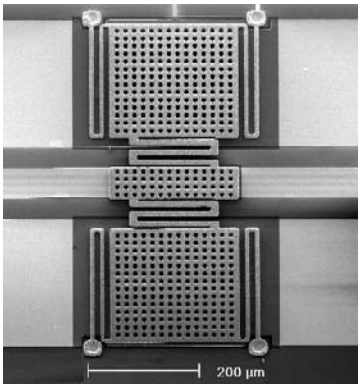

(b)

Figure 9.19 Resonant MEMS switch: (a) concept and simplified equivalent circuit (at resonance, the impedance equals to *R*); and (b) optical picture of a MEMS switch. (© 2000 IEEE [47].)

9.3 Active-Circuit Applications

An active-circuit application integrates transistor-based circuits with passive components to perform amplification or signal processing functions. Typical examples are oscillators, mixers, and low noise amplifiers (LNA). The integrated circuit performs the amplification or signal processing, and the passive component, the resonator in our case, is used as time-varying or frequency-varying impedance. The IC and resonator integration may be hybrid, monolithic, or heterogeneous, as it has been demonstrated by academic researchers and industrial companies. We discuss implementations of both kinds in this section.

9.3.1 Oscillators

An oscillator is a closed-loop circuit with positive feedback. That means that the signal running around the loop is constructively amplified in such a way that the output signal grows and oscillates in the absence of input signal. Instead of that, the noise in the system is enough to start up the oscillation given that two conditions are met:

1. The gain around the loop must be equal or higher than 1 (0 dB).
2. The total phase shift in the loop must equal to 0°.

These conditions are known as the Barkhausen criteria [50].

The oscillator can also be viewed as a two-port negative resistance circuit, which is somehow compensated by a positive-resistance load at the oscillation frequency [51]. Both representations of the oscillator are depicted in the equivalent circuits of Figure 9.20. According to the negative resistance representation, the oscillator is designed through large-signal analysis of the active negative resistance circuit in order to find the circuit parameters that exactly cancel the load or any other positive resistance in the closed loop circuit [52].

There exist many circuit topologies and kinds of oscillators, though the crystal oscillator is the main concern of this book. Crystal oscillators are widely used to generate standard reference frequencies in modern electronic systems. The influence of parasitic elements on crystal oscillators and the oscillation start-up conditions have been studied in the past [53]. In a crystal oscillator, the positive resistance compensation is provided through the frequency-varying impedance of a crystal resonator. The first crystal oscillators implemented quartz-crystal resonators, which have been systematically replaced by miniaturized MEMS, NEMS, SAW, and FBAR resonators. The general theory that allows the linear and nonlinear analysis of any crystal oscillator circuit was developed by Vittoz et al.; for a reference guide, see [54]. Next, we discuss some of these implementations and the major achievements of the miniature integrated oscillators.

The 5-GHz FBAR-based balanced oscillator developed by Aissi et al. monolithically integrates the FBAR resonator above the AMI semiconductor 0.35-μm BiCMOS IC oscillator. The balanced, differential configuration of the oscillator allows division by two the electrode resistance of the FBAR, which leads to better phase noise in comparison to single-ended oscillators. The measured phase noise is –121 dBc/Hz at 100 kHz from a 5.46-GHz carrier frequency. Another benefit of the differential output configuration is that it allows direct driving of the divider and mixer, which are generally balanced, without the need for a single-ended to differential converter [55]. The schematic circuit of the balanced Colpitts oscillator is shown in Figure 9.21(a). The core oscillator transistors T1 and T2 are

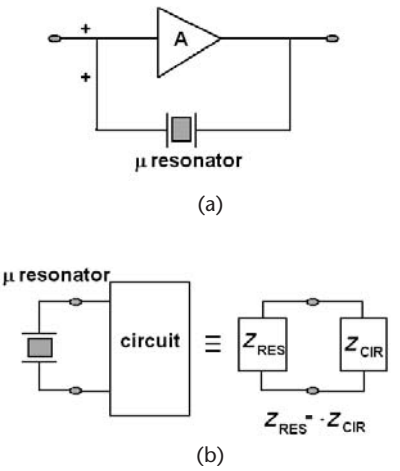

Figure 9.20 Equivalent circuits for oscillators: (a) positive feedback oscillator; and (b) negative resistance oscillator.

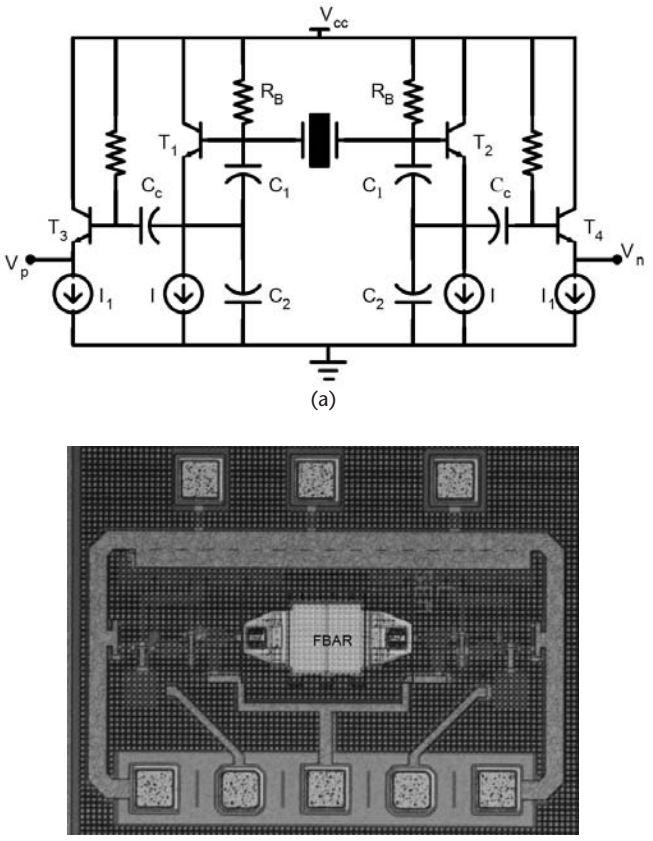

Figure 9.21 Above-IC FBAR low phase noise balanced oscillator: (a) schematic circuit of the balanced Colpitts oscillator; and (b) chip layout micrograph. (© 2006 IEEE [55].)

equally sized, and the buffers T3 and T4 isolate the core oscillator from 50Ω impedance loads also having the same size. The chip occupies $650 \times 830\ \mu$m of silicon area, with the resonator area including contacts to the BiCMOS IC last metal being $170 \times 300\ \mu$m. The micrograph of Figure 9.21(b) shows the FBAR above the oscillator circuit.

A quite different approach is the MEMS oscillator developed by Lin et al. The circuit replaces the single resonator normally used in crystal oscillators with a mechanically coupled array to effectively raise the power-handling ability at the working frequency. Lin and colleagues integrate a mechanically coupled array of up to nine 60-MHz wine-glass disk resonators embedded in a positive feedback loop to attain oscillation. The circuit achieves a phase noise of –123 dBc/Hz at 1-kHz offset and –136 dBc/Hz at far-from-carrier offsets, beating the GSM phase noise requirements by 8 dB and 1 dB, respectively [56]. A detailed schematic of the circuit showing the sustaining transresistance amplifier and the placement of the resonator array is depicted in Figure 9.22(a). A SEM image of the disk array comprised by three wine-glass resonators is observed in Figure 9.22(b).

The self-excited, nanocantilever resonator-based CMOS oscillator developed by Verd et al. is used for mass detection applications, and it can achieve 1 ag/Hz

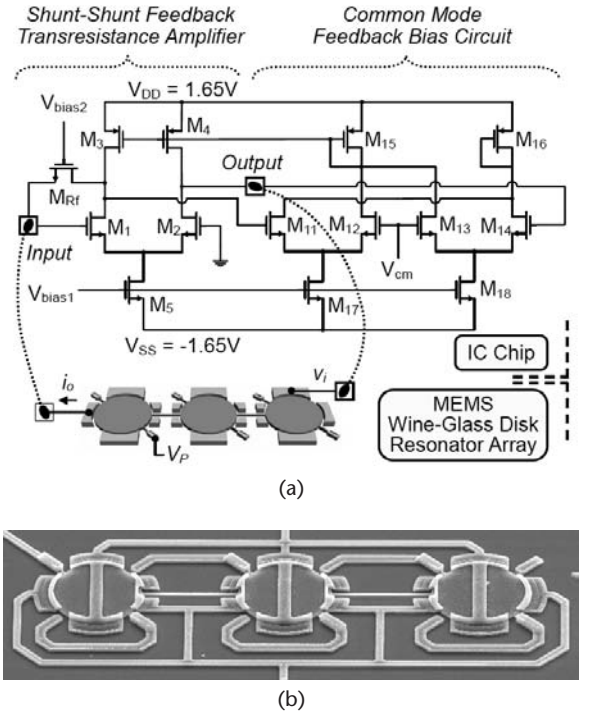

Figure 9.22 Wine-glass disk-resonator array MEMS oscillator. (a) Detailed circuit schematic of the single-stage sustaining transresistance amplifier, implemented by a fully differential amplifier in a one-sided shunt-shunt feedback configuration. (© 2005 IEEE [56].) (b) SEM image of the three-wine-glass disk resonator array. (© 2005 IEEE [56].)

mass sensitivity [57] (Figure 9.23). The mechanical resonator is monolithically integrated above the commercial 0.35-μm AMS035 CMOS process and implemented using the top metal layer and post-CMOS processed through simple mask-less wet etching. The MEMS-adapted Pierce oscillator vibrates at a frequency of 6 MHz with a 1.6-Hz frequency stability in air environment. The submicrometer-scale resonator is based on a cantilever structure 10 μm long, 600 nm wide, and 750 nm thick, and it features three electrodes for DC voltage biasing, electrostatic excitation, and capacitive read-out.

Discera (Ann Arbor, Michigan) has developed and sells a complete line of silicon-based MEMS oscillators [18]. The DSC8002 is a programmable, MEMS-based oscillator fabricated with the Discera PureSilicon technology. This circuit can be programmed to any frequency from 1 to 150 MHz, with a nominal operational range of 1.8V to 3.3V. The DSC8002 incorporates a robust silicon MEMS resonator that is intended for industrial and portable applications like mobile, consumer electronics, and CCD clocks for VTR cameras, among others. The oscillator and resonator circuit exhibits low operating and standby current of 3 mA (at 40 MHz) and 1 μA, respectively, within a small footprint of $2.5 \times 2.0 \times 0.85$ mm and a temperature stability of ±25 ppm to ±50 ppm. The micrograph of Figure 9.24(a) shows the footprint of the oscillator, wherein the resonator is smaller than the ASIC. This is a remarkable difference from previous art quartz-crystal oscillators whose resonators dominated the size of the package. The block diagram of

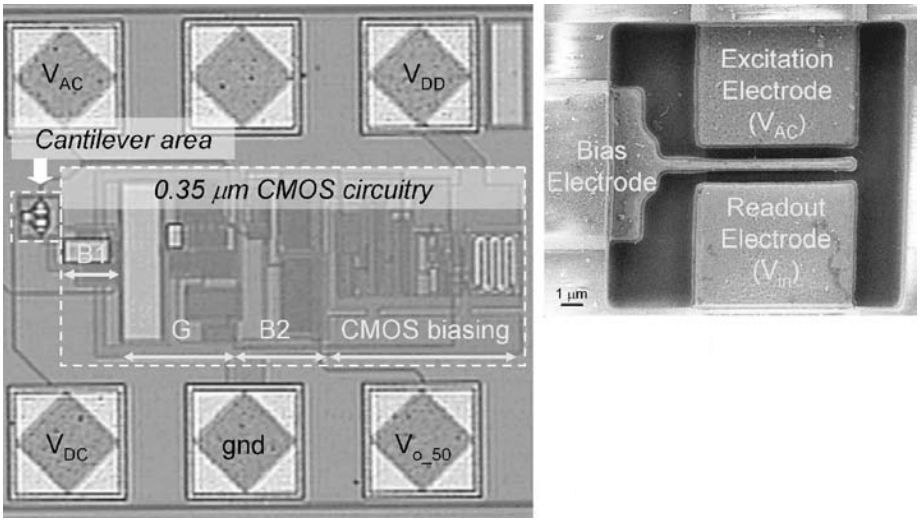

(a) (b)

Figure 9.23 Submicrometer resonator-based oscillator: (a) photograph of the cantilever-based oscillator monolithically integrated in AMS's 0.35-μm CMOS process; and (b) SEM image of a fabricated 10-μm-long, 0.6-μm-wide metal cantilever. (© 2008 IEEE [57].)

Figure 9.24(b) depicts the architecture of the VCO oscillator, including an N-divider to perform the frequency programming. The MEMS resonator and the ASIC are integrated by wire bonding [58].

SiTime is another company that nowadays commercializes silicon MEMS oscillators [19]. The SiTime SiT3701 is one of the smallest programmable voltage-controlled MEMS oscillators (VCMO) on the market today. The SiT3701 all-silicon VCMO comes in four-pin packages with the smallest footprint being 2.5×2.0 mm. The circuit is programmable to obtain oscillation at any frequency from 1 MHz to 80 MHz, and at selected frequencies between 80 MHz and 110 MHz, with supply voltage options of 1.8V, 2.5V, 2.8V, and 3.3V, and frequency stability from ±25 ppm to ±100 ppm. This oscillator is also oriented for portable consumer applications [59].

Other oscillator implementations may be mentioned as well, like the SAW oscillator circuit of Schmitt et al. [60], the ultra-low-power injection locked transmitter for wireless sensor networks based on FBAR by Chee et al. [61], or the commercially available SAW and QMEMS oscillators by Epson Toyocom [31].

9.3.2 Mixers and Mixlers

A mixer is a nonlinear circuit that performs frequency conversion from the RF frequency to intermediate frequencies. In essence, a mixer is a signal multiplier that uses a reference signal of a certain frequency to downconvert the frequency spectrum of the input signal. Taking advantage of signal processing and well-known trigonometric relationships, the product of the RF and the reference signals generates a couple of new signals. The first one is at the difference of the central frequen-

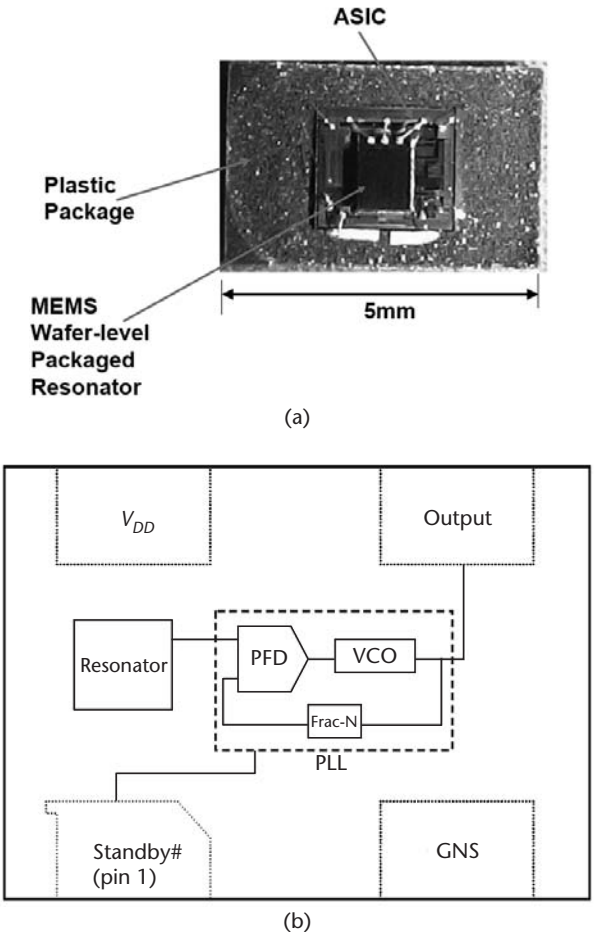

Figure 9.24 Discera's DSC 8002 MEMS oscillator: (a) footprint of the oscillator showing the MEMS resonator above the ASIC; and (b) block diagram. (© 2009 Discera [58].)

cies of the RF and reference signals, and the second one is centered at the sum of such frequencies:

$$f_{IF} = f_{RF} - f_{LO} \tag{9.1}$$

$$f_{M} = f_{RF} + f_{LO} \tag{9.2}$$

where f_{IF} is the intermediate frequency, f_M is the high-frequency image of f_{IF}, f_{RF} is the RF frequency, and f_{LO} is the local-oscillator reference frequency. In a down converter, the f_M signal is discarded by using a lowpass (or bandpass) filter, while the f_{IF}-centered signal is then delivered to the baseband stages to perform further signal processing and information recovery. An upconverter operates in the opposite way, by taking the added-frequency signal and filtering out the difference signal. Traditionally, the mixers have been built with conventional transistor-based circuits. Herein, we study how new MEMS-based mixer implementations are also able to achieve RF signal downconversion with good performance.

MEMS mixer filters exploit the voltage-squared nonlinearity of the electrostatic force driving the resonators, as studied by Fedder et al. [62]. Mixing and IF filtering can be accomplished in a 0.02-mm^2 area with less than 1 mW of input power. The square geometry at the head of the 2.29-MHz cantilever of Figure 9.25 reduces feedthrough by distancing the RF and IF electrodes. Application of RF voltage V_{RF} to the stationary electrode and local oscillator voltage V_{LO} to the cantilever generates an electrostatic force proportional to $(V_{RF} - V_{LO})^2$ that acts on the moving cantilever. The $V_{RF} \times V_{LO}$ force component then has a frequency of $(f_{RF} - f_{LO})$. The mechanical vibration of the cantilever is amplified by the mechanical Q value and read-out capacitively through the IF electrode. Successful mixing with these resonators has been observed up to 3.2-GHz input frequencies. The circuit is monolithically integrated within a tunable RF front end fabricated within the Jazz SiGe60 4-metal BiCMOS process [63].

The term *mixler* is a neologism to designate the combination of a mixer and a filter. A mixler is a device comprised of MEMS resonators and mixer transducers performing both frequency translation and selective filtering of the electrical input signal [64]. Figure 9.26(a) presents the schematic representation of a mixler device. The structure of this device is basically the same as that of a microelectromechanical filter comprised of two clamped-clamped beam resonators, each with center frequency f_{IF}, coupled at low-velocity locations by a flexural mode beam. The SEM image of Figure 9.26(b) shows the 37-MHz microelectromechanical mixler indicating key features and dimensions of the beams, electrodes, and so on. The device converts the electrical input signal to a mechanical force. Next, it processes this signal mechanically via its network of flexural-mode beams, and then it reconverts the resulting signal to an electrical output signal that can be further processed by subsequent transceiver electronics. The key to mixing in this device is its capacitive electromechanical transduction, which converts electrical energy to mechanical energy through a square law transfer function, as conventional mixers do [65].

A second example is the fully integrated CMOS-MEMS mixler using the commercial AMS035 0.35-μm technology of Uranga et al. [66]. The MEMS structure is a clamped-clamped beam resonator implemented with the polysilicon capacitance

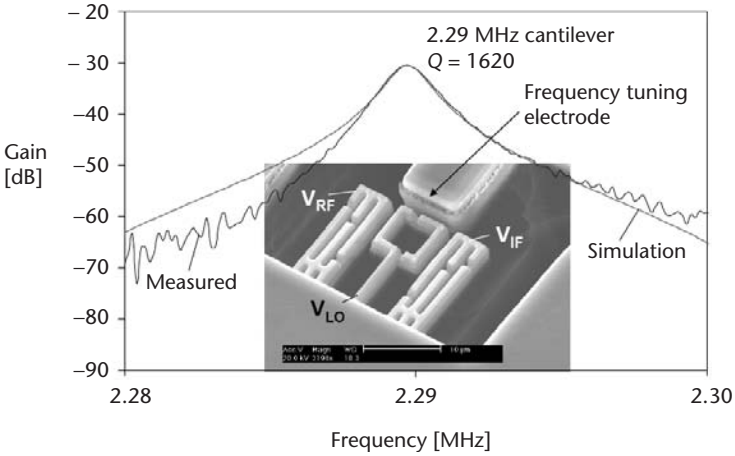

Figure 9.25 RF MEMS mixer filter fabricated within the Jazz SiGe60 4-metal BiCMOS process. (© 2005 IEEE [62].)

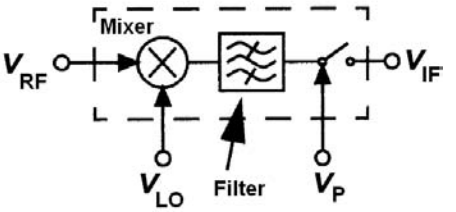

(a)

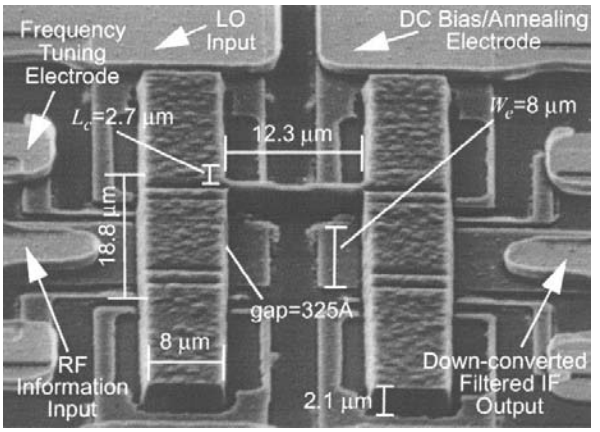

(b)

Figure 9.26 MEMS mixler: (a) schematic representation comprising a filter and a mixer; and (b) full-view of a 37-MHz microelectromechanical mixler indicating key features and dimensions of the beams, electrodes, and ports. (© 2004 IEEE [65].)

module of the CMOS process, thus achieving a fundamental lateral resonance frequency of 22.5 MHz. To operate the MEMS as a mixler, two different approaches were proposed to generate the nonlinear signal: the quadratic relationship of the voltage against the excitation force, and the amplitude modulation of the excitation signal. Figure 9.27 shows a SEM image of the released MEMS structure, which is a clamped-clamped beam 13 μm long, 350 nm wide, and having a 150-nm capacitive transducing gap. The polysilicon capacitance module of the AMS process was used to define both the excitation and read-out electrodes, as well as the mobile structure. Wet etching of the sacrificial silicon oxide layer was carried out to release the MEMS. The vibration is detected through electrostatic actuation and capacitive read-out of the generated motional current through an on-chip integrated transimpedance amplifier [66].

9.3.3 Tuned Low-Noise Amplifiers

A low-noise amplifier (LNA) is placed on the receiver path of RF communication systems to amplify the low-level signal incoming at the antenna port after the band selection stage. An LNA features a low-noise figure, typically around 3–5 dB, hence its name. LNA circuits implement moderate gain amplifiers, RF chocks and coupling capacitors for frequency compensation, and input and output impedances to match the 50-ohm transmission line impedance of most RF circuits.

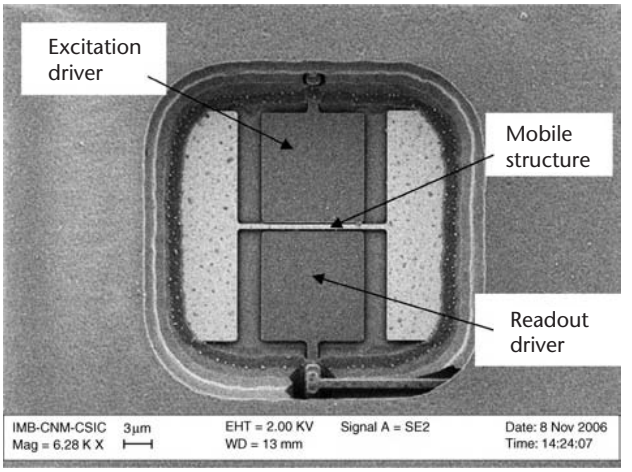

Figure 9.27 Full CMOS MEMS mixler: the clamped-clamped beam resonator is fabricated with the polysilicon capacitance module of the AMS035 CMOS process. (© 2007 IEEE [66].)

The recent monolithic integration of FBAR and CMOS technologies has enabled the design of new circuits such as the tuned differential LNA of Figure 9.28(a) for 2.2-GHz WCDMA applications [67]. The filtering LNA comprises two differential broadband (1 dB-BW of 5 GHz) current feedback amplifiers connected on each side of an FBAR filter, thus ensuring the frequency selectivity of the circuit. The curves of Figure 9.28(b) show a measured gain larger than 20 dB and a noise figure of 3 dB in the passband. The input gain compression at 1 dB is –26 dBm. This moderate linearity comes from the tradeoff between the amplifier's bandwidth, the high gain, the good noise performance, and the low power consumption (10 mA at 3V for each stage). Thus, better linearity can be achieved if one of these parameters is sacrificed.

The design of tuned RF circuits also involves the implementation of impedance-matching techniques. Although this example is the first demonstration of FBAR-based tuned RF amplifiers, nothing impedes the realization of new concepts like tuned power amplifiers for RF transmitters.

9.3.4 RF Front-End Systems

At this point, we have seen how individual blocks in the RF chain can be implemented with available microresonator technologies. Moreover, these RF blocks are suitable for further integration toward the single chip, thus constituting an integrated RF front end. An RF front end integrates the set of components present in a receiver from the antenna to the intermediate frequency (IF) stage. Depending on the receiver architecture, different components can be part of the front end. However, most receivers are constituted by matching networks, channel selection switches, band selection filters, duplexers (or any other multiplexer), LNAs, and phase-matching arrays. The main challenge of RF front-end systems is the efficient handling of power and bandwidth, mainly related to insertion losses of the switches and the filters, noise figures of the LNA, or quality factors and selectivity of the filters.

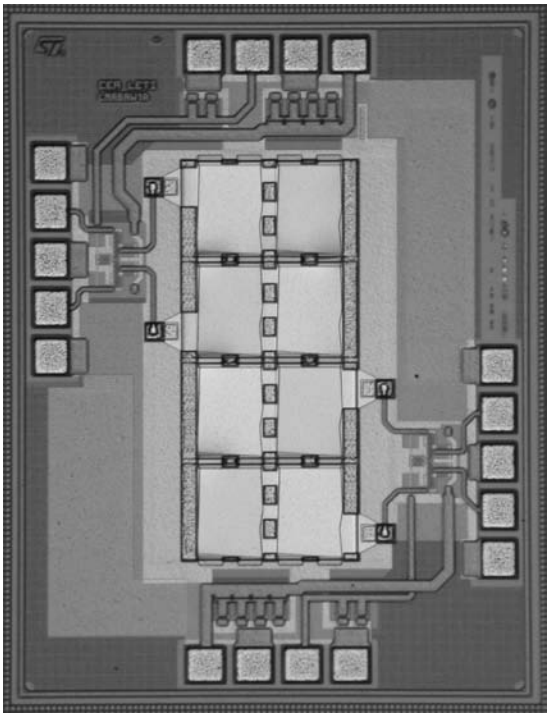

(a)

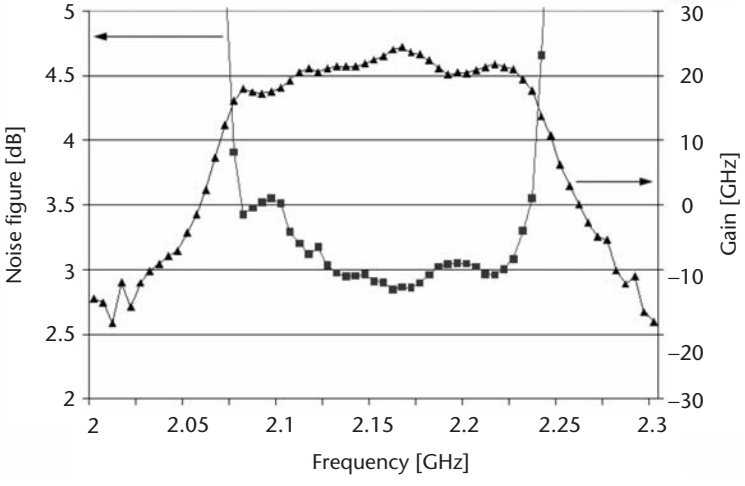

(b)

Figure 9.28 (a, b) Tuned LNA integrated with above-IC FBAR filter: noise figure and gain. (© 2005 IEEE [67].)

Single-chip integration of RF front ends has long been a dream for RF system designers; however, only recently, thanks to the RF MEMS contribution, has the integration of different components and technologies been possible. New receiver architectures, like the massively parallel switchable RF front end, enable simultaneous reception and transmission of narrowband signals located in different fre-

quency bands. These architectures are suitable for multiband 3G and B3G mobile communication systems, and they solve the problem of multiple and bulky user handsets. The diagram of Figure 9.29 exemplifies the massively parallel front end concept.

In the past few years, MEMS- and FBAR-based integrated front ends have appeared in the market of RF components. The circuit proposed in [68] is a simplified implementation of a zero-IF front end, and it consists of LNA, FBAR filter, and mixer. The RF front-end circuit architecture is depicted in Figure 9.29(a). The design and integration of the RF front end for WCDMA applications utilize the above-IC FBAR bandpass filter between the LNA and the mixer in order to relax linearity constraints and, thus, power consumption for the downconversion mixers. This first experimental chip is designed and fabricated in a 0.25-μm SiGe:C BiCMOS process enhanced with above-IC capabilities, whose layout is observed in the micrograph of Figure 9.29(b). The BAW filter is fabricated by CEA-LETI and CSEM. The above-IC BAW process is plugged over the BiCMOS final passivation layer, and the electrical contact with the rest of the circuit is realized at the last IC metal layer [68].

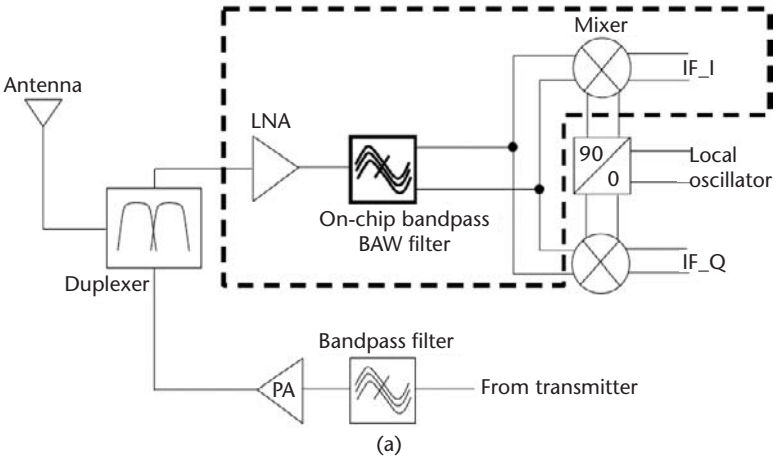

(a)

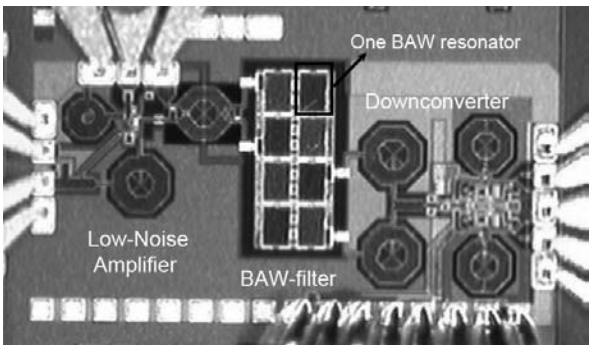

(b)

Figure 9.29 RF front end consisting of monolithically integrated BiCMOS LNA, FBAR filter, and downconversion mixer: (a) block diagram of the WCDMA-ZIF transceiver and (b) micrograph of the front end (LNA, filter, and mixer). (© 2005 IEEE [68].)

At the industrial level, Epcos offers the D5013 SAW-switch front-end module for GSM850, EGSM, DCS, PCS, and WCDMA2100 services. The D5013 is a low-loss SAW module for mobile telephone system integrating TX lowpass filters, switches, and decoders. Besides, it integrates SAW filters for reception of GSM 850, EGSM, PCN, and PCS signals, and ESD protection at the antenna port to 8 kV for possible contact discharges [69]. The schematic drawing of Figure 9.30 depicts the parallel architecture of the D5013 front end. Each one of the bands is selected by a multiple-switch selector controlled by the decoder. The maximum insertion loss value, including all the received and transmitted bands is 3.6 dB. The front end is assembled in SMT, with an approximate weight of 100 mg, a height of 1.1 mm, and a footprint of 3.2×4.5 mm.

Another integrated front-end concept is the Avago Technologies ALM-1712, which is a 1.575-GHz GPS front-end module combining an LNA with GPS FBAR filters. The LNA uses Avago's proprietary GaAs enhancement-mode (pHEMT) process to achieve a high gain with very low noise figure and high linearity. The integrated filter utilizes an FBAR filter for rejection at cellular- and PCS-band frequencies with the small footprint of 4.5×2.2 mm and a height of 1 mm. The LNA has a gain of 12.8 dB, a noise figure of 1.65 dB, and cellular-band and PCS-band rejections of 95 dBc and 90 dBc, respectively, among other specifications [70]. The schema of Figure 9.31(a) depicts the block diagram of the ALM-1712, where the RF input signal is filtered first by an FBAR GPS filter, then amplified by the LNA, and postfiltered and delivered to the RF output by another FBAR GPS fil-

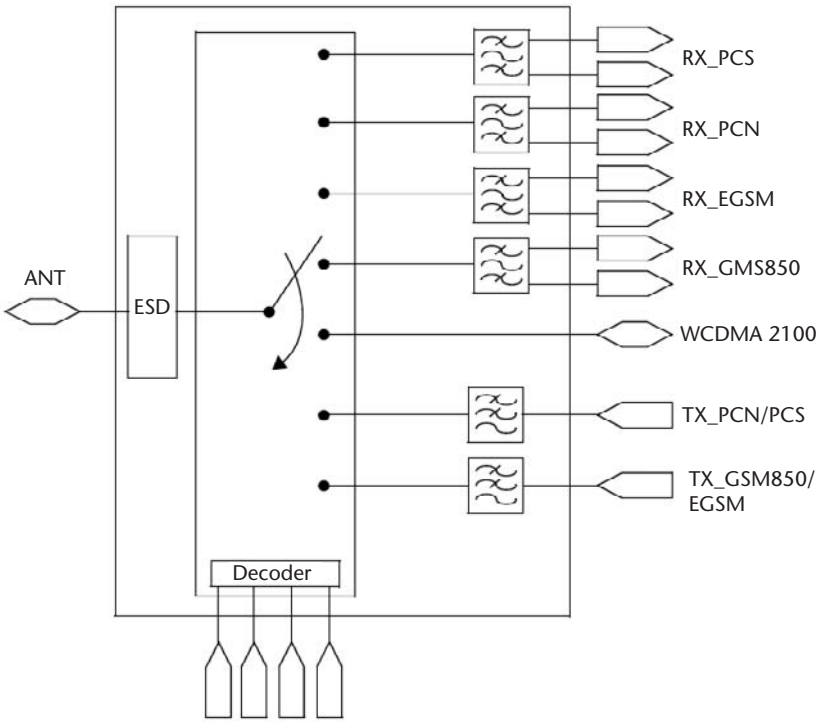

Figure 9.30 Epcos D5013 parallel RF front-end module for GSM850, EGSM, DCS, PCS, and WCDMA2100: the D5013 integrated SAW filters for band selection by means of switches and the decoder. (© 2009 Epcos [69].)

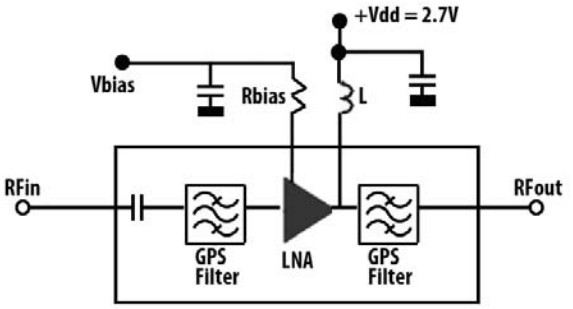

(a)

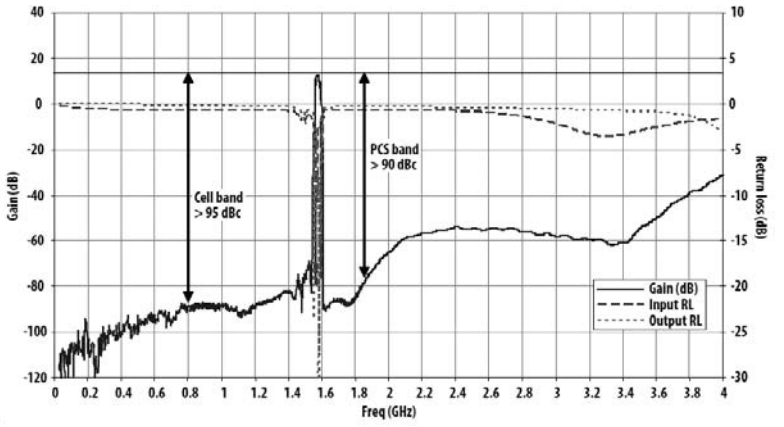

(b)

Figure 9.31 Avago Technologies' ALM-1712 front-end module: the chip integrates an LNA with GPS FBAR filters: (a) block diagram and (b) gain and return loss versus frequency. (© 2009 Avago [70].)

ter. The 12.8-dB gain and return loss of the front-end module are observed in Figure 9.31(b). The curves are taken when the chip is powered with a voltage supply of 2.7 VDC and current of 8 mA.

9.4 Summary

In this chapter, we have reviewed the major RF applications of acoustic and electromechanical microresonators. These applications and the MEMS technology behind them are known as the RF MEMS field. As we studied, RF MEMS applications are diverse and have high market impact. Nowadays, RF MEMS have passed from concept demonstration to intense commercialization, and different acoustic and microelectromechanical technologies are available in the market. Nevertheless, while acoustic SAW and BAW resonator technologies—including FBAR and SMR—have reached the required maturity for mass production and commercialization, most silicon-based RF MEMS are still in development, or they have already been developed but are in the consolidation process. Thus, filters, duplexers, and filter-based front ends have been successfully miniaturized using SAW and

FBARs, and millions of units of them are sold every year. On the other hand, MEMS-based RF oscillators are beginning their commercialization and have a promising future, and the highly anticipated RF switches are still being developed to reach industrial standards.

In this context, the RF MEMS market is very concentrated in a few companies, in spite of the big size of the overall MEMS industry. Mobile telephony FBAR and BAW applications dominate the market and represent nearly 40% of the total sales. From the oscillator and switch side, they are seen as interesting because of volume and economy scales, although reliability and CMOS integration issues are to be solved. Besides, design efforts will be intensive, because new RF architectures are to be developed to fully exploit the potential of integrated RF MEMS. This is a challenge and an opportunity for RF designers. We have seen in this chapter how the integration of RF MEMS is increasing and how, to date, the single-chip front end is a market reality that has left the laboratory and conceptual promises to occupy a place in the RF MEMS commercial applications. Of course, further integration, miniaturization, and process compatibility is expected for the next few years to build even more powerful and cost-efficient RF front ends.

References

[1] Apple, iPhone, http://www.apple.com/iphone/.

[2] Universal Mobile Telecommunications System (UMTS), http://www.umts-forum.org.

[3] Wi-Fi Alliance, Wi-Fi: Local area wireless networking based on IEEE 802.11 standards, http://www.wi-fi.org.

[4] High Speed Packet Access HSPA technology, GSM World, the GSM Association, http://www.gsmworld.com/technology/hspa.htm.

[5] Global System for Mobile Communications, GSM World: the GSM Association, http://www.gsmworld.com.

[6] Enhanced Data Rates for GSM Evolution EDGE Technology, GSM World: the GSM Association, http://www.gsmworld.com/technology/edge.htm.

[7] Bluetooth Technology, http://www.bluetooth.com.

[8] Global Positioning System, http://www.gps.gov.

[9] Nokia N97 Mobile Phone, Nokia: Connecting People, http://europe.nokia.com/n97#.

[10] Samsung Omnia mobile phone, Samsung Mobile, http://uk.samsungmobile.com/mobile-phones/samsung-omnia.

[11] LG Arena, LG Mobile, http://www.lgmobile.com.

[12] Nguyen, C. T.-C., "Microelectromechanical Components for Miniaturized Low-Power Communications," *Dig. of Tech. Papers IEEE MTT-S Intl. Microwave Symposium RF MEMS Workshop 1999*, Anaheim, CA, June 18, 1999, pp. 48–77.

[13] Bouchaud, J., B. Knoblich, and H. Wicht, "RF MEMS Market," Wicht Technologie Consulting, Munich, Germany, 2005.

[14] Avago Technologies, http://www.avagotech.com.

[15] Epcos AG, http://www.epcos.com.

[16] TriQuint Semiconductor, http://www.triquint.com.

[17] Skyworks, http://www.skyworksinc.com.

[18] Discera, http://www.discera.com.

[19] SiTime Corporation, http://www.sitime.com.

[20] Royal Philips, http://www.philips.com.

[21] Baolab Microsystems, http://www.baolab.com.

[22] Fujishima, S., "The History of Ceramic Filters," *IEEE Trans. on Ultrason. Ferroelec. Freq. Control*, Vol. 47, 2000, pp. 1–7.

[23] Lakin, K. M., G. R. Kline, and K. T. McCarron, "Development of Miniature Filters for Wireless Applications," *IEEE Trans. on Microw. Theory Tech.*, Vol. 43, 1995, pp. 2933–2939.

[24] Ruby, R., et al., "Ultra-Miniature High-Q Filters and Duplexers Using FBAR Technology," *Dig. of Tech. Papers IEEE Intl. Solid-State Circuits Conf. ISCC 2001*, San Francisco, CA, February 5–7, 2001, pp. 120–121.

[25] Kim, K.-W., et al., "Resonator Size Effects on the TFBAR Ladder Filter Performance," *IEEE Microw. Wirel. Compon. Lett.*, Vol. 13, 2003, pp. 335–337.

[26] Centro Nacional de Microelectrónica (CNM), Two-Metal CNM25 CMOS Technology, http://www.cnm.es.

[27] Avago Technologies, ACPF-7003 "High Reception and Image Rejection Transmission Filter for the US PCS Band," 2006, http://www.avagotech.com.

[28] Avago Technologies, "ACPF-7002 High Rejection Transmission Filter for the US PCS Band," 2007, http://www.avagotech.com.

[29] TriQuint Semiconductor, 880404, "1575 MHz BAW Filter," 2007, http://www.triquint.com.

[30] TriQuint Semiconductor, 880369 "5775 MHz BAW Filter," 2007, http://www.triquint.com.

[31] Epson Toyocom, http://epsontoyocom.co.jp/english/.

[32] Epcos AG, Surface Acoustic Wave Components Division, SAW MC WT, B7843, "1855 MHz Low-Loss Filter for Mobile Communications," 2002, http://www.epcos.com.

[33] Avago Technologies, ACMD-7602, "Miniature UMTS Band I Duplexer," 2008, http://www.avagotech.com.

[34] Epcos AG, Surface Acoustic Wave Components Division, SAW MC WT, B7692, "BAW Duplexer WCDMA Band II," 2008, http://www.epcos.com.

[35] Epcos AG. Surface Acoustic Wave Components Division, SAW MC WT, B9100, "SAW CELL/GPS/PCS Triplexer," 2008, http://www.epcos.com.

[36] Avago Technologies, ACFM-7102, "PCS/Cellular/S-GPS Quintplexer," 2007, http://www.avagotech.com.

[37] Epcos AG, Surface Acoustic Wave Components Division, SAW MC WT, B7686, "BAW/SAW Duplexer WCDMA Band II (PCS)," 2008, http://www.epcos.com.

[38] Bannon, F. D., J. R. Clark, and C. T. -C. Nguyen, "High-Q HF Microelectromechanical Filters," *IEEE J. Solid-State Circuits*, Vol. 35, 2000, pp. 512–526.

[39] Nguyen, C. T. C., "Integrated Micromechanical Circuits for RF Front Ends," *Proc. 36th European Solid-State Device Research Conference ESSDERC 2006*, Montreux, Switzerland, September 18–22, 2006, pp. 7–16.

[40] Li, S.-S., et al., "An MSI Micromechanical Differential Disk-Array Filter," *Dig. of Tech. Papers 14th International Conference on Solid-State Sensors, Actuators and Microsystems TRANSDUCERS 2007*, Lyon, France, June 10–14, 2007, pp. 307–311.

[41] Sony Corporation, Bandpass Filter Developed Using MEMS Technology Integration with Peripheral Circuits Also Possible, http://www.sony.net/Products/SC-HP/cx_news/vol43/pdf/sideview43.pdf.

[42] Clark, J. R., et al., "Parallel-Coupled Square-Resonator Micromechanical Filter Arrays," http://www.discera.com.

[43] Demirci, M. U., M. A. Abdelmoneum, and C. T.-C. Nguyen, "Mechanically Corner-Coupled Square Microresonator Array for Reduced Series Motional Resistance," *Dig. of Tech. Papers 12th Int. Conf. on Solid-State Sensors & Actuators TRANSDUCERS 2003*, Boston, MA, June 8–12, 2003, pp. 955–958.

[44] De Los Santos, H. J., *RF MEMS Circuit Design for Wireless Communications*, Norwood, MA: Artech House, 2002.

[45] De Los Santos, H. J., "MEMS for RF/Wireless Applications: The Next Wave—Part I," *Microwave J.,* Vol. 44, 2001, pp. 20–41.

[46] De Los Santos, H. J., "MEMS for RF/Wireless Applications: The Next Wave—Part II," *Microwave J.,* Vol. 44, 2001, pp. 142–152.

[47] Peroulis, D., et al., "RF MEMS Devices for High Isolation Switching and Tunable Filtering," *Dig. of Tech. Papers IEEE MTT-S Intl. Microwave Symposium*, Vol. 2, Phoenix, AZ, June 11–16, 2000, pp. 217–1220.

[48] Peroulis, D., "RF MEMS Devices for Multifunctional Integrated Circuits and Antennas," Ph.D. thesis, University of Michigan, Ann Arbor, MI, 2003.

[49] Wang, X., L. P. B. Katehi, and D. Peroulis, "AC Actuation of Fixed-Fixed Beam MEMS Switches," *Dig. of Tech. Papers Topical Meeting on Silicon Monolithic Integrated Circuits in RF Systems, 2006*, San Diego, CA, January 18–20, 2006.

[50] Jones, M. H., *A Practical Introduction to Electronic Circuits*, Cambridge, U.K.: Cambridge University Press, 1982.

[51] Rhea, R. W., *Oscillator Design and Computer Simulation*, Atlanta, GA: Noble Publishing, 1995.

[52] Dearn, A., *How to Design an RF Oscillator*, London: Institution of Electrical Engineers, 2000, pp. 7/1–7/7.

[53] Unkrich, M. A., and Robert G. Meyer, "Conditions for Start-Up in Crystal Oscillators," *IEEE J. Solid-State Circuits*, Vol. SC-17, 1982, pp. 87–90.

[54] Vittoz, E. A., "High-Performance Crystal Oscillator Circuits: Theory and Application," *IEEE J. Solid-state Circuits*, Vol. SC-17, 1982, pp. 774–783.

[55] Aissi, M., et al., "A 5 GHz Above-IC FBAR Low Phase Noise Balanced Oscillator," *Proc. IEEE Radio Frequency Integrated Circuits Symposium RFIC-2006*, Vol. 1, San Francisco, CA, June 11–13, 2006, pp. 25–28.

[56] Lin, Y.-W., et al., "Low Phase Noise Array-Composite Micromechanical Wine-Glass Disk Oscillator," *Dig. of Tech. Papers IEEE Intl. Electron Devices Meeting IEDM 2005*, Washington, D.C., December 5–7, 2005, pp. 281–284.

[57] Verd, J., et al., "Monolithic CMOS MEMS Oscillator Circuit for Sensing in the Attogram Range," *IEEE Electron Dev. Lett.*, Vol. 29, 2008, pp. 146–148.

[58] Discera, DSC8002 Series 1.8 to 3.3V PureSilico Programmable Oscillator: http://www.discera.com.

[59] SiTime Corporation, SiT3701 Smallest Programmable VCMO Voltage Controlled MEMS Oscillator, http://www.sitime.com.

[60] Schmitt, R. F., J. W. Allen, and R. Wright, "Rapid Design of SAW Oscillator Electronics for Sensor Applications," *Sens. Actuators B: Chem.*, Vol. 76, 2001, pp. 80–85.

[61] Chee, Y. H., A. M. Niknejad, and J. M. Rabaey, "An Ultra-Low-Power Injection Locked Transmitter for Wireless Sensor Networks," *IEEE J. Solid State Circuits*, Vol. 41, 2006, pp. 1740–1748.

[62] Fedder, G. K., and T. Mukherjee, "Tunable RF and Analog Circuits Using On-Chip MEMS Passive Components," *Dig. of Tech. Papers IEEE Intl. Solid-State Circuits Conf. ISCC 2005*, San Francisco, CA, February 6–10, 2005, pp. 390–391.

[63] Jazz Semiconductor, http://www.jazzsemi.com.

[64] Wong, A.-C., H. Ding, and C.T.-C. Nguyen, "Micromechanical Mixer and Filters," *Dig. of Tech. Papers IEEE Intl. Electron Devices Meeting IEDM 1998*, San Francisco, CA, December 6–9, 1998, pp. 471–474.

[65] Wong, A. C., and C. T. C. Nguyen, "Micromechanical Mixer-Filters ('Mixlers')," *J. Microelectromech. Systems*, Vol. 13, 2004, pp. 100–112.

[66] Uranga, A., et al., "Fully Integrated MIXLER Based on VHF CMOS-MEMS Clamped-Clamped Beam Resonator," *Electron. Lett.*, Vol. 43, 2007, pp. 452–454.

[67] Dubois, M.-A., et al., "Integration of High-Q BAW Resonators and Filters Above IC," *Dig. of Tech. Papers IEEE Intl. Solid-State Circuits Conf. ISCC 2005*, San Francisco, CA, February 6–10, 2005, pp. 392–393.

[68] Carpentier, J. F., et al., "A SiGe:C BiCMOS WCDMA Zero-IF RF Front-End Using an Above-IC BAW Filter," *Dig. of Tech. Papers IEEE Intl. Solid-State Circuits Conf. ISCC 2005*, San Francisco, CA, February 6–10, 2005, pp. 394–395.

[69] Epcos AG, Surface Acoustic Wave Components Division, SAW MC WT, D5013, "SAW Frontend Module GSM 850/EGSM/DCS/PCS/WCDMA 2100," 2008, http://www.epcos.com.

[70] Avago Technologies, "ALM-1712 GPS Low-Noise Amplifier Front-End Module with Integrated Pre and Post Filters and Variable Current/Shutdown Function," 2009, http://www.avagotech.com.

CHAPTER 10

Case Studies: Modeling, Design, and Fabrication of FBAR and MEMS-Based Systems

So far, we have studied the concepts, modeling, design, fabrication, and integration of FBAR and MEMS resonator-based microsystem and nanosystems. In addition, we have reviewed some of their main sensor and RF applications. This chapter carries out an in-depth study of specific implementation cases of FBAR and MEMS systems.

To get started, we establish a methodological approach for the design of MEMS-resonator and IC systems. Technological and conceptual aspects at both the resonator and IC sides are considered. The purpose of this section is to define a working reference passing through the different stages of system design. Designers will learn the appropriate steps to should follow to build a successful resonator-IC system, including modeling, characterization, parameter extraction, and process design.

Next, we study the first case: the fabrication of an FBAR and its compatibility with silicon technologies. In this way, we build a diary of the step-by-step fabrication process of an FBAR, and we go through a run by describing each of the implemented processes and the required actions to supervise compatibility with the global process. In Chapter 4 we reviewed surface and bulk-micromachined FBAR implementations, and we defined the main issues regarding process compatibility. In this chapter, we will learn how the compatibility requirements of FBAR and silicon processes can be met and discover the interactions between the different processes. Thus, the combination of structural materials, their deposition and patterning, and the micromachining techniques have to be compatible with the previous process steps. We propose a list of the materials currently implemented in FBARs and their combination.

The second case we will revise herein is the high-level design of a temperature-compensated FBAR-based oscillator. We begin the discussion by defining the topology of FBAR oscillators and the impact of temperature in the oscillator stability. Next, we perform the small-signal analysis of the oscillator by using the FBAR's MBVD model and the CMOS small-signal parameters. Then, we carry out the temperature compensation analysis by high-level modeling of the temperature-compensated oscillator. A Verilog-A model of the FBAR is useful to illustrate the design approach.

In the last section of the chapter, we design a read-out circuit for a 434-MHz silicon-MEMS resonator. We take the lessons learned in the first section to systemati-

cally design the circuit, passing from the system level to reach the circuit-level implementation. First, we see how the circuit is specified as a function of the MEMS characteristics and its extracted RLC model. We make a digression to describe the integration approach of the MEMS and the read-out circuit. The study also describes the implemented testing routines to predict and experimentally characterize the circuit performance.

10.1 Methodological Approach for MEMS-IC Integration

In Chapter 3, the different levels of FBAR and MEMS resonator design and modeling were analyzed. Now, we use modeled FBAR or MEMS resonators to integrate them with an IC. Thus, the extracted models will serve to specify the circuit requirements and expected performance so we can build a functional system.

The flow diagram of Figure 10.1 depicts the proposed methodology for MEMS-IC integration, whose central axis represents all the actions involving integration of the left-side FBAR/MEMS resonator design steps and the right-side integrated circuit steps. First, the integration technology has to be defined. In this step, monolithic, hybrid, or heterogeneous integration strategy is decided. This decision

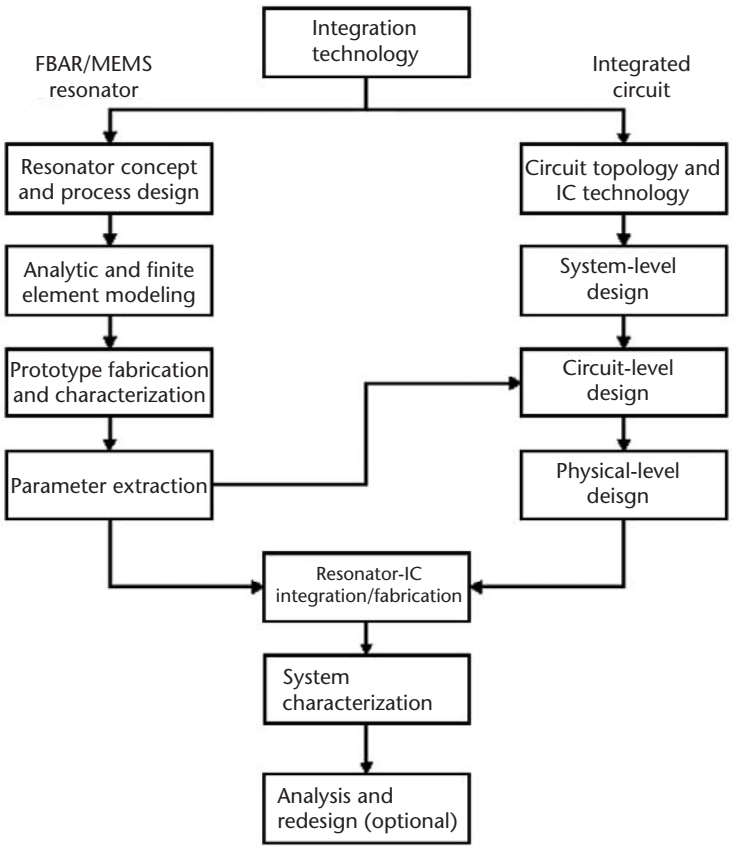

Figure 10.1 Integrated MEMS-IC design methodology.

will support the resonator concept and process design, involving compatibility issues with the IC, like temperatures and materials. At the layout level, it also requires previsions of the resonator active area, electrode design and contact pad area, dicing design (if needed), through vias (if needed), temperature budget, and process contamination, among other process elements. The integration approach also affects decisions on the required IC technology and circuit topology. In the case of monolithic integration, the considerations are the number of layers of the microelectronic process (typically CMOS or BiCMOS), thicknesses and materials of the upper process layers, and other requirements concerning the postprocess of the IC wafer. Whether the resonator is fabricated before, in the middle, or after the IC process is also a matter of design. The IC layers to be used for this purpose have to be decided in this step as well. On the other hand, the IC technology requirements for hybrid and heterogeneous integrations are less demanding, and they are more related to functional (system level) and layout (physical level) design.

The analytical and finite element modeling (FEM) of the resonator can now be performed. After some iterations, the FEM analysis and the theoretical design will provide information of the structural, motional, and dynamic response of the resonator, which will be useful to generating the final process and layout design (provided that the resonator fabrication technology is already known and controlled). A MEMS prototype can now be fabricated. If the monolithic approach is implemented, prototyping does not necessarily require full integration with the IC, and the resonator is usually accompanied with a dummy circuit for characterization and parameter extraction purposes. Different test and de-embedding structures are used at this stage to extract the resonator material constants, the quality factor, the equivalent-circuit parameters, the insertion losses, and the parasitic impedance. Along with the system-level design (system analysis at the transfer function level), the extracted information is vital to complete the circuit-level design. Specifically, input impedance matching with the resonator, amplification gain, or minimum and maximum levels of the input current are some of the IC-design parameters depending on the resonator characterization. At the application level, the bandwidth, oscillation frequency, output impedance and buffering, and power consumption are among the designed specifications.

The resonator-IC interface has to be modeled at the circuit level. In this way and depending on the integration approach, accurate quantification of the parasitic effects of the wire-bonding, bumping, or IC via-holes will enable a reliable prediction of the circuit response. Only after good-practice physical layout design and postlayout simulations can the final response of the resonator-IC system be predicted within reasonable security margins. In general, if the resonator is monolithically integrated and due to its nonstandard design, the design rule checking (DRC) tools will notice the designer with a great amount of warning and error messages. It is a nontrivial task of the design team to distinguish between involuntary mistakes and design-driven, purposely induced rule violations.

After completing the physical design, the IC is fabricated and integrated with the resonator. Please note that the previous steps of the left-sided branch of the flow diagram were concerned with resonator prototyping and not necessarily with the final device. Thus, we can proceed with final-resonator fabrication, and, if the integration is monolithic, this is performed simultaneously with the IC fabrication,

given the process sequence. Otherwise, wire-bonding, flip-chip, and MCM, packaging or related hybridization techniques are implemented now to complete the integration. Testing and characterization of the integrated system provide enough feedback to determine the feasibility of our integration process and the application by itself. Corrective design and technological actions are performed here, in case of malfunctioning or poor system performance. The diagram of Figure 10.1 shows only an iteration of the resonator-IC integration process, although various iterations are normally required to achieve satisfactory results. This methodology is implemented in the following sections to explain the FBAR oscillator and the Si-MEMS resonator with integrated read-out circuit. First, we focus on the detailed fabrication process, technology compatibility, and characterization results of an FBAR.

10.2 Case I: Compatibility of FBAR and Silicon Technologies

In Chapter 4 we studied different FBAR fabrication processes, putting special emphasis on the aluminum nitride (AlN) layer deposition technology and material characterization. At the same time, the compatibility issues and the actions to solve them were explained. We also discussed some inspection techniques, like scanning-electron-microscope (SEM), interferometer and confocal microscopy, and their application to structural analysis of fabricated devices. In this section, the technology compatibility tests are explained. Then, we go through step-by-step descriptions of two bulk micromachining-based FBAR processes. Although the fabrication sequences are specific for the exemplified devices, they are suitable reference guides of generic MEMS resonator and FBAR processes.

10.2.1 Compatibility Testing

10.2.1.1 AlN and Metal Electrode Compatibility

The FBAR studied herein is made of AlN with Pt/Ti electrodes, fabricated on silicon substrate, and bulk micromachined by two technological options: front-side reactive ion etching and back-side anisotropic wet etching. Thus, we begin the study by reviewing the compatibility testing required to pattern the AlN in order to preserve the electrodes, and vice versa. For this reason, the study involves different metals and AlN etchants. Once selected Pt/Ti as the FBAR metallization, the objective is patterning the electrodes with no damage to the AlN. The same considerations for preserving the FBAR structure are taken into account for the micromachining processes.

The study starts with the AlN etching techniques. AlN is patterned by wet etching, after immersion of wafers on certain etchant solutions. Different chemical solutions are commercially available to accomplish this purpose. In considering the Si/SiO_2/metal-bottom/AlN/metal-top structure of the FBAR, AlN patterning has to be completed with no damage to the bottom-electrode metal and the SiO_2 layers (i.e., the etchant has to be highly selective to AlN). The experiments required to test the AlN selectivity consist of taking wafer samples with a different bottom-electrode metal composition and photoresist configuration, and etching them with dif-

ferent chemical solutions. In this way, a matrix with metals in the rows and etchants in the columns is built, like that shown in Table 10.1. The goal of these experiments is to find the metal-resist combinations able to survive the etching process. In the present case study, three commercial etchants are employed: KOH, TMAH, and OPD-4262, which is a TMAH-like solution. The bottom electrode metallization is made of Al, Ti, Pt, Au, Ni, and combinations of these materials. In all the cases, Ti is used as adhesive metal for the structural metals (Pt, Au, or Ni) (candidate substrates for AlN deposition), and the AlN has a thickness of 1,000 nm. Table 10.1 shows that the OPD-4262 and Pt/Ti combination ensures reasonable etching times, with no damage to the Pt/Ti layers. Additionally, the 1,000-nm lateral etching is negligible in comparison to the size of the FBAR electrodes (tens of micrometers). Etching rates and etch-stop times are determined after visual inspection and profile measurements of the sample.

Table 10.1 Compatibility Matrix for AlN Etching

Metal Electrode (Bottom)	*OPD-4262 (With/Without Resist)*	*KOH (With/Without Resist)*	*TMAH[1] (With/Without Resist)*
Al (2,000Å) (mask, resist)	Time: 30 minutes, with intervals (3 minutes) Result: Bad (metal attacked, resist preserved)	KOH attacks both resist and metal	TMAH attacks both resist and metal
Ti+Pt (300Å, 2.000Å) (mask, resist)	Time: 2 hours, with intervals Result: OK (no resist lifting, no metal etching, no lifting)	Time: 1 hour, with intervals Result: Bad (resist is attacked, metal lifted off)	—
Ti (2.000Å) (no mask, resist)	Time: 2 hours, with intervals Result: OK	Time: 2 hours, with intervals Result: Bad (resist is slowly attacked, metal lifted off)	—
Ti+Pt+AlN (300Å, 1,000Å, 5,000Å) (no mask, no resist)	Time: 5/10 minutes, with 1-minute intervals Result: OK. (AlN is etched, 1,000 Å/min, 500 Å/min, respectively)	Time: 1 minute Result: OK (metal preserved, AlN etched, 5.000Å/min)	Time: 1+1 minutes (AlN) Result: OK (metal preserved, AlN etched, 2,500 Å/min)
Ti+Au (300Å, 500Å) (mask, resist)	Time: 1 hour, with intervals Result: OK	Time: 1 hour, with intervals Result: Bad (resist is etched, metal "blows up")	—
Ti+Au (300Å, 500Å) (no mask, no resist)	Time: 1 hour, with intervals Result: OK	Time: 1 hour, with intervals Result: OK	Time: 1 hour, with intervals Result: OK
Ti+Ni (300Å, 500Å) (mask, resist)	Time: 1 hour, with intervals Result: OK	Time: 1 hour, with intervals Result: BAD (resist is etched, metal lifted off)	—
Ti+Ni (300Å, 500Å) (no mask, no resist)	Time: 1 hour, with intervals Result: OK	Time: 1 hour, with intervals Result: OK	Time: 1 hour, with intervals Result: OK

Two samples are observed in the micrographs of Figure 10.2, before and after AlN etching with OPD-4262. In the sample of Figure 10.2(a) the AlN is deposited on Al, and we can see how the metallization has disappeared after the etching (right side). The Al layer (the brightest in the image) remains only in those areas where the AlN protects it (see how the connecting lines and testing pads have disappeared). The second sample consists of AlN deposited on Ti/Pt, and Figure 10.2(b) shows it after the same etching conditions of the previous sample. This time, the connecting pads and the coplanar transmission line are preserved.

From the previous tests, we discarded Al as suitable bottom-electrode metal because it was attacked by the tested etchants. Next, we examine the top electrode compatibility with the AlN layer and the bottom electrode, the analyses being per-

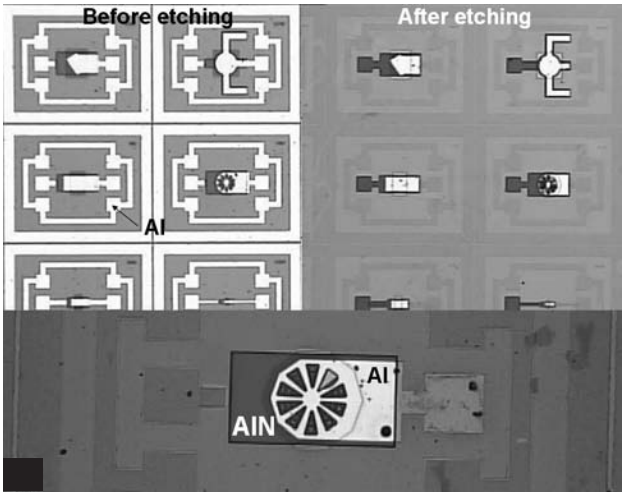

(a)

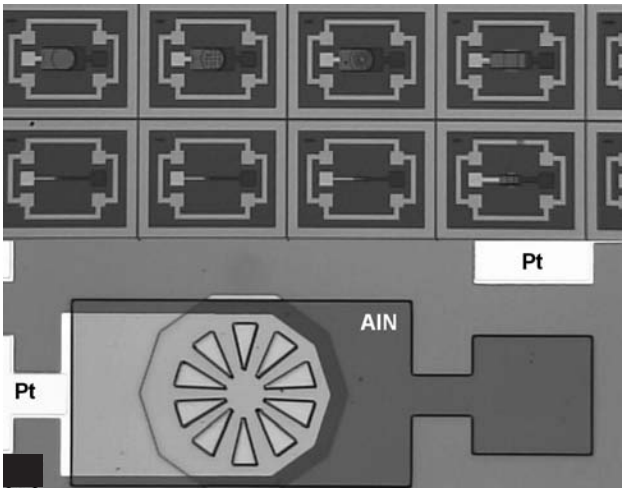

(b)

Figure 10.2 AlN compatibility testing results using OPD-4262 etchant: (a) AlN deposited on Al, before (left) and after (right) etching (the Al layer in white has disappeared after etching); and (b) AlN deposited on Pt/Ti, which remains after AlN etching.

formed with Pt, Au, and Ni metallization (all of them implementing Ti as the adhesive layer). In these tests, the metals are patterned through lift-off after immersion of the samples in acetone. Additional ultrasound shaking helps increasing the efficacy of the resist removal. Table 10.2 shows that, again, the Pt/Ti combination achieved the best lift-off results with no damage to the previous layers.

It is worth mentioning that, in spite of the good results obtained in this study, many other techniques and materials can also be employed to achieve similar performance. Electrodes made of tungsten (W) have also been tested to be compatible with AlN processing [1]. The compatibility of AlN with Al-, Cu-, and Mo-made electrodes patterned through lift-off techniques have been demonstrated as well [2].

The third topic we review in this section is the selectivity of the Si etching process. Let's consider two bulk micromachining processes: RIE-based and KOH-based anisotropic etchings. A short description of both processes is provided in Section 4.2.4. Previously, it was noted that the FBAR structure is supported on a thin SiO_2 layer to isolate the metal electrodes and the substrate.

10.2.1.3 RIE-Based Si Etching Compatibility

Front-side RIE-based etching of the Si substrate requires a mask to open the SiO_2 covering the wafer. The only exceptions are areas where the etching window is opened. Also, we know that the etching selectivity between Si and SiO_2 is about 1:6. Extensive testing has demonstrated that insignificant etchings of AlN or the metal layers occur for long exposures to etching plasma, yet the SiO_2 layer may suffer from important etching. For example, etching of 30 μm of Si leads to 5 μm of attacked SiO_2. Typically, passivation SiO_2 has a thickness less than 1 μm, which means that etching is completed in a few minutes before resonator releasing. Since the metal electrodes of the FBAR are deposited on top of SiO_2, high under-etching of Si conducts to instability of the oxide and metal layers. Also, the SiO_2 passivation loses its functionality due to full etching along the noncovered areas. The situation can be monitored by SEM analysis, as shown in Figure 10.3(a). The figure shows the aspect of the test structure after RIE (the layer configuration of the structure is

Table 10.2 Compatibility Testing for Metal-Layer Patterning

Metal Electrode (Bottom)	*Lift-Off (Only Wafers with Resist, Acetone)*
Ti+Pt (300Å, 2.000 Å) (mask, resist)	Time: 10 minutes Result: OK
Ti+Au (300Å, 500Å) (mask, resist)	Time: 10 minutes Result: Fair-poor. Resist lifted-off for small patterns (max. 50%), and for bigger ones (~50%)
Ti+Ni (300Å,500Å) (mask, resist)	Time: 10 minutes, with intervals Result: Bad (metal did not lift off)

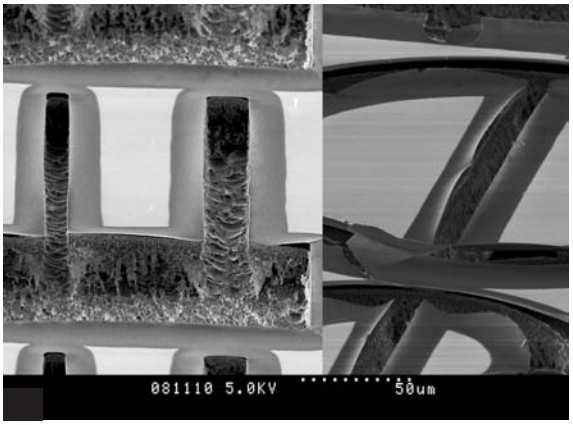

(a)

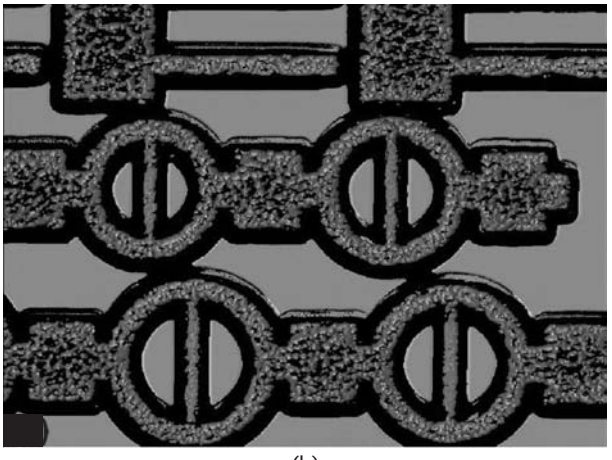

(b)

Figure 10.3 Under-etching test of a metal-on-oxide structure attacked through front-side RIE: (a) SEM image showing that the metal in gray bends after Si and SiO_2 etching; and (b) confocal image of the same structure (the black borders are the bent metal regions).

Si/SiO_2/metal). Due to lateral under-etching of both the Si substrate and the SiO_2 layer, the metal layer (in light) loses its support, thus bending and being released from the substrate (the gray and dark-gray areas are "flying" metal with no SiO_2 support). In the confocal image of Figure 10.3(b), we observe the same structure. Here, the smooth gray regions are the metal, the rough darker-gray regions are etched Si substrate, and the black contour is the (bent) metal with no underlying SiO_2. Longer etching times widen the bent metal contour and eventually complete destruction of the electrode structure.

At least there are two ways for reaching compatibility of the Si RIE and the SiO_2 layer. The trivial one, but not feasible, is to reduce the etching time of Si. The second option is to protect the wafer with a material selective to the plasma recipe. Then, the wafer is etched, and, after etching completion, the cushion material is removed. If such a protective layer can be deposited and properly patterned to provide a window to the Si substrate, the etching time can be arbitrarily long (from the selectivity point of view).

If we use the same mask of the etching window, and a protective Al/Cu layer, for example, the previous goals can be accomplished. Figure 10.4(a) shows a sample FBAR and its coplanar access line with the brightest Al/Cu cushion covering the ensemble. The dark area around the device is the Si substrate seen through the etching window and the corrugated region around the window is the under-etched SiO_2 area. Once the RIE finishes, the Al/Cu cushion is removed by a wet-etching process. The micrograph of Figure 10.4(b) shows full-fabricated FBARs at the end of the process: the darkest gray is the Si substrate at the bottom (several tens of micrometers), the dark gray is SiO_2 with no Si underneath it, and the clear gray is SiO_2 supported on nonetched Si. Some traces of the Al/Cu (bright) still remain on the under-etched SiO_2 region. The detailed, step-by-step description of this process is carried out in Section 10.2.2.

The previous RIE process may be modified through deep RIE (DRIE) processing. When implemented from the back side of wafers, DRIE of Si offers two advantages: (1) under-etching of SiO_2 is avoided, and (2) the Al/Cu cushion is no longer

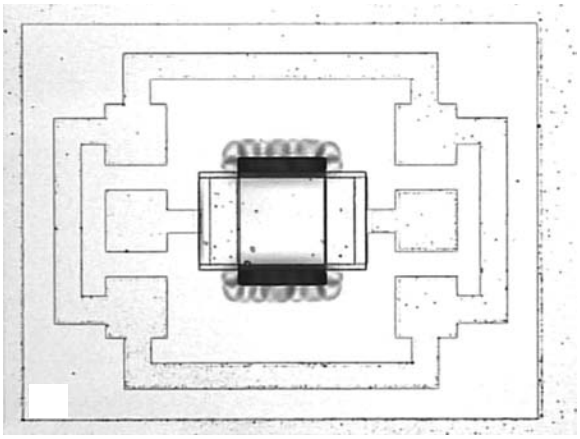

(a)

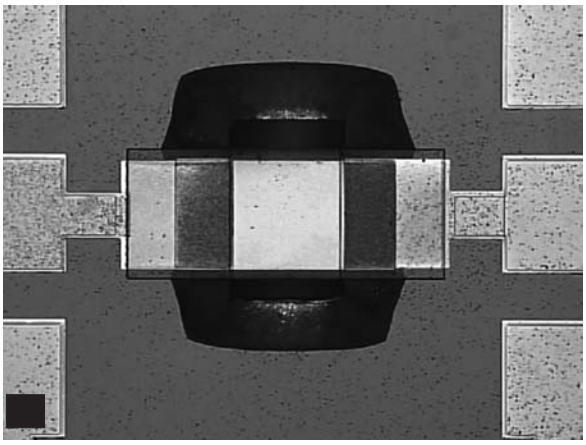

(b)

Figure 10.4 Compatibility of the Si etching and protection of SiO_2: (a) Al/Cu cushion on the SiO_2 to avoid its etching (the etched region in dark black, and the laterally under-etched SiO_2 in rough gray); and (b) the FBAR and the coplanar transmission line after the Al/Cu cushion removal.

needed to protect SiO_2 or structural layers of components. The drawback of this approach is that etching of the full wafer is required to release the resonators, thus increasing fragility.

10.2.1.4 KOH-Based Wet-Etching Compatibility

Anisotropic wet etching of Si has been used for a long time in MEMS and FBAR fabrication, mainly based on KOH etchants. The KOH wet etching is, in a certain way, an auto-controlled process because the process stops when a specific angle in the crystallographic structure of Si is reached. This advantage can be exploited if proper mask design is carried out, to make the desired pattern size coincident with the stopping angle. Selectivity of KOH to other materials also helps to control the etching. For a given substrate thickness, KOH concentration, and appropriate mask design, rough calculations of the etching times are enough for compatibly design the process.

In the KOH process, the front-side Al/Cu cushion layer is replaced by a back-side mask protecting selected regions of the Si substrate from undesired etching. The schematic drawing of Figure 10.5(a) depicts the cross-section of the process, detailing the back-side mask, the stopping front-side SiO_2 layer, and the etching angle. The back-side mask may be a silicon nitride, Si_3N_4, for example. The micrograph of Figure 10.5(b) shows an implementation of this process, the round device being observed at the end of the wafer (500-mm depth). The SiO_2 layer has a thickness of 4,000Å and it avoids contact of the KOH with the structural layers of the FBAR, thus preventing them from being etched. The squared shape of the 1,800-Å Si_3N_4 mask is also observed in the picture, where the gray area around the etched volume is the mask. Due to the etching angle, the base area of the so-formed truncated pyramid is bigger than the top area at the end (where the device is located). The Si walls are the dark gray regions. In Section 10.2.3, we examine in detail an implementation of the back-side FBAR process.

10.2.2 Front-Side, Reactive-Ion-Etching-Based Process

Our fabrication diary begins with the case of RIE-micromachined FBARs. Since the resonators can be implemented in several ways and with an infinite variety of equipment and processes, the manufacturing conditions discussed herein are exclusively a reference guide of current-art FBAR processing. To structure the diary, we have divided it in five main stages: (1) wafer preparation and front-side etching window opening, (2) bottom electrode, (3) AlN deposition and patterning, (4) top electrode, and (5) micromachining (RIE). The fabrication sequences of each stage are illustrated by corresponding Figures 10.6 through 10.10. The global process number is indicated below each drawing, regardless of the stage depicted in the figure, though.

10.2.2.1 Wafer Preparation and Front-Side Etching Window Opening

We start the process by preparing the wafers for clean room processing. Commercial silicon wafers of diameter 100 mm and thickness of 500 μm can be employed. Although not necessary, it is desirable to prepare high-resistivity substrates able to

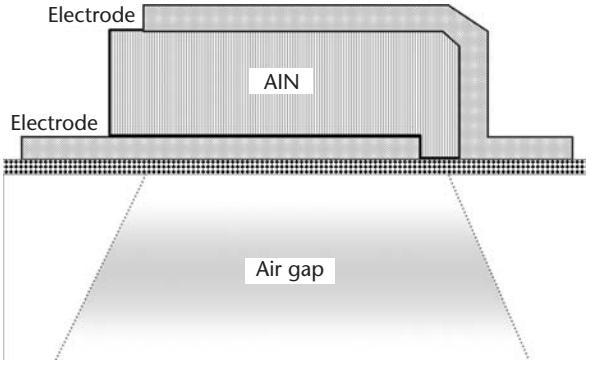

(a)

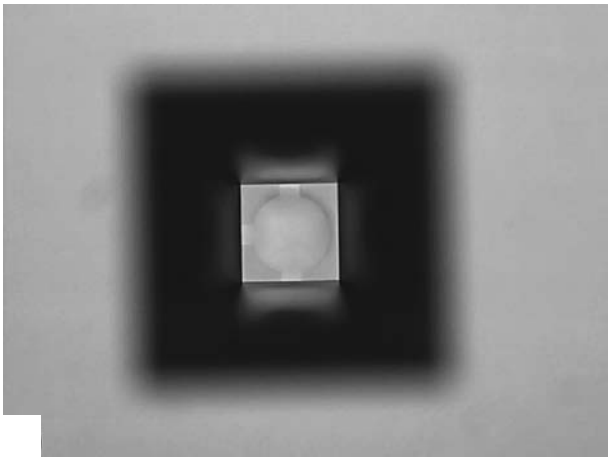

(b)

Figure 10.5 (a, b) Compatibility of the Si wet-etching process: cut-view of the technology (the SiO_2 layer and the crystallography of the Si prevent further etching, and the Si_3N_4 mask protects the Si substrate).

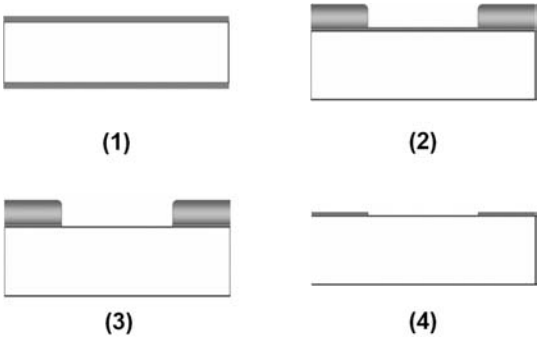

Figure 10.6 Front-side RIE-based process, wafer preparation, and front-side etching window opening: (1) thermal oxidation; (2) photolithography; (3) oxide etching; and (4) resist removal.

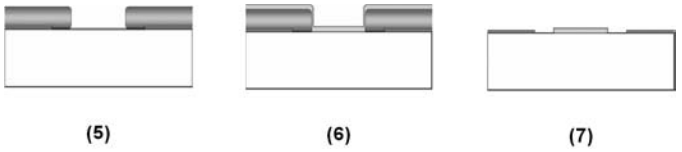

Figure 10.7 Front-side RIE-based process, bottom electrode: (5) photolithography; (6) metal deposition; and (7) resist removal and metal lift-off.

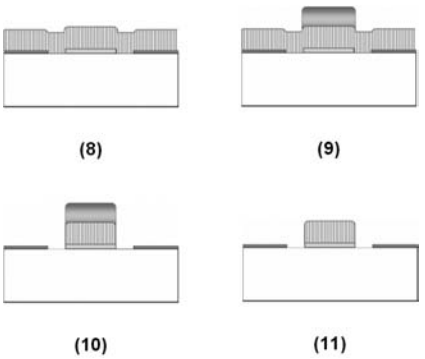

Figure 10.8 Front-side RIE-based process, AlN deposition, and patterning: (8) AlN deposition; (9) photolithography; (10) AlN etching; and (11) resist removal and cleaning.

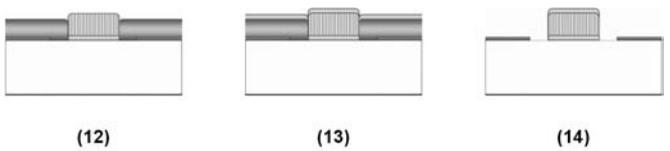

Figure 10.9 Front-side RIE-based process, top electrode: (12) photolithography; (13) metal deposition; and (14) resist removal and metal lift-off.

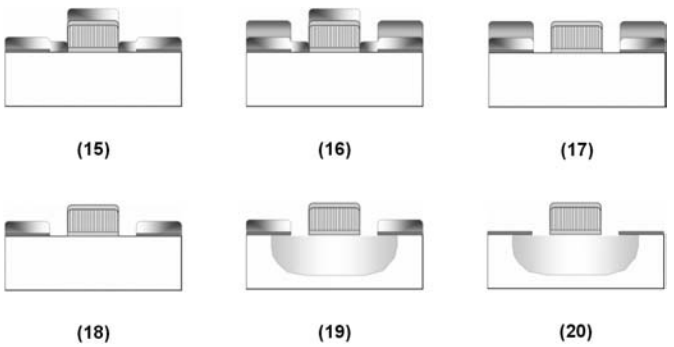

Figure 10.10 Front-side RIE-based process, bulk micromachining: (15) Al/Cu cushion deposition; (16) photolithography; (17) Al/Cu etching; (18) resist removal; (19) RIE-assisted Si micromachining; and (20) Al/Cu cushion removal. Process completed.

reduce the RF losses. Once inside the clean room, standard cleaning on all the wafers is performed with cascade and in-track rinsing. The cleaning can be carried out in three steps: (1) 10–15 minutes of cleansing in sulfuric acid H_2SO_4 and H_2O_2 solution (2:1), (2) immersion in de-ionized water H_2O for another 5 minutes, and (3) additional 10-minute cleansing in de-ionized H_20. Drying of the wafers in heater at 110–125°C completes the preparation.

The wafer preparation process for front-side etching is depicted in the sequence of Figure 10.6. First, a thermal SiO_2 layer of 400 nm is grown on both surfaces of the wafer (1). This is done in an oven at 1,100°C, alternating dry and wet environments. Typically, it starts with a short exposition to oxygen (O_2) flow for about 10 minutes. Next, the flow changes to H_2+O_2 for the longer time of about one hour. To finish the oxidation, O_2 flows again in the chamber for a short time (another 10 minutes, for example). The flow is controlled to be between 3–6 sccm. In this process, only the front-side oxide is useful (to isolate the electrodes and the substrate), so the back-side oxide can be removed up to the designer decision.

Next, in step (2), a photolithographic step is performed with a mask corresponding to etching window patterns. Prior to the photoresist coating, the SiO_2 surface is usually treated with hexa-methyl-disilazane (HMDS) vapor (20 to 30 seconds) to improve the adhesion between the wafer and the resist. With the aid of a spinner, the resist is coated on the wafer, with typical thickness of 1–2 μm. Soft-baking is normally performed in hot plate at 100°C and contact times of 20–30 seconds. Then, the wafer alignment and exposure to UV are carried out. For contact-mode masks, the resist exposition is about 10 seconds or less and the developing times between 20 and 30 seconds. Additional hard baking in hot plate at 115°C for about 30 seconds ameliorates the shape and consistence of the resist.

The exposed areas of SiO_2 are now etched using dry-etching techniques, step (3). For a 400-nm-thick layer, the typical etching times go from half an hour to a couple of hours. Once the etching is completed, the remaining resist is removed by two means: acid solution and dry etching (4). After a first acid-base resist removal, an in-depth cleaning of the wafer is performed in oxygen plasma equipment. Typical operation ranges are 500-W power, 1-mbar pressure or less, and 10% oxygen flow, for about 30–45 minutes.

10.2.2.2 Bottom Electrode

Patterning of the metal electrode can be done through metal etching or lift-off. In this case study, metal lift-off for electrode patterning is implemented, with the sequence of Figure 10.7 depicting the bottom electrode fabrication. First, the photolithography defining the electrode shape is performed, with resist characteristics and processing similar to those referred to in the previous stage (5). Thicknesses of 2 μm and soft baking at 100–115°C are enough to obtain a resist suitable for lift-off. Then, the metallic thin film is deposited on the wafer (6); for example, a 150-nm Pt is sputtered by RF/magnetron sputtering (a 30-nm adhesive Ti layer is deposited prior to Pt). By using argon (Ar) gas and a Pt target, typical deposition times are about 20–30 minutes when the flow of the gas is 50 sccm, the RF power is 100W, and the chamber pressure while sputtering is 110^{-2} mbar. The wafer is then immersed in acetone to perform the metal lift-off (7). To aid this process, ultra-

sound shaking is combined with the acetone to increase the efficacy and the speed. The frequency of the ultrasonic signal can be set to variable or sweeping mode. Evaluation of this step is done through visual inspection of the wafer. Further cleansing of the wafer may be carried out prior to the next step.

10.2.2.3 AlN Deposition and Patterning

The AlN deposition is the key technology of this process. Reactive sputtering and epitaxial growth are the most popular techniques. In this example, reactive magnetron/RF sputtering is implemented in the sequence of Figure 10.8. The 1,000-nm-thick AlN layer is deposited on the wafer surface (8). Having an Ar-N_2 atmosphere (50%–50%) and Al target, the deposition takes place with a rate of 6–7 nm per minute when the RF power is 1 kW and the chamber pressure is 1×10^{-2} mbar. The same resist and setup of step (5) can also be implemented in the photolithography of the AlN (9). Then, wet etching of AlN is done with the OPD-4262 etchant (10). For the thickness of 1,000 nm, the estimated etching rate is between 33–66 nm per minute. Finally, the resist and possible residues are removed through O_2-plasma-based cleaning of the wafers (11).

10.2.2.4 Top Electrode

The top electrode processing sequence is essentially the same as the bottom electrode, and it is depicted in Figure 10.9: resist coating and photolithography with the top electrode mask (12), sputtered-Pt deposition (13), and resist etching and metal lift-off (14). Improved cleaning of the wafer may be performed by O_2 plasma etching.

10.2.2.5 FBAR Micromachining (RIE)

Once the structural layers of the FBAR are fabricated, RIE-based micromachining is the last, and perhaps the most critical, stage of the process. In Section 10.2.1 a compatible process with the low Si-to-SiO_2 RIE selectivity was introduced. Now, we describe the steps required for the device releasing, the sequence illustrated in Figure 10.10. First, the wafer is covered with the Al/Cu cushion layer (15). A thickness of 500 nm is enough to protect the oxide during the RIE. The photolithography to pattern the Al/Cu can thus be performed using the same mask of the etching window opening (which coincides with the exposed SiO_2 surface) (16). Etching of the Al/Cu defines the protected SiO_2 area (17), and the remaining resist on the Al/Cu can be removed by using the previously described plasma techniques (18). The sample is now introduced in the RIE chamber, setting up an SF_6+O_2 atmosphere with Ar buffer at 75 mTorr pressure, and 100W of RF power, which etches Si with a 3:1 to 4:1 anisotropy ratio (19). FBARs are typically sized between 50 and 100 μm, so the required lateral etching is half these values. The last step of the process is the removal of the Al/Cu (20), which can be done in selective dry etching or wet etching, according to the available technology. At this point, the FBAR is completely released and the fabrication is completed.

10.2.3 Back-Side Wet-Etching Process

The second part of our fabrication diary is concerned with the back-side KOH-based wet-etching process of FBARs. At the structural level of the FBAR, the process is essentially the same as that of the RIE-processed case. However, the wafer and etching preparation and the etching process stages substantially differ from those presented in the previous section. Again, the diary structure is divided into five stages: (1) wafer preparation and back-side etching window opening, (2) bottom electrode, (3) AlN deposition and patterning, (4) top electrode, and (5) micromachining (KOH). Since most of the processes involved in the wet-etched FBAR fabrication are the same as described in the previous case, we will focus on the etching preparation and the wet etching in itself.

10.2.3.1 Wafer Preparation and Back-Side Etching Window Opening

The cleaning and preparation steps are the same as described in Section 10.2.2.1. In this case, however, it is useful to implement thinner wafers to reduce the etching times. For this reason, 300-μm-thick wafers are usually implemented in back side etching processes. The first step in the fabrication sequence of Figure 10.11 depicts the growing of thermal SiO_2 with a thickness of 400 nm (1), which is employed as sacrificial material to open a region in the back side of the wafer for Si etching. Next, a silicon nitride, Si3N4, for example, is deposited on the back-side of the wafer (2). This nitride will be used as a mask during the Si etching due to its high selectivity to KOH.

Next, in step (3), the first photolithographic step is performed with a mask corresponding to the membrane area. By considering the wafer thickness and the KOH-driven etching angle of the wafer, one calculates the size of patterns (54.7 deg between the {100} and {111} planes, or 35.3° respect to the normal). Thus, the back-side membrane size (which designed in the mask) is projected through the 300-μm-thick wafer to fit the front-side membrane size. In step (4), the noncovered nitride is attacked through plasma etching. Then, an acid solution and posterior O_2 plasma etching remove the resist and remaining particles (5). The O_2 plasma also etches the thermal oxide on the front side and the noncovered areas of the wafer's back side (6). The wafer is now prepared for deposition of the FBAR structural layers and for the back-side etching steps performed at the end of the process.

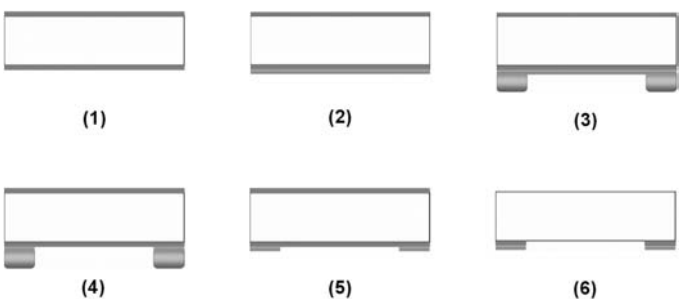

Figure 10.11 Back-side KOH-based process, wafer preparation, and back-side etching window opening: (1) thermal oxidation; (2) nitride deposition (back-side); (3)photolithography; (4) nitride etching; (5) resist removal; and (6) oxide etching.

10.2.3.2 Bottom Electrode

The same techniques described in Section 10.2.2.2 are used to fabricate the bottom electrode, whose process sequence depicts Figure 10.12. First of all, a low-pressure plasma-enhanced chemical vapor-deposited (LPECVD) oxide layer is deposited on the front-side surface of the wafer (7). In this way, we achieve better electrode-substrate isolation and, at the same time, provide an effective barrier to the wet etching. This means that, as a difference to the previous process, the SiO_2 membrane will support the FBAR, instead of being suspended only by its structural layers. Next, one performs the photolithography defining the Pt electrode (8), the Pt layer deposition (9), and the lift-off of the resist and the on-resist metal (10). The Pt thickness is again 150 nm. Further cleansing may be required prior to performing further processing of the wafer.

10.2.3.3 AlN Deposition and Patterning

The AlN deposition and patterning sequences are identical to those presented in Section 10.2.2.3, as depicted in Figure 10.13. The 1,000-nm-thick AlN layer is deposited on the wafer surface (11). Then, the photolithography is performed (12), and the AlN is etched with OPD-4262 to pattern the resonator shape (13). Finally,

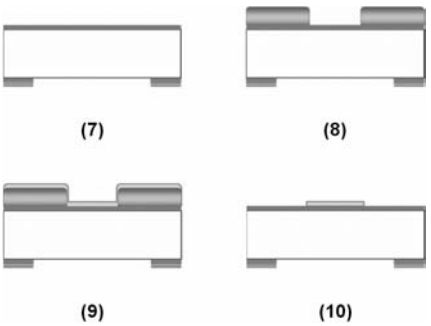

Figure 10.12 Back-side KOH-based process, bottom electrode: (7) LPCV-deposited oxide; (8) photolithography; (9) metal deposition; and (10) resist removal and metal lift-off.

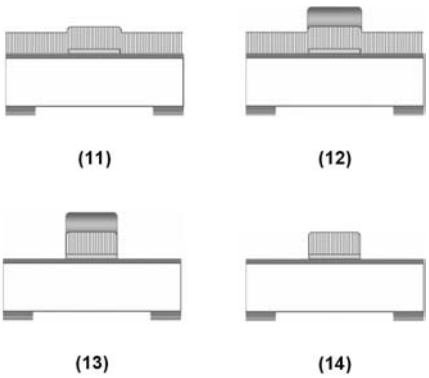

Figure 10.13 Back-side KOH-based process, AlN deposition, and patterning: (11) AlN deposition; (12) photolithography; (13) AlN etching; and (14) resist removal and cleaning.

O_2-plasma-based cleaning removes the resist and possible residues of the wafers (14).

10.2.3.4 Top Electrode

The top electrode processing sequence is essentially the same as for the bottom electrode shown in previous sections. The sequence is depicted in the schematic drawings of Figure 10.14: resist coating and photolithography with the top electrode mask (15), sputtered-Pt deposition (16), and resist etching and metal lift-off (17). In addition, the wafer may be deeply cleaned with in O_2 plasma.

10.2.3.5 FBAR Micromachining (KOH)

Last, but not least, the KOH-assisted back-side micromachining of the wafer is carried out, as depicted in step (18) of the sequence in Figure 10.15. As previously commented, the angle between the back-side plane and the normal is 54.7°, and the etching stops just at the oxide-silicon interface. Additionally, we can remove the back-side Si_3N_4 and SiO_2, if desired. At this point, the FBAR is released, and the process is completed.

10.3 Case II: High-Level Design of a Temperature-Compensated (TC) Oscillator

Resonator-based crystal oscillators (RXO) are one of the most appealing applications of FBAR and MEMS resonators. They are a subject of study and industrial production, as we extensively reviewed in Chapter 9. In spite of the high Q factor of such microresonators and the availability of different integration technologies with current IC processes, RXOs (as well as virtually any oscillator) suffer frequency

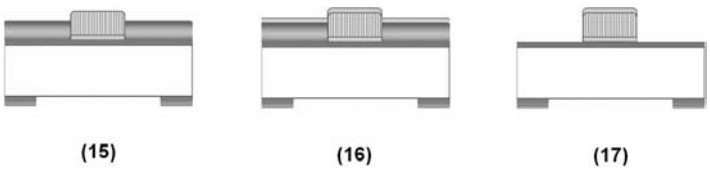

Figure 10.14 Back-side KOH-based process, top electrode: (15) photolithography; (16) metal deposition; and (17) resist removal and metal lift-off.

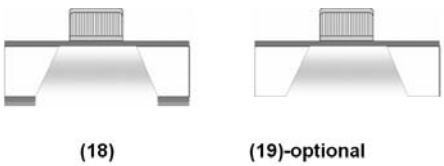

Figure 10.15 Back-side KOH-based process, micromachining: (18) KOH-based wet-etching of Si; and (19) back-side nitride and oxide removal (optional).

instability from aging- and temperature-related issues. Both the IC and the resonator contribute to the frequency drifting of the RXO. Already in Chapter 6, we analyzed the temperature coefficient factor of FBARs and studied a process-based compensation strategy.

In this section, we will study the case of a temperature-compensated FBAR oscillator. First, we introduce the impact of temperature on the frequency stability, the phase noise, and the application requirements of RXOs. Next, we focus on current-art FBAR-oscillator implementations and their phase noise performance. With this at hand, both technology-level and system-level solutions for the RXO frequency drifting are proposed. In the present study, we assume that the temperature coefficient factor (TCF) of the FBAR can be tailored at the process level. Thus, the analysis will be oriented to reduce the TCF of the IC-plus-FBAR ensemble. For this purpose, codesign of the RXO is carried out, by performing a Verilog-A model of the temperature-compensated FBAR and the circuit-level modeling of the ensemble. The compensation strategies and their implementations are discussed at the end of the section.

10.3.1 The Temperature Stability Issue in Oscillators

As previously stated in Chapter 6, oscillators are closed-loop circuits with positive feedback. If the Barkhausen criteria are met, the oscillation is sustained without the need for input signal. An RXO is constituted by two components: the resonator and the amplification circuit. The components are interconnected to be part of the oscillator loop to attain enough gain and phase shift, imposed by the Barkhausen conditions (0 dB and 360°, respectively). The resonance frequency mainly determines the RXO frequency of the crystal, which can be a quartz plate, a MEMS resonator, a SAW, or an FBAR. Small variations of this frequency do not normally jeopardize the Barkhausen conditions, because the RXO is designed with adequate gain and phase margins. However, since the performance of an oscillator depends on its frequency stability, one may intuit that the frequency variations should be controlled to guarantee operation within the application limits.

The oscillator frequency stability is quantified by defining its phase noise. The phase noise is the amount of fluctuations in the phase of the oscillation, which leads to frequency deviation of the ideal pure-sinusoidal oscillator behavior. The phase noise adds to the ideal sinusoidal wave so as the oscillation power is spread to adjacent frequencies:

$$a(t) = A_0 \sin\left(2\pi f_0 + \theta(t)\right) \tag{10.1}$$

where f_0 is the central frequency of the oscillation and $\theta(t)$ is the phase noise. Thus, the phase noise modulates the ideal oscillation frequency in a random way. The severity depends on the temperature fluctuations, among many factors. The phase noise density is measured in dBc/Hz at various offsets referencing the central frequency. It is assumed that, typically, the phase noise includes both low-frequency flicker noise and broadband white noise, so it has a monotonically descending sideband shape in the frequency domain, as depicted in Figure 10.16. Ultimately, the phase noise is responsible for limiting the signal-to-noise ratio and the proper demodulation of RF signals. Thus, the phase noise has to be kept as low as possible.

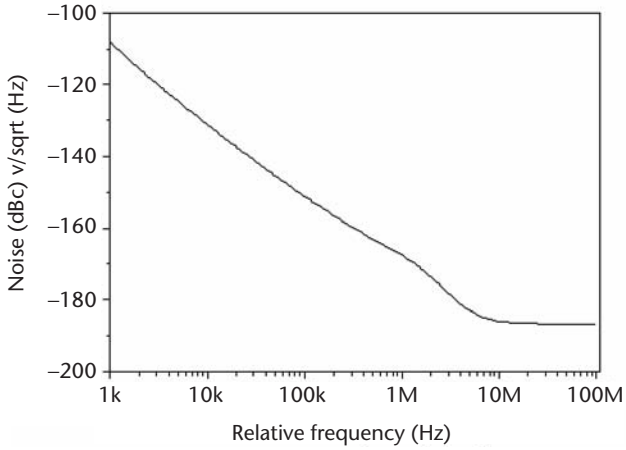

Figure 10.16 Frequency-domain representation of phase noise.

The oscillator phase noise depends to a great extent on the resonator's temperature coefficient factor (TCF). Thus, if we are able to reduce the TCF, the oscillator phase noise will be improved [3]. In Chapter 6 we already defined the TCF of a resonator, and some temperature compensation strategies to control the resonance frequency of FBARs were discussed. At the process level, the mainstream strategy is adding a compensation layer made of a material with a TCF of magnitude opposite to that of the active layer. In AlN-made FBARs, a properly designed SiO_2 layer can accomplish this task to reduce the TCF to values as low as –1.5 ppm/°C, which are pretty competitive to the performance of quartz [4, 5].

At the system level, various circuit topologies and frequency control strategies exist to compensate for the temperature-dependent phase noise. They include analog, digital, and mixed-signal techniques. Analog techniques address temperature compensation by building a current or voltage reference that is independent of the power supply and fabrication process. Also, such a reference exhibits a well-known temperature behavior. The temperature dependence may assume one of three forms: (1) proportional to absolute temperature (PTAT), (2) constant transconductance g_m behavior, and (3) temperature independent [6]. In this way, analog compensation circuits may implement bandgap and PTAT voltage generators [7–10], varactors or capacitor banks [11, 12], or built-in heating of the resonator for constant-temperature operation [13], among many others.

Digital compensation is carried out by an EPROM memory and a resistive temperature sensor. Thus, the sensor converts the resistance temperature value to a proportional voltage, which is then converted to a digital signal. This signal is subsequently used to address the EPROM containing the calibrated control voltage necessary for compensating the measured temperature. M. A. Taslakov implemented this method to temperature compensation of a 1-GHz surface transverse wave (STW)–based oscillator with a temperature precision of ±1.25 ppm from –30°C to +60°C [14]. Mixed compensation techniques attempt to combine the good repeatability and low phase noise of analog compensation and the simpler structure and stability of digital techniques (e.g., the double compensated TCXO presented by Zhou et al. [15]).

10.3.2 Low Phase Noise FBAR-Based Oscillators

To date, FBAR oscillator implementations with low phase-noise performance have been demonstrated. The high Q factor of the FBAR and the phase noise performance of the oscillator in gigahertz bands make them attractive to 3G applications. Although attractive, the phase noise can still be reduced by modifying the FBAR process, the circuit design, or both. To illustrate the impact of the resonator TCF reduction in phase noise, let's analyze the 5-GHz RXO implemented by Zhang et al. [16]. The noncompensated FBAR performing a –60 ppm/°C TCF was modified to feature a SiO_2 temperature compensation layer. In this way, the compensated TCF was reduced to –8.7 ppm/°C, thus achieving a phase noise of –109.5 dBc/Hz at 100 kHz.

The balanced Colpitts configuration proposed by Aissi et al. succeeds in halving the phase noise of the oscillator to a value of –121 dBc/Hz at 100 kHz from 5.46-GHz carrier frequency [17]. In this case, the FBAR does not implement any temperature compensation layer. A third oscillator designed by Chee et al. drastically reduces the phase noise by combining a 1.9-GHz FBAR oscillator with an injection locked power oscillator [18]. Prior to locking, the power oscillator shows a poor phase noise of –98 dBc/Hz at 100 kHz. When the power and the FBAR oscillators are locked in, the phase noise is improved to –120 dBc/Hz at the offset frequency of 100 kHz. The phase noise performances of the circuit before and after injection locking are shown in the plot of Figure 10.17.

The previous examples are just samples of the several ways conceived to improve the oscillator performance. Of course, many other techniques are also suitable for reducing the FBAR oscillator phase noise, like the varactor-controlled low-TCF circuit. Once the FBAR is optimized to attain low-TCF, further actions can be taken to reduce the oscillator's TCF. Thus, codesigning the FBAR and the circuit can lead us to very low TCF values, as we analyze in the following section. We carry out this task by modeling the temperature and frequency responses of the FBAR, the oscillator, and the varactors.

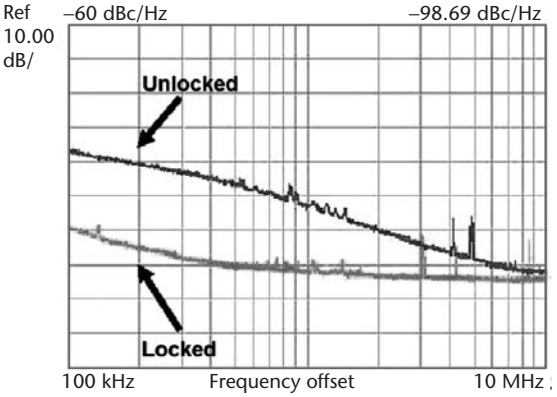

Figure 10.17 Phase noise performance of the injection locking oscillator transmitter: a phase noise improvement higher than 20 dBc/Hz at 100 kHz is observed after locking of the power and FBAR oscillators. (© 2006 IEEE [18].)

10.3.3 Codesign of an FBAR-Based TC Oscillator

Codesign of an electronic system is a working philosophy understanding that the different components of the circuit have to be designed with regard to global system performance. Instead of their individual optimization, codesign studies the interaction among components modifying the response of the system [19]. Individual optimization is thus nonuseful or, in general, it only leads to local variable optimization. Although many methodologies for electronic system codesign exist, all of them make use of cosimulation of the circuit components. This is done through specifically created system description languages, like Verilog-A, SystemC, or VHDL-AMS, among others [20–23]. In recent years, the integration of MEMS and FBARs with ICs make these methodologies necessary to optimum system design.

In our case, codesigning the FBAR and the circuit can lead us to very low TCF value. Of course, we can optimize the circuit without considering the TCF of the FBAR. At the process level, we can reduce the FBAR's TCF by implementing temperature compensation layers as described in Chapter 6. None of these solutions imply that the integrated system will perform the lowest possible TCF. For this purpose, we first model the temperature and frequency responses of the FBAR, the oscillator, and the varactors. Then, we integrate them and see how the integrated system responds to temperature, so we can determine the design values suitable for TCF reduction.

First, it is useful to get previous knowledge of the oscillator architecture and the circuit-level operating principles. The Figure 10.18(a) depicts the schematic circuit of a Pierce oscillator. Transistor M_1 is the oscillator's core providing enough transconductance gain to sustain the oscillation, I_{BIAS} supplies the bias current of the circuit including the M1 drain-to-source current I_{DS}, C_1 and C_2 modulate the amplification gain, and the crystal is an FBAR that fixes the oscillation frequency through the feedback network between the drain and gate of $M1$. C_1 and C_2 are external,

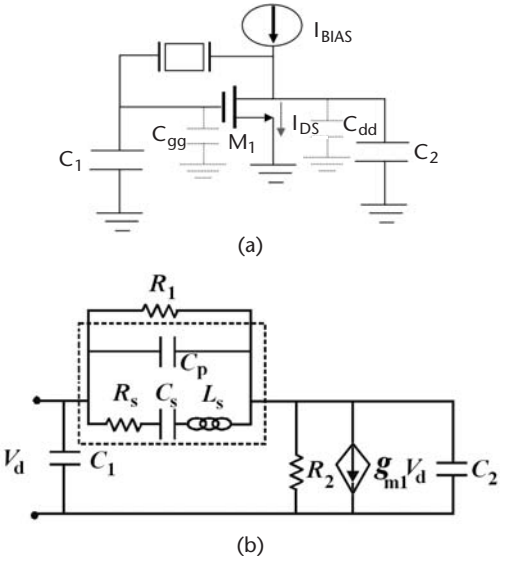

Figure 10.18 Pierce oscillator: (a) schematic circuit with the FBAR between gate and drain of M_1; and (b) small-signal representation.

monolithic, or the input and output capacitances of M_1. In a lesser way, they also serve as frequency pulling parameters. The crystal resonator is implemented with an FBAR, which we will model by the MBVD equivalent-circuit representation. I_{BIAS} is implemented by a CMOS current source, and the DC biasing of M_1 is fixed by placing a feedback resistance R_3 between gate and drain. The small-signal oscillator circuit is shown in Figure 10.18(b). A more realistic circuit should include the gate and drain capacitances C_{gg} and C_{dd}. They may be comparable to C_1 and C_2 for a big-area transistor M_1 with high transconductance gain g_m.

The Barkhausen conditions are examined by breaking the loop at the output of the voltage-controlled current source ($g_m v_1$) and introducing a test current i across R_2 and C_2. In this way, the open-loop gain $T(s)$ must be higher than unity, and the phase shift introduced by the FBAR must be equal to −180° to obtain a total phase shift of 360°:

$$T(s) = -\frac{g_m v_1}{i} \tag{10.2}$$

$$T(s) = \frac{g_m R_1 R_2}{Z_c(s)(1+R_1C_1s)(1+R_2C_2s) + R_1(1+R_2C_2s) + R_2(1+R_1C_1s)} \tag{10.3}$$

Equivalently, the real component of the circuit impedance (Z_c) must be negative and higher in module than the equivalent parallel impedance formed by the FBAR and the biasing resistance R_3:

$$Z(s) = \frac{1}{C_0 s} \| R_3 \| \left(R_m + L_m s + \frac{1}{C_m s} \right) \tag{10.4}$$

$$Z(s) = -Z_c \tag{10.5}$$

Note that the parasitic impedance due to FBAR-to-IC interconnection is excluded from the analysis. Depending on the integration strategy, they can be significant, and they should be considered for realistic results. In a first approximation, though, we also neglect R_3 and the output resistance R_2 to find the values of the real and imaginary components of the circuit impedance Z_C:

$$\mathrm{Re}(Z_c) = -\frac{g_m C_1 C_2}{(g_m C_0)^2 + \omega^2 (C_1C_2 + C_2C_0 + C_1C_0)^2} \tag{10.6}$$

$$\mathrm{Im}(Z_c) = -\frac{g_m^2 C_0 + 2\omega^2 (C_1 + C_2)(C_1C_2 + C_2C_3 + C_1C_3)}{\omega\left[(g_m C_0)^2 + \omega_0^2 (C_1C_2 + C_2C_3 + C_1C_3)\right]} \tag{10.7}$$

From the previous equations, we see how the circuit's negative resistance can be larger than that of the FBAR by controlling C_1, C_2, and g_m, thus allowing the oscillation to start up. As we said before, C_{gg} and C_{dd} may be included in the analysis. Actually, they replace C_1 and C_2 in most circuits because of their large size. In summary,

we have three temperature-dependent components controlling the oscillation frequency:

1. Transistor M_1, through g_m, C_{gg}, and C_{dd}, all of them also dependent of I_{DS}, which is also affected by temperature variations;
2. External capacitors C_1, C_2 (monolithic or discrete components);
3. FBAR modeled through the motional impedance elements L_m, R_m, and C_m.

Now, let's state the codesign strategies of the temperature-compensated oscillator, assuming that the circuit has been designed to meet the Barkhausen conditions (i.e., that the g_m, I_{DS}, C_1, and C_2 values are enough to sustain the oscillation given an FBAR model):

1. Controlling the equivalent-circuit parameters of the FBAR L_m, C_m, and C_0: Although not of a physical meaning, thus not controllable by circuit-design techniques, the temperature dependence of L_m, C_m, or C_0 can be modeled through a system-level language. In this way, the FBAR behavioral model is integrated into the circuit-level model of the oscillator to obtain the FBAR-plus-IC temperature response.
2. Controlling the C_{gg}/C_{dd} ratio: It assumes that by controlling the I_{DS} value, the values of C_{gg} and C_{dd} can be changed to contribute compensating the temperature variations. This is done by parametric analysis of the I_{BIAS} current source.
3. Controlling the C_1/C_2 ratio: The oscillation frequency depends on the total circuit's reactance at that frequency. The temperature variations modify the reactance, and the oscillation frequency. The C_1/C_2 ratio is modified to compensate the modeled L_m/C_m temperature variations.

First, we need an FBAR description suitable for integration with Spice or Spectre models used in the circuit-level design environment. The parameters of such a description are the equivalent-circuit elements and TCF of the FBAR and the temperature. According to the examples of Chapter 6, where resonators with linear TCF were studied, the mathematical model provided by (6.2) to (6.4) gives us the basis for building the behavioral model. We reproduce here (6.2) to (6.4) for convenience of the description:

$$f_0^{Ti} = f_0^{ref}\left(1 - TCF \times \left(T_{ref} - T_i\right)\right) \tag{10.8}$$

$$f_0 = \frac{1}{2\pi\sqrt{L_m C_m}} \tag{10.9}$$

$$L_m^{Ti} = \frac{L_m^{ref}}{\left(1 - TCF \times \left(T_{ref} - T_i\right)\right)^2} \tag{10.10}$$

where f_0 is the resonance frequency, f_0^{Ti} is the resonance frequency at temperature T_i, f_0^{ref} is the resonance frequency at the reference temperature T_{ref}, L_m and C_m are

the motional inductance and capacitance of the MBVD FBAR model, L_m^{Ti} is the L_m value at temperature T_i, and L_m^{ref} is the L_m value at temperature T_{ref}. This temperature-dependent model of L_m can be implemented by different means, as the following Verilog-A script:

```
'include "constants.vams"
'include "disciplines.vams"
module Lm_T(vp, vn) ;
inout vp, vn ;
electrical vp, vn ;
parameter real Lm = 0 ;  //Lm: reference motional inductance
parameter real Temp = 40 ;  //Temp: reference temperature (°C)
parameter real TCF = –5 ;  //TCF: temperature coefficient factor
      analog
V(vp, vn) <+ ddt(Lm*I(vp, vn)) /((1 – TCF/1e6 *(40 – Temp))*(1-TCF/1e6 *(40 –
Temp)));
Endmodule
```

According to the Verilog sintaxis, L_m_T is a two-terminal *module* with input-output voltage nodes *vp* and *vn* representing L_m^{Ti}. Next, the initial values of the model parameters are defined, and the voltage-to-current relationship of the *module* is described. Thus, we see that the voltage across L_m^{Ti} is a function of the derivative instruction *ddt* of the current, the reference L_m, the reference temperature *Temp*, and the *TCF*. This model can then be instantiated in the circuit design environment (e.g., Cadence Virtuoso Schematic). The circuit representation of the model and other circuit components is depicted in Figure 10.19(a), and the Cadence dialog box for object property edition of the inductor in Figure 10.19(b). The frequency response in parts per million (ppm) against the temperature is similar to that already presented in Figure 6.9(b), although with a TCF = –5 ppm/°C (according to the previous script). By modifying the *TCF* parameter, the process-based temperature compensation of the FBAR can be simulated. The resonator model can now be integrated with the other circuit components to analyze their combined temperature performance.

Before the FBAR-IC integration, the circuit is simulated to check its own TCF value. This will give us an idea of the amount of compensation due to the IC we will need to introduce in the system. To carry out this simulation, we replace the Verilog-A model of the FBAR by ideal RLC counterparts with no performance variations due to temperature. Also, we are interested on studying the variations of the transconductance g_m. The curves of Figures 10.20(a) and 10.20(b) show the temperature-due variations of g_m and the oscillation frequency, respectively. The circuit was simulated using the Spectre models of the AMS035C3B4 CMOS technology for the +20°C to +80°C range, and, according to the figures, it has a negative TCF. Analyzing the curves of g_m, its TCF equals –3,125 ppm/°C, which is very high. However, if we look at the behavior of the oscillation frequency, its TCF has the very low value of –0.5 ppm/°C. This would mean that the variations of g_m are absorbed or compensated by the other circuit components.

Now, we connect the FBAR(T°) and the IC(T°) models. For given values of *Temp*, *TCF*, and *Lm*, the available Spice or Spectre models in the CAD environment

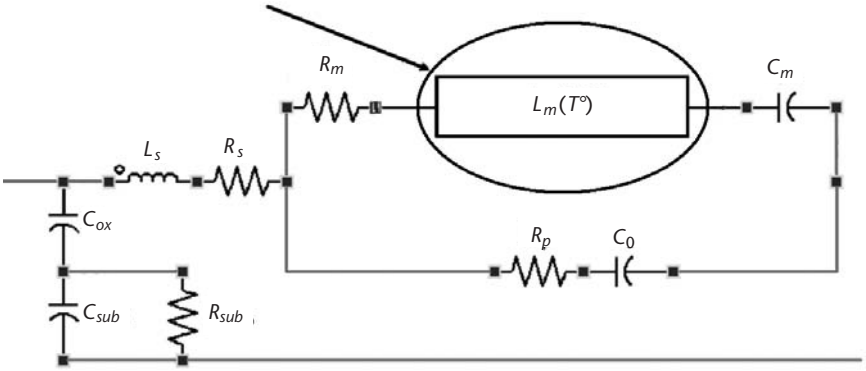

(a)

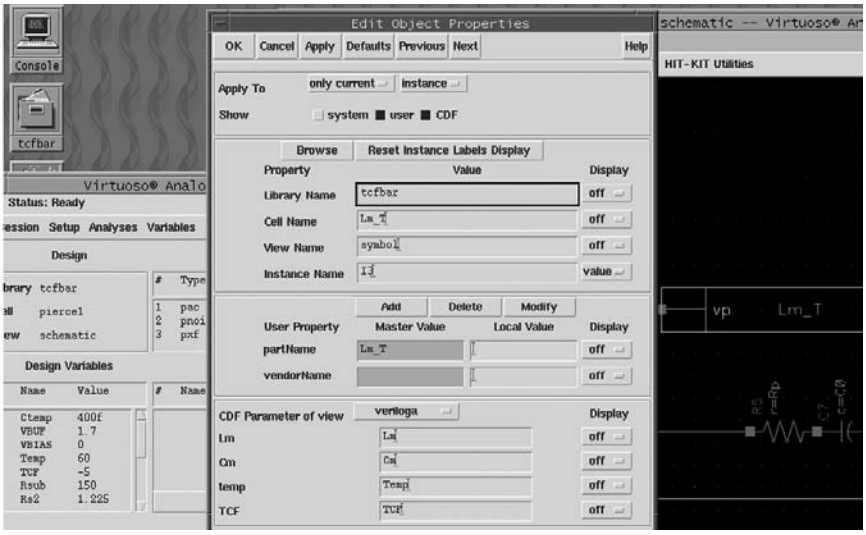

(b)

Figure 10.19 Behavioral implementation of an FBAR in the Cadence environment: (a) schematic circuit of the MBVD model of the FBAR with the Verilog-A model of the motional inductance L_m^{Ti} (in the oval); and (b) edit dialog box for setting the initial values of the model.

perform the open-loop and close-loop circuit analysis. Let's remember that, previously, we used TCF values equal to –5 ppm/°C for the FBAR, and obtained an IC TCF of –0.5 ppm/°C. The TCF of the integrated system is carried out by sweeping the temperature range of 20–80°C in both the Spectre modeling setup and the FBAR's edit dialog box. The results are shown in Figure 10.21, where the obtained TCF is –6.5 ppm/°C. We conclude that the TCF of the FBAR and the IC are added, but resulting in a higher value than the sum of their individual TCFs.

Then, we implement our compensation strategies to test their suitability. First, we analyze the C_{gg}/C_{dd} ratio. From the previous analysis, we find out that the drain-source current I_{DS} is also sensitive to the temperature variations, as the points in the plot of Figure 10.22 demonstrate. Thus, it is impossible to control the C_{gg}/C_{dd}

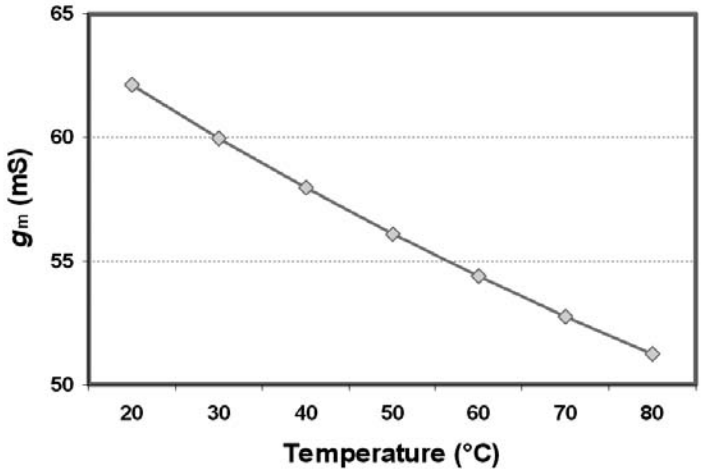

(a)

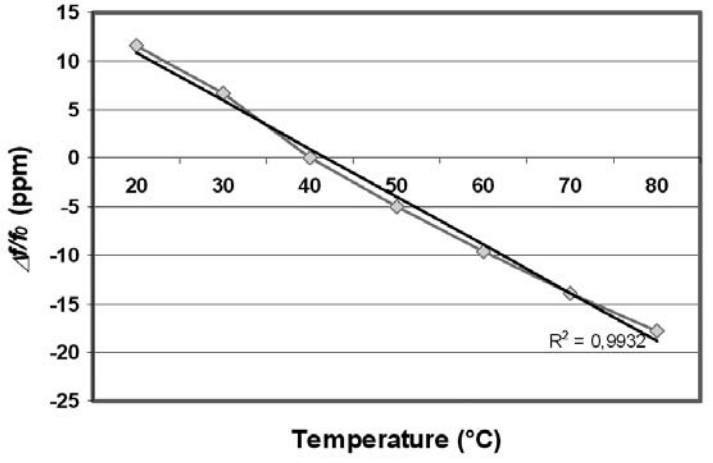

(b)

Figure 10.20 Circuit-level simulation of the Pierce oscillator TCF (ideal MBVD elements in the FBAR): (a) transconductance g_m; and (b) oscillation frequency (ppm).

values due to I_{DS} via I_{BIAS}. For this reason, we discard the implementation of this strategy.

We consider now controlling the C_1/C_2 ratio. In a first stage of the analysis, we assume that we are able to change the value of C_1, C_2, or both. This can be done by implementing digitally controlled capacitor banks, or integrated MEMS or discrete varactors. To modify C_1, for example, we assume a tuning range relative to the values of C_{gg}. Thus, we implement a first bank tunable up to a maximum C_1 value equal to the 50% of C_{gg}. In the second implementation, C_1 is tuned in the range of the 100% of C_{gg}. Results in the plots of Figure 10.23 compare these implementations and the noncompensated circuit. A TCF reduction up to –1.8 ppm/°C was obtained with this approach.

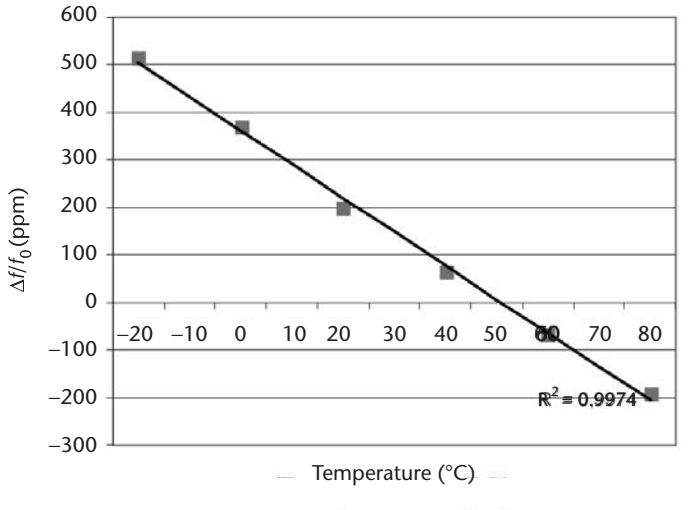

Figure 10.21 Thermal response of the integrated FBAR-IC oscillator (no temperature compensation): the system TCF is –6.5 ppm/°C.

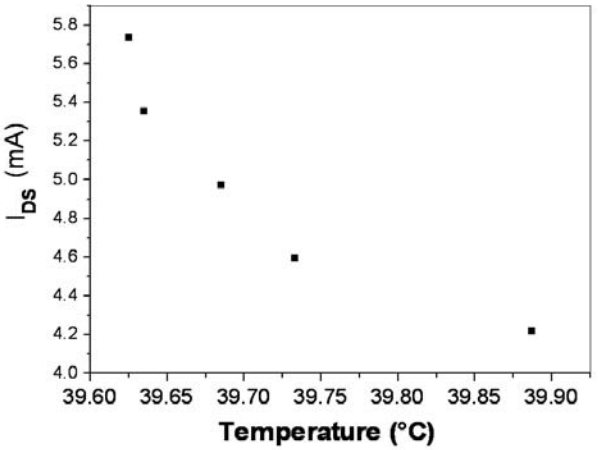

Figure 10.22 Thermal response of the drain-to-source current I_{DS} of transistor M_1.

In conclusion, one can say that the latter strategy will be useful to reduce the TCF of the circuit. However, many challenges have to be faced, most of them related to the implementation of the variable C_1-C_2 capacitor set. Tuning range and quality factor of current-art varactors has to be kept in mind. Nevertheless, we have learned that both the FBAR and the IC have to be analyzed in a joint way to obtain more realistic results. Codesign methodologies like that introduced in these paragraphs are useful to accomplish this purpose.

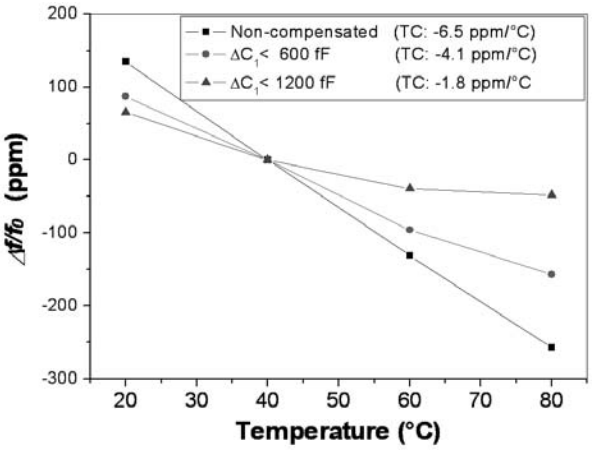

Figure 10.23 Thermal response of the integrated FBAR-IC oscillator implementing the C_1/C_2 ratio compensation strategy: the system TCF is reduced up to –1.8 ppm/ºC (full range of C_1 equals the C_{gg} value).

10.4 Case III: Read-Out Circuit Design of a 434-MHz MEMS Resonator

Integration of MEMS resonators with microelectronic circuits often requires previous characterization and parameter extraction of the resonator, as we examined in the previous case. These tasks provide the designer with enough information for dimensioning the IC's large and small signal specifications, like biasing, required gain level, and bandwidth. However, equivalent-circuit models of small MEMS devices may be hardly extracted due to very low output currents, high insertion losses, and noise levels. In some cases, the engineer only has at hand rough parameter estimations based on simulations to complete the circuit-level design. A second issue is the impedance matching between the characterization instrument and the resonator.

To overcome these issues, read-out circuits are integrated with MEMS to accomplish two purposes: (1) signal amplification of the MEMS output current to reach the minimum signal levels to de-embed the resonator model; and (2) impedance matching with the characterization equipment. Broadly, Figure 10.24 repre-

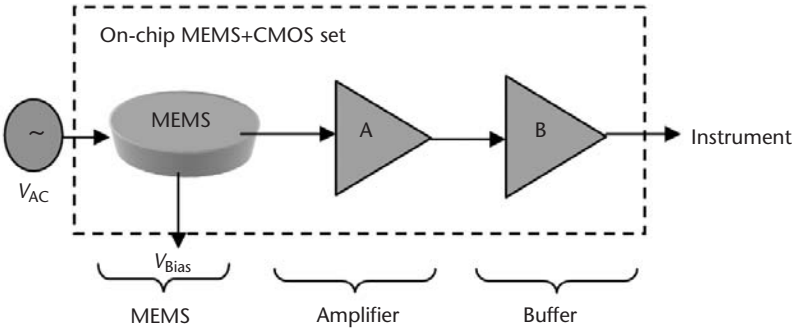

Figure 10.24 MEMS resonator and read-out circuit integration scheme: the output MEMS current is amplified and impedance-matched to the instrument input port.

sents the scheme of MEMS resonator and read-out circuit integration. The drawing assumes electrostatic actuation of the resonator with an AC voltage V_{AC}, which is biased through the DC voltage V_{BIAS}. The time-varying current i_{AC} is delivered to the amplifier with gain A for increasing and conditioning the signal level, and the buffer provides impedance matching to the characterization instrument. The dotted line represents the on-chip MEMS and CMOS read-out circuit set. Typically, the characterization setup for this chip includes a signal generator with sweeping capability to excite the MEMS and a spectrum analyzer or a network analyzer to perform both functions directly.

Several circuit architectures and measurement techniques are applicable to perform characterization of a MEMS resonator. In this case study, we focus on a linear-mode circuit able to develop broadband characterization of the frequency response of an electrostatically actuated MEMS resonator. The specification and design of the read-out amplifier includes the amplifier architecture, values for passive components, output impedances, dynamic range, bandwidth, and gain range, among other parameters.

10.4.1 MEMS-CMOS Integration Technology

Better comprehension of the read-out circuit is reached if we first understand the MEMS-CMOS integration technology and physical layout. Monolithic integration of the MEMS and CMOS circuit reduces the parasitic effects introduced by wire-bonding or discrete integration. In the present case, the integration is implemented by designing the MEMS with the Poly1 and Poly2 layers of the AMS035c3b4 CMOS technology [24]. The MEMS is released after a wet etching postprocess. The cross section of the AMS device chip after CMOS process completion will look like the schema of Figure 10.25(a). As observed, the passivation layer PROT is opened during the CMOS process to allow access to the upper IMD layer.

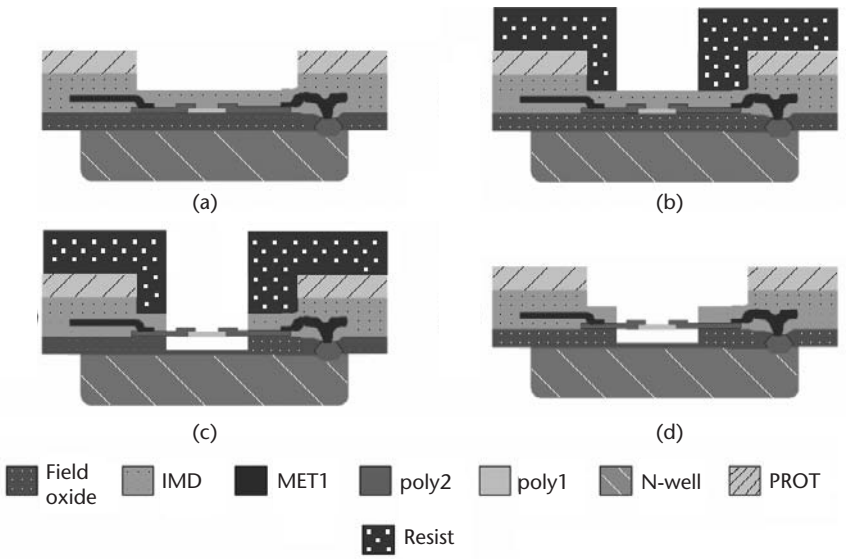

Figure 10.25 (a–d) MEMS resonator postprocess implementation using the AMS035C3B4 CMOS process. (Courtesy of Zachary J. Davis, DTU Nanotech, Copenhagen, Denmark.)

Since the Poly1 and Poly2 layers are patterned using the AMS mask layers, we only need to release the structures. First, a thick layer of photo-resist is deposited and a window opened directly over the MEMS area, as shown in Figure 10.25(b). Then, HF-based wet-etching releases the resonator, attacking the SiO_2-made layers, the field oxide, and the IMD in Figure 10.25(c). In the last step, the protection resist is removed and the processing is finished, as depicted in Figure 10.25(d).

The driving and read-out electrodes of the MEMS current are implemented with the first metal layer MET1, as suggested in Figures 10.25. Because of the monolithic integration, the current flows to the IC through MET1. In this way, the read-out circuit architecture has to be designed to match this current and make proper signal conditioning, as we discuss in the next sections.

10.4.2 Read-Out Circuit Specification and Circuit Architecture

The main function of read-out circuits is amplification of the MEMS resonator output current. We expect this current to be a resonant signal produced at a specific mode shape in the hundreds of megahertz range and to be very weak, with AC amplitudes in the order of nano-amperes. Regarding these matters, a set of requirements for the read-out amplifier is listed in Table 10.3.

By using an RLC-circuit-based electromechanical model of the resonator [25], one can estimate the dynamic range of the read-out amplifier. As the MEMS device is designed to resonate in a narrow frequency range, the input-current mode of the amplifier couples to the current flowing out of the MEMS. In general, the circuit and the MEMS present high impedance mismatching. Additionally, it is highly desirable that the circuit has output impedance near 50Ω, given that this value corresponds to the input-port impedance of the network analyzer used in the MEMS characterization. This will maximize the matching and minimize the losses. In order to characterize the amplifier, linearity is important. However, due to the expected high Q shape of the MEMS current, distortion would be negligible in a very narrow bandwidth, making the linearity issue irrelevant. Other aspects concerning maxi-

Table 10.3 Read-Out Amplifier Specifications

Issue	*Requirement*
Dynamic range	Wide, running from hundreds of nA to units of μA
Bandwidth	Cutoff frequency in the order of 400 MHz
Power	Not restricted
Size	Not restricted
IC technology	AMS 0.35 μm CMOS
Linearity	Yes
Input mode	Current mode
Feedback configuration	Open/closed loop
MEMS integration	Impedance matching not required
Output matching	Near 50Ω

mum size or power consumption can be neglected initially, only a selection of CMOS as the target technology is required.

Different circuit architectures are applicable to perform characterization of MEMS resonators, such as transimpedance amplifier (TIA), current comparator, current amplifier, and low-noise amplifier. In our case, let's choose the TIA architecture as the target configuration to perform read-out of the MEMS resonator. Figure 10.26 depicts a TIA amplifying the MEMS current, followed by further amplification and buffering stages. The TIA architecture takes the input current signal and amplifies it through an impedance to generate an output voltage signal. Because of this, the TIA is also referred to as current-to-voltage converter.

Typically, the gain of the current-to-voltage converter V_{out}/I_{in} is not high enough to meet the circuit specifications, and depending on the IC technology it assures a higher bandwidth than a voltage-mode amplifier of the same gain. In this sense, additional amplifying stages are usually cascaded to the TIA to achieve a desired V_{fin}/I_{out} gain specification. Finally, buffering is required to match the output circuit and input instrumentation impedances. If the instrument is a network analyzer with 50Ω input impedance, the output buffer impedance has to be close to this value. The buffer gain V_{RF}/V_{fin} approximates to unity, although high input-output mismatching leads to lower gains. Additionally, external matching networks could also be integrated to the setup in order to refine the impedance matching. Thus, the total AC transimpedance gain V_{RF}/I_{in} equals the cascaded gain of each stage:

$$\frac{V_{RF}}{I_{in}} = \frac{V_{out}}{I_{in}} \cdot \frac{V_{fin}}{V_{out}} \cdot \frac{V_{RF}}{V_{fin}} \tag{10.11}$$

10.4.3 Read-Out Implementation and Characterization

The implementation requirements for a typical TIA are a high bandwidth, high transimpedance gain, adequate power consumption, low noise, low input impedance, and small area. Improved Wilson current mirrors perform the current-to-voltage conversion. The mirrors connect to resistive transistor loads to attain transimpedance gain of 60 dBΩ. Its output node then connects to the DC coupling and biasing stage, which is required for achieving two main objectives. First, one isolates the voltage amplifier from the biasing deviations of the TIA. This is

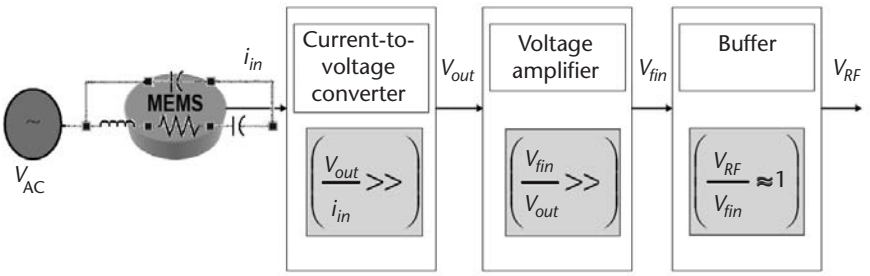

Figure 10.26 Transimpedance amplifier: current-to-voltage converter followed by voltage amplifier and buffer.

done by DC blocking at the output node of this stage. The second objective is to provide DC biasing to the subsequent voltage amplifier. Further voltage amplification was conceived to assure sufficient voltage gain to the circuit. This block is implemented as a three-stage, nondifferential, resistive load amplifier configuration adding a 20-dB voltage gain.

The output buffer is implemented with transistors connected in a feedback loop to reduce the output impedance to the range of 50Ω. When in comparison to traditional source follower topology, this configuration is capable of achieving design values with smaller transistor sizes. Nevertheless, a reduction on the global gain happens due to the high mismatching between the input and output impedances of the buffer, which leads to a buffer voltage gain lower than unity. In the end, the overall transimpedance gain of the read-out circuit is 70 dBΩ. For a detailed discussion of circuit design implementation and characterization, see [26].

Traditionally, TIAs with high bandwidth are built with GaAS, InP, or SiGe technologies. As CMOS processes were downscaled to submicron gate lengths, new TIA designs appeared to offer higher bandwidths. On the other hand, the maximum power supply is also reduced to prevent the field oxide breakdown, although the threshold voltage still needs reduction [27–30]. Since the megahertz-bandwidth requirements of the read-out circuit are within the current CMOS capabilities, we choose this technology for implementing the circuit. Figure 10.27 shows the footprint of the CMOS MEMS-IC chip with the composing blocks of the system being signaled in the picture. AC characterization of the IC is performed by a 50Ω network analyzer and DC power supplies.

10.5 Summary

In this chapter, we have studied three implementation cases of FBAR and MEMS resonators. In the first one, we reviewed the detailed fabrication processes of bulk-micromachined FBARs. The second case addressed the design of a temperature-compensated FBAR-based oscillator. The third one dealt with the design of a MEMS-resonator read-out circuit.

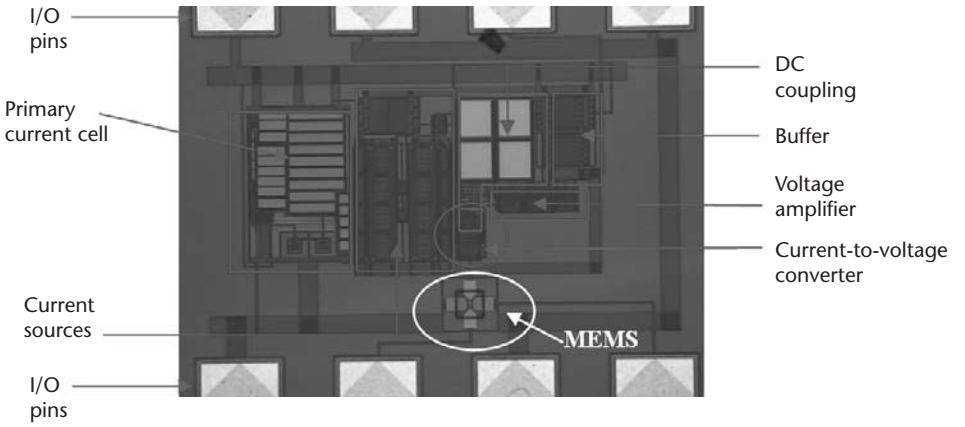

Figure 10.27 Die photograph of the integrated MEMS-to-read-out circuit. (© 2005 SPIE [29].)

From these examples, we have learned that MEMS-based system design is a multidisciplinary area that requires understanding of different fields, from processing and fabrication technologies to integrated circuit implementation. Codesign methodologies are useful to integrate the efforts of the engineering team in the purpose of building a complete MEMS-CMOS system.

References

[1] Akiyama, M., et al., "Influence of Metal Electrodes on Crystal Orientation of Aluminum Nitride Thin Films," *Vacuum*, Vol. 74, 2004, pp. 699–703.

[2] Lee, J.-B., et al., "Effects of Bottom Electrodes on the Orientation of AlN Films and the Frequency Responses of Resonators in AlN-Based FBARs," *Thin Solid Films*, Vol. 447–448, 2004, pp. 610–614.

[3] Gribaldo, S., et al., "Experimental Study of Phase Noise in FBAR Resonators," *IEEE Trans. on Ultrasonics, Ferroelectrics, Freq. Control*, Vol. 53, 2006, pp. 1982–1986.

[4] Vanhelmont, F., et al., "A 2 GHz Reference Oscillator Incorporating a Temperature Compensated BAW Resonator," *Proc. IEEE Intl. Ultrason. Symp. 2006*, Vancouver, BC, October 3–6, 2006, pp. 333–336.

[5] Pang, W., et al., "A Temperature-Stable Film Bulk Acoustic Wave Oscillator," *IEEE Electron Dev. Lett.*, Vol. 29, 2008, pp. 315–318.

[6] Razhavi, B., *Design of Analog CMOS Integrated Circuits*, New York: McGraw-Hill, 2001.

[7] Tanzawa, T., et al., "A 2.4-GHz Temperature-Compensated CMOS LC-VCO for Low Frequency Drift Low-Power Direct-Modulation GFSK Transmitters," *IEICE Trans. Electron.*, Vol. E88-C, 2005, pp. 490–495.

[8] Stadius, K., et al., "A Monolithic Temperature Compensated 1.6 GHz VCO," *Proc. GAAS Conference 1998, GAAS98*, Amsterdam, the Netherlands, October 5–6, 1998, pp. 626–630.

[9] Ho, G. K., et al., "Temperature Compensated IBAR Reference Oscillators," *Proc. IEEE Intl. Conf. MEMS 2006*, Istanbul, Turkey, January 22–26, 2006, pp. 737–741.

[10] Sundaresan, K., et al., "Electronically Temperature Compensated Silicon Bulk Acoustic Resonator Reference Oscillators," *IEEE J. Solid-State Circuits*, Vol. 42, 2007, pp. 1425–1434.

[11] Schodowski, S., *A New Approach to a High Stability Temperature Compensation Crystal Oscillator*, Schaumburg, IL: Motorola Communications Systems Division, 1970.

[12] Kinsman, R. G., *Temperature Compensation of Crystals with Parabolic Temperature Coefficients*, Schaumburg, IL: Motorola Communications Systems Division, 1978.

[13] Jha, C. M., et al., "In-Chip Device-Layer Thermal Isolation of MEMS Resonator for Lower Power Budget," *Proc. ASME International Mechanical Engineering Congress and Exposition IMECE2006*, Chicago, IL, November 5–10, 2006, pp. 1–7.

[14] Taslakov, M. A., "1 GHz STW Based Oscillator with Continuous Temperature Compensation," *IEEE Trans. on Ultrason. Ferroelec. Freq. Control*, Vol. 45, 1998, pp. 192–195.

[15] Zhou, W., et al., "Comparison Among Precision Temperature Compensated Crystal Oscillators," *Proc. IEEE Intl. Frequency Control Symposium 2005*, Vancouver, BC, August 29–21, 2005, pp. 575–579.

[16] Zhang, H., et al., "5GHz Low Phase-Noise Oscillator Based FBAR with Low TCF," *Proc. 13th International Conference on Solid-State Sensors, Actuators and Microsystems Transducers 2005*, Seoul, Korea, June 5–9, 2005, pp. 1100–1101.

[17] Aissi, M., et al., "A 5 GHz Above-IC FBAR Low Phase Noise Balanced Oscillator," *Proc. IEEE Radio Frequency Integrated Circuits Symposium RFIC-2006*, Vol. 1, San Francisco, CA, June 11–13, 2006, pp. 25–28.

[18] Chee, Y. H., A. M. Niknejad, and J. M. Rabaey, "An Ultra-Low-Power Injection Locked Transmitter for Wireless Sensor Networks," *IEEE J. Solid State Circuits*, Vol. 41, 2006, pp. 1740–1748.

[19] Churchman, C. W., *The Systems Approach,* New York: Delacorte Press, 1968.

[20] IEEE Std. 1364-2001, *IEEE Standard Verilog Hardware Description Language*, New York: Institute of Electrical and Electronics Engineers, 2001.

[21] IEEE Std. 1666-2005, *IEEE Standard SystemC Language Reference Manual*, New York: Institute of Electrical and Electronics Engineers, 2005.

[22] Bakalar, C. E., "VHDL-AMS: A Hardware Description Language for Analog and Mixed-Signal Applications," *Proc. IEEE Trans. on Circuits Systems II: Analog Digital Signal*, Vol. 46, 1999, pp. 1263–1272.

[23] IEEE Std. 1076.1-1999, *VHSIC Hardware Description Language Analog And Mixed-Signal*, New York: Institute of Electrical and Electronics Engineers, 1999.

[24] Austria Microsystems 2-poly 4-metal 0.35 μm CMOS technology, http://www.austriamicrosystems.com.

[25] Nguyen, C. T.-C., and R. T. Howe, "An Integrated CMOS Micromechanical Resonator High-Q Oscillator," *IEEE J. Solid-State Circuits*, Vol. 34, 1999, pp. 440–455.

[26] Mohan, S. S., et al., "Bandwidth Extension in CMOS with Optimised On-Chip Inductors," *IEEE J. of Solid-State Circuits*, Vol. 35, 2000, pp. 346–355.

[27] Kossel, M., et al., "Wideband CMOS Transimpedance Amplifier," *Electronics Letters*, Vol. 39, 2003, pp. 587–588.

[28] Kromer, C., et al., "A Low Power 20 GHz 52 dBOhm Transimpedance Amplifier in 80 nm CMOS," *IEEE J. Solid-State Circuits*, Vol. 39, 2004, pp. 885–894.

[29] Campanella, H., et al., "Band-Pass Transimpedance Read Out Circuit for UHF MEMS Resonator Applications," *Proc. SPIE Symposium on Microtechnologies for the New Millennium 2005*, Vol. 5837, Sevilla, Spain, May 9–11, 2005, pp. 300–309.

[30] Fay, P., C. Caneau, and I. Adesia, "High-Speed MSM/HEMT and p-I-n/HEMPT Monolithic Photo Receivers," *IEEE Trans. on Microwave Theory Tech.*, Vol. 50, 2002, pp. 62–67.

About the Author

Humberto Campanella is a research fellow at the Consejo Superior de Investigaciones Científicas (CSIC) assigned to the Instituto de Microelectrónica de Barcelona IMB-CNM, Spain, and associate professor in the Department of Telecommunications and System Engineering at the Universitat Autònoma de Barcelona. He holds a B.Sc. in electronics engineering from the Pontificia Universidad Javeriana, Bogotá, Colombia; an M.Sc. in telecommunication systems from the Universidad Politécnica de Madrid, Spain; a Ph.D. in microelectronics and automated systems from the Université de Montpellier, France; and another Ph.D. in electronics engineering from the Universitat Autonoma de Barcelona, Spain. Dr. Campanella has more than 15 years of industry and academic experience in research, development, and engineering of integrated circuits, microelectromechanical systems, telecommunications, and signal processing. He has published several scientific papers and holds one patent on the heterogeneous integration of FBAR and MEMS resonators with CMOS technologies. He has served as a reviewer of indexed scientific journals and as a referee for public-funded projects in the United States, Europe, and South America.

Index

Recent Titles in the Artech House Integrated Microsystems Series

Acoustic Wave and Electromechanical Resonators: Concept to Key Applications, Humberto Campanella

Adaptive Cooling of Integrated Circuits Using Digital Microfluidics, Philip Y. Paik, Krishnendu Chakrabarty, and Vamsee K. Pamula

Fundamentals and Applications of Microfluidics, Second Edition, Nam-Trung Nguyen and Steven T. Wereley

Integrated Interconnect Technologies for 3D Nanoelectronic Systems, Muhannad S. Bakir and James D. Meindl, editors

Introduction to Microelectromechanical (MEM) Microwave Systems, Héctor J. De Los Santos

An Introduction to Microelectromechanical Systems Engineering, Nadim Maluf

MEMS Mechanical Sensors, Stephen Beeby et al.

Micro and Nano Manipulations for Biomedical Applications, Tachung C. YihIlie Talpasanu

Microfluidics for Biotechnology, Second Edition, Jean Berthier and Pascal Silberzan

Organic and Inorganic Nanostructures, Alexei Nabok

Post-Processing Techniques for Integrated MEMS, Sherif Sedky

Pressure-Driven Microfluidics, Václav Tesař

RFID-Enabled Sensor Design and Applicatons, Amin Rida, Li Yang, and Manos Tentzeris

RF MEMS Circuit Design for Wireless Communications, Héctor J. De Los Santos

Wafer-Level Testing and Test During Burn-in for Integrated Circuits, Sudarshan Bahukudumbi Krishnendu Chakrabarty

Wireless Sensor Network, Nirupama Bulusu and Sanjay Jha

For further information on these and other Artech House titles, including previously considered out-of-print books now available through our In-Print-Forever® (IPF®) program, contact:

Artech House
685 Canton Street
Norwood, MA 02062
Phone: 781-769-9750
Fax: 781-769-6334
e-mail: artech@artechhouse.com

Artech House
16 Sussex Street
London SW1V 4RW UK
Phone: +44 (0)20 7596-8750
Fax: +44 (0)20 7630-0166
e-mail: artech-uk@artechhouse.com

Find us on the World Wide Web at: www.artechhouse.com